UNIVERSITÉ DE STRASBOURG

ÉCOLE DOCTORALE DES SCIENCES CHIMIQUES

Laboratoire d'Electrochimie et de Chimie Physique du Corps Solide

THÈSE

présentée par :

HUO Zhaohui

soutenue le : 22, Septembre 2015

pour obtenir le grade de : **Docteur de l'université de Strasbourg**

Discipline/ Spécialité: Chimie

Polyoxométallate – porphyrine: application pour la génération de photocourant et la photocatalyse.

THÈSE dirigée par :

[Pr. Laurent Ruhlmann] Professeur, Université de Strasbourg

RAPPORTEURS :

[DR. Fethi BEDIOUI] Directeur de recherche, Université Paris Descartes

[Pr. Emmanuel CADOT] Professeur, Université Versailles-Saint-Quentin

---

AUTRES MEMBRES DU JURY :

[DR. Emmanuel LACÔTE] Directeur de recherche, Université de Lyon

[Pr. Elena SAVINOVA] Professeur, Université de Strasbourg

Acknowledgements

I want to first acknowledge the jury members for agreeing to evaluate this thesis:

- Prof. Laurent RUHLMANN, Université de Strasbourg
- DR. Fethi BEDIOUI, Université Paris Descartes
- Prof. Emmanuel CADOT, Université Versailles-Saint-Quentin
- DR. Emmanuel LACÔTE, Université de Lyon
- Prof. Elena SAVINOVA, Université de Strasbourg

The present study was established in Laboratoire d'Electrochimie et de Chimie Physique du Corps Solide at the Institut de Chimie, Université de Strasbourg under the direction of Prof. Laurent Ruhlmann. I gratefully acknowledge Prof. Laurent Ruhlmann for having given me the opportunity to perform a PhD thesis in his working group. It is difficult to overstate my gratitude to my supervisor Prof. Laurent Ruhlmann with his enthusiasm, inspiration, great knowledge, and plentiful experience. In this context I also like to emphasise the advantageous working conditions at the Université de Strasbourg: the technical equipment and the advanced training possibilities in various domains were outstanding. I would like to thank all the members of the in Laboratoire d'Electrochimie et de Chimie Physique du Corps Solide and the chemistry department who have contributed to my work. These are in particular:

- DR. Jean-Paul Gisselbrecht for sharing with me his tremendous knowledge on programming, electrochemistry and helped me analyze my experimental results.
- Prof. Corinne Boudon for her scientific contribution to my three-year work in the framework of my thesis and her valuable comments in every group discussion.
- Dr. BONNEFONT Pierre-Antoine for his assistance in X-ray spectroscopy and impedance spectroscopy.

I would like to express my gratitude to the partners of the scientific collaboration that have enriched the outcome of my thesis. In this context I would like to address:

- Prof. Christophe Bucher (Ecole Normale Supérieure de Lyon—Université Lyon 1) who helped us to synthesize the 1,1''-(1,3-propanediyl)bis-4,4'-bipyridinium and his assistance in analysing the spectroelectrochemical data.

• Prof. Anna Proust (Universit éPierre et Marie Curie-Paris6) who collaborated with us to establish the design and functionalization of polyoxometalates: towards advanced applications in catalysis and materials science

• Dr. Rana Farha (Universit éPierre et Marie Curie-Paris6) for AFM measurement.

• Prof. Petra HELLWIG and MELIN Frederic (Universit éde Strasbourg) for the raman measurement.

• Prof. XU Hualong (Fudan University) for the TEM and XPS measurements and the assistance in analysing the experimental data.

• Dr. Thierry Dintzer (Universit éde Strasbourg) for the SEM measurement.

I am also indebted to my many colleagues for providing a friendly and fine academic environment. I am especially grateful to Dr. Iban Azcarate, Dr. Iftikhar Ahmed, Mr. Zang Dejin and Miss Yang Shu for their great help.

I would like to thank my husband, Zhang Gang, whose love, optimistic and support were essential to my success. I would also like to thank all my family.

I wish grateful again to the admirable couple, Prof. Laurent RUHLMANN and Madame Tao YANG-RUHLMANN for their warm-hearted care on my foreign life.

Last, I would like to express my great gratitude to the foundation of Oversea Study Program of Guangzhou Elite Project (GEP).

List of publications

[1] **Z.H. Huo**, J.P. Gisselbrecht, R. Farha, M. Goldmann, E.S. Aman, C. Bucher, L. Ruhlmann, Alternating electro-copolymerization of zinc-β-octaethylporphyrin with a flexible bipyridinium. Electrochim Acta, 122 (2014) 108.

[2] **Z.H. Huo**, D.J. Zang, S. Yang, R. Farha, M. Goldmann, B. Hasenknopf, H.L. Xu, L. Ruhlmann, Synthesis and characterization of Lindqvist-type polyoxometalate–porphyrin copolymers. Electrochim Acta, in press, DOI: 10.1016/j.electacta.2015.03.178.

[3] **Z.H. Huo**, I. Azcarate, R. Farha, M. Goldmann, H.L. Xu, B. Hasenknopf, E. Lacôte, L. Ruhlmann, Copolymeric films obtained by electropolymerization of porphyrins and dipyridyl-spacers including Dawson-type polyoxometalates J Solid State Electrochem, in press, DOI : 10.1007/s10008-015-2828-5.

[4] I. Azcarate, **Z.H. Huo**, R. Farha, M. Goldmann, H. L. Xu, B. Hasenknopf, E. Lacôte, L. Ruhlmann, Generation of photocurrent from visible light irradiation of conjugated Dawson polyoxophosphovanadotungstate-porphyrin copolymers. Chem-Eur. J., 21 (2015) 8271.

[5] I. Ahmed, R. Farha, **Z.H. Huo**, C. Allain, X.X. Wang, H.L. Xu, M. Goldmann, B. Hasenknopf, L. Ruhlmann, Porphyrin–polyoxometalate hybrids connected via a tris-alkoxo linker for the generation of photocurrent. Electrochimica Acta 110 (2013) 726.

Résumé en français

Introduction

Les recherches liées à l'emploie de l'énergie solaire comme source d'énergie propre sont de plus en plus étudiées ses dernières années. Le principe de la photoconversion de la lumière en énergie électrique des cellules photovoltaïques mais aussi des dispositifs photosynthétiques artificiels reposent sur la formation d'une séparation de charge électronique photoinduite avec une durée de vie appropriée et une faible recombinaison des charges.[1]

Les polyoxométallates (POMs) constituent une classe unique de clusters inorganiques anioniques du type métal-oxygène à l'échelle moléculaire, dans lesquels les élements métalliques, coordinés dans un environement octahédrique d'atomes d'oxygène, se trouvent dans un état d'oxydation élevé (souvent de configuration d^0). Ils sont de bons accepteurs d'électrons. Ils ont par exemple de bons atouts pour des applications en photocatalyse ou en photoélectrocatalyse comme en témoignent les travaux récents présents dans la littérature. Du fait de leurs bonnes stabilités et de leurs robustesses les POMs peut subir des transferts multi-électroniques sans décomposition.

Cependant, les POMs peuvent être excités (POMs*) principalement sous irradiation UV. Une solution pour remédier à ce problème consiste à associer au POM un photosensibilisateur qui absorberait dans le domaine du visible tel que la porphyrine, qui peut jouer un rôle clé dans la collecte de l'énergie lumineuse. La porphyrine excitée est un bon donneur d'électron et peut ainsi transfèrer l'électron au POM, connu pour être un excellent accepteur d'électron.

Les POMs étant des groupes anioniques, des hybrides électrostatiques peuvent être fabriqués en présence de chromophores cationiques tels que des colorants organiques,[2,3,4] des complexes polypyridyles du Ru ou du Re,[5,6,7] ou des porphyrines et phthalocyanines.[8,9] Ruhlmann et al[10] ont proposé un assemblage hybride multicouche $[H_2TPhN(Me)_3P^{4+}/\alpha_2\text{-}Fe(P_2W_{17}O_{61})^{7-}]_n$ construit via une stratégie « couche par couche » pour la génération de photocourant sous illumination dans le domaine du visible (Fig. 1).

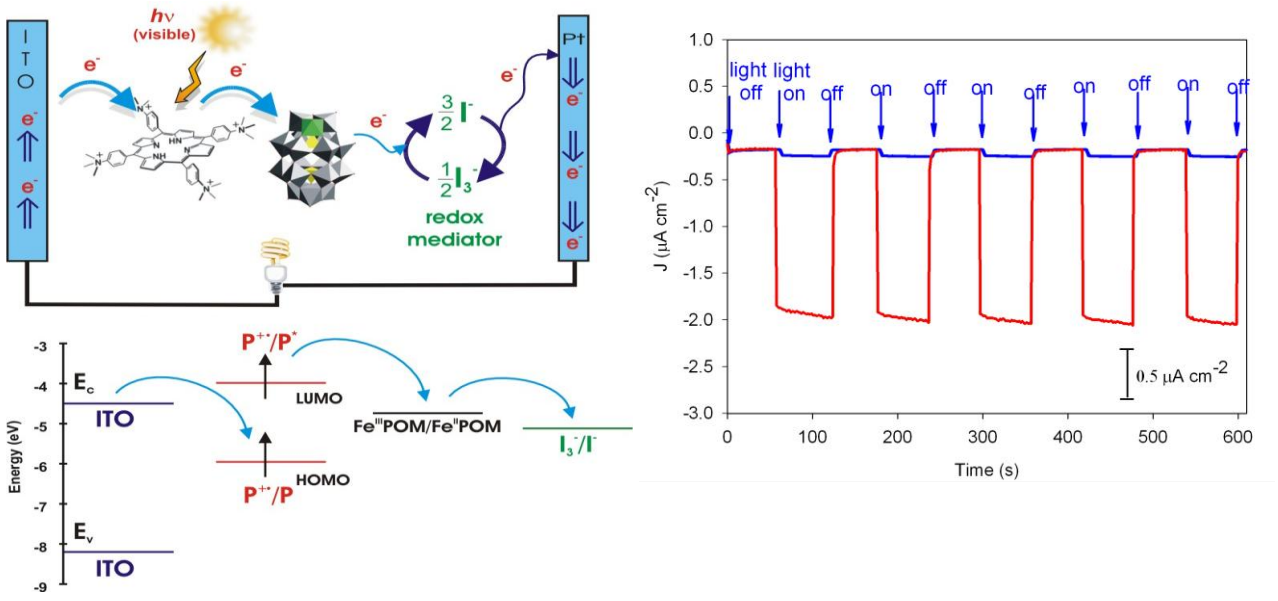

Fig. 1. Gauche: représentation schématique de la structure d'une couche du film $[\alpha_2\text{-}Fe^{III}P_2W_{17}O_{61}^{7-}$ / $H_2TN(Me)_3PhP^{4+}]_n$ (n = nombre de cycle de trempage) sur électrode ITO de la cellule photoélectrochimique et diagramme schématique montrant les transferts d'électrons. Droite : réponse photoélectrochimique pour la monocouche $[H_2TPhN(Me)_3P^{4+}]$ (courbe bleue) et du film $[\alpha_2\text{-}Fe^{III}P_2W_{17}O_{61}^{7-}$ / $H_2TPhN(Me)_3P^{4+}]_{25}$ (courbe rouge) avec et sans illumination (lampe à Arc Xe 300 W, $\lambda > 385$ nm, filtre passe haut). Milieu : acetonitrile contenant I_3^- (0.1 mol L^{-1}) et I^- (0.5 mol L^{-1}). E = -0.1 V / ECS.

Des complexes de coordination POM-porphyrine(s) ont été aussi rapportés, basés sur la coordination de groupements pyridyles greffés sur un POM du type Anderson ou Linqvist sur le métal central d'une porphyrine[11,12] ou inversement la coordination d'un substituant pyridyle périphérique de la porphyrine sur le métal (Ni, Co et Fe) substitué en position α_2 d'un POM du type Keggin (Fig. 2).[13]

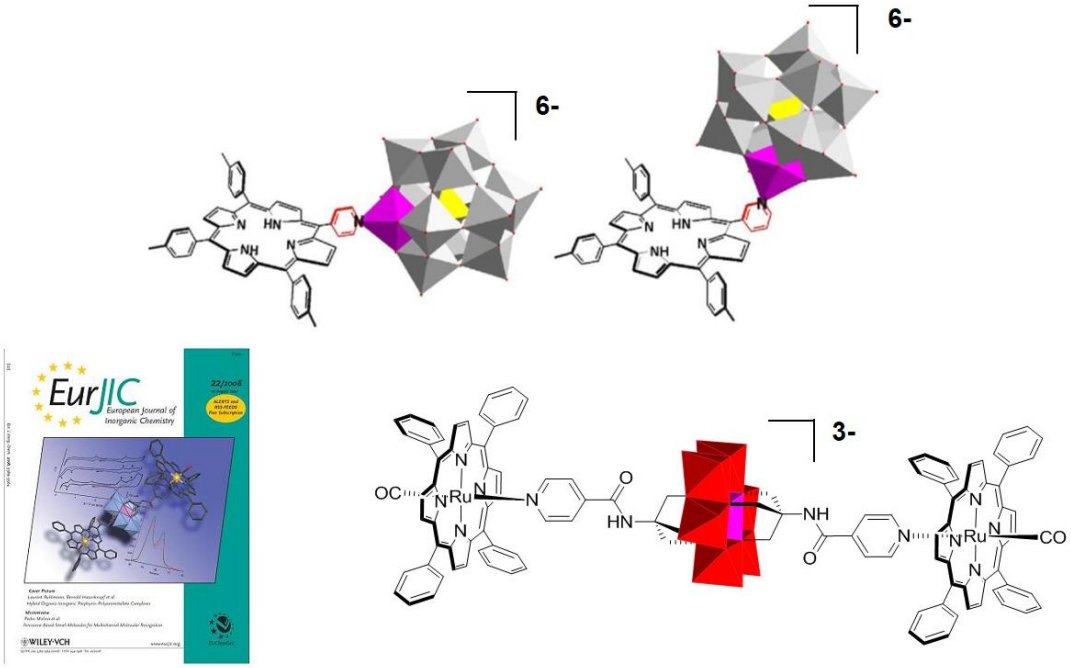

Fig. 2. Complexes de coordination porphyrine(s)– polyoxométallate.

La troisième approche est basée sur un lien covalent entre le POM (du type Dawson ou Anderson) et le photosensibiliseur porphyrine (Fig. 3).[14]

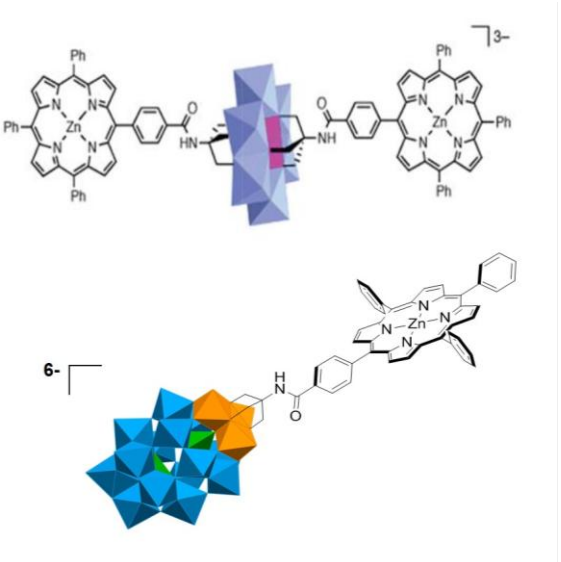

Fig. 3. Complexes covalents porphyrine(s)– polyoxométallate.

Un transfert Langmuir-Shaeffer inverse a également été réalisé sur électrode ITO du complexe covalent du type Dawson montrant une efficacité pour la génération de photocourant sous illumination dans le domaine visible (Fig. 4) en milieu aqueux en présence de I_3^- 0,1 mol L^{-1} et de I^- 0,5 mol L^{-1}.

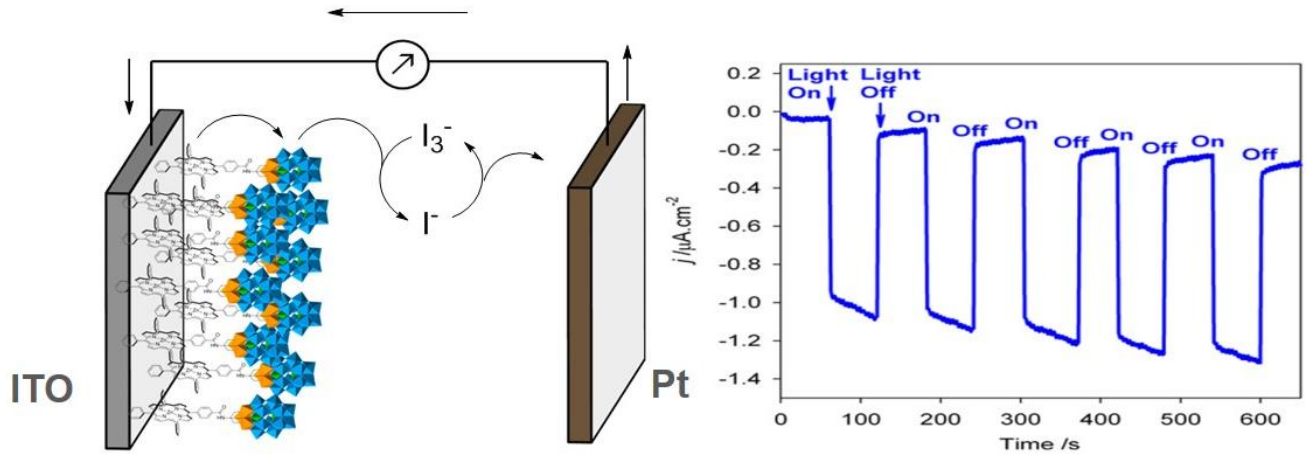

Fig. 4. Electrode ITO modifiée suite à un transfert Langmuir-Shaeffer inversé et réponse photoélectrochimique sous illumination visible.

Deux types d'ancrage sont reportés dans la littérature avec des fonctionalisations polyalkoxo[15,16] ou imido[17]. Les complexes hybrides peuvent aussi être préparés à l'aide des fragments organiques greffés de manière covalente sur un hétéroatome inseré à partir d'un POM monolacunaire.[18,19,20] Par exemple, Anna Proust et al ont rapporté la synthèse et l'étude des propriétés photophysiques d'une série de complexes Ir(III)-POM conjugués.[21] Parmi eux, l'hybride organosilyl du type Dawson $[P_2W_{17}O_{61}\text{-}\{O(SiC_{36}H_{23}N_3O_2Ir)_2\}]^{6-}$ offre le meilleur compromis entre l'efficacité de la séparation de charge et son grand temps de vie. Ce système a également permi la production de dihydrogène de manière photocatalytique sous la illumination dans le domaine visible sans perte significative de performance après de plus d'une semaine de photolyse en continue.[22]

D'après la littérature, un seul exemple de polymère à base de polyoxométallate a été reporté par Peng et al où l'étude des propriétés photovoltaïques a également été mesurée.[23] Les groupes hexamolybdate sont incorporés de manière covalente sur une chaîne principale du type poly(phénylène-acétylène). Ce copolymère, utilisé comme un composant d'un dispositif photovoltaïque monocouche (ITO/polymer/Ca), a montré cependant une efficacité limité avec un rendement de conversion de 0.15 %.[23]

Enfin, récemment, Ruhlmann et al ont rapporté la formation de copolymères covalents à base de POMs du type Anderson et de porphyrines (Fig. 5) en utilisant une méthode d'électropolymerisation basée sur l'attaque de nucleophilic de groupes pyridyles (groupement greffé sur le POM : $[MnMo_6O_{18}\{(OCH_2)_3CNHCO(4\text{-}C_5H_4N)\}_2]^{3-}$) sur un dication porphyrine généré électrochimiquement

(bioxydée). Les films obtenus ont été utilisés comme photocatalyseurs hétérogènes pour la réduction d'ions Ag^+ ou $AuCl_4^-$ sous illumination dans le domaine du visible.[24] La protection de deux des quatre positions par deux groupements pyridinium ou chlorure de la porphyrine a aussi permi de contrôler la direction de l'électropolymérisation (Fig. 6) et d'éviter la formation d'un copolymère en « zig-zag » présenté sur la Figure 5.

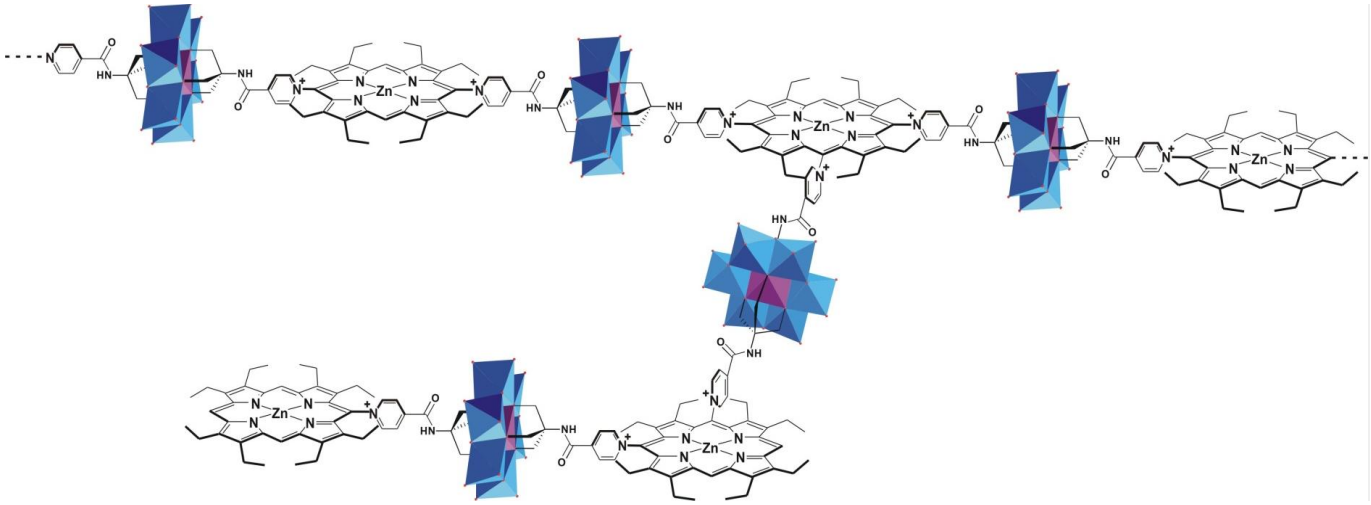

Fig. 5. Représentation du copolymère $\{[MnMo_6O_{18}\{(OCH_2)_3CNHCO(4\text{-}py^+)\}_2]^{3-}\text{-}ZnOEP\}_n$.

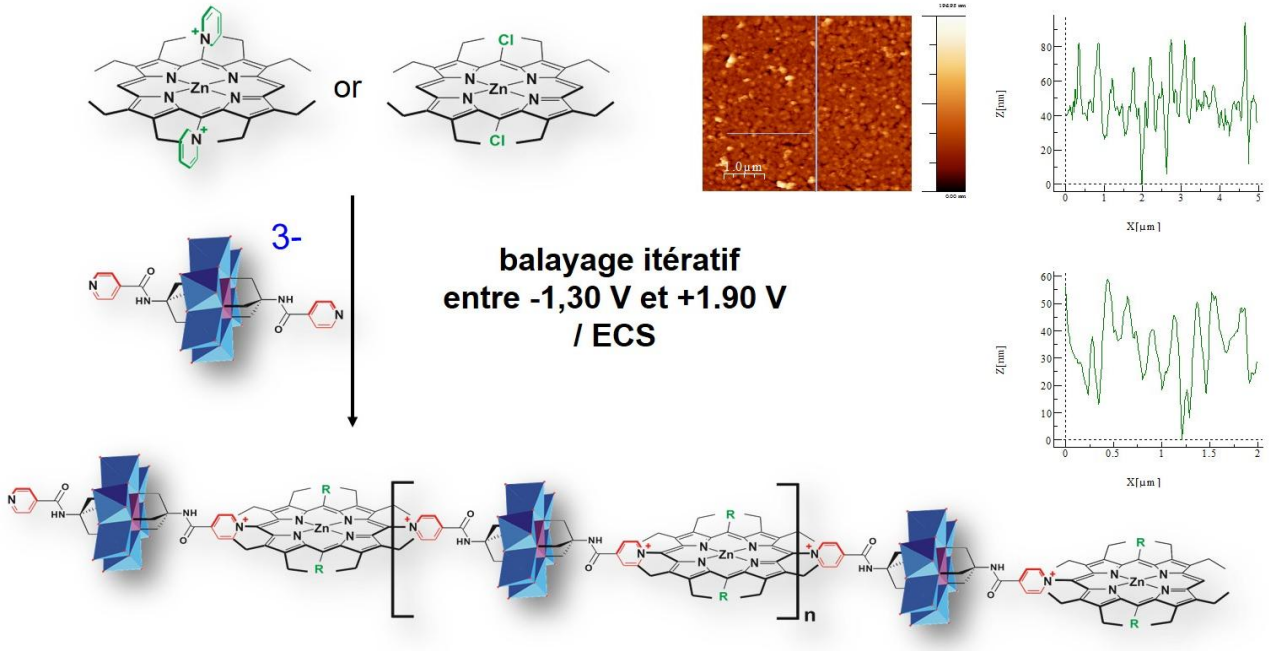

Fig. 6. Représentation du copolymère $\{[MnMo_6O_{18}\{(OCH_2)_3CNHCO(4\text{-}py^+)\}_2]^{3-}\text{—}ZnOEP(R)_2\}_n$ (R = Py^+ ou Cl).

Le mécanisme pour l'obtention du copolymère est du type $E(EC_NEC_B)_nE$ où E correspond à une étape électrochimique, C_N correspond à une étape chimique, celle de l'attaque nucléophile (py) sur la position *méso* de la porphyrine pour formation un intermédiaire réactionnel (isoporphyrine) et C_B est une étape chimique de réaromatisation et élimination du proton. La formation du copolymère nécessite la formation du dication porphyrine plus réactive vis-à-vis d'un nucléophile (Fig. 7).

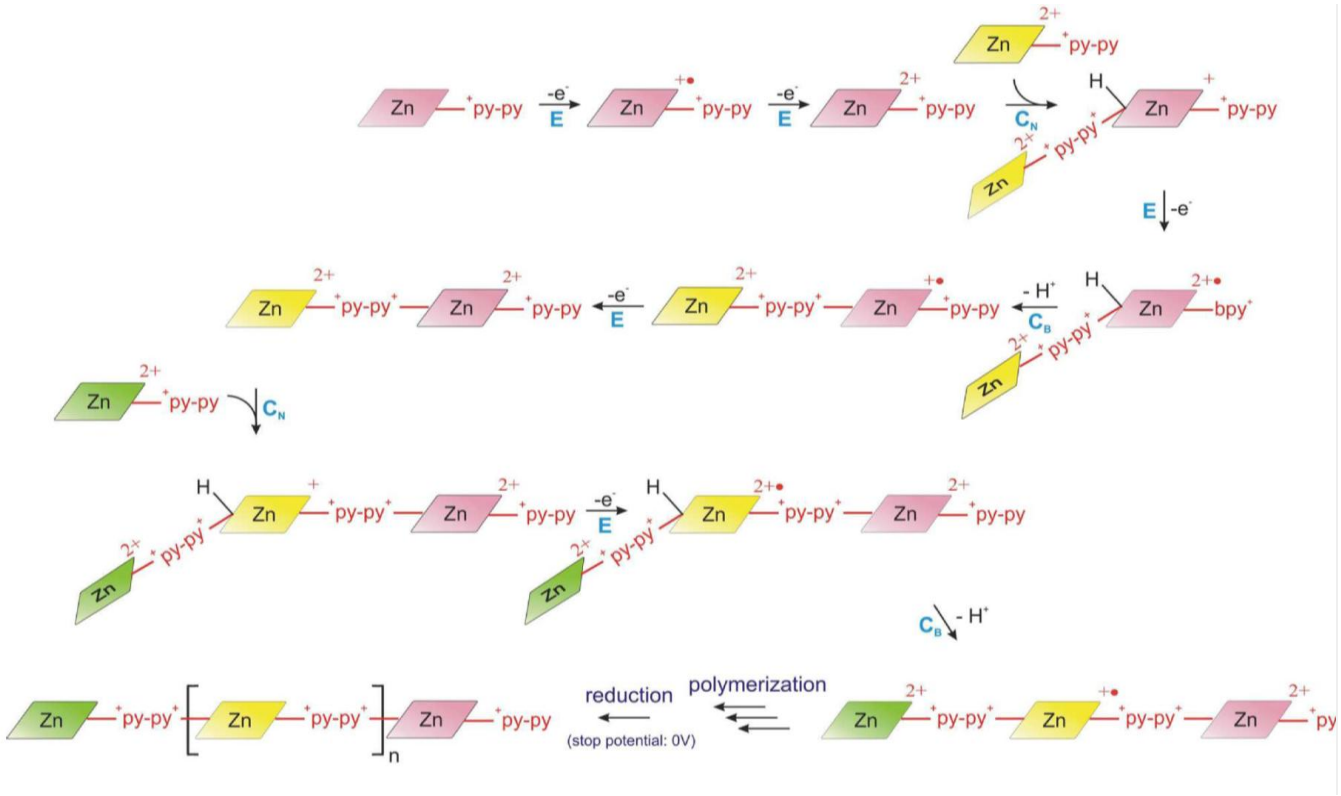

Fig. 7. Représentation du mécanisme $E(EC_NEC_B)_nE$ pour la formation du copolymère.

L'objectif de cette thèse est d'aller au-delà de cette preuve de principe et d'étudier de nouveaux systèmes POM-porphyrines et de montrer qu'il est possible d'utiliser les propriétés catalytiques des POMs tout en utilisant la lumière visible, en leur associant des phototosensibilisateurs absorbant dans le domaine visible. Plusieurs assemblages hybrides porphyrines-POMs ont alors été étudiés successivement au cours de ce travail. Tout d'abord, nous avons développé de nouveaux copolymères POMs-porphyrines obtenus par voie électrochimique avec des POMs de géométrie variée. Outre les méthodes électrochimiques, la spectroscopie d'aborption UV-visible et la spectroscopie XPS, la spectroscopie d'impédance électrochimique, les microscopies AFM et MET, et les mesures de microbalance à quartz

sont autant de techniques qui ont permis d'apporter des éléments de réponses quant à l'organisation des films POM-porphyrines.

Dans un second temps, des systèmes POM-porphyrines ioniques ; et POM-porphyrinse dopés par des nanoparticules métalliques (Ag, Au ou Pt) ont été développés et étudiés.

La détermination des performances de ces films soit inclus dans une cellule photovoltaïque ou bien utilisés comme photocatalyseurs pour la réduction d'ions métalliques (Ag^{I} ou Pt^{IV}) a également été menée.

1 – Films copolymères Polyoxométallates – porphyrines covalents

Les copolymères hybrides POMs-porphyrines ont été directement obtenus par l'oxydation électrochimique de la zinc-*ß*-octaethyl porphyrin (**ZnOEP**, Fig. 8A) ou de la 5,15-ditolylporphyrine (**H_2T_2P**, Fig. 8B) en présence de type différent POMs portant deux groupes pyridyles pendants (**Py-POM-Py**, Fig. 9) via un mécanisme $E(EC_NEC_B)_nE$ (Fig. 7).

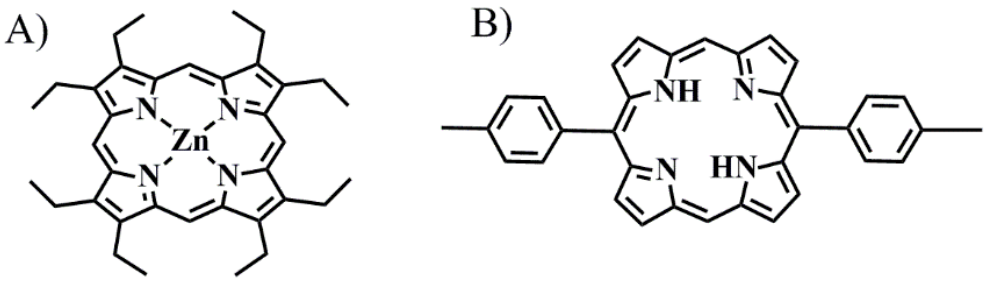

Fig. 8. Représentation de A) **ZnOEP**, B) **H_2T_2P**.

Le premier système étudié (cf. ***chapitre II***) a été obtenu par électropolymerization d'une base libre (**H_2T_2P**) ou de la métalloporphyrine **ZnOEP** en présence du dérivé Lindqvist polyoxovanadate (Figs. 9 et 10) où a été greffé deux groupes pyridyles attachés au POM via un groupement Tris-alkoxo : $[V_6O_{13}\{(OCH_2)_3CNHCO(4\text{-}C_5H_4N)\}_2]^{2-}$, (**Py-$V_6O_{13}$-Py**)).

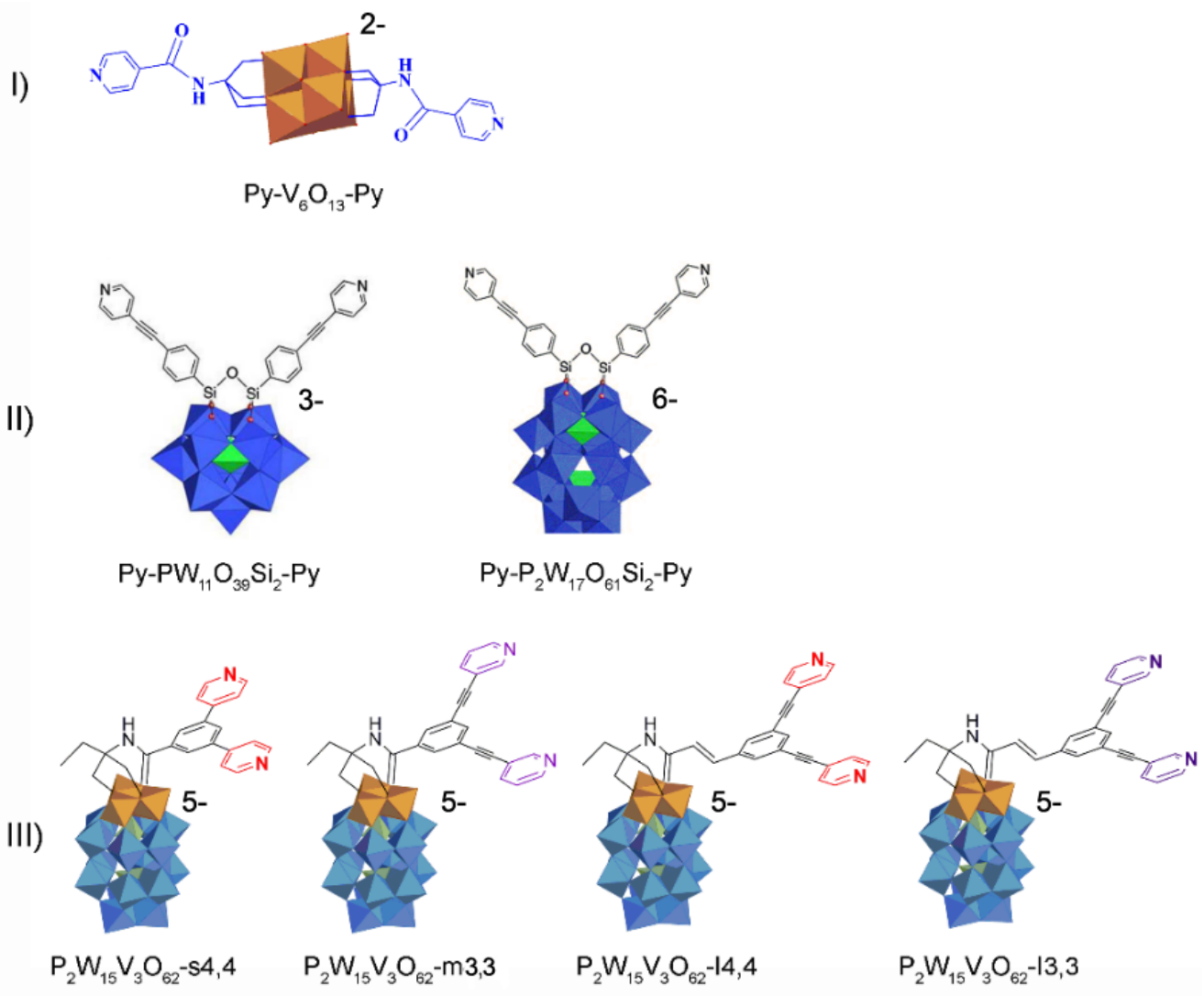

Fig. 9 Structures de trois séries de POM(py)$_2$, I) Lindqvist (**Py-V_6O_{13}-Py**), II) Keggin et Dawson (**Py-$PW_{11}Si_2$-Py** et **Py-$PW_{17}Si_2$-Py** respectivement), III) Dawson (fonctionnalisation bis-alkoxo-amide).

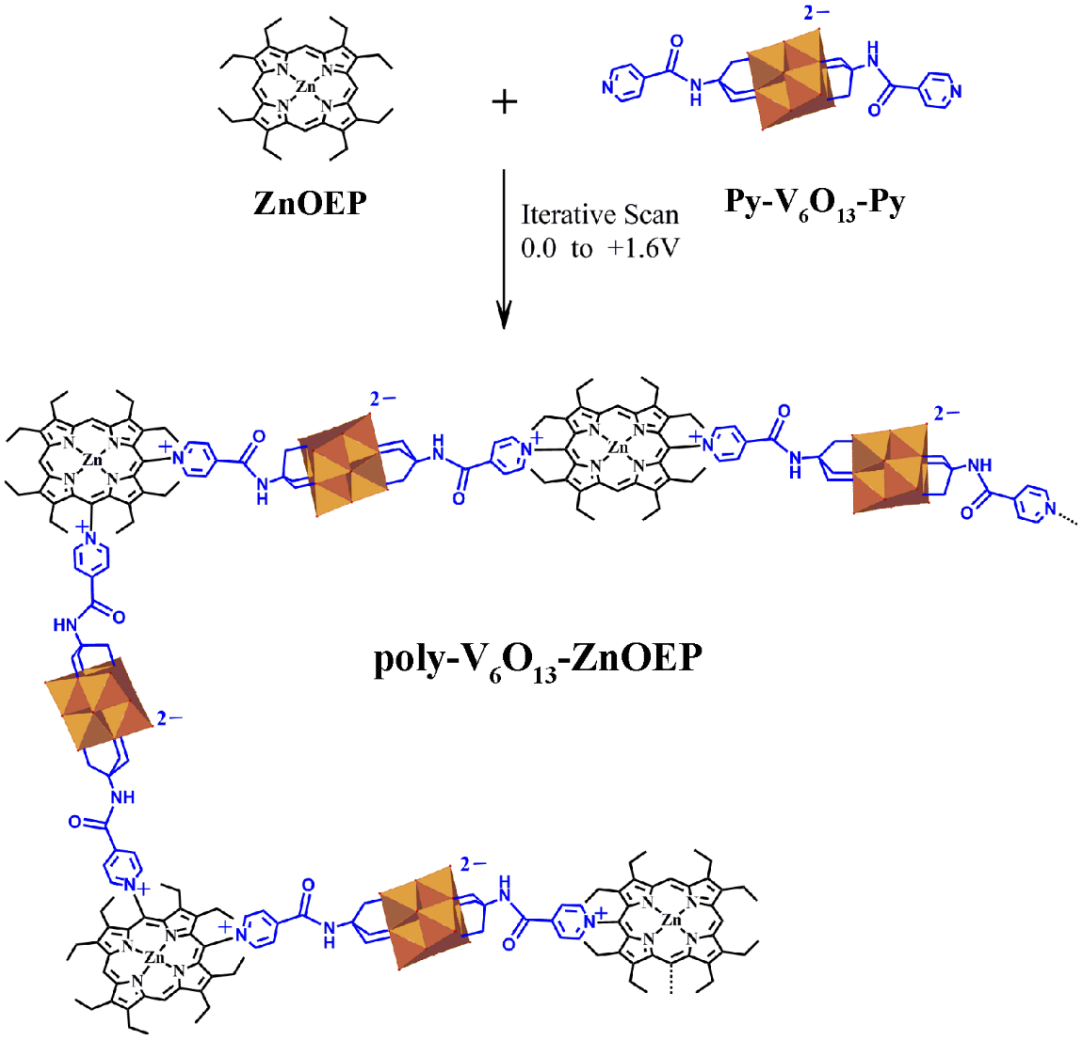

Fig. 10 Représentation du **poly-V_6O_{13}-ZnOEP**.

Un second système décrit dans le ***chapitre III*** a été préparé à partir de polyoxométallate du type Keggin ou Dawson : $[PW_{11}Si_2O_{40}C_{26}H_{16}N_2]$.3TBA (**Py-$PW_{11}Si_2$-Py**) et $[P_2W_{17}Si_2O_{62}C_{26}H_{16}N_2]$.6TBA (**Py-$P_2W_{17}Si_2$**) respectivement. Les copolymères ont été directement obtenus par électrooxydation des mêmes porphyrines **ZnOEP** ou de **H_2T_2P** en présence de **Py-$PW_{11}Si_2$-Py** ou **Py-$P_2W_{17}Si_2$-Py** (Fig. 11).

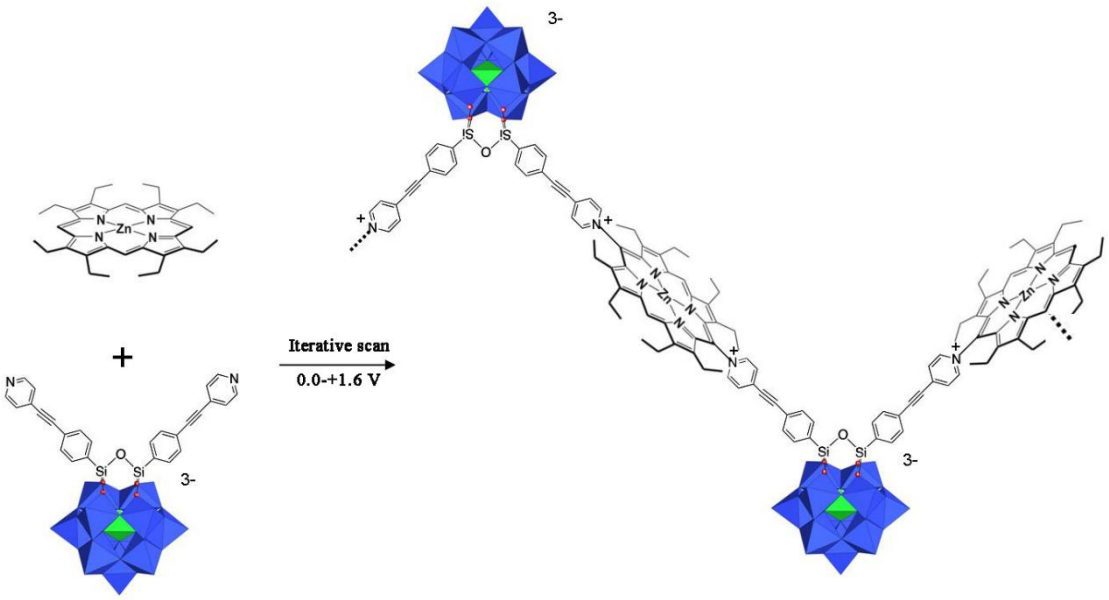

Fig. 11 Schéma de l'electropolymérisation de **ZnOEP** en présence de **Py-PW$_{11}$Si$_2$-Py**.

On peut noter dans le cas, par exemple de la formation du **poly-Py-PW$_{11}$Si$_2$-Py-ZnOEP**, que lors de l'électropolymérisation, l'évolution des voltammogrammes cycliques montre la croissance de deux vagues en réduction associées à la réduction du ligand **Py-PW$_{11}$Si$_2$-Py** (couples $W^{VI/V}$) démontrant un dépôt à l'électrode d'un film constitué en partie du POM.

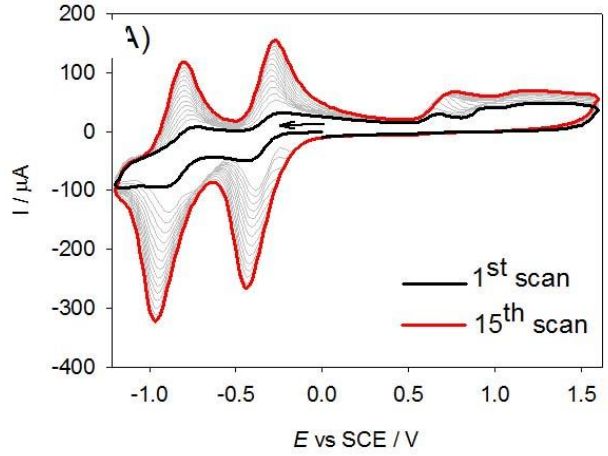

Fig. 12. Voltammogrammes cycliques enregistrés entre −1,20 V et +1,60 V / ECS durant l'électropolymérisation de 0,25 mmol/dm^3 **ZnOEP** en présence de 0,25 mmol/dm^3 de **Py-PW$_{11}$Si$_2$-Py**. Milieu : CH_3CN/1,2-$C_2H_4Cl_2$ (3/7) + 0.1 mol/dm^3 de NBu_4PF_6. Electrode de travail : ITO. S =1 cm^2; vitesse de balayage : 0.1 V/s.

Un troisième système hybride POM-porphyrine a été synthétisé et étudié (***chapitre IV***). Une série de quatre films a été obtenue à partir de POMs de structure du type Dawson $[P_2W_{15}V_3O_{62}]^{9-}$ où a été

greffé, via une fonctionnalisation bis-alkoxo-amide, des groupements dipyridyle variés dont un exemple est décrit sur la Figure 13.

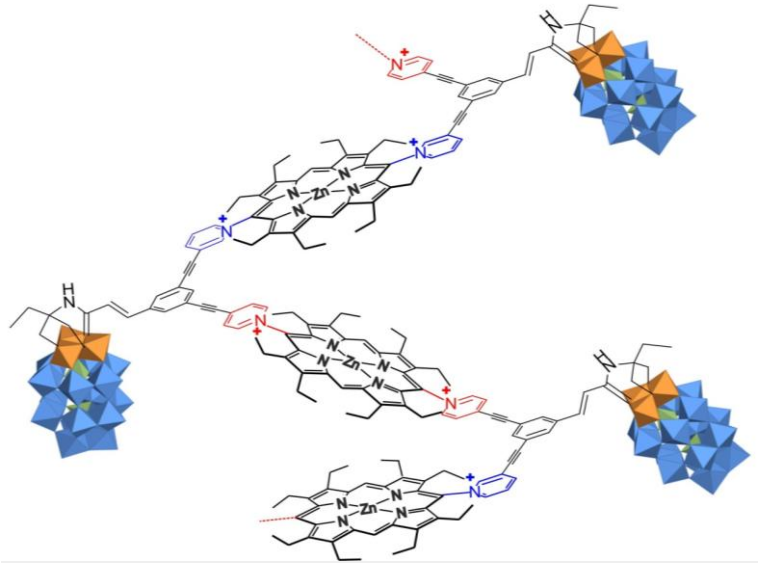

Fig. 13 Schéma de l'electropolymérisation de **ZnOEP** en présence du **POM-l4,3**.

Tous les copolymères ont été caractérisés par spectroscopie d'absorption UV-visible, XPS, AFM (microscopie à force atomique), EQCM (nanobalance électrochimique à cristal de quartz) et électrochimie. Des mesures en spectroscopie d'impédance électrochimique ont également été menées, dans le noir ou sous illumination dans le domaine du visible.

La réponse photoélectrochimique a été mesurée sur l'ensemble des copolymères synthétisés. Par exemple dans le cas des copolymères obtenus à partir de POMs du type Dawson $[P_2W_{15}V_3O_{62}]^{9-}$ **poly-POM-s4,4-ZnOEP**, **poly-POM-m3,3-ZnOEP**, **poly-POM-l4,4-ZnOEP** et **poly-POM-l3,3-ZnOEP**, la meilleur photoréponse sous illumination visible de la série est obtenue pour le copolymère **poly-POM-l4,4-ZnOEP** (Fig. 14).

Sur l'ensemble des copolymères développés, l'hybride silyl-Dawson-ZnOEP est le candidat le plus prometteur pour la génération de photocourant sous illumination dans le domaine du visible (Fig. 15A et Fig. 15C) où l'efficacité de la génération du photocourant est directement corrélée à la résistance de transfert de charge mesurée (sous immumination) par spectroscopie d'impédance électrochimique (Fig. 15B). En effet, plus la résistance de transfert de charge est faible, plus l'intensité du photocourant généré est grande.

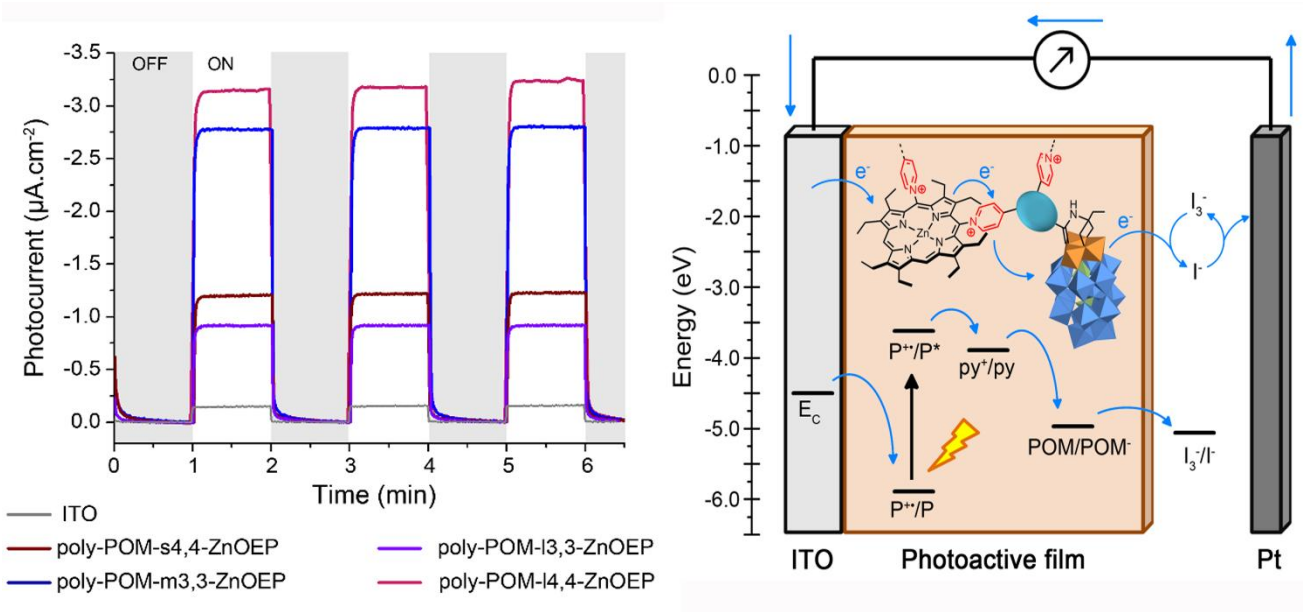

Fig. 14 Gauche : réponse photoélectrochimique de **poly-POM-s4,4-ZnOEP**, **poly-POM-m3,3-ZnOEP**, **poly-POM-l4,4-ZnOEP** et **poly-POM-l3,3-ZnOEP** (préparation du film entre –0,05 V et +1,90 V / ECS, 3 balayages itératifs) en milieu aqueux contenant $Na^+I_3^-$ 0.1 mol.L^{-1} et Na^+I^- 0.5 mol.L^{-1}. Remarque : seulement une face de l'électrode est recouverte d'ITO et donc du film. Illumination avec une lampe à Arc Xe 300 W (λ = 385 nm, filtre passe-haut). Potentiel BIAS : –0,10 V. La ligne grise correspond à la photoréponse de l'électrode ITO nue. Droite : représentation schématique de la structure d'une couche interne du film et le diagramme énergétique montrant le processus de transfert d'électron.

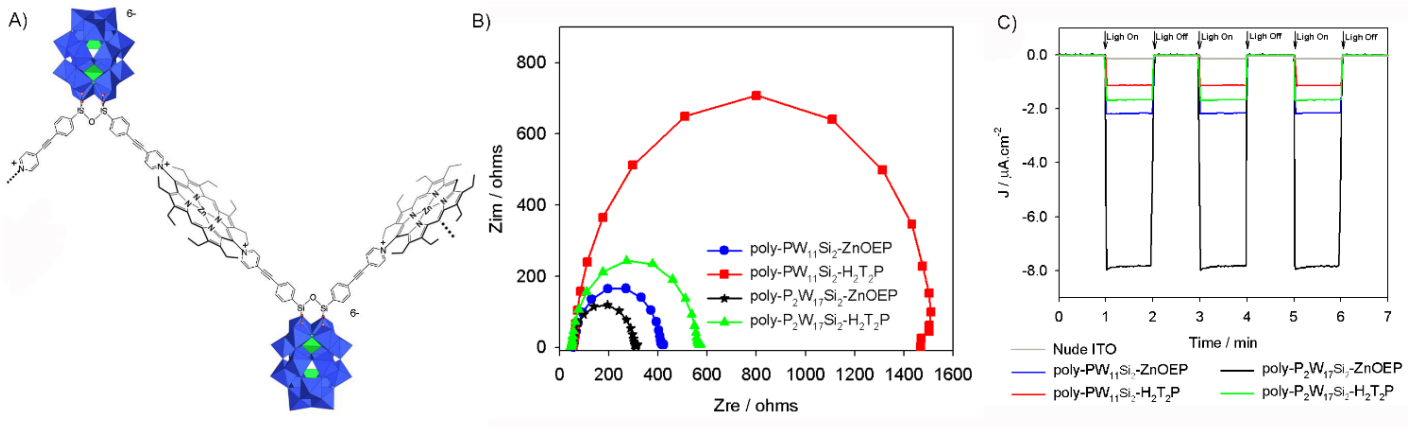

Fig. 15 A) Schéma de copolymère **poly-$PW_{11}Si_2$–ZnOEP**, B) courbe de Nyquist et C) réponse photoélectrochimique du **poly-PW_{11}-ZnOEP** (obtenue après 5 balayages itératifs), **poly-PW_{11}-H_2T_2P** (5 balayages itératifs), **poly-P_2W_{17}-ZnOEP** (3 balayages itératifs) et **poly-P_2W_{17}-H_2T_2P** (3 balayages itératifs). Préparation du film entre 0,00 V et +1,60 V / ECS. Mesures sous irradiation avec une lampe Arc Xe 300 W (λ ≥ 385 nm, filtre passe-haut) dans H_2O + I_3^- 5 mmol L^{-1} et I^- 0.5 mol L^{-1} ; potentiel BIAS : 0,00 V.

On peut noter que le type de porphyrine employé est aussi important, par exemple le copolymère hybride silyl-Dawson-**ZnOEP** présente une résistance de transfert de charge inférieure au film hybride silyl-Dawson-**H_2T_2P** obtenu à partir de la porphyrin base libre **H_2T_2P** (Fig. 15, centre).

Dans le cas des copolymères à base de POM du type Lindqvist, **poly-V_6O_{13}-ZnOEP** et **poly-V_6O_{13}-ZnOEP**, le changement de la réponse photoélectrochimique, en comparant le film à base de la porphyrine base libre ou de la métalloporphyrine, est par contre beaucoup moins important (Fig. 16).

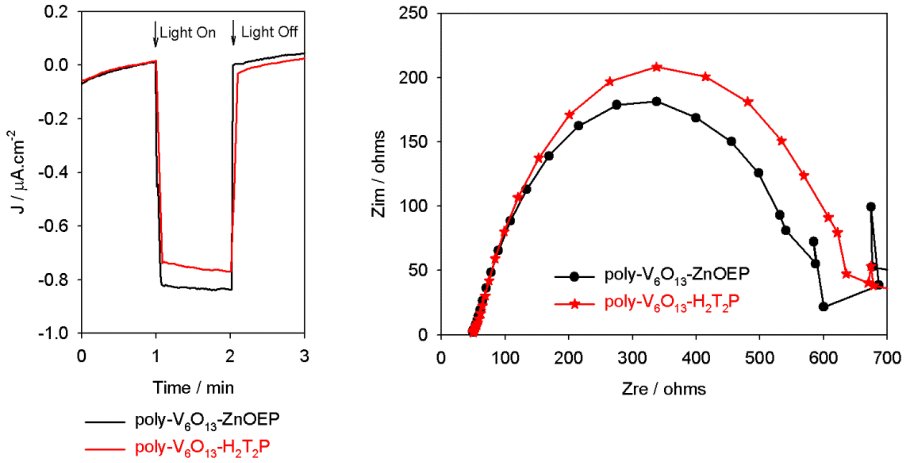

Fig. 16 Gauche : réponse photoélectrochimique du copolymère **poly-V_6O_{13}-ZnOEP** (3 balayages itératifs, courbe noire) et de **poly-V_6O_{13}-H_2T_2P** (3 balayages itératifs, courbe rouge) (copolymère préparés par balayage itératif entre 0,00 V et +1,60 V / ECS). Remarque : seulement un côté de l'électrode est recouverte d'ITO et donc du copolymère. Illumination dans le domaine visible avec une lampe à Arc Xenon 300 W ($\lambda \geq 385$ nm filtre passe haut). Potentiel BIAS : 0,00 V. Droite : courbe de Nyquist pour le **poly-V_6O_{13}-ZnOEP** (3 scans, courbe noire) et pour le **poly-V_6O_{13}-H_2T_2P** (3 balayages itératifs, courbe rouge). Potentiel DC : 0,00 V.

Ces films ont ensuite été utilisés pour l'étude de la réduction photocatalytiques de métaux (Ag^I et Pt^{IV}). La topologie des nanostructures d'argent obtenues (Figs. 17 et 18) en photocatalyse est très dépendante du type de POM présent dans le copolymère. Dans le cas des nanostructures à base de Pt^0, leur morphologie a très peu été influencée par la nature du POM ou de la porphyrine employée (Fig. 19).

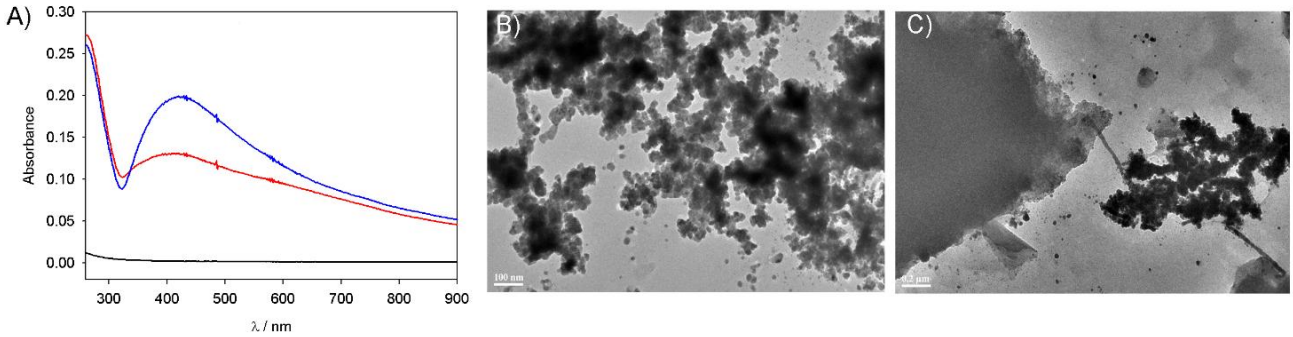

Fig. 17 A) Spectres UV-visible des nanoparticules d'argent présentes en solution après photocatalyse en employant comme catalyseur le copolymère **poly-V_6O_{13}-ZnOEP** (courbe rouge) ou le copolymère **poly-V_6O_{13}-H_2T_2P** (courbe bleue). Image MET des nanoparticules d'argent obtenues à partir des films (catalyseur hétérogène) : B) **poly-V_6O_{13}-ZnOEP** et C) **poly-V_6O_{13}-H_2T_2P**.

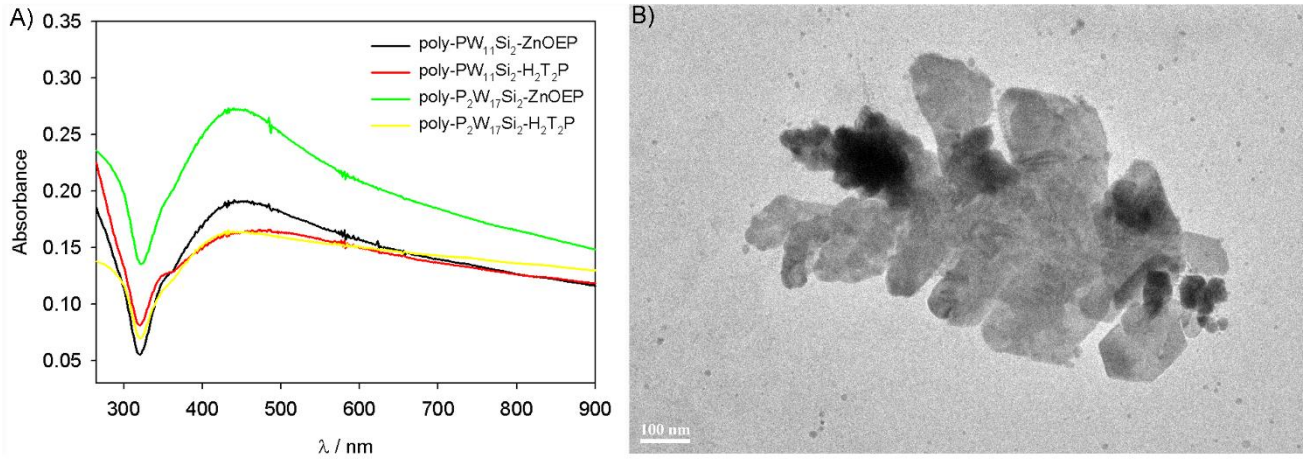

Fig. 18 A) Spectres UV-visible des nanoparticules d'argent obtenues en solution après photocatalyse préparées à partir des copolymères **poly-Py-$PW_{11}Si_2$-Py-Porphyrine** et **poly-Py-$PW_{17}Si_2$-Py-Porphyrine** (Porphyrine = **ZnOEP** ou **H_2T_2P** ; polyoxométallate du type Keggin ou Dawson : $[PW_{11}Si_2O_{40}C_{26}H_{16}N_2].3TBA$ (**Py-$PW_{11}Si_2$-Py**) et $[P_2W_{17}Si_2O_{62}C_{26}H_{16}N_2].6TBA$ (**Py-$P_2W_{17}Si_2$**)) B) Image MET des nanoparticules d'argent obtenues en prenant comme catalyseur le film **poly-$PW_{11}Si_2$-H_2T_2P**.

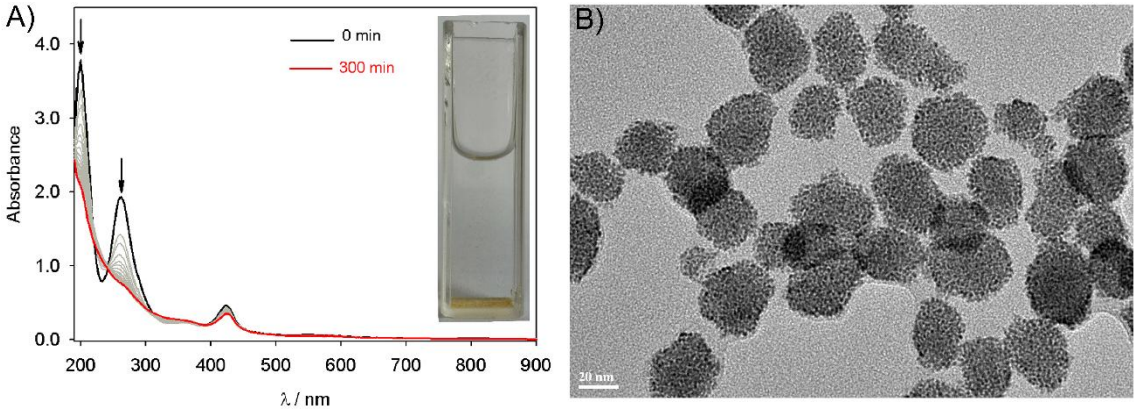

Fig. 19 A) Evolution du spectre UV-visible d'une solution desaérée de $H_2Pt^{IV}Cl_6$ 1,6 × 10^{-4} mol L^{-1} en présence de 0,13 mol L^{-1} de propan-2-ol contenant une plaque de quartz modifiée avec le copolymère **poly-$PW_{11}Si_2$-ZnOEP** sous illumination dans le domaine visible. Encart : photographie de la solution de nanoparticules de Pt après irradiation. B) Image MET des nanostructures de platine obtenues à partir du catalyseur **poly-$PW_{11}Si_2$-ZnOEP**.

2 – Films électrostatiques polyoxométallates – copolymère de porphyrines

Dans le ***chapitre V***, nous avons utilisé la même méthode d'électropolymérization décrite dans les chapîtres 2 à 4. Elle est basée sur l'attaque de nucleophile de groupes pyridyle (4,4'-bipyridine ou 1,1''-(1,3-propanediyl)bis4,4'-bipyridinium) sur les dications électrogénés pour l'obtention de copolymères de porphyrines. Par exemple lors de l'utilisation du 1,1''-(1,3-propanediyl)bis4,4'-bipyridinium, un copolymère **poly-ZnOEP-V^{2+}-$(CH_2)_3$-V^{2+}** (**poly-ZnOEP2**) avec un bis-viologène comme espaceur est obtenu (Fig. 20). Les propriétés électrochimiques et spectroélectrochimiques montrent dans ce cas la formation de π-dimères lors de la première réduction des viologènes caractérisé par une bande d'absorption au-delà de 1000 nm lors de l'étude spectroélectrochimique (Fig. 21B). La formation de ce π-dimère explique également de dédoublement de la seconde vague de réduction des unités viologènes (pices IIa et IIb, Fig. 21A) lors de l'étude électrochimique. Il caractérise une forte interaction entre des groupes $V^{+\bullet}$ proches (probablement intermoléculaire, c'est-à-dire entre différent espaceurs du même copolymère ou entre deux copolymères proche dans le film).

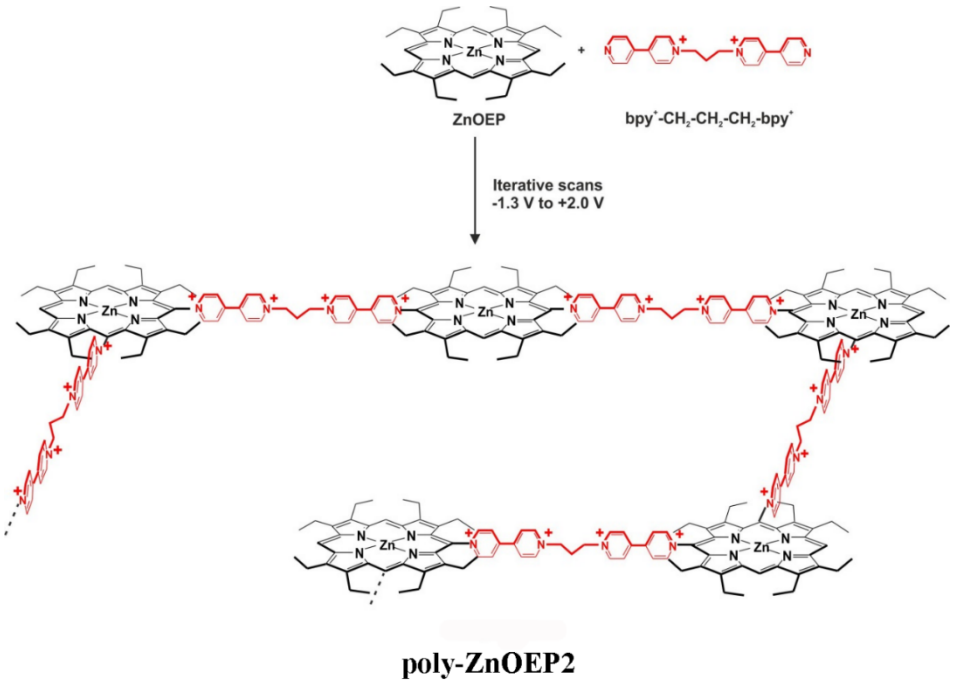

Fig. 20 Schéma d'électropolymérisation en "zig-zag" de **ZnOEP** en présence du $bpy^{+}–CH_2–CH_2–CH_2–{}^{+}bpy\ 2PF_6^-$ pour l'obtention du film **poly-ZnOEP2**.

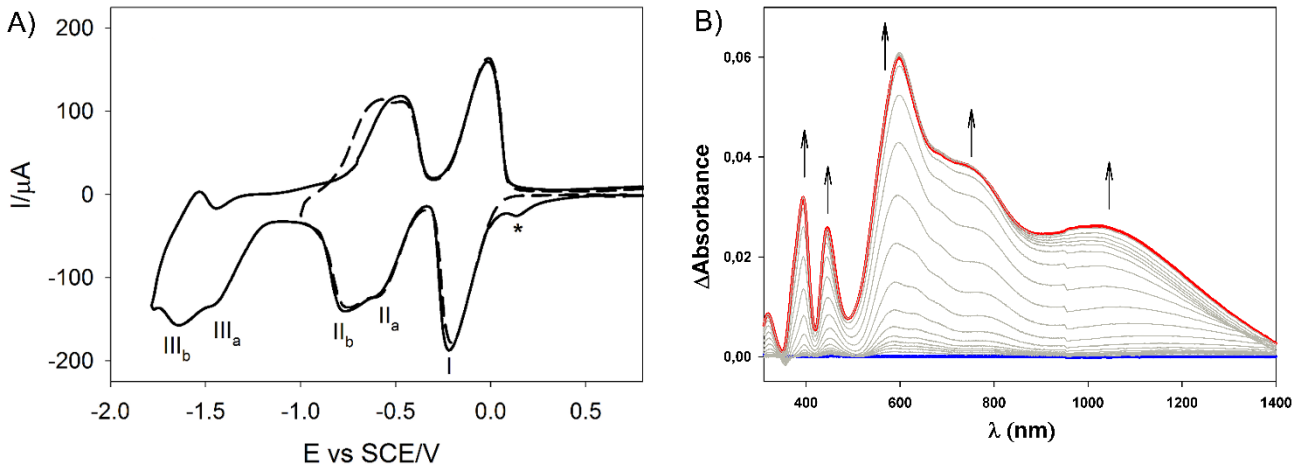

Fig. 21 A) Voltammogramme cyclique du film **poly-ZnOEP2** obtenu après 25 balayages itératifs en milieu 1,2-$C_2H_4Cl_2$/CH_3CN (4/1) et 0,1 mol L^{-1} $TBAPF_6$. B) Spectres UV-visible-proche IR au cours de la réduction exhaustive au potentiel du pic I (1 électron par unité viologen) pour le copolymère **poly-ZnOEP2** en milieu H_2O et 0,2 mol L^{-1} $TEAPF_6$. Electrode de travail : ITO. S = 1 cm^2.

L'épaisseur des films a également été étudiée par AFM montrant que celle-ci tend vers un plateau (Fig. 22). L'allure de la courbe est similaire à celle obtenue lors des mesures des propriétés d'absorption UV-visibles des films. Ceci est probablement du au potentiel de dépôt employé, mais aussi sans doute aux propriétés de conductivité du film déposé.

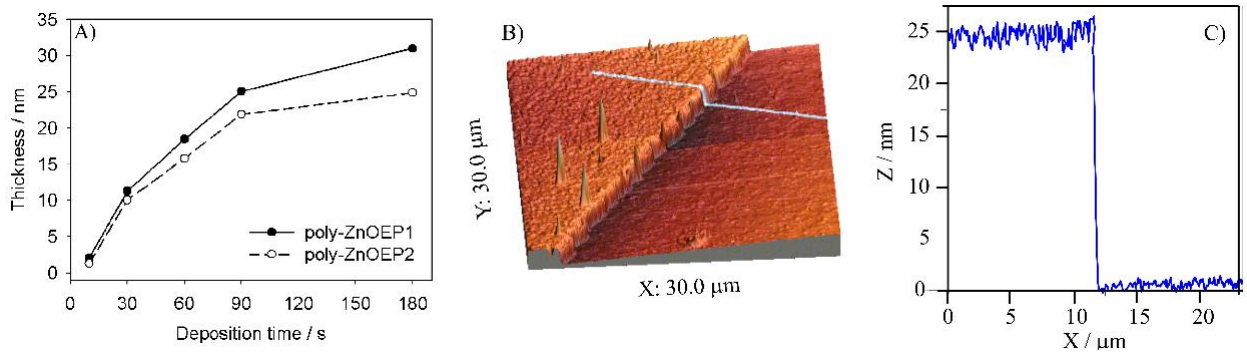

Fig. 22 A) Mesure de l'épaisseur des films, B) image AFM montrant la topologie enregistrée pour **poly-ZnOEP2** (dépot au potential appliqué +1.90 V durant 180 secondes) et C) analyse de la section marquées en bleue de l'image AFM.

Dans un second temps les POMs peuvent être incorporés sur les copolymères de porphyrines cationiques via une réaction de méthathèse (échange des contre anions PF_6^- par des groupements POMs comme le polyanion du type Presseyler $NaP_5W_{30}O_{110}^{14-}$). Deux films hybrides ont ainsi pu être obtenus : le **poly-ZnOEP-V^{2+} / $[NaP_5W_{30}O_{110}]^{14-}$** (**poly-ZnOEP1 / P_5W_{30})** (et le **poly-ZnOEP-V^{2+}-$(CH_2)_3$-V^{2+} / $[NaP_5W_{30}O_{110}]^{14-}$** (**poly-ZnOEP2 / P_5W_{30})** où le viologène est abrégé V^{2+}. Ces films possèdent respectivement un photocourant 3,4 fois et 1,3 fois plus grand par rapport aux films où le polyanion $NaP_5W_{30}O_{110}^{14-}$ est absent. Ceci est lié à la présence de $NaP_5W_{30}O_{110}^{14-}$ en surface du film permettant une cascade de transfert d'électron ad-hoc de la porphyrine excitée au viologène, puis du radical viologène formé (monoréduit) au POM (Fig. 23). Ceci n'est possible que grâce au potentiel redox approprié de $[NaP_5W_{30}O_{110}]^{14-}$ qui peut agir comme un accepteur fort d'électron.

En changeant uniquement le solvant H_2O par CH_3CN, avec le même film et le même médiateur rédox (I_3^-/I^-) et dans les mêmes conditions d'illumination, on peut remarquer un changement de la direction du transfert d'électrons passant d'un processus cathodique en milieu aqueux à un processus anodique avec un solvant du type acétonitrile (Fig. 23). On peut expliquer ce phénomène par la grande influence du solvant sur le potentiel de réduction notamment de l'unité POM qui impose le sens du transfert d'électron.

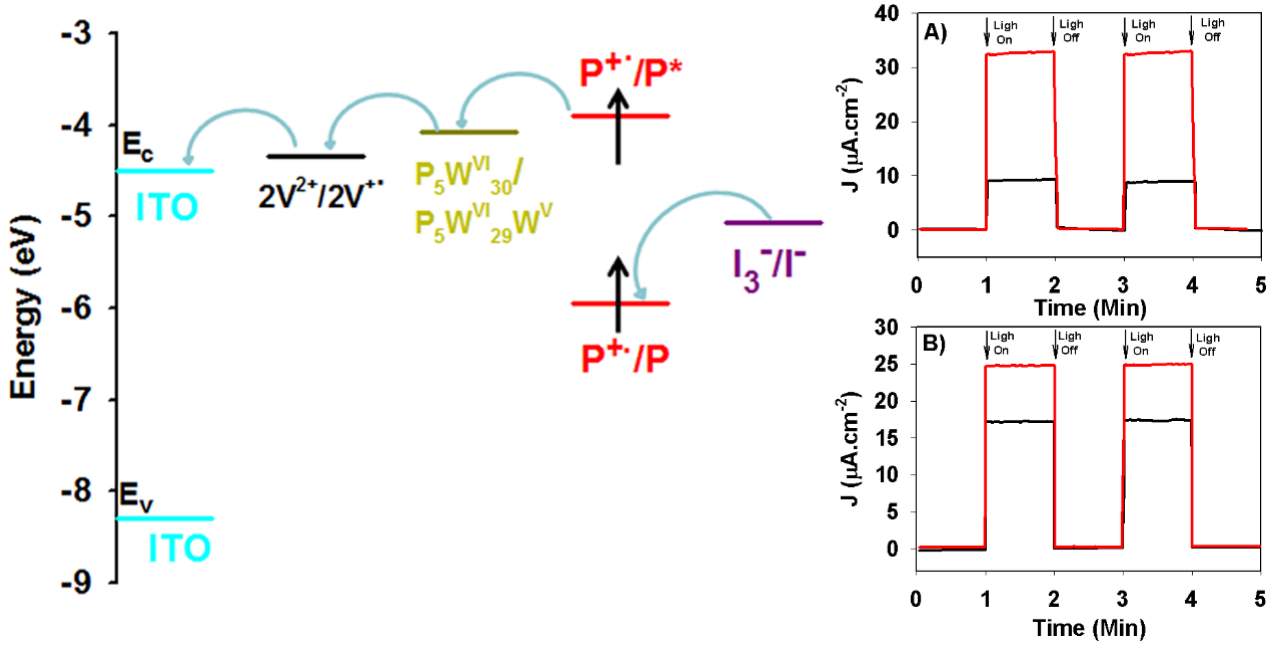

Fig. 23 Gauche : diagramme d'énergie schématique montrant les processus de transfert d'électrons photoinduit. Droite : A) Réponse photoélectrochimique de **poly-ZnOEP-V^{2+}/[$NaP_5W_{30}O_{110}$]$^{14-}$ (poly-ZnOEP1/P_5W_{30})** et de B) **poly-ZnOEP-V^{2+}-$(CH_2)_3$-V^{2+}/[$NaP_5W_{30}O_{110}$]$^{14-}$ (poly-ZnOEP2/P_5W_{30})** dans le noir ou sous illumination à l'aide d'une lampe à arc Xe 300 W (λ > 385 nm, filtre passe haute) en milieu acetonitrile contenant I_3^- 5 mmol L^{-1} et I^- 0,5 mol L^{-1}. Potentiel BIAS : 0,00 V / potentiel à circuit ouvert (OCP).

Des mesures en spectroscopie d'impédance électrochimique dans le noir et sous illunination visible des systèmes **poly-ZnOEP-V^{2+}/[$NaP_5W_{30}O_{110}$]$^{14-}$** (**poly-ZnOEP1/P_5W_{30}**) et **poly-ZnOEP-V^{2+}-$(CH_2)_3$-V^{2+}/[$NaP_5W_{30}O_{110}$]$^{14-}$** (**poly-ZnOEP2/P_5W_{30}**) ont été également étudiées. Elle montrent d'une part que la résistance de transfert de charge diminue sous illunination (associé à la génération d'un photocourant). D'autre part une diminution des résistances de transfert de charge lors de la présence de **P_5W_{30}** en surface du film dans le noir ou sous illumination a également été observée (Fig. 24). Ces résultats montrent que lorsque la résistance du transfert de charge diminue, la génération du photocourrant est plus efficace.

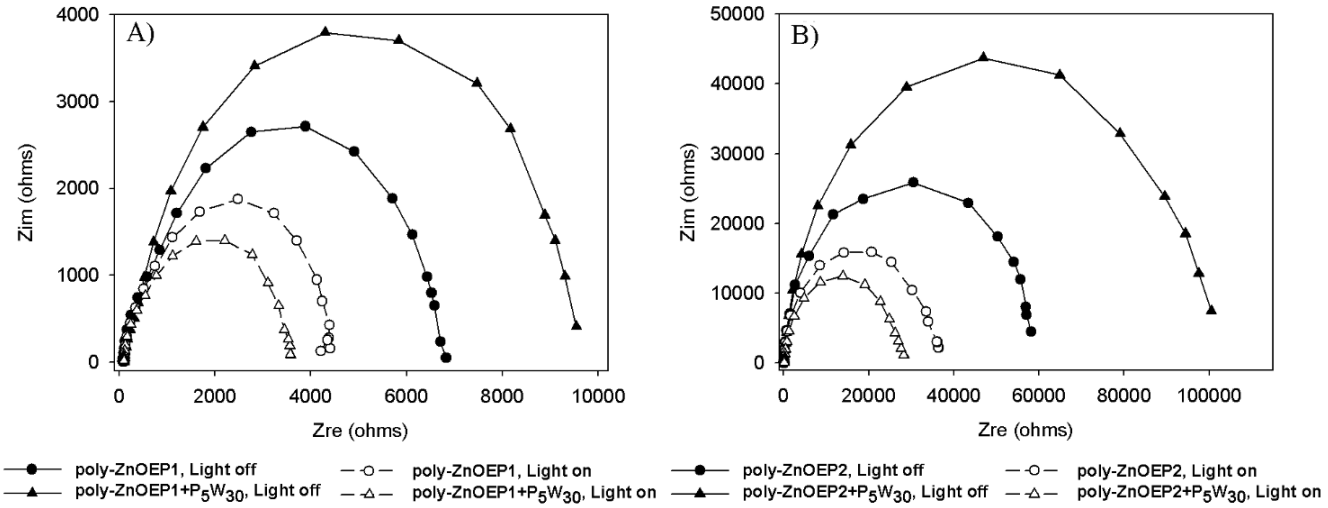

Fig. 24 Spectroscopie d'impédance électrochimique. A) copolymère **poly-ZnOEP1** et copolymère **poly-ZnOEP1/P_5W_{30}** (temps de trempage du film dans la solution aqueuse de POM : 60 min). B) copolymère**poly-ZnOEP2** et copolymère **poly-ZnOEP2/P_5W_{30}** (temps de trempage : 30 min) avec et sans illumination (lampe à Arc Xe 300 W, $\lambda > 385$ nm filtre passe haute). Milieu acetonitrile contenant I_2 5 mmol L^{-1} et NaI 0,5 mol L^{-1} (BIAS : 0,00 V. La gamme de fréquence explorée était de 0.1 Hz à 10^5 Hz. Potentiel 0,00 V.

La nanobalance électrochimique à cristal de quartz (EQCM) a été aussi employées pour mesurer les masses déposées lors de la formation des copolymères intiales de porphyrines **poly-ZnOEP-V^{2+}** et **poly-ZnOEP-V^{2+}-$(CH_2)_3$-V^{2+}** (7,9 et 5,7 µg.cm^{-2} respectivement, au potentiel appliqué de +1,90 V durant 180 s). La nanobalance à cristal de Quartz (QCM) a ensuite été utilisée pour peser la quantité de PF_6^- échangée par $[NaP_5W_{30}O_{110}]^{14-}$ lors de la réaction de méthathèse (0,61 et 0,77 µg.cm^{-2} respectivement, pour un temps de trempage de l'électrode modifiée dans une solution aqueuse de $[NaP_5W_{30}O_{110}]^{14-}$ d'une heure.

3 – Films électrostatiques copolymère de porphyrines – nanoparticules P_5W_{30}@MNPs (P_5W_{30} = $[NaP_5W_{30}O_{110}]^{14-}$, Preyssler)

La résonance plasmon observée à la surface de nanostructures d'argent ou d'or permet une amélioration de manière importante l'excitation électronique de molécules ancrées en surface de ces nanostructures et permet la génération de transporteur de charge.

Dans le ***chapitre VI***, une stratégie facile et simple pour l'obtention de nanoparticules (Ag, Au et Pt) par photocatalyse a été utilisée avec l'aide du polyanion du type Preyssler $[NaP_5W_{30}O_{110}]^{14-}$ (abrégé **P_5W_{30}**). Le polyanion $[NaP_5W_{30}O_{110}]^{14-}$ joue un rôle double, il agit comme agent réducteur (photocatalyseurs pour la réduction des ions métalliques sous illumination UV en présence du médiateur rédox propan-2-ol) et aussi comme agent stabilisant (surfactant) permettant la formation des nanostructures **P_5W_{30}@MNPs**. Ici, le POM du type Pressler $[NaP_5W_{30}O_{110}]^{14-}$ englobe le métal réduit permettant ainsi sa stabilisation (Fig. 25).

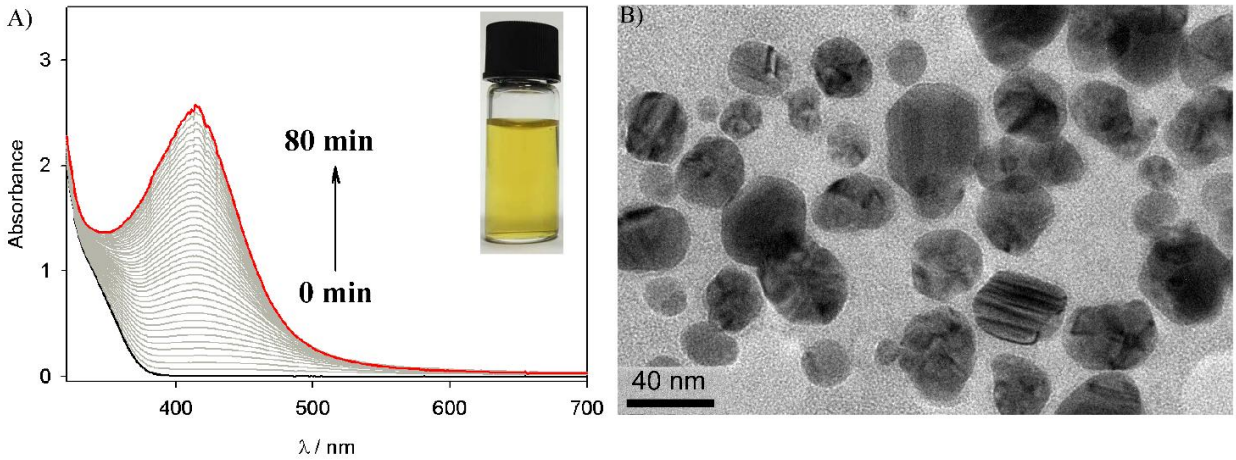

Fig. 25 A) Spectres d'absorption UV-visible des nanoparticules d'argent formées sous illumination UV en solution aqueuse contenant **$Na_{14}[NaP_5W_{30}O_{110}]$** (**$P_5W_{30}$**) en présence de Ag_2SO_4 (0,2 mM) et de 0,13 M de propan-2-ol. Encart : image de la solution de nanoparticles. B) Image MET des nanoparticules **P_5W_{30}@Ag**.

Par réaction de méthathèse, il est ensuite possible d'échanger des contre-anions PF_6^- de copolymère de porphyrine cationique à espaceur pyridinium et d'obtenir des systèmes hybrides **P_5W_{30}@MNPs-porphyrine** (Fig. 26). La masse initiale de copolymère bis-porphyrine **poly-*cis*-$H_2Py_2Ph_2P$-ZnOEP** déposée a été mesurée par EQCM (nanobalance électrochimique à cristal de quartz, Fig. 27A) tandis que la quantité de nanoparticules introduites a été mesurée une nouvelle fois par nanobalance à cristal de quartz (QCM, Fig. 27B).

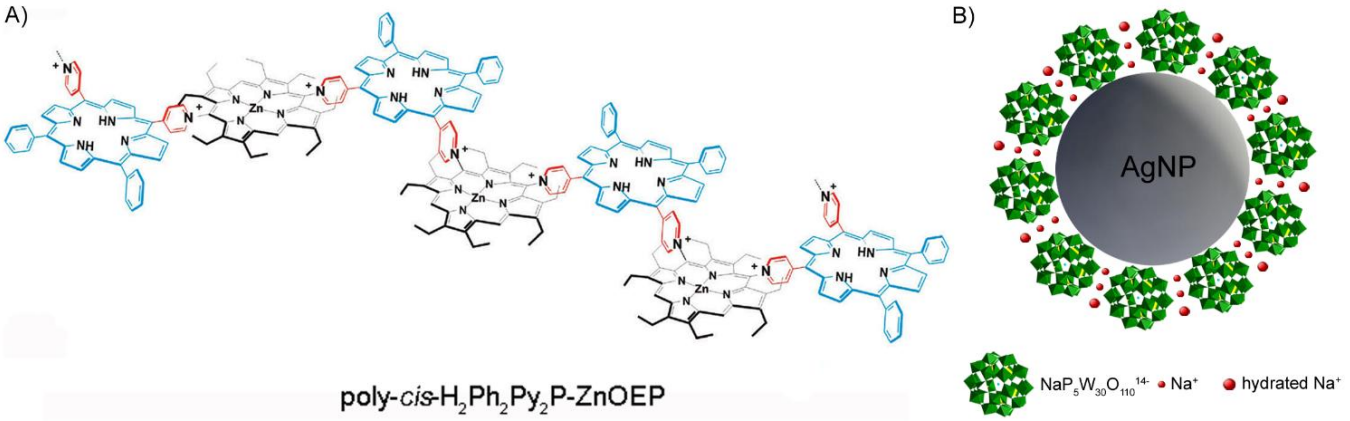

Fig. 26 A) Structure moléculaire de **poly-cis-$H_2Ph_2Py_2$P-ZnOEP**. B) Schéma proposé de la nanostructure **P_5W_{30}@AgNPs**.

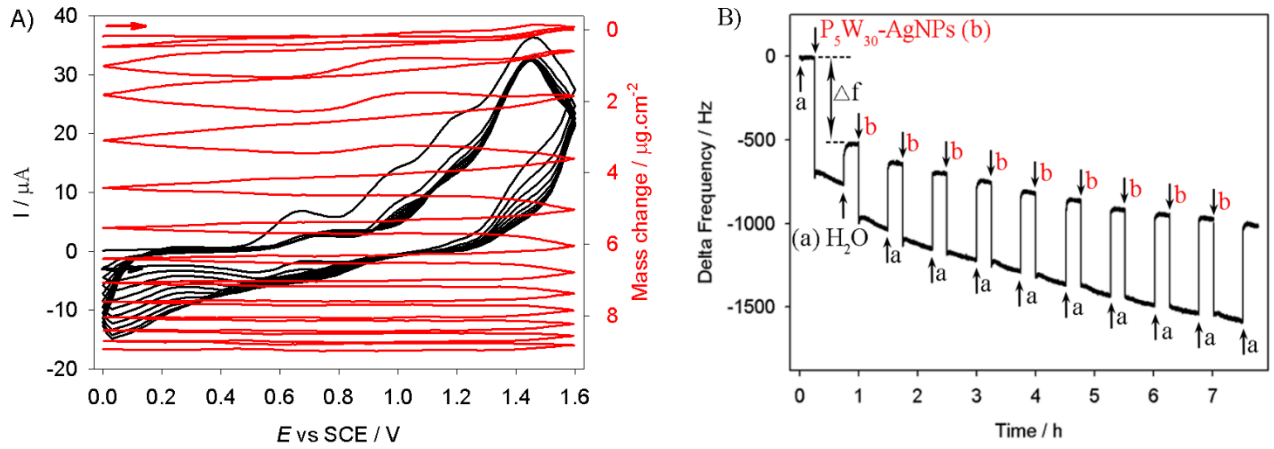

Fig. 27 A) Voltammogramme cyclique au cours de l'électropolymérization (15 premiers balayages) et mesure de la variation de masse obtenue par EQCM (nanobalance électrochimique à cristal de quartz) avec **ZnOEP** (0,25 mmol L^{-1}) et ***cis*-$H_2Py_2Ph_2$P** (0,25 mmol L^{-1}). Milieu : $CH_3CN/1,2\text{-}C_2H_4Cl_2$ (3/7) en présence de 0.1 mol L^{-1} $TBAPF_6$. Electrode de travail : ITO (S = 0.2 cm^2) déposé sur un cristal de quartz (9.08 MHz). v = 100 mV s^{-1}. B) Variation de la fréquence (QCM) d'une électrode ITO modifiée avec le film copolymère bis-porphyrine **poly-*cis*-$H_2Py_2Ph_2$P-ZnOEP** en fonction du temps de trempage dans une solution aqueuse contenant **$[NaP_5W_{30}O_{110}]^{14-}$@AgNPs** (b) (S = 0.2 cm^2)). La ligne de base (point de repère a) correspond au film de départ. La flèche ↓ indique l'injection de la solution de **P_5W_{30}@Ag**. La flèche ↑ indique le lavage à l'eau.

Une amélioration notable du photocourant a été observée en présence de **P_5W_{30}@MNPs** en surface du film où la nature du métal M (Au, Ag, Pt) semble aussi jouer un rôle.

Dans le cas où uniquement le POM du type Pressler $[NaP_5W_{30}O_{110}]^{14-}$ est incorporé au copolymère (bis-porphyrine à espaceur pyridinium), le photocourant mesuré sous illumination visible est 1,3 fois plus grand montrant l'effet de la présence du POMs permettant une cascade des transfers d'électrons. Ceci a tendance à diminuer la recombinaison des charges du fait de l'éloignement du radical cation

porphyrine et du POM réduit. Dans le cas de l'incorporation de nanostructures du type **P_5W_{30}@AgNPs** en surface du film, une augmentation du photocourant de 400 % a été mesurée (Fig. 28).

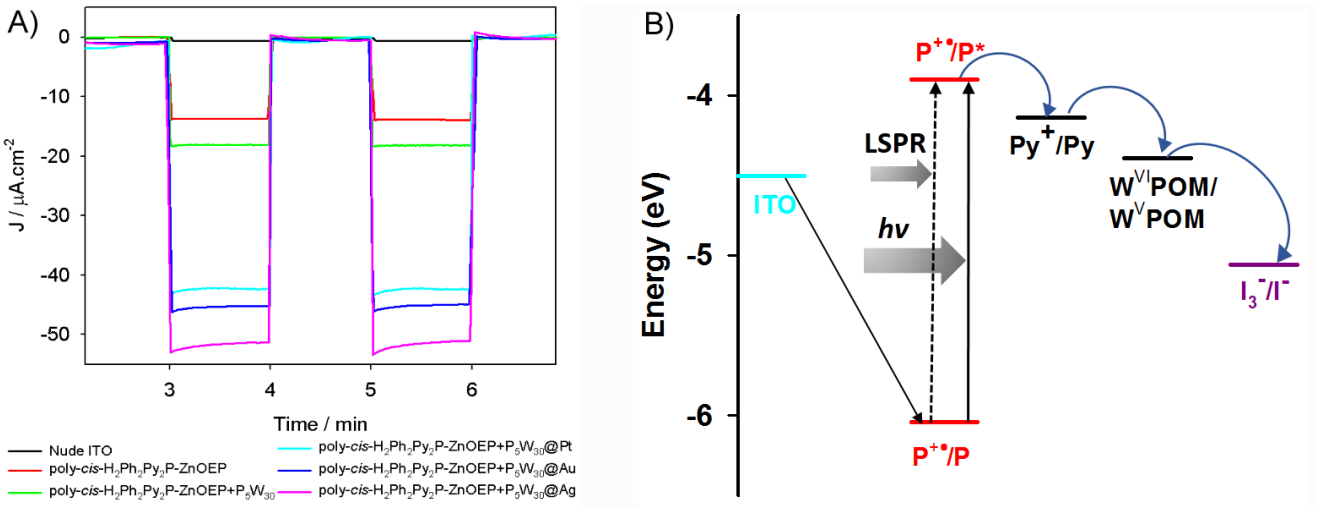

Fig. 28 A) Courbes J-t pour une série de copolymères porphyrines dopés à l'aide de nanoparticules P_5W_{30}@MNPs (M = Ag, Au et Pt) mesurées dans le noir ou sous illumination dans le domaine du visible en milieu H_2O contenant I_3^- 5 mmol L^{-1} et I^- 0,5 mol L^{-1}. Potentiel BIAS : -0,10 V par rapport au potentiel en circuit ouvert (OCP). $[NaP_5W_{30}O_{110}]^{14-}$ = P_5W_{30}. B) Diagramme d'énergie schématique présentant le processus de transfert électronique. (Py = pyridine, P = porphyrine).

Ce résultat peut être attribué à la présence de nouveau de transfert d'électron photoinduit en cascade : de la porphyrine vers le pyridinium, puis du radical pyridinium vers **P_5W_{30}** ce qui retarde la recombinaison des charges. L'augmentation de l'efficacité peut aussi être due également au plasmon de résonance des nanoparticules **P_5W_{30}@MNPs** (M = Ag, Pt, Au) qui améliore considérablement l'excitation électronique mais aussi probablement la conductivité du film sous illumination. Les mesures en spectroscopie d'impédance électrochimique sous illumination (Fig. 29) montrent de nouveau une résistance de transfert de charges beaucoup plus faible en présence de **P_5W_{30}@MNPs** (M = Ag, Pt, Au) en surface du film relié à une meilleur efficacité de la génération du photocourant (Figs. 28 et 29).
Dans ce cas la simulation de la courbe en spectroscopie d'impédance électrochimique semble montrer la présence d'un second processus de transfert de charge.
Comparé au circuit équivalent n°1 (Fig. 29A) correspondant au copolymère **poly-*cis*-$H_2Py_2Ph_2$P-ZnOEP**, une résistance de transfert de charge additional R_{ct2} en parallèle avec la capacitance C_2 est

obtenue en série pour le circuit équivalent n°2 pour **poly-*cis*-$H_2Py_2Ph_2P$-ZnOEP/P_5W_{30}@Ag**.

R_{ct2} et R_{ct1} peuvent être interprétés comme les résistances de transfert de charges de la solution aux nanoparticules et des nanoparticules à l'électrode (**poly-cis-$H_2Py_2Ph_2P$-ZnOEP**) respectivement. L'impédance globale *Z(w)* du circuit n°2, qui correspond au « fit » (courbe rouge), correspond ainsi à l'équation 1 ci-dessous :

$$Z(w)=R_e+ R_{ct1}/(1+R_{ct1}C_1(jw)^n)+R_{ct2}/(1+R_{ct2}C_2jw) \qquad \text{équation (1)}$$

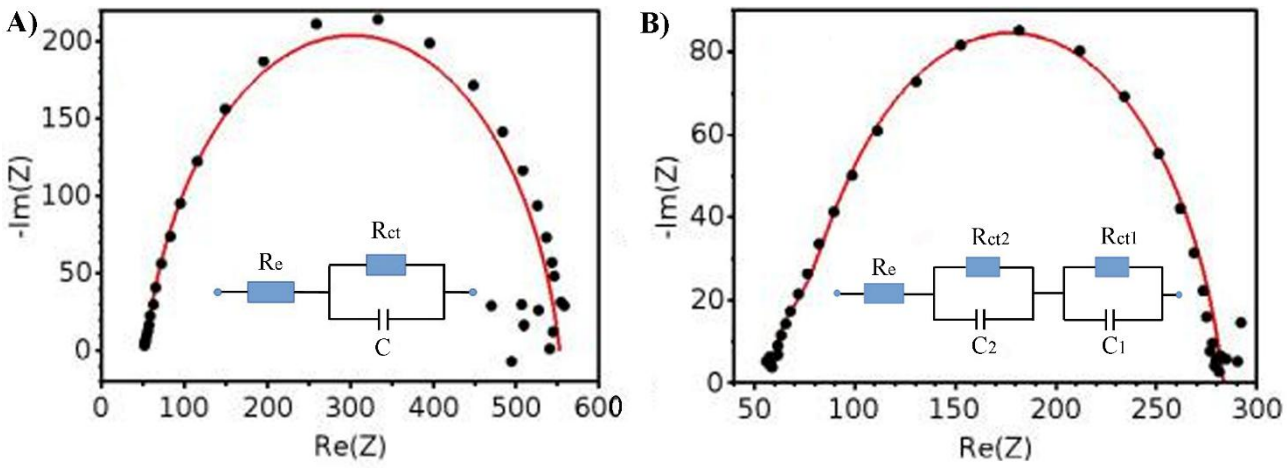

Fig. 29 Spectroscopie d'impédance électrochimique du copolymère **poly-*cis*-$H_2Py_2Ph_2P$-ZnOEP** (A), et du copolymère **poly-*cis*-$H_2Py_2Ph_2P$-ZnOEP/P_5W_{30}@Ag** (B). Encarts : circuit équivalent utilisé pour la simulation (courbes rouges).

Conclusion

Pour conclure, les résultats présentés dans cette thèse portent sur le développement de nouveaux systèmes hybrides porphyrines-POMs où le type de porphyrine, la nature de l'espaceur entre les unités porphyrines et la nature du groupement POM ont été modulés. Ces nouveaux systèmes hybrides ont été caractérisés par spectroscopie d'absorption UV-visible, XPS, AFM, EQCM, spectroscopie d'impédance électrochimique et électrochimie. L'évaluation de la génération de photocourant ainsi que la photocatalyse de la réduction d'ions métaliques (Ag^I, Au^{III}, Pt^{IV}) sous illumination dans le domaine visible en présence de I_3^-/I^- ou de propan-2-ol a également été étudiée.

Les perspectives de ces travaux sont nombreuses tant au niveau des applications en photoélectrocatalyse qu'en photocatalyse pour la réduction d'ions d'interêt environmentale (Hg^{II}, Cr^{VI}, Pb^{II}, etc…) voire la photodégradation de polluants organiques (pesticides, colorants, etc …) en milieu aqueux aérié.

Des études pour la génération de photocourant à l'aide d'une lampe Arc Xe couplée à un monochromateur sont prévues de manière à montrer que l'efficacité de la génération de photocourant est meilleure au niveau de l'absorption du photosensibilisateur : la porphyrine. La mesure des rendements à partir de cellule scellées sera également un point à développer dans un avenir proche.

Le développement des études sur le « dopage » des films avec des nanoparticules POM@MNPs semblent être également très prometteur et nécessite des études plus poussées, notamment l'effet de la taille des nanoparticles, l'utilisation de nanoparticules stabilisées avec du citrate et pas le POM, etc...

Références

(1) Long, D.-L.; Tsunashima, R.; Cronin, L. *Angew. Chem. Int. Ed. Engl.* **2010**, *49* (10), 1736.
(2) Xie, J.; Abrahams, B. F.; Wedd, A. G. *Chem. Commun. (Camb).* **2008**, No. 5, 576.
(3) Nie, S.; Zhang, Y.; Liu, B.; Li, Z.; Hu, H.; Xue, G.; Fu, F.; Wang, J. *J. Solid State Chem.* **2010**, *183* (12), 2957.
(4) Zhang, H.; Peng, J.; Shen, Y.; Yu, X.; Zhang, F.; Mei, J.; Li, B.; Zhang, L. *Chem. Commun.* **2012**, *48* (37), 4462.
(5) Ruhlmann, L.; Costa-Coquelard, C.; Hao, J.; Jiang, S.; He, C.; Sun, L.; Lampre, I. *Can. J. Chem.* **2008**, *86* (11), 1034.
(6) Ettedgui, J.; Diskin-Posner, Y.; Weiner, L.; Neumann, R. *J. Am. Chem. Soc.* **2011**, *133* (2), 188.
(7) Walsh, J. J.; Long, D.-L.; Cronin, L.; Bond, A. M.; Forster, R. J.; Keyes, T. E. *Dalton Trans.* **2011**, *40* (9), 2038.
(8) Santos, I. C. M. S.; Rebelo, S. L. H.; Balula, M. S. S.; Martins, R. R. L.; Pereira, M. M. M. S.; Simões, M. M. Q.; Neves, M. G. P. M. S.; Cavaleiro, J. a. S.; Cavaleiro, A. M. V. *J. Mol. Catal. A Chem.* **2005**, *231* (1-2), 35.
(9) Costa-Coquelard, C.; Sorgues, S.; Ruhlmann, L. *J. Phys. Chem. A* **2010**, *114* (22), 6394.
(10) Ahmed, I.; Wang, X.; Boualili, N.; Xu, H.; Farha, R.; Goldmann, M.; Ruhlmann, L. *Appl. Catal. A Gen.* **2012**, *447-448*, 89.
(11) Piepenbrink, M.; Triller, M. U.; Gorman, N. H. J.; Krebs, B. *Angew. Chemie - Int. Ed.* **2002**, *41* (14), 2523.
(12) Yokoyama, A.; Kojima, T.; Ohkubo, K.; Shiro, M.; Fukuzumi, S. *J. Phys. Chem. A* **2011**, *115* (6), 986.
(13) Schaming, D.; Costa-Coquelard, C.; Lampre, I.; Sorgues, S.; Erard, M.; Liu, X.; Liu, J.; Sun, L.; Canny, J.; Thouvenot, R.; Ruhlmann, L. *Inorganica Chim. Acta* **2010**, *363* (10), 2185.
(14) Allain,C.; Schaming,D.; Sorgues, S.; Gisselbrecht,J.-P.; Lampre, I.; Ruhlmann, L.; Hasenknopf, B. *Dalton Trans.* **2013**, *42* (8), 2745.
(15) Chen, Q.; Chen, Q.; Goshorn, D. P.; Goshorn, D. P.; Scholes, C. P.; Scholes, C. P.; Tan, X. L.; Tan, X. L.; Zubieta, J.; Zubieta, J. *J. Am. Chem. Soc.* **1992**, *114* (12), 4667.
(16) Li, J.; Huth, I.; Chamoreau, L. M.; Hasenknopf, B.; Lacôte, E.; Thorimbert, S.; Malacria, M. *Angew. Chemie - Int. Ed.* **2009**, *48* (11), 2035.
(17) Kang, J.; Nelson, J. a; Lu, M.; Xie, B.; Peng, Z.; Powell, D. R. *Inorg. Chem.* **2004**, *43* (20), 6408.
(18) Odobel, F.; Séverac, M.; Pellegrin, Y.; Blart, E.; Fosse, C.; Cannizzo, C.; Mayer, C. R.; Elliott, K. J.; Harriman, A. *Chem. - A Eur. J.* **2009**, *15* (13), 3130.
(19) Harriman, A.; Elliott, K. J.; Alamiry, M. a H.; Pieux, L. Le; Séverac, M.; Pellegrin, Y.; Blart, E.; Fosse, C.; Cannizzo, C.; Mayer, C. R.; Odobel, F. *J. Phys. Chem. C* **2009**, *113* (14), 5834.
(20) Elliott, K. J.; Harriman, A.; Le Pleux, L.; Pellegrin, Y.; Blart, E.; Mayer, C. R.; Odobel, F. *Phys. Chem. Chem. Phys.* **2009**, *11* (39), 8767.
(21) Matt, B.; Xiang, X.; Kaledin, A. L.; Han, N.; Moussa, J.; Amouri, H.; Alves, S.; Hill, C. L.; Lian, T.; Musaev, D. G.; Izzet, G.; Proust, A. *Chem. Sci.* **2013**, *4* (4), 1737.
(22) Matt, B.; Fize, J.; Moussa, J.; Amouri, H.; Pereira, A.; Artero, V.; Izzet, G.; Proust, A. *Energy Environ. Sci.* **2013**, *6* (5), 1504.
(23) Lu, M.; Xie, B.; Kang, J.; Chen, F.-C.; Peng, Z. *Chem. Mater.* **2005**, *17* (2), 402.
(24) Schaming, D.; Allain, C.; Farha, R.; Goldmann, M.; Lobstein, S.; Giraudeau, A.; Hasenknopf, B.; Ruhlmann, L. *Langmuir* **2010**, *26* (7), 5101.

Abstract

Solar energy, as the cleanest and least limited energy source, becomes increasingly hot over recent years. Polyoxometalates (POMs) are a structurally diverse family of anionic metal oxide molecular compounds with extent applications in photocatalysis and photoelectrocatalysis. Unfortunately, POMs can be excited (POMs*) mainly under UV irradiation. To address this problem, POMs can be linked to visible light sensitizer, such as porphyrins, which possess strong visible absorptions and ultrafast photoinduced charge separation.

1 - Covalent polyoxometalate – porphyrin copolymeric films

Hybrid POM-porphyrin copolymeric films were directly obtained by the electro-oxidation of zinc-β-octaethyl porphyrin (ZnOEP) or 5,15-ditolyl porphyrin (H_2T_2P) through $E(EC_NEC_B)_nE$ process in the presence of different type POMs bearing two pyridyl groups (Py-POM-Py). **System I** (chapter II): the electropolymerization of free base H_2T_2P or metalloporphyrin ZnOEP are reported in the presence of a functionalized Lindqvist polyoxovanadate bearing two pyridyl groups which are tethered to the POM through tris-alkoxo functionalization ($[V_6O_{13}\{(OCH_2)_3CNHCO(4\text{-}C_5H_4N)\}_2]^{2-}$ (Py-V_6O_{13}-Py)). **System II** (chapter III): we have firstly chosed Keggin-type POMs $[PW_{11}Si_2O_{40}C_{26}H_{16}N_2]$ TBA_3 (Py-$PW_{11}Si_2$-Py) and Dawson-type POMs $[P_2W_{17}Si_2O_{62}C_{26}H_{16}N_2]$ TBA_6 (Py-$P_2W_{17}Si_2$-Py) of which the two pyridyl groups were connected to the POM through organosilyl functionalization. Then, copolymeric films were directly obtained by the electro-oxidation of ZnOEP or H_2T_2P in the presence of Py-$PW_{11}Si_2$-Py or Py-$P_2W_{17}Si_2$-Py. **System III** (chapter IV): we introduce a bottom-up synthesis and have characterized four other films obtained from dipyridyle-substituted organo-polyoxometallic bricks using bis-alkoxo-amide functionalizations of Dawson structure $[P_2W_{15}V_3O_{62}]^{9-}$. All of the copolymers have been characterized by UV-vis spectroscopy, XPS (X-ray photoelectron spectroscopy), AFM (atomic force microscopy), EQCM (electrochemistry quartz crystal microbalance) and electrochemistry. Then, they were applied for photocurrent generation and photocatalytical recovery of metals (Ag and Pt).

By comparison, the silyl-Dawson-ZnOEP hybrid was the most promising candidate for photocurrent generation because of silyl-Dawson with better electron-reservoir ability and an acceptable compromise

between the rate of charge separation and the charge recombination. If changing the type of the porphyrin, for instance the silyl-Dawson-ZnOEP hybrid had lower charge transfer resistance than silyl-Dawson-H_2T_2P hybrid film. The obtained Ag nanostructures through photocatalysis were also affected by the type of POM, however, the getting Pt nanostructures were not influenced by the size and the charges of the POM to a large extent.

2 – Electrostatic polyoxometalate – porphyrin copolymeric films

In chapter V, we firstly used an electropolymerization method which based on the nucleophilic attack of pyridyl groups (4,4'-bipyridine or 1,1''-(1,3-propanediyl)bis-4,4'-bipyridinium) as Lewis bases onto electrogenerated dications to prepare porphyrin copolymers. POMs which are anionic clusters can be incorporated onto the aforementioned cationic porphyrin polymer to obtain POM-porphyrin copolymeric film. Both poly-ZnOEP-V^{2+}/$[NaP_5W_{30}O_{110}]^{14-}$ and poly-ZnOEP-V^{2+}-$(CH_2)_3$-V^{2+} /$[NaP_5W_{30}O_{110}]^{14-}$ (viologen abbreviated to V^{2+}) composite film electrodes possessed a 3.4 times and 1.3 times higher photocurrent response than in the absence of $[NaP_5W_{30}O_{110}]^{14-}$, respectively. This was due to the appropriate redox potential of $[NaP_5W_{30}O_{110}]^{14-}$ which acted as strong electron acceptor. EQCM and QCM was employed to monitor the mass change during the poly-ZnOEP-V^{2+} and poly-ZnOEP-V^{2+}-$(CH_2)_3$-V^{2+} copolymers electrodeposition (7.9 and 5.7 $\mu g.cm^{-2}$ respectively, applied potential: +1.9 V, elapsed time:180 s) and also for the incorporation process of $[NaP_5W_{30}O_{110}]^{14-}$ (0.61 and 0.77 $\mu g.cm^{-2}$ respectively, soaking time: 1 hour).

3 – Electrostatic porphyrin-Preyssler POM@MNPs copolymeric films

Surface plasmon resonance that occurs at the surface of silver (or gold) metal has substantially enhanced the electronic excitation of surface-anchored molecules and the charge carrier generation. In the chapter VI, one facile and easier strategy to get MNPs (Ag, Au, and Pt) with the help of Preyssler POM ($Na_{14}[NaP_5W_{30}O_{110}]$) (abbreviated P_5W_{30}) as photoelectrocatalyst has been used to get various core-shell POM@MNPs. Here, the POMs play a dual role, acting as both reducing agents and stabilizing anions. Then, we have introduced POM@MNPs at the surface of the bis-porphyrin copolymer (with pyridiniums as spacers) through metathesis reaction to further improve the efficiency of the

photocurrent generation.

If only P_5W_{30} was incorporated to the bis-porphyrin copolymer, the increase was 1.3 times. However, the incorporation of P_5W_{30}@AgNPs increase the photocurrent respond of bis-porphyrin copolymer with the greatest extent (up to four times). This can be attributed to the occurrence of the photoinduced electron transfer between pyridinium and P_5W_{30}, which decrease back electron combination, meantime, the localized surface plasmon resonance that occurs at the surface of silver nanoparticles has substantially enhanced the electronic excitation of surface-anchored porphyrin, and the excellent eletroconductivity of silver nanoparticles promoted the electronic transmission.

To conclude, the results presented in this thesis is an effort to further enhance the application of POM-porphyrin based hybrid materials. Various systems with designed geometries and structures have beed prepared and characterized by UV-vis spectroscopy, XPS, AFM, EQCM and electrochemistry. Then, we focus on the assessment of the reactivity of the materials under visible light irradiation for photocurrent generation or/and photocatalytic recovery of metals.

List of Abbreviations

H_2T_2P	5, 15 ditolylporphyrin
ZnOEP	zinc-β-octaethylporphyrin
TBA	tetrabutylammonium
HOMO	hightest occupied molecular orbital
LUMO	lowest unoccupied molecular orbital
H_2TPP	tetraphenylporphyrin
ZnTPP	zinc-tetraphenylporphyrin
NMR	nuclear magnetic resonance
DSSC	dye sensitized solar cell
POM	polyoxometalate
MNPs	metal nanoparticles
η	electric power conversion efficiency
PSSC	porphyrin-sensitized solar cells
J_{SC}	short-circuit current density
IPCE	incident photons to current
$H_2TPhN(Me)_3P^{4+}$	5,10,15,20-(4-trimethylammoniophenyl) porphyrin
ZnQMA	5,10,15,20-tetrakis(2,4,6-trimethylphenyl)-6'-arboxyquinoxalino[2,3-
ITO	indium tion oxide
SPR	surface plasmon resomance
PEI	polyethyleneimine
$(NH_4)_{42}\{Mo_{132}\}$	$(NH_4)_{42}[Mo_{132}O_{372}(CH_3COO)_{30}(H_2O)_{72}]$ *ca*.$300H_2O$ *ca*. $10CH_3COONH_4$
Mo_{154}	$[Mo_{154}O_{462}H_{14}(H_2O)_{70}]^{14-}$
Mo_{368}	$[H_xMo_{368}O_{1032}\ (H_2O)_{240}(SO_4)_{48}]^{48-}$
bmimpm	bis(1-methylimidazol-2-yl)-4-methoxyphen-1-ylmethanol
acac	acetylacetonate
H_2DPP	dodecaphenyl porphyrin
ET	electron transfer
D*	electron donor in its excited state
A	electron acceptor in its ground-state
BET	back electron transfer
H_2T_3P-4-py	5,10,15-tritolyl-20-(4-pyridyl) porphyrin
H_2T_3P-3-py	5,10,15-tritolyl-20-(3-pyridyl) porphyrin
H_2P_3P-4-py	5,10,15-triphenyl-20-(4-pyridyl) porphyrin
IC	internal conversion

MLCT	metal-to-ligand charge-transfer
ZnP	Zn-metallated porphyrin
FbP	free-base porphyrin
EnT	energy transfer
HT	hole transfer
cryo-TEM	cryogenic transmission electron microscopy
SAM	self-assembled monolayer
CNTs	carbon nanotubes
GNSs	graphene nanosheets
GNSs	graphene nanosheets
NN	nanonet
NW	nanowires
HRTEM	high-resolution TEM
XPS	X-ray photoelectron spectroscopy
AFM	atomic force microscopy
EQCM	electrochemistry quartz crystal microbalance
V_6O_{13}	$[V_6O_{13}\{(OCH_2)_3CNHCO(4\text{-}C_5H_4N)\}_2]^{2-}$
SCE	saturated calomel electrode
CV	cyclic voltammogram
f	frequency
Δm	mass change
GC	glassy carbon
UV	ultra violet
DMF	N,N-dimethylformamid
ε	molar extinction coefficient
Γ	surface coverage
EIS	electrochemical impedance spectroscopy
NHE	normal hydrogen electrode
$PW_{11}Si_2$	$[PW_{11}Si_2O_{40}C_{26}H_{16}N_2]^{3-}$
$P_2W_{17}Si_2$	$[P_2W_{17}Si_2O_{62}C_{26}H_{16}N_2]^{6-}$
Fc	ferrocene
$P_2W_{15}V_3$	$[P_2W_{15}V_3O_{62}]^{9-}$
bpy	4,4’-bipyridine
V	viologen
P_5W_{30}	$[NaP_5W_{30}O_{110}]^{14-}$
IR	infrared

LBL	layer-by-layer
BnOH	benzylalcohol
PPV	poly(p-phenylenevinylene) derivatives
EV^{2+}	ethylviologen
MV^{2+}	methylviologen

Contents

General introduction

Solar energy, as the cleanest and least limited energy source, becomes increasingly hot over recent years. Photoconversion of light into energy such as photovoltaic cells and artificial photosynthetic devices relies on the formation of photoinduced electronic charge separation with suitable lifetime and low back-electron transmission. Polyoxometalates (POMs) are a unique family of molecular-scale oxide clusters with remarkable diverse structural and electronic properties.[1] POMs are negatively charged electron acceptors with highly tunable redox potentials. Because of their robustness and the large number of high-oxidation-state transition metal atoms, POMs can undergo multi-electron photoredox processes without decomposition. However, POMs can be excited (POMs*) mainly under UV irradiation. To address this problem, POMs can be linked to visible light sensitizer, such as porphyrins, which play a key role in light harvesting and transfer the excited electrons to POMs, on the other hand, POMs as an excellent electron acceptor can retard undesirable backward charge recombination of the excited porphyrins.

POMs are anionic clusters, electrostatic hybrids can be fabricated with cationic chromophores such as organic dyes,[2,3,4] Ru or Re polypyridyl complexes,[5,6,7] or porphyrins and phthalocyanine[8,9], conveniently. Ruhlmann and coworkers[10] reported multilayer assembly $[H_2TPhN(Me)_3P^{4+}/\ \alpha_2\text{-}Fe(P_2W_{17}O_{61})^{7-}]_n$ constructed by layer-by-layer self-assembly strategy for the photocurrent generation.

POM–porphyrin coordination complexes were also reported, however, which are based on largely empirical oxo-coordination of transition metal complexes onto surface of POMs[11,12] and the coordination of the peripheral substituents of porphyrins and metal substituted POMs.[13]

The third approach is based on covalent linkage between the POM and the visible light photosensitizer. The target complexes can be tethered to POMs by grafting organic ligands onto the oxometallic framework which are more predictable and with well-defined geometries and anchoring mode. From the literature review, polyalkoxo[14, 15] and imido[16] functionalizations are the mainly two types of method to graft organic ligands to the POMs surface. Hybrids can also be prepared by covalent grafting organic moieties through heteroatom-insertion in a lacunary POM. [17,18,19] Anna Proust and coworkers have reported the synthesis and photophysical properties of a series of heteroleptic carbocyclometalated iridium(III)–POM conjugates.[20] Among them, Dawson-type organosilyl hybrid $[P_2W_{17}O_{61}\text{-}\{O(SiC_{36}H_{23}N_3O_2Ir)_2\}]^{6-}$ offers the best compromise between efficient charge separation and long-lived

charge-separated state and also able to perform photocatalytic hydrogen production under visible light without significant loss of performance over more than 1 week of continuous photolysis.[21]

To the best of our knowledge, for building functional devices with photovoltaic properties, there is only one example of covalent POM–chromophore polymers. Peng et al. reported a hybrid conjugated poly(phenylene acetylene) copolymer with hexamolybdate clusters embedded into the main chain through covalent bonds. The polymer was used as a component of a singlelayer photovoltaic device (indium tin oxide (ITO)/polymer/Ca configuration), which exhibited a power conversion efficiency of 0.15%.[22]

Recently, Ruhlmann et al has reported the formation of covalent Anderson type-POM–porphyrin film using an electropolymerization method based on the nucleophilic attack of pyridyl groups (bound on the Anderson type POM framework, $[MnMo_6O_{18}\{(OCH_2)_3CNHCO(4\text{-}C_5H_4N)\}_2]^{3-}$) onto electrogenerated porphyrin dications. The obtained film was used as a heterogeneous photocatalyst for the reduction of Ag^+ under visible light.[23]

The aim of the present thesis is to go beyond this proof of principle and to investigate new covalent and electrostatic POM – porphyrin hybrids and applied for photocurrent generation and/or photorecovery metal ions (Ag(I) and Pt(IV)).

In the last decade, the metal nanoparticles (MNPs) has emerged as a new kind of compound that has attracted intensive attention due to its unique optical, electronic, catalytic, and magnetic properties.[24,25,26] Significantly, localized surface plasmon resonance that occurs at the surface of silver (or gold) metal has substantially enhanced the electronic excitation of surface-anchored molecules and the charge carrier generation.[27,28] However, pure MNPs are unstable and easily gather together,[24] which restricts their utility in the catalyst industry.

In this thesis, one facile and easier strategy to get stable MNPs (M = Ag, Au, or Pt) with the use of POMs has been applied to get various P_5W_{30}@MNPs nanoparticles.[29] Here, the Preyssler's type POMs ($Na_{14}[NaP_5W_{30}O_{110}]$) ($P_5W_{30}$) play a dual role, acting as both reducing agents and stabilizing anions (surfactant). To further increase the conversion efficiency of photon energy to electrical energy, we introduce P_5W_{30}@MNPs (M = Ag, Au, Pt) nanoparticles on to the surface of the bis-porphyrin copolymer in order to try to promote more the efficiency of the photocurrent generation.

References

(1) Long, D.-L.; Tsunashima, R.; Cronin, L. *Angew. Chem. Int. Ed. Engl.* **2010**, *49* (10), 1736.
(2) Xie, J.; Abrahams, B. F.; Wedd, A. G. *Chem. Commun. (Camb).* **2008**, No. 5, 576.
(3) Nie, S.; Zhang, Y.; Liu, B.; Li, Z.; Hu, H.; Xue, G.; Fu, F.; Wang, J. *J. Solid State Chem.* **2010**, *183* (12), 2957.
(4) Zhang, H.; Peng, J.; Shen, Y.; Yu, X.; Zhang, F.; Mei, J.; Li, B.; Zhang, L. *Chem. Commun.* **2012**, *48* (37), 4462.
(5) Ruhlmann, L.; Costa-Coquelard, C.; Hao, J.; Jiang, S.; He, C.; Sun, L.; Lampre, I. *Can. J. Chem.* **2008**, *86* (11), 1034.
(6) Ettedgui, J.; Diskin-Posner, Y.; Weiner, L.; Neumann, R. *J. Am. Chem. Soc.* **2011**, *133* (2), 188.
(7) Walsh, J. J.; Long, D.-L.; Cronin, L.; Bond, A. M.; Forster, R. J.; Keyes, T. E. *Dalton Trans.* **2011**, *40* (9), 2038.
(8) Santos, I. C. M. S.; Rebelo, S. L. H.; Balula, M. S. S.; Martins, R. R. L.; Pereira, M. M. M. S.; Simões, M. M. Q.; Neves, M. G. P. M. S.; Cavaleiro, J. a. S.; Cavaleiro, A. M. V. *J. Mol. Catal. A Chem.* **2005**, *231* (1-2), 35.
(9) Costa-Coquelard, C.; Sorgues, S.; Ruhlmann, L. *J. Phys. Chem. A* **2010**, *114* (22), 6394.
(10) Ahmed, I.; Wang, X.; Boualili, N.; Xu, H.; Farha, R.; Goldmann, M.; Ruhlmann, L. *Appl. Catal. A Gen.* **2012**, *447-448*, 89.
(11) Piepenbrink, M.; Triller, M. U.; Gorman, N. H. J.; Krebs, B. *Angew. Chemie - Int. Ed.* **2002**, *41* (14), 2523.
(12) Yokoyama, A.; Kojima, T.; Ohkubo, K.; Shiro, M.; Fukuzumi, S. *J. Phys. Chem. A* **2011**, *115* (6), 986.
(13) Schaming, D.; Costa-Coquelard, C.; Lampre, I.; Sorgues, S.; Erard, M.; Liu, X.; Liu, J.; Sun, L.; Canny, J.; Thouvenot, R.; Ruhlmann, L. *Inorganica Chim. Acta* **2010**, *363* (10), 2185.
(14) Chen, Q.; Chen, Q.; Goshorn, D. P.; Goshorn, D. P.; Scholes, C. P.; Scholes, C. P.; Tan, X. L.; Tan, X. L.; Zubieta, J.; Zubieta, J. *J. Am. Chem. Soc.* **1992**, *114* (12), 4667.
(15) Li, J.; Huth, I.; Chamoreau, L. M.; Hasenknopf, B.; Lacôte, E.; Thorimbert, S.; Malacria, M. *Angew. Chemie - Int. Ed.* **2009**, *48* (11), 2035.
(16) Kang, J.; Nelson, J. a; Lu, M.; Xie, B.; Peng, Z.; Powell, D. R. *Inorg. Chem.* **2004**, *43* (20), 6408.
(17) Odobel, F.; Séverac, M.; Pellegrin, Y.; Blart, E.; Fosse, C.; Cannizzo, C.; Mayer, C. R.; Elliott, K. J.; Harriman, A. *Chem. - A Eur. J.* **2009**, *15* (13), 3130.
(18) Harriman, A.; Elliott, K. J.; Alamiry, M. a H.; Pieux, L. Le; Séverac, M.; Pellegrin, Y.; Blart, E.; Fosse, C.; Cannizzo, C.; Mayer, C. R.; Odobel, F. *J. Phys. Chem. C* **2009**, *113* (14), 5834.
(19) Elliott, K. J.; Harriman, A.; Le Pleux, L.; Pellegrin, Y.; Blart, E.; Mayer, C. R.; Odobel, F. *Phys. Chem. Chem. Phys.* **2009**, *11* (39), 8767.
(20) Matt, B.; Xiang, X.; Kaledin, A. L.; Han, N.; Moussa, J.; Amouri, H.; Alves, S.; Hill, C. L.; Lian, T.; Musaev, D. G.; Izzet, G.; Proust, A. *Chem. Sci.* **2013**, *4* (4), 1737.
(21) Matt, B.; Fize, J.; Moussa, J.; Amouri, H.; Pereira, A.; Artero, V.; Izzet, G.; Proust, A. *Energy Environ. Sci.* **2013**, *6* (5), 1504.
(22) Lu, M.; Xie, B.; Kang, J.; Chen, F.-C.; Peng, Z. *Chem. Mater.* **2005**, *17* (2), 402.
(23) Schaming, D.; Allain, C.; Farha, R.; Goldmann, M.; Lobstein, S.; Giraudeau, A.; Hasenknopf, B.; Ruhlmann, L. *Langmuir* **2010**, *26* (7), 5101.
(24) Reiss, G.; Hutten, A. *Nat Mater* **2005**, *4* (10), 725.
(25) Singamaneni, S.; Bliznyuk, V. N.; Binek, C.; Tsymbal, E. Y. *J. Mater. Chem.* **2011**, *21* (42), 16819.
(26) Georgakilas, V.; Gournis, D.; Tzitzios, V.; Pasquato, L.; Guldi, D. M.; Prato, M. *J. Mater. Chem.* **2007**, *17* (26), 2679.
(27) Akiyama, T.; Aiba, K.; Hoashi, K.; Wang, M.; Sugawa, K.; Yamada, S. *Chem. Commun. (Camb).* **2010**, *46* (2), 306.
(28) Akiyama, T.; Nakada, M.; Terasaki, N.; Yamada, S. *Chem. Commun.* **2006**, No. 4, 395.
(29) Troupis, A.; Hiskia, A.; Papaconstantinou, E. *Angew. Chem. Int. Ed. Engl.* **2002**, *41* (11), 1911.

Chapter I

Chapter I: Introduction and literature review

1. Porphyrins

1.1 Structure, nomenclature and properties

1.1.1 Structure and nomenclature

Porphyrins are substituted derivatives of porphine, an organic macrocycle consisting of four pyrrole rings linked together by four methine bridges. This macrocycle is composed of 20 carbon atoms with 22 electrons, 18 relocatable impart its aromaticity. The carbon atoms are numbered from 1 to 20 according to the nomenclature adopted by IUPAC in 1987. Porphine rings inlcude three types of carbon atoms: α, β (located on the pyrroles), and meso (located at the methine bridges) (Fig.1.1). The substituents could be tethered either on the β positions or meso positions.[1]

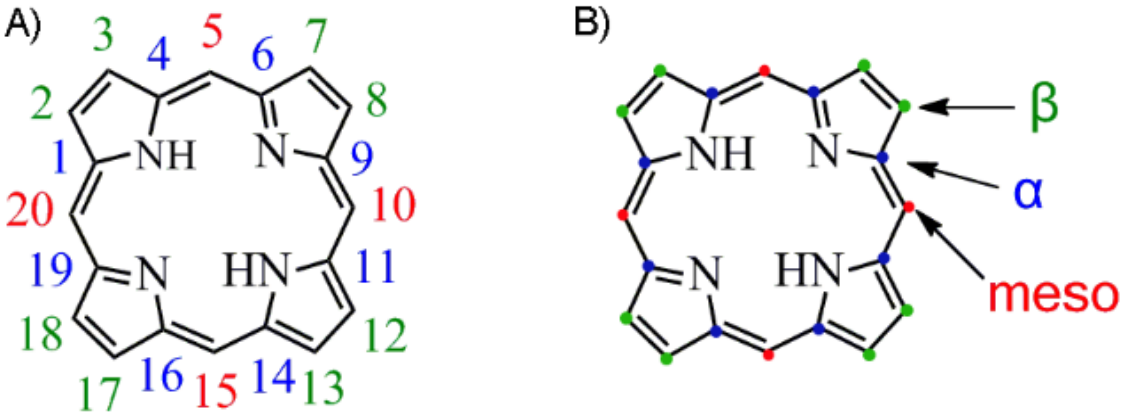

Fig. 1.1 Porphine macrocycle A) I.U.P.A.C nomenclature, B) localization of the α, β and *meso* positions.

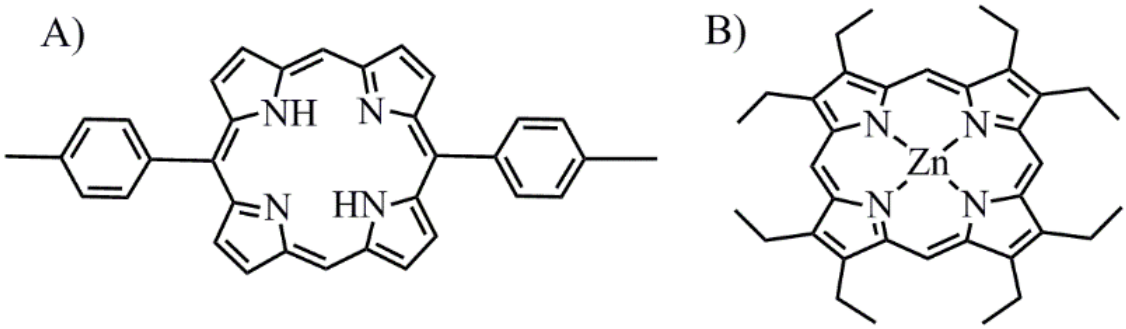

Fig. 1.2. A) free base 5, 15-ditolylporphyrin (**H_2T_2P**) and B) zinc-β-octaethylporphyrin (**ZnOEP**).

There are two types of porphyrins, which differ in the occupation of the central porphine core: the free base porphyrins, for which the the macrocycle center is occupied by two hydrogen atoms (Fig. 1.2A) and metalloporphyrins, for which the central region is a metal cation (Fig. 1.2B).

1.1.2 Electrochemical properties

The free base porphyrins are oxidized in two reversible one-electron steps to yield the radical monocation and the dication.[2,3] Similarly, their reduction process is also reversible in general, leading to the radical monoanion and dianion (Fig. 1.3). However, the redox processes of the porphyrin derivatives may become irreversible affected by the substituents. Moreover, for some porphyrins in anhydrous solvents and with a specially selected working electrode (usually a mercury drop electrode), it is possible to observe up to two additional reduction waves, corresponding to the formation of the tri-anion radical and the tetra-anion.[4,5]

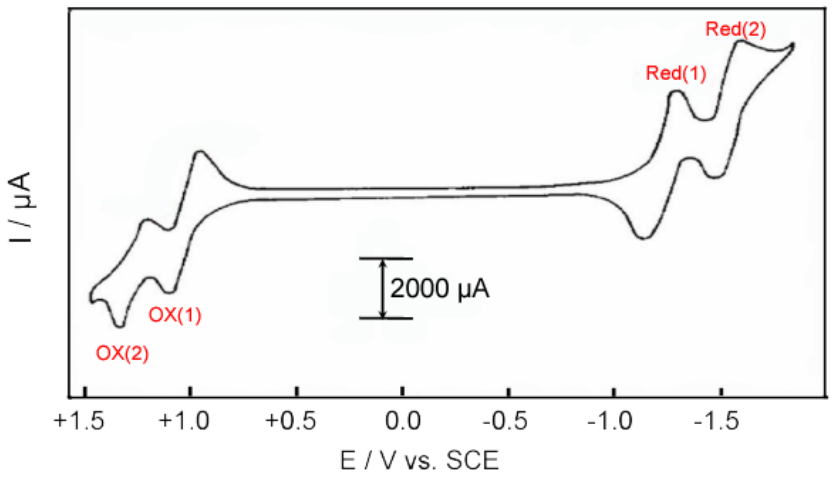

Fig. 1.3. Cyclic voltammogram of 2.5 × 10^{-4} mol L^{-1} octaethylporphyrin H_2OEP in 1,2-CH_2Cl_2 containing 0.1 mol L^{-1} $TBAPF_6$, scan rate : 50 mV s^{-1}.

Metalloporphyrins include two types of redox behavior, lying on the nature of the central cation.[3] One type is the metalloporphyrin with an electrochemically inert metal cation (Zn^{2+}, Ru^{2+}, Mg^{2+}, Pd^{2+}, Cu^{2+}). Redox process is similar as the corresponding free base porphyrin, however, the metal is able to affect the redox potentials. The second type is that metalloporphyrins with electroactive metal cation (Fe^{3+}, Ni^{2+}, Co^{2+}, Au^{3+}, Mn^{2+}). In this case, an additional wave of the reduction or oxidation of the metal cation is observable.

Empirical rules derived from experimental results of series of tetraphenylporphyrin and octaethylporphyrin[2,3] can be extended to study the redox processes of the porphyrin cycle with other substituents or central metal cation:

1. The difference between the potentials of the first and second reduction of the porphyrin ring is 0.42 ± 0.05 V;

2. The potential difference between the first and second oxidation of the porphyrin ring is 0.29 ± 0.05 V;

3. The distance between the potentials of the first reduction and first oxidation of the porphyrin ring is 2.25 ± 0.15 V. Moreover, this potential difference may be associated with the energy gap between the highest occupied molecular orbital (HOMO) and the lowest unoccupied molecular orbital (LUMO).

1.1.3 Spectral properties

1.1.3.1 UV-visible absorption spectroscopy

Porphyrin macrocycles are highly conjugated systems and consequently they typically have very intense absorption bands in the visible region and deeply colored; the name "porphyrin" comes from the greek word porphyros, meaning purple. Porphyrins possess a very intense absorption band ($5 \times 10^5 > \varepsilon > 10^5$ mol L^{-1} cm^{-1}), named Soret or B band, located between 390 and 450 nm (sometimes on highter wavelength which depends on the substituent), as well as several bands with lower intensity, called Q bands, which also located in the visible range, between 450 and 800 nm (Fig. 1.4).

The transition of $3a_{2u}$ (π)→$4e_g$ (π^*) leads to the first excited state S_1 which is a forbidden transition in theory, but is still observable because of a vibratory ionic coupling. The transition of $S_0 \rightarrow S_1$ generates Q bands. For metalloporphyrins, the spectra show two Q bands, named α (band at higher wavelength) and β (band at lower wavelength), and corresponding to vibrational transitions v = 0→v' = 0 and v = 0→v' = 1, respectively.

The non-equivalent HN-NH and N-N axis in free base porphyrin induce D_{2h} symmetry (D_{4h} for metallated porphyrin) and the presence of two electric dipole transitions, so, free base porphyrins possess four Q bands. Q bands are very sensitive to the geometry and substituents of the macrocycle and the nature of the central metal cation. The Soret band comes from the transition $1a_{1u}(\pi) \rightarrow 4e_g(\pi^*)$

which is a type of $S_0 \rightarrow S_2$ transition. It should be pointed out that it is possible to observe additional absorption bands in some porphyrins in the ultra-violet region, called N and L corresponding to the transitions of $S_0 \rightarrow S_3$ and $S_0 \rightarrow S_4$ respectively.[1]

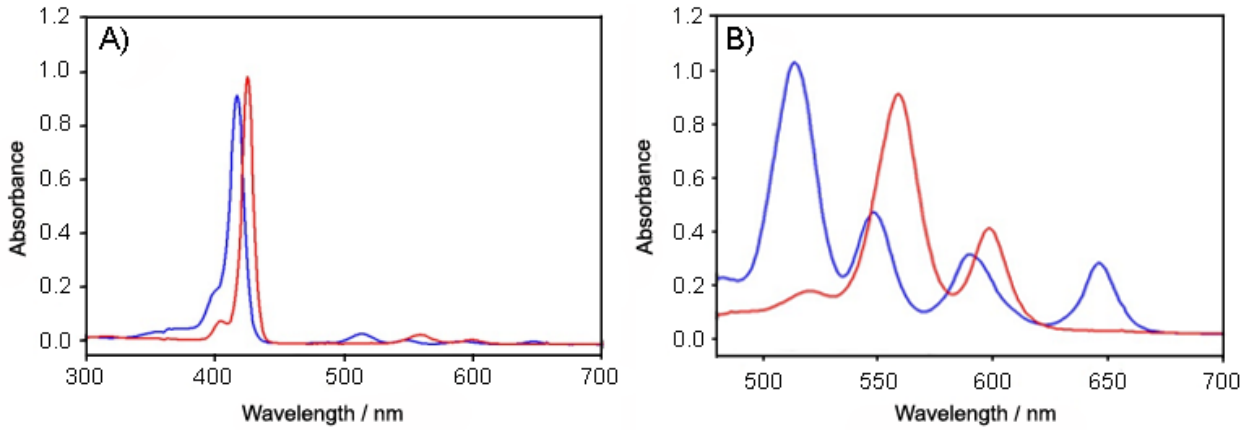

Fig. 1.4. UV-visible absorption spectra of free base tetraphenylporphyrine, H_2TPP (—) and Zinc tetraphenylporphyrin, ZnTPP (—). A) c = 2.5 $\times 10^{-6}$ mol L^{-1} (full spectra) and B) c = 5 $\times 10^{-5}$ mol L^{-1} (Q bands region) in DMF.

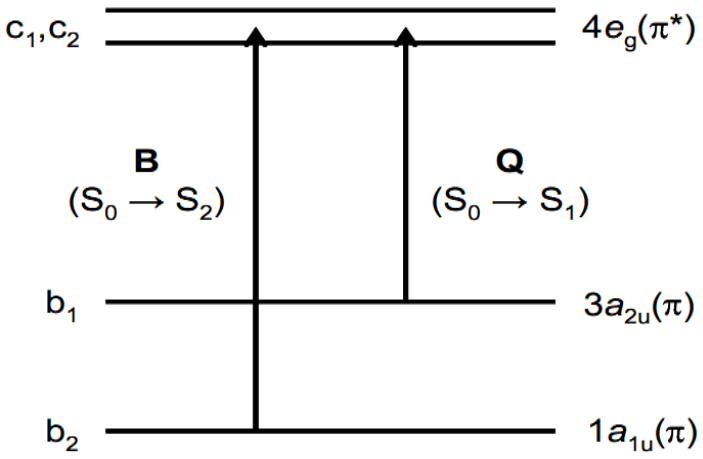

Fig. 1.5. Electron transmission diagram of porphyrin.

1.1.3.2 Fluorescence spectroscopy

The excitation of porphyrins in one of excited states S_x is followed by a rapid internal conversion to the lowest excited state S_1 in 10^{-12}-10^{-13} s. Thus, depending on the excitation is nonradiative or radiative processes, porphyrins are fluorescent or non-fluorescent, respectively. In practice, if porphyrin with a quantum efficiency greater than 10^{-3}, it can be affirmed as fluorescent porphyrin.[1]

The occupation of the macrocycle center master the fluorescent characteristic of the porphyrins. Generally, the free base porphyrins are highly fluorescent. Metalloporphyrins depend on the nature of central metal cation, for example, the zinc porphyrin (Fig 1.5) is fluorescent while the iron porphyrin is non-fluorescent.

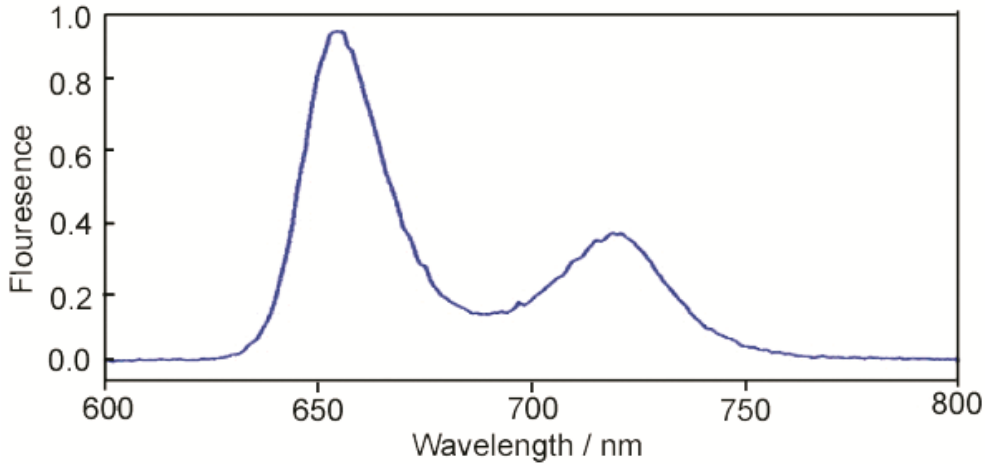

Fig. 1.6 Fluorescence spectrum (λ_{exc} = 510 nm) of the ZnOEP in DMF.

1.1.4 ^{1}H NMR characterization

The ring current induced by the magnetic field imposed by the spectrometer generates a large magnetic anisotropy cone whose axis is perpendicular to the plane of the macrocycle. Thus, the protons located outside of this cone are strongly deshielded (between 7 and 10 ppm), while those located inside (NH porphyrin free bases) are heavily armored ($\delta < 0$) (Fig. 1.7).

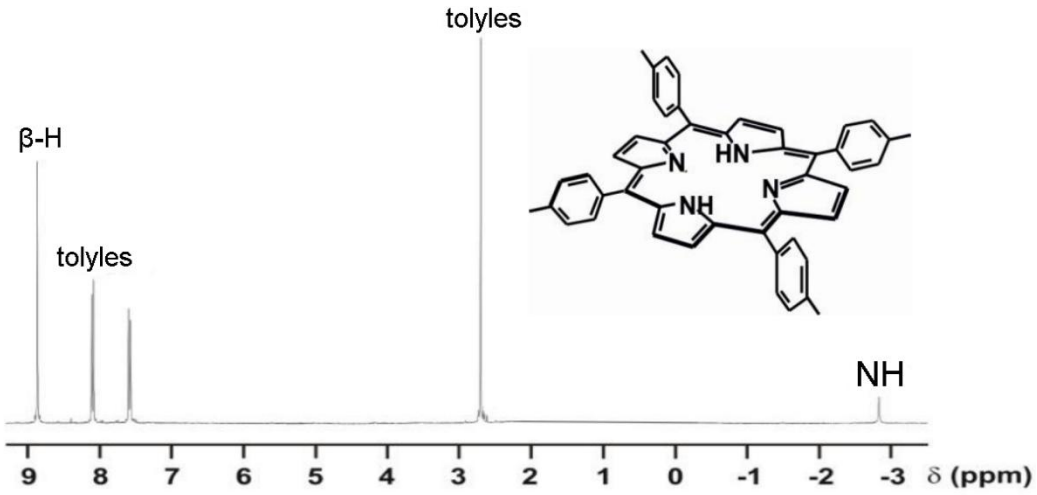

Fig. 1.7. ^{1}H NMR spectrum of H_2TPP in CD_2Cl_2. Frequency: 300 MHz.

1.2 Porphyrin-based artificial light-harvesting systems

Nature has selected chlorophylls as antennae in plants to harvest light for the conversion of solar energy in the photosynthetic processes. Inspired by natural photosynthesis, scientists attempted to import artificial chlorophylls – the porphyrins – as efficient centers to absorb light for opto-electronic applications.

1.2.1 Porphyrin/TiO_2

In 1991, O'Regan and Grätzel firstly demonstrated the concept of low cost, high efficiency dye sensitized solar cells (DSSC) using a ruthenium dye-sensitized colloidal TiO_2 films and an iodide/triiodide redox mediator.[6]

Fig. 1.8 shows the schematic diagram of a typical DSSC device, which is comprised of a dye-sensitized mesoporous working electrode (TiO_2, anode) and a counter electrode (Pt-coated, cathode), and the electrolyte (iodine-based or cobalt complexes, redox mediator) filling in the space between the anode and the cathode. The critical elements of the cell are light absorption and initial charge separation by the dye molecule (eqn (1)), followed by charge stabilisation through rapid electron injection into the TiO_2 conduction band (eqn (2)) and dye regeneration by the I^- (or Co^{2+}) (eqn (3)). Finally, the reduction of I_3^- (or Co^{3+}) at the counter electrode completes the cycle (eqn (4)).

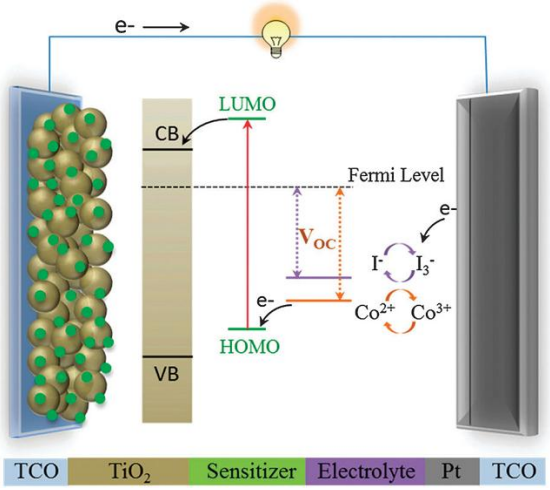

$$TiO_2\text{–}P + h\nu \rightarrow TiO_2\text{–}P^* \quad (1)$$

$$TiO_2\text{–}P^* \rightarrow TiO_2(e^-)\text{–}P^+ \quad (2)$$

$$2TiO_2(e^-)\text{–}P^+ + 3I^- \rightarrow 2TiO_2(e^-)\text{–}P + I_3^- \quad (3)$$

$$I_3^- + 2e^- \rightarrow 3I^- \quad (4)$$

Figure 1.8 Structure and operating principle of a typical DSSC.(Pigment named P).

Since 2000, lots of effort has been expended to enhance optical power convention efficiency on

porphyrin-based materials. According to my literature review, there are three primary strategies adopted to boost this value:

a) Modification of the porphyrin properties, exploring the electron transfer photophysics and establish a correlation between the films structure and the photocurrent efficiency;
b) Construction of complicated molecular systems employing a cascade architecture such as supermolecular assemblies of porphyrins with semiconductor or semiconductor-like materials (I chose polyoxometalate (POM) in my research), metal nanoparticles (MNPs) (I chose POM@MNPs in my research), fullerene or carbon nanomaterials, based on the efficient charge separation.
c) Mimicry of the photosynthetic reaction center using a porphyrin slipped cofacial dimer.

In ruthenium-based sensitized nanocrystalline TiO_2 solar cells, the light to electric power conversion efficiencies (η) up to 12.1 %, however, which is employing both DX1 and the traditional sensitizer N719 as sensitizer (η of the single DX1 is 10.4%).[7–13] The rarity, cost, and environmental issues of ruthenium complexes hinder their wide application, and encourage to explor the sufficient, cheaper and safer sensitizers. Researchers have made tremendous efforts in seeking new and efficient sensitizers suitable for practical use in DSSC.[9–45] Fig. 1.9 shows the evolution of photovoltaic performances of DSSC from 1991 to 2015 based on three types of potential and widely investigated photosensitizers.[46] For the ruthenium-based sensitizers, the efficiency of the N3 dye already reached 10.0% in 1993;[47] the benchmark performance of the N3/N719 family was reported to be 11.2% in 2005,[7] and the record efficiency of the C106 dye was 11.7% in 2010.[11] The efficiencies of metal-free organic dyes were reported to be 9–10% during 2005-2013 with the best-performed organic dye (C219) reaching η = 10.3%.[34] The development of metal-free organic sensitizers seems to meet a bottleneck, until 2014, the appearence of ADEKA-1 brough a new hope. However, recent developments of porphyrin-sensitized solar cells (PSSC) with a feature of exponential rise attracts more and more attention of scientists.[18–25,48,49]

As previously mentioned, the intrinsic superiority of porphyrin-based dyes are their rigid molecular structures with large absorption coefficients in the visible region and many chemical reaction active sites. Porphrins possess four meso and eight β positions, which are available for functionalization, in

order to telic tuning of the optical, electrochemical, physical, and photovoltaic properties.

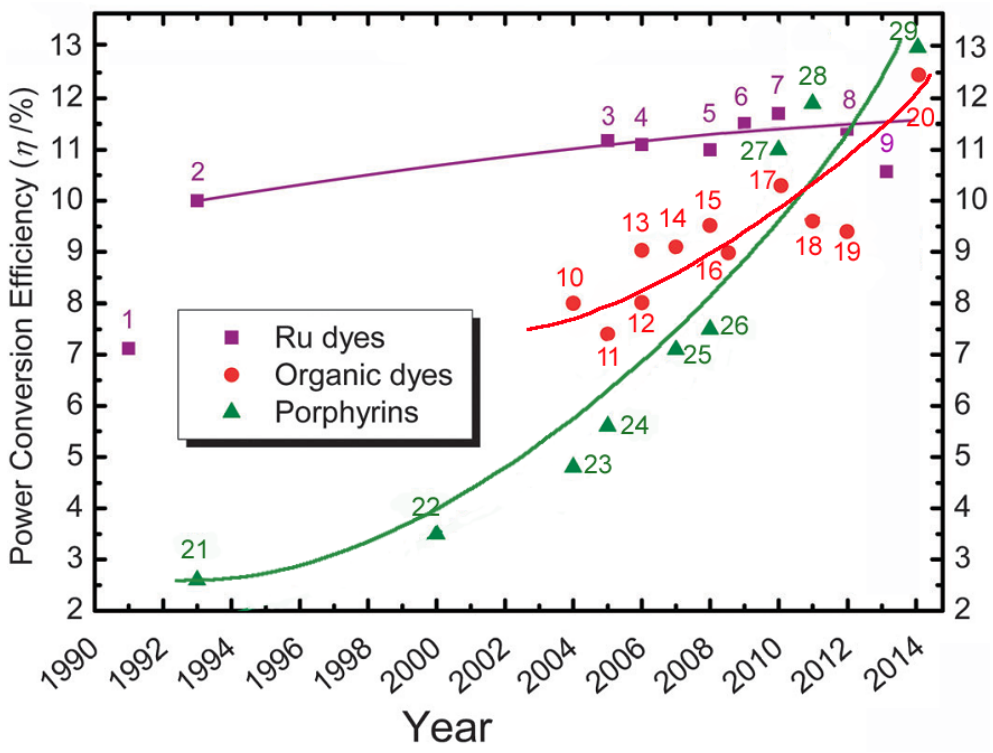

Fig. 1.9 Efficiency progressing records of DSSC from 1991 to 2015 on the basis of three representative sensitizers labelled **1–9** for Ru-based complexes (■), **10–20** for organic dyes (●) and **21–29** for porphyrin dyes (▲). The labelled sensitizers may have an alternative given name or a specific code given by the authors: (1) trinuclear Ru dye,[6] (2) N3,[47] (3) N3,[7] (4) N719,[8] (5) C101,[26] (6) CYC-B11,[9] (7) C106,[11] (8) black dye,[12] (9) DX1,[13] (10) indoline dye,[27] (11) NKX-2677,[28] (12) JK2,[29] (13) D149,[30] (14) TA-St-CA,[31] (15) MK-2,[32] (16) D205,[33] (17) C219,[34] (18) Y123,[35] (19) C218,[36] (20) ADEKA-1,[48] (21) Cu-2-a-oxymesoisochlorin,[37] (22) TCPP,[38] (23) Zn-1a,[39] (24) Zn-3,[40] (25) GD2,[41] (26) tda-2b-bd-Zn,[42] (27) YD-2,[43] (28) YD2-oC8,[25] and (29) SM315.[49]

Porphyrins with linkers at *β*-position. In 1993, Kay and Grätzel firstly reported a porphyrin type copper chlorophyll as a photosensitizer for PSSC with η = 2.6%,[37] then, no breakthrough of PSSC until 2004 Burrell, Grätzel and their co-workers reported *β*-linked zinc porphyrins.[39,44] In 2007, the same groups published *β*-linked zinc porphyrin sensitizers in another series with the best one (GD2, Fig. 1.10a) reaching η =7.1%[41] opening up a promising possibility for the creation of new porphyrin sensitizers to boost the efficiency of DSSC.

Porphyrins with linkers at meso-position. Diau, Yeh and co-workers[50] reported meso-substituted zinc porpyrin derivatives, for which YD0 (Fig. 1.10b) acted as a reference. YD1 (η = 6.0%) with the

diarylamino group linked at the meso-position of the porphyrin (Fig. 1.10c) was comparable to that of N3 dye (η= 6.1%) under the same experimental conditions in 2009.[50] YD1 demonstrated outstandingly great short-circuit current density (J_{SC}) which was attributed to the high efficiency of conversion of incident photons to current (IPCE) broadly extending beyond 700 nm. The electron donor in YD1 not only extend the absorption region but also push the excited electrons toward TiO_2 in order to improve the charge separation. The push–pull framework of YD1 indicates the arrival of the era of PSSC.

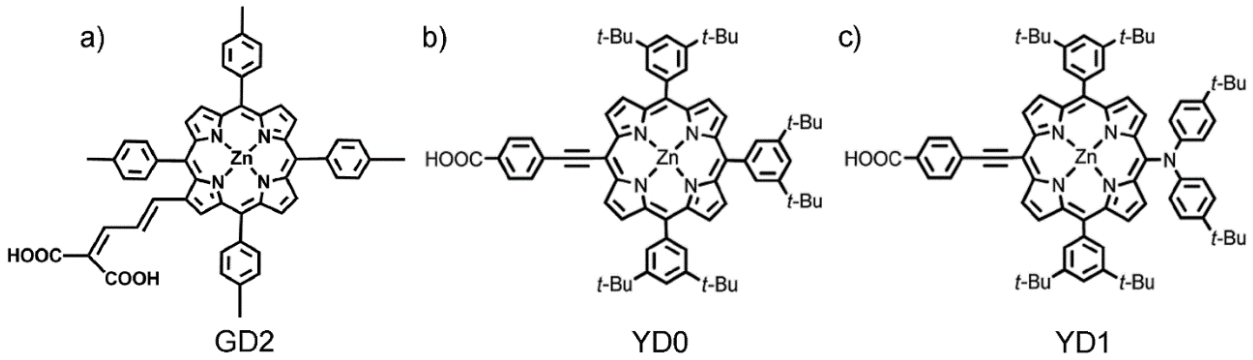

Fig. 1.10 Molecular structures of a) GD2, b)YD0, and c) YD1.

Porphyrins with extended spsctral feature. The most viable way to increase J_{SC} is to harvest a broader region of the solar spectrum. To extend the absorption of porphyrin dyes to the near infrared region, we must decrease the energy gap between HOMO and LUMO. For this purpose, the first strategy is to introduce a highly conjugated π-extended chromophore coupled with the porphyrin ring: Lin and Diau designed anthracene-functionalized porphyrin (LAC-3, Fig. 1.11a),[51] fluorene-functionalized porphyrin (LD22, Fig. 1.11b)[52] with η = 7.3% and pyrene-functionalized porphyrin (LD4, Fig. 1.11c)[53] with η = 10.1%, which was superior to that of N719(η = 9.3%) ;

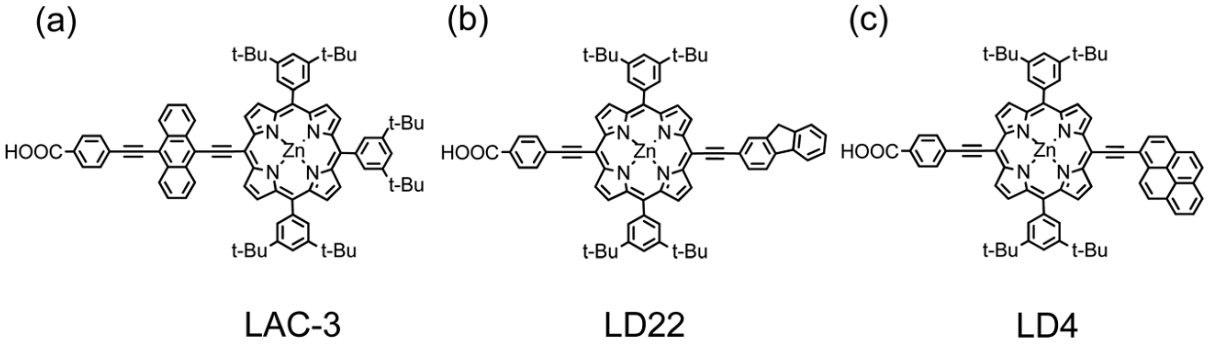

Fig. 1.11 Molecular structures of (a) LAC-3, (b) LD22 and (c) LD4.

The second strategy is to synthesise fused porphyrins : this idea became mature and practical when

Imahori and co-workers[54,55,] reported their first examples, of which a device fabricate with a naphthalene-based meso-*β*-edge fused zinc porphyrin (fused-Zn-1, Fig. 1.12a) (η = 4.1%) (5.0% under co-sensitization), which was improved by half relative to the reference cell with an unfused porphyrin. Then, they achieved an unsymmetrical π-elongation[56] to build quinoxaline-based *β*-*β*-edge fused zinc porphyrins, of which one anchoring group (5,10,15,20-Tetrakis(2,4,6-trimethylphenyl)-6'-carboxyquinoxalino[2,3-*β*]porphyrinatozinc (II) (ZnQMA), Fig. 1.12b) gained η= 5.2%, nearly 80% performance of N719 device under the same conditions.

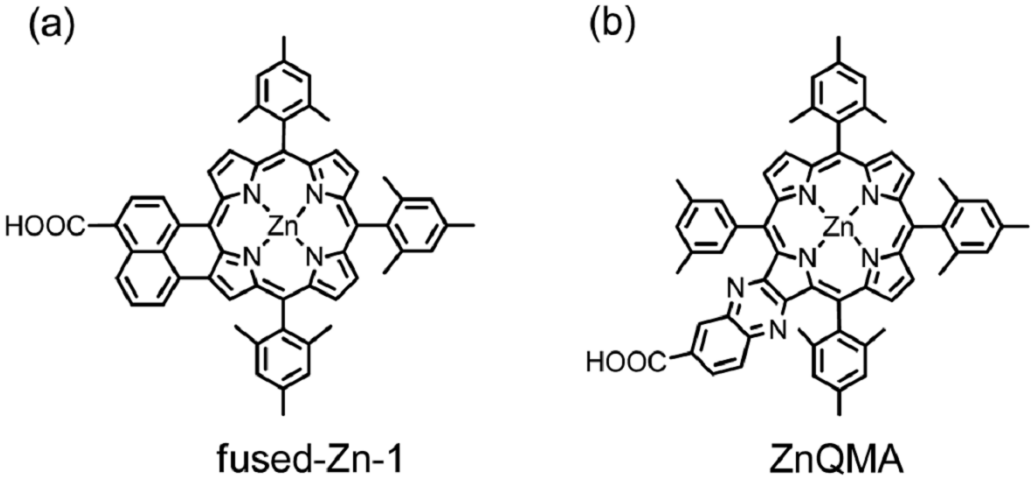

Fig. 1.12 Molecular structures of (a) fused-Zn-176, and (b) ZnQMA.

The third strategy is to form dimeric porphyrins: Derived from the structure of YD0 (Fig. 1.10b), Diau and Yeh[57] designed two porphyrin dimers, YDD0 (Fig. 1.13a) and YDD1 (Fig. 1.13b). Similar to the results of Kim and Osuka,[58] the spectrum of YDD1 only showed slightly red-shifted compared to that of the monomeric YD0. However, due to effective excitonic coupling between the two nearly perpendicular porpyrin units in YDD1, the gap in the IPCE spectrum of YD0 was completely filled in the spectrum of YDD1, leading to enhancement of the J_{SC} in the YDD1 device. With the link of an ethynyl group between the two monomeric units, YDD0 exhibit red shifts, split Soret bands between 400 and 500 nm, and broadening of the Q bands to nearly 800 nm. Because of the co-planar structural feature of YDD0 leading to serious dye aggregation, the broad IPCE spectrum of YDD0 exhibit much smaller efficiency, < 40%, than those of YD0 and YDD1 (~70%). Analogous to the structural design of YDD0, Segawa and co-workers[59] added a carbazole electron-donating groups (EDG) at the meso-

position of the porphyrin edge to form a push–pull porphyrin dimer, DTBC (Fig. 1.14c). The absorption spectrum of DTBC was similar to that of YDD0, but its IPCE spectrum showed much greater efficiency than that of YDD0, and DTBC obtained an optimized device performance η = 5.2%[59] higher than the performance of YDD0, η = 4.1%.[57]

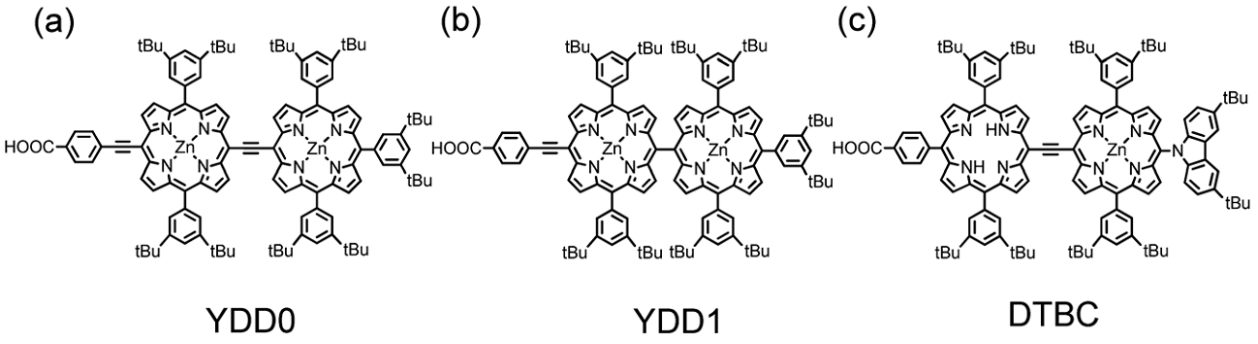

Fig. 1.13 Molecular structures of (a)YDD0, (b) YDD1, and DTBC.

Porphyrin-based donor–π–acceptor (D–π–A) dyes. The porphyrin chromophores possess intrinsically strong light absorption in the Soret and Q-bands, however, the lack of significant absorption in the spectral region between these two features need to be overcomed. In 2014, Grätzel[49] reengineered the prototypical structure of D–π–A porphyrins: the porphyrin core with the bulky bis (2′, 4′-bis(hexyloxy)-[1,1′-biphenyl]-4-yl) amine[60] donor and a 4-ethynyl-benzoic acid yielded the green dye SM371, which exhibited slightly better performance (12.0%) than the previous state-of-the-art YD2-o-C8 (11.9%).[25] Incorporation of the proquinoidal benzothia-diazole unit into this structure afforded the dye SM315, a panchromatic porphyrin sensitizer (Fig. 1.14 left). Relatively to SM371, SM315 exhibited significant broadening of Soret and Q-band absorbance features yielding improved light harvesting in both the green (500–600 nm) and red (up to 800 nm) region of the spectrum, leading to an improved J_{SC} (18.1 versus 15.9 mA cm^{-2} for SM315 and SM371, respectively) in the DSSC (Fig. 1.14 right). Ultimately, without the requirement of a co-sensitizer, the panchromatic sensitizer SM315 achieved a record η=13.0% at full sun illumination.[49]

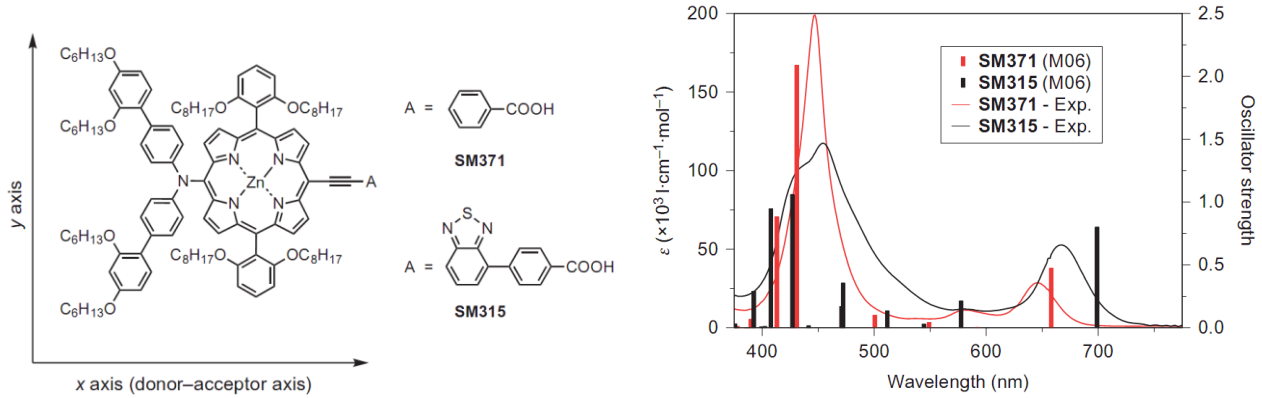

Fig. 1.14 Left: structures of SM371 and SM315. Right: absorption spectra of SM371 and SM315.

1.2.2 Porphyrin/metal nanoparticles

Metal nanoparticles (MNPs) have been caught much attention for their unique optical properties and have been utilized to improve the efficiency of photoelectric conversion in solar cells,[61,62,63] solid-state photodiodes,[64–69], photodetecters,[70,71] and so on. Specially, in 2005, Yamada[72] constructed multistructure assemblies of the self-assembled monolayered disulfide derivative of porphyrin ($[Po]_2$) on the surface of gold nanoparticals (AuNP, diameyer = 14 ± 1 nm) film that was generated at liquid/liquid interface at the level of nanoparticle layer and then transferred onto the the surface of a planar gold electrode, named ITO/AuNP/Po (ITO: indium tion oxide). This assemblies exhibits enhancement of photocurrent from the self-assembled monolayer of Po in a wide wavelength region, where the AuNP localized plasmon resonance (LPR) was responsible. Based on LPR, gold nanoparticles with several to several tenths of nanometers diameters show distinct absorption bands in the visible to near-infrared region. Thus, their multistructures are expected to intensify the electronic excitation of surface-anchored molecules by localized field of surface plasmon, generating enhanced electron-transfer (that is photocurrent), more efficiently in visible to near-infrared region. Remarkably, a noteworthy superiority of using the LPR-responsible gold nanoparticles is that the localized plasmon itself is independent of the incident angle differ from the surface plasmon resomance (SPR), as illustrated in Fig. 1.15a and Fig. 1.15b. As reference, AuNP was replaced by a planar gold electrode using vacuum deposition of gold onto the ITO electrode as: ITO/Au/Po. The photocurrent intensities of ITO/AuNP/Po at longer wavelengths are relatively larger as compared with those of ITO/Au/Po (Fig 1.16a).

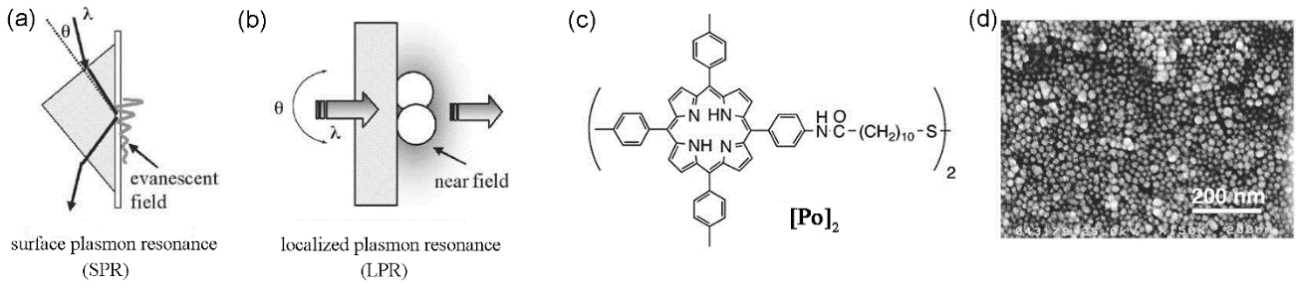

Fig. 1.15 Illustrated outline of (a) surface plasmon resonance and (b) localized plasmon resonance. (c) Structure of a disulfide derivative of porphyrin $[Po]_2$. (d) SEM image of ITO/AuNP/Po.

Fig. 1.16b showed the photocurrent comparison of ITO/AuNP/Po to ITO/Au/Po, which was not equal to Po molecules ratios of ITO/AuNP to ITO/Au electrodes, and dependent of the irradiation wavelength. It is clear that the photocurrent ratio is increasing in ~500 – ~700 nm region which was corresponding to the broad plasmon band of the multistructured assembly of gold nanoparticles. The authors did not make certain this time why the photocurrent ratios show a peak around 460 nm.

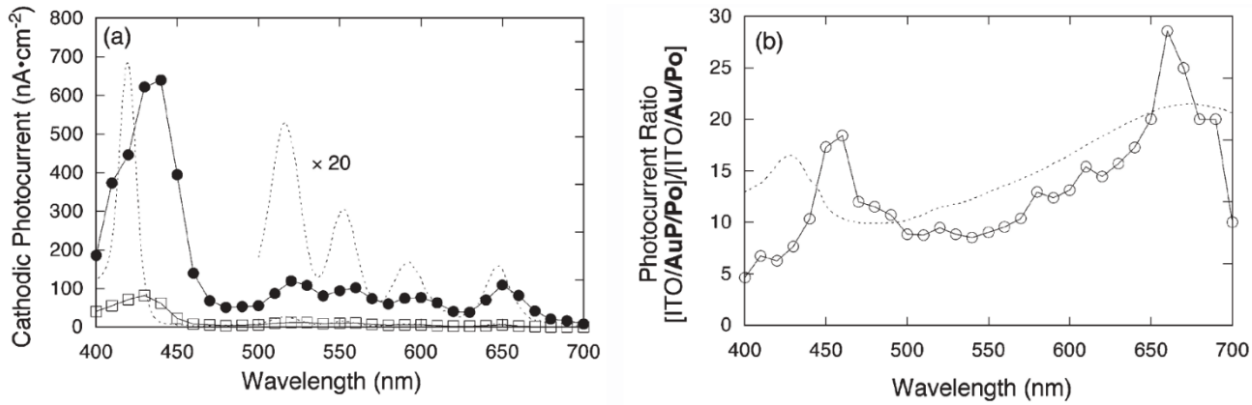

Fig. 1.16 (a) Photocurrent action spectra of ITO/AuNP/Po (●), ITO/Au/Po (□), and absorption spectrum of $[Po]_2$ in CH_2Cl_2 (…). (b) Photocurrent ratios of ITO/AuP/Po to ITO/Au/Po (○), and transmission absorption spectrum of ITO/AuP/Po (⋯).

After that, in 2010, Yamada[73] reported a self-assembled monolayer of the same porphyrin $[Po]_2$ fabricated on the surface of an electrochemically deposited gold nanostructure (named AuB/Po, Fig. 1.17a) exhibits large increase of photocurrent due to porphyrin excitation, especially in the near-infrared region, due to the LPR (Fig.1.17b and Fig.1.17c). As reference, AuB was replaced by a planar gold electrode using vacuum deposition of gold onto the ITO electrode as: Au/Po.

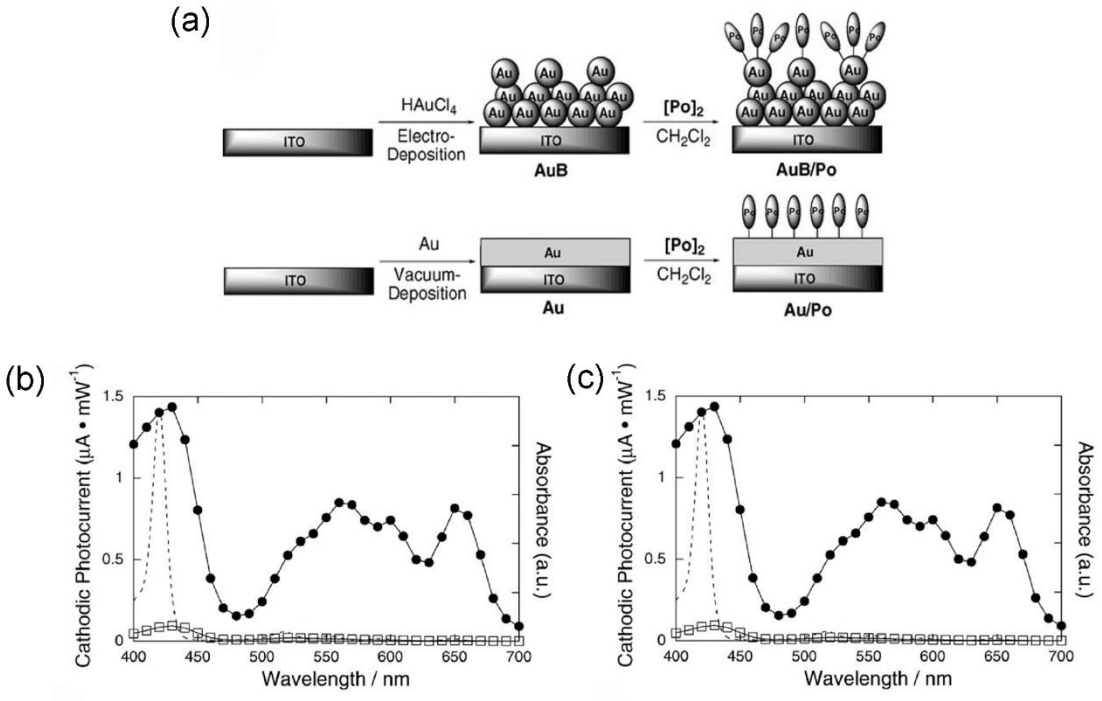

Fig. 1.17 (a) Fabrication procedure of AuB/Po and Au/Po. (b) Photocurrent action spectra of AuB/Po (●), Au/Po (□), and absorption spectrum of $[Po]_2$ in CH_2Cl_2 (···). (c) Photocurrent ratios of AuB/Po to Au/Po (○).

In 2013, Yamada[74] fabricated zinc tetraphenyl porphyrin (ZnTPP)−silver nanoparticle (AgNP) composite films on ITO electrodes by the electrostatic layer-by-layer adsorption method (Fig. 1.18). The degree of immobilization of AgNP on the ITO electrodes was depended on the immersion time into the aqueous colloidal solution of AgNP. The morphology of AgNP affected the lifetime of singlet excited state of ZnTPP (ZnTPP*), due to AgNP aggregates is competitive with the photoinduced electron-transfer from ZnTPP* to O_2 in the photocurrent measurements.

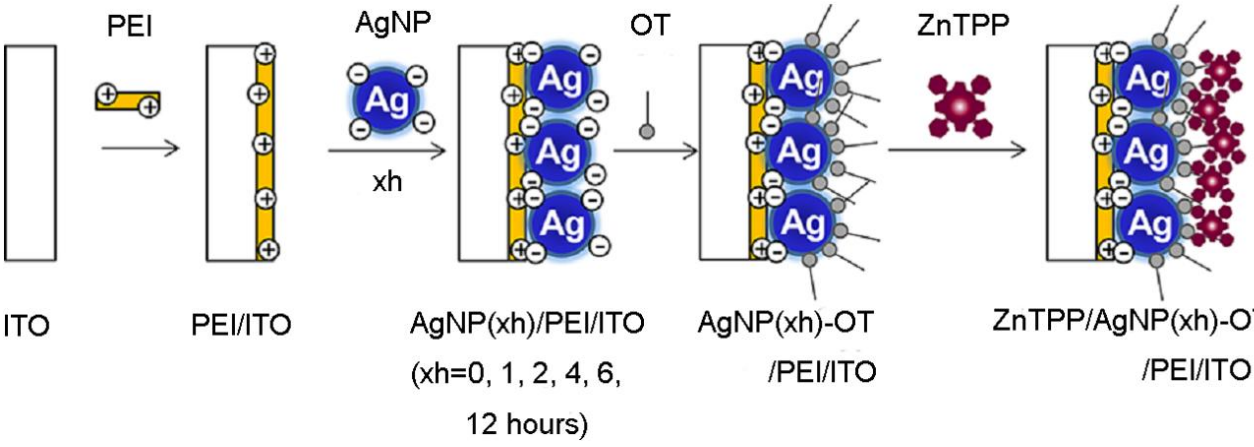

Fig. 1.18 Schematic illustration for the fabrication of zinc tetraphenyl porphyrin (ZnTPP)−AgNP composite films on the ITO electrode. (PEI = poly ethyleneimine).

2. Polyoxometalates

2.1 Structure, properties and representation of polyoxometalates

2.1.1 Structure of POMs

Polyoxometalates (POMs) are a structurally diverse family of anionic metal oxide molecular compounds with applications in analytics, catalysis, photocatalysis, medicine, electronics and materials science. POMs are mainly composed by [MO_6] octahedron, where M is largely restricted to the group 5 and 6 metals, vanadium, niobium, tantalum, molybdenum, and tungsten in their highest oxidation state. The large family of POMs is divided into iso- and heteropolyoxometalate. The former only involve one type of transition metal. The latter can involve not only some hetero early transition metals, but also other metals or non-metals such as Fe^{3+}, Zn^{2+}, [SO_4^{2-}], and [PO_4^{3-}]. This class of POMs has been deeply studied. The primary building block is the [MO_6] octahedron and [MO_4] tetrahedron, metal atoms are displaced toward the vertexes that lie at the surface of the cluster. However, trigonal [MO_3], square [MO_4], trigonal bipyramidal [MO_5], or square pyramidal [MO_5] units also occur. The classical POMs, such as Anderson-, Lindqvist-, Keggin-, and Wells-Dawson-type have been researched extensively (Fig. 1.19).

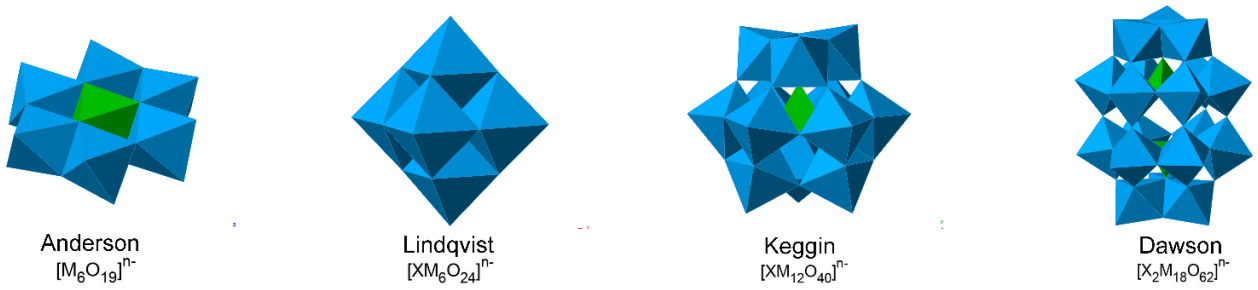

Fig. 1.19 The classical Anderson-, Lindqvist-, Keggin-, and Wells-Dawson-type POMs.

However, the development of crystal synthesis techniques enable to discovery more POMs with complex structures.[75–79] The synthesis of crown-shaped [$NaP_5W_{30}O_{110}$]$^{14-}$,[75] nano-wheel {Mo_{154}},[80] nano-sphere {Mo_{132}},[81] and a giant cluster {Mo_{368}}[82] have been published (Fig. 1.20)

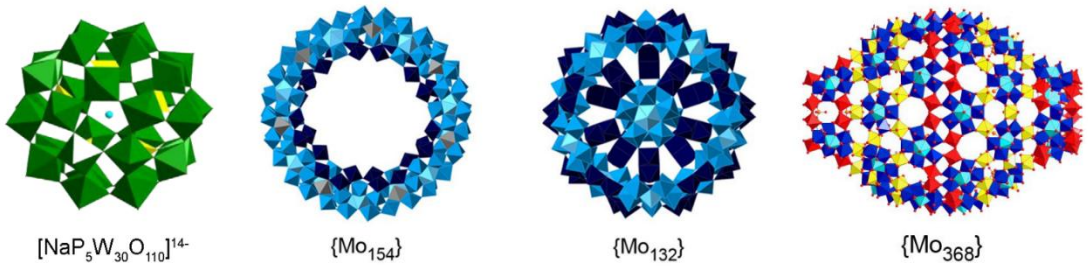

Fig 1.20 Structures of crown-shaped $[NaP_5W_{30}O_{110}]^{14-}$, nano-wheel $\{Mo_{154}\}$, nano-sphere $\{Mo_{132}\}$ and giant cluster $\{Mo_{368}\}$.

2.1.2 Properties of POMs

POMs possess unique electric, photonic and magnetic properties, and chemical reactivity. Furthermore, considering POMs' extensive structural variety, the attractive applications of POMs are continually reported since the invention of POMs nearly160 years ago.

For most POMs especially those high-symmetry species, the additional charges, which reduce POMs, always equally distribute in the whole molecule and all the octahedrons. So, one cannot indicate which atoms keep the electrons and change valence, that is to say, the POMs molecule is a conjugating system. The broad range of POMs' applications is based on (i) the ability of POMs to act as conjugated electron reservoirs and (ii) the extreme variability of their molecular properties, including size, shape, redox potential, charge density, solubility, acidity, etc. The particular interest is POMs as electron-accepting moieties in charge-transfer systems including organic ligand as electron donors. It's also worth pointing out the donor/acceptor interactions in such charge-transfer materials are critically controlled by the size and shape of the POMs as well as by their redox potentials, which are readily tuned by varying the metal centers.

POMs can undergo reversible, stepwise, multielectron-transfer reactions, which are the basis for many catalytic processes. Since 1916 Ridle reported the reversible photochemical action of POMs, many studies disclosured that these compounds exhibit a fascinating photoredox chemistry owing to their robustness and large number of metallic centers, POMs can undergo reversible and multi- electron photoredox processes and keeping their structure intact. These properties make POMs as electron mediators in solar cell and photocatalytic process.

2.2 Multi-functional polyoxometalates - based hybrids

2.2.1 Hybrids based on electrostatic interaction without previous anchor organic ligands onto POMs

POMs are anionic clusters, electrostatic hybrids can be fabricated with cationic chromophores such as organic dyes,[83–85] Ru or Re polypyridyl complexes,[86] or porphyrins and phthalocyanines,[87,88]. Many papers have been published the photovoltaic electrode of POM included multi-component systems based on electrostatic interaction. Tia E. Keyes and Robert J. Forster[89,90,91] have investigated thin layers of an electrostatically associated adduct formed between the polyoxomolybdate, $[S_2Mo_{18}O_{62}]^{4-}$, and the metallopolymers $[Ru(bpy)_2(PVP)_{10}]^{2+}$ which have been deposited onto electrodes by layer-by-layer (LBL) method (Fig. 1.21). Photocurrents of 38 and 100 $nA.cm^{-2}$ were measured under the visible radiation (> 480 nm) when the film is dipped respectively in a benzyl alcohol solution at a potential of 0.4 V and in acetonitrile : benzyl alcohol (4 : 6) at a potential of 0.6 V. Compared with the single POM, the presence of the photosensitive polymer strongly increase the photocurrents (in benzyl alcohol under visible radiation), however, the photocurrents measured for these POM / Ru-PVP systems are particularly low. The benzyl alcohol, used as sacrificial electron donor, has been chosen because the presence of electrolyte (or redox mediator such as I_3^-/I^-) tends to disrupt the electrostatic binding of ruthenium complexes to POMs. Thus, in these conditions, a low conductivity of the films is observed. This poor conductivity of the films should explain the low photocurrent generation. Moreover, such films show that the photocurrent take on the order of 30–100 s to reach a time-independent value.

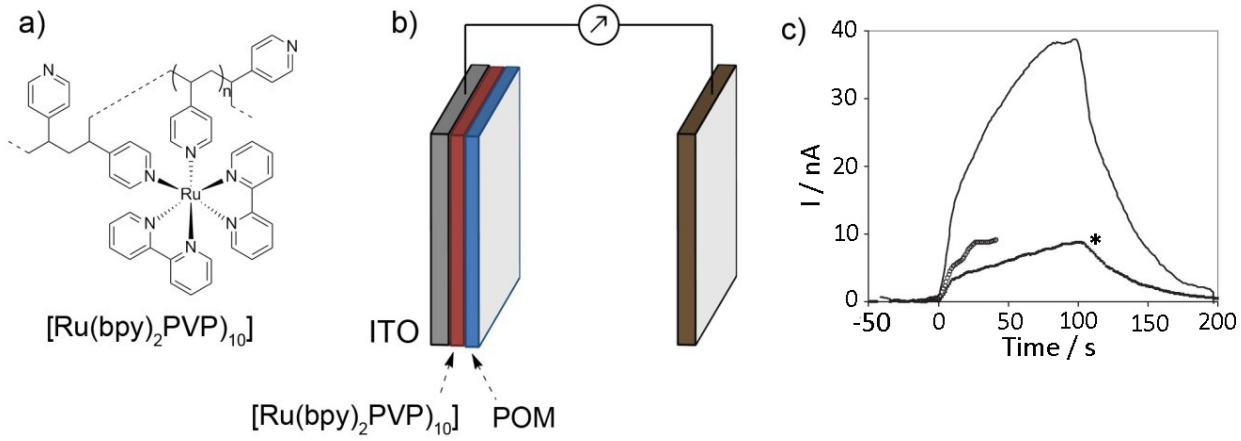

Fig. 1.21 a) Structure of $[Ru(bpy)_2PVP)_{10}]$, b) Representation of the LbL cell ($[Ru (bpy)_2PVP)_{10}]$/ POM) (POM=S_2Mo_{18} or P_2W_{18}). c) Photocurrent of $[Ru (bpy)_2PVP)_{10}]/S_2Mo_{18}$ (solid line), $[Ru(bpy)_2(CO\text{-}PIC)_7]^{2+}$/ S_2Mo_{18} (open circles) and $[Hx_4N]_4[S_2Mo_{18}]$ (*) formed on ITO electrodes in contact with pure benzyl alcohol containing 0.1M $TBATBF_4$ as supporting electrolyte. BIAS: 0.4 V.

Moreover, Li-Hua Gao has reported a series of related studies on photovoltaic properties of films produced by assembling hemicyanines with different POMs *via* LbL method. The structures of hemicyanine used in these studies, denoted H^a and N^b, are shown in Fig. 1.22.[92,93,94] The prepared films absorb in the visible between 400 and 600 nm through the transfer bands of intramolecular charge of the chromophore. For all these systems, the cathodic current (negative) were measured under white irradiation (325 <λ <730 nm) under zero or negative potential (-0.2 or -0.3 V). The system shows the strongest currents for $Zn_4(PW_9)_2/N^3)_3$ (J = 13.7 $\mu A.cm^{-2}$). Several common trends can be observed in these studies. The first is that the optimal number of bilayer is between 3 and 4. Beyond 4, the photocurrent starts to fall. Only the system $(Cd_4(PW_9)_2/N^6)_n$ is an exception since the best results are obtained for the monolayer $(Cd_4(PW_9)_2/N^6)_1$. Even when POM is used, hemicyanide H^3 and N^3, having a spacer $(CH_2)_3$ give better results than with shorter or longer spacers (n = 1, 6 or 10). Applying a negative potential enables to increase the measured photocurrents. Similarly, the addition of an electron acceptor, like the methyl viologen, in the electrolyte solution improves the performance. Both observations are consistent with the direction of transfer of electrons. A selection of photocurrent response for some systems are collected in table of general conclusion.

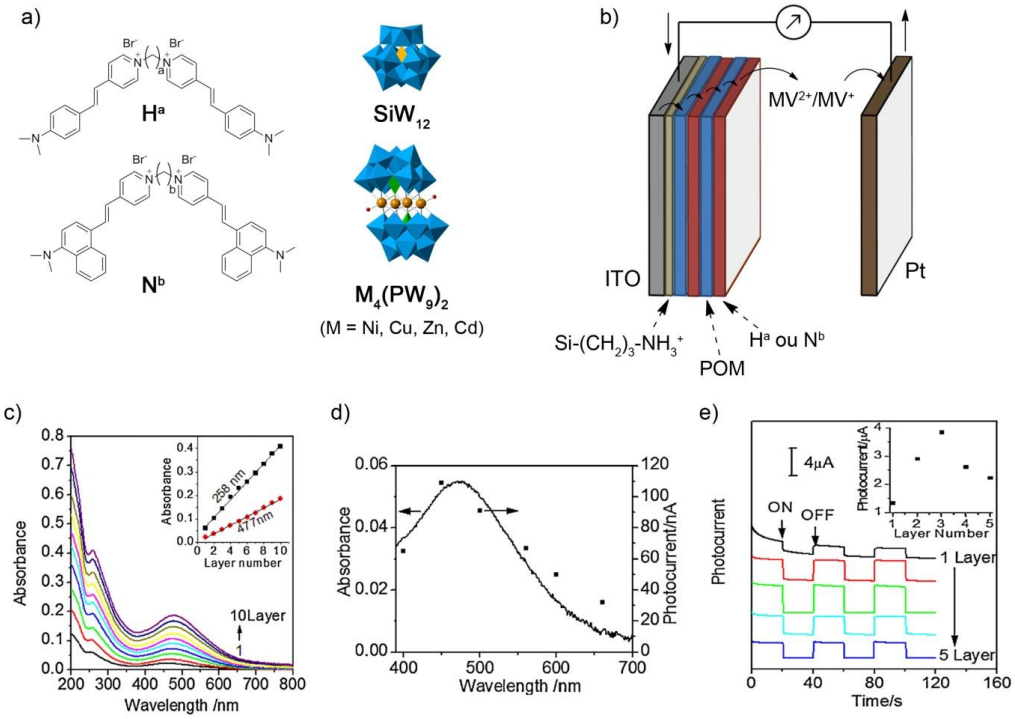

Fig. 1.22 a) Structures of hemicyanine H^a and N^b, and POMs of SiW_{12} and $M_4(PW_9)_2$. b) The LbL cell of $(POM/hemicyanine)_n$. c) UV-vis absorption spectra of $Zn_4(PW_9)_2/N^3)_n$ films on quartz. d) Comparison between the absorption spectrum of $Zn_4(PW_9)_2/N^3)_3$ and the photocurrent values under irradiation at different wavelengths. e) Photocurrent of $Zn_4(PW_9)_2/N^3)_n$ with n = 1 to 5, BIAS: -0.3 V.

Z. Sun has prepared the assemblies that POMs were sensitized by various phthalocyanine. Dawson type-POM: P_2Mo_{18} and tetraaminophthalocyanine cationic cobalt (CoTAPc) are deposited on ITO by LbL method (Fig. 1.23) [95]. The films are stabilized by the inclusion of bilayer PAH/PSS between each P_2Mo_{18}/CoTAPc bilayer. Although films $(CoTAPc/PSS)_5$ are capable of generating photocurrent under UV irradiation, the films included POMs and CoTAPc show better results. However, the measured photocurrents are of the order of 30 $nA.cm^{-2}$. More recently, the $SiMo_{12}$ assembled with a copper phthalocyanine (CuPc) on ITO plates by LbL method[96] has also been studies. In UV and visible irradiation, the photocurrent of $(CuPc/SMo_{12})_9$ was 0.6 $\mu A.cm^{-2}$ under BIAS of 0.6 V. In comparison, the film of only phthalocyanine or only POM produce smaller photocurrents (6 times lower). If the radiation is restricted to the visible, a photocurrent can be measured, but is less intense. This suggests that the irradiation of the phthalocyanine are not sufficient and that the synergistic effect between the POM and CuPc requires radiation in both the visible and UV. Surface photovoltage measurements also show a strong response of the film in the visible and UV, due to a charge transfer of the phthalocyanine to the POM. Analysis of I-V curves indicate, however, that the performance of films $(CuPc/SMo_{12})_9$ is extremely low ($\eta = 3.41\times10^{-4}$ %).

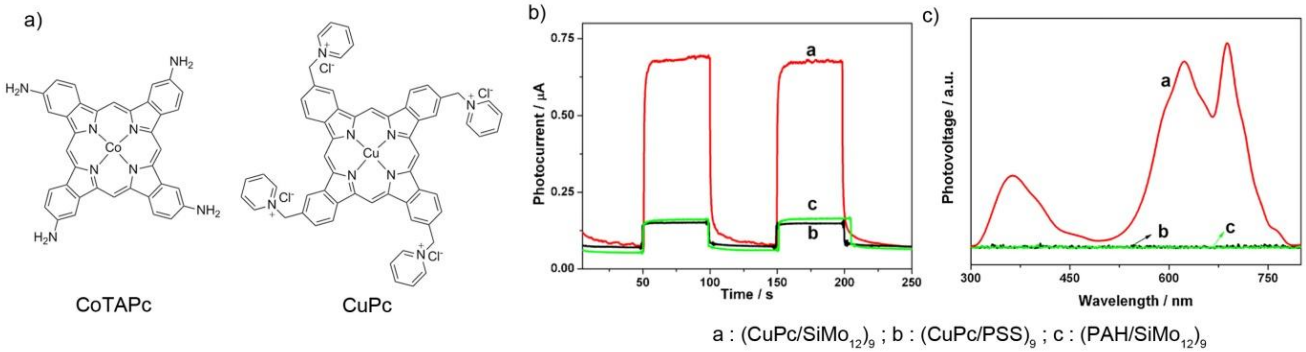

Fig. 1.23 a) Representation phthalocyanine CoTAPc and CuPc. B) Photocurrent measurements and b) surface photovoltage for the films $(CuPc/SiMo_{12})_9$, $(CuPc/PSS)_9$ and $(PAH/SiMo_{12})_9$ under UV and visible light.

Ruhlmann and coworkers[97] reported films based on electrostatic interactions between tetracationic porphyrin, 5,10,15,20-(4-trimethylammoniophenyl) porphyrin tetra(*p*-toluenesulfonate), $[H_2TPhN(Me)_3P]^{4+}$ and Dawson type polyoxometalate α_2-$[Fe(P_2W_{17}O_{61})]^{7-}$ were constructed by layer-by-layer (LBL) self-assembly strategy (Fig. 1.21a). This film has been applied for the photoreduction of silver ions. Indeed, with propan-2-ol as sacrificial donor, porphyrins can be excited by visible light

and give electrons to POM known to be as good catalyst (Fig. 1.24c). Giant silver dendrites have been obtained (Fig. 1.24b). Their photovoltaic performances are also investigated by photocurrent transient measurements. The presence of α2-$[Fe^{III}P_2W_{17}O_{61}]^{7-}$ enhanced the photocurrent around 25 times than only $H_2TPhN(Me)_3P^{4+}$ film, due to α2-$Fe^{III}P_2W_{17}O_{61}^{7-}$ is a strong acceptor of electrons and can take one electron from the excited porphyrin (Fig. 1.25).[98]

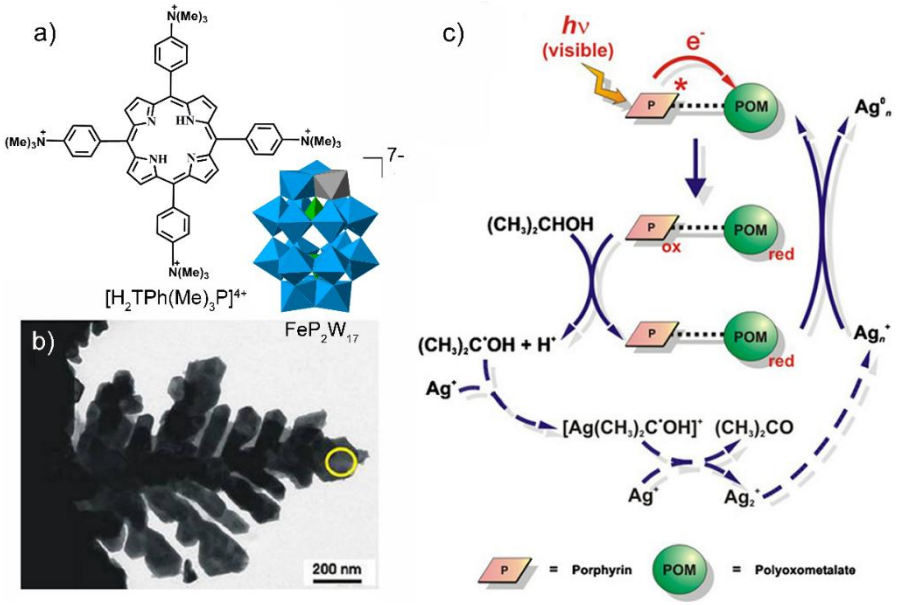

Fig. 1.24 a) Representation of $[H_2TPhN(Me)_3P]^{4+}$ and α2-$[Fe(P_2W_{17}O_{61})]^{7-}$. b) TEM of the getting silver dendrites. c) Schematic proposed mechanism for the photoreduction of silver cations using the $[H_2TPhN(Me)_3P^{4+}/\ \alpha_2\text{-}Fe(P_2W_{17}O_{61})^{7-}]_n$ films.

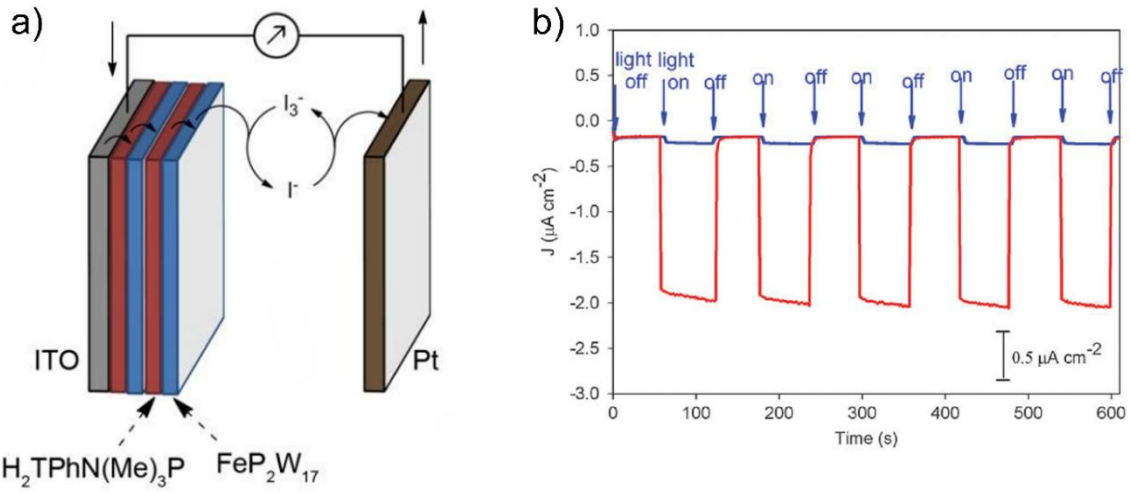

Fig. 1.25 a) Schematic illustration of the multilayer assembly $[H_2TPhN(Me)_3P^{4+}/\ \alpha_2\text{-}Fe(P_2W_{17}O_{61})^{7-}]_n$ for the photocurrent generation. b) Photoelectrochemical response of $[H_2TPhN(Me)_3P]^{4+}$ (blue curve) and $[[H_2TPhN(Me)_3P^{4+}/\ \alpha_2\text{-}Fe(P_2W_{17}O_{61})^{7-}]_{25}$ films (red curve).

In 2015, two recent papers report the formation of electrostatically self-assembled POM included films. Gao and coworkers[99] designed four Keggin-type POMs of $[BW_{12}O_{40}]^{5-}$, $[PW_{12}O_{40}]^{3-}$, $[SiW_{12}O_{40}]^{4-}$ or $[PMo_{12}O_{40}]^{3-}$ with a hemicyanine (named, H^1Br_2) and demonstrated that in order to act as good electron shuttles by balancing their electron-accepting ability and the electron-donating capacity of their reduced states, the LUMOs of POMs should be compromised to a medium value. Shi, Zhang and coworkers[100] synthetized composite films with optical nonlinearities derived from the water-soluble Keplerate-type POM $(NH_4)_{42}[Mo_{132}O_{372}(CH_3COO)_{30}(H_2O)_{72}]$ *ca.* $300H_2O$ *ca.* $10CH_3COONH_4$ (denoted $(NH_4)_{42}\{Mo_{132}\}$) and chloroform-soluble tetra-phenylporphyrin perchlorate $[H_2TPP](ClO_4)_2$ (Fig. 1.26). Because of the interfacial charge transfer induced by laser from $[H_2TPP](ClO_4)_2$ to $(NH_4)_{42}\{Mo_{132}\}$ in the films, the composite film possessed remarkably enhanced optical nonlinearities (Fig. 1.26).

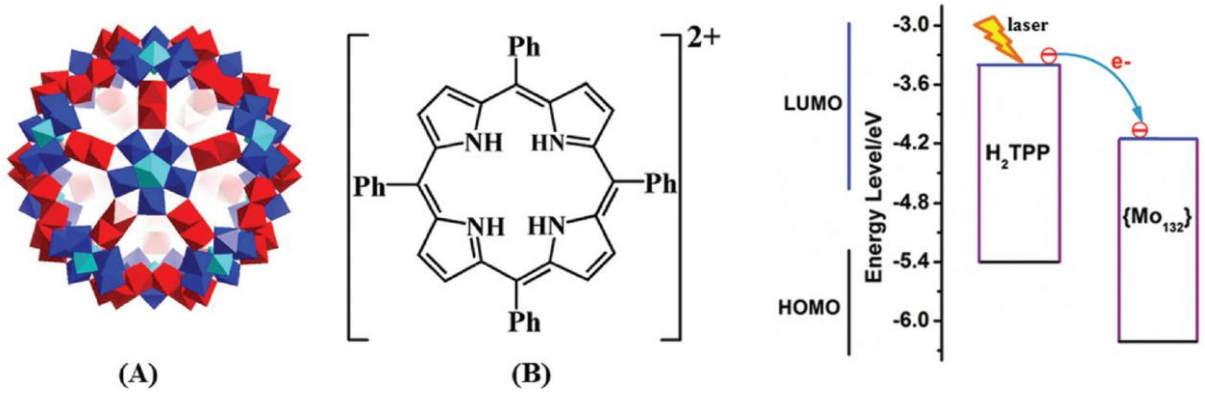

Fig. 1.26 Structures of the Keplerate-type polyoxometalate anion $\{Mo_{132}\}$ (A) and divalent cations of porphyrin $[H_2TPP]^{2+}$ (B). Right: Energy level and electron-transfer process diagram of $H_2TPP](ClO_4)_2$, $\{Mo_{132}\}$ molecules. Color code: blue, LUMO level; black, HOMO level.

2.2.2 Hybrids based on coordination interaction

Krebs et al. were the precursor to combine the POM chemistry with classic coordination chemistry, mediated by oxo ligands of the POM framework.[101] Aming to direct oxygen-transfer processes, they focused their attention on the polyoxovanadate family. By mixing bmimpm and $[VO(acac)_2]$ in MeOH (bmimpm = bis(1-methylimidazol-2-yl)-4-methoxyphen-1-ylmethanol; acac = acetylacetonate), they obtained a prototype hybrid of a $\{V_6O_{13}(OCH_3)_6\}^{n-}$ Lindqvist-type core capped by two vanadyl complexes $\{VO(bmimpm)(acac)\}^+$ (Fig. 1.27). The coordination sphere of the external vanadium ions can be worked as a model for researching the reactivity of enzymatic active sites (e.g. sites in vanadium-

containing haloperoxidases). Self-assembly is an attractive method to construct functional assemblies on several length scales. But, it remains weakness to be selected to build-up blocks that possess poorly directional coordination sites such as $\{V_6O_{13}(OCH_3)_6\}^{n-}$ unit. That is to say, it's significant to seek more elaborate precursors torward incorporating several complementary moieties into a single molecule based on self-assembly.

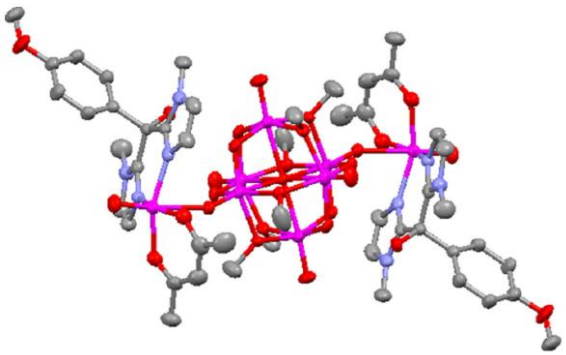

Fig. 1.27 Molecular structure of $[\{VO(bmimpm)(acac)\}_2\{V_6O_{13}(OCH_3)_6\}]$ (ORTEP dia-gram, thermal ellipsoids are represented at 50% probability; H atoms were omitted for clarity; C = grey; O = red; V = pink); N = pale blue.

Kojima, Fukuzumi et al. committed themselves to the development of the formation of nanosized discrete hybrids combining POMs and metalloporphyrins.[102,103] The selection of metalloporphyrins was not only encouraged by the aforementioned rich and tunable electronic, redox and optical characters, but also by the merits with (I) a controlled coordination mode (only two axial positions on the metal are available as coordination sites), (II) tunable properties through chemical derivatization of the porphyrin framwork (which can be also further used for covalent linking with coordination complexes and other units, making it possible to compaire the two type of linkage, vide infra) and (III) a possible neutral charge (realized by compensation of charges between the anionic porphyrin and the metal cation). Fukuzumi firstly prepared a silicododecatungstate Keggin ion "sandwiched" between two molybdo-dodecaphenyl porphyrins $[\{Mo^{V}(DPP)(O)\}_2(H_2SiW^{VI}_{12}O_{40})]$ (H_2DPP = dodecaphenyl porphyrin) (Fig. 1.28a). H_2DPP is a highly directional group which provids only one available site for coordination in the axial direction. In view of the Lewis acidity of the Mo^{V} center which originates from its highly distorted structure, and the bulky volume of H_2DPP, trans-terminal oxo ligands on the POM are more suitable for the linkage.

Further inspired by the association of metalloporphyrins with POMs as D*-A dyads (D* = electron

donor in its excited state; A = electron acceptor in its ground-state) for photoinduced electron transfer and enhanced hole-electron separation, they continued their study through replacing paramagnetic Mo(V) by diamagnetic and hard Lewis acid Sn(IV) because photoexcited Sn(IV)-porphyrins are known as excellent electron donors and with longer the excited state than paramagnetic Mo(V)-porphyrin. They synthesized the $[Sn(TMPP(Ph)_8)(OMe)(\alpha\text{-}[PW_{12}O_{40}])]^{2-}$ hybrid by substitution of one sterically hindered and axial MeO^- ligand on the precursor $[Sn(TMPP(Ph)_8)(OMe)_2]$ ($TMPP(Ph)_8$ = 5,10,15,20-tetrakis(4-methoxyphenyl)-2,3,7,8,12,13,17,18-octaphenylporphyrinato) Fig. 1.28b) with a stability constant $K = 7.5 \times 10^2$. Femtosecond laser flash photolysis results demonstrated that the quenching of the luminescent metalloporphyrin were accelerated when linked to the POM. Unfortunately, the relatively large reorganization energy for the one-electron transfer and the short distance of the separating lead to fast back electron transfer and undetectable charge-separation (rate constant of electron transfer $k_{ET} = 1.0 \times 10^7\ s^{-1}$ vs. rate constant of back electron transfer $k_{BET} = 1.2 \times 10^{11}\ s^{-1}$).

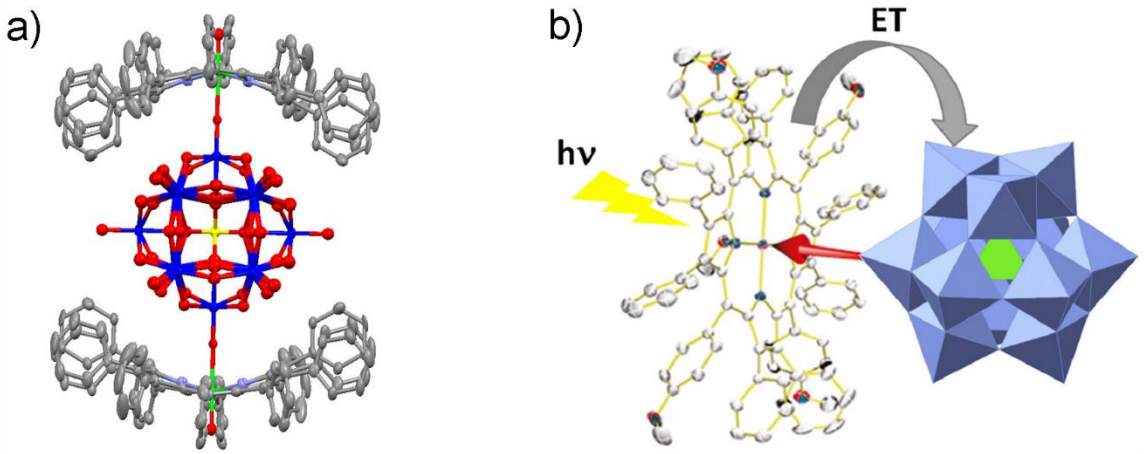

Fig. 1.28a) Molecular structure of the "sandwich" hybrid $[\{Mo(DPP)(O)\}_2(H_2SiW_{12}O_{40})]$ (ORTEP diagram, thermal ellipsoids are represented at 50% probability; H atoms were omitted for clarity; C = grey; O = red; N = pale blue; Mo = green; W = blue; Si = yellow).[102] b) Representation of the photoinduced electron transfer (ET) from the excited porphyrin to POM, leading to a charge-separated state in the Sn-phorphyrin-POM dyad $[Sn(TMPP(Ph)_8)(OMe)(\alpha\text{-}[PW_{12}O_{40}])]^{2-}$ (ORTEP diagram for the metalloporphyrin: H atoms were omitted for clarity, C = grey, O = red, N = blue, Sn = pink; polyhedra representation for the POM: P = green, W = pale blue).[103]

In 2010, Rulmann et al extend to new type coordination[104] between functional groups attached to the peripheral substituents of porphyrins (5,10,15-tritolyl-20-(4-pyridyl) porphyrin (named H_2T_3P-4-py) or

5,10,15-tritolyl-20-(3-pyridyl) porphyrin (named H_2T_3P-3-py) or 5,10,15-triphenyl-20-(4-pyridyl) porphyrin (named H_2P_3P-4-py)) and metal substituted POMs (α-$[MSiW_{11}O_{39}]^{6-}$, M = Co^{2+}or Ni^{2+}). The formation constants are of the same order of magnitude (3–9 ×10^6 L mol^{-1}) with the exception of that of H_2T_3P-3-Py-{CoSiW11} (1.3 ×10^5 L mol^{-1}). A strong quenching of the porphyrin fluorescence is observed upon addition of the POM and formation of the complexes. The paramagnetic ^1H NMR study gave evidence on the formation of a 1/1 coordination complex of between $MSiW_{11}$ (M = Co^{2+} or Ni^{2+}) and a pyridyl-porphyrin (Fig. 1.29).[105]

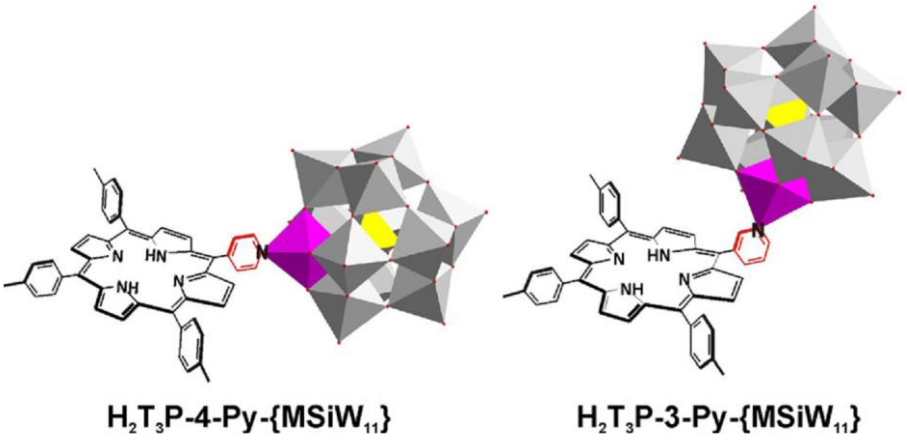

Fig. 1.29 Postulated structure of the 1:1 complex between H_2T_3P-4-Py or H_2T_3P-3-Py and $MSiW_{11}$ (M = Co^{2+} or Ni $^{2+}$). Co or Ni: violin color.

Based on our research and literature review, distance between units, it can also present serious disadvantages for functional materials and devices such as poor regioselectivity and weaker linkage. Well-organized and stronger POM–chromophore bonds are definitely needed.

In this section, the development of the coordination POM–chromophore hybrids is only introduce, in which the POM don't have previous anchored organic ligands. In section 2.23 and 2.24 the description of hybrids in which the organic ligands grafted to the POM framework will be done..

2.2.3 Hybrids with organic ligands grafted to the POM surface

Contrary to the aforementioned largely empirical oxo-coordination of transition metal complexes onto surface of POMs and the coordination of the peripheral substituents of porphyrins and metal substituted POMs, the target complexes can be tethered to POMs by grafting organic ligands onto the oxometallic framework which are more predictable and with well-defined geometries and anchoring mode. In this section, hybrids have been classified according to the way of POM functionalization.

2.2.3.1 Polyalkoxo functionalization

In order to prepare predictable POM structures with organic ligands, researchers focused on polyalkoxo functionalization. Zubieta et al firstly introduced the tris-alkoxo functionalization of POMs in organic media.[106] More recently, Hasenknopf, Lacôte et al. created an original bis-alkoxo-amide tripodal decorated Dawson phosphovanadotungstate, featuring the rare incorporation of the carbonyl group from diol-amide ligands into the POM framework[107] (Fig. 1.30).

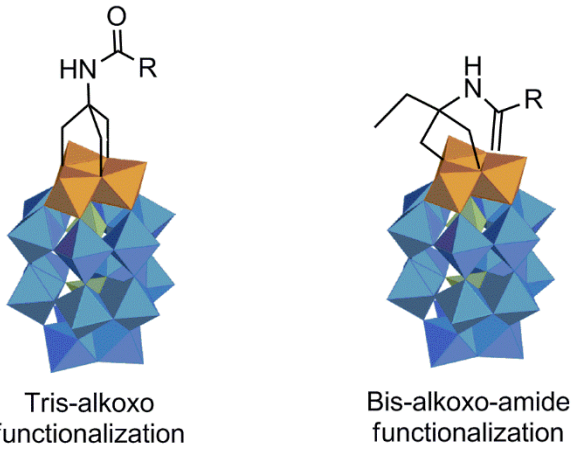

Fig. 1.30 Representation of tris-alkoxo and bis-alkoxo-amide functionalizations of Dawson structures.

Hasenknopf, Ruhlmann et al. synthesized symmetric discrete arrays by axial coordination of 4-pyridyl functionalized Anderson and Lindqvist type POMs respectively, ($[M'Mo_6O_{18}\{(OCH_2)_3CNHCO(4\text{-}C_5H_4N)\}]^{3-}$ with M' = Fe(III), Mn(III)); $[V_6O_{13}\{(OCH_2)_3CCH_2OC(O)(4\text{-}C_5H_4N)\}_2]^{2-}$ and $[V_6O_{13}\{(OCH_2)_3CNHCO(4\text{-}C_5H_4N)\}_2]^{2-}$) onto metalloporphyrins [M''TPP(CO)] (M'' = Zn(II), Ru(II); TPP = tetraphenylporphyrin) (Fig. 1.31).[108] ^1H NMR titration indicated that the pyridyl-POM was more strongly bound to Ru(II) ($K \sim 10^7$–10^8) than to Zn(II) centers and absorption spectroscopy demonstrated some competitive coordination between CH_3CN and the pyridyl-POM onto the metalloporphyrin. Fluorescence spectroscopy revealed that the excess POM was necessary to avert decomplexation and to quench the emission of ZnTPP by energy transfer. Electronic communication between the POMs and the porphyrin was established. But, regrettably, decomplexation of the POM from the Ru center (under electrochemical conditions) and nucleophilic attack of the POM-grafted pyridyl groups at meso and/or the β positions of the porphyrin limit the extension use of this type of hybrid.

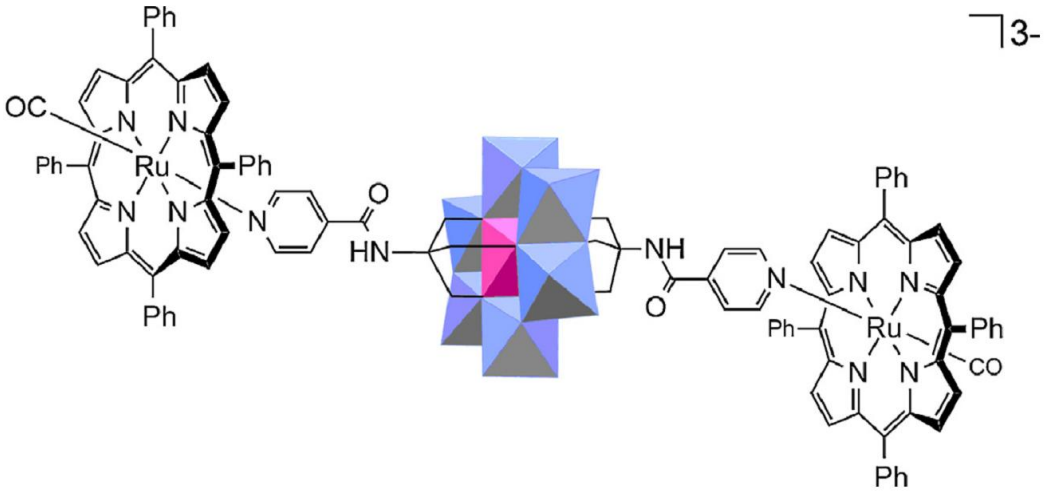

Fig. 1.31 Postulated structure of Ru(CO)TPP - dipyridyl-Anderson type POM.

A stronger association between the two components of the complexes was desirable. Covalent attachment between all of the moieties appears as the way of choice.[109] The introduction of the necessary triol ligand on the porphyrin, aiming direct grafting on the POM, was achieved in two steps by Zn(II) metallation of 5-(4-carboxyphenyl)-10,15,20-triphenylporphyrin followed by amidation with tris(hydroxymethyl) aminomethane. Hybrids $[N(C_4H_9)_4]_3[MnMo_6O_{18}\{(OCH_2)_3CNHCO(ZnTPP)\}_2]$ (**2**) and $[N(C_4H_9)_4]_5H[P_2V_3W_{15}O_{59}\{(OCH_2)_3CNHCO(ZnTPP)\}]$ (**3**) (Fig. 1.32) were finally obtained by reacting the ZnTPP-tris moiety ($\{(HOCH_2)_3CNHCO(ZnTPP)\}$) with metallic precursors, the functionalized POMs being formed in situ. Electrochemical results showed the separate redox processes on the organic and inorganic parts, and the lack of communication between units in the ground state. Fluorescence quenching of the ZnTPP moieties was more rapid when linked to the Dawson structure (up to 97%) but not to the Anderson.

For both, the Gibbs free energy changes for electron transfer were allowable (less for Anderson hybrid), however, the transfer was ineffective in the Anderson hybrid, in which the excited triplet-state of ZnTPP relaxed faster because of the heavy and paramagnetic atom effects. For the Dawson hybrid, a multi-exponential decay was observed due to the existence of different conformers in solution. Photoinduced electron transfer from the excited ZnTPP to Dawson type POM ($k_{ET} = 1.6 \times 10^{10}\ s^{-1}$) result in a charge-separated state has been revealed, which initiate further photochemical applications. Schematic diagram in Fig. 1.33 showing the assumed deactivation processes occurring in Dawson-ZnTPP molecular hybrid.

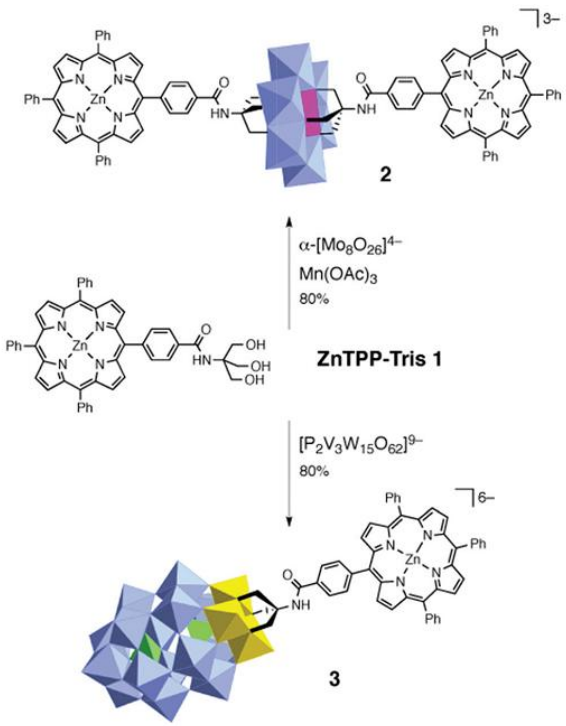

Fig. 1.32 Synthesis of covalent $[N(C_4H_9)_4]_3[MnMo_6O_{18}\{(OCH_2)_3CNHCO(ZnTPP)\}_2]$ and $[N(C_4H_9)_4]_5H[P_2V_3W_{15}O_{59}\{(OCH_2)_3CNHCO(ZnTPP)\}]$ POM–porphyrin arrays.

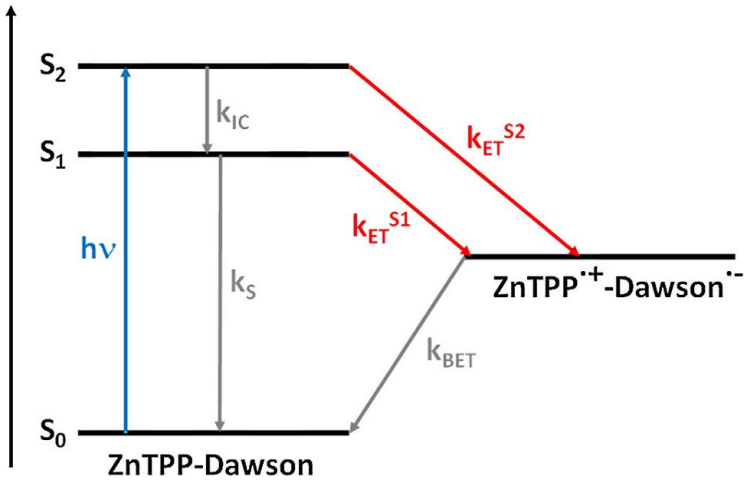

Fig. 1.33 Schematic diagram showing the assumed deactivation processes occurring in the Dawson upon absorption of a photon (hν), the excited hybrid undergoes internal conversion from S_2 to S_1 (k_{IC} = 7.7×10^{11} s^{-1}), electron transfer from the S_2 state ($k_{S2/ET}$ = 4.3×10^{11} s^{-1}), electron transfer from the S_1 state ($k_{S1/ET}$ = 1.6×10^{10} s^{-1}), radiative and nonradiative decay processes from S_1 to S_0, intersystem crossing from S_1 to T_1 ($k_S + k_{ISC}$ = 5.3×10^8 s^{-1}) and back electron transfer ($k_{BET} < 1 \times 10^9$ s^{-1}).[109]

Subsequently, the promising photoinduced charge separation observed for this Dawson-ZnTPP molecular hybrid was further exploited for photocurrent generation (Fig. 1.34).[110] Rulmann et al prepared this Dawson-ZnTPP hybrid films onto ITO based on the Langmuir–Schaefer inverted transfer method (Fig. 1.34a). Under light irradiation, ZnTPP subunit is worked as photosensitizer that delivers

electrons to POM. Then in turn, the reduced form of the POM relay electrons to a redox mediator/electrolyte (I_3^-/I^- redox couple) which is reoxidized at Pt counter-electrode. To complete the circuit, the oxidized porphyrin would be regenerated by accepting one electron from the ITO conduction band (Fig. 1.34b). To the best of our knowledge, this system is the first example of POM-based photoactive molecular covalent hybrid for chemically-modified electrodes which becomes to a hot topic for light transducing devices such as DSSC and water-splitting photoelectrochemical cells.

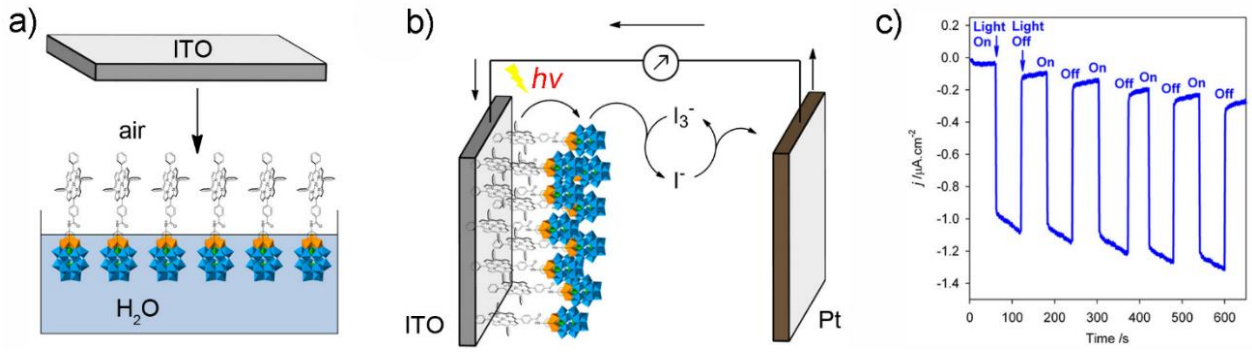

Fig. 1.34 a) Deposition of the POM-Porphyrin monolayer on ITO by Langmuir–Schaefer inverted transfer method. b) Photovoltaic cell constructed from the modified ITO plate and against a Pt electrode. c) Photoelectrochemical response of this Langmuir–Schaefer film.

Introduction of polydentate coordination sites onto the POMs through designing the structure of covalent organic ligands of the POMs, is another promising approach in building-up multi-functional POM-containing assemblies. Hasenknopf, Hanan et al. firstly designed tris-alkoxo-pyridyl ligands of various denticity (from pyridyl[111] to bipyridyl (bpy)[112] and terpyridyl (tpy)[113]) and grafted them on Anderson manganese-templated molybdates, Lindqvist vanadates and Dawson vanadotungstates, respectively. In the recent publication, a successful complexation of the neutral $[Re^{I}(CO)_3Br]$ unit on a bpy-functionalized Dawson type POM revealed the combined intrinsic properties of both subunits (Fig. 1.35). Because of the high reactivity of the reduced species $[Re^{I}(L)(CO)_3X]$ (L = derivatized bipyridine; X = halide), $[Re(L)(CO)_3(X)]$ complexes are relatively stable and possess rich photochemistry. Attributed to radiative relaxation of the metal-to-ligand charge-transfer (MLCT) transition, emission was located in 500–600 nm range. In general, radiative decay of the triplet state to the ground state accompanied with two other competitive processes: non-radiative decay (NR) and electron transfer (ET)

to the charge separated state with subsequent back electron transfer (BET). In this covalent POM–Re hybrid, the luminescence was totally quenched by rapid photoinduced electron transfer (ET) from the MLCT ($*Re^{I}$) state to the POM (Fig. 1.35 right). Due to the magnitude of the redox potential of the subunits, the excited state oxidation potential of Re^{I} (1.8 V vs. SCE) was sufficient to reduce the POM moiety (0.08 V vs. SCE) proving a large driving force for the photoinduced reduction of the POM unit in this hybrid. This driving force is a significant proof for photocatalytical application.

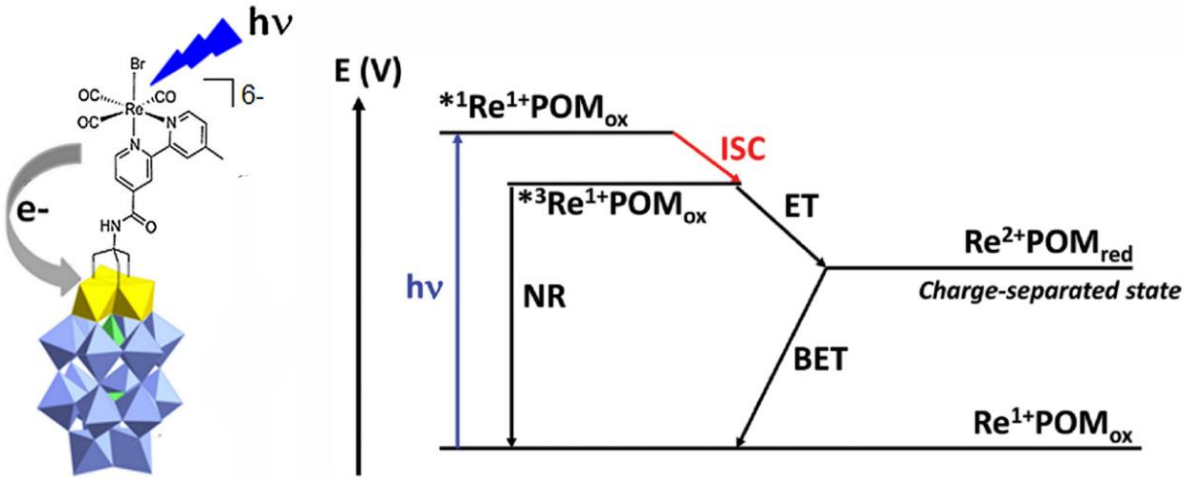

Fig. 1.35 Representation of the hybrid $[P_2W_{15}V_3O_{63}C_{16}H_{16}N_3Re(CO)_3Br]^{6-}$ and the schemetic energy level diagram. The observed luminescence quenching of the Re is attributed to electron transfer from the $*Re^{I}$ to the POM.[112]

2.2.3.2 Imido functionalization

The replacement of terminal oxo ligands O^{2-} by imido ligands RN^{2-} is a general strategy to bond organic moiety R to the POM skeleton. Two decades ago, Maatta et al firstly reported one hybrid featuring the covalent attachment of an oxidizable organometallic donor to a reducible POM acceptor[114]: the linkage between a hexamolybdate cluster and a ferrocenyl moiety was realized through a Mo=N imido bond obtainning the hybrid $[((\eta^5\text{-}C_5H_5)Fe\text{-}(\mu\text{-}\eta^5\text{:}\sigma\text{-}C_5H_4N))Mo_6O_{18}]^{2-}$. Peng et al. have made a contribution for investigating imido-POMs charge transfer systems through extended π-conjugated bridge. They try to realize a charge-transfer resonance between subunits and an increased delocalization of the π-electrons over the entire molecule. Using Pd-catalyzed coupling reactions on monoiodo- or diiodo-functionalized Lindqvist POMs, they synthesized $[Mo_6O_{18}(NAr^1)]^{2-}$ and $[Mo_6O_{17}(NAr^2)_2]^{2-}$ (Ar^1 = 4-iodo-2,6-dimethylphenyl and Ar^2 = 4-iodo-2,6-diisopropylphenyl) with one and two ferrocenyl units, respectively (Fig. 1.36).[115] The broad absorption extended to beyond 550 nm, indicating the existence

of a charge-transfer from the ferrocenyl donor to the POM acceptor, even though with long D−A separation distance (11.29 Å).

Further, Peng devoted to synthesize copolymers with conjugated photoactive organic skeletons and POM moieties inserted in the main-chain or as side-chain pendants.[116,117] Hexamolybdate subunits were embedded through covalent bonding to the main chain of poly-(phenylene acetylene)s. These hybrids were synthesized also by the palladium-catalyzed coupling reactions of a diethynyl functionalized cluster with a diiodobenzene derivative or a diiodo functionalized cluster with a diethynylbenzene derivative. These polymeric hybrids possessed intense visible absorption, however without fluorescence emissions, indicating efficient fluorescence quenching of the incorporated POM subunits on the organic phenylene acetylene moieties. The polymer was further applied for prototype photovoltaic cell fabrication (single-layer of photoactive hybrid polymer with a configuration ITO/polymer/Ca-cathode) and obtained a power conversion efficiency of 0.15% (Fig. 1.37).[116]

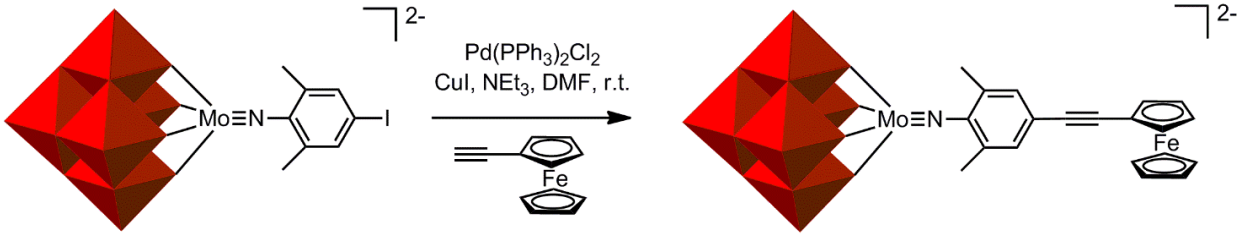

Fig. 1.36 Synthetic process of covalent imido-molybdate POM–ferrocenyl hybrids ($[Mo_6O_{18}(NAr^1)]^{2-}$, Ar^1 = 4-iodo-2,6-dimethylphenyl).[115]

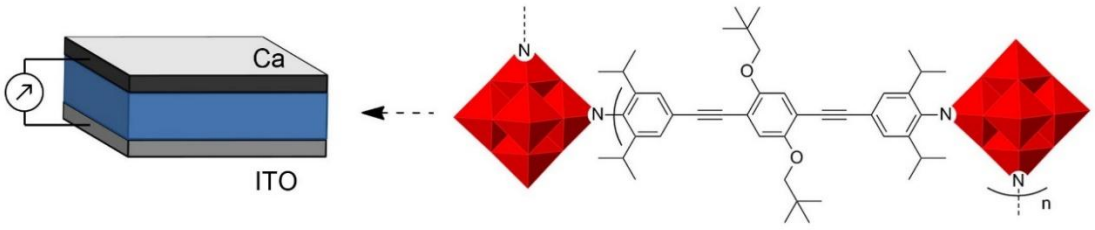

Fig. 1.37 Representation of the photovoltaic cell of hexamolybdate-poly phenylenevinylene.

2.2.4 Hybrids with covalent grafting through heteroatom-insertion in a lacunary POM

The substitution of one or more oxometallic units from the POM skeleton by controlled hydrolysis forms lacunary structures. Electrophilic groups and organometallic fragments can filled these vacancies. Purposely, organic moieties are attached to the POM through a heteroatom.

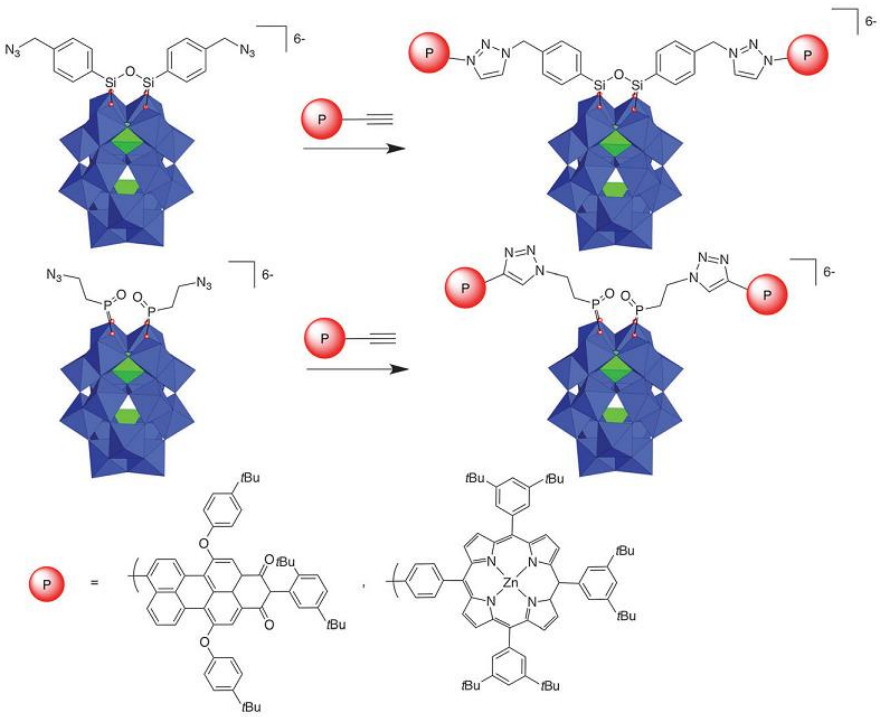

Fig 1.38 Synthesis of POM-based hybrids through Huisgen 1,3-dipolar cycloadditions. Green tetrahedra, {PO_4}. Blue octahedra, {WO_6}.

Seeking photoactivation of POMs in the visible region, Odobel, Harriman et al. reported covalent hybrids with two perylene or metalloporphyrins grafted through organosilyl (semi-rigid) and organophosphoryl (flexible) anchors (Fig 1.38).[118,119] Although no charge-separated excited states could be detected from laser flash photolysis, luminescence quenching was detectable and attributed to intramolecular electron transfer to the POM. The quenching was more efficient in hybrids with more flexible linker, matching with greater thermodynamic driving force and shorter "through-space" separation of units. The flexible linker conquer the insulator effect by adopting several conformations in solution which was testified by the pressure-dependent fluorescence results. Further, to realize the multi-electron charge accumulation, they linked two porphyrin clusters onto one POM group, selecting a flexible linker for through-space electron transfer (Fig. 1.39).[120] A porphyrin cluster consist of three Zn-metallated porphyrins (ZnP), as photon collectors, and one free-base porphyrin (FbP), as energy reservoir. ZnP absorb light energy and transmit energy (EnT = energy transfer) to FbP. Efficient charge separation achieved by electron transfer (ET) from FbP to the POM and by hole transfer (HT) from FbP to a ZnP. The POM subunit play the role of electron pool capable of storing up to two electrons under visible-light irradiation.[120]

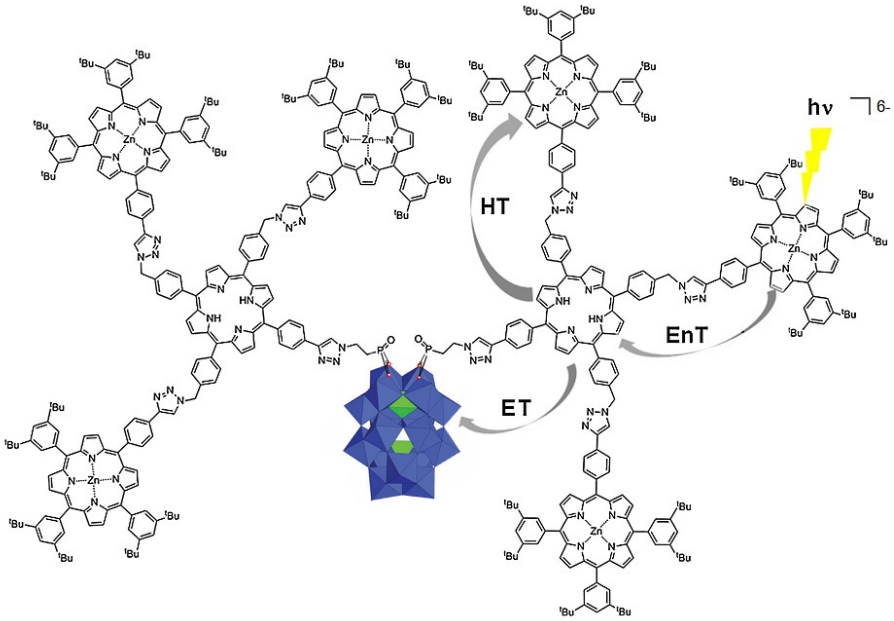

Fig. 1.39 Schematic representation of charges transfer.

Proust et al also devoted a long-term research on POM photosensitization choosing silyl-derivatized Keggin- and Wells-Dawson-type POMs and utilizing Sonogashira cross coupling (Fig. 1.40).[121,122,123] POM–pyrene system revealed a complete quenching of the chromophore luminescence, while for the POM–ruthenium the quenching was partial (ca. 15 to 30%). As expected from the redox potentials of the subunits, rate of charge separation was faster in silyl hybrids than in stannyl hybrids and in silyl-Keggin than in silyl-Dawson POMs. Computations demonstrated that the picolinate linker offered directionality for the photoinduced electron transfer as directing the charge localization which lead to a favored charge separation and retarded charge recombination. Due to smaller HOMO–LUMO gap, the silyl-Keggin showed faster electron transfer rate (consistent with its lower reduction potential and thus inducing a larger driving force for forward electron transfer). However, faster electron transfer was accompainded with faster charge recombination. By comparison, the silyl-Dawson hybrid was the most promising candidate providing an acceptable compromise between the rate of charge separation and charge recombination (k_{CS} = 1.92 $\times 10^9$ s^{-1} and k_{CR} = 3.71 $\times$107 s^{-1}, respectively).

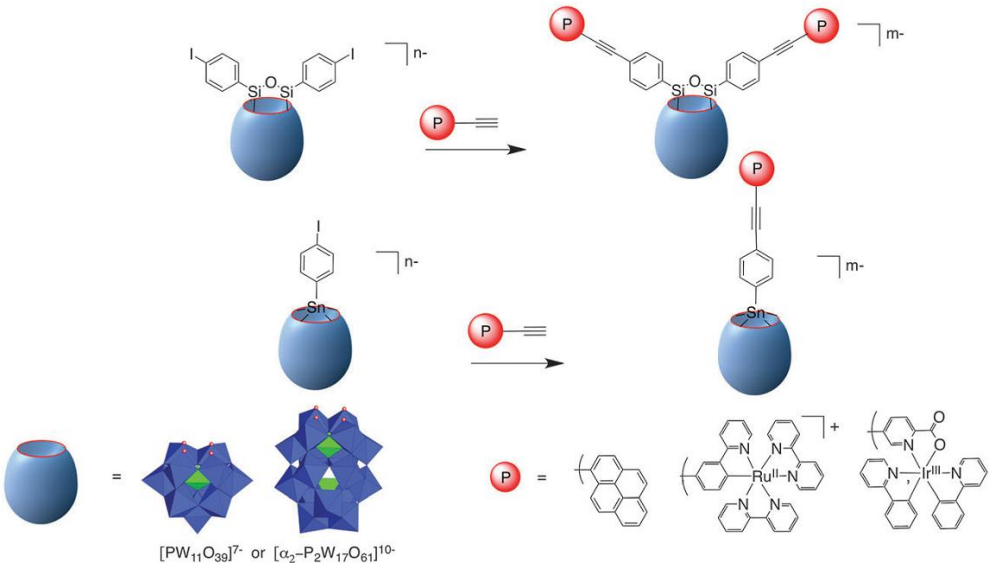

Fig. 1.40 Schematic representation of POM-based hybrids through Sonogashira coupling reactions.

Recently, the appearence of a tretraruthenium substituted polyoxotungstate ($[Ru_4(\mu\text{-}O)_4(\mu\text{-}OH)_2(H_2O)_4(\gamma\text{-}SiW_{10}O_{36})_2]^{10-}$) was a breakthrough in the field of photoelectrochemical water oxidation,[124,125] in which the tetra-Ru(IV) μ-oxo core mimicks the oxygen-evolving complex of natural photosynthesis by undergoing four consecutive oxidation steps, followed by nucleophilic attack and water oxidation.[126] Bonchio, Campagna et al combined a tetranuclear Ru(II) dendrimeric photosensitizer ($[Ru\{(m\text{-}dpp)Ru(bpy)_2\}_3)^{8+}$, bpy = 2,2'-bipyridine; dpp = 2,3-bis(2'-pyridyl) pyrazine)) (**1**) and ($[Ru_4(\mu\text{-}O)_4(\mu\text{-}OH)_2(H_2O)_4(\gamma\text{-}SiW_{10}O_{36})_2]^{10-}$) (**2**) as the catalyst enables photoinduced oxygen evolution in water at 550 nm with an excellent quantum yield of 0.30 (Fig. 1.41).[127]

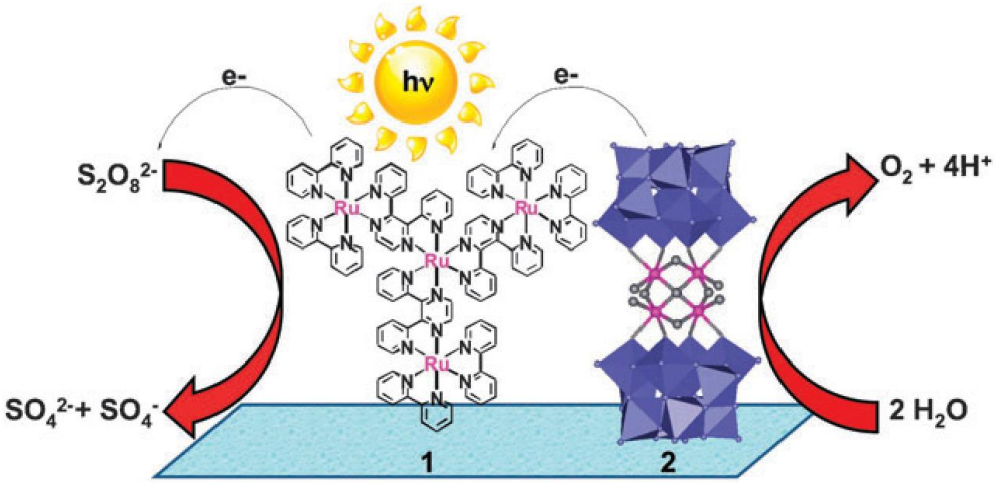

Fig 1.41 Photocatalytic mechanism in $Ru_4(\mu\text{-}O)_4(\mu\text{-}OH)_2(H_2O)_4(\gamma\text{-}SiW_{10}O_{36})_2]^{10-}$/$[Ru_4(\mu\text{-}O)_4(\mu\text{-}OH)_2(H_2O)_4(\gamma\text{-}SiW_{10}O_{36})_2]^{10-}$ for water oxidation.

2.2.5 Hybrids of POM with nanomaterials

When ligand-to-metal (O→M) charge-transfer bands are stimulated by UV irradiation, excited POMs can reduce the metal salts to metal(0) nanpparticles (NPs). Here, the POMs play a dual role, acting as both reducing agents and stabilizing anions (Fig. 1.42a).

2.2.5.1 Metal nanoparticle/POM bi-component hybrids

In 2002, Papaconstantinou et al[128] firstly reported α-$PW_{12}O_{40}^{3-}$-stabilized Ag(0), Au(0), Pt(0), and Pd(0) metal nanoparticals (MNPs) by reacting the corresponding metal–salt precursors ($AgNO_3$, $HAuCl_4$, K_2PtCl_6, and $PdCl_2$) with photochemically-reduced forms of α-$H_3PW_{12}O_{40}$. Further, Weinstock used cryogenic transmission electron microscopy (cryo-TEM) to directly image the intact ‘‘solution-state’’ structures of POM-MNPs[129,130] in water. The cryo-TEM images clearly showed that POMs form monolayer shells on Ag(0) (Fig 1.42b) and Au(0) (Fig 1.42c) NPs, conceptually analogous to self-assembled monolayer (SAM) protecting shells of alkanethiolate ligands. The POM monolayers are electrostatic in nature which are unlike the hydrophobic alkanethiolate-ligand shells.

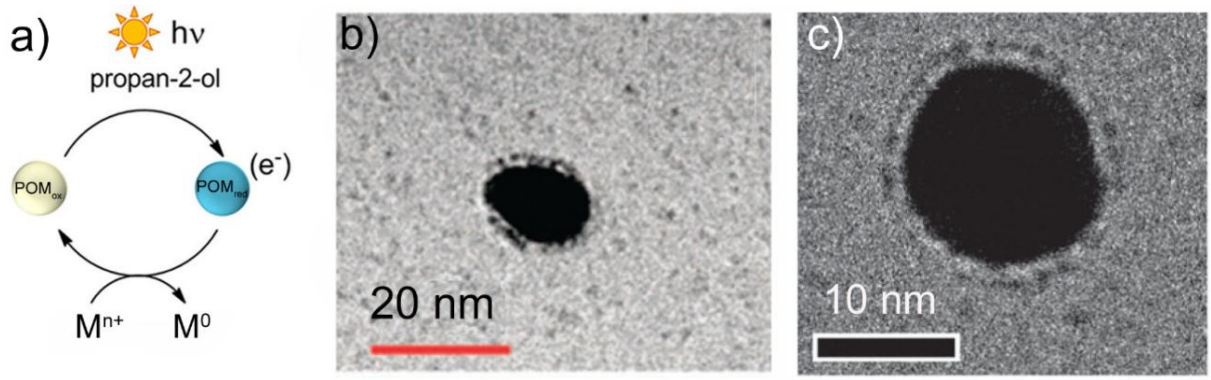

Fig 1.42 a) POM-catalyzed photochemical reduction of metal ions to metal (0) nanoparticles. Higher-magnification cryo-TEM image, revealing individual molecules of α-$AlW_{11}O_{39}^{9-}$ on b) Ag(0) NP and c) Au(0)NP. Freely solvated POMs appear as small dark objects in the background.

Weinstock et al introduced a structural model to feature the extensive incorporation of counter-cations into the POM monolayer itself, using 14 nm AuNPs. Fig. 1.43 reveals five α-$AlW_{11}O_{39}^{9-}$ molecules at actual center-to-center distances (drawn to scale) on the AuNPs surface. The fully hydrated K^+ cation, with its ~17 waters of hydration, located near the outer region of the monolayer, matches the dimension of the space between α-$AlW_{11}O_{39}^{9-}$ molecules. A fully dehydrated cation is closer to the metal surface.

There, the hydrophobic feature of the gold surface maybe promoted partial dehydration of K^+, that would be compensated by direct linkage between K^+ and the bridging and terminal O^{2-} ligands of the POM.[130]

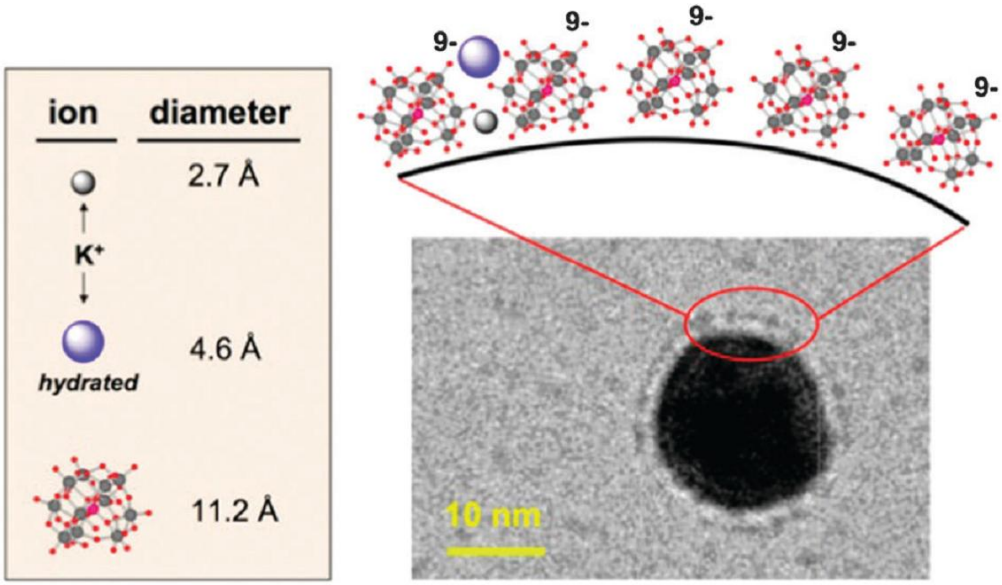

Fig. 1.43 Scale model of α-$AlW_{11}O_{39}^{9-}$ and K^+ counter cations on the surface of a 14-nm AuNP. The left diagram illustrates the crystallographic and hydrated sizes of K^+ relative to a scale model of α-$AlW_{11}O_{39}^{9-}$ (drawn with their defect sites facing the gold surface, although this may not be the only viable orientation.)

2.2.5.2 POM included tri-component hybrids

Carbon-based materials, especially one-dimensional (1D) carbon nanotubes (CNTs) and two-dimensional (2D) graphene nanosheets (GNSs) have been extensively applied as catalysts or as the conducting supports of other catalysts.[131,132,133] Decorating carbon nanotubes/graphene with various metal nanoparticles has became a highlight.

Inspired by the aforementioned facile and easier strategy for the synthesis of MNPs (Ag, Au, Pd, and Pt) with the help of POMs, in 2011, Zhang et al reported an one-pot synthesis of well-defined AuNPs@PW_{12}-CNTs tri-component nanohybrids (Fig. 1.44, up). In this system, $H_3PW_{12}O_{40}$ (PW_{12}) worked as reducing, encapsulating and bridging molecules, meantime, avoid introducing other organic toxic molecules.

Fig. 1.44(down) shows the TEM images of the bare CNTs (a) and well defined AuNPs@ PW_{12}–CNTs (b). The magnified image reveals a clear core–shell nanostructure and AuNPs with an average size of 35 ± 3 nm in diameter (Fig. 1.44c and Fig. 1.44d). From high resolution TEM (HRTEM), the well-

defined lattice fringe of the Au(111) crystalline face (0.23) demonstrated its highly mono-crystalline feature (Fig. 1.44e). To further certify the existence of the $H_3PW_{12}O_{40}$, in situ energy dispersive X-ray spectroscopy (EDX) was studied. In Fig. 1.44f, besides strong peaks of Au, the appearence of tungsten peaks validated the $H_3PW_{12}O_{40}$ around Au NPs. The study of inductively coupled plasma–mass spectroscopy (ICP-MS) revealed the actual Au loading of the hybrid was about 29.1 wt%.[134] To expand the research, this lab successfully incorporate well defined Pt (2.5 ± 0.5 nm) and Ag (5.0 ± 0.5 nm) NPs onto the CNTs. The actual Pt and Ag loadings of the hybrids were about 18.1 wt% and 33.1 wt% respectively, which are conformed with the initial design (20 wt% and 36 wt%).[135,136]

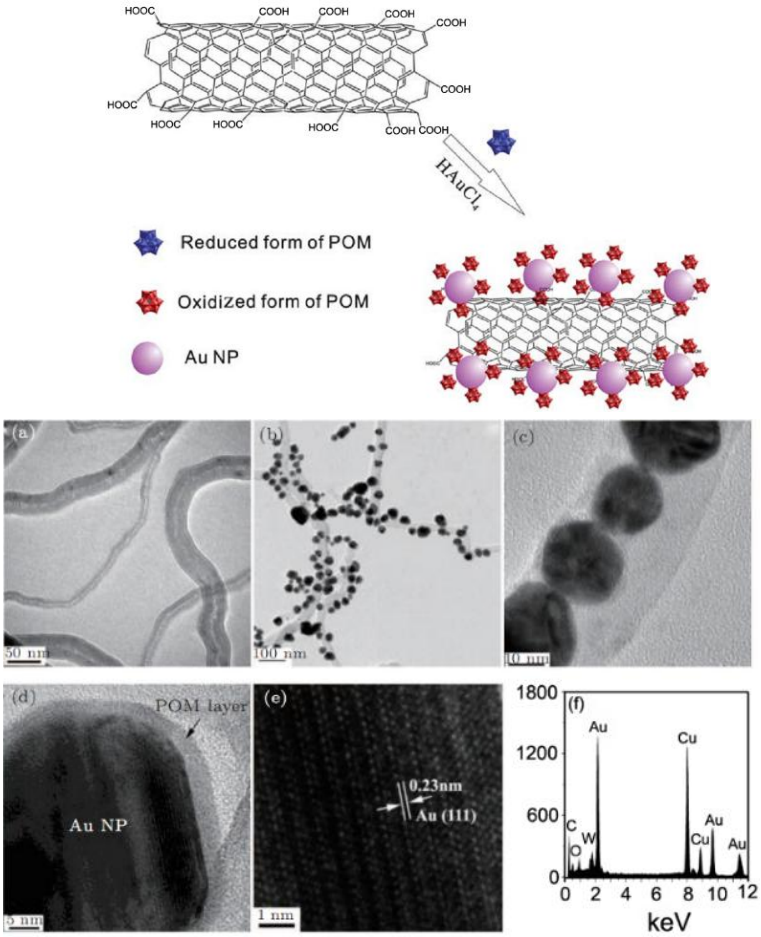

Fig. 1.44 Up: The synthesis route of AuNP@PW_{12}–CNTs at room temperature. Down: a) TEM image of bare CNTs; (b) AuNP@ PW_{12}–CNTs composites; (c) four aligned AuNPs on the surface of a single CNT; (d) magnified image of one AuNP@ PW_{12} core–shell structure; (e) HRTEM image of a single Au NP.

It's worth to mention that the prepared AuNPs@ PW_{12}–CNTs nanohybrids owned enhanced photocatalytic activities for photodegradation of RhB under visible light irradiation (Fig. 1.45 right).[134] Benefited by the intrinsic electronic characteristics, POMs show semiconductor-like photochemical

behaviors.[137] In the current system, under UV light, charge transfer from an O^{2-} to a W^{6+} at W–O–W bonds leading to the formation of a pair of trapped electron (W^{5+}) and hole (O^{-}). The trapped electron can further be oxidized by oxygen, while the hole works as an oxidant for a solution species. Unfortunatly, the aformentioned circulation only can be activated under UV light irradiation, while, when AuNPs were anchored on POMs, the excitation of the LPR of AuNPs induced the charge transfer from the Au NPs to POM. The visible light-induced electron transfer endows AuNPs with oxidizing ability, and able to oxidize organic pollutants (Fig. 1.45 left). So, the prepared AuNPs@PW_{12}–CNTs nanohybrids owned enhanced photocatalytic activities for photodegradation of RhB under visible light irradiation (Fig. 1.45 right).

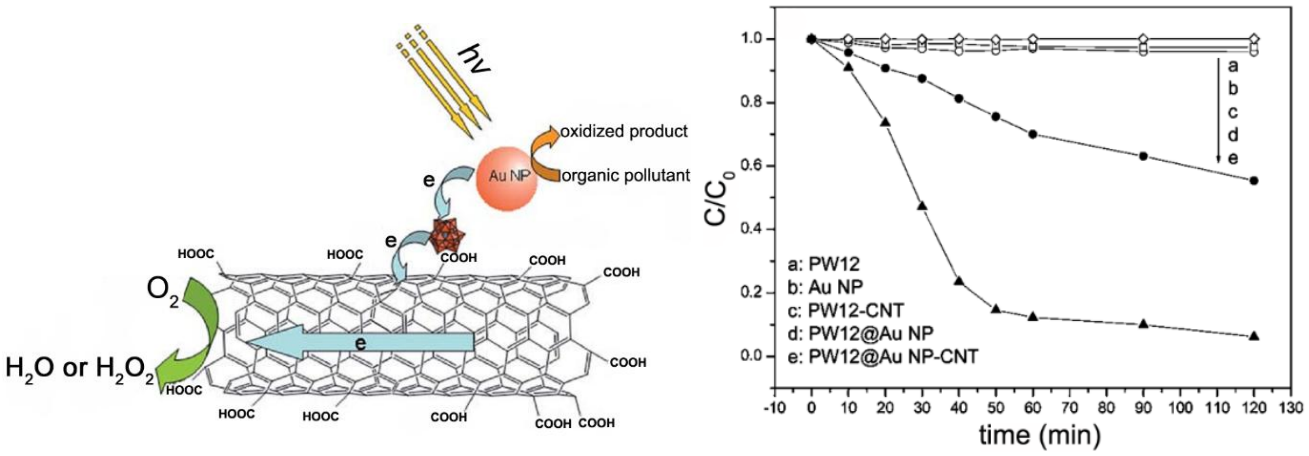

Fig. 1.45 Left: The photocatalytic mechanism of AuNP@PW_{12}-CNTs tri-component nanohybrid. Right: Temporal evolutions of the photodegradation of RhB of different catalytic materials under visible light irradiation ($\lambda > 420$ nm).

Since 2004, graphene nanosheets (GNSs) has been discovered by Novoselov et al.,[138] which were composed of an atomically thin 2D lattice of sp2 carbon atoms packed into a dense honeycomb and evaluated as "the thinnest known material in the universe and the strongest ever measured". Graphene nanosheets have been honoured as a "rising star" material attributed to high electrical conductivity, large surface-to-volume ratio, high electron transfer rate, and exceptional thermal stability.[139,140] Using the same synthesis route as indicated above, Liu, Zhang et al replaced carbon nanotubes by graphene nanosheets (GNSs) to synthesize a series of MNPs@POM–GNSs (M=Au, Pt, Pd)[141,142] and AgNN@POM–GNS[143] (Fig. 1.46a) (where NN stands for the nanonet) with an interesting surface

topography looking like tiny threads in which POM served as both reducing agent and bridge molecules.

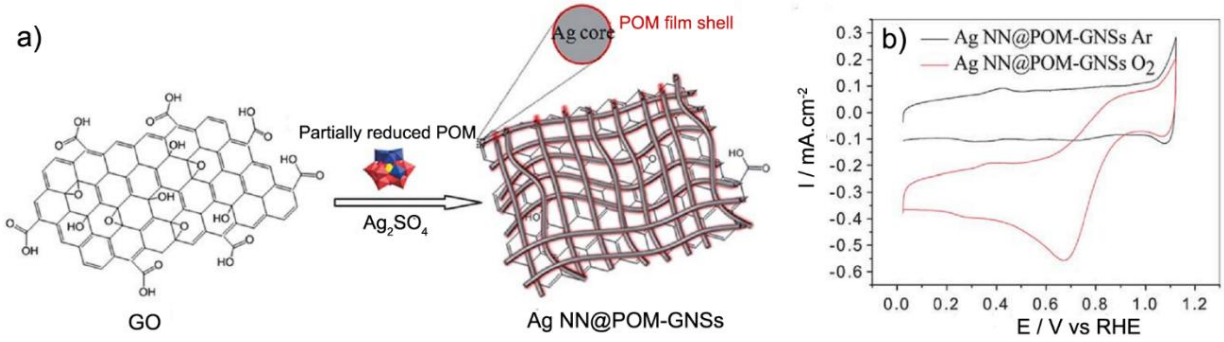

Fig. 1.46 a) The preparation procedure of 2D AgNN@POM–GNSs tri-component hybrids. b) Cyclic voltammetry curves of the dioxygen reduction reaction on AgNN@POM–GNSs in Ar (black curves) and O_2 (red curves) in saturated 0.1M NaOH solutions.

Fig. 1.47(a) and (b) showed that Ag networks were formed by self-weaving of Ag nanowires (AgNW) (40 nm – 50 nm in diameter, exceeding 100 μm in length) disperse on the spreading graphene sheets. The core–shell structure can be clearly observed in Fig. 1.47(c), which is in consistent with the above discussion.[134,135] The high-resolution TEM (HRTEM) image and the electronic diffraction of the nanowires verify their high crystallinity (Fig. 1.47(d)).

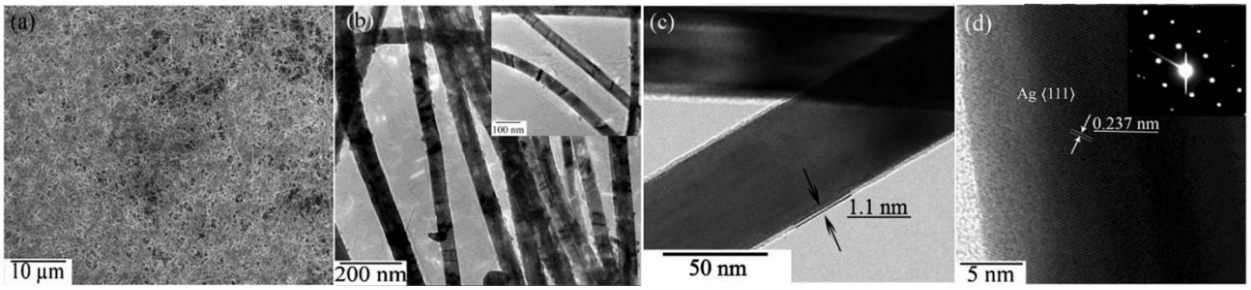

Fig. 1.47 (a) Typical SEM image of AgNW@POM–GNSs. (b) TEM image of AgNW@POM–GNSs, the inset is a magnified image. (c) Magnified TEM image of core–shell AgNW@POM structures. (d) HRTEM of one Ag NW, the inset is the electronic diffraction of the nanowires.

The prepared AgNN@POM–GNSs nanohybrids possessed excellent electro-catalytic activity towards the oxygen reduction reaction since the high catalytic activity of the Ag NN and the brilliant electron transfer ability of GNSs, and also their synergistic effect, reinforced by the presence of POM moieties (Fig. 1.46b). In addtion, I speculate these hybrids may be potential candidates in energy fields, such as photoelectric materials for solar cells.

3. Electrochemical pathway based on nucleophilic substitution onto porphyrin

3.1 Electrosynthesis of monosubstituted porphyrins

The electrochemical properties of porphyrins are now well established. The oxidation of the π-ring of a porphyrin proceeds via two one-electron steps to yield the radical monocation and the dication. The reactivity of porphyrin cations and dications with nucleophilic compounds has been also well researched. In 1974, Dolphin and Felton firstly reported the reactivity of oxidized porphyrins with nucleophilic solvents.[144] However, the π-radical cations have been in most cases prepared by chemical ways, which was confronted with multistep chemical syntheses with low overall yields of the desired products.

Giraudeau et al. firstly reported the reactivity of the electrogenerated radical cation of the zinc meso-tetraphenylporphyrin (ZnTPP) in the presence of pyridine through direct electrochemical oxidation of the macrocycle, leading to a macro-cycle substituted by a pyridinium in *β*-position.[145] Afterwards, a similar work has achieved the substitution of pyridinium in meso-position of the zinc-*β*-octaethylporphyrin (ZnOEP).[146] Lucas et al. reported electrochemical nucleophilic substitutions onto the totally unsubstituted porphyrin (magnesium porphin).[147] Indeed, an electrolysis at a potential allowing the formation of the radical cation of the porphin in the presence of pyridine led to a regioselective mono *meso*-substitution of a pyridine with a yield of 73%. A similar regioselective mono meso-substitution of phosphane has been observed with a yield of 78%. These reactions indicated that substitutions into meso-position are more favorable.

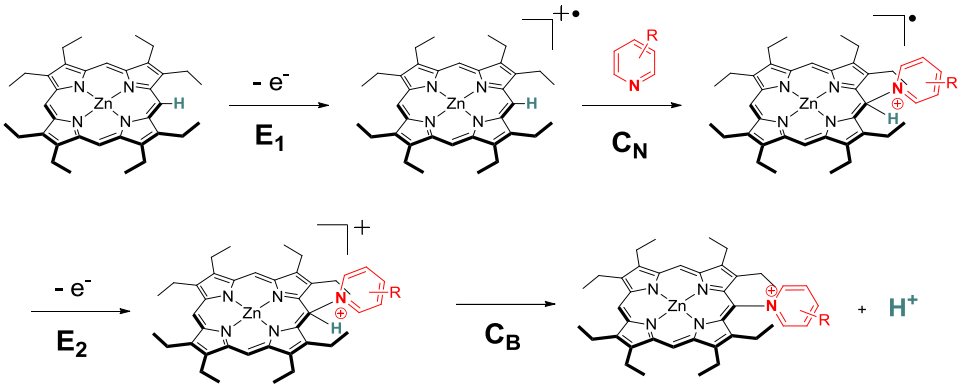

Fig. 1.48 $E_1C_NE_2C_B$ proposed mechanism for the substitution of ZnOEP on one of its meso positions with a pyridine derivative.

The $E_1C_NE_2C_B$ process can well explain the electrochemical substitution of a nucleophile in meso-

position of the ZnOEP macrocycle (Fig. 1.48).[148]

Firstly, the electrogenerated porphyrin radical cation ($ZnOEP^{+\bullet}$, step E_1) can be attacked by a nucleophile (abbreviated Nu) (step C_N) onto a methine bridge (meso-carbon) to yield an isoporphyrin. During the continuous electrolysis, the isoporphyrin is then spontaneously oxidized (step E_2) and the proton present initially on this meso-carbon is released (step C_B) to give the mono-substituted $ZnOEP(Nu)^+$. The global reaction is:

$$ZnOEP + 2\ Nu \rightarrow ZnOEP(Nu)^+ + 2\ e^- + Nu\text{-}H^+$$

The global reaction indicated two equivalents of Lewis base were needed. One equivalent of Lewis base acts as a nucleophile which attacks the *meso*-position, while the second equivalent of nucleophile acts as Brønsted base which helps to remove the proton at the meso-position achieving the rearomatization of the porphyrin.

3.2 Electropolymerization of porphyrin polymers

When 4,4'-bipyridine is used instead of pyridine, dimers even the polymer of porphyrins can be also electrosynthesized.[148] 4,4'-bipyridine presents two accessible nucleophilic sites which can react one after the other with two porphyrin rings. The proposed $E(EC_NEC_B)_nE$ mechanism for the electropolymerization was shown in Fig. 1.49.

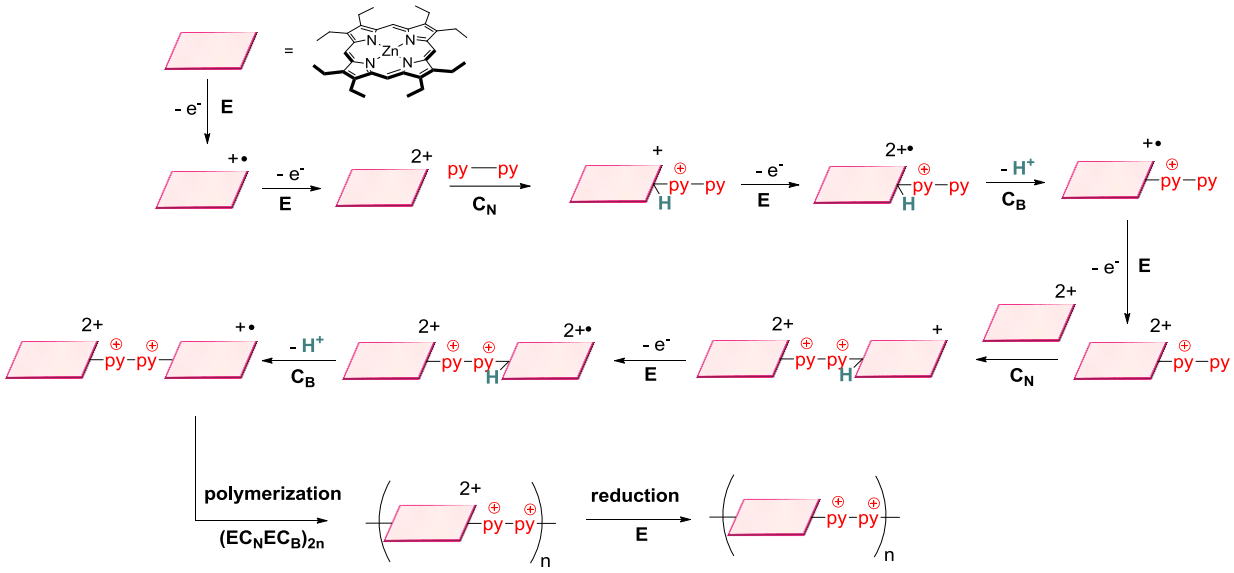

Fig. 1.49 $E(EC_NEC_B)_nE$ mechanism proposed for the electropolymerization.

One important reminder: while the formation of radical cation is sufficient to obtain monosubstituted porphyrins,[148] the formation of dication is demanded to realize the electropolymerization. Firstly, a kinetic factor: the nucleophilic attack is faster onto the dication than onto the radical cation. Consequently, if the iterative scans stopped at a potential allowing only the formation of the radical cation, the nucleophilic attack cannot be performed because of the lack of time (in regard of the speed of the sweep), the reverse scan in the cathodic part being too rapid. The other point regards to the degree of substitution of macrocycles. Indeed, during the process of the polymer synthesis, porphyrins are at least substituted twice by positively charged moieties. Moreover, when the chain of polymer grows, the quantity of positive charge enhances. As a result, porphyrins are more and more difficult to be oxidized. That is to say an increase of the oxidative potential is required to accomplish the polymerization.[146,149] If we use ZnOEP, the four meso-positions are free, and the nucleophilic attack can occur on each of them. Thus, "zigzag" polymers and eventually hyper-branched polymers can be obtained.[150] Conversely, if ZnOEP are substituted by two protecting groups such as chlorides (see Fig. 1.50)[149,150] or pyridiniums[151] on two *meso*-positions (positions 5 and 15), the linear polymers can be obtained.

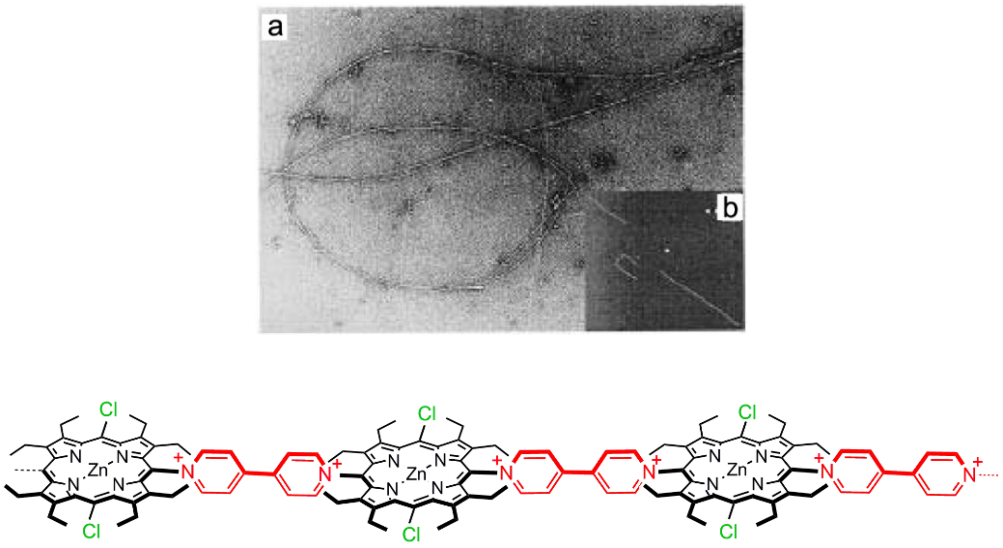

Fig.1.50 a) TEM image of a linear fiber obtained by electropolymerization of $ZnOEP(Cl)_2(bpy)^+$ b) AFM picture (up). Linear polymer obtained from $ZnOEP(Cl)_2(bpy)^+$ monomer (down).

More interestingly, this method allows to easily build functional materials by using inorganic compounds with select properties, provided that these compounds had been previously functionalized with two pendant pyridyl groups in order to use them as spacers between porphyrin macrocycles. As aforementioned review, because POMs possessed rich photoredox chemistry, we planed to synthesize

POMs derivatives functionalized with two pyridyl groups (py-POM-py), then mixed with porphyrin for the electropolymerization through $E(EC_NEC_B)_nE$ process to get POM-porphyrin copolymers. Recently, in our laboratory, we have firstly reported the formation of POM–porphyrin copolymer film with an Anderson type py-POM-py $[MnMo_6O_{18}\{(OCH_2)_3CNHCO(4\text{-}C_5H_4N)\}_2]^{3-}$ and ZnOEP (or 5,15-ZnOEP(py)$^{2+}$) via this original electropolymerization process. The films showed excellent photoactive ability for the reduction of Ag^+ under visible light.[151]

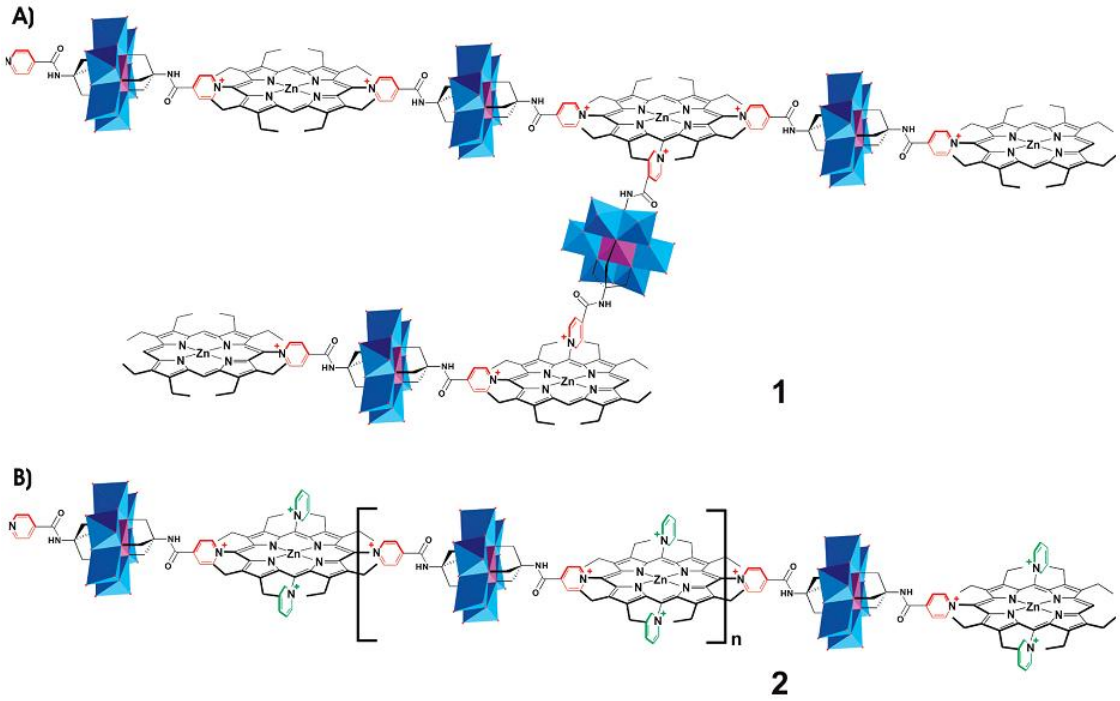

Fig. 1.51 Copolymers 1 and 2 obtained with A) ZnOEP and B) 5,15-ZnOEP(py)$_2^{2+}$, respectively, in the presence of Anderson type py-POM-py $[MnMo_6O_{18}\{(OCH_2)_3CNHCO(4\text{-}C_5H_4N)\}_2]^{3-}$.

Based on the state of the art, the topic of this thesis will be to to explore and to form new type of pophyrin-POM hybrid systems based onto the electrostatic interactions between copolymer of porphyrin obtained by electropolymerization and POM or new copolymers porphyrin-POM obtained directly with **Py-POM-Py** and porphyrin. Thus, in chatpers II to IV, various new type of porphyrin-POM copolymers will be described and studied, where the nature of the **Py-POM-Py** bridge will be selected for their specific chemical or structural properties: rigid or not; long or short; electron conducting or not; with conjugated π-bonds (alkene, alkyne or aromatic chains) or successive σ-bonds (alkyl chains), etc., allowing one to modulate the communication between porphyrin macrocycles within the polymeric chains. The nature of the POM will be also change (Lindqvist, Keggin, Dawon type POM). In chapter V, the hybrid porphyrin-POM systems obtained via the electrostatic interaction between

cationic copolymer of porphyrin and the Preyssler anions will be studied. Finally in the last chapter, POM@MNPs will be included instead of the POM which will give new POM porphyrin - POM@MNPs hybrid systems in order to increase the photosensibilization of the porphyrin.

The effection of the type of POMs and porphyrins used (variation of the charge, the size, the metal and the redox potential of the POM, and variation of the type of the porphyrin: free base versus metalloporphyrin), for the photocatalysis and the photoelectrocatalysis properties, will be examinated in this work.

References

(1) Bajema, L.; Gouterman, M.; Meyer, B. *J. Mol. Spectrosc.* **1961**, *27* (1-4), 225.
(2) Fajer, J.; Borg, D. C.; Forman, a; Dolphin, D.; Felton, R. H. *J. Am. Chem. Soc.* **1970**, *92* (11), 3451.
(3) Fuhrhop, J. H.; Kadish, K. M.; Davis, D. G. *J. Am. Chem. Soc.* **1973**, *95* (16), 5140.
(4) Wolberg, a; Manassen, J. *J. Am. Chem. Soc.* **1970**, *92* (10), 2982.
(5) Potentials, S. O. R. *J. Am. Chem. Soc.* **1965**, *104* (3), 4238.
(6) O'Regan, B.; Grätzel, M. *Nature*, ***1991***, *353* (6346), 737.
(7) Nazeeruddin, M. K.; De Angelis, F.; Fantacci, S.; Selloni, A.; Viscardi, G.; Liska, P.; Ito, S.; Takeru, B.; Grätzel, M. *J. Am. Chem. Soc.* **2005**, *127* (48), 16835.
(8) Wang, Q.; Ito, S.; Grätzel, M.; Fabregat-Santiago, F.; Mora-Seró, I.; Bisquert, J.; Bessho, T.; Imai, H. *J. Phys. Chem. B* **2006**, *110* (50), 25210.
(9) Chen, C.-Y.; Wang, M.; Li, J.-Y.; Pootrakulchote, N.; Alibabaei, L.; Ngoc-le, C.-H.; Decoppet, J.-D.; Tsai, J.-H.; Grätzel, C.; Wu, C.-G.; Zakeeruddin, S. M.; Grätzel, M. *ACS Nano* **2009**, *3* (10), 3103.
(10) Cao, Y.; Bai, Y.; Yu, Q.; Cheng, Y.; Liu, S.; Shi, D.; Gao, F.; Wang, P. *J. Phys. Chem. C* **2009**, *113* (15), 6290.
(11) Yu, Q.; Wang, Y.; Yi, Z.; Zu, N.; Zhang, J.; Zhang, M.; Wang, P. *ACS Nano* **2010**, *4* (10), 6032.
(12) Han, L.; Islam, A.; Chen, H.; Malapaka, C.; Chiranjeevi, B.; Zhang, S.; Yang, X.; Yanagida, M. *Energy Environ. Sci.* **2012**, *5* (3), 6057.
(13) Kinoshita, T.; Dy, J. T.; Uchida, S.; Kubo, T.; Segawa, H. *Nat. Photonics* **2013**, *7* (7), 535.
(14) Robertson, N. *Angew. Chemie., Int. Ed.* **2006**, *45* (15), 2338.
(15) Ooyama, Y.; Harima, Y. *Eur. J. Org. Chem.* **2009**, *2009* (18), 2903.
(16) Mishra, A.; Fischer, M. K. R.; Bäuerle, P. *Angew. Chemie., Int. Ed.* **2009**, *48* (14), 2474.
(17) Ning, Z.; Fu, Y.; Tian, H. *Energy Environ. Sci.* **2010**, *3* (9), 1170.
(18) Imahori, H.; Umeyama, T.; Ito, S. *Acc. Chem. Res.* **2009**, *42* (11), 1809.
(19) Radivojevic, I.; Varotto, A.; Farley, C.; Drain, C. M. *Energy Environ. Sci.* **2010**, *3* (12), 1897.
(20) Martínez-Díaz, M. V.; de la Torre, G.; Torres, T. *Chem. Commun.* **2010**, *46* (38), 7090.
(21) Griffith, M. J.; Sunahara, K.; Wagner, P.; Wagner, K.; Wallace, G. G.; Officer, D. L.; Furube, A.; Katoh, R.; Mori, S.; Mozer, A. J. *Chem. Commun.* **2012**, *48* (35), 4145.
(22) Imahori, H.; Umeyama, T.; Kurotobi, K.; Takano, Y. *Chem. Commun.* **2012**, *48* (34), 4032.
(23) Panda, M. K.; Ladomenou, K.; Coutsolelos, A. G. *Coord. Chem. Rev.* **2012**, *256* (21-22), 2601.
(24) Hasobe, T.; Imahori, H.; Kamat, P. V.; Tae, K. A.; Seong, K. K.; Kim, D.; Fujimoto, A.; Hirakawa, T.; Fukuzumi, S. *J. Am. Chem. Soc.* **2005**, *127* (4), 1216.
(25) Yella, a.; Lee, H.-W.; Tsao, H. N.; Yi, C.; Chandiran, a. K.; Nazeeruddin, M. K.; Diau, E. W.-G.; Yeh, C.-Y.; Zakeeruddin, S. M.; Gratzel, M. *Science* **2011**, *334* (6056), 629.
(26) Gao, F.; Wang, Y.; Shi, D.; Zhang, J.; Wang, M.; Jing, X.; Humphry-Baker, R.; Wang, P.; Zakeeruddin, S. M.; Grätzel, M. *J. Am. Chem. Soc.* **2008**, *130* (32), 10720.
(27) Horiuchi, T.; Miura, H.; Sumioka, K.; Uchida, S. *J. Am. Chem. Soc.* **2004**, *126* (39), 12218.
(28) Hara, K.; Wang, Z.; Sato, T.; Furube, A.; Katoh, R.; Sugihara, H.; Dan-oh, Y.; Kasada, C.; Shinpo, A.; Suga, S. *J. Phys. Chem. B* **2005**, *109* (32), 15476.
(29) Kim, S.; Lee, J. K.; Kang, S. O.; Ko, J.; Yum, J.-H.; Fantacci, S.; De Angelis, F.; Di Censo, D.; Nazeeruddin, M. K.; Grätzel, M. *J. Am. Chem. Soc.* **2006**, *128* (51), 16701.
(30) Ito, S.; Zakeeruddin, S. M.; Humphry-Baker, R.; Liska, P.; Charvet, R.; Comte, P.; Nazeeruddin, M. K.; Péchy, P.; Takata, M.; Miura, H.; Uchida, S.; Grätzel, M. *Adv. Mater.* **2006**, *18* (9), 1202.
(31) Hwang, S.; Lee, J. H.; Park, C.; Lee, H.; Kim, C.; Park, C.; Lee, M.-H.; Lee, W.; Park, J.; Kim, K.; Park, N.-G.; Kim, C. *Chem. Commun.* **2007**, (46), 4887.
(32) Wang, Z. S.; Koumura, N.; Cui, Y.; Takahashi, M.; Sekiguchi, H.; Mori, A.; Kubo, T.; Furube, A.; Hara, K. *Chem. Mater.* **2008**, *20* (12), 3993.
(33) Ito, S.; Miura, H.; Uchida, S.; Takata, M.; Sumioka, K.; Liska, P.; Comte, P.; Péchy, P.; Grätzel, M. *Chem. Commun.* **2008**, 5194.
(34) Zeng, W.; Cao, Y.; Bai, Y.; Wang, Y.; Shi, Y.; Zhang, M.; Wang, F.; Pan, C.; Wang, P. *Chem. Mater.* **2010**, *22* (5), 1915.
(35) Tsao, H. N.; Yi, C.; Moehl, T.; Yum, J. H.; Zakeeruddin, S. M.; Nazeeruddin, M. K.; Grätzel, M. *ChemSusChem* **2011**, *4* (5), 591.
(36) Xu, M.; Zhang, M.; Pastore, M.; Li, R.; De Angelis, F.; Wang, P. *Chem. Sci.* **2012**, *3* (4), 976.
(37) Kay, A.; Graetzel, M. *J. Phys. Chem.* **1993**, *97* (23), 6272.
(38) Cherian, S.; Wamser, C. C. *J. Phys. Chem. B* **2000**, *104* (15), 3624.

(39) Nazeeruddin, M. K.; Humphry-Baker, R.; Officer, D. L.; Campbell, W. M.; Burrell, A. K.; Grätzel, M. *Langmuir* **2004**, *20* (15), 6514.
(40) Wang, Q.; Campbell, W. M.; Bonfantani, E. E.; Jolley, K. W.; Officer, D. L.; Walsh, P. J.; Gordon, K.; Humphry-Baker, R.; Nazeeruddin, M. K.; Grätzel, M. *J. Phys. Chem. B* **2005**, *109* (32), 15397.
(41) Campbell, W. M.; Jolley, K. W.; Wagner, P.; Wagner, K.; Walsh, P. J.; Gordon, K. C.; Schmidt-Mende, L.; Nazeeruddin, M. K.; Wang, Q.; Grätzel, M.; Officer, D. L. *J. Phys. Chem. C* **2007**, *111* (32), 11760.
(42) Park, J. K.; Lee, H. R.; Chen, J.; Shinokubo, H.; Osuka, A.; Kim, D. *J. Phys. Chem. C* **2008**, *112* (42), 16691.
(43) Bessho, T.; Zakeeruddin, S. M.; Yeh, C. Y.; Diau, E. W. G.; Grätzel, M. *Angew. Chemie., Int. Ed.* **2010**, *49*, 6646.
(44) Campbell, W. M.; Burrell, A. K.; Officer, D. L.; Jolley, K. W. *Coord. Chem. Rev.* **2004**, *248* (13-14), 1363.
(45) He, H.; Gurung, A.; Si, L. *Chem. Commun.* **2012**, *48* (47), 5910.
(46) Hagfeldt, A.; Boschloo, G.; Sun, L.; Kloo, L.; Pettersson, H. *Chem. Rev.* **2010**, *110*, 6595.
(47) Nazeeruddin, M. K.; Kay, A; Miiller, E.; Liska, P.; Vlachopoulos, N.; Grätzel, M. *J. Am. Chem. Soc.* **1993**, *115* (4), 6382.
(48) Kakiage, K.; Aoyama, Y.; Yano, T.; Otsuka, T.; Kyomen, T.; Unno, M.; Hanaya, M. *Chem. Commun.* **2014**, *50* (48), 6379.
(49) Mathew, S.; Yella, A.; Gao, P.; Humphry-Baker, R.; Curchod, B. F. E.; Ashari-Astani, N.; Tavernelli, I.; Rothlisberger, U.; Nazeeruddin, M. K.; Grätzel, M. *Nat. Chem.* **2014**, *6* (3), 242.
(50) Lee, C.-W.; Lu, H.-P.; Lan, C.-M.; Huang, Y.-L.; Liang, Y.-R.; Yen, W.-N.; Liu, Y.-C.; Lin, Y.-S.; Diau, E. W.-G.; Yeh, C.-Y. *Chem. Eur. J.* **2009**, *15* (6), 1403.
(51) Lin, C. Y.; Wang, Y. C.; Hsu, S. J.; Lo, C. F.; Diau, E. W. G. *J. Phys. Chem. C* **2010**, *114* (1), 687.
(52) Wu, C.-H.; Pan, T.-Y.; Hong, S.-H.; Wang, C.-L.; Kuo, H.-H.; Chu, Y.-Y.; Diau, E. W.-G.; Lin, C.-Y. *Chem. Commun.* **2012**, *48* (36), 4329.
(53) Wang, C.-L.; Chang, Y.-C.; Lan, C.-M.; Lo, C.-F.; Wei-Guang Diau, E.; Lin, C.-Y. *Energy Environ. Sci.* **2011**, *4* (5), 1788.
(54) Tanaka, M.; Hayashi, S.; Eu, S.; Umeyama, T.; Matano, Y.; Imahori, H. *Chem. Commun.* **2007**, *3* (20), 2069.
(55) Hayashi, S.; Tanaka, M.; Hayashi, H.; Eu, S.; Umeyama, T.; Matano, Y.; Araki, Y.; Imahori, H. *J. Phys. Chem. C* **2008**, *112* (39), 15576.
(56) Eu, S.; Hayashi, S.; Umeyama, T.; Matano, Y.; Araki, Y.; Imahori, H. *J. Phys. Chem. C* **2008**, *112* (11), 4396.
(57) Mai, C.-L.; Huang, W.-K.; Lu, H.-P.; Lee, C.-W.; Chiu, C.-L.; Liang, Y.-R.; Diau, E. W.-G.; Yeh, C.-Y. *Chem. Commun.* **2010**, *46* (5), 809.
(58) Park, J. K.; Chen, J.; Lee, H. R.; Park, S. W.; Shinokubo, H.; Osuka, A.; Kim, D. *J. Phys. Chem. C* **2009**, *113* (52), 21956.
(59) Liu, Y.; Lin, H.; Dy, J. T.; Tamaki, K.; Nakazaki, J.; Nakayama, D.; Uchida, S.; Kubo, T.; Segawa, H. *Chem. Commun.* **2011**, *47* (13), 4010.
(60) Gao, P.; Kim, Y. J.; Yum, J.-H.; Holcombe, T. W.; Nazeeruddin, M. K.; Grätzel, M. *J. Mater. Chem. A* **2013**, *1* (18), 5535.
(61) Pillai, S.; Catchpole, K. R.; Trupke, T.; Green, M. a. *J. Appl. Phys.* **2007**, *101* (9).
(62) Stuart, H. R.; Hall, D. G. *Appl. Phys. Lett.* **1996**, *69* (16), 2327.
(63) Hägglund, C.; Zäch, M.; Petersson, G.; Kasemo, B. *Appl. Phys. Lett.* **2008**, *92* (5), 10.
(64) Schaadt, D. M.; Feng, B.; Yu, E. T. *Appl. Phys. Lett.* **2005**, *86* (6), 1.
(65) Sundararajan, S. P.; Grady, N. K.; Mirin, N.; Halas, N. J. *Nano Lett.* **2008**, *8* (2), 624.
(66) Lim, S. H.; Mar, W.; Matheu, P.; Derkacs, D.; Yu, E. T. *J. Appl. Phys.* **2007**, *101* (10), 104309.
(67) Konda, R. B.; Mundle, R.; Mustafa, H.; Bamiduro, O.; Pradhan, a. K.; Roy, U. N.; Cui, Y.; Burger, a. *Appl. Phys. Lett.* **2007**, *91* (19), 191111.
(68) Kwon, M. K.; Kim, J. Y.; Kim, B. H.; Park, I. K.; Cho, C. Y.; Byeon, C. C.; Park, S. J. *Adv. Mater.* **2008**, *20* (7), 1253.
(69) Pillai, S.; Catchpole, K. R.; Trupke, T.; Zhang, G.; Zhao, J.; Green, M. a. *Appl. Phys. Lett.* **2006**, *88* (16), 1.
(70) Stuart, H. R.; Hall, D. G. *Appl. Phys. Lett.* **1998**, *73* (26), 3815.
(71) Collin, S.; Pardo, F.; Pelouard, J. L. *Appl. Phys. Lett.* **2003**, *83* (8), 1521.
(72) Akiyama, T.; Nakada, M.; Terasaki, N.; Yamada, S. *Chem. Commun.* **2006**, (4), 395.
(73) Akiyama, T.; Aiba, K.; Hoashi, K.; Wang, M.; Sugawa, K.; Yamada, S. *Chem. Commun.* **2010**, *46* (2), 306.
(74) Matsumoto, R.; Yonemura, H.; Yamada, S. *J. Phys. Chem. C* **2013**, *117* (6), 2486.

(75) Alizadeh, M. H.; Harmalker, S. P.; Jeannin, Y.; Martin-Frere, J.; Pope, M. T. *J. Am. Chem. Soc.* **1985**, *107* (9), 2662.
(76) Müller, A.; Peters, F.; Pope, M. T.; Gatteschi, D. *Chem. Rev.* **1998**, *98* (1), 239.
(77) Long, D.-L.; Burkholder, E.; Cronin, L. *Chem. Soc. Rev.* **2007**, *36* (1), 105.
(78) Müller, a.; Kögerler, P.; Dress, a. W. M. *Coord. Chem. Rev.* **2001**, *222* (1), 193.
(79) Müller, a.; Roy, S. *Coord. Chem. Rev.* **2003**, *245* (1-2), 153.
(80) Müller, A.; Krickemeyer, E.; Meyer, J.; Bogge, H.; Peters, F.; Plass, W.; Diemann, E.; Dillinger, S.; Randerath, M.; Menke, C. *Angew. Chem., Int. Ed.* **1995**, *4* (19), 2122.
(81) Müller, A.; Krickemeyer, E.; Bögge, H.; Schmidtmann, M.; Peters, F. *Angew. Chem., Int. Ed.* **1998**, *37* (24), 3359.
(82) Achim, M.; Beckmann, E.; Bögge, H.; Schmidtmann, M.; Dress, A. *Angew. Chem., Int. Ed.* **2002**, *41*(7), 1162.
(83) Xie, J.; Abrahams, B. F.; Wedd, A. G. *Chem. Commun.* **2008**, *5*, 576.
(84) Nie, S.; Zhang, Y.; Liu, B.; Li, Z.; Hu, H.; Xue, G.; Fu, F.; Wang, J. *J. Solid State Chem.* **2010**, *183* (12), 2957.
(85) Zhang, H.; Peng, J.; Shen, Y.; Yu, X.; Zhang, F.; Mei, J.; Li, B.; Zhang, L. *Chem. Commun.* **2012**, *48* (37), 4462.
(86) Ruhlmann, L.; Costa-Coquelard, C.; Hao, J.; Jiang, S.; He, C.; Sun, L.; Lampre, I. *Can. J. Chem.* **2008**, *86* (11), 1034.
(87) Santos, I. C. M. S.; Rebelo, S. L. H.; Balula, M. S. S.; Martins, R. R. L.; Pereira, M. M. M. S.; Simões, M. M. Q.; Neves, M. G. P. M. S.; Cavaleiro, J. a. S.; Cavaleiro, A. M. V. *J. Mol. Catal. A Chem.* 2005, 231 (1-2), 35.
(88) Costa-Coquelard, C.; Sorgues, S.; Ruhlmann, L. *J. Phys. Chem. A* 2010, 114 (22), 6394.
(89) Zhu, J.; Walsh, J. J.; Bond, A. M.; Keyes, T. E.; Forster, R. J. *Langmuir* 2012, 28 (37), 13536.
(90) Walsh, J. J.; Zhu, J.; Zeng, Q.; Forster, R. J.; Keyes, T. E. *Dalton Transactions*, 2012, 41, 9928.
(91) Zhu, J.; Zeng, Q.; O'Carroll, S.; Bond, A.; Keyes, T. E.; Forster, R. *J. Electrochem. commun*. 2011, 13 (9), 899.
(92) Gao, L.; Sun, Q.; Lin, X.; Qi, J.; Wang, K. *Colloids Surfaces A Physicochem. Eng. Asp.* 2013, 423, 162.
(93) Gao, L.; Sun, Q.; Wang, K. J. *Colloid Interface Sci.* 2013, 393 (1), 92.
(94) Gao, L. H.; Sun, Q. L.; Qi, J. M.; Lin, X. Y.; Wang, K. Z. *Electrochim. Acta* 2013, 92, 236.
(95) Yang, Y.; Xu, L.; Li, F.; Du, X.; Sun, Z. *J. Mater. Chem.* 2010, 20 (48), 10835.
(96) Sun, Z.; Fang, S.; Li, F.; Xu, L.; Hu, Y.; Ren, J. *J. Photochem. Photobiol. A Chem.* 2013, 252, 25.
(97) Ahmed, I.; Wang, X.; Boualili, N.; Xu, H.; Farha, R.; Goldmann, M.; Ruhlmann, L. *Appl. Catal. A Gen.* 2012, 447-448, 89.
(98) Ahmed, I.; Farha, R.; Goldmann, M.; Ruhlmann, L. Chem. Commun. (Camb). 2013, 49 (5), 496.
(99) Gao, L.-H.; Zhang, J.-F.; Wang, H.-L.; Lin, X.-Y.; Qi, J.-M.; Wang, K.-Z. *Electrochim. Acta* **2015**, *166*, 215.
(100) Shi, Z.; Zhou, Y.; Zhang, L.; Yang, D.; Mu, C.; Ren, H.; Shehzad, F. K.; Li, J. *Dalt. Trans.* **2015**, *44* (9), 4102.
(101) Piepenbrink, M.; Triller, M. U.; Gorman, N. H. J.; Krebs, B. *Angew. Chemie., Int. Ed.* **2002**, *41* (14), 2523.
(102) Yokoyama, A.; Kojima, T.; Ohkubo, K.; Fukuzumi, S. *Chem. Commun.* **2007**, *7345* (39), 3997.
(103) Yokoyama, A.; Kojima, T.; Ohkubo, K.; Shiro, M.; Fukuzumi, S. *J. Phys. Chem. A* **2011**, *115* (6), 986.
(104) Ko, M.; Rhyu, G. I.; So, *H. Bull. Korean Chem. Soc.* **1993**, *14* (4), 500.
(105) Schaming, D.; Costa-Coquelard, C.; Lampre, I.; Sorgues, S.; Erard, M.; Liu, X.; Liu, J.; Sun, L.; Canny, J.; Thouvenot, R.; Ruhlmann, L. *Inorganica Chim. Acta* **2010**, *363* (10), 2185.
(106) Chen, Q.; Chen, Q.; Goshorn, D. P.; Goshorn, D. P.; Scholes, C. P.; Scholes, C. P.; Tan, X. L.; Tan, X. L.; Zubieta, J.; Zubieta, J. *J. Am. Chem. Soc.* **1992**, *114* (12), 4667.
(107) Li, J.; Huth, I.; Chamoreau, L. M.; Hasenknopf, B.; Lacôte, E.; Thorimbert, S.; Malacria, M. *Angew. Chemie., Int. Ed.* **2009**, *48* (11), 2035.
(108) Allain, C.; Favette, S.; Chamoreau, L. M.; Vaissermann, J.; Ruhlmann, L.; Hasenknopf, B. *Eur. J. Inorg. Chem.* **2008**, *2008* (22), 3433.
(109) Allain, C.; Schaming, D.; Karakostas, N.; Erard, M.; Gisselbrecht, J.-P.; Sorgues, S.; Lampre, I.; Ruhlmann, L.; Hasenknopf, B. *Dalton Trans.* **2013**, *42* (8), 2745.
(110) Ahmed, I.; Farha, R.; Huo, Z.; Allain, C.; Wang, X.; Xu, H.; Goldmann, M.; Hasenknopf, B.; Ruhlmann, L. *Electrochim. Acta* **2013**, *110*, 726.
(111) Santoni, M.-P.; Pal, A. K.; Hanan, G. S.; Tang, M.-C.; Venne, K.; Furtos, A.; Ménard-Tremblay, P.; Malveau, C.; Hasenknopf, B. *Chem. Commun.* **2012**, *48* (2), 200.

(112) Santoni, M.-P.; Pal, A. K.; Hanan, G. S.; Tang, M.-C.; Furtos, A.; Hasenknopf, B. *Dalton Trans.* **2014**, *43* (19), 6990.
(113) Santoni, M. P.; Pal, A. K.; Hanan, G. S.; Proust, A.; Hasenknopf, B. *Inorg. Chem.* **2011**, *50* (14), 6737.
(114) Stark, J. L.; Young, V. G.; Maatta, E. A. *Angew. Chemie., Int. Ed.* **1995**, *34* (22), 2547.
(115) Kang, J.; Nelson, J. a; Lu, M.; Xie, B.; Peng, Z.; Powell, D. R. *Inorg. Chem.* **2004**, *43* (20), 6408.
(116) Lu, M.; Xie, B.; Kang, J.; Chen, F.-C.; Peng, Z. *Chem. Mater.* **2005**, *17* (2), 402.
(117) Xu, B.; Lu, M.; Kang, J.; Wang, D.; Brown, J.; Peng, Z. *Chem. Mater.* **2005**, *17* (11), 2841.
(118) Odobel, F.; Séverac, M.; Pellegrin, Y.; Blart, E.; Fosse, C.; Cannizzo, C.; Mayer, C. R.; Elliott, K. J.; Harriman, A. *Chem. Eur. J.* **2009**, *15* (13), 3130.
(119) Harriman, A.; Elliott, K. J.; Alamiry, M. a H.; Pieux, L. Le; Séverac, M.; Pellegrin, Y.; Blart, E.; Fosse, C.; Cannizzo, C.; Mayer, C. R.; Odobel, F. *J. Phys. Chem. C* **2009**, *113* (14), 5834.
(120) Elliott, K. J.; Harriman, A.; Le Pleux, L.; Pellegrin, Y.; Blart, E.; Mayer, C. R.; Odobel, F. *Phys. Chem. Chem. Phys.* **2009**, *11* (39), 8767.
(121) Matt, B.; Coudret, C.; Viala, C.; Jouvenot, D.; Loiseau, F.; Izzet, G.; Proust, A. *Inorg. Chem.* **2011**, *50* (16), 7761.
(122) Matt, B.; Renaudineau, S.; Chamoreau, L. M.; Afonso, C.; Izzet, G.; Proust, a. *J. Org. Chem.* **2011**, *76* (9), 3107.
(123) Matt, B.; Moussa, J.; Chamoreau, L. M.; Afonso, C.; Proust, A.; Amouri, H.; Izzet, G. *Organometallics* **2012**, *31* (1), 35.
(124) Geletii, Y. V.; Huang, Z.; Hou, Y.; Musaev, D. G.; Lian, T.; Hill, C. L. *J. Am. Chem. Soc.* **2009**, *131* (22), 7522.
(125) Orlandi, M.; Argazzi, R.; Sartorel, A.; Carraro, M.; Scorrano, G.; Bonchio, M.; Scandola, F. *Chem. Commun.* **2010**, *46* (18), 3152.
(126) Sartorel, A.; Miró, P.; Salvadori, E.; Romain, S.; Carraro, M.; Scorrano, G.; Di Valentin, M.; Llobet, A.; Bo, C.; Bonchio, M. *J. Am. Chem. Soc.* **2009**, *131* (44), 16051.
(127) Puntoriero, F.; La Ganga, G.; Sartorel, A.; Carraro, M.; Scorrano, G.; Bonchio, M.; Campagna, S. *Chem. Commun.* **2010**, *46* (26), 4725.
(128) Troupis, A.; Hiskia, A.; Papaconstantinou, E. *Angew. Chemie., Int. Ed.* **2002**, *41* (11), 1911.
(129) Neyman, A.; Meshi, L.; Zeiri, L.; Weinstock, I. *J. Am. Chem. Soc.* **2008**, *130* (49), 16480.
(130) Wang, Y.; Neyman, A.; Arkhangelsky, E.; Gitis, V.; Meshi, L.; Weinstock, I. *J. Am. Chem. Soc.* **2009**, *131* (47), 17412.
(131) Jeon, I.-Y.; Choi, H.-J.; Ju, M. J.; Choi, I. T.; Lim, K.; Ko, J.; Kim, H. K.; Kim, J. C.; Lee, J.-J.; Shin, D.; Jung, S.-M.; Seo, J.-M.; Kim, M.-J.; Park, N.; Dai, L.; Baek, J.-B. *Sci. Rep.* **2013**, *3*, 2260.
(132) Liang, Y.; Li, Y.; Wang, H.; Zhou, J.; Wang, J.; Regier, T.; Dai, H. *Nat. Mater.* **2011**, *10* (10), 780.
(133) Wang, S.; Yu, D.; Dai, L. *J. Am. Chem. Soc.* **2011**, *133* (14), 5182.
(134) Li, S.; Yu, X.; Zhang, G.; Ma, Y.; Yao, J.; Keita, B.; Louis, N.; Zhao, H. *J. Mater. Chem.* **2011**, *21* (7), 2282.
(135) Li, S.; Yu, X.; Zhang, G.; Ma, Y.; Yao, J.; De Oliveira, P. *Carbon* **2011**, *49* (6), 1906.
(136) Liu, R.; Li, S,; Yu, X.; Zhang, G.; Ma, Y; Yao, J.; *J. Mater. Chem.* **2011** *21*(7) 14917.
(137) Guo, Y.; Hu, C. *J. Mol. Catal. A Chem.* **2007**, *262* (1-2), 136.
(138) Novoselov, K. S.; Geim, A. K.; Morozov, S. V; Jiang, D.; Zhang, Y.; Dubonos, S. V; Grigorieva, I. V; Firsov, A. A. *Science* **2004**, *306* (5696), 666.
(139) Wang, Y.; Shao, Y.; Matson, D. W.; Li, J.; Lin, Y. *ACS Nano* **2010**, *4* (4), 1790.
(140) Shao, Y.; Wang, J.; Engelhard, M.; Wang, C.; Lin, Y. *J. Mater. Chem.* **2010**, *20* (4), 743.
(141) Liu, R.; Li, S.; Yu, X.; Zhang, G.; Zhang, S.; Yao, J.; Keita, B.; Nadjo, L.; Zhi, L. *Small* **2012**, *8* (9), 1398.
(142) Liu, R.; Li, S.; Yu, X.; Zhang, G.; Zhang, S.; Yao, J.; Zhi, L. *J. Mater. Chem.* **2012**, *22* (8), 3319.
(143) Liu, R.; Yu, X.; Zhang, G.; Zhang, S.; Cao, H.; Dolbecq, A.; Mialane, P.; Keita, B.; Zhi, L. *J. Mater. Chem. A* **2013**, *1* (38), 11961.
(144) D. Dolphin，R. H. Felton. *Acc. Chem. Res.* **1974**, *7*, 26.
(145) El Kahef, L.; El Meray, M.; Gross, M.; Giraudeau, a. *J. Chem. Soc. Chem. Commun.* **1986**, *12* (8), 621.
(146) Giraudeau, A.; Lobstein, S.; Ruhlmann, L.; Melamed, D.; Barkigia, K. M.; Fajer, J. *J. Porphyrins Phthalocyanines* **2001**, *05* (11), 793.
(147) Devillers, C. H.; Dime, A. K. D.; Cattey, H.; Lucas, D. *Chem. Commun.* **2011**, *47* (6), 1893.
(148) Giraudeau, A.; Ruhlmann, L.; El Kahef, L.; Gross, M. *J. Am. Chem. Soc.* **1996**, *118* (12), 2969.
(149) Ruhlmann, L.; Schulz, A. *J. Am. Chem. Soc.* **1999**, *121* (8), 6664.
(150) Xia, Y.; Schaming, D.; Farha, R.; Goldmann, M.; Ruhlmann, L. *New J. Chem.* **2012**, *36* (3), 588.
(151) Schaming, D.; Allain, C.; Farha, R.; Goldmann, M.; Lobstein, S.; Giraudeau, A.; Hasenknopf, B.; Ruhlmann, L. *Langmuir* **2010**, *26* (7), 5101.

Chapter II

Covalent Lindqvist polyoxovanadate – porphyrin hybrid films for the photocurrent generation and the photocatalytical recovery of metal

Chapter II: Covalent Lindqvist polyoxovanadate – porphyrin hybrid films for the photocurrent generation and the photocatalytical recovery of metals

In the following three chapters (chapters II, III, and IV), we have prepared three series of covalent POM–porphyrin copolymers using an electropolymerization method based on the nucleophilic attack of pyridyl groups (bound on the POM framework, Py-POM-Py) as Lewis bases onto electrogenerated porphyrin dications through an $E(EC_NEC_B)_nE$ process.[1]

In the present chapter II, the electropolymerization of the free base type 5,15-ditolyl porphyrin (**H_2T_2P**) or of the metalloporphyrin type zinc-*β*-octaethylporphyrin (**ZnOEP**) in the presence of a functionalized Lindqvist polyoxovanadate bearing two pyridyl groups which were tethered to the POM through tris-alkoxo functionalization ($[V_6O_{13}\{(OCH_2)_3CNHCO(4\text{-}C_5H_4N)\}_2]^{2-}$ (**Py-V_6O_{13}-Py**)) is reported.

The resulting films have been characterized by UV–visible absorption spectroscopy, X-ray photoelectron spectroscopy, atomic force microscopy and electrochemistry. Electrochemical quartz crystal microbalance was employed to investigate the copolymer mass. Their photovoltaic performance has been investigated by photocurrent transient measurements. The two hybrid films also applied for photocatalytical recovery of noble metal (Ag and Pt).

1. Introduction

Polyoxometalates (POMs), a large family of transition metal oxygen anion clusters with d^0 electronic configurations, exhibits overall similar photocatalytic behaviors like semiconductor metal oxides. Upon light irradiation, electrons are promoted from an oxygen-centered 2p orbital to an empty metallic d-orbital, generating a highly reactive charge-separated state.[2] With this concept Anandan et al. impregnated POM in polyvinylidene fluoride polymer as a solid polymer electrolyte in DSSCs and obtained expectant results.[3] The above-mentioned excellent properties and pioneering studies indicate that POMs will be promising candidates to optimize the efficiency of electrolytes in photocurrent generation. Furthermore, POMs also play an important role in environmentally benign oxidative

photodegradation of organic compounds in water purification technology.[4] While photolysis in the presence of a sacrificial electron donor reduces POMs which in turn lead to the reduction of metallic ions, it appears finally as a useful alternative for synthesis and recovery of metallic nanoparticles.[5,6]

Unfortunately, POMs can be excited only under UV irradiation (O → M, LMCT absorption band) which strongly limits the use of POMs in solar visible light conversion materials. To address this problem, POMs can be linked to visible light sensitive molecules via covalent, coordination or non-covalent bonding. In the first chapter, a review of the development of POM – based hybrids has been given. The electrochemical synthesis of the POM-porphyrin copolymers uses the previously published nucleophilic substitution on porphyrins via an $E(EC_NEC_B)_nE$ process..[7,8,9,10,11,12] A polarization of a working electrode at the first ring-oxidation potential of porphyrins in the presence of pyridine induced a nucleophilic attack and leading to the attachment of the pyridyl nitrogens to the *meso* positions of the porphyrin. If the applied the potential at the second ring-oxidation potential of porphyrins in the presence of bipyridine, copolymer with viologen spacers can be obtained. In this chapter, the nucleophile pyridine groups came from the functionalized POM (Py-POM-Py), [1,13,14] where copolymers $\{POM\text{-}porphyrin\}_n$ can be obtained. Recently, Ruhlmann et al has reported the formation of Anderson type-POM–porphyrin copolymer film with an Anderson type POM $[MnMo_6O_{18}\{(OCH_2)_3CNHCO(4\text{-}C_5H_4N)\}_2]^{3-}$ and **ZnOEP** via this electropolymerization/deposition process.

The global reaction, for a degree of polymerization n, can be written as (eq 1):

$$(n+1)Porph + (n+1)Py\text{-}POM\text{-}Py \rightarrow Porph\text{-}(Py^{+}\text{-}POM\text{-}Py^{+}\text{-}Porph)_n\text{-}Py^{+}\text{-}POM\text{-}Py + (2n+1)H^{+} + (4n+2)e^{-} \quad (1)$$

(where Porph = porphyrin)

The obtained film was used as a heterogeneous photocatalyst for the reduction of Ag^+ under visible light.[1]

2. Formation and characterization

2.1. Electropolymerization of copolymers

The syntheses of the copolymers were achieved via our electropolymerization method, as reported

earlier.[15,16] It relied on the addition of the dipyridyl-substituted Lindqvist-type polyoxovanadate $[V_6O_{13}\{(OCH_2)_3CNHCO(4\text{-}C_5H_4N)\}_2]^{2-}$ (**Py-V_6O_{13}-Py**) (Fig. 2.1C) to an electro-generated dicationic 5,15-ditolylporphyrin (**H_2T_2P**) (Fig. 2.1A) or zinc-*β*-octaethylporphyrin (**ZnOEP**) (Fig. 2.1B) by iterative scans between –1.10 V and +1.60 V *vs.* SCE (Fig. 2.3).

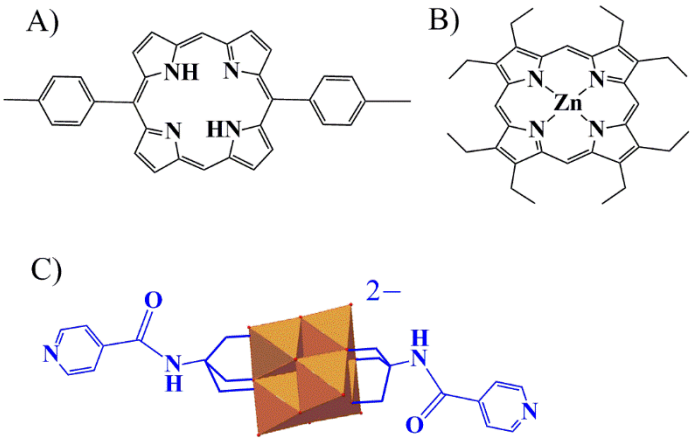

Fig. 2.1 Representation of A) **H_2T_2P**, B) **ZnOEP** and C) Lindqvist type POM $[V_6O_{13}\{(OCH_2)_3CNHCO(4\text{-}C_5H_4N)\}_2]^{2-}$ (**Py-V_6O_{13}-Py**).

The described electrochemical synthesis of the copolymers uses the previously reported $E(EC_NEC_B)_nE$ process of nucleophilic substitution on porphyrins.[16,17,8,9,10,18] As soon as the iterative scans were performed at an anodic potential sufficiently high to allow the formation of the porphyrin dication, the formation of a copolymer coating the working electrode was observed (Fig. 2.2).

CVs in Figs. 2.3 - 2.6 testify in favor of formation of passivating films. Indeed, the redox response of the monomer reaction at the covered electrode surface completely vanishes in the course of a few cycles, besides the reversible charging-discharging processes are absent. Moreover, the proposed copolymer structure (Fig. 2.2) includes TRIS fragment ($(\text{-O-}CH_2)_3$C-NH-CO-py)) with two neighboring carbon atoms in sp3-configuration inside the principal chain which breaks the conjugation so that there is no sufficiently high overlap of π-orbitals to ensure the electron (polaron) transport along the copolymer chain typical for conducting (conjugated) polymers. Therefore, one may think that the experimentally observed electroactivity of the film related to redox transitions of the functional groups is due to a different electron-transport ("hopping") mechanism via the electron transfer between the groups in different oxidation states.

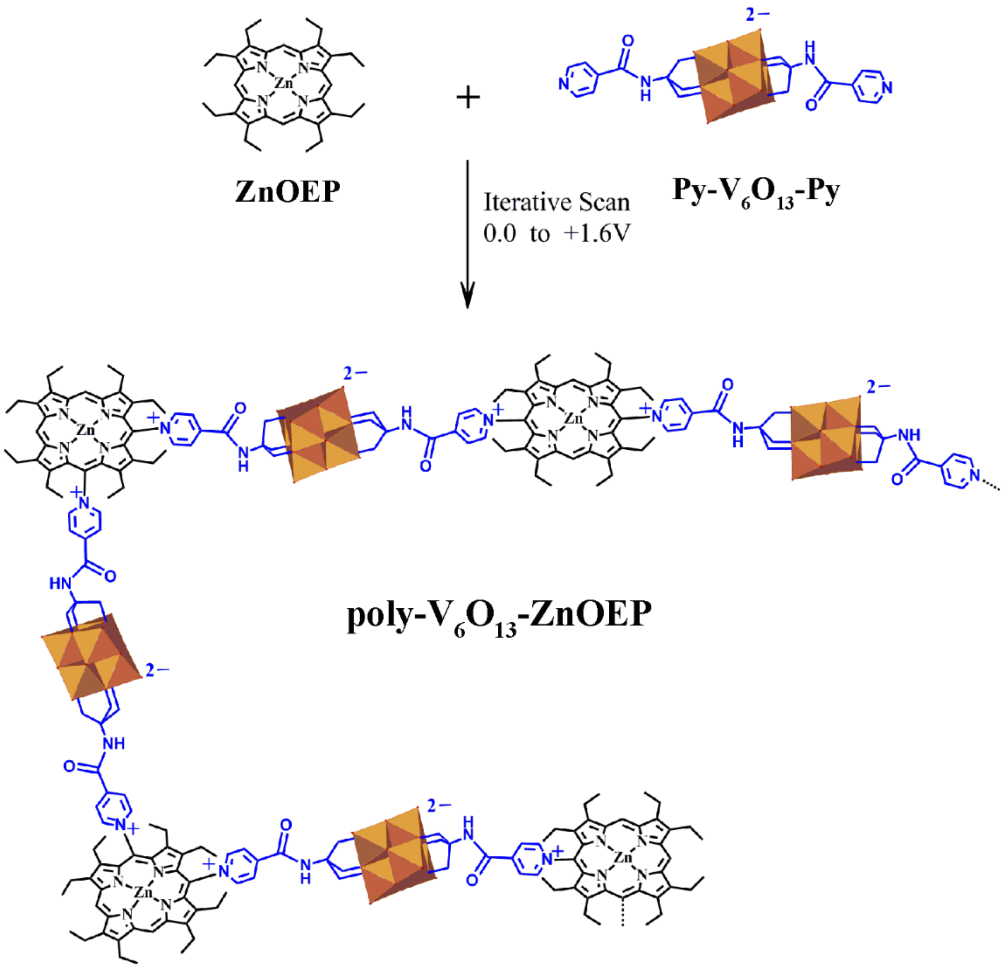

Fig. 2.2 Electropolymerization scheme of **ZnOEP** in the presence of $[V_6O_{13}\{(OCH_2)_3CNHCO(4\text{-}C_5H_4N)\}_2]^{2-}$ (**Py-V_6O_{13}-Py**).

We were unable to determine the polymerization degree n by gel permeation chromatography because of the very high affinity of the compound to the column used. We tested the solubility of Porph-Py^+-POM-Py^+-Porph obtained by electrosynthesis (using 0.7 V as applied potential), which are sufficiently soluble. Therefore, our compounds obtained by the above method must correspond to oligomers or more likely polymers were less soluble.

Equation 1 is correct if it describes the mechanism depicted in Fig. 2.2 with only two substitutions per porphyrin ring. It must be noted that according to the reached potential (1.60 V *vs.* SCE) during the electropolymerization process, **ZnOEP** can be possibly tri- and tetrasubstituted giving a branched polymer, as already observed for the electrolysis of **ZnOEP** in the presence of excess of pyridine leading to the tetrasubstituted porphyrin (because of the presence of four substitutable *meso* positions for **ZnOEP**).[9] However, the kinetics to form the trisubstituted and the tetrasubstituted porphyrin are

probably slower in the case of using Py-POM-Py because of the steric hindrance. Thus, the bisubstitution is probably mainly present in this case with of course the possibility sometimes to have the branched copolymer. Of course, in the case of the formation of the branched copolymer, the corresponding global equation is more complicated.

Moreover, in the case of the use of the 5,15-ditoly-porphyrin, because the free base porphyrin is harder to oxidize (1.01 V *vs.* SCE) and also because the presence of only two *meso* positions are substitutable, only the bisubstitution (per porphyrin ring) at positions 10 and 20 can be proposed. Furthermore, substitution at the β-positions seems to be impossible in the case of the 5,15-ditoly-porphyrin based on a preliminary study of electrosynthesis using pyridine as a Lewis base in similar conditions where only the substitution at the *meso* position is obtained.

The reactions thus generate H^+ ions, which can demetalate **ZnOEP** or even protonate the free base **H_2T_2P**, and stop the reaction. In our case, the protons generated do not perturb the coating of the electrodes. The large volume of solution used is certainly an advantage, but the main reason is likely the presence of the free pyridine groups (Py-POM-Py), which can trap the released protons in the form HPy^+-POM-Py or HPy^+-POM-$^+$PyH. Moreover, the cycling during the electropolymerization process reduces the released protons and regenerates Py-POM-Py (see equations 2 and 3):

$$HPy^+\text{-POM-Py} + e^- \rightarrow \text{Py-POM-Py} + 1/2H_2 \qquad (2)$$

$$HPy^+\text{-POM-}^+\text{PyH} + 2e^- \rightarrow \text{Py-POM-Py} + H_2 \qquad (3)$$

The absence of demetalation of **ZnOEP** monomer or the protonation of the free base **H_2T_2P** monomer in solution, was verified by UV-visible spectroscopy after several depositions of the film which shows no change compared to the initial spectrum of the corresponding solution. In the case of the deposited film, no demetalation of **ZnOEP** or protonation of the free base **H_2T_2P** subunits of the copolymer was also attested by the UV-visible spectra of the films.

The reduction of the hexavanadate core (redox couples V^V/V^{IV} –0.82 V *vs.* SCE), which was not well defined on the ITO electrode, occurred upon the first cathodic scans (Fig. 2.3 A, B black line). In the case of the copolymer obtained from **ZnOEP** and **Py-POM-Py** (abbreviated **Poly-ZnOEP-POM**) (Fig. 2.3A), an increase of a reduction peak (poorly resolved) near –0.82 V was observed as the copolymer was formed. For the copolymer obtained from **H_2T_2P** and **Py-POM-Py** (abbreviated **poly-POM-**

H_2T_2P), a similar reduction peak (poorly resolved) was growing near –0.73 V. This was attributed to the superimposed signals from the reduction of the forming bridging pyridiniums and the reduction of the vanadium atoms.

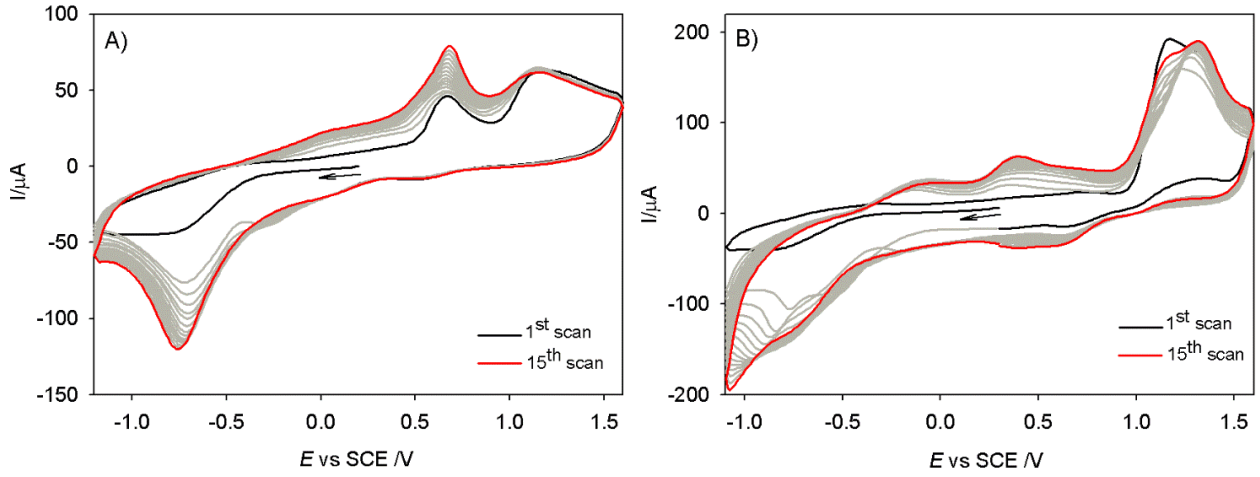

Fig. 2.3 Cyclic voltammograms recorded between −1.10 V and +1.60 V *vs.* SCE during the electropolymerization of A) 0.25 mmol L^{-1} **ZnOEP**, and of B) 0.25 mmol L^{-1} **H_2T_2P** with 0.25 mmol L^{-1} **Py-V_6O_{13}-Py** in CH_3CN/1,2-$C_2H_4Cl_2$ (3/7) in the presence of 0.1 mol L^{-1} $TBAPF_6$. Working electrode: ITO. (←) Start of the scan. S =1 cm^2; scan rate: 0.1 V s^{-1}.

It must be noted that the reduction of the pyridinium groups is irreversible. In fact the reduction of the spacer -Py^+-V_6O_{13}-Py^+-, leads to the formation of the di-radical Porph-Py•-V_6O_{13}-Py•-Porph. The radical of Py• is not delocalized onto the porphyrin-ring (or onto the polyoxometalate) but is localized only onto the pyridyl group. Thus, during the iterative scan between -1.10 V and +1.60 V, the pyridyl radical Py• formed can react with other Py• in proximity by radical coupling leading to branched copolymer. The C-C bond of the dipyridyl bridge can be formed inside the same copolymer or between two copolymers (intra- or intermolecular reaction). Similar reactivity has been reported in the literature.[19,20] Upon the limitation of the iterative scans between 0.00 V and +1.60 V, the reduction potential of the Py^+ groups is not reached. In such case, we are sure to avoid the formation of the dipyridyl linker.

For the **poly-V_6O_{13}-ZnOEP** copolymer only *meso*-substitutions occurred as all the *β*-positions of **ZnOEP** were occupied by ethyl groups, which are not substitutable. It is likely that some **ZnOEP** can be substituted three (or even four) times, and constitutes therefore branching points of the polymer (see above).

In the case of 5,15-ditolyl porphyrin (**H_2T_2P**), the nucleophilic attack is allowed only at the 5,15 *meso*

positions of the porphyrin to form the isoporphyrin intermediate.[16,18] Oxidation of this porphyrin alone yield first the radical cation $\mathbf{H_2T_2P^{+\bullet}}$. From there, at least three kinds of dimers are expected via a radical coupling reaction with *meso-meso, meso-β* or *β-β* link, but previous work in the literature using the 5,15-bis(3,5-di-tert-butylphenyl) porphyrin shows only the formation of a mixture of *meso-meso* and *meso-β* linked dimers. These dimers must presented a splitting of the Soret band at 412.6 nm and 446.6 nm and 414.8 nm and 434.6 nm respectively.[21, 22,23]

In our case, only the reaction between the $\mathbf{H_2T_2P^{2+}}$ and **Py-V_6O_{13}-Py** occurred which lead to the copolymer **poly-V_6O_{13}-H_2T_2P**. The UV-vis spectra of the mother solution after the electropolymerization and also the UV-vis spectra of the copolymer deposited showed clearly that no dimer $\mathbf{(H_2T_2P)_2}$ was formed via a radical coupling between the two radical cation $\mathbf{H_2T_2P^{+\bullet}}$ showing that only the nucleophilic substation occurred.

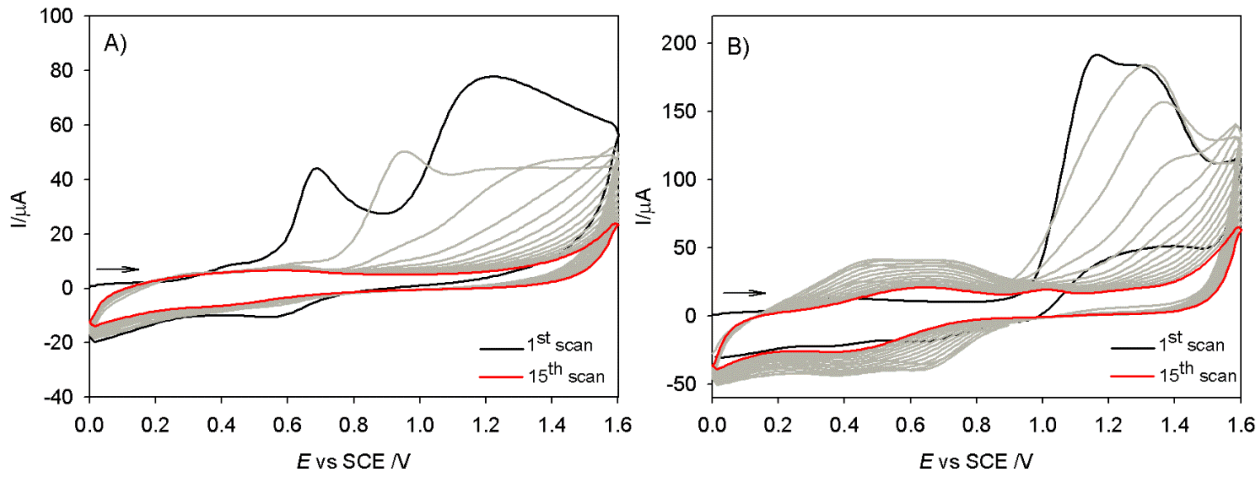

Fig. 2.4 Cyclic voltammograms recorded during the electropolymerization of A) 0.25 mmol/dm^3 **ZnOEP**, and of B) 0.25 mmol L^{-1} **H_2T_2P** with 0.25 mmol L^{-1} **Py-V_6O_{13}-Py** in CH_3CN/1,2-$C_2H_4Cl_2$ (3/7) in the presence of 0.1 mol L^{-1} $TBAPF_6$. Working electrode: ITO. (←) Start of the scan. S =1 cm^2; scan rate: 0.1 V/s. Cyclic scanning was applied at potentials between 0.00 and +1.60 V *vs.* SCE.

When the scanning was limited to iterative scans between 0.00 V and +1.60 V, we observed that the oxidation peak regularly shifted anodically during the electropolymerisation of **ZnOEP** and **Py-V_6O_{13}-Py** (Fig. 2.4A). This is an indication of the growing difficulty to oxidize the porphyrin of the film with increased film thickness. A similar observation has been made previously[8,24] and is probably due to the presence of the positive charge of the dipyridinium groups which renders more difficult the oxidation of the copolymer chain.

2.2. EQCM for the copolymer deposition

The electrosynthesis by iterative scans between 0.00 and +1.60 V of **poly-V_6O_{13}-ZnOEP** and **poly-V_6O_{13}-H_2T_2P** has been monitored by EQCM. Fig. 2.5 and Fig. 2.6 illustrate the simultaneously recorded cyclic voltammograms and frequency change.

The quartz resonance frequency (Δf) presented a decrease at each cycle, which corresponded to the increase of the polymer mass during the electrosynthesis. Using the Sauerbrey's equation,[25] change in mass of working electrode during the electropolymerization was quantified from the changes in the resonance frequency. Besides, the trace of the first scan in Fig. 2.5 shows that a significant decrease of the frequency and consequently the mass increase occurs above the second oxidation peak; i. e. electropolymerization happened upon the formation of the dication porphyrin. The steady frequency decrease with time was an indication of the smooth increase of the copolymer mass. The quartz resonance frequency and thus the mass change (Δm) presented a quasi linear variation with time (Fig. 2.5B), which according to some authors could be an indication of the formation of a homogeneous film.[26] Similar behavior was observed for the electropolymerization of **poly-V_6O_{13}-H_2T_2P** (Fig. 2.6).

In the present investigation, coverages after 20 iterative scans were about 45.8 and 8.8 μg/cm^2 for **poly-V_6O_{13}-ZnOEP** and **poly-V_6O_{13}-H_2T_2P**, respectively. It should be noted that the lower coverage of **poly-V_6O_{13}-H_2T_2P** is probably due to the higher redox potential of the second oxidation of **H_2T_2P** (+1.27 V) than **ZnOEP** (+1.08 V). In such a case, we reached more rapidly the end potential used +1.60 V, where the growth of the chain of the copolymer was stopped in the case of the use of **H_2T_2P**. A minor factor is also the lower molecular weight of **H_2T_2P** (490.60 g mol^{-1}) than **ZnOEP** (598.15 g mol^{-1}). It can also be explained by the number of *meso* positions available for the substitution: two for **H_2T_2P** versus four for **ZnOEP**.

In the case of the calculation with two **Py-POM-Py** per one **ZnOEP**, 9.8 mg/C is calculated which is closer to 11.9 mg/C. It suggests that two Py-POM-Py per ZnOEP unit is detected by EQCM. This result can be explained to the presence *i)* of the trisubstituted **ZnOEP** porphyrin or *ii)* of **ZnOEP** mainly bisubstituted with Py-POM-Py and additionally coordinated by one Py-POM-Py monomer. The slight higher value measured (11.9 mg/C versus 9.8 mg/C) can also indicate that a small portion of the **ZnOEP** is probably tribustituted and with one additional **Py-V_6O_{13}-Py** group showing that the substitution yield is almost quantitative.

In the case of **poly-V_6O_{13}-H_2T_2P**, the theoretical yield of the copolymer mass deposited per charge unit according to Fig. 2.6 can be calculated and is equal to 5.8 mg/C for **poly-V_6O_{13}-H_2T_2P** (with one **Py-V_6O_{13}-Py** per **H_2T_2P** unit). However, the experimental copolymer mass deposited per charge unit gives only 1.4 mg/C.

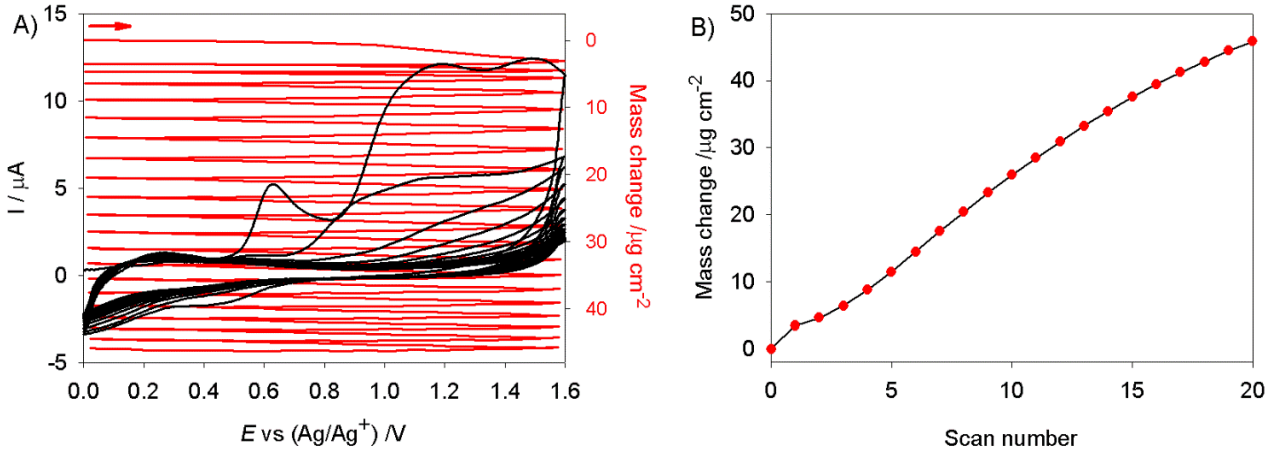

Fig. 2.5 A) Consecutive cyclic voltammograms (first 20 scans) and electrochemical quartz crystal microbalance measurements for the first 20 scans during the electropolymerization of 0.25 mmol L^{-1} **ZnOEP** with 0.25 mmol L^{-1} **Py-V_6O_{13}-Py** in CH_3CN/1,2-$C_2H_4Cl_2$ (3/7) in the presence of 0.1 mol L^{-1} $TBAPF_6$. Working electrode: ITO (A = 0.2 cm^2) deposited on a 9.08 MHz AT-cut quartz crystal. v = 100 mV s^{-1}. B) Mass change (Δm) calculated from Sauerbrey's equation versus the number of scan n.

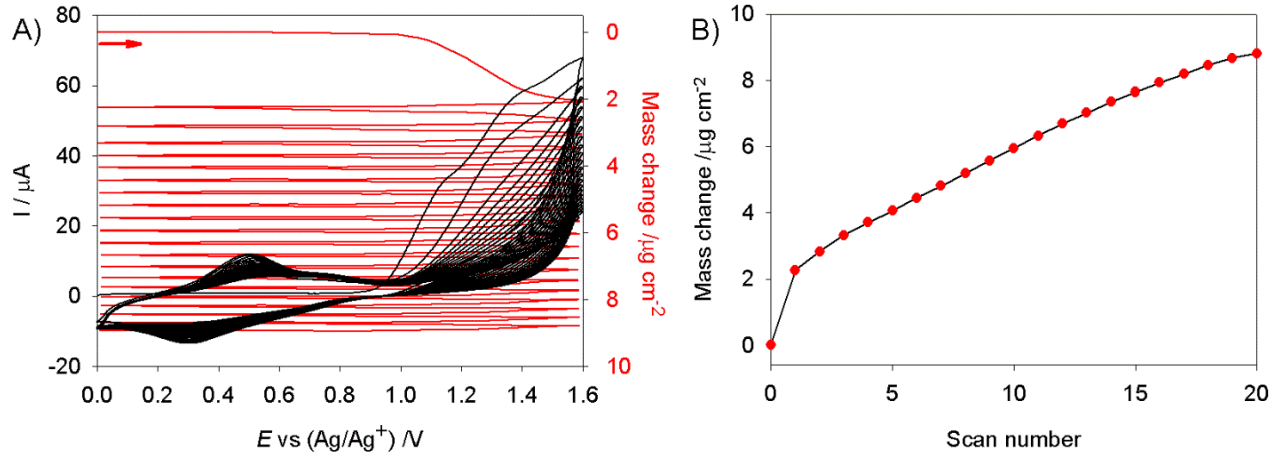

Fig. 2.6 A) Consecutive cyclic voltammograms (first 20 scans) and electrochemical quartz crystal microbalance measurements for the first 20 scans during the electropolymerization of 0.25 mmol L^{-1} **H_2T_2P** with 0.25 mmol L^{-1} **Py-V_6O_{13}-Py** in CH_3CN/1,2-$C_2H_4Cl_2$ (3/7) in the presence of 0.1 mol L^{-1} $TBAPF_6$. Working electrode: ITO (A = 0.2 cm^2) deposited on a 9.08 MHz AT-cut quartz crystal. v = 100 mV s^{-1}. B) Mass change (Δm) calculated from Sauerbrey's equation versus the number of scan n.

This result can be explained by the competitive reaction of protonation of the free base porphyrin during

the electropolymerization. In such a case, oxidation of the free base porphyrin gives first the formation of $H_4T_2P^{2+}$ which can in turn react with **Py-V_6O_{13}-Py** to exchange the proton leading to the formation of the large quantity of Py-V_6O_{13}-PyH^+ and/or HPy$^+$-V_6O_{13}-PyH^+ detected during the electropolymerization. Indeed, the peaks at +0.3 to +0.4 V during the formation of **poly-H_2T_2P-V_6O_{13}** were probably due to the couple Py-H^+/Py+1/2H_2 as already observed in previous work but at different potential.[9] In such a case, the proton can be present at the end of the copolymer chain (namely H_2T_2P-(Py$^+$-V_6O_{13}-Py$^+$-H_2T_2P)$_n$-Py$^+$-POM-Py$^+$-H) or in the monomer (Py-V_6O_{13}-Py$^+$-H and/or H-Py$^+$-V_6O_{13}-Py$^+$-H). Similar redox potential reduction of the protonated H-Py$^+$-POM-Py$^+$-H has been measured for Py-POM-Py in the presence of $HClO_4$ (Fig. 2.7).

Mest et al have shown such reactivity of the free base porphyrin upon their oxidation even in strictly anhydrous solvents.[27] In this case, oxidation of the free base gives rise to a quantitative chemical reaction and protonation, the protonation being induced by radical reaction, the protons coming from the solvent or the conducting salt. In such condition, the calculated yield is only around 25 %. It explains well why the current exchanged is very important with a lower deposited mass for **poly-V_6O_{13}-H_2T_2P** and explains also the new redox process between +0.2 V and +0.6 V (Fig. 2.6).

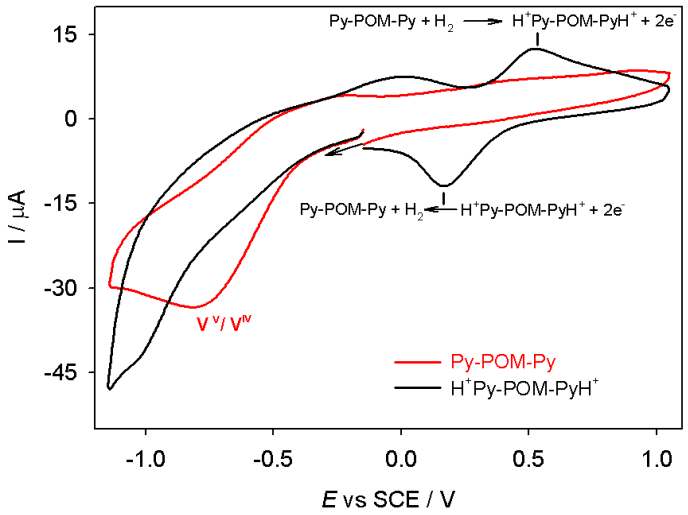

Fig. 2.7 Cyclic voltammograms of 0.25 mmol L^{-1} **Py-V_6O_{13}-Py** before (red curve) and after (black curve) added of 2 eq. of $HClO_4$ in 10 mL CH_3CN/1,2-$C_2H_4Cl_2$ (3/7) in the presence of 0.1 mol L^{-1} $TBAPF_6$. Working electrode: ITO. (←) Start of the scan. S =1 cm^2; scan rate: 0.1 V s^{-1}.

2.3. Cyclic voltammetric investigations of the two polymeric films

The electrochemical behaviour of the films obtained has been studied by cyclic voltammetry (Table 1 and Fig. 2.8). Characteristically, one reduction peak appeared at -0.73 V (for **poly-V_6O_{13}-H_2T_2P**) and

at -0.82 V (for **poly-V_6O_{13}-ZnOEP**) which correspond to the superimposed signals from the reduction of the forming bridging pyridiniums and the reduction of the Lindqvist-type polyoxovanadate (couple $V^{V/IV}$). In the case of **poly-V_6O_{13}-ZnOEP**, the presence of only one reduction peak of the pyridinium at -0.82 V, are consistent with only the bisubstituted **ZnOEP** porphyrin. Indeed, previous works have shown that the bisubstitution in 5,15 positions give only one peak reduction of the two pyridinium in the case of **ZnOEP** bisubstituted with two Py^+. In the case of the hypothetical additional *meso* substitution, the **ZnOEP** porphyrin will be tri-substituted (three pyridiniums per macrocycle), which generally displays the splitting of the reduction of the three pyridiniums and the successive reduction of the three py^+ which is not the case in this study.

Consequently, the second **Py-V_6O_{13}-Py** group detected by EQCM for the **poly-V_6O_{13}-ZnOEP** seem to be not substituted on to the porphyrin ring at the *meso* position but is only coordinated to the zinc atoms of the macrocycle. Moreover, the redshift of 20 nm of the Soret band (see section 2.4.) fits also well to the bisubstituted porphyrin with the coordination of the zinc atom by the second **Py-V_6O_{13}-Py** group.

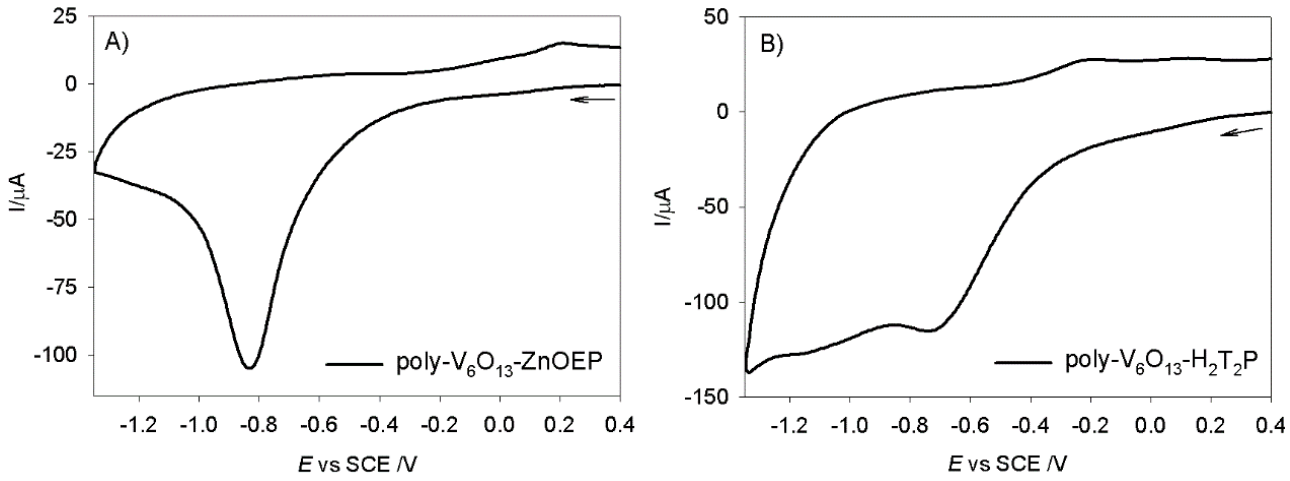

Fig. 2.8 Cyclic voltammograms of A) **poly-V_6O_{13}-ZnOEP** and B) **poly-V_6O_{13}-H_2T_2P** film (obtained after 20 scans, between 0.00 V and +1.60 V) in CH_3CN/1,2-$C_2H_4Cl_2$ (3/7) with 0.1 mol/dm^3 $TBAPF_6$. (←) Start of the scan. S =1 cm^2; scan rate: 0.1 V s^{-1}.

Table 1. Electrochemical data for **ZnOEP**, **H_2T_2P**, **Py-V_6O_{13}-Py**, **poly-V_6O_{13}-ZnOEP** and **poly-V_6O_{13}-H_2T_2P**.

Compounds	**Ring oxidation**		**Reduction of py^+ and of V^V of Py-V_6O_{13}-Py**	**Ring reduction**	
ZnOEP [a]	1.08	0.71		-1.66	
	(0.13)	(0.13)			
H_2T_2P [a]	1.27	1.01		-1.20	-1.66
				(0.17)	(0.32)
Py-V_6O_{13}-Py [a]			-0.82 [c]		
poly-V_6O_{13}-ZnOEP [b]			-0.82 [c]		
poly-V_6O_{13}-H_2T_2P [b]			-0.73 [c]	-1.11 [c]	-1.67[c]

[a] Potentials in V *vs.* SCE were obtained from cyclic voltammetry in 1,2-$C_2H_4Cl_2$ with 0.1 mol/dm^3 $TBAPF_6$. Scan rate = 100 mV s^{-1}. Working electrode: ITO, S=1 cm^2.

[b] Potentials in V *vs.* SCE were obtained from cyclic voltammetry in in CH_3CN/1,2-$C_2H_4Cl_2$ (3/7) with 0.1 mol/dm^3 $TBAPF_6$. Scan rate = 100 mV s^{-1}. Working electrode: ITO, S=1 cm^2. The given half-wave potentials are equal to $E_{1/2} = (E_{pa} + E_{pc})/2$. Under bracket: $\Delta E_p = |E_{pa} - E_{pc}|$.

[c] Irreversible.

2.4. UV-vis spectroscopy

UV-visible spectra of both copolymers on ITO electrodes presented similar characteristics. They exhibit a large Soret absorption band, which was red shifted by 15 and 20 nm compared to the **ZnOEP** and **H_2T_2P** monomer respectively (Table 2 and Fig. 2.9).

This change can be explained by intra- or intermolecular excitonic interactions between the porphyrin subunits.[8,24] In regard of our experience of the substitution of porphyrin with pyridinium groups,[28] these red shifts are in agreement with the presence of the bisubstituted porphyrin ring inside the copolymer. In addition, the absorption intensity of the chromophores increased progressively for each iterative scan during the deposition (Inset of Fig. 2.9) and tended to reach a plateau. This shows well that the thickness

of the film increased with the number of iterative scans (n) up to a certain limit.

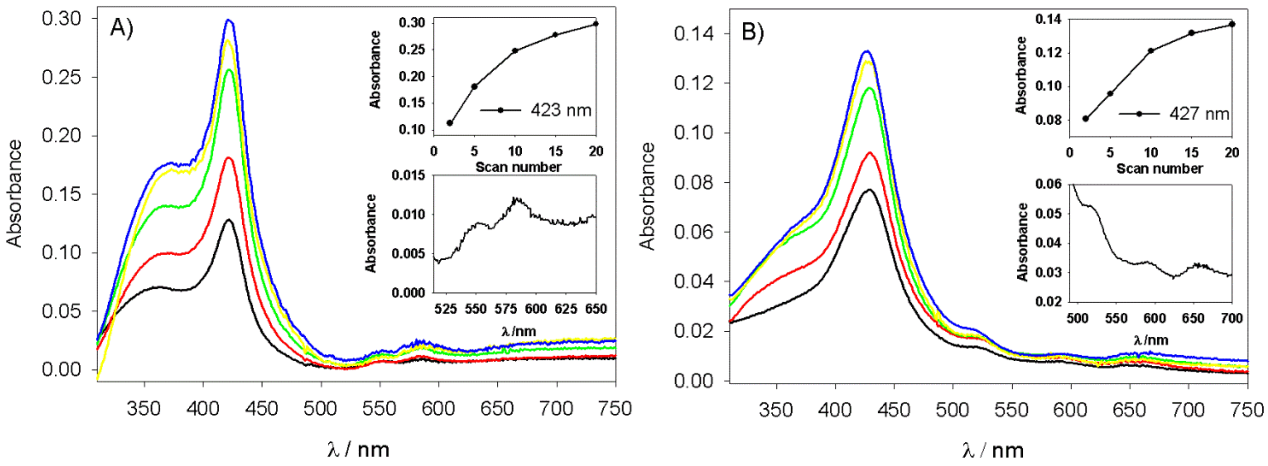

Fig. 2.9 UV–vis absorption spectra of A) **poly-V_6O_{13}-ZnOEP** and B) **poly-V_6O_{13}-H_2T_2P** obtained after n iterative scans between 0.00 and +1.60 V *vs.* SCE on ITO.

Table 2 UV–visible spectral data for **ZnOEP** and **H_2T_2P** in DMF, **Py-V_6O_{13}-Py** in CH_3CN, **poly-V_6O_{13}-ZnOEP** and **poly-V_6O_{13}-H_2T_2P** on ITO. In brackets: molar extinction coefficient (ε /10 ^{3} dm^3 mol^{-1} cm^{-1}).

Compound	Soret band/nm	Q bands/nm	π-π*Band/nm
ZnOEP	408 (672.3)	538 (34.3), 674 (37.7)	
H_2T_2P	407 (402.3)	502 (16.6), 537 (5.8), 577 (4.6), 631 (1.4)	
Py-V_6O_{13}-Py			257 (29.0), 375 (6.6)
poly-V_6O_{13}-ZnOEP	423	547, 583	
poly-V_6O_{13}-H_2T_2P	427	516, 561, 592, 658	

2.5. X-ray photoelectron spectroscopy (XPS)

XPS was used to determine the chemical composition of the films. **Poly-V_6O_{13}-H_2T_2P** (Fig. 2.10) exhibited peaks corresponding to C1s (284.6 eV), N1s (400.3 eV and 398.6 eV) of the porphyrin ligand, the organic part of the spacer and the TBA countercation, while the O1s (537.2 eV), and V2p3 (V2p$_{1/2}$

= 523.4 eV and $V2p_{3/2}$ = 516.0 eV) are coming from the vanadium, and oxygen atoms in the POM. F1s signals (686.8 eV) and P2p (133.8eV) corresponding to PF_6^- trapped in the copolymer structure were also observed.

The XPS data thus confirmed that the Lindqvist-type polyoxovanadate $TBA_2[V_6O_{13}\{(OCH_2)_3CNHCO(4\text{-}C_5H_4N)\}_2]$ and the **H_2T_2P** porphyrin were incorporated into the films, in agreement with the UV-vis absorption spectra. Similar XPS spectra were obtained for **poly-V_6O_{13}-ZnOEP** (Fig. 2.11) where in addition the signal of the Zn element, not well defined, but still detectable was near 1022.4 eV.

In the case of **poly-V_6O_{13}-H_2T_2P** (obtained after 20 iterative scans between 0.00 and +1.60 V *vs.* SCE), the calculation of the atomic ratios C:N, O:V, N:V give: 9.4, 4.2, and 1.2 respectively (see Fig S2 in the appendix) which are not very far from the theoretical atomic ratios calculated (C:N = 8.6, O:V = 3.5, N:V = 1.7) for the proposed formula of the copolymer, with one porphyrin macrocycle for one Py-POM-Py.

In the case of **poly-V_6O_{13}-ZnOEP**, the experimental atomic ratio V/Zn give aberrant value. In fact the Zn 2p3 signal is very difficult to be measured and even sometime is not detected. Here, because of the ill-defined signal, the atomic ratio calculated (170) is incorrect and very far from the expected value (V:Zn = 12). For the atomic ratio C/N, only the presence of two Py-POM-Py groups per **ZnOEP** porphyrin can be proposed and give nearly the experimental atomic ratio C/N measured. The result gave similar results as already observed from EQCM measurements.

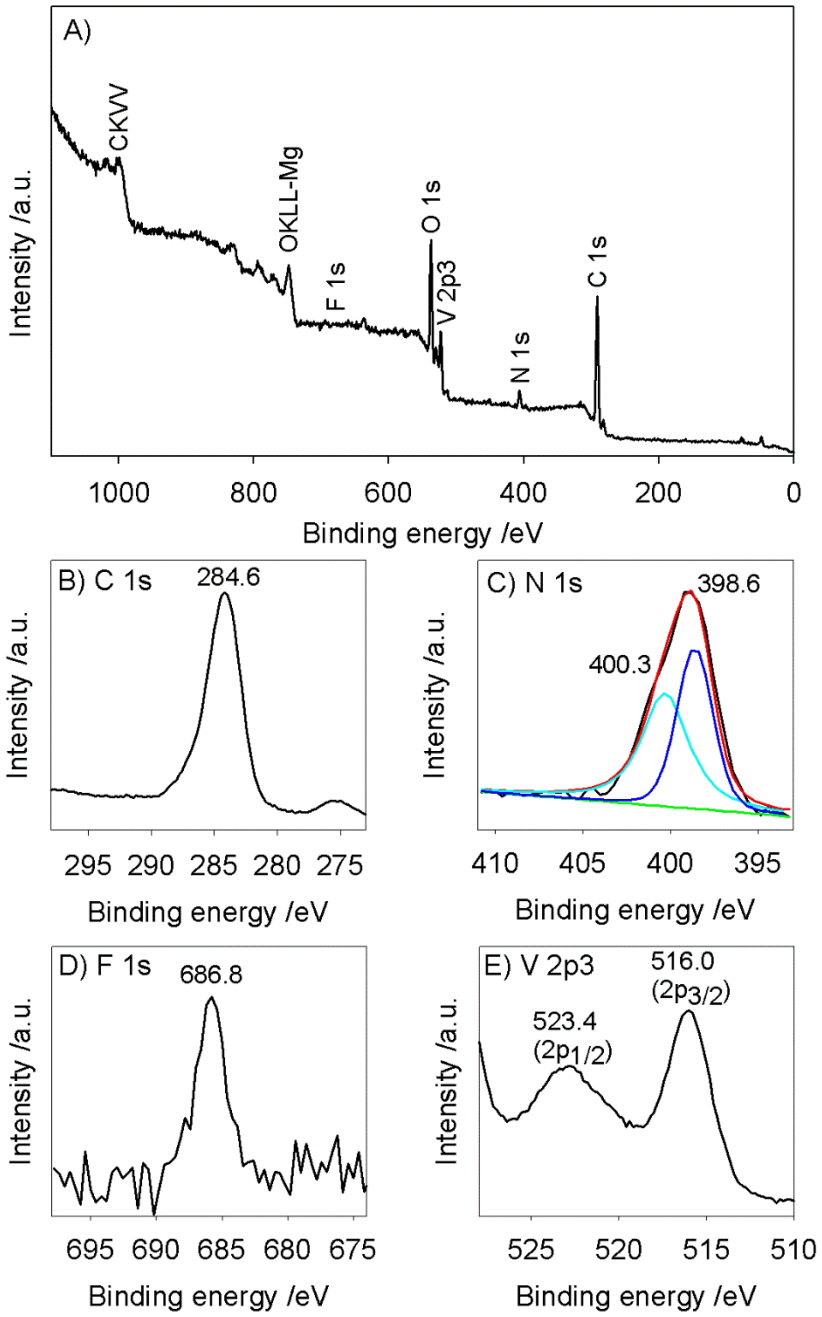

Fig. 2.10 XPS spectra of the modified ITO electrodes with **poly-V_6O_{13}-H_2T_2P** obtained after 20 iterative scans between 0.00 and +1.60 V *vs.* SCE. (A) Global XPS spectra, (B) C 1s, (C) N 1s, (D) F 1s, (E) V 2p3.

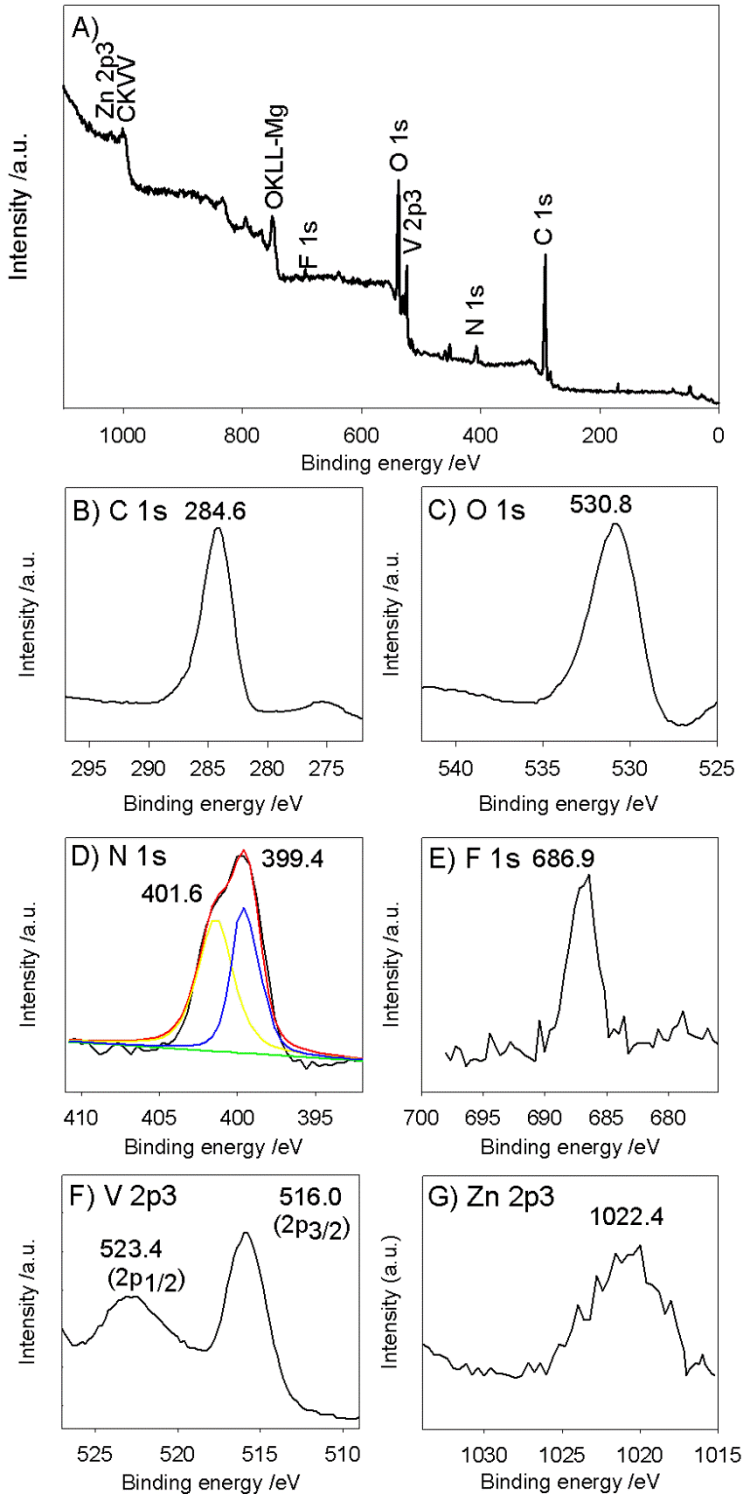

Fig. 2.11 XPS spectra of the modified ITO electrodes with **poly-V_6O_{13}-ZnOEP** obtained after 20 iterative scans between 0.00 and +1.60 V *vs.* SCE. (A) Global XPS spectra, (B) C 1s, (C) O 1s, (D) N 1s, (D) F 1s, (E) V2p3, (E) Zn2p3.

2.6. Film morphology (Atomic force microscopy)

The films were examined by scanning atomic force microscopy (AFM). In a typical observation, **poly-V_6O_{13}-ZnOEP** appeared as tightly packed coils with average diameters of 60-80 nm and a height of 10 nm (Fig. 2.12A,B). The rms surface roughness of the film was 6.61 nm for 1 μm^2 area. Thickness of the deposited polymeric film (obtained after 20 scans between 0.00 V and +1.60 V) is about 61 nm (measured by scratching the films with the metallic tip). Similar behavior was observed for **poly-V_6O_{13}-H_2T_2P** but with average diameters of 40-60 nm and a height of 5 nm (Fig. 2.12C,D). The rms surface roughness was 3.48 nm. Thickness of the deposited polymeric film (obtained after 20 scans between 0.00 V and +1.60 V) is about 25 nm.

In the case of **poly-V_6O_{13}-ZnOEP** the diameter and the height of the coils were nearly two times larger. This result is in agreement with the EQCM measurements where the mass deposition was about five times more important in using **ZnOEP** instead of **H_2T_2P**. This is probably because of the presence of longer chains and also the coordination of one additional Py-POM-Py onto the Zn, as discussed above.

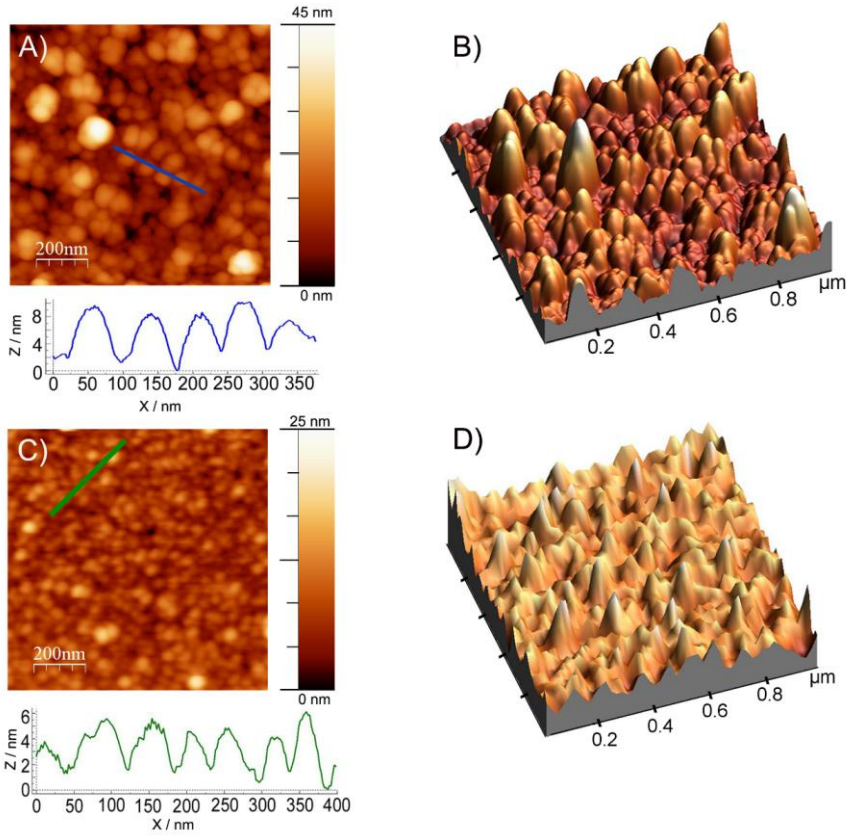

Fig. 2.12 Tapping mode AFM topography of A) and B) **poly-V_6O_{13}-ZnOEP**, and C) and D) **poly-V_6O_{13}-H_2T_2P** films (obtained after 20 scans, between 0.00 V and +1.60 V) and section analysis of the aggregate marked by a blue line for A) and green line for C). (For interpretation of the references to color in this figure legend, the reader is referred to the web version of the article).

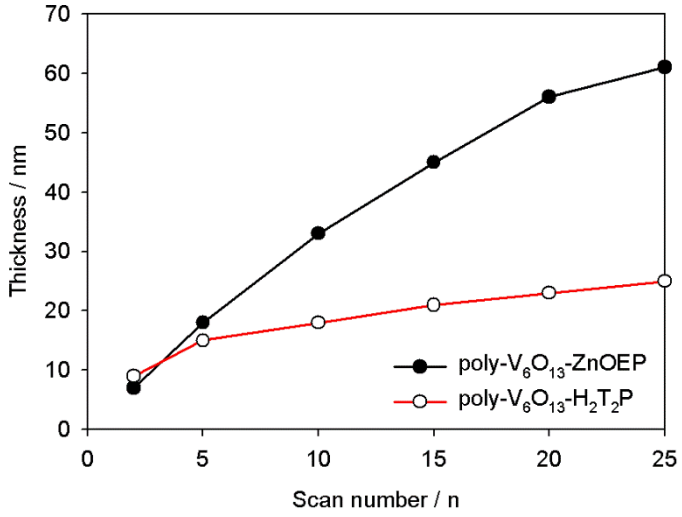

Fig. 2.13 Thickness of **poly-V_6O_{13}-ZnOEP** and **poly-V_6O_{13}-H_2T_2P** measured by AFM versus different numbers of iterative scans.

Table 3 Thickness (measured from AFM), Δm (measured from AFM and EQCM respectively) and surface coverage Γ calculated versus the number of iterative scan n.

poly-V_6O_{13}-ZnOEP

Number of iterative scan n	Thickness (nm)	Δm ($\mu g\ cm^{-2}$)	Γ (10^{-9} mol cm^{-2})
2	7	4.64	2.15
5	18	11.47	5.32
10	33	25.95	12.02
15	45	37.55	17.40
20	56	45.84	21.24
25	61	-	-

poly-V_6O_{13}-H_2T_2P

Number of iterative scan n	Thickness (nm)	Δm ($\mu g\ cm^{-2}$)	Γ (10^{-9} mol cm^{-2})
2	9	2.82	1.38
5	15	4.06	1.98
10	18	5.94	2.90
15	21	7.64	3.73
20	23	8.81	4.30
25	25	-	-

3. Photocurrent generation

We have evaluated the photochemical performance of these two hybrids based on the application of photocurrent generation and photocatalytical recovery of metals under visible-light illumination (Fig. 2.14).

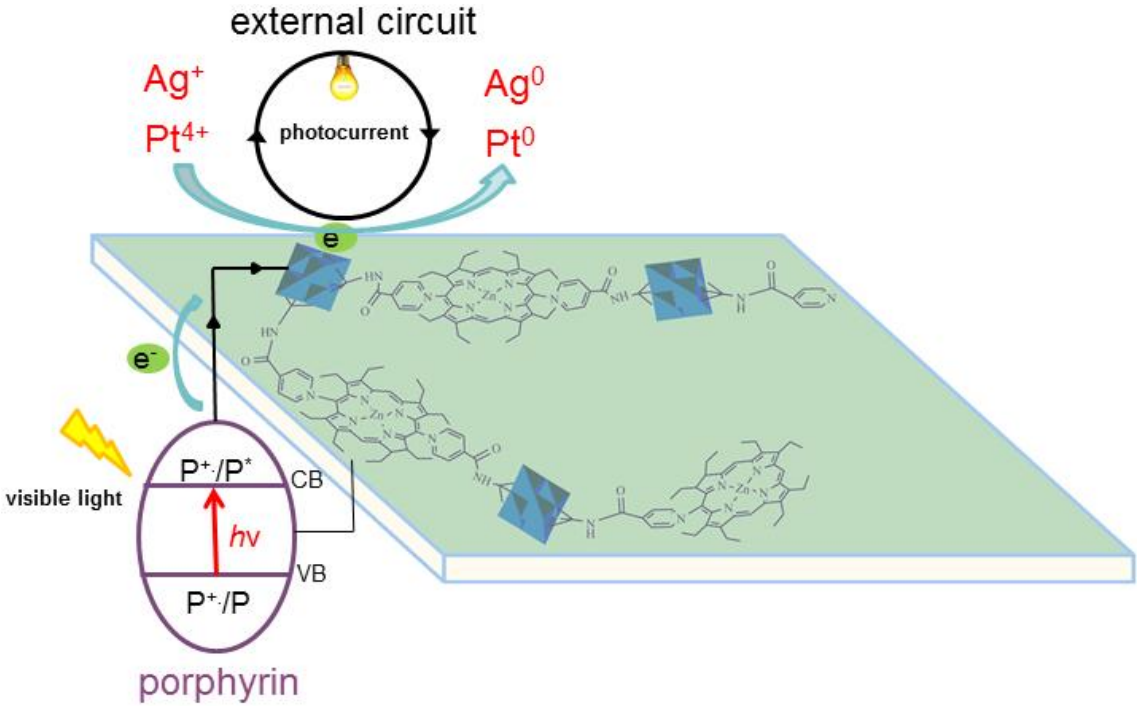

Fig. 2.14 Schematic representation of the process of photocurrent generation or photocatalytical recovery of metal with the **poly-V_6O_{13}-ZnOEP** modified ITO electrode under visible illumination.

3.1. Effect of the film thickness

Fig. 2.15 shows amperometric J–t curves for the photocurrent response of six different **poly-V_6O_{13}-ZnOEP** films deposited on ITO electrodes with increasing scan numbers during the electropolymerization process. The ITO electrode covered by **poly-V_6O_{13}-ZnOEP** film was immerged in aqueous solutions in the presence of I_3^- 5 mmol L^{-1} and I^- 0.5 mol L^{-1} reversible redox mediator, which also acted as electrolyte to improve the conductivity and thus increase the current magnitude. Irradiations were performed using a 300 W Xe lamp equipped with a water cell filter to absorb the near-IR radiations and a 385 nm cut-off filter, so the POM subunits cannot be excited. The bias potential was set at 0.0 V and the device was exposed under visible light for 1 min then kept in the dark for 1 min. In Fig. 2.15, the films generated the photocurrent as the illuminant was switched on, when it was turned

off the photocurrent disappear. The obtained photocurrent intensity was on the same order of magnitude as those in previous literature on porphyrin/POM or chromophore/POM systems.[29]

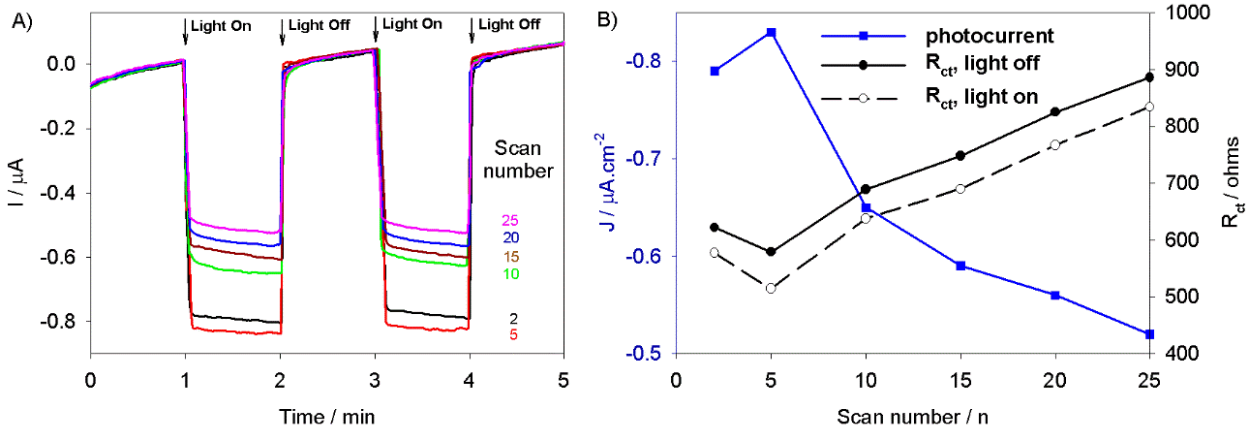

Fig. 2.15 A) photoelectrochemical response of **poly-V_6O_{13}-ZnOEP** with different numbers of iterative scans used for the preparation of the film (between 0.00 V and +1.60 V versus SCE). Only one side is recovered by ITO with on-off light illumination from 300 W Xe Arc lamp (with $\lambda \geq 385$ nm long pass filter). BIAS potential: 0.00 V. B) (■) plots of the photocurrent, and plots of R_{ct} without illumination (●), and with illumination (○) in aqueous solution containing I_3^- 5 mmol L^{-1} and I^- 0.5 mol L^{-1} versus the numbers of iterative scans, DC potential: 0.00V.

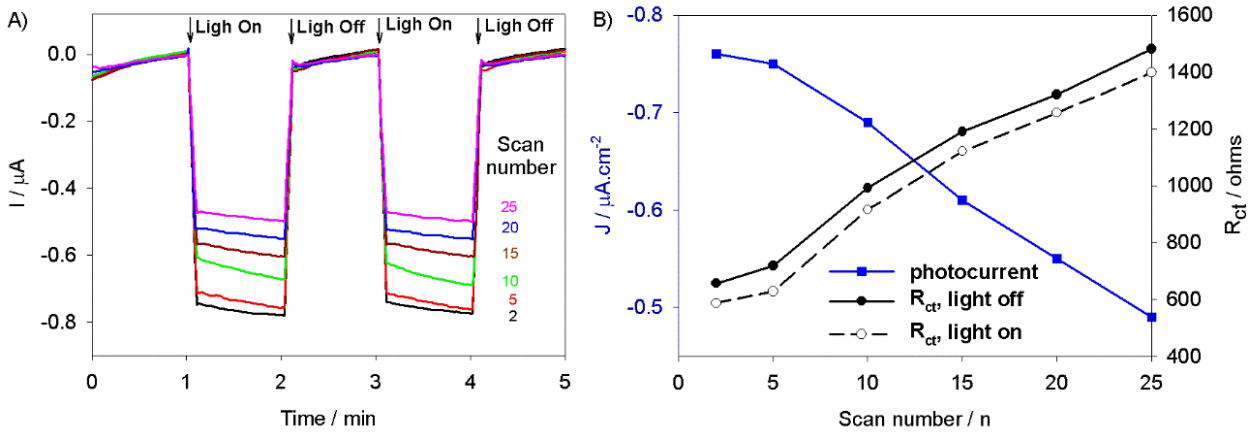

Fig. 2.16 A) photoelectrochemical response of **poly-V_6O_{13}-H_2T_2P** with different numbers of iterative scans used for the preparation of the film (between 0.00 V and +1.60 V versus SCE). Only one side is recovered by ITO with on-off light illumination from 300 W Xe Arc lamp (with $\lambda \geq 385$ nm long pass filter). BIAS potential: 0.00 V. B) (■) plots of the photocurrent, and plots of R_{ct} without illumination (●), and with illumination (○) in aqueous solution containing I_3^- 5 mmol L^{-1} and I^- 0.5 mol L^{-1} versus the numbers of iterative scans, DC potential: 0.00 V.

Comparable photoelectrochemical responses have also been reported in the literature for various assemblies, such as poly(p-phenylenevinylene)/POM or photosensitizer/POM (photosensitizer: ruthenium complexes, phthalocyanine, hemicyanine; see Table 2 (Page 225) and the first

chapter).[1,30,31,32,33] However, because of the wide variation of the measurement, a more detailed comparison is very difficult to carry out.

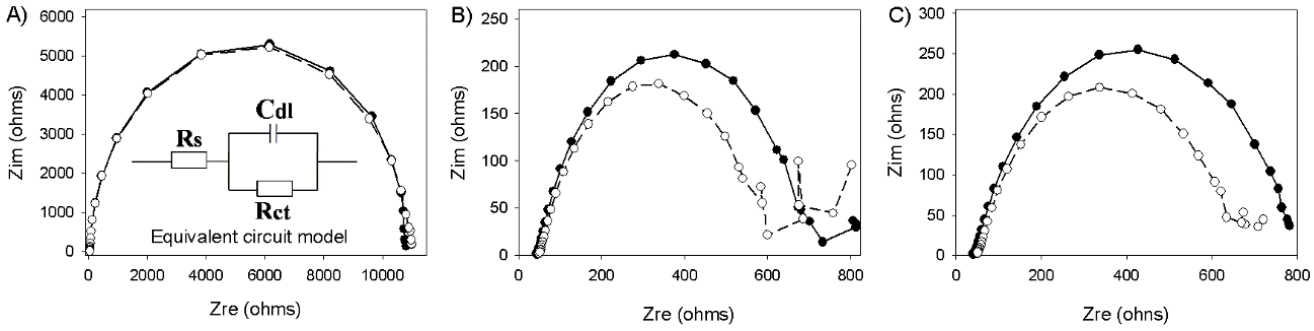

Fig. 2.17 Nyquist plot of A) **bare ITO**, B) **poly-V_6O_{13}-ZnOEP** (scan number = 5) and C) **poly-V_6O_{13}-H_2T_2P** (scan number = 2), DC potential 0.0V, with (dotted line) and without (full line) visible irradiation from 300 W Xe Arc lamp (with $\lambda \geq 385$ nm long pass filter) in H_2O containing I_3^- 5 mmol L^{-1} and I^- 0.5 mol L^{-1}. Inset of A): circuit description code (CDC) of the system.

Interestingly, the photocurrent response of these two porphyrin-POM hybrids depend on the iterative scan number (n) used for the electrodeposion of the film. The magnitude of the photocurrent is high in low scan numbers (n = 2 or 5) and then as the scan number increases the magnitude of photocurrent decreases. This follows the same trend as the charge transfer resistance (R_{ct}, diameter of the semi-circle in the Nyquist plot) with the same modified electrode in same condition (Fig. 2.15B, Fig. 2.16B). It suggests that the photocurrent efficiency is mainly dependent on the charge transfer resistance of the film. Remarkably, charge transfer resistance (R_{ct}) is lower under the irradiation than that in the dark, which fully prove that the generation of extra electron flow under illumination. The optimized photocurrent of **poly-V_6O_{13}-ZnOEP** (0.83 $\mu A.cm^{-2}$) is a little higher than that of **poly-V_6O_{13}-H_2T_2P** (0.76 $\mu A.cm^{-2}$), attributed to two reasons: i) the molar extinction coefficient of ZnOEP is higher than that of **H_2T_2P** (see table 2) and the **poly-V_6O_{13}-ZnOEP** films possess higher absorbance than **poly-H_2T_2P-V_6O_{13}** which lead to **poly-V_6O_{13}-ZnOEP** is able to absorb the visible light energy more efficiently, ii) the **poly-V_6O_{13}–ZnOEP** owns a little lower charge transfer resistance than **poly-V_6O_{13}-H_2T_2P** on both dark and irradiation conditions (Fig. 2.17B and Fig. 2.17C).

3.2. Different BIAS potential

To further verify the photocurrent polarity, the photocurrent dependence on the BIAS potential for both **poly-V_6O_{13}-ZnOEP** and **poly-V_6O_{13}-H_2T_2P** films was investigated, and the results are shown in Fig.

2.18 and Fig. 2.19, respectively.

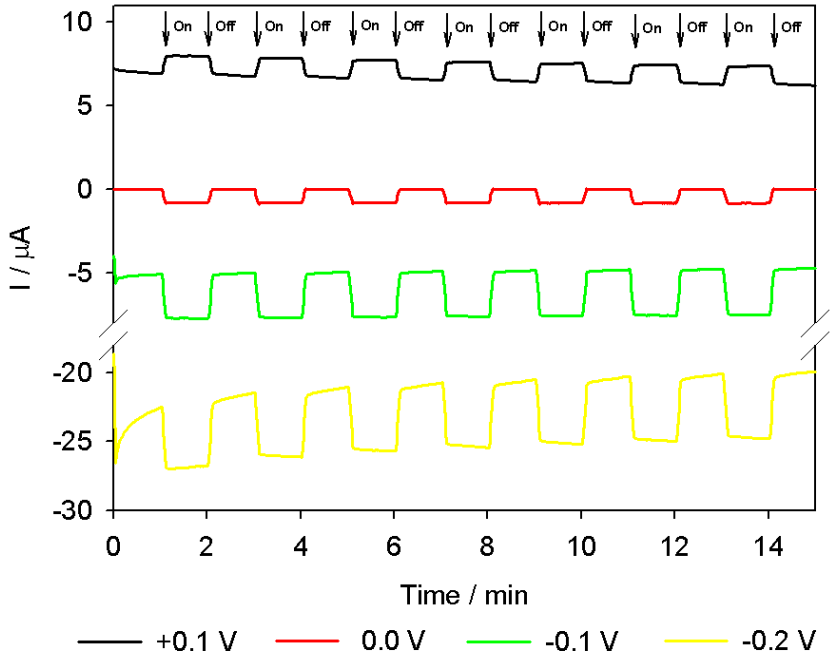

Fig. 2.18 Photoelectrochemical response of **poly-V_6O_{13}-ZnOEP** (5 scans) (preparation of the film between 0.00 V and +1.60 V versus SCE) under irradiation from 300 W Xe Arc lamp (with $\lambda \geq 385$ nm long pass filter) in H_2O containing I_3^- 5 mmol L^{-1} and I^- 0.5 mol L^{-1} with different BIAS potential.

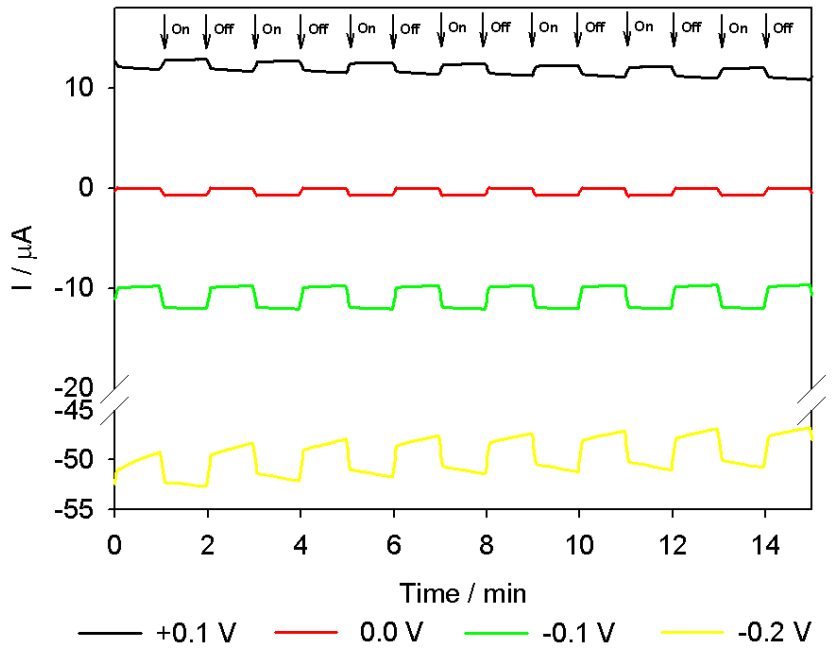

Fig. 2.19 Photoelectrochemical response of **poly-V_6O_{13}-H_2T_2P** (2 scans) (preparation of the film between 0.00 V and +1.60 V versus SCE) under irradiation from 300 W Xe Arc lamp (with $\lambda \geq 385$ nm long pass filter) in H_2O containing I_3^- 5 mmol L^{-1} and I^- 0.5 mol L^{-1}, BIAS potential 0.00 V.

It can be seen that the photocurrents of the two films increased with deceasing BIAS potential, similarly to the behaviors of previously reported (Keggin-type POM/hemicyanine)$_n$ film.[34] The photocurrent of both films depend on the BIAS voltages over 0.0 to –0.2 V range. When applied BIAS voltages are lower than 0.0 V, the photocurrents of both films are cathodic, i.e. the electrons flow from ITO electrode through the hybrid films to the electrolyte solution. In contrast, when the BIAS voltage is positive, the photocurrents are anodic.

3.3. Energy diagram of the electron transfer processes

We attempt to explore the electron transfer process in the system, the energies of the relevant electronic states should be calculated. For **poly-V_6O_{13}-ZnOEP**, the energy level diagram can be built using the oxidation potential of **ZnOEP** subunit and the reduction potential of V^V/V^{IV} in the POM cluster and the pyridinium subunits, together with the optical excitation of **ZnOEP** within the film. It describes the thermodynamics for spectral sensitization of the ITO electrode.

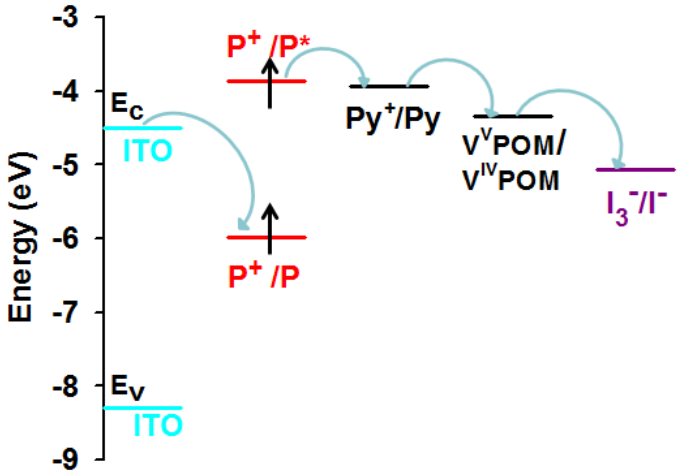

Fig. 2.20 Schematic energy level diagram showing the electron transfer process.

The oxidation potential of **ZnOEP** subunit (P) provides a measurement of the energy of the HOMO. An estimate for the potential of t the excited **ZnOEP*** ($P^{+\bullet}/P^*$) can be obtained by subtracting the energy for excitation light of the film from its oxidation potential

$$E(P^{+\bullet}/P^*) = E(P^{+\bullet}/P) - E_{S0\rightarrow S1}$$

The oxidation potential of the **ZnOEP** will correlate with the ability of the oxidized porphyrin to accept electrons from the ITO conduction band. From the electron affinity, the conduction band (E_c) and valence band (E_v) edges of ITO electrode surface are estimated to be –4.5 and –8.3 eV.[52] The level of the excited state (–3.87 eV for $P^{+\bullet}/P^*$) and the ground state (–5.98 eV for $P^{+\bullet}/P$) for the film are taken in reference to the oxidation potential of the porphyrin (+1.48V *vs*. ENH with a band gap of 2.11 eV at λ = 589 nm, measured from the film). The energy level of the couples $Py^+/Py^\bullet$, $V^{V}POM/V^{IV}POM$ and I_3^-/I^- on the absolute scale are –3.94 eV (–0.56 V *vs.* NHE), , –4.35 eV (-0.15 V *vs.* NHE) and –5.13 eV (+0.63 V *vs.* NHE) as represented in Fig. 2.20. Due to it is incapable of detecting the redox potentials of **poly-V_6O_{13}-ZnOEP** using ITO electrode, we electropolymerized the **poly-V_6O_{13}-ZnOEP** film on the glass carbon substrate, then measured the cyclic voltammogram of the obtained film in the aqueous solution with NaI as conducting salt. The **V_6O_{13}** subunit acted as a strong electron acceptor and can oxidize the pyridyl radical initially formed from electron transfer from the excited porphyrin to the pyridinium, which is an asset for preventing reverse charge transfer of the exited porphyrin.

4. Photocatalytical recovery of metals

Metal recovery is a topic of great concern from economic and environmental aspect. Since many metals are either valuable or toxic, the development of methods that aim to recovery of metals could contribute to save the finite resources and solve the environmental problems.

Metallic nanoparticles can be produced using various methods, such as thermal decomposition,[35] electrochemical techniques,[36,37] sonochemical synthesis,[38,39] radiolysis,[40] microwave irradiation[41] and photocatalysis.[42] In particular, POMs can be used in photocatalytical processes for the recovery of metals or the synthesis of nanoparticles. Our main objective was to study that covalent copolymers of POMs with chromophores (it is porphyrin in this thesis) allow us to activate the POMs by visible light which further reduced silver and platinum ions. A charge transfer between the porphyrin units and the POM can be shown by transient absorption spectroscopy.[43] The study of supported photosensitized systems coupled with POMs to perform heterogeneous photocatalysis has also been reported for the elaboration of metallic silver nanosheets and nanowires using covalent copolymers with porphyrin and Anderson-type POM subunits.[1]

4.1 Photocatalytical recovery of silver

The electrochemically deposited **poly-V_6O_{13}-ZnOEP** or **poly-V_6O_{13}-H_2T_2P** copolymers were dissolved and removed from ITO with dimethyl formamide (DMF). Subsequently, the copolymer in DMF solution was deposited on a quartz slide, and the DMF solvent was evaporated in air. Then the quartz slide was plunged in an optical cell containing a deaerated aqueous solution with 8×10^{-5} mol L^{-1} Ag_2SO_4 and 0.13 mol L^{-1} propan-2-ol. Finally, the whole sample was illuminated under visible light with a high-pass filter at 385 nm (that is to say, allowing only wavelengths above 385 nm) allows only the excitation of the porphyrin. Fig. 2.21 presents the absorption spectra recorded during the experiment performed with the **poly-V_6O_{13}-ZnOEP** (Fig. 2.21A) or **poly-V_6O_{13}-H_2T_2P** (Fig. 2.21B) films in deaerated aqueous solution with silver cations. The absorbance intensity increases in the whole visible domain during illumination and the solution becomes slightly yellow which demonstrate the formation of silver nanoparticles.[1, 44] The initial rate of Ag^+ reduction is determined to be 3.4×10^{-5} mol L^{-1} min^{-1} for **poly-V_6O_{13}-ZnOEP** and 3.1×10^{-5} mol L^{-1} min^{-1} for **poly-V_6O_{13}-H_2T_2P**. After almost 95 min (for **poly-V_6O_{13}-ZnOEP**) and 105 min (for **poly-V_6O_{13}-H_2T_2P**) of visible light irradiation, the absorption spectrum does not evolve anymore which indicates the end of the reaction.

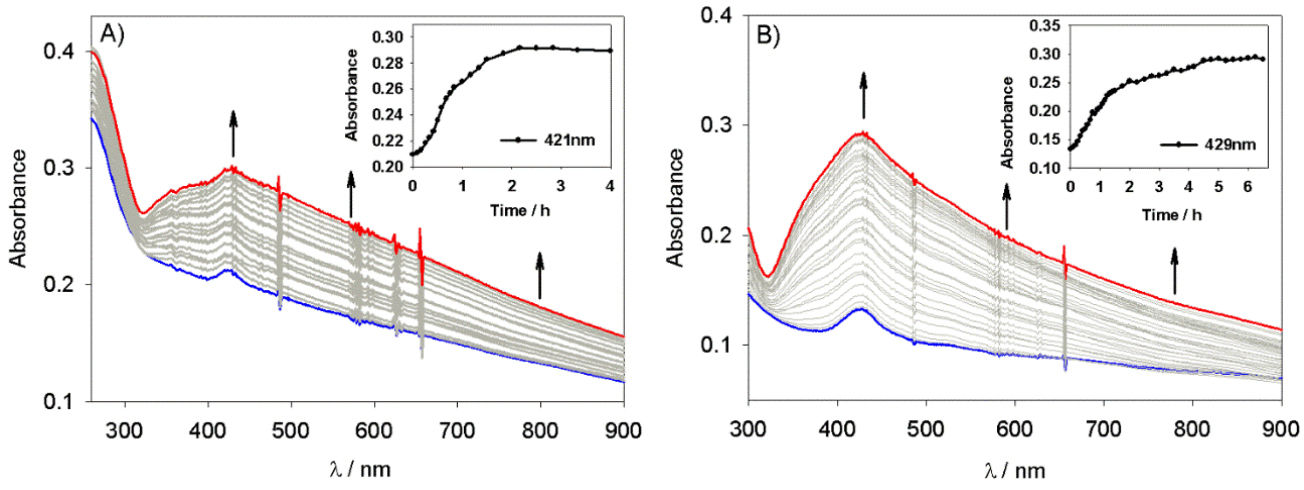

Fig. 2.21 Change in the UV–vis absorption spectrum of a deaerated aqueous solution of 8.0×10^{-5} mol L^{-1} Ag_2SO_4 and 0.13 mol L^{-1} propan-2-ol containing a slide of quartz modified with A) **poly-V_6O_{13}-ZnOEP**, B) **poly-V_6O_{13}-H_2T_2P** film under illumination. Inset: plot of the intensity of the absorbance at A) λ = 421 and B) λ = 429 versus the time of irradiation.

If we take out the quartz slide covered with the film, the UV–visible spectrum of the silver nanoparticles

can be obtained and possess a large plasmon band of the AgNPs in the whole visible domain with a maximum around 410 nm (Fig. 2.22). No change in the solution spectrum is observed for one week indicating the stability of the silver nanoparticles toward oxidation. Moreover, it has been found that slides of quartz after the catalysis can be reused at least three times nearly without change of the efficiency of the photocatalysis.

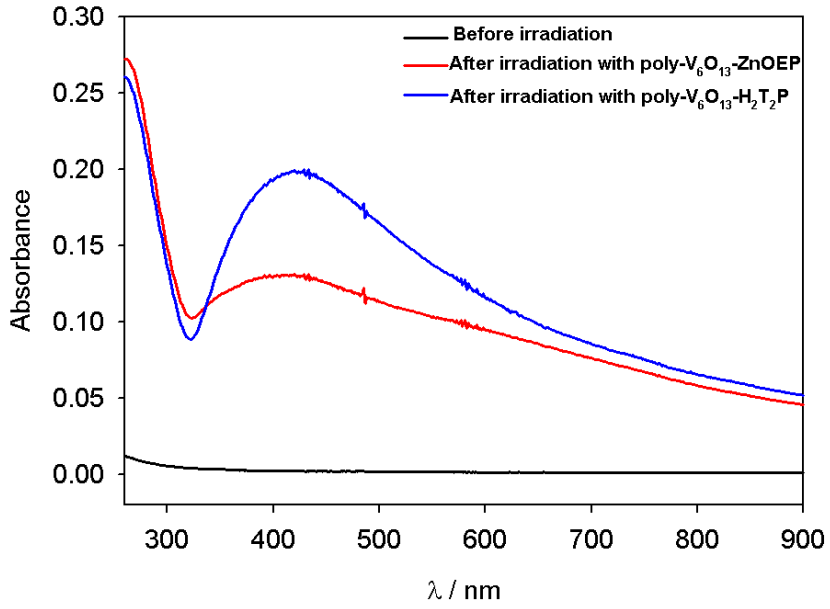

Fig. 2.22 Spectrum of the silver nanomaterial solution before and after the photocatalysis using the **poly-V_6O_{13}-ZnOEP** (red curve) or the **poly-V_6O_{13}-H_2T_2P** (blue curve) films.

The TEM micrographs confirmed the formation of silver particles (Fig. 2.23 and Fig. 2.24). The nanoparticles obtained with **poly-V_6O_{13}-ZnOEP** were semi-homogenous in size with an average of 20 nm, but are agglomerated (Fig. 2.23). Conversely, the nanostructures obtained with **poly-V_6O_{13}-H_2T_2P** were inhomogeneous in size and shape, because the samples presented not only spherical, elongated particles but also long linear silver nanowires (thickness ca. 20-40 nm and length ca. 200-500 nm) and silver nanosheets (Fig. 2.24).

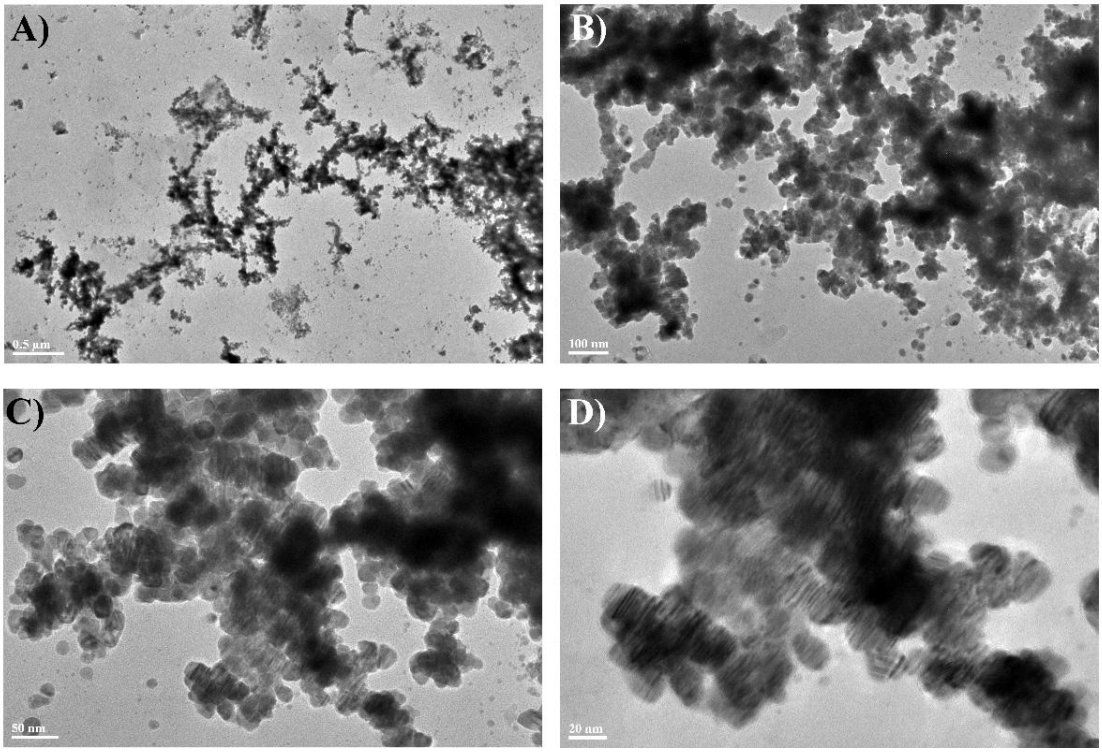

Fig. 2.23 TEM images of the silver nanoparticles obtained with the **poly-V_6O_{13}-ZnOEP** film in deaerated solutions 8.0×10^{-5} mol L^{-1} Ag_2SO_4.

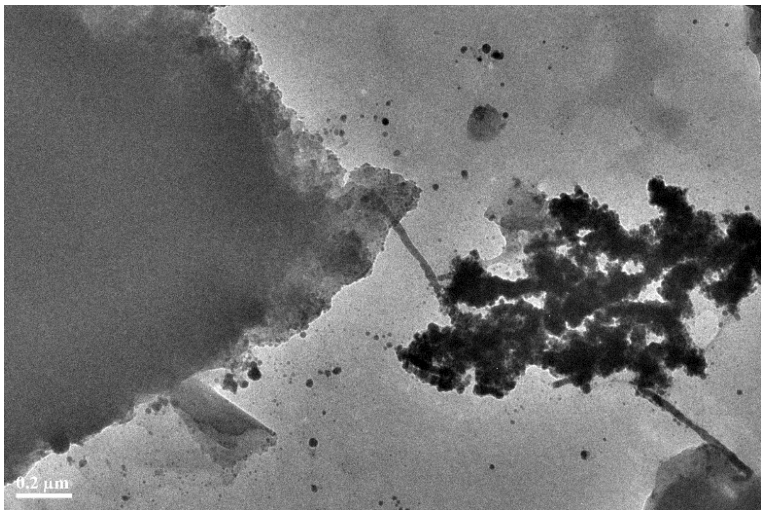

Fig. 2.24 TEM images of the silver nanomaterials obtained with the **poly-V_6O_{13}-H_2T_2P** film in deaerated solutions 8.0×10^{-5} mol L^{-1} Ag_2SO_4.

4.2. Photocatalytical recovery of platinum

To extend the photocatalytical application, we have explored the photocataysis of the reduction of $Pt^{IV}Cl_6^{2-}$ anions using the two covalent porphyrin-Lindqvist type POM copolymers. The study is conducted under deaerated medium in the presence of 1.6×10^{-4} mol L^{-1} $H_2Pt^{IV}Cl_6$ (to keep the same concentration of metal ions) and 0.13 mol L^{-1} propan-2-ol. Fig. 2.25 illustrates the change in the UV-vis absorption spectrum recorded during the illumination of a quartz slide covered with **poly-V_6O_{13}-ZnOEP** in a deaerated aqueous solution containing 1.6×10^{-4} mol L^{-1} H_2PtCl_6 and 0.13 mol L^{-1} propan-2-ol during visible light irradiation. The initial absorbance of $Pt^{IV}Cl_6^{2-}$ anions decreased during illumination and disappeared completely after 100 min, however, because the Pt nanoparticles do not possess plasmon band or other type of UV-visible absorbance, it's impossible to monitor the creation of the Pt nanoparticles from the UV-visible spectroscopy. Fortunately, after 24 hours illumination, we can see the yellow sediment on the bottom of the cuvette, and after stirring, the absorbance in the whole domain increase.

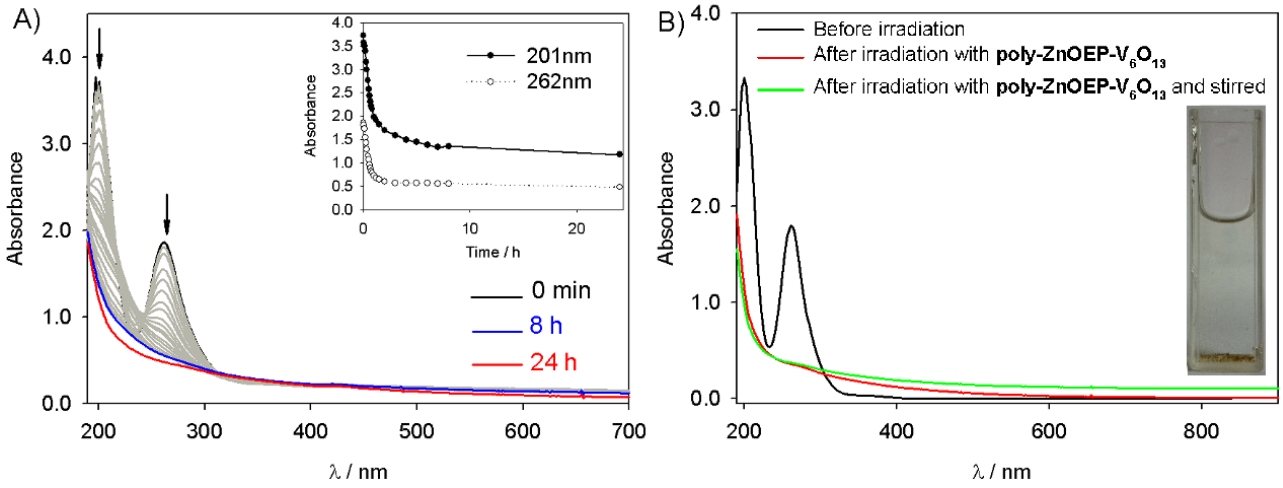

Fig. 2.25 A) Change in the UV–vis absorption spectrum of a deaerated aqueous solution of 1.6×10^{-4} mol L^{-1} H_2PtCl_6 and 0.13 mol L^{-1} propan-2-ol containing a slide of quartz modified with **poly-V_6O_{13}-ZnOEP** film under illumination. Inset: plot of the intensity of the absorbance at λ = 201 and 262 nm versus the time of irradiation. B) Spectrum of the platinum solution before and after photocatalysis. Inset: photo of the obtained solution in the cuvette after the irradiation.

The TEM micrographs confirm the formation of the Pt nanoparticles with closed-packed spherical structure. The diameter of the basic nanoparticles subunit is 1.0-1.5 nm which form the closed-packed

nanoparticles with a diameter of 10-20 nm (Fig. 2.26).

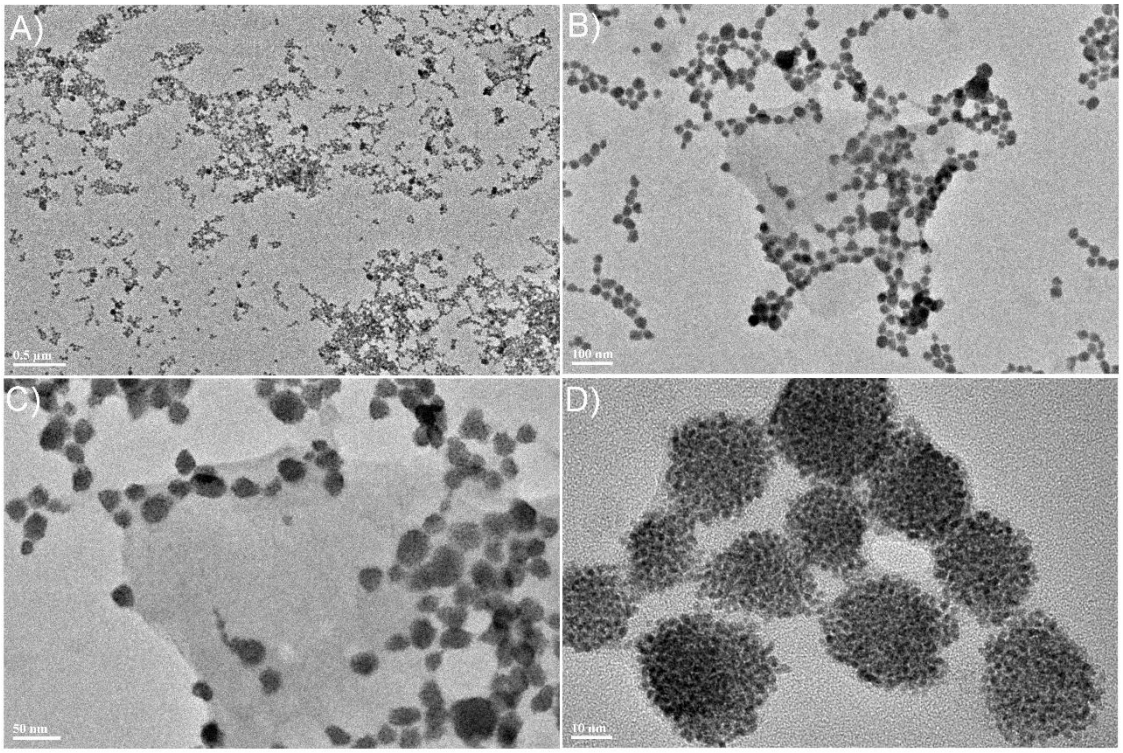

Fig. 2.26 TEM images of the platinum nanomaterial obtained with the **poly-V_6O_{13}-ZnOEP**.

Fig. 2.27 presents the absorption spectra of a deaerated aqueous solution containing 1.6×10^{-4} mol L^{-1} H_2PtCl_6 and 0.13 mol L^{-1} propan-2-ol with **poly-V_6O_{13}-H_2T_2P** covered quartz slide during visible light irradiation. The initial absorbance of $Pt^{IV}Cl_6^{4-}$ anions disappeared completely after 110 min which is a little slower than for **poly-V_6O_{13}-ZnOEP**. After 24 h illumination, we obtained an uniform and faint yellow solution which is unlike the sediment of using **poly-V_6O_{13}-H_2T_2P**. The TEM micrographs of the getting Pt nanostructures are presented in Fig. 2.28. The Pt nanoparticles showed again closed-packed spherical structure similar that was obtained using **poly-V_6O_{13}-ZnOEP** film. Nevertheless, such structures is also mixed with big nanosheets. The obtained Pt nanomaterial is in this case inhomogeneous in size and shape.

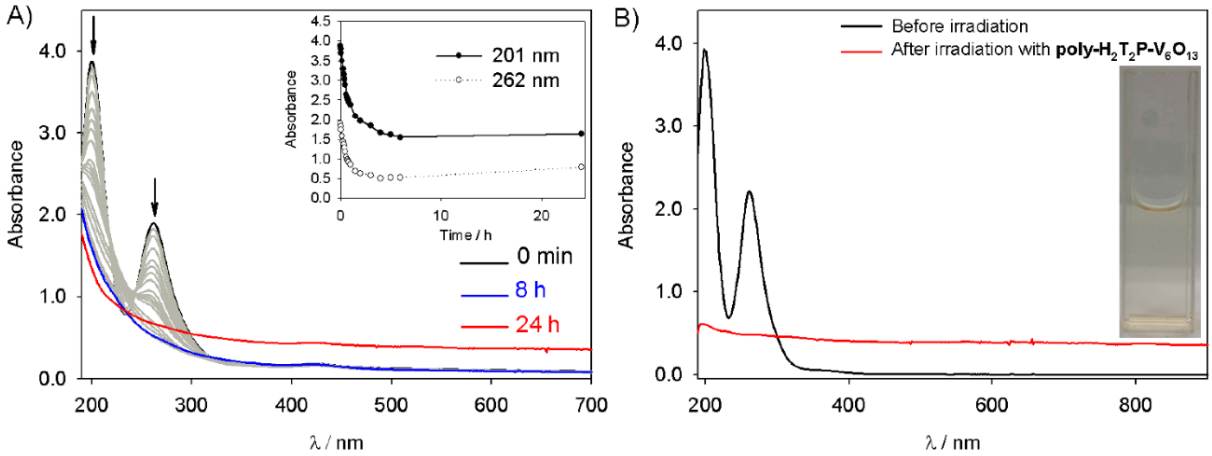

Fig. 2.27 A) Change in the UV–vis absorption spectrum of a deaerated aqueous solution of 1.6×10^{-4} mol L^{-1} H_2PtCl_6 and 0.13 mol L^{-1} propan-2-ol containing a slide of quartz modified with **poly-V_6O_{13}-H_2T_2P** film under illumination. Inset: plot of the intensity of the absorbance at λ = 201 and 262 nm versus the time of irradiation. B) Spectrum of the platinum solution before and after photocatalysis. Inset: photo of the obtained solution in the cuvette after the irradiation.

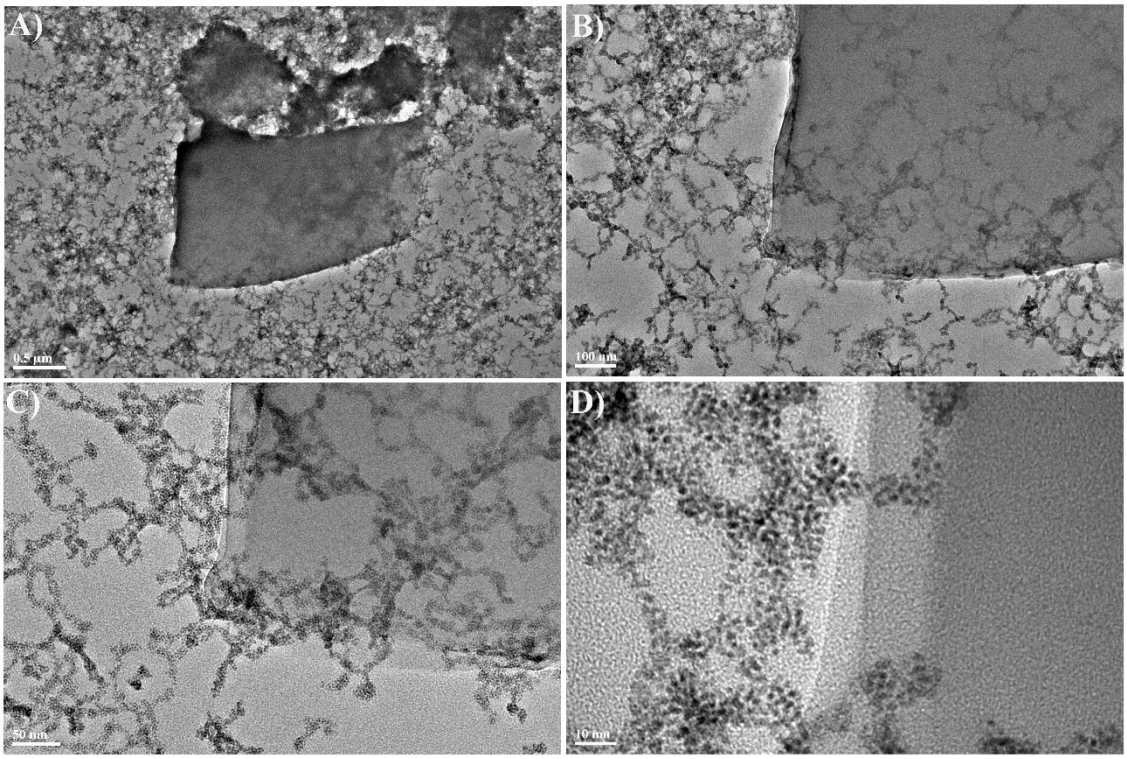

Fig. 2.28 TEM images of the platinum nanomaterials obtained with the **poly-V_6O_{13}-H_2T_2P** film in deaerated solutions 1.6×10^{-4} mol L^{-1} H_2PtCl_6.

5. Conclusion

In this chapter, covalent **poly-V_6O_{13}-ZnOEP** and **poly-V_6O_{13}-H_2T_2P** electroactive films were obtained

on ITO electrode surfaces during repetitive potential cycling. When the potential high enough to get porphyrin dications, the pyridyl nucleophile (**Py-V_6O_{13}-Py**) will react with them to start the electrodeposition and the formation of the copolymers. Homogeneous charge transport through these films and significant photocurrent response were observed. Controlling the thickness of the film is crucial for the photocurrent-generation efficiency. We demonstrated the efficiency of the two copolymers in the photocatalytic reduction of Ag(I) and Pt(IV) using visible light.

The **poly-V_6O_{13}-ZnOEP** copolymers with the **ZnOEP** as chromophores possessed more efficient photocurrent response and a little higher kinetic performance during photocatalytical process than **poly-V_6O_{13}-H_2T_2P**, which are ascribed to the higher light collection (higher visible absorbance) and lower charge transfer resistance of **poly-V_6O_{13}-ZnOEP**.

The obtained Ag nanomaterials by **poly-V_6O_{13}-ZnOEP** were semi-homogenous. Conversely, the nanostructures obtained with **poly-V_6O_{13}-H_2T_2P** were inhomogeneous in size and shape. The morphology of the Pt nanomaterials obtained by **poly-V_6O_{13}-ZnOEP** were spherical nanoparticles packed by much smaller nanoparticle subunits. When **poly-V_6O_{13}-H_2T_2P** has been taken as photocatalyst, the closed packed Pt nanoparticles units were mixed with big Pt nanosheets.

References

(1) Schaming, D.; Allain, C.; Farha, R.; Goldmann, M.; Lobstein, S.; Giraudeau, A.; Hasenknopf, B.; Ruhlmann, L. *Langmuir* **2010**, *26* (7), 5101.

(2) Long, D.-L.; Tsunashima, R.; Cronin, L. *Angew. Chem. Int. Ed. Engl.* **2010**, *49* (10), 1736.

(3) Anandan, S.; Pitchumani, S.; Muthuraaman, B.; Maruthamuthu, P. *Sol. Energy Mater. Sol. Cells* **2006**, *90* (12), 1715.

(4) Mylonas, a.; Hiskia, a.; Papaconstantinou, E. *J. Mol. Catal. A Chem.* **1996**, *114* (1-3), 191.

(5) Troupis, a.; Hiskia, a.; Papaconstantinou, E. *Appl. Catal. B Environ.* **2003**, *42* (3), 305.

(6) Costa-Coquelard, C.; Schaming, D.; Lampre, I.; Ruhlmann, L. *Appl. Catal. B Environ.* **2008**, *84* (3-4), 835.

(7) Kahef, L. El; Gross, M.; Giraudeau, A. *J. Chem. Soc, Chem. Commun.* **1989**, *49*, 1989.

(8) Giraudeau, A.; Ruhlmann, L.; El Kahef, L.; Gross, M. *J. Am. Chem. Soc.* **1996**, *118* (12), 2969.

(9) Ruhlmann, L.; Lobstein, S.; Gross, M.; Giraudeau, A. *J. Org. Chem.* **1999**, *64* (4), 1352.

(10) Giraudeau, A.; Lobstein, S.; Ruhlmann, L.; Melamed, D.; Barkigia, K. M.; Fajer, J. *J. Porphyr. Phthalocya.* **2001**, *05* (11), 793.

(11) Ruhlmann, L.; Giraudeau, A. *Chem. Commun.* **1996**, *17*, 2007.

(12) Ruhlmann, L.; Giraudeau, A. *Eur. J. Inorg. Chem.* **2001**, 659.

(13) Favette, S.; Hasenknopf, B.; Vaissermann, J.; Gouzerh, P.; Roux, C. *Chem. Commun. .* **2003**, *21*, 2664.

(14) Allain, C.; Favette, S.; Chamoreau, L.; Vaissermann, J.; Ruhlmann, L.; Hasenknopf, B. *Eur. J. Inorg. Chem.* **2008**, *2008* (22), 3433.

(15) Ruhlmann, L.; Schulz, A. *J. Am. Chem. Soc.* **1999**, *121* (8), 6664.

(16) Ruhlmann, L.; Hao, J.; Ping, Z.; Giraudeau, A. *J. Electroanal. Chem.* **2008**, *621* (1), 22.

(17) Giraudeau, A.; Schaming, D.; Hao, J.; Farha, R.; Goldmann, M.; Ruhlmann, L. *J. Electroanal. Chem.* **2010**, *638* (1), 70.

(18) Schaming, D.; Ahmed, I.; Hao, J.; Alain-Rizzo, V.; Farha, R.; Goldmann, M.; Xu, H.; Giraudeau, A.; Audebert, P.; Ruhlmann, L. *Electrochim. Acta* **2011**, *56* (28), 10454.

(19) Huang, S.-C.; Lin, C.-Y. *Chem. Commun.* **2015**, *51* (3), 519.

(20) Schaming, D.; Marggi-Poullain, S.; Ahmed, I.; Farha, R.; Goldmann, M.; Gisselbrecht, J.-P.; Ruhlmann, L. *New J. Chem.* **2011**, *35* (11), 2534.

(21) Ogawa, T.; Ogawa, T.; Nishimoto, Y.; Ono, N.; Yoshida, N.; Osukua, A. *Chem. Commun.* **1998**, 337.

(22) Ogawa, T.; Nishimoto, Y.; Yoshida, N.; Ono, N.; Osuka, A. *Angew. Chemie Int. Ed.* **1999**, *38* (1-2), 176.

(23) Dime, A. K. D.; Devillers, C. H.; Cattey, H.; Habermeyer, B.; Lucas, D. *Dalt. Trans.* **2012**, *41*, 929.

(24) Sessler, J. L.; Johnson, M. R.; Creager, S. E.; Fettinger, J. C.; Ibers, J. a. *J. Am. Chem. Soc.* **1990**, *112* (25), 9310.

(25) Bruckenstein, S.; Shay, M. *Electrochim. Acta* **1985**, *30* (10), 1295.

(26) Schmidt, V. M.; Heitbaum, J. *Electrochim. Acta* **1993**, *38* (2-3), 349.

(27) Inisan, C.; Saillard, J.-Y.; Guilard, R.; Tabard, A.; Le Mest, Y. *New J. Chem.* **1998**, *22* (8), 823.

(28) Schaming, D.; Xia, Y.; Thouvenot, R.; Ruhlmann, L. *Chem. Eur. J.* **2013**, *19* (5), 1712.

(29) Ahmed, I.; Farha, R.; Goldmann, M.; Ruhlmann, L. *Chem. Commun.* **2013**, *49* (5), 496.

(30) Li, J.; Huth, I.; Chamoreau, L. M.; Hasenknopf, B.; Lacôte, E.; Thorimbert, S.; Malacria, M. *Angew. Chemie. Int. Ed.* **2009**, *48* (11), 2035.

(31) Jin, G.; Wang, S.-M.; Chen, W.-L.; Qin, C.; Su, Z.-M.; Wang, E.-B. *J. Mater. Chem. A* **2013**, *1* (23), 6727.
(32) Chen, X.; Gao, L. H.; Zheng, Z. B.; Wang, K. Z. *Mater. Res. Bull.* **2013**, *48* (2), 595.
(33) Gao, L. H.; Sun, Q. L.; Qi, J. M.; Lin, X. Y.; Wang, K. Z. *Electrochim. Acta* **2013**, *92*, 236.
(34) Gao, L.-H.; Zhang, J.-F.; Wang, H.-L.; Lin, X.-Y.; Qi, J.-M.; Wang, K.-Z. *Electrochim. Acta* **2015**, *166*, 215.
(35) Kim, Y. H.; Lee, D. K.; Kang, Y. S. *Colloids Surfaces A Physicochem. Eng. Asp.* **2005**, *257-258*, 273.
(36) Reetz, M.; Helbig, W. *J. Am. Chem. Soc.* **1994**, *116* (11), 7401.
(37) Starowicz, M.; Stypuła, B.; Banaś, J. *Electrochem. commun.* **2006**, *8* (2), 227.
(38) Nagata, Y.; Watananabe, Y.; Fujita, S.; Dohmaru, T.; Taniguchi, S. *J. Chem. Soc. Chem. Commun.* **1992**, *21*, 1620.
(39) Fujimoto, T.; Terauchi, S. Y.; Umehara, H.; Kojima, I.; Henderson, W. *Chem. Mater.* **2001**, *13* (3), 1057.
(40) Belloni, J.; Mostafavi, M.; Remita, H.; Marignier, J. L.; Delcourt, M. O. *New J. Chem.* **1998**, *11* (22), 1239.
(41) Yin, H.; Yamamoto, T.; Wada, Y.; Yanagida, S. *Mater. Chem. Phys.* **2004**, *83* (1), 66.
(42) Ohtani, B.; Kakimoto, M.; Miyadzu, H.; Nishimoto, S.; Kagiya, T. *J. Phys. Chem.* **1988**, *92* (20), 5773.
(43) Costa-Coquelard, C.; Sorgues, S.; Ruhlmann, L. *J. Phys. Chem. A* **2010**, *114* (22), 6394.
(44) Ahmed, I.; Wang, X.; Boualili, N.; Xu, H.; Farha, R.; Goldmann, M.; Ruhlmann, L. *"Applied Catal. A, Gen.* **2012**, *447-448*, 89.
(45) Hao, J.; Giraudeau, A.; Ping, Z.; Ruhlmann, L. *Langmuir* **2008**, *24* (5), 1600.
(46) Brisach-Wittmeyer, A.; Lobstein, S.; Gross, M.; Giraudeau, A. *J. Electroanal. Chem.* **2005**, *576* (1), 129.
(47) Schaming, D.; Giraudeau, A.; Lobstein, S.; Farha, R.; Goldmann, M.; Gisselbrecht, J.-P.; Ruhlmann, L. *J. Electroanal. Chem.* **2009**, *635* (1), 20.
(48) Baraka, M. El; Jannot, J. M.; Ruhlmann, L.; Giraudeau, A.; Deumie, M.; Seta, P. *Photochem. Photobio. A: Chem.* **1998**, *113* (2), 163.
(49) Ponomarev, E. A.; Peter, L. M. *J. Electroanal. Chem.* **1995**, *397* (1-2), 45.
(50) Kuang, D.; Brillet, J.; Chen, P.; Takata, M.; Uchida, S.; Miura, H.; Sumioka, K.; Zakeeruddin, S. M.; Grätzel, M. *ACS Nano* **2008**, *2* (6), 1113.
(51) Matt, B.; Xiang, X.; Kaledin, A. L.; Han, N.; Moussa, J.; Amouri, H.; Alves, S.; Hill, C. L.; Lian, T.; Musaev, D. G.; Izzet, G.; Proust, A. *Chem. Sci.* **2013**, *4* (4), 1737.
(52) Sereno, L.; Silber, J.; Otero, L.; Bohorquez, M. D. V.; Moore, A. L. *J. Phys. Chem.* **1996**, *100* (2), 814.
(53) Witten Jr, T.; Sander, L.; *Phys. Rev. Lett.* **1981**, *47* (19) 1400.
(54) Azcarate, I.; Ahmed, I.; Farha, R.; Goldmann, M.; Wang, X.; Xu, H.; Hasenknopf, B.; Lacôte, E.; Ruhlmann, L. *Dalton Trans.* **2013**, *42* (35), 12688.
(55) Azcarate , I.; Huo, Z.; Farha , R.; Goldmann , M.; Xu, H.; Hasenknopf, B.; Lacôte , E.; Ruhlmann, L. *Chem. Eur. J.* **2015**, *21* (22), 8271.
(56) Aldebert, P.; Audebert, P.; Armand, M.; Bidan, G.; Pineri, M. *J. Chem. Soc. Chem. Commun.* **1986**, *22*, 1636.
(57) Audebert, P.; Aldebert, P.; Pineri, M.; *Synthetic Metals* **1989**, *32* (1), 1.
(58) Genies, E. M.; Hany, P.; Lapkowski, M.; Santier, C.; Olmedo, L. *Synth. Met.* **1988**, *25* (1), 29.
(59) Lowe, J.; Holdcroft, S. *Macromolecules* **1995**, *28* (13), 4608.
(60) Keita, B.; Brudna Holzle, L. R.; Ngo Biboum, R.; Nadjo, L.; Mbomekalle, I. M.; Franger, S.; Berthet, P.; Brisset, F.; Miserque, F.; Ekedi, G. a. *Eur. J. Inorg. Chem.* **2011**, *4* (8), 1201.

Chapter III

Covalent Keggin and Dawson silyl polyoxophosphotungstate – porphyrin copolymers for the photocurrent generation and the photocatalytical recovery of metals

Chapter III: Covalent Keggin and Dawson silyl polyoxophosphotungstate – porphyrin copolymers for the photocurrent generation and the photocatalytical recovery of metals

In the present chapter, we have obtained and studied four covalent POM–porphyrin copolymers based on the nucleophilic attack of pyridyl groups (bound on the POM framework, Py-POM-Py) onto electrogenerated porphyrin dications through an $E(EC_NEC_B)_nE$ process.[1] All of the copolymers have been characterized by UV-vis spectroscopy, X-ray photoelectron spectroscopy, atomic force microscopy, impedance spectroscopy, electrochemical quartz crystal measurement and electrochemistry.

The photochemical active performances were evaluated by photocurrent transient measurements and photocatalytical recovery of metals. The photosynthetic activity and efficiency vared with types of POM (Keggin *vs.* Dawson-type, of which the two pyridyl groups were connected to the POM through organosilyl functionalization) and type of photosensitizers (metal porphyrin *vs.* free base porphyrin).

1. Introduction

The design of artificial photosynthetic materials is emerging for the development of a sustainable economy. Photoconversion of light into chemical fuels relies on the formation of photoinduced electronic charge separation with suitable lifetime to permit redox reactions with external substrates to proceed. In the search for alternative materials, polyoxometalates (POMs) have recently attracted particular attention, which are well-known molecular electron reservoirs and electrocatalysts.[2] POMs can be reduced in several steps and to accommodate several electrons. [3,4,5,6]

The covalent linkage between a POM and a photosensitizer, compared to electrostatic association, is expected to facilitate better control of the interaction and orientation between the POM and the chromophore.

As starting hybrid POM platforms, Anna Proust reported silyl (or organotin)-derivatized Keggin- and Wells-Dawson-type POMs used Sonogashira cross coupling for providing rigid linkers (Chapter I, section 2.2.4). The nature of the POM and its functionalization impact the redox potential of the polyanion and both can be tuned in order to optimize the charge separation in the polyanion. Up to now,

among the reported hybrids, the iridium(III) photosensitized silyl-Dawson hybrid seems to have the most interesting photophysical properties (relative to silyl-Keggin, tin-Keggin and tin-Dawson hybrids) which can be ascribed to its very effective charge separation while its charge-separated state is a *priori* still long enough to permit redox reactions with external substrates to proceed.[7,8,9,10]

Excited by these achievements, we want to extended the research of silyl-Keggin and silyl-Dawson hybrid with other chronophers for instance porphyrins, so organosilyl functionalized Keggin-type POMs $[PW_{11}Si_2O_{40}C_{26}H_{16}N_2]TBA_3$ (abbreviated **Py-$PW_{11}Si_2$-Py**) and Dawson-type POMs $[P_2W_{17}Si_2O_{62}C_{26}H_{16}N_2]TBA_6$ (abbreviated **Py-$P_2W_{17}Si_2$-Py**) bearing two pyridyl groups were used for electrochemical preparation of the copolymers with porphyrin (**ZnOEP** and **H_2T_2P**) using the previously reported $E(EC_NEC_B)_nE$ process.[11,12,13,14,15,16] We herein describe the electropolymerization and the characterization of the four hybrids and their applications for photocurrent generation and photoreduction of Ag_2SO_4 and H_2PtCl_6 under visible irradiation.

2. Formation and characterization

2.1. Redox behavior of the two organo-POM monomers

A collaboration with the group of Prof. Anna Proust and Dr. Guillaume Izzet let us to have two silyl functionalized Keggin and Dawson type POMs $[PW_{11}Si_2O_{40}C_{26}H_{16}N_2]TBA_3$ (abbreviated **Py-$PW_{11}Si_2$-Py**) and $[P_2W_{17}Si_2O_{62}C_{26}H_{16}N_2]TBA_6$ (abbreviated **Py-$P_2W_{17}Si_2$-Py**) (see Fig. 3.2).

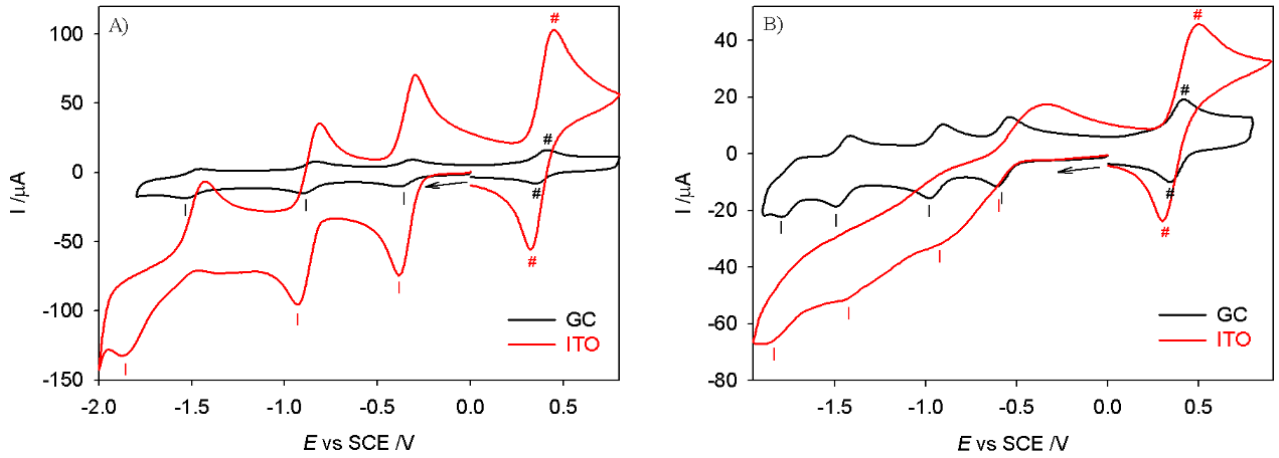

Fig. 3.1 Cyclic voltammograms of 0.25 mmol L^{-1} A) $[PW_{11}Si_2O_{40}C_{26}H_{16}N_2]TBA_3$ and B) $[P_2W_{17}Si_2O_{62}C_{26}H_{16}N_2]TBA_6$ in CH_3CN in the presence of 0.1 mol L^{-1} $TBAPF_6$. Working electrode: ITO, S = 1 cm^2 and glass carbon (GC), d = 3 mm. (←) Start of the scan. Scan rate: 0.1 V s^{-1}. Peak #: Fc/Fc^+ internal reference.

The redox behavious of **Py-$PW_{11}Si_2$-Py** and **Py-$P_2W_{17}Si_2$-Py** show three and four successive reduction processes respectively, from the W^{VI}/W^{V} (Fig. 3.1) using glassy carbon electrode. However, the redox process of **Py-$P_2W_{17}Si_2$-Py** shows only ill-defined waves using ITO electrode (Fig. 3.1B). In the case of **Py-$PW_{11}Si_2$-Py**, the redox process shows similar behaviors using glass carbon and ITO electrode (Fig. 3.1A).

2.2. Electropolymerization of copolymers

All of the electropolymerizations were carried out under the same experimental conditions by iterative scans in 0.1 mol L^{-1} solutions of tetrabutylammonium hexafluorophosphate ($TBAPF_6$) in 1,2-$C_2H_4Cl_2/CH_3CN$ (7:3) containing the studied porphyrin (**ZnOEP** or **H_2T_2P**) (0.25 mmol L^{-1}) and **Py-POM-Py** (**Py-$PW_{11}Si_2$-Py** or **Py-$P_2W_{17}Si_2$-Py**) (0.25 mmol L^{-1}) under an argon atmosphere. The reported electrochemical synthesis of the copolymers uses the previously reported $E(EC_NEC_B)_nE$ process of nucleophilic substitution on porphyrins. The polarization of a working electrode at the porphyrin's second ring-oxidation potential in the presence of Py-POM-Py,[17,18] lead to the formation of hybrid films $[POM\text{-}porphyrin]_n$ (Fig. 3.3).

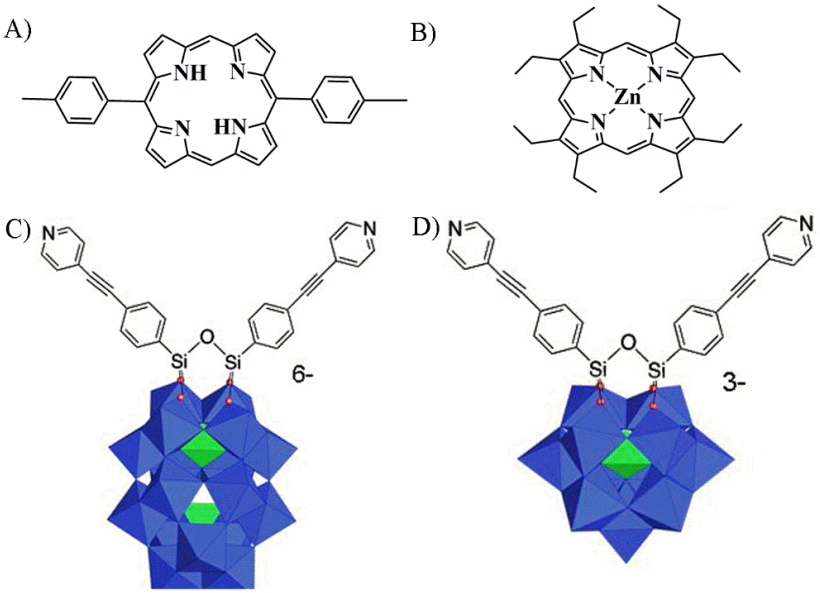

Fig. 3.2 Representation of A) **H_2T_2P**, B) **ZnOEP**, C) Dawson type POM $[P_2W_{17}Si_2O_{62}C_{26}H_{16}N_2]TBA_6$ (**Py-$P_2W_{17}Si_2$-Py**) and D) Keggin type POM $[PW_{11}Si_2O_{40}C_{26}H_{16}N_2]TBA_3$ (**Py-$PW_{11}Si_2$-Py**)

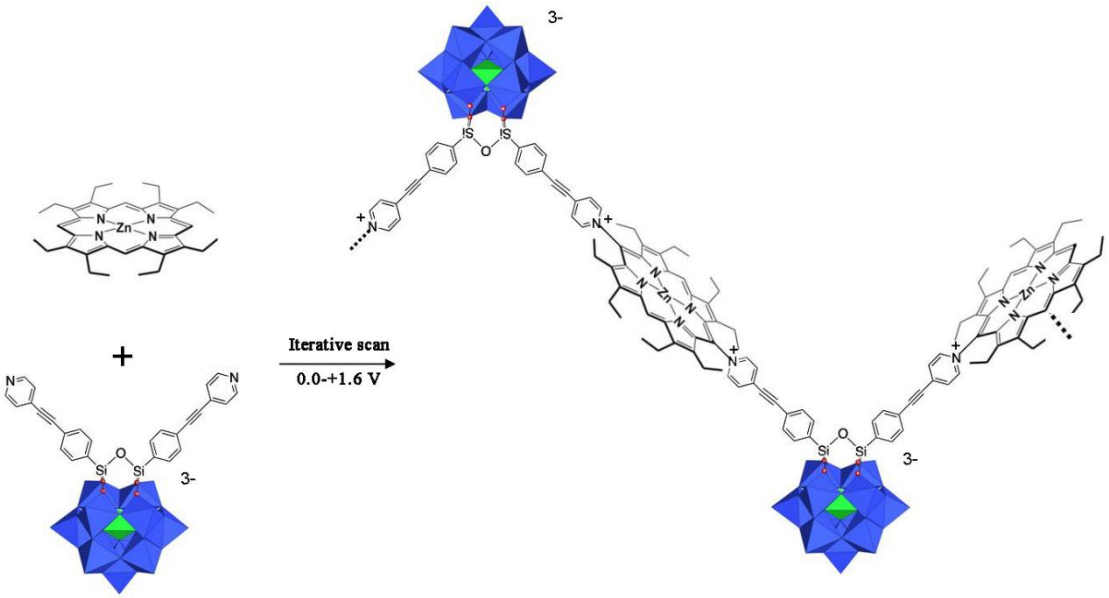

Fig. 3.3 Electropolymerization scheme of **ZnOEP** in the presence of **Py-PW$_{11}$Si$_2$-Py**.

The reactions generated H^+ ions. Scanning between -1.2 V and +1.6 V reduced these protons to H_2, and they were accumulated in solution when the scan was limited between 0.0 to +1.6 V. In the both cases, they did not perturb the coating of the electrodes. UV-visible spectroscopy demonstrated that the demetalation of the **ZnOEP** did not occur in any cases. Two types of porphyrins were used for the polymerizations. First, we used **ZnOEP**, for which the four *meso* positions are free, and nucleophilic attack could occur at positions 5, 10, 15, and 20. As a result, various branched forms of the copolymer were expected. **ZnOEP** was then replaced by **H$_2$T$_2$P**. In this case, only positions 5 and 15 were free, leading to the formation of linear 1D copolymers by the above reaction.

Fig. 3.4 illustrates the evolution of the CVs during the electropolymerization of **ZnOEP** in the presence of equimolar amounts of **Py-PW$_{11}$Si$_2$-Py**. During the first scan in reduction, two clearly reduction peaks coming from the POM units were detected on -0.36 V and -0.87 V *vs.* SCE. In the second scan, an irreversible reduction peak appeared at ca. -0.77 V *vs.* SCE (peak b, Fig. 3.4 A'), which was the reduction of the pyridinium units of the dipyridinium-POM spacers of the generated polymer (ZnOEP-Py$^+$-POM-Py$^+$)$_n$.[19,20,14,15] The intensity of these peaks increased with repetitive scans which indicated the regular growth of the conducting polymeric films at the electrode. The irreversibility of the signal indicated that the generated pyridyl radicals were not stable and reacted further.[21,22]

When we used *meso*-substituted porphyrin **H$_2$T$_2$P** (in positions 5 and 15) instead of **ZnOEP** to carry out the electropolymerization with **Py-PW$_{11}$Si$_2$-Py**, the well-defined redox peaks of the W^{VI}/W^{V} were

also obtained in the first san. And in the second scan, the appearance of an irreversible reduction peak ca. -0.70 V versus SCE (peak b, Fig. 3.4B') indicated the the generation of dipyridinium-POM spacers. In the case of the preparation of **poly-$PW_{11}Si_2$-ZnOEP**, in the positive potential range three oxidation peaks (d, e and f) in Fig. 3.4A' were recorded. The first and the second one-electron oxidation peak (peaks d and e) represented the generation of the π-radical porphyrin cation and dication, and the third peak (peak e) might be attributed to the oxidation of the intermediate isoporphyrin.[23] A similar redox behavior at the positive potential scan was also observed using **H_2T_2P** instead of **ZnOEP** (Fig. 3.4B') but in this case only two irreversible signals were observed. The oxidation of **H_2T_2P** units need also a higher positive potential, and as scans go on the oxidation peaks merged each other. It must be noted that in contrast of chapter II, the use of free base porphyrin **H_2T_2P** does not induce protonation during the oxidation followed by the proton exchange with **Py-$PW_{11}Si_2$-Py**. It suggests that the kinetic of the reaction between **$H_2T_2P^{2+}$** and **Py-$PW_{11}Si_2$-Py** is probably faster than the proton abstraction of **$H_2T_2P^{2+}$**.

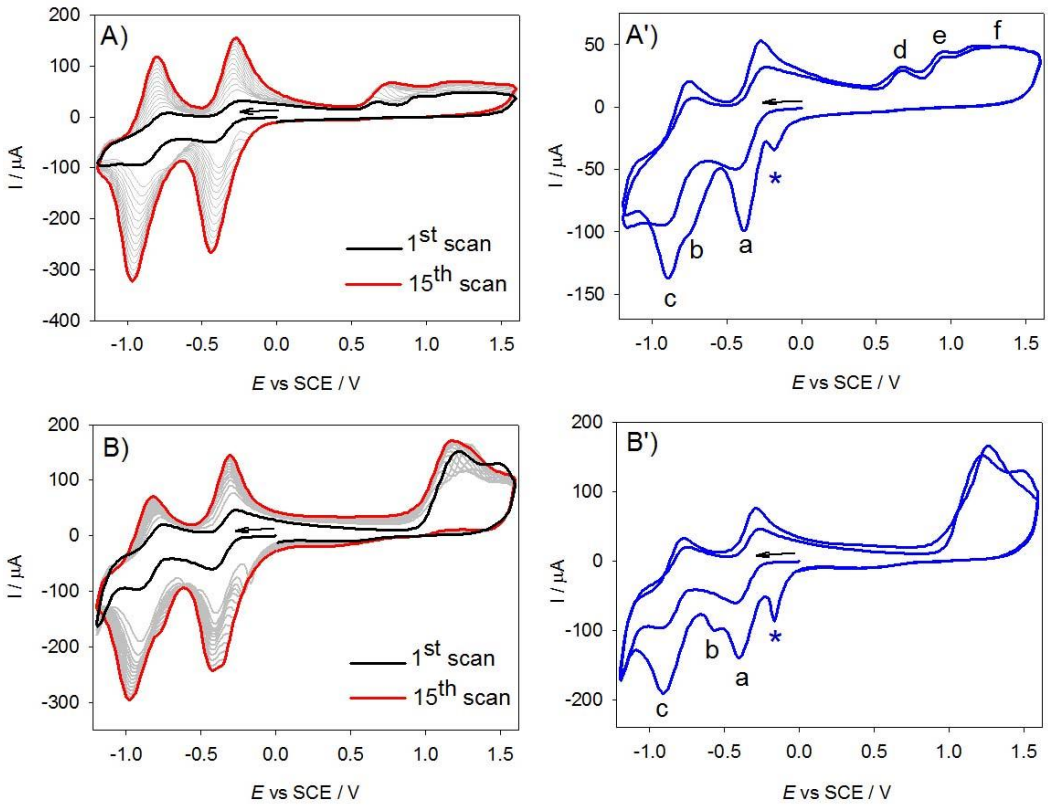

Fig. 3.4 Cyclic voltammograms recorded between −1.20 V and +1.60 V *vs.* SCE during the electropolymerization of 0.25 mmol L^{-1} **ZnOEP** with 0.25 mmol L^{-1} **Py-$PW_{11}Si_2$-Py**, (A) first 15 scans and A ʾ) first 2 scans), and of 0.25 mmol L^{-1} **H_2T_2P** with 0.25 mmol L^{-1} **Py-$PW_{11}Si_2$-Py** (B) first 15 scans and (B ʾ) first 2 scans in $CH_3CN/1,2\text{-}C_2H_4Cl_2$ (3/7) in the presence of 0.1 mol L^{-1} $TBAPF_6$. Working electrode: ITO. (←) Start of the scan. S =1 cm^2; scan rate: 0.1 V s^{-1}. Peak *: reduction of the isoporphyrin.

In the case of the use of **Py-$P_2W_{17}Si_2$-Py** as Py-POM-Py subunits, the redox peaks of W^V/W^{VI} was harder to be detected using ITO as working electrode, even in the pure **Py-$P_2W_{17}Si_2$-Py** solution without porphyrin (Fig. 3.1B). From the second iterative scan in the presence of porphyrin, the reduction of the pyridinium appeared and the intensity of this peak increased as the iterative scan number increased between −1.20 V and +1.60 V *vs.* SCE (Fig. 3.5 A' and Fig. 3.5 B').

Copolymers were also obtained by cyclic scanning (0.1 Vs^{-1}) in the potential range from 0 to +1.60 V *vs.* SCE. The obtained copolymers exhibited redox behavior similar to that observed when scanning from -1.20 to +1.60 V *vs.* SCE.

The additional wave near +0.5 V (Fig. 3.5B' and Fig. 3.8B) in the case of the formation of copolymer **poly-$P_2W_{17}Si_2$-H_2T_2P** can be attributed to the formation of the protonated **$H_4T_2P^{2+}$** intermediate which then exchange proton with **Py-$P_2W_{17}Si_2$-Py** and form **H^+Py-$P_2W_{17}Si_2$-Py** and/or **H^+Py-$P_2W_{17}Si_2$-Py$^+$H** as already observed in chapter II when using this free base porphyrin.

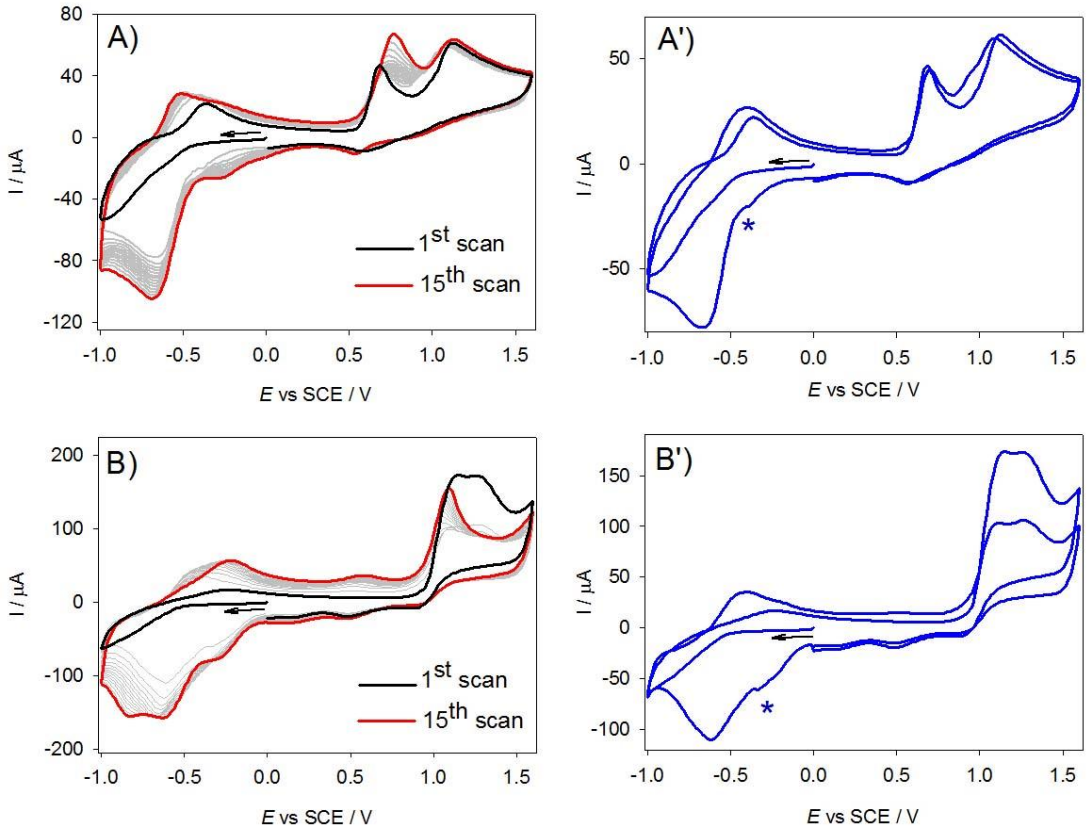

Fig. 3.5 Cyclic voltammograms recorded between −1.00 V and +1.60 V *vs.* SCE during the electropolymerization of 0.25 mmol L^{-1} **ZnOEP** with 0.25 mmol L^{-1} **Py-$P_2W_{17}Si_2$-Py**, (A) first 15 scans and (A') first 2 scans, and of 0.25 mmol/dm^3 **H_2T_2P** with 0.25 mmol L^{-1} **Py-$P_2W_{17}Si_2$-Py** (B) first 15 scans and (B') first 2 scans in CH_3CN/1,2-$C_2H_4Cl_2$ (3/7) in the presence of 0.1 mol L^{-1} $TBAPF_6$. Working electrode: ITO. (←) Start of the scan. S =1 cm^2; scan rate: 0.1 V s^{-1}. Peak *: reduction of the isoporphyrin.

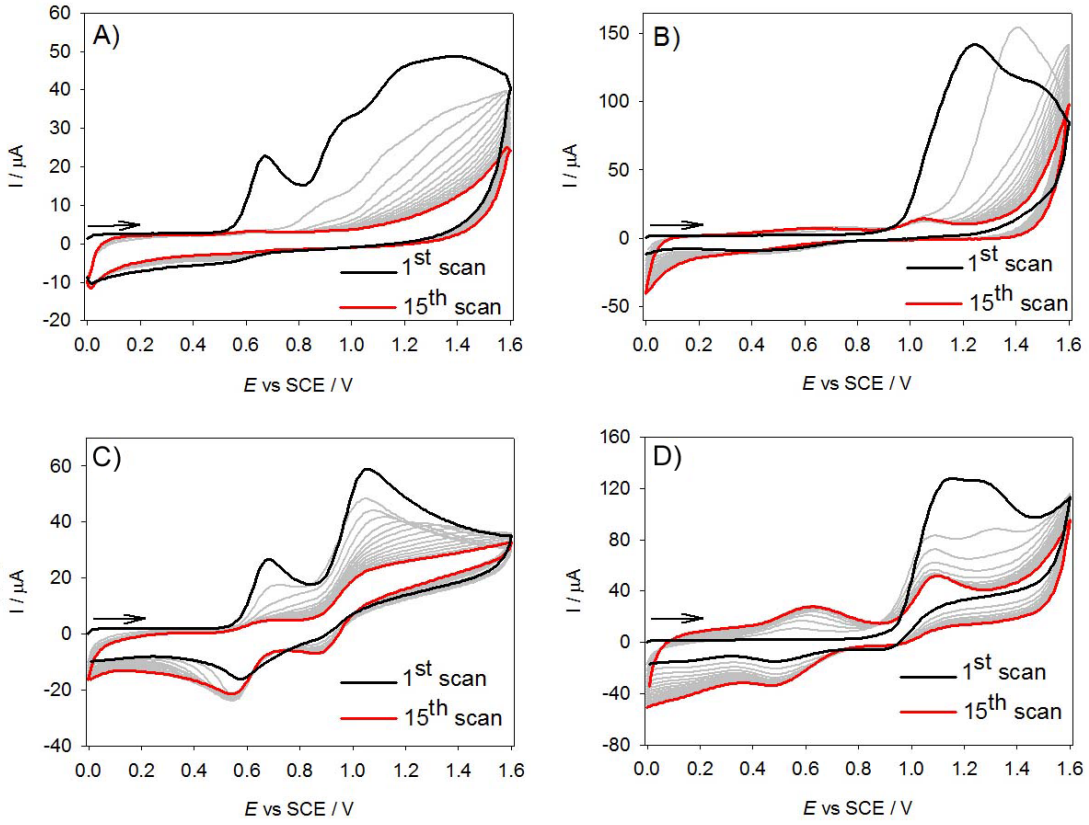

Fig. 3.6 Cyclic voltammograms recorded between 0.00 V and +1.60 V *vs.* SCE during the electropolymerization of 0.25 mmol L^{-1} **ZnOEP** (A), and of 0.25 mmol L^{-1} **H_2T_2P**, (B) with 0.25 mmol L^{-1} **Py-$PW_{11}Si_2$-Py**, and the electropolymerization of 0.25 mmol L^{-1} **ZnOEP** (C), and of 0.25 mmol L^{-1} **H_2T_2P** (D) with 0.25 mmol L^{-1} **Py-$P_2W_{17}Si_2$-Py** in CH_3CN/1,2-$C_2H_4Cl_2$ (3/7) in the presence of 0.1 mol L^{-1} $TBAPF_6$. Working electrode: ITO. (←) Start of the scan. S =1 cm^2; scan rate: 0.1 V s^{-1}.

2.3. EQCM for the copolymer deposition

The electropolymerization process of the four copolymers was monitored by EQCM. Fig. 3.7 and Fig. 3.8 showed the simultaneously recorded mass changes Δm and cyclic voltammograms between 0.00 and +1.60 V with an ITO working electrode deposited on an AT-cut quartz crystal resonator, the quartz resonance frequency Δf decreased with each consecutive cycle, with a concomitant increase in the mass of the copolymer. By using the Sauerbrey equation,[24] this change in mass was calculated. The smooth drop in quartz resonance frequency and the simultaneous mass increase Δm show continuous growth of the copolymer.

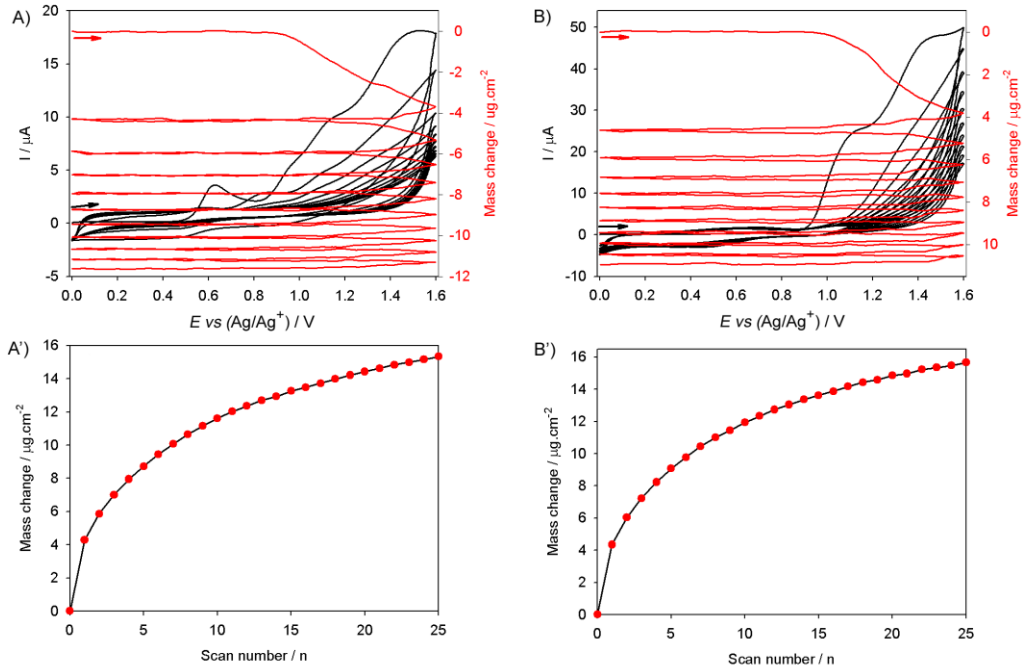

Fig. 3.7 Consecutive CVs (first 10 scans) and EQCM measurements for the first 10 scans during the electropolymerization of 0.25 mmol L^{-1} (A) **ZnOEP** or (B) **H_2T_2P** with 0.25 mmol L^{-1} **Py-$PW_{11}Si_2$-Py** in CH_3CN/1,2-$C_2H_4Cl_2$ (3/7) in the presence of 0.1 mol L^{-1} $TBAPF_6$. Working electrode: ITO (S = 0.2 cm^2) deposited on a 9.08 MHz AT-cut quartz crystal. v = 100 mV s^{-1}. (A') and (B') Mass change (Δm) versus the number of scan n.

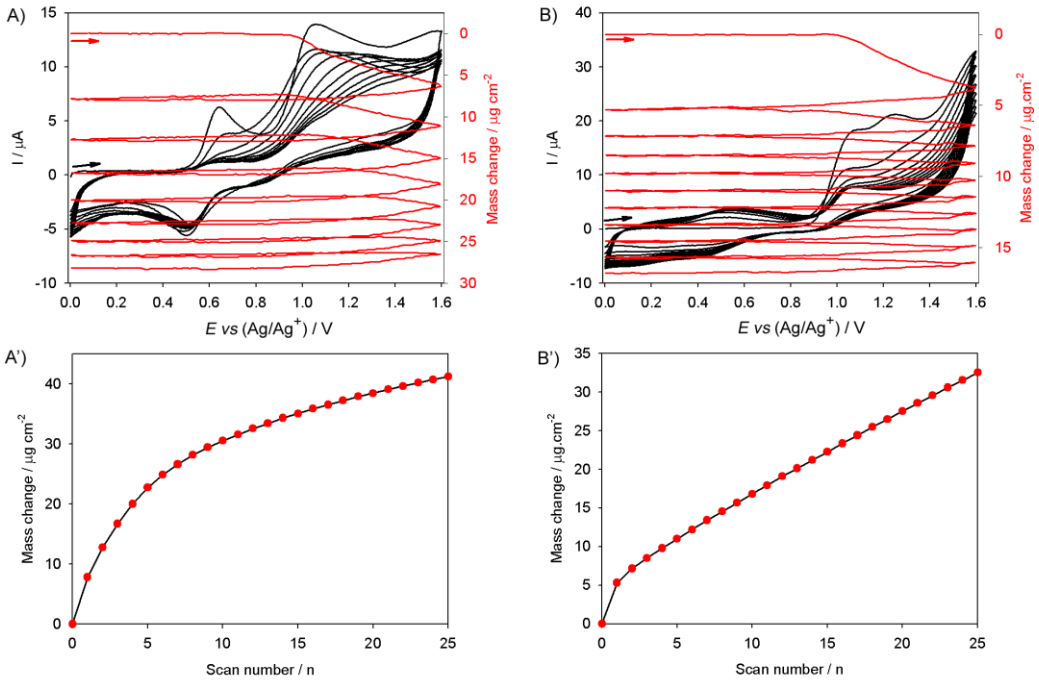

Fig. 3.8 Consecutive CVs (first 10 scans) and EQCM measurements for the first 10 scans during the electropolymerization of 0.25 mmol L^{-1} (A) **ZnOEP** or (B) **H_2T_2P** with 0.25 mmol L^{-1} **Py-$P_2W_{17}Si_2$-Py** in CH_3CN/1,2-$C_2H_4Cl_2$ (3/7) in the presence of 0.1 mol L^{-1} $TBAPF_6$. Working electrode: ITO (A = 0.2 cm^2) deposited on a 9.08 MHz AT-cut quartz crystal. v = 100 mV s^{-1}. (A') and (B') Mass change (Δm) calculated versus the number of scan n.

In the present investigation, the coverage after 25 iterative scans between 0 and +1.60 V was about 15.3, 15.7, 41.2 and 32.5 mg cm^{-2} for **poly-$PW_{11}Si_2$-ZnOEP**, **poly-$PW_{11}Si_2$-H_2T_2P**, **poly-$P_2W_{17}Si_2$-ZnOEP** and **poly-$P_2W_{17}Si_2$-H_2T_2P** copolymers, respectively. The **poly-$P_2W_{17}Si_2$-ZnOEP** and **poly-$P_2W_{11}Si_2$-ZnOEP** copolymers obtained the highest coverage probably due to the molecular mass of **Py-$P_2W_{17}Si_2$-Py** subunit (6046 g mol^{-1}) which possess higher formula weight than **Py-$PW_{11}Si_2$-Py** subunit (3833 g mol^{-1}).

2.4. Cyclic voltammetric investigations of the films

The electrochemical behaviors of the four films have been studied by cyclic voltammetry (Fig. 3.9). For **poly-$PW_{11}Si_2$-ZnOEP** and **poly-$PW_{11}Si_2$-H_2T_2P**, two well-defined reduction peaks (named as peak a, and peak c in Fig. 3.9A and Fig. 3.9B) were assumed to the reduction of W^{VI} to W^{V} on the basis of peak potential of the **Py-$PW_{11}Si_2$-Py**. Peak b corresponds to the irreversible pyridinium reductions, deduced from the CVs of electropolymerization (Fig. 3.4), in which from the second scan, an additional reduction peak appeared between the first reduction and second reduction of W^{VI} to W^{V}. Because **H_2T_2P** was easier to be reduced (first and second ring reduction at -1.20 V and -1.66 V *vs.* SCE for the porphyrin monomer) than **ZnOEP** (first ring reduction at -1.66 V *vs.* SCE), **poly-$PW_{11}Si_2$-H_2T_2P** presented also two peaks corresponding to the first and second reduction of the **H_2T_2P** subunits (peaks d and e, Fig. 3.9B), whereas in the case of **poly-$PW_{11}Si_2$-ZnOEP** only the first reduction of the **ZnOEP** subunit was detectable (peak d, Fig. 3.9A). These peaks might corresponded to the reduction of the macrocycle, however, the last reduction process might also be the overlap of the signal of reduction of the porphyrin and the reduction of the W^{VI} to W^{V} of the hybrid polyanion **$PW_{11}Si_2$** (see Table 1) which might explained that the current peak were higher.

In the case of the use of **Py-$P_2W_{17}Si_2$-Py** as Py-POM-Py, because the reductions of W^{VI} to W^{V} were harder to be measured and present ill-defined waves on ITO, we assumed the peaks a and b corresponded to the pyridinium reduction indicating the presence of the “zig-zag” copolymer and the substitution in *meso* positions 5,10 or 5,15. Moreover, the peak c could be attributed to the reduction of porphyrin macrocycle (Fig. 3.9C, and Fig. 3.9D).

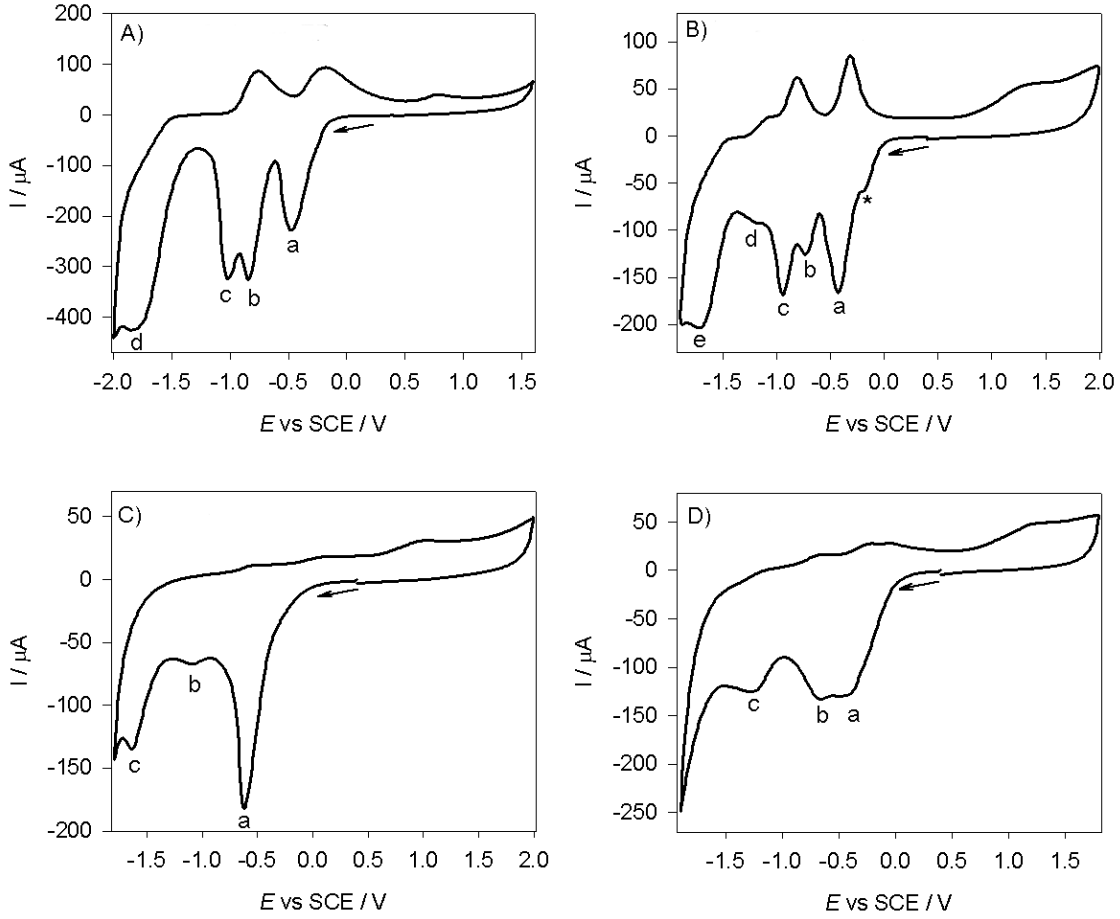

Fig. 3.9 Cyclic voltammograms of A) **poly-$PW_{11}Si_2$-ZnOEP**, B) **poly-$PW_{11}Si_2$-H_2T_2P**, C) **poly-$P_2W_{17}Si_2$-ZnOEP** and D) **poly-$P_2W_{17}Si_2$-H_2T_2P** (obtained after 25 scans, between 0.00 V and +1.60 V) in CH_3CN/1,2-$C_2H_4Cl_2$ (3/7) with 0.1 mol L^{-1} $TBAPF_6$. (←) Start of the scan. S =1 cm^2; scan rate: 0.1 V s^{-1}.

Table 1. Electrochemical data for **ZnOEP**, **H_2T_2P**, **Py-$PW_{11}Si_2$-Py**, **Py-$P_2W_{17}Si_2$-Py**, **poly-$PW_{11}Si_2$-ZnOEP**, **poly-$PW_{11}Si_2$-H_2T_2P**, **poly-$P_2W_{17}Si_2$-ZnOEP** and **poly-$P_2W_{17}Si_2$-H_2T_2P**.

Compounds	**Ring oxidation**		**Reduction of py^+ and of W^{VI}**		**Ring reduction**	
ZnOEP [a]	1.08 (130)	0.71 (128)			-1.66	
H_2T_2P [a]	1.27	1.01			-1.20 (170)	-1.66 (320)
$PW_{11}Si_2$ [a,GC]			-0.34 (75) -1.50 (84)	-0.87 (59)		
$PW_{11}Si_2$ [a,ITO]			-0.34 (91) -1.65 (445)	-0.88 (110)		
$P_2W_{17}Si_2$ [a, GC]			-0.57 (78) -1.45 (72)	-0.94 (78) -1.73 (105)		
$P_2W_{17}Si_2$ [a, ITO]			-0.49 (286) -1.42 (25)	-0.90 (40) -1.76 (190)		
poly-$PW_{11}Si_2$-ZnOEP [b]	1.24 [irr]		-0.38 (130) -0.91 (138)	-0.81[irr]	-1.81[irr]	
poly-$PW_{11}Si_2$-H_2T_2P [b]	1.63 [irr]		-0.37 (60) -0.89 (50)	-0.75[irr]	-1.17 (133)	-1.70[irr]
poly-$P_2W_{17}Si_2$-ZnOEP [b]	1.26 [irr]		-0.60 [irr]	-1.04 [irr]	-1.61[irr]	
poly-$P_2W_{17}Si_2$-H_2T_2P [b]	1.66 [irr]		-0.37 [irr]	-0.68 [irr]	-1.26 [irr]	

[a] Potentials in V *vs.* SCE were obtained from cyclic voltammetry in 1,2-$C_2H_4Cl_2$ with 0.1 mol $L^{-1}TBAPF_6$. Scan rate = 100 mV s^{-1}. Working electrode: ITO, S=1 cm^2.

[b] Potentials in V *vs.* SCE were obtained from cyclic voltammetry in in CH_3CN/1,2-$C_2H_4Cl_2$ (3/7) with 0.1 mol $L^{-1}TBAPF_6$. Scan rate = 100 mV s^{-1}. Working electrode: ITO, S=1 cm^2. The given half-wave potentials are equal to $E_{1/2} = (E_{pa} + E_{pc})/2$. Under bracket: $\Delta E_p = |E_{pa} - E_{pc}|$.

2.5. UV-vis spectroscopy

The UV–visible absorption spectra of the porphyrin monomers (**H_2T_2P** and **ZnOEP**, black line) in solution and the **poly-$PW_{11}Si_2$-H_2T_2P** and the **poly-$P_2W_{17}Si_2$-ZnOEP** copolymer films deposited on ITO are shown for comparison in Fig. 3.10A and Fig. 3.10B. This superimposition reveals that both of the Soret band of **poly-$PW_{11}Si_2$-H_2T_2P** and of **poly-$P_2W_{17}Si_2$-ZnOEP** copolymers, attributed to the main porphyrin-based π–π^* electronic transition, are broader and red-shifted in copolymers (onto ITO electrode) than in monomers (Table 2). This evolution can be explained by the exciton coupling theory concerning intra- or intermolecular excitonic interactions between the porphyrin subunits, together with a greater deformation of the macrocycles within the polymer. After electropolymerization, the films were found to be fully soluble in DMF. Analysis of the resulting solutions by UV–vis absorption spectroscopy revealed a sharper Soret band and a little hypochromatic shift than that recorded on the solid film (Fig. 3.10). This evolution suggested that for the most part intramolecular interactions remain when the copolymers were in solution. UV-visible absorption spectra of the mother solution, containing **ZnOEP** and Py-POM-Py (**Py-$PW_{11}Si_2$-Py** or **Py-$P_2W_{17}Si_2$-Py**), after the deposition of several film clearly shows no demetallation of the starting ZnOEP and no demetallation of the ZnOEP units of the films.

Fig. 3.11A revealed a spectum for **poly-$P_2W_{17}Si_2$-ZnOEP** with different iterative scans. Plotting the absorbance of the Soret band recorded for the four prepared films as a function of the number of iterative scans (Fig. 3.11B) showed a similar curves featuring an increase reaching a plateau after nearly 25 scans. The films using **ZnOEP** as porphyrin subunit gave a higher absorbance intensity than hybrids used **H_2T_2P** after 25 iterative scans between 0 and +1.60 V *vs.* SCE.

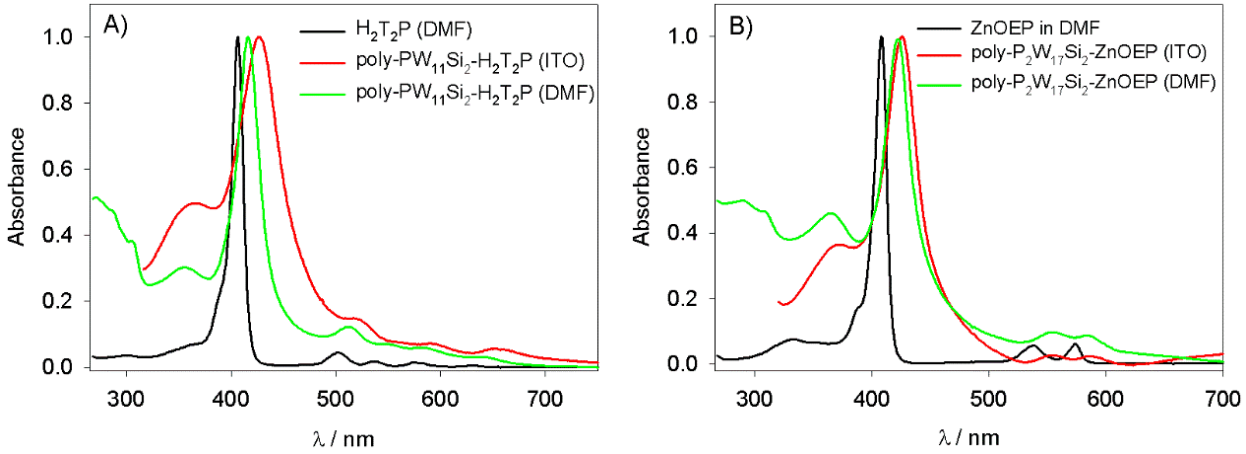

Fig. 3.10 A) Normalized UV-vis spectra of **H_2T_2P** in DMF (black), **poly-$PW_{11}Si_2$- H_2T_2P** on ITO (red), **poly-$P_2W_{17}Si_2$-H_2T_2P** in DMF (green). B) Normalized UV-vis spectra of **ZnOEP** in DMF (black), **poly-$PW_{11}Si_2$-ZnOEP** on ITO (red), **poly-$P_2W_{17}Si_2$-ZnOEP** in DMF (green).

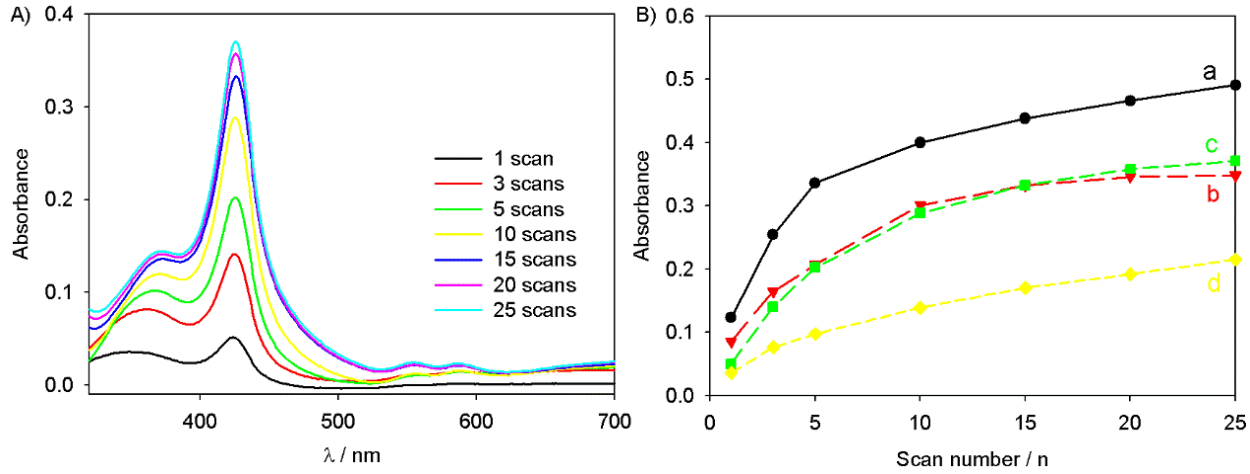

Fig. 3.11 UV–vis spectra of A) **poly-$P_2W_{17}Si_2$-ZnOEP** obtained after n iterative scans (n = 1, 3, 5, 10, 15, 20 and 25) on ITO. B) Plot of the intensity of the absorbance of the Soret band *versus* the iterative scan number between 0 and +1.60 V versus SCE. Line a: **poly-$PW_{11}Si_2$-ZnOEP**, line b: **poly-$PW_{11}Si_2$-H_2T_2P**, line c: **poly-$P_2W_{17}Si_2$-ZnOEP** and line d: **poly-$P_2W_{17}Si_2$-H_2T_2P**.

Table 2 UV–visible spectral data for **ZnOEP** and **H_2T_2P** in DMF, **Py-$PW_{11}Si_2$-Py** and **Py-$P_2W_{17}Si_2$-Py** in CH_3CN, **poly-$PW_{11}Si_2$-ZnOEP**, **poly-$PW_{11}Si_2$-H_2T_2P**, **poly-$P_2W_{17}Si_2$-ZnOEP** and **poly-$P_2W_{17}Si_2$-H_2T_2P** on ITO or in DMF. Under brackets: molar extinction coefficient (ε /10^3 dm^3 mol^{-1} cm^{-1}).

Compound	Soret band /nm	Q bands / nm	POM band / nm
ZnOEP	408 (672.3)	538 (34.3), 674 (37.7)	
H_2T_2P	407 (402.3)	502 (16.6), 537 (5.8), 577 (4.6), 631 (1.4)	
Py-$PW_{11}Si_2$-Py			268 (57.9), 335 (63.0)
Py-$P_2W_{17}Si_2$-Py			288 (142.4), 305 (135.2)
poly-$PW_{11}Si_2$-ZnOEP (ITO)	426	552, 586	
poly-$PW_{11}Si_2$-ZnOEP (DMF)	424	551, 582	271, 286, 306
poly-$PW_{11}Si_2$-H_2T_2P (ITO)	425	521, 559, 591, 658	
poly-$PW_{11}Si_2$-H_2T_2P (DMF)	421	509, 549, 586, 643	271, 285, 305
poly-$P_2W_{17}Si_2$-ZnOEP (ITO)	426	555, 589	
poly-$P_2W_{17}Si_2$-ZnOEP (DMF)	422	554, 586	290, 308
poly-$P_2W_{17}Si_2$-H_2T_2P (ITO)	425	517, 557, 594, 654	
poly-$P_2W_{17}Si_2$-H_2T_2P (DMF)	422	515, 555, 590, 652	291, 307

2.6. X-ray photoelectron spectroscopy

Although the XPS measurement gives only a semi quantitative elemental analysis, the C, N, O, P, W, Si, Zn and F elements enable to confirm the presence of **poly-$PW_{11}Si_2$-ZnOEP** (Fig. 3.12). In the case of the **poly-$PW_{11}Si_2$-ZnOEP** copolymer, the Zn 2p3/2 (1023.2 eV) is assigned to the zinc in **ZnOEP**. Three types of nitrogen (N 1s) with different chemical states are observed, which appear at 398.6 eV, 400.0 eV and 402.3 eV (corresponding to the pyridinium spacer, the nitrogen of the porphyrin and may be also to the TBA countercation). However, because Dawson-type POMs subunit bear two times negative charges than Keggin-type POMs subunit and need two times counter cations (TBA), so the N1s of **poly-$P_2W_{17}Si_2$-ZnOEP** (Fig.S.3.6) and **poly-$P_2W_{17}Si_2$-H_2T_2P** (Fig.S.3.7) hybrids were dominated by the ammonium peak on 402.4 eV and even overlap other peaks. W 4f7 (36.1 eV for W 4f7/2 and 38.2 eV for W 4f5/2) peaks and the spectrum signal of O 1s (532.0 eV) and P 2p3 (134.3 eV) come from P−O bond in POM.

The F 1s (686.8 eV) is ascribed to counter ion PF_6^-. While O 1s signal (531.1 eV) comes from H_2O on the copolymer surface. However, when we replaced **ZnOEP** by **H_2T_2P**, Zn 2p3/2 signal disappeared (Fig. S3.5 and Fig. S.3.7).

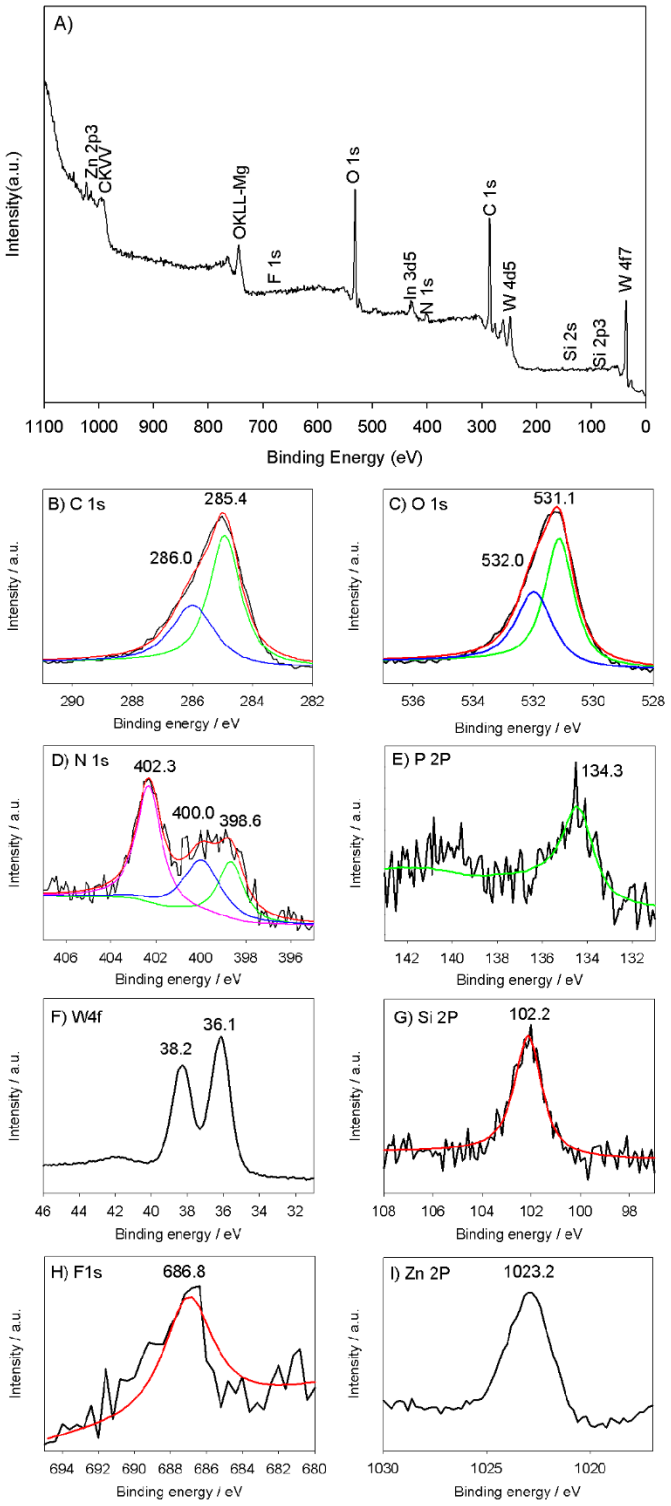

Fig. 3.12 XPS of **poly-$PW_{11}Si_2$-ZnOEP** global XPS spectra (A), C 1s (B), O 1s (C), N 1s (D), P 2p3 (E), W 4f7 (H), Si 2p3 (G), F 1s (H), Zn 2p3 (I).

2.7 Film morphology (Atomic Force Microscopy)

The coated electrodes were washed with CH_2Cl_2 to remove any residual of the conducting salt present on the film. In a typical image, **poly-$PW_{11}Si_2$-ZnOEP** and **poly-$PW_{11}Si_2$-H_2T_2P** appeared as tightly packed coils with average diameters of 45 ± 5 nm and 55 ± 5 nm and a height of 2.9 ± 0.2 nm and 3.8 ± 0.2 nm (Fig. 3.13), respectively. The root mean square (RMS) surface roughness of the film obtained after 25 iterative scans from 0 to +1.60 V*versus* SCE was 1.9 and 2.3 nm in an area of 1 μm^2 for **poly-$P_2W_{11}Si_2$-ZnOEP** and **poly-$P_2W_{11}Si_2$-H_2T_2P**, respectively. When using **Py-$P_2W_{17}Si_2$-Py** as Py-POM-Py unit instead of **Py-$PW_{11}Si_2$-Py**, the size of the tightly packed coils was bigger. The average diameters were 60 ± 5 nm and 75 ± 5 nm, and the height were 11.2 ± 0.3 nm and 7.9 ± 0.3 nm for **poly-$P_2W_{17}Si_2$-ZnOEP** and **poly-$P_2W_{17}Si_2$-H_2T_2P** (Fig. 3.14), respectively.

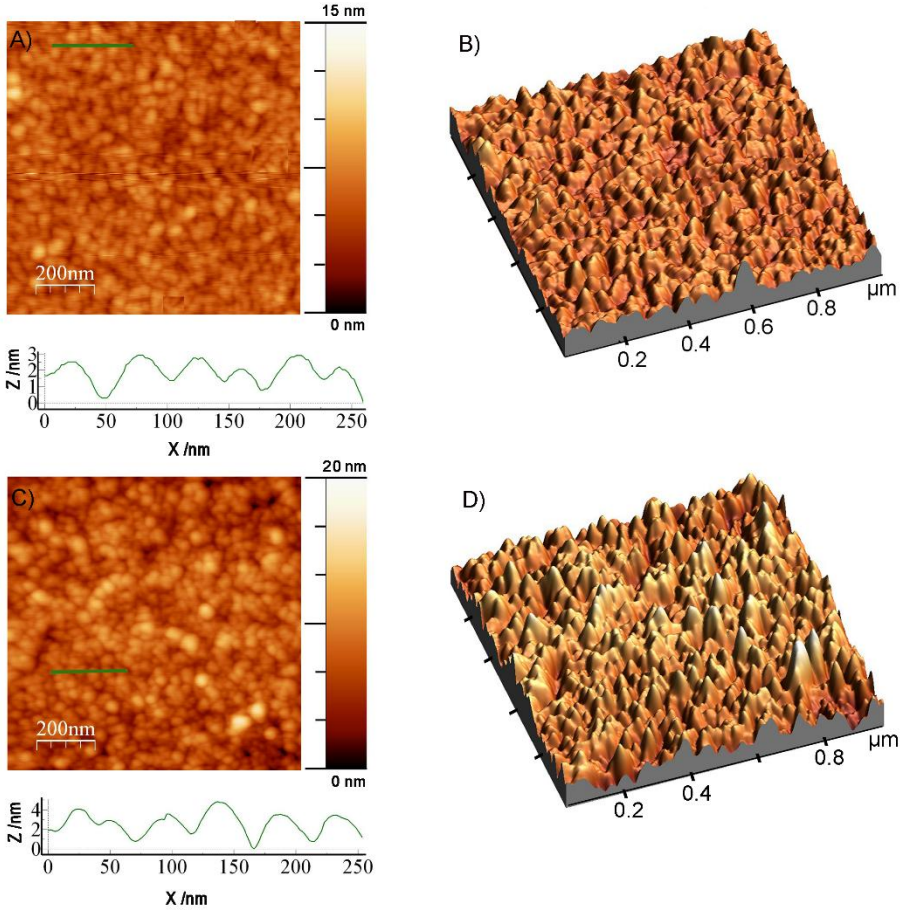

Fig. 3.13 Tapping mode AFM topography of A) and B) **poly-$PW_{11}Si_2$-ZnOEP**, and C) and D) **poly-$PW_{11}Si_2$-H_2T_2P** films and section analysis of the aggregate marked by a green line.

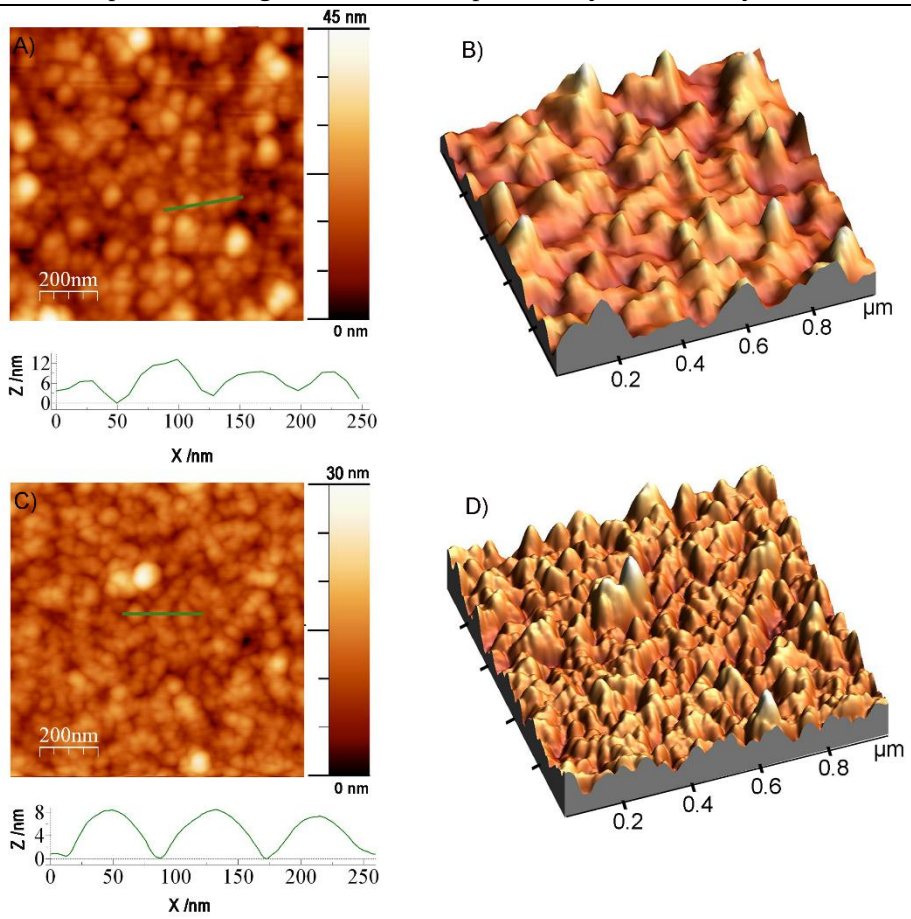

Fig. 3.14 Tapping mode AFM topography of A) and B) **poly-$P_2W_{17}Si_2$-ZnOEP**, and C) and D) **poly-$P_2W_{17}Si_2$-H_2T_2P** films obtained after deposition from 0 to +1.60 V *versus* SCE and section analysis of the aggregate marked by a green line.

To measure the thickness of the coated film on ITO, we have removed the copolymer by scratching the film with a metallic tip. We observed some puffiness induced by the removal of the material. Analysis of the bottom proved that the ITO substrate had been touched. The thickness was the height difference on each side, far from the puffiness. The estimated thickness increased with increasing number of scans, following the nearly same trend as the UV/Vis absorbance intensity (Fig. 3.15).

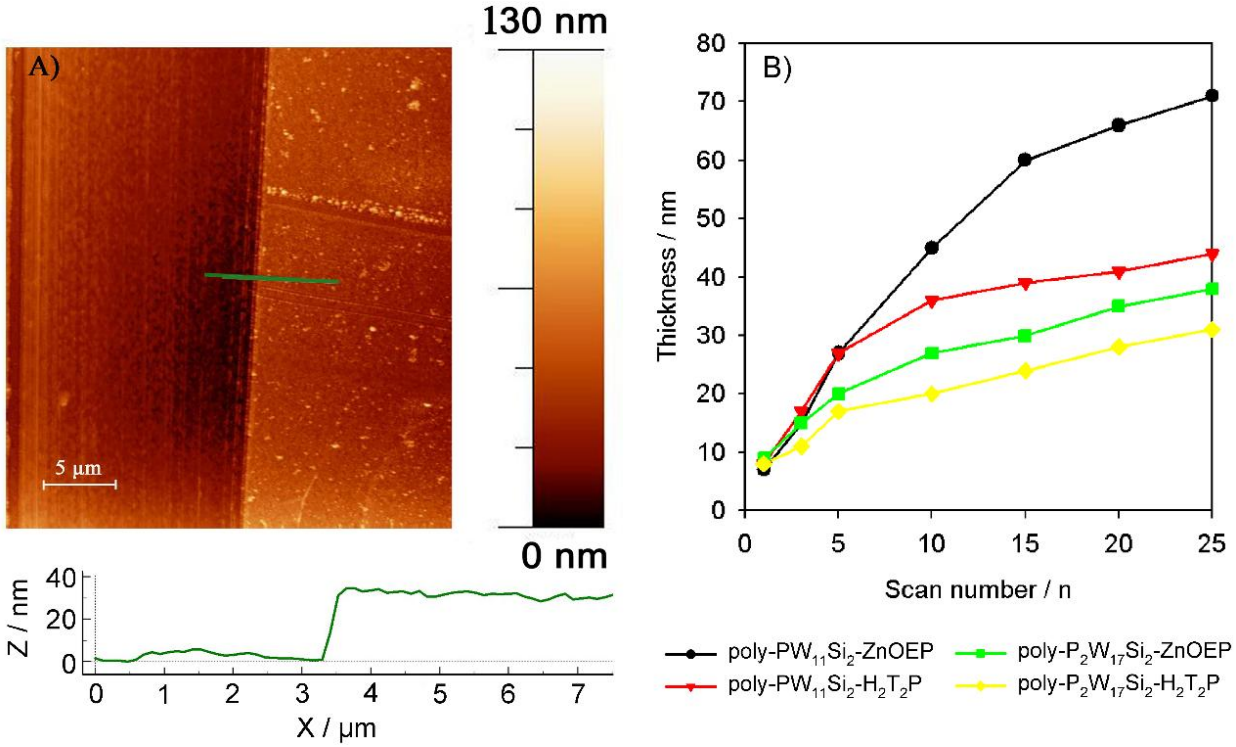

Fig. 3.15 A) AFM image of the ITO electrode modified with **poly-$P_2W_{11}Si_2$-ZnOEP** obtained after 25 iterative scans from 0 to +1.60 V *versus* SCE. Bottom: section analysis. B) Thickness measured by AFM versus different numbers of iterative scans.

Table 3 Thickness, Δm (measured from AFM and EQCM respectively) and surface coverage Γ calculated versus the number of iterative scan n.

poly-$PW_{11}Si_2$-ZnOEP

Number of iterative scan n	Thickness (nm)	Δm (µg/cm^2)	Γ (10^{-9} mol cm^{-2})
1	7	4.29	0.94
3	15	7.01	1.54
5	27	8.72	1.92
10	45	11.61	2.55
15	60	13.26	2.92
20	66	14.43	3.17
25	71	15.34	3.37

poly-$PW_{11}Si_2$-H_2T_2P

Number of iterative scan n	Thickness (nm)	Δm ($\mu g/cm^2$)	Γ (10^{-9} mol cm^{-2})
1	8	4.43	0.99
3	17	7.22	1.63
5	27	9.07	2.04
10	36	11.93	2.69
15	39	13.63	3.07
20	41	14.85	3.36
25	44	15.66	3.53

poly-$P_2W_{17}Si_2$-ZnOEP

Number of iterative scan n	Thickness (nm)	Δm ($\mu g/cm^2$)	Γ (10^{-9} mol cm^{-2})
1	9	7.80	1.15
3	15	16.70	2.47
5	20	22.75	3.36
10	27	30.55	4.52
15	30	35.05	5.18
20	35	38.44	5.69
25	38	41.19	6.09

poly-$P_2W_{17}Si_2$-H_2T_2P

Number of iterative scan n	Thickness (nm)	Δm ($\mu g/cm^2$)	Γ (10^{-9} mol cm^{-2})
1	8	5.30	0.80
3	11	8.50	1.28
5	17	10.99	1.65
10	20	16.81	2.53
15	24	22.26	3.35
20	28	27.53	4.14
25	31	32.53	4.89

3. Photocurrent generation

3.1. Effect of the film thickness

First of all, we have optimized the film thickness for the photocurrent response of the hybrid films deposited on ITO electrodes. Fig. 3.16 shows amperometric J–t curves for the photocurrent response for **poly-$P_2W_{17}Si_2$-ZnOEP** films obtained with increasing scan numbers during the electropolymerization step. The supported films were immerged in aqueous solutions and left under visible light ($\lambda > 385$ nm; the POM subunits do not have absorption in this domain). The photocurrent was measured in the presence of NaI_3 (5 mmol L^{-1})/NaI (0.1 molL^{-1}) as reversible redox mediator. The bias potential was set at 0.00 V and the device was exposed under visible light for 1 min followed by the dark for 1 min. The photocurrent response depends on the number of deposition scans used for preparation of the film. The magnitude of the photocurrent increased appreciably from n=1 to n=3, and then as deposition scans increas the photocurrent magnitude decrease. This follows the same trend of the charge transfer resistance (R_{ct}) (diameter of the Nyquist plot on X axial)[25,26] of the films in the same measurement conditions. It suggests that the photocurrent efficiency is dependent on charge transfer resistance on the film to some extent, whereby the best performance for **poly-$P_2W_{17}Si_2$-ZnOEP** film is obtained by only three iterative scans between 0.00 and 1.60 V *versus* SCE. Under irradiation the R_{ct} is lower than the value measured in the dark. For instance, an important decrease of the R_{ct} in the case of the film prepared with 3 iterative scans is observed: R_{ct} (light off) = 444.2 ohms *versus* R_{ct}(light on) = 256.8 ohms. Fig. 3.17B shows CVs of **poly-$P_2W_{17}Si_2$-ZnOEP** (prepared with n = 3 scans between 0.00 V and +1.60 V *versus* SCE) in the same measuring environment. Under irradiation the current magnitude increase a little and the difference between light on and light off corresponds to the photocurrent. Thus, I_3^- was a little bit easier to be reduced under visible illumination (Fig. 3.17B).

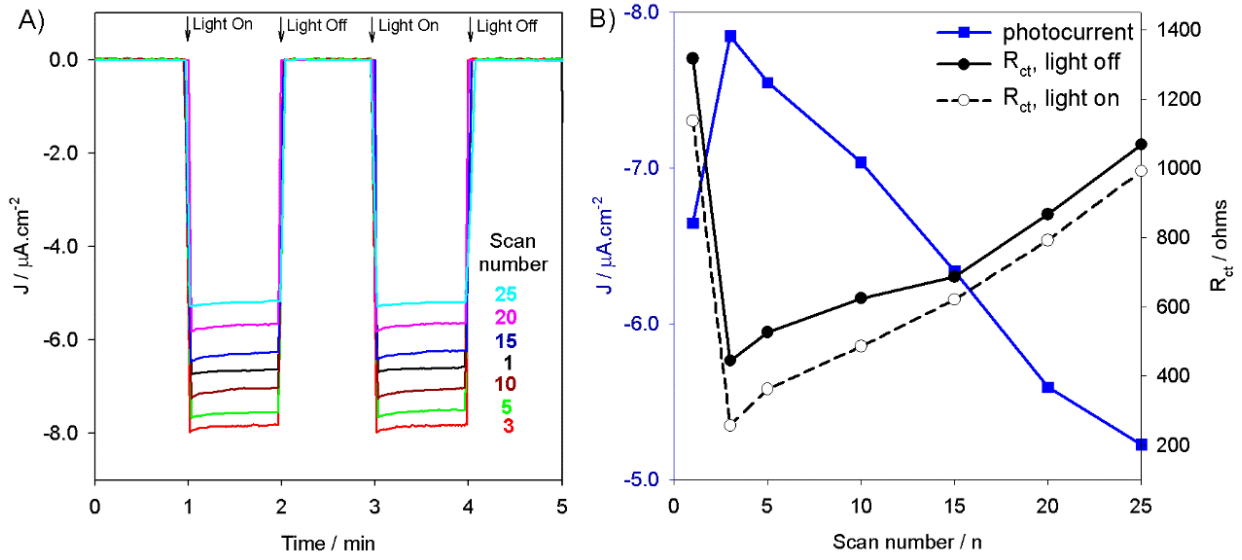

Fig. 3.16 A) Photoelectrochemical response of **poly-$P_2W_{17}Si_2$-ZnOEP** with different numbers of iterative scans used for the preparation of the film (between 0.00 V and +1.60 V *versus* SCE). Only one side is recovered by ITO with on-off light illumination from 300 W Xe Arc lamp (with $\lambda \geq 385$ nm long pass filter). BIAS potential: 0.00 V. B) (■) plots of the photocurrent, and plots of R_{ct} without illumination (●), and with illumination (○) in aqueous solution containing I_3^- 5 mmol L^{-1} and I^- 0.5 mol L^{-1} versus the numbers of iterative scans.

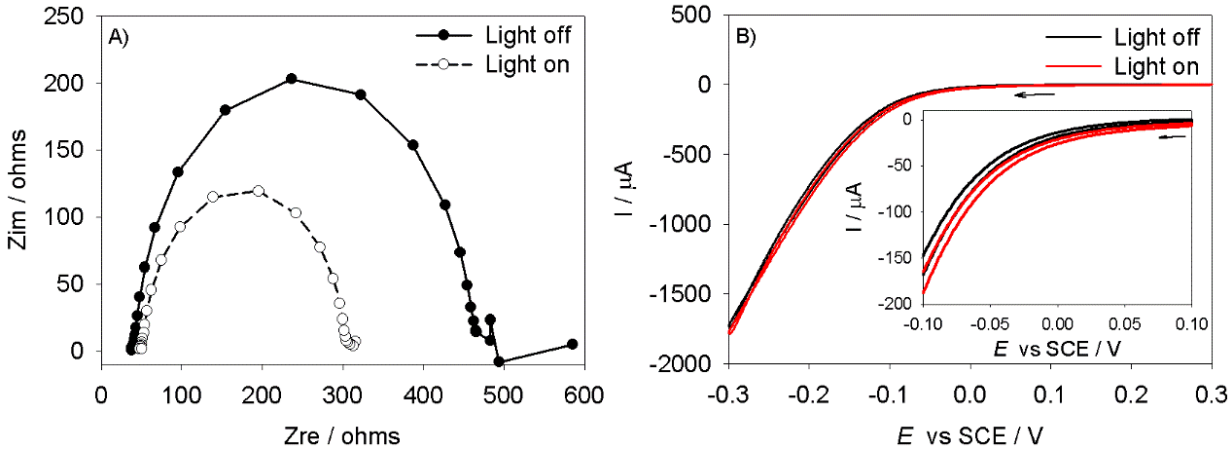

Fig. 3.17 A) Nyquist plot and B) CVs of **poly-$P_2W_{17}Si_2$-ZnOEP** (prepared with n = 3 scans between 0.00 V and +1.60 V *versus* SCE) without and with illumination from 300 W Xe Arc lamp (with $\lambda \geq 385$ nm long pass filter) in H_2O containing I_3^- 5 mmol L^{-1} and I^- 0.5 mol L^{-1}, DC potential 0.0 V for impedance measurement.

3.2 Effect of the type of polyoxometalates and of porphyrins

Proust and Amouri reported POM photosensitization choosing silyl-derivatized Keggin- and Wells-Dawson-type POMs. Their studies revealed that limited communication between subunits in the ground state and the variation in the electron acceptor character of the POMs depending on the structual class

and the chemical anchor.

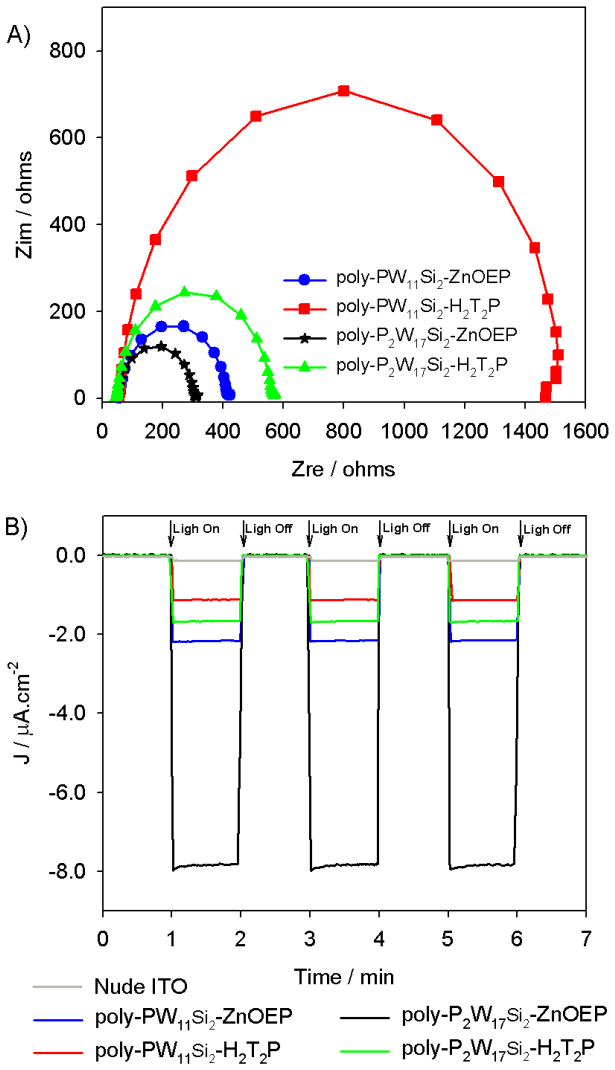

Fig. 3.18 A) Nyquist plot and B) photoelectrochemical response of **poly-PW_{11}-ZnOEP** (obtained after n = 5 iterative scans), **poly-PW_{11}-H_2T_2P** (5 scans), **poly-P_2W_{17}-ZnOEP** (3 scans) and **poly-P_2W_{17}-H_2T_2P** (3 scans). Preparation of the film between 0.00 V and +1.60 V *versus* SCE) under irradiation from 300 W Xe Arc lamp (with $\lambda \geq 385$ nm long pass filter) in H_2O containing I_3^- 5 mmol L^{-1} and I^- 0.5 mol L^{-1}, BIAS potential: 0.00 V.

By comparison, Proust reported that the Ir-cyclometalated silyl-Dawson hybrid was the most promising candidate in photoelectron transfer which provided an acceptable compromise between the rate of charge separation and charge recombination ($k_{CS} = 1.92 \times 10^9\ s^{-1}$ and $k_{CR} = 3.71 \times 10^7\ s^{-1}$, respectively).[7] In this present work, Nyquist plot of the four prepared films in H_2O containing I_3^- 5 mmol L^{-1} and I^- 0.5 mol L^{-1} under visible irradiation have been measured. The charge transfer resistance (R_{ct}) of **poly-$P_2W_{17}Si_2$-ZnOEP** (obtained after 3 iterative scans) is the lowest (Fig. 3.18A) in the four copolymers. It corresponds also to the highest photocurrent respond in the magnitude (Fig. 3.18B). We observed a

direct relationship between the R_{ct} and the photocurrent magnitude, the more the R_{ct} is lower, higher is the intensity of the photcurrent.

3.3 Different BIAS potential

To study the effect of the polarity on photocurrent responds, different BIAS potentials are used for the four films as shown in Fig. 3.19. It can be seen that the electron transfer direction for **poly-$PW_{11}Si_2$-ZnOEP** and **poly-$PW_{11}Si_2$-H_2T_2P** (obtained both with 5 iterative scans) depended on the bias potential. When applied negative and zero bias voltages, the photocurrents for **poly-$PW_{11}Si_2$-ZnOEP** and **poly-$PW_{11}Si_2$-H_2T_2P** films were cathodic, i.e the electrons flow from ITO electrode through the copolymeric films to the electrolyte solution. In contrast, when the bias voltages switched to positive potential, the photocurrents became anodic. Futhermore, in the case of **poly-$P_2W_{17}Si_2$-ZnOEP** and of **poly-$P_2W_{17}Si_2$-H_2T_2P** films for BIAS potentials between -0.3 V to +0.2 V, the electron transfer were always cathodic.

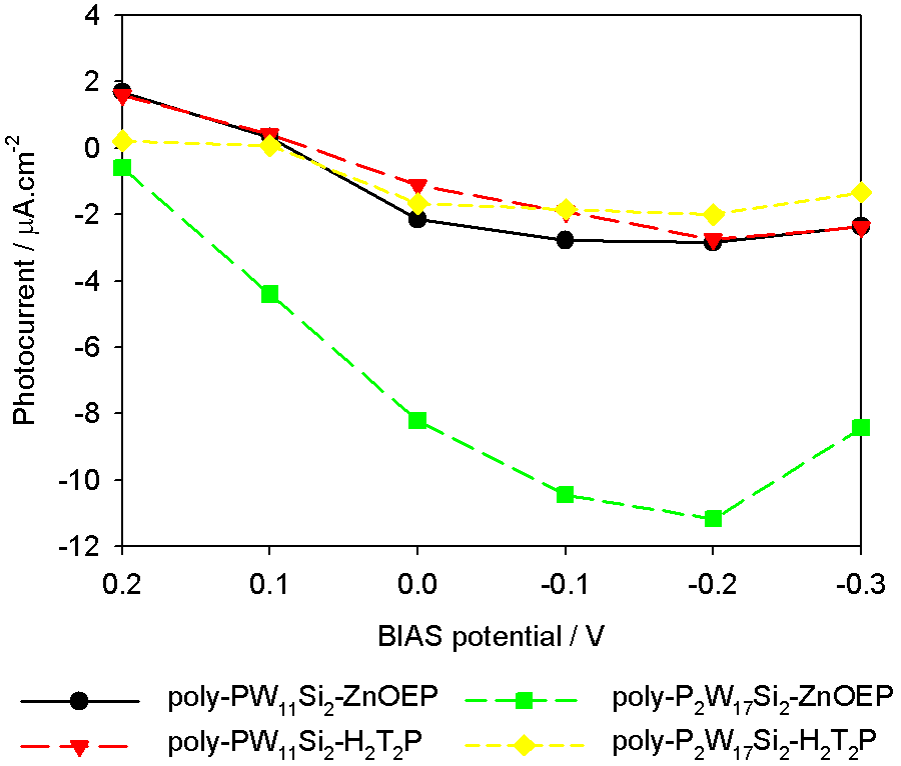

Fig. 3.19 Effects of bias voltage on the photocurrents of **poly-$PW_{11}Si_2$-ZnOEP** (5 scans), **poly-$PW_{11}Si_2$-H_2T_2P** (5 scans), **poly-$P_2W_{17}Si_2$-ZnOEP** (3 scans), and **poly-$P_2W_{17}Si_2$-H_2T_2P** (3 scans) films on ITO electrode under irradiation from 300 W Xe Arc lamp (with $\lambda \geq 385$ nm long pass filter) in H_2O containing I_3^- 5 mmol L^{-1} and I^- 0.5 mol L^{-1}. Preparation of the film between 0.00 V and +1.60 V *versus* SCE.

3.4 Energy diagram of the electron transfer processes

To further investigate the electron transfer mechanism in the system, we have estimated the energies of the relevant electronic states. In the case of copolymer **poly-$P_2W_{17}Si_2$-ZnOEP**, an energy level diagram can be built using the oxidation potential of **ZnOEP** subunit and the reduction potential of W^{VI}/W^{V} of the POM cluster and the reduction potential of pyridinium subunits, together with the optical excitation of **ZnOEP** within the film (Fig. 3.20). It describes the thermodynamics for spectral sensitization of the ITO electrode. The level of the excited porphyrin (–3.77 eV for $P^{+\bullet}/P^{*}$) and the ground state porphyrin (–6.00 eV for $P^{+\bullet}/P$) for the film are taken in reference to the oxidation potential of the porphyrin (+1.50 V *vs.* ENH with a band gap of 2.23 eV at λ = 555 nm; measured from the film). The energy level of the couples W^{VI}POM/W^{V}POM, $Py^{+}/Py^{\bullet}$ and I_3^{-}/I^{-} on the absolute scale are – 4.18 eV (– 0.36 V *vs.* NHE), –3.96 eV (– 0.54 V *vs.* NHE), and –5.13 eV (+0.63 V *vs.* NHE) as represented in Fig. 3.20. Due to it is incapable of detecting the redox potentials of **poly-$P_2W_{17}Si_2$-ZnOEP** using ITO electrode, we have electropolymerized the **poly-$P_2W_{17}Si_2$-ZnOEP** film on the glass carbon substrate, then measured the cyclic voltammogram of the obtained film in the aqueous solution containing NaI as the conducting salt.

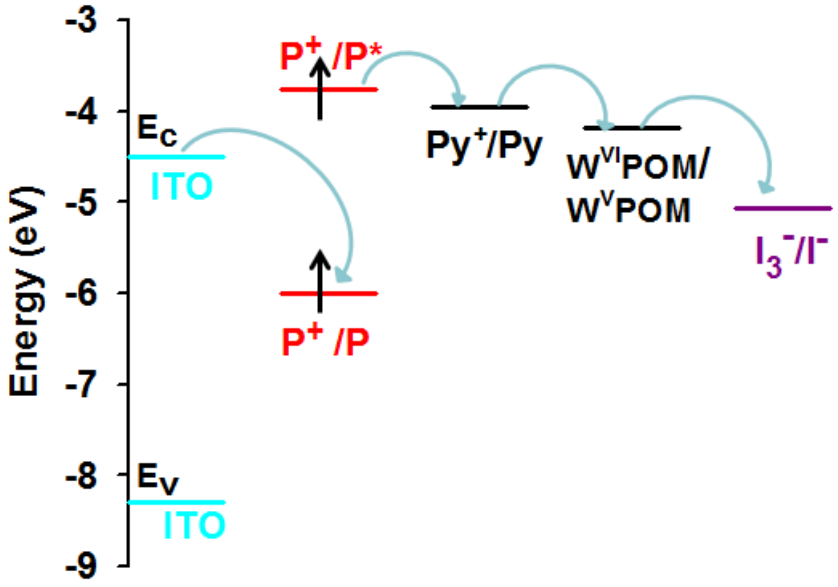

Fig. 3.20 Schematic energy level diagram showing the electron transfer process.

The **$P_2W_{17}Si_2$** subunit acted as a strong electron acceptor and can oxidize the pyridyl radical initially formed from electron transfer from the excited porphyrin to the pyridinium. The reduced POM can then in turn give one electron to reduced I_3^{-}, while I^{-} can be reoxidized at the platinum counter electrode

(Fig. 3.20). The **$P_2W_{17}Si_2$** subunit therefore participated to the electron relay via a downhill electrochemical cascade, which stabilized the separated charges (oxidized porphyrin and reduced POM) and hampered the charge recombination.

4. Photocatalytical recovery of metals

4.1. Photocatalytical recovery of silver

Photocatalysis performed under deaerated conditions with **poly-$PW_{11}Si_2$-ZnOEP**, **poly-$PW_{11}Si_2$-H_2T_2P**, **poly-$P_2W_{17}Si_2$-ZnOEP**, and **poly-$P_2W_{17}Si_2$-H_2T_2P** coated quartz plate placed in aqueous solution of 8.0×10^{-5} mol L^{-1} Ag_2SO_4 and in the presence of 0.13 mol L^{-1} propan-2-ol, respectively. Fig. 3.21 A and B show the change of the UV-vis spectra during the photocatalysis using **poly-$PW_{11}Si_2$-ZnOEP** and **poly-$PW_{11}Si_2$-H_2T_2P**. At the first 150 min, the Soret bands of the porphyrin (**ZnOEP** and **H_2T_2P**) remained nearly unchanged, and the plasmon band of the obtained Ag nanostructure in the whole visible range increased as time go on. If the irradiation continued, the porphyrin undergoes an important degradation, however, the plasmon band keep unchanged with **poly-$PW_{11}Si_2$-ZnOEP** coated quartz and increased slightly with **poly-$PW_{11}Si_2$-H_2T_2P** coated quartz. It demonstrated that the obtained Ag nanostructures were not breakdown, but **poly-$PW_{11}Si_2$-ZnOEP** and **poly-$PW_{11}Si_2$-H_2T_2P** film were unable to be reuse because of the degradation of the film.

As a contrast, during the whole photoreduction process using **poly-$P_2W_{17}Si_2$-ZnOEP** and **poly-$P_2W_{17}Si_2$-H_2T_2P**, the porphyrin remained stable, since the Soret band and Q bands were intact even after prolonged visible irradiation (240 min) (Fig. 3.22). The kinetic performances were also better than that of **poly-$PW_{11}Si_2$-ZnOEP** and **poly-$PW_{11}Si_2$-H_2T_2P**. In the case of **poly-$P_2W_{17}Si_2$-ZnOEP**, after only 15 min of irradiation, the absorbance spectrum remained unchanged illustrating the end of the photoreduction (Fig. 3.22A).

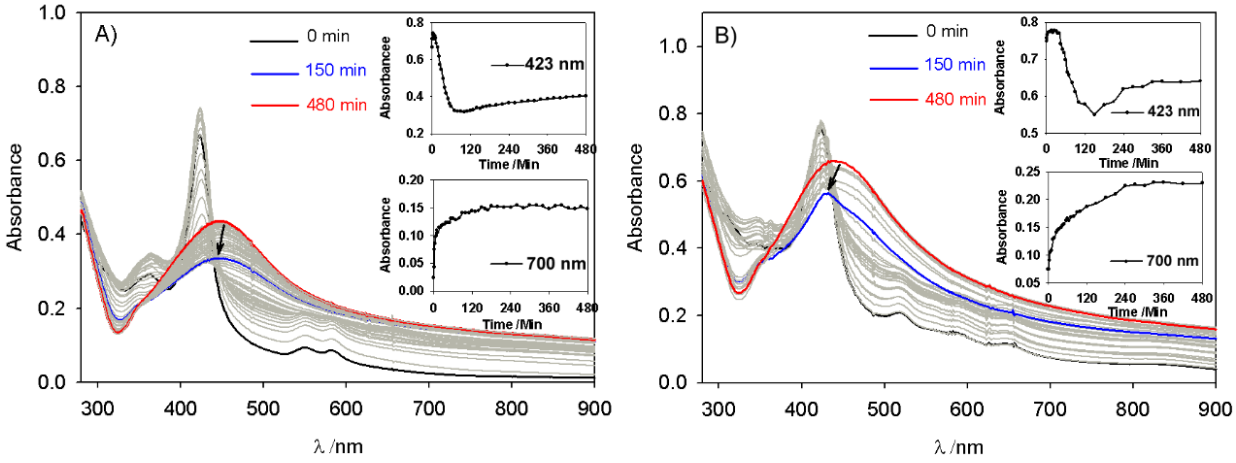

Fig. 3.21 Changes in the UV–vis absorption spectrum of a deaerated aqueous solution of 8.0×10^{-5} mol L^{-1} Ag_2SO_4 and 0.13 mol L^{-1} propan-2-ol containing a slide of quartz modified with A) **poly-$PW_{11}Si_2$-ZnOEP** and B) **poly-$PW_{11}Si_2$-H_2T_2P** film under illumination. Inset: plot of the intensity of the absorbance at λ = 423 nm versus the time of visible irradiation.

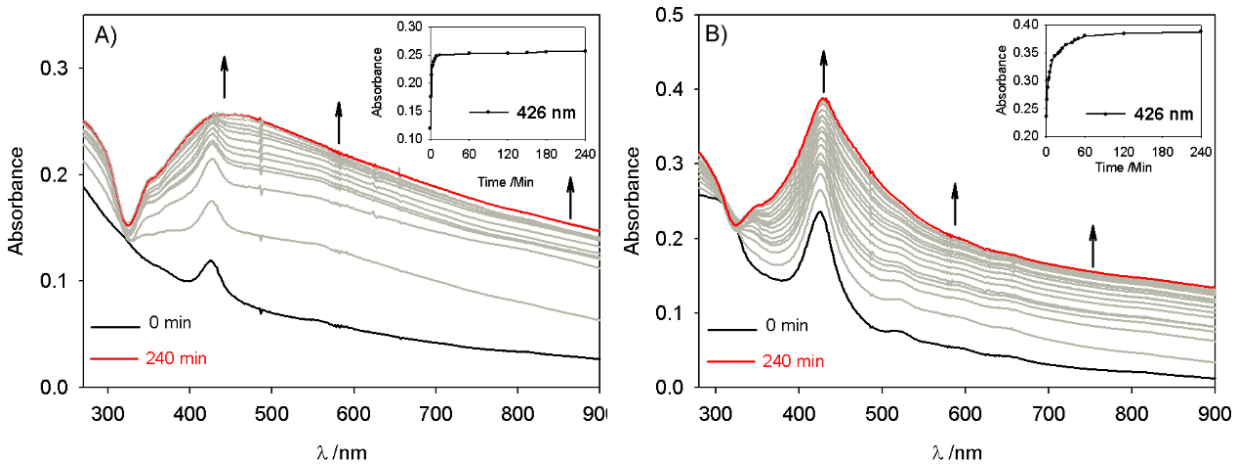

Fig. 3.22 Changes in the UV–vis absorption spectrum of a deaerated aqueous solution of 8.0×10^{-5} mol L^{-1} Ag_2SO_4 and 0.13 mol L^{-1} propan-2-ol containing a slide of quartz modified with A) **poly-$P_2W_{17}Si_2$-ZnOEP** and B) **Poly-$P_2W_{17}Si_2$-H_2T_2P** film under illumination. Inset: plot of the intensity of the absorbance at λ = 426 nm versus the time of irradiation.

After the end of the illumination, we remove the quartz slide covered with the film. The UV–visible spectra of the silver nanoparticles obtained by the four prepared photocatalytic films showed the presence of the large plasmon band in the whole visible domain with a maximum around 430 nm (Fig. 3.23). The broad plasmon band indicated that the formed silver nanostructure were not uniform in size and in shape.

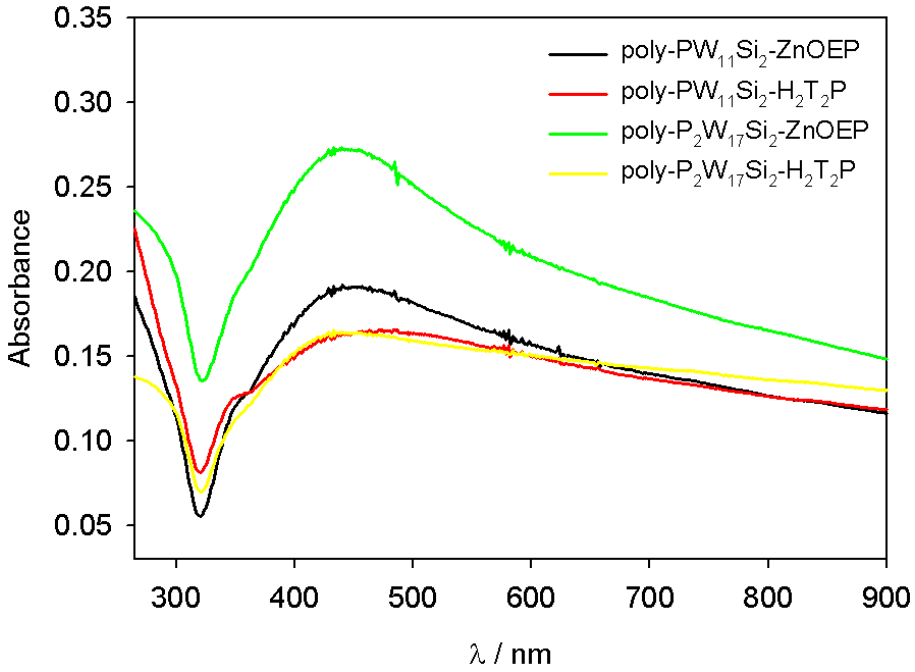

Fig. 3.23 Spectrum of the silver nanoparticles solution after the photocatalysis.

TEM images of the samples after irradiation were shown in Figs. 3.24-3.26. The silver nanostructures obtained using **poly-$PW_{11}Si_2$-ZnOEP** (Fig. 3.24) were mixed in the form and shape including irregular nanosheets in size (200-400 nm), nanoribbons (length of 300-400 nm) surrounded by spherical non symmetric particles (9-15 nm).

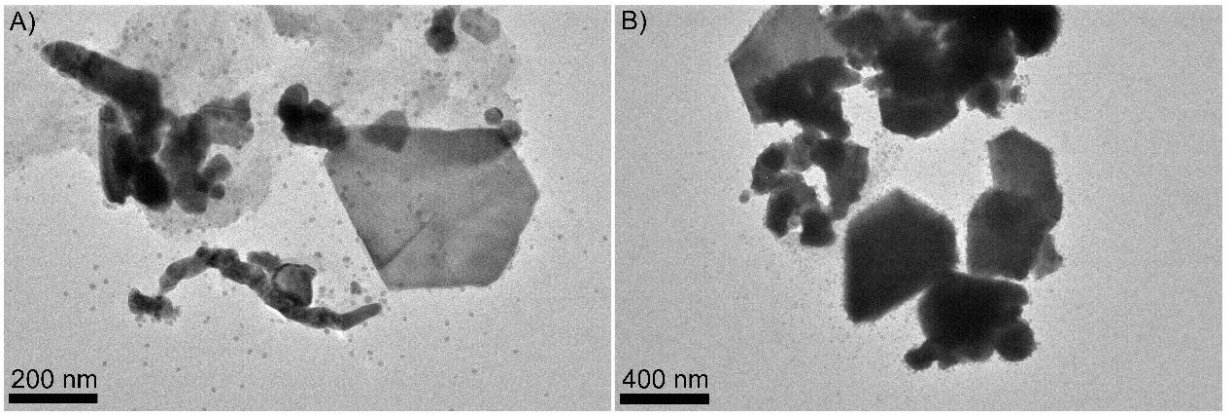

Fig. 3.24 TEM images of silver nanostructure (irregular nanosheets, naonoribbon and spherical form) obtained with **poly-$PW_{11}Si_2$-ZnOEP**.

The TEM images of the silver nanostructure obtained in the case of **poly-$PW_{11}Si_2$-H_2T_2P** (Fig. 3.25) showed the presence of nanoplates like asymmetric dendrite. Formation of these dendrites could be explained by diffusion-limited aggregation DLA model[27] which illustrated it as a diffusion control domination process. Fig. 3.26 presents TEM micrographs of the silver nanostructure obtained by the

use of **poly-$P_2W_{17}Si_2$-ZnOEP** (Fig. 3.26A) and **poly-$P_2W_{17}Si_2$-H_2T_2P** (Fig. 3.26B) which were inhomogeneous in size and shape because the samples presented not only spherical, elongated, or bent particles but also silver nanosheets.

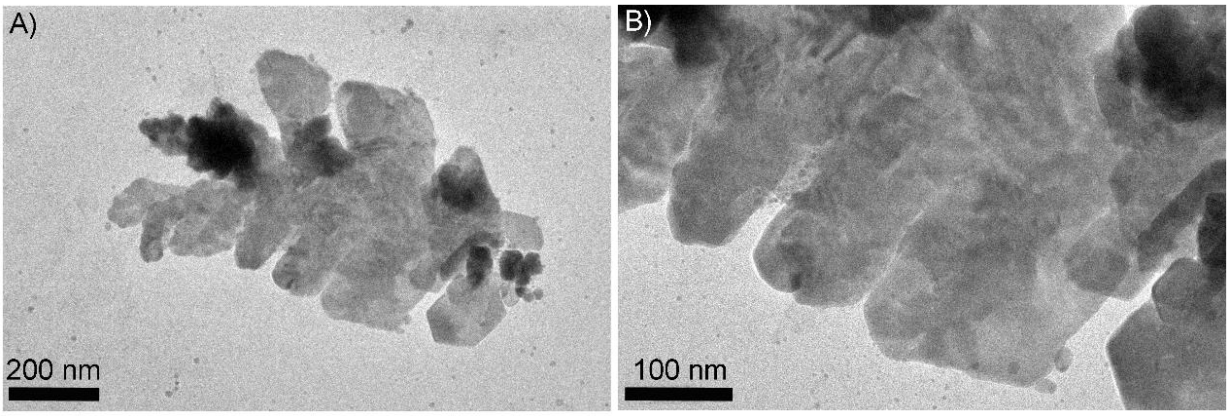

Fig. 3.25 TEM images of silver nanostructure obtained with **poly-$PW_{11}Si_2$-H_2T_2P**.

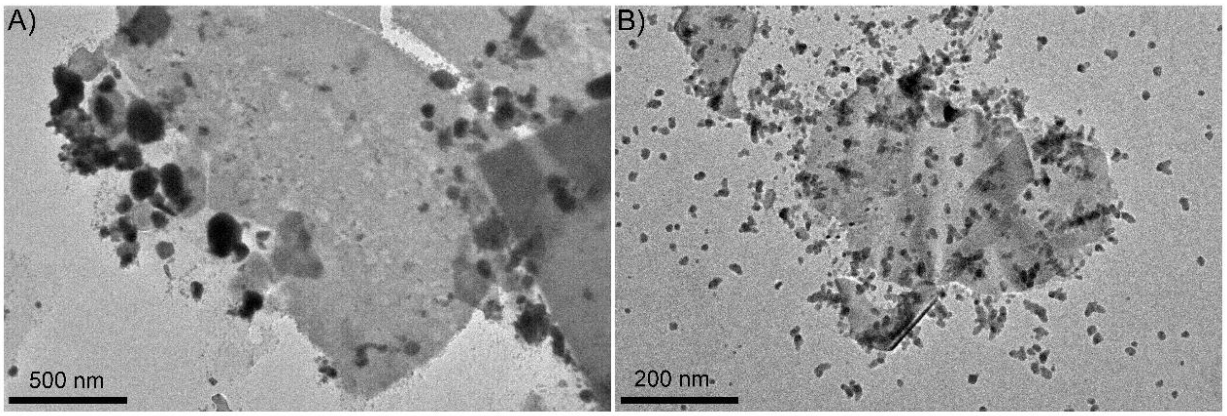

Fig. 3.26 TEM images of silver nanostructure (irregular nanosheets and spherical form) obtained with A) **poly-$P_2W_{17}Si_2$-ZnOEP**, B) **poly-$P_2W_{17}Si_2$-H_2T_2P**.

This photoreduction processes should involve the reduction of the excited porphyrin (Porph*) by propan-2-ol leading to the formation of the reduced porphyrin ($Porph^{\bullet -}$) and the alcohol radical according to the global reaction:

$$Porph^* + (CH_3)_2CHOH \rightarrow Porph^{\bullet -} + (CH_3)_2C^{\bullet}OH + H^+ \qquad (1)$$

This reaction is thermodynamically favourable. Indeed, the reduction potentials of the excited porphyrins are evaluated according to the relation:

$$E(Porph^* / Porph^{\bullet -}) = E(Porph / Porph^{\bullet -}) + E_{S_0 \rightarrow S_1}$$

where $E(Porph/Porph^{\bullet -})$ is the first reduction potential of the porphyrin and $E_{S_0 \rightarrow S_1}$ corresponds to the energy of the lowest electronic transition determined from the absorbance spectrum.

The calculated $E(Porph^*/Porph^{\bullet -})$ values are higher than the reported values for $(CH_3)_2C^{\bullet}OH/(CH_3)_2CHOH$ (E = 0.8 V *vs.* NHE [28])

However, the redox properties of the formed radical species are not favourable to explain the subsequent photoreduction of Ag^+ ions. Indeed, the redox potential of the (Ag^+/Ag^0) couple is too low (E = -1.75 V *vs.* NHE[29]) to permit the direct reduction by the reduced porphyrin or by the alcohol radical ($E((CH_3)_2CO/ (CH_3)_2C^{\bullet}OH)$ = -1.71 V *vs.* NHE[30]). But as in the case of the reduction by the polyoxometalate, referring to radiolytic studies, a complexation step between alcohol radical and silver ions can take place and initiate the formation of silver clusters : [6, 29, 31,]:

$$(CH_3)_2C^{\bullet}OH + Ag^+ \rightarrow Ag(CH_3)_2C^{\bullet}OH^+ \quad (2)$$

$$Ag(CH_3)_2C^{\bullet}OH^+ + Ag^+ \rightarrow Ag_2^+ + (CH_3)_2C{=}O + H^+ \quad (3)$$

$$2Ag_2^+ \rightarrow Ag_4^{2+} \quad (4)$$

$$Ag_m^{x+} + Ag_p^{y+} \rightarrow Ag_{(m+p)}^{(x+y)+} \quad (5)$$

Later, as the redox potential of the silver cluster, $E(Ag^{n+}/Ag_n)$, increases with the nuclearity n, for large enough clusters, their direct reduction by the reduced porphyrin or the alcohol radical become thermodynamically favourable.

Two possible mechanisms can be involved to explain the formation of silver nanoparticles. The first mechanism (Fig. 3.27A) consists in the reduction of the excited complexed porphyrins by propan-2-ol, followed by electron transfer within the complex to the POM. Then, the reduced complexed POM can reduce silver ions by a similar way to that reported for the POM alone.[6] As previously, a complexation step between alcohol radical and silver ions can initiate the formation of silver clusters (reactions (2)–(5)) before a thermodynamically possible reduction with the reduced POM or with the alcohol radical when the nuclearity of initial silver aggregates is sufficient.

The second mechanism (Fig. 3.27B) corresponds to a direct intramolecular electron transfer from the excited porphyrins to polyoxometalate. Then, the reduced POM can reduce silver ions according to a

similar mechanism to the one considered for the photocatalysis by POM alone. A fast intramolecular electron transfer is in agreement with fluorescence quenching of our films and is also favourable thermodynamically. Previous works in our laboratory are more in favor of this mechanism.

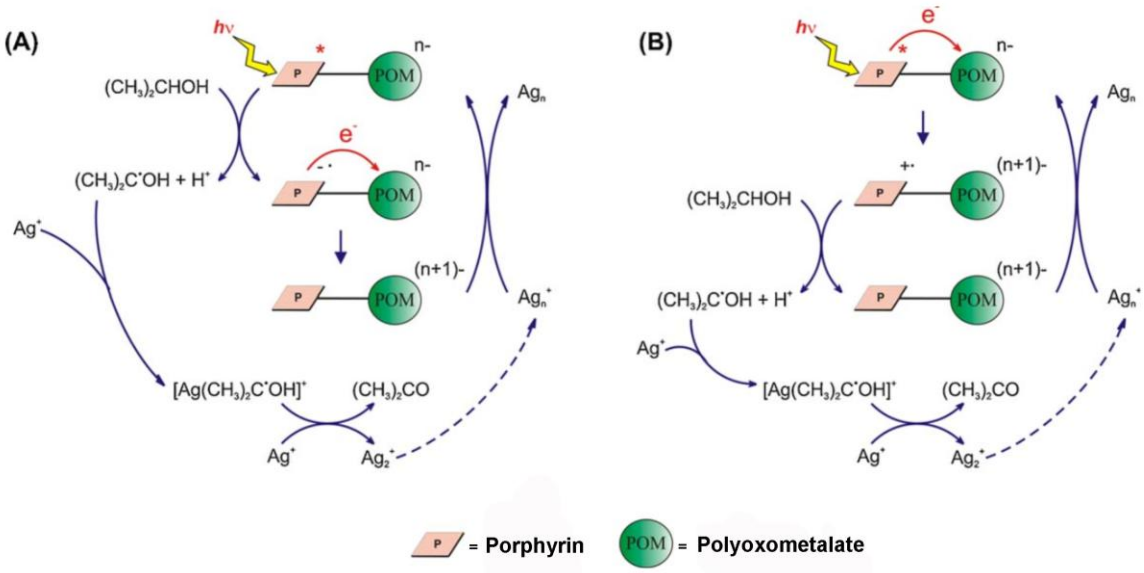

Fig. 3.27 Two possible mechanisms for the photoreduction of silver ions by the use of the porphyrins–POM complexes.

4.2. Photocatalytical recovery of platinum

Photoreduction application of the four prepared films also extend to the recovery of platinum ions. Fig. 3.28 represents the evolution of the UV–vis absorption spectrum recorded during the illumination of a quartz slide covered with **poly-$PW_{11}Si_2$-ZnOEP** in a deaerated aqueous solution containing 1.6×10^{-4} mol L^{-1} $H_2Pt^{IV}Cl_6$ and 0.13 mol L^{-1} propan-2-ol. Under illumination **poly-$PW_{11}Si_2$-ZnOEP** is able to rapidly reduce the $Pt^{IV}Cl_6^{2+}$ ions proved by the decrease of the characteristic absorption of Pt^{IV}. However, it's not accompanied by any increase of the absorbance in the visible range. Finally, the precipitation of the nanoparticles observed as a black-brown sediment on the bottom of cuvette (Fig. 3.28).

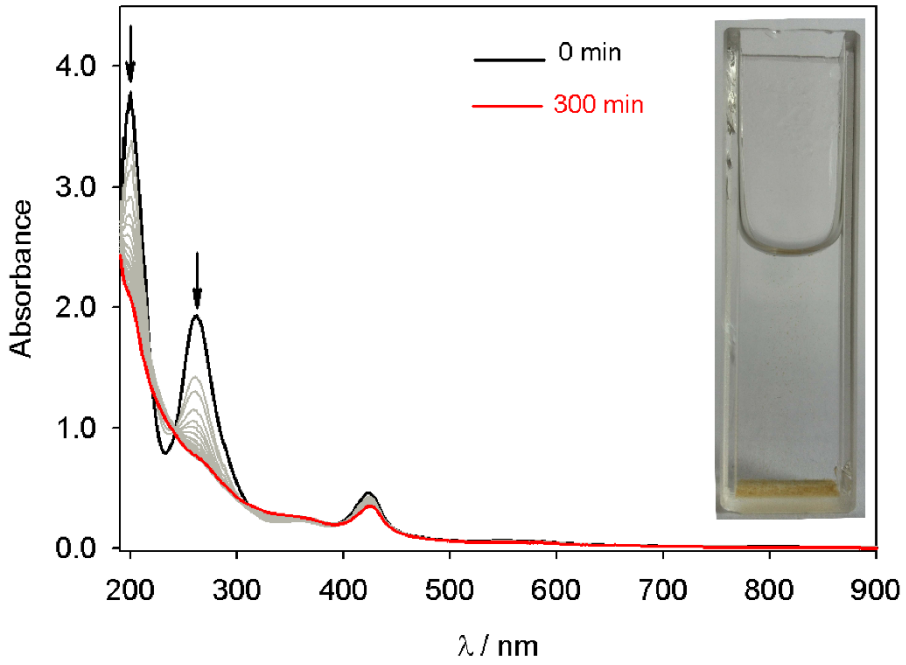

Fig. 3.28 Changes in the UV–vis absorption spectrum of a deaerated aqueous solution of 1.6 $\times 10^{-4}$ mol L^{-1} H_2PtCl_6 and 0.13 mol L^{-1} propan-2-ol containing a slide of quartz modified with **poly-$PW_{11}Si_2$-ZnOEP** film under illumination. Inset: photo of the PtNPs solution after the irradiation.

Then, we stirred evenly the solution in the cuvette and prepared TEM samples. The TEM micrographs confirmed the formation of platinum nanoparticles (PtNPs) which were homogeneous in size and shape using **poly-$PW_{11}Si_2$-ZnOEP** (Fig. 3.29). It can be seen that the smaller PtNPs with the diameter of 2.5 ± 0.2 nm aggregated to bigger PtNPs with the diameter of 22.5 ± 2.0 nm. Similar PtNPs were obtained using **poly-$PW_{11}Si_2$-H_2T_2P** and **poly-$P_2W_{17}Si_2$-ZnOEP** (Fig. 3.30 and Fig. 3.31). Remarkably, the platinum nanostructures obtained with **poly-$P_2W_{17}Si_2$-H_2T_2P** were aggregated spheres in diameter of 29.5 ± 2.0 nm together with a triangular nanosheet (length 1.8-2.4 μm) (Fig. 3.32). Plots of the intensity of the absorbance at λ = 201 and λ = 262 nm versus the time of irradiation revealed that **poly-$P_2W_{17}Si_2$-ZnOEP** possessed the hightest photocatalytic reaction rate (2.1 $\times 10^{-4}$ mol L^{-1} min^{-1}) which is consistent with the hightest photocurrent density generated by **poly-$P_2W_{17}Si_2$-ZnOEP** film (Fig. 3.33).

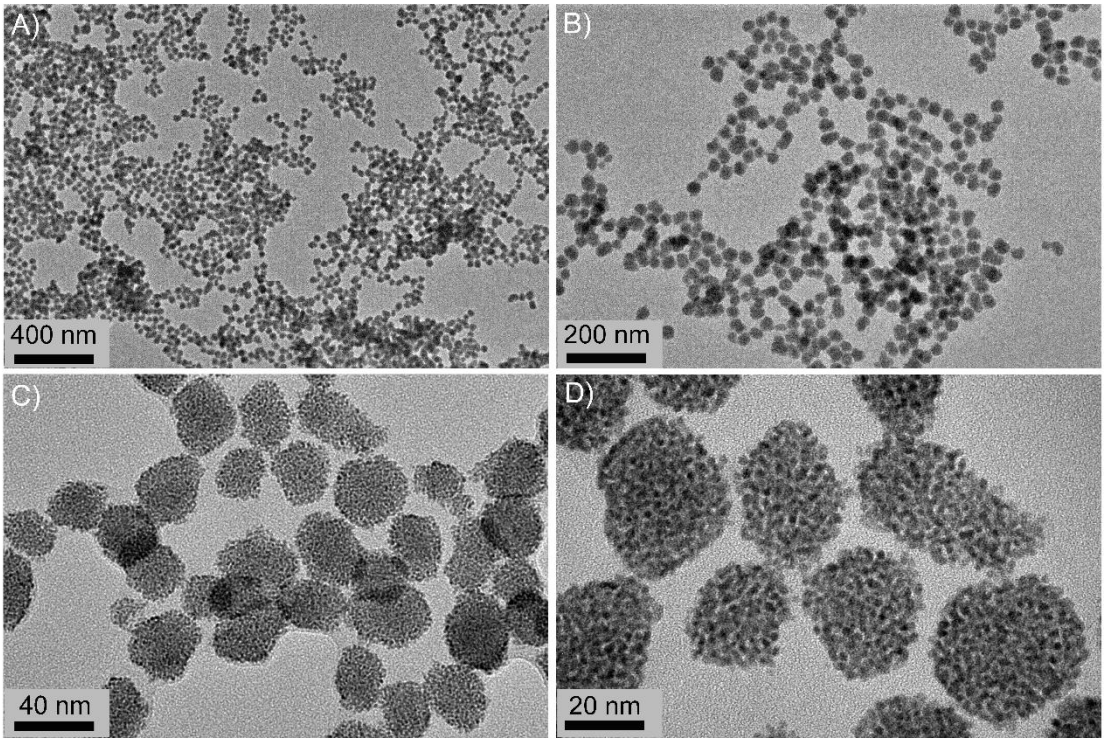

Fig. 3.29 TEM images of platinum nanostructure obtained with **poly-$PW_{11}Si_2$-ZnOEP**.

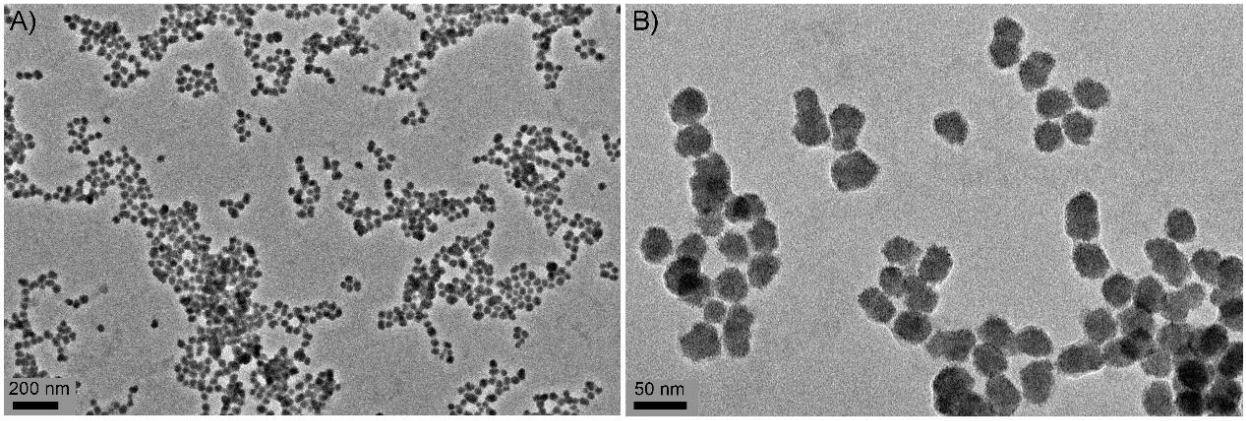

Fig. 3.30 TEM images of platinum nanostructure obtained with **poly-$PW_{11}Si_2$-H_2T_2P**.

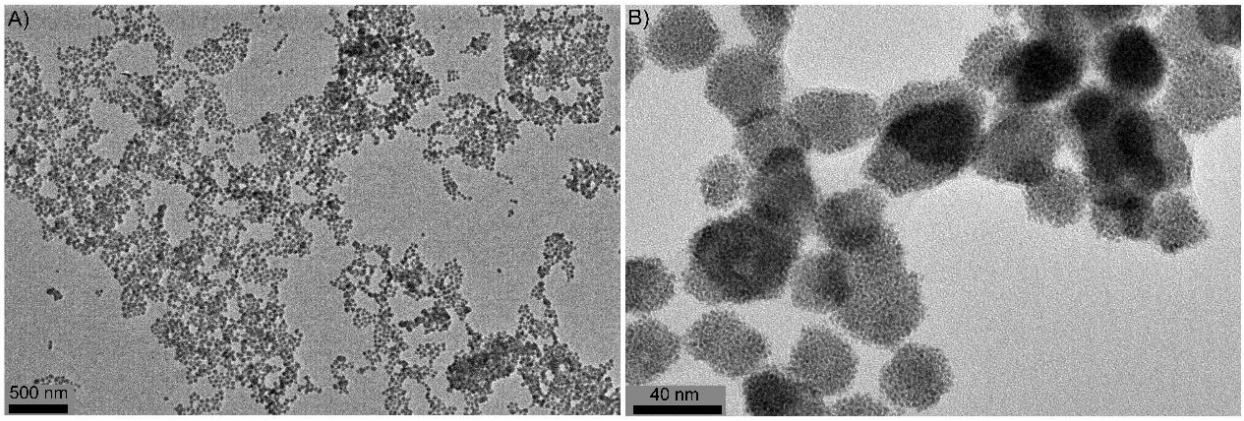

Fig. 3.31 TEM images of platinum nanostructure obtained with **poly-$P_2W_{17}Si_2$-ZnOEP**.

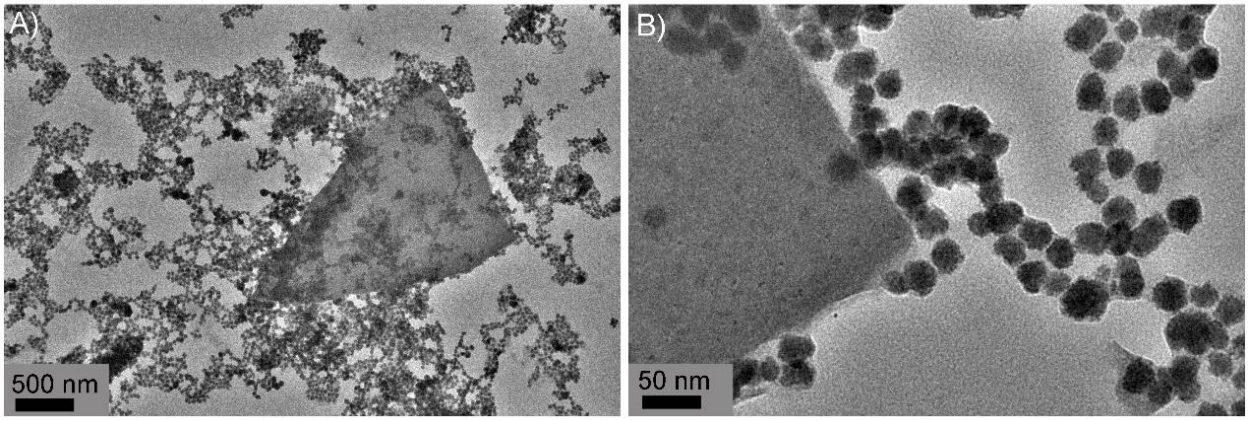

Fig. 3.32 TEM images of platinum nanostructure obtained with **poly-$P_2W_{17}Si_2$-H_2T_2P**.

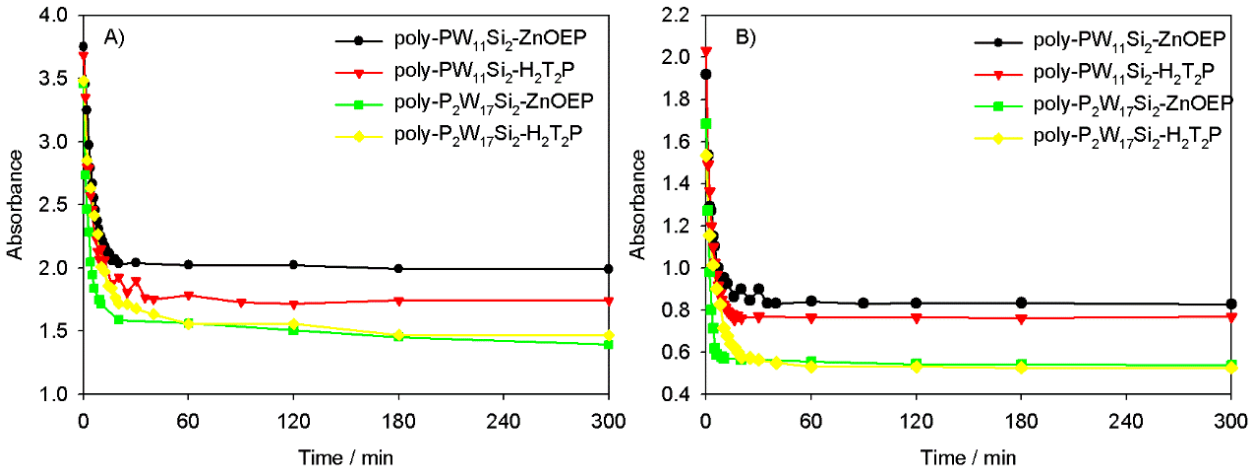

Fig. 3.33 Plot of the intensity of the absorbance at A) λ = 201 and B) λ = 262 nm versus the time of irradiation.

5. Conclusion

Electropolymerization of organosilyl Keggin and Dawson-type POM derivatives bearing two pyridyl moieties with **ZnOEP** and **H_2T_2P** has allowed us to prepare four covalently bonded POM-porphyrin copolymers. In this series of photoactive assemblies the redox behavior of the POM, acting as an electron acceptor, can be tuned according to its structural class (Keggin *vs.* Dawson). The properties of the porphyrin (molar extinction coefficient: **ZnOEP** > **H_2T_2P**) dominate the light collection ability of the POM-porphyrin copolymers, and the order of the visible absorbance magnitude: **poly-$PW_{11}Si_2$-ZnOEP** > **poly-$PW_{11}Si_2$-H_2T_2P**, **poly-$P_2W_{17}Si_2$-ZnOEP** > **poly-$P_2W_{17}Si_2$-H_2T_2P**. The impedance measurements indicate **poly-$P_2W_{17}Si_2$-ZnOEP** with the lowest charge transfer resistance. The performance of **poly-$P_2W_{17}Si_2$-ZnOEP** in photocurrent generation and the photocatalytical kinetic are the best during all of the covalent POM-porphyrin copolymers that we have prepared (ten covalent copolymers in total).

References

(1) Schaming, D.; Allain, C.; Farha, R.; Goldmann, M.; Lobstein, S.; Giraudeau, A.; Hasenknopf, B.; Ruhlmann, L. *Langmuir* **2010**, *26* (7), 5101.
(2) Long, D.-L.; Tsunashima, R.; Cronin, L. *Angew. Chem. Int. Ed. Engl.* **2010**, *49* (10), 1736.
(3) Anandan, S.; Pitchumani, S.; Muthuraaman, B.; Maruthamuthu, P. *Sol. Energy Mater. Sol. Cells* **2006**, *90* (12), 1715.
(4) Mylonas, a.; Hiskia, a.; Papaconstantinou, E. *J. Mol. Catal. A Chem.* **1996**, *114* (1-3), 191.
(5) Troupis, a.; Hiskia, a.; Papaconstantinou, E. *Appl. Catal. B Environ.* **2003**, *42* (3), 305.
(6) Costa-Coquelard, C.; Schaming, D.; Lampre, I.; Ruhlmann, L. *Appl. Catal. B Environ.* **2008**, *84* (3-4), 835.
(7) Matt, B.; Xiang, X.; Kaledin, A. L.; Han, N.; Moussa, J.; Amouri, H.; Alves, S.; Hill, C. L.; Lian, T.; Musaev, D. G.; Izzet, G.; Proust, A. *Chem. Sci.* **2013**, *4* (4), 1737.
(8) Matt, B.; Coudret, C.; Viala, C.; Jouvenot, D.; Loiseau, F.; Izzet, G.; Proust, A. *Inorg. Chem.* **2011**, *50* (16), 7761.
(9) Matt, B.; Fize, J.; Moussa, J.; Amouri, H.; Pereira, A.; Artero, V.; Izzet, G.; Proust, A. *Energy Environ. Sci.* **2013**, *6* (5), 1504.
(10) Matt, B.; Moussa, J.; Chamoreau, L.-M.; Afonso, C.; Proust, A.; Amouri, H.; Izzet, G. *Organometallics* **2012**, *31* (1), 35.
(11) Giraudeau, A.; Ruhlmann, L.; El Kahef, L.; Gross, M. *J. Am. Chem. Soc.* **1996**, *118* (12), 2969.
(12) Ruhlmann, L.; Lobstein, S.; Gross, M.; Giraudeau, A. *J. Org. Chem.* **1999**, *64* (4), 1352.
(13) Giraudeau, A.; Lobstein, S.; Ruhlmann, L.; Melamed, D.; Barkigia, K. M.; Fajer, J. *J. Porphyr. Phthalocya.* **2001**, *05* (11), 793.
(14) Ruhlmann, L.; Hao, J.; Ping, Z.; Giraudeau, A. *J. Electroanal. Chem.* **2008**, *621* (1), 22.
(15) Giraudeau, A.; Schaming, D.; Hao, J.; Farha, R.; Goldmann, M.; Ruhlmann, L. *J. Electroanal. Chem.* **2010**, *638* (1), 70.
(16) Schaming, D.; Ahmed, I.; Hao, J.; Alain-Rizzo, V.; Farha, R.; Goldmann, M.; Xu, H.; Giraudeau, A.; Audebert, P.; Ruhlmann, L. *Electrochim. Acta* **2011**, *56* (28), 10454.
(17) Favette, S.; Hasenknopf, B.; Vaissermann, J.; Gouzerh, P.; Roux, C. *Chem. Commun. (Camb).* **2003**, No. 21, 2664.
(18) Allain, C.; Favette, S.; Chamoreau, L.; Vaissermann, J.; Ruhlmann, L.; Hasenknopf, B. *Eur. J. Inorg. Chem.* **2008**, *2008* (22), 3433.
(19) Ruhlmann, L.; Schulz, A. *J. Am. Chem. Soc.* **1999**, *121* (8), 6664.
(20) Hao, J.; Giraudeau, A.; Ping, Z.; Ruhlmann, L. *Langmuir* **2008**, *24* (5), 1600.
(21) Brisach-Wittmeyer, A.; Lobstein, S.; Gross, M.; Giraudeau, A. *J. Electroanal. Chem.* **2005**, *576* (1), 129.
(22) Schaming, D.; Giraudeau, A.; Lobstein, S.; Farha, R.; Goldmann, M.; Gisselbrecht, J.-P.; Ruhlmann, L. *J. Electroanal. Chem.* **2009**, *635* (1), 20.
(23) Baraka, M. El; Janot, J. M.; Ruhlmann, L.; Giraudeau, A.; Deumié, M.; Seta, P. *J. Photochem. Photobio. A: Chemistry*, 1998, *113*, 163.
(24) Bruckenstein, S.; Shay, M. *Electrochim. Acta* **1985**, *30* (10), 1295.
(25) Ponomarev, E. a.; Peter, L. M. *J. Electroanal. Chem.* **1995**, *397* (1-2), 45.
(26) Kuang, D.; Brillet, J.; Chen, P.; Takata, M.; Uchida, S.; Miura, H.; Sumioka, K.; Zakeeruddin, S. M.; Grätzel, M. *ACS Nano* **2008**, *2* (6), 1113.
(27) Witten Jr, T.; Sander, L.; *Phys. Rev. Lett.* **1981**, *47* (19) 1400.
(28) Gachard, E.; Remita, H.; Khatouri, J.; Keita, B.; Nadjo, L.; Belloni, and J. *New J. Chem.* **1998**, *22* (11), 1257.
(29) Henglein, A. *Berichte der Bunsengesellschaft für Phys. Chemie* **1977**, *81* (6), 556.
(30) H. A. Schwarz and R. W. Dodson. *J. Phys. Chem.* **1989**, *93* (1), 409.
(31) Tausch-Treml, R.; Henglein, A.; Lilie, J. *Berichte der Bunsengesellschaft für Phys. Chemie* **1978**, *82* (12), 1335.

Chapter IV

Conjugated Dawson polyoxophosphovanadotungstate – porphyrin copolymers for the photocurrent generation and the photocatalytical recovery of metals

Chapter IV: Conjugated Dawson polyoxophosphovanadotungstate – porphyrin copolymers for the photocurrent generation and the photocatalytical recovery of metals

Four hybrid polyoxometalate-porphyrin copolymeric films were obtained by the electro-oxidation of zinc octaethylporphyrin in the presence of four different dipyridyle-substituted organo-polyoxometallic bricks using bis-alkoxo-amide functionalizations of Dawson structure $[P_2W_{15}V_3O_{62}]^{9-}$. The POM monomers were designed around 1,3,5-trisubstituted benzene rings. Two of the substituents of the benzene ring are linked to the pyridines, while the last one is connected to the POM subunit. The four monomers vary by the relative positions of the nitrogen atoms of the pyridines, or by the distance from the carbonyl function. The copolymers have also been characterized by UV-vis spectroscopy, XPS, electrochemistry and AFM. Their photovoltaic performances under visible light irradiation were investigated by photocurrent transient measurements under visible illumination. The four hybrids also applied for photocatalytical recovery of metals (Ag^+ and Pt (VI)).

1. Introduction

Polyoxometalates (POMs) form a distinctive class of inorganic metal-oxygen cluster compounds with applications in analytics, medicine, catalysis and photocatalysis, electronics and material science. [1] POMs are negatively charged electron acceptors with highly tunable redox potentials. Because of their robustness and the large number of high oxidation-state transition metals, POMs can undergo multi-electron photoredox processes without decomposition. This is a significant advantage for photophysical applications, which generally involve electron transfers and/or storage. The above-mentioned excellent properties and pioneering studies indicate that POMs will be promising candidates to optimize the efficiency of electrolytes in photocurrent generation. Furthermore, POMs also play an important role in environmentally benign oxidative photodegradation of organic compounds in water purification technology.[2] While photolysis in the presence of a sacrificial electron donor reduces POMs which in

turn lead to the reduction of metal cations, it appears finally as a useful alternative for synthesis and recovery of metal nanoparticles.[3,4]

Unfortunately, POMs can be excited (POM*) only under UV irradiation (O → M LMCT absorption band). Not only does this mean that merely a small fraction of the sunlight can be converted into electrical energy, it also implies that reaction vessels must be transparent in this wavelength range. This severely limits their applications in photoelectric devices.

To address this problem, POMs can be linked to visible light sensitive molecules via covalent, coordination or non-covalent bonding. In the first chapter, a review of the development of POM – based hybrids has been proposed. The electrochemical synthesis of the POM-porphyrin copolymers based on the nucleophilic substitution (Py-POM-Py) on porphyrins via an $E(EC_NEC_B)_nE$ process[5,6,7,8,9,10,11,12,13] have already depicted in chapters II and III.

In this study, we introduce the bottom-up synthesis and characterization of four films obtained from bis-pyridine-substituted organo-polyoxometallic bricks using $[P_2W_{15}V_3O_{62}]^{9-}$ diolamide-grafting method with different geometries, and evaluate the impact of the monomer structure of POM on the architecture of the Dawson-type POM–porphyrin copolymers in the photocurrent response and photocatalytical recovery of metals.

2. Formation and characterization

2.1. Electropolymerization of copolymers

The four organic connectors (Fig. 4.1, bottom) were selected to modulate the communication between porphyrin macrocycles within the polymeric chains, and between the porphyrins and the POMs. All of them relied on diolamide grafting[14] to establish full conjugation between the organic backbone and the pendant POM framework in the copolymer. The POM monomers were designed around 1,3,5-tri substituted benzene rings, which serve as conjugated hubs. Two of the substituents of the benzene ring are connected to the pyridine rings, while the remaining one is connected to the POM subunit. The four monomers differ in the relative positions of the nitrogen atoms of the pyridine rings or in the distance from the carbonyl group. The numbers in the acronyms used in Fig. 4.1 indicate the position at which

the pyridyl group is grafted to the benzene ring (3- or 4-position of the heterocycle), while the letters indicate the nature of the spacers connecting the POM and the pyridine rings ("s" stands for short, i.e., the pyridine rings are directly connected to the aromatic platform, which is itself directly connected to the POM; "m" stands for medium, in which case one triple-bond connector has been inserted between the pyridine ring and the aromatic platform; "l" stands for long, in which a double bond is inserted between the POM and the aromatic platform, in addition to the alkyne group).

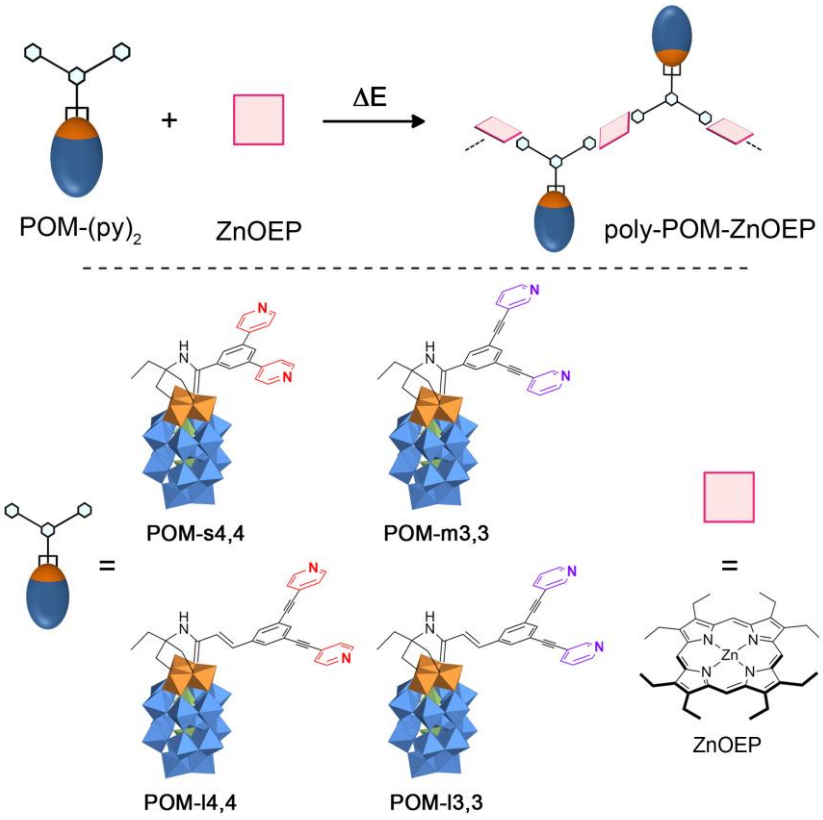

Fig. 4.1 Top: schematic representation of the electrosynthesis of POM-porphyrin copolymer. Bottom: representation of the diol-amide (**POM-s4,4**, **POM-m3,3, POM-l4,4** and **POM-l3,3**) ligands and of **ZnOEP** photosensitizer.

The copolymers were synthesized by the method like before, which involved addition of the various dipyridyl-substituted phosphovanadotungstates to an electro-generated dicationic porphyrin (Fig. 4.1, top and Fig. 4.2).[11,15,16] As soon as the iterative scans were performed at a potential in the anodic part sufficiently high to allow the formation of the porphyrin dication, the formation of a coating film on working electrode was observed. The reactions thus generate H^+ ions, which can demetalate the porphyrin and stop the reaction. In our case, the protons generated did not perturb the coating on the

electrodes because of the large volume of solution used. The absence of demetalation of **ZnOEP** was verified by UV-vis spectroscopy. We prepared POM–porphyrin copolymer films from the four different Dawson-type Py-POM-Py monomers.[17]

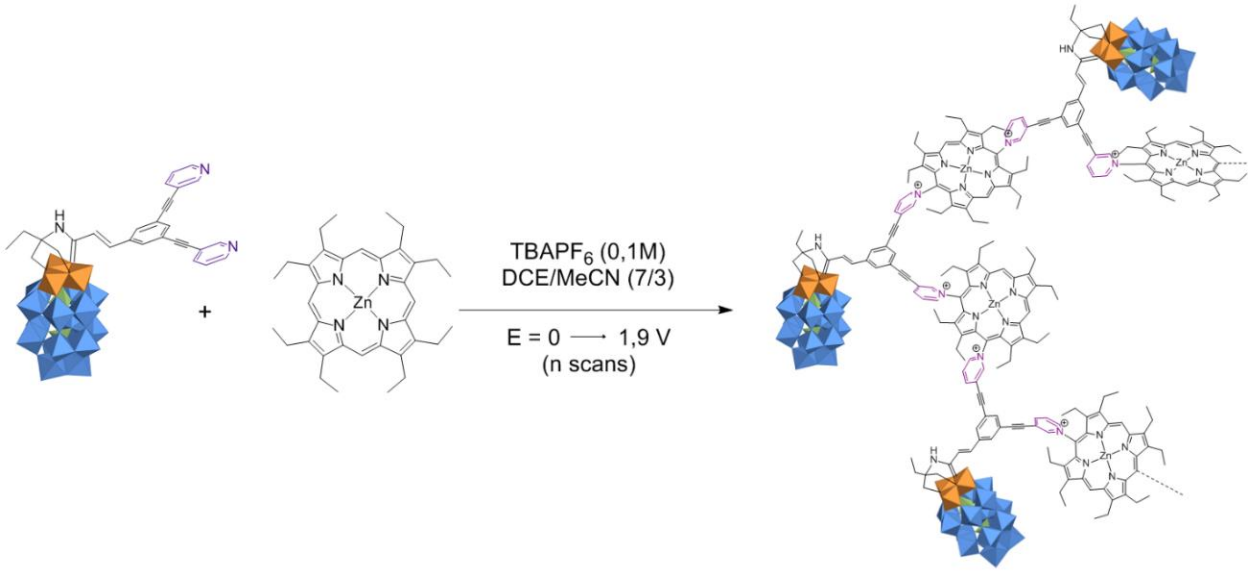

Fig. 4.2 Synthesis of copolymer **poly-POM-l4,4-ZnOEP**.

All electropolymerizations were carried out under conditions similar to the aforementioned research,[11] by iterative scans between -0.05 and +1.90 V *vs.* SCE or -1.3 and +1.90 V *vs.* SCE (Fig. 4.3 and S4.2, see appendix) in 0.1 mol L^{-1} solutions of $TBAPF_6$ in 1,2-$C_2H_4Cl_2$/MeCN (7:3) containing **ZnOEP** (0.25 mmol L^{-1}) and Py-POM-Py (0.25 mmol L^{-1}) under argon atmosphere. Moreover, all the further studies of the properties of the films have been conducted using modified electrode obtained from iterative scan between –0.05 V and +1.90 V *vs*. SCE in order to avoid the irreversible reduction of the pyridium groups. In the case of the preparation of the **poly-POM-s4,4-ZnOEP** copolymer, the signal observed during the first scan (Fig. 4.3, left, red line) corresponds to the reduction of the three vanadium ions in POM-s4,4 (redox couples V^V/V^{IV}) which were not well defined using an ITO electrode. With iterative scans between –1.30 V and +1.90 V, an increase of a reduction peak at –0.95 V *vs*. SCE as well as a poorly resolved peak near –0.80 V were observed as the copolymer was formed. They were attributed to the superimposed signals from the reduction of the forming bridging pyridiniums (Table 1) and the reduction of the vanadium atoms (V^V/V^{IV}).

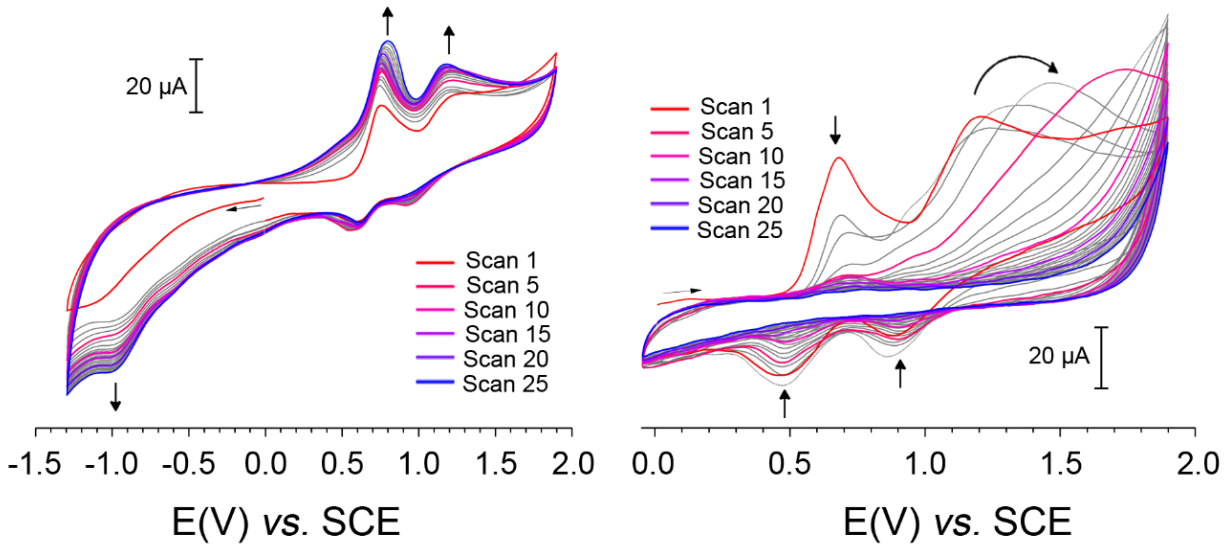

Fig. 4.3 Cyclic voltammograms for the electropolymerization of **ZnOEP** (0.25 mmol L^{-1}) in the presence of **POM-m3,3** (0.25 mmol L^{-1}) in 1,2-$C_2H_4Cl_2$/CH_3CN (7:3) containing 0.1 mol L^{-1} $TBAPF_6$. Working electrode ITO. S = 1 cm^2. Counter electrode: Pt, Reference: SCE. Cyclic scanning (0.1 $V.s^{-1}$) was applied at potentials between -0.05 V and +1.90 V *vs.* SCE (right) or between -1.30 V and +1.90 V *vs.* SCE (left). (←) Start of the scan.

2.2. EQCM for the copolymer deposition

The electropolymerization of the four copolymers was monitored by EQCM. Fig. 4.4 illustrates the simultaneously recorded mass changes Δm and cyclic voltammograms. In the electropolymerization of **ZnOEP** and **POM-l4,4** by iterative scans between -0.05 and +1.90 V (Fig. 4.4D) with an ITO working electrode deposited on an AT-cut quartz crystal resonator. The quartz resonance frequency Δf decreased with each consecutive cycle, with a concomitant increase in the mass of the copolymer. By using the Sauerbrey equation,[18] this change in mass was calculated (Fig. 4.4D'). The smooth drop in quartz resonance frequency and the simultaneous mass increase Δm show continuous growth of the copolymer. Similar behaviors were observed for the electropolymerization of **POM-m3,3** and **ZnOEP**, **POM-l3,3** and **ZnOEP**, as well as **POM-s4,4** and **ZnOEP** (Fig. 4.4).

In the present investigation, the coverage after 25 iterative scans between 0.00 and +1.90 V was about 18.5 µg cm^{-2} for **poly-POM-l4,4-ZnOEP**. Similar Δm values were measured for **poly-POM-l3,3-ZnOEP**, **poly-POM-m3,3-ZnOEP**, and **poly-POM-s4,4-ZnOEP** (10.9, 12.5, and 13.2 µg cm^{-2}, respectively). Surface coverage Γ was estimated from mass coverage Δm to be 3.52×10^{-9}, 2.08×10^{-9}, 2.39×10^{-9}, and 2.55×10^{-9} mol cm^{-2} for **poly-POM-l4,4-ZnOEP**, **poly-POM-l3,3-ZnOEP**, **poly-POM-**

m3,3-ZnOEP, and **poly-POM-s4,4-ZnOEP**, respectively, where the amounts calculated correspond to the subunits of the chain, namely, (ZnOEP-py^{+}-POM^{5-}-py^{+})TBA$_5$ (PF$_6$)$_2$.

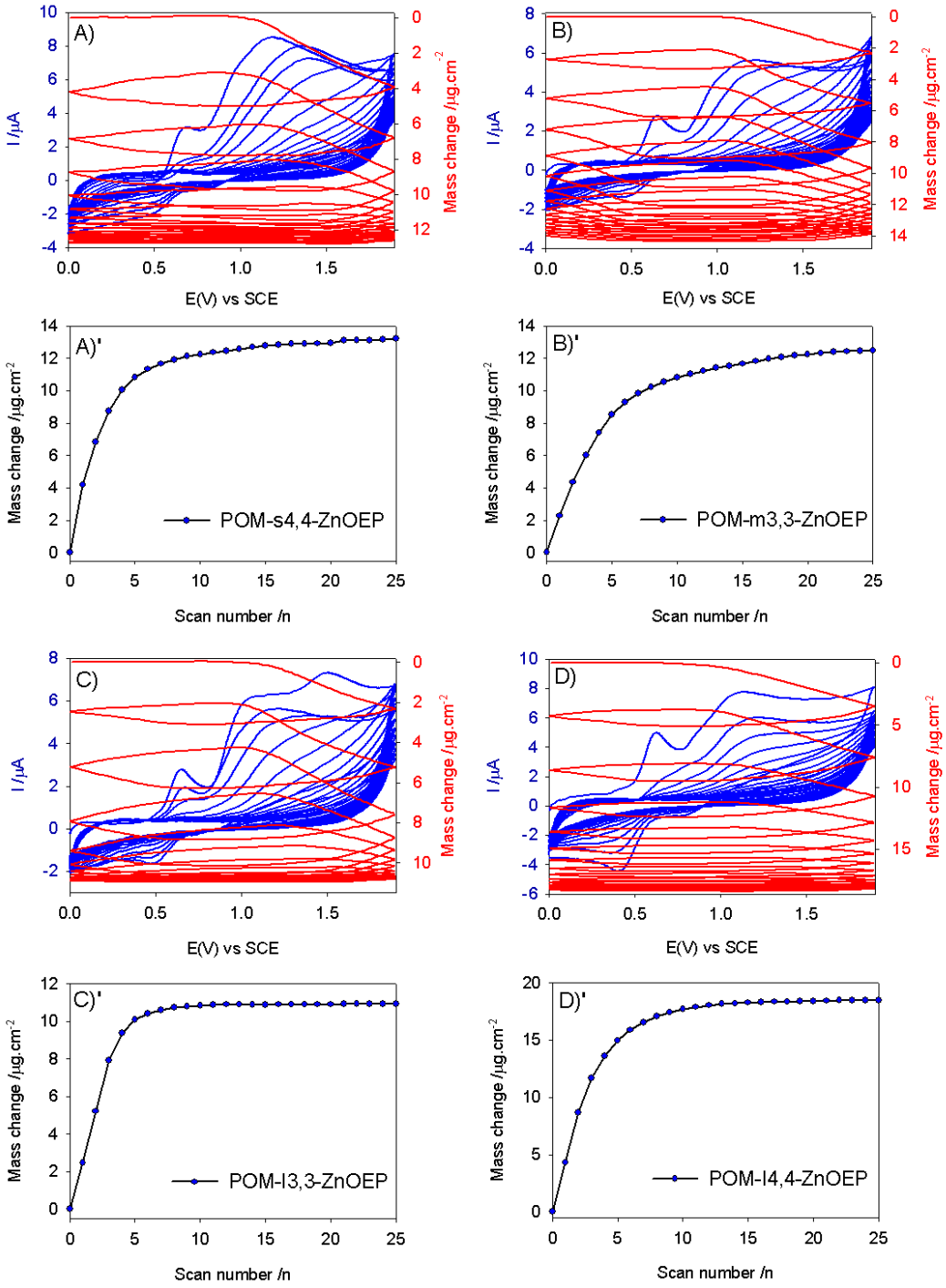

Fig. 4.4 Consecutive cyclic voltammograms (first 10 scans) and electrochemical quartz crystal microbalance measurements (Δm) during the electropolymerization of 0.25 mmol L^{-1} ZnOEP with 0.25 mmol L^{-1} A) and A') **poly-POM-s4,4-ZnOEP**, B) and B') **poly-POM-m3,3-ZnOEP**, C) and C') **poly-POM-l3,3-ZnOEP** and D) and D') **poly-POM-l4,4-ZnOEP** in 1,2-$C_2H_4Cl_2$–CH_3CN (7/3) in the presence of 0.1 mol L^{-1} $TBAPF_6$. Working electrode: ITO (A = 0.2 cm^2) deposited on a 9.08 MHz AT-cut quartz crystal. v = 100 mV s^{-1}.

2.3. Cyclic voltammetric investigations of the polymeric films

The electrochemical behavior of the films was studied by cyclic voltammetry (Table 1, Fig. 4.5 and Figs. S4.3-S4.5 in the Appendix). Characteristically, two reduction peaks appeared, corresponding to the reduction of the pyridinium groups and the first reduction of the **ZnOEP** macrocycles (Table 1). The pyridinium reductions were observed at -0.79, -1.02, and -0.98 *vs*. SCE for **poly-POM-l4,4-ZnOEP**, **poly-POM-l3,3-ZnOEP**, and **poly-POM-m3,3-ZnOEP** respectively, and split into two waves at -0.78 and -0.95 V for **poly-POM-s4,4-ZnOEP**. This shows the strong influence of the linker on the reduction potential of the pyridinium spacers. For the two isomers **poly-POM-l4,4-ZnOEP** and **poly-POM-l3,3-ZnOEP**, easier reduction of the pyridinium spacers were observed when the pyridyl groups were connected at the 4-position (para positions). Similar behavior was observed for the two other copolymers, except for the splitting of the pyridinium reductions at -0.78 and -0.95 V for **poly-POM-s4,4-ZnOEP**. This can tentatively be explained in terms of π conjugation. For **poly-POM-l4,4-ZnOEP** or **poly-POM-s4,4-ZnOEP**, the delocalization of the pyridyl radical is greater than for **poly-POM-l3,3-ZnOEP** or **poly-POM-m3,3-ZnOEP** because the conjugation with the central benzene ring leads to stabilization of the reduced intermediate. In the particular case of **poly-POM-s4,4-ZnOEP**, the splitting of the pyridinium reduction peak is likely due to the proximity of the two py^+ centers. Because of this proximity and the delocalization of the radical after the first reduction, the electron density increases near the second pyridinium center and the second reduction is expected to be more difficult. In the case of **poly-POM-l3,3-ZnOEP** or **poly-POM-m3,3-ZnOEP** with attachment at the 3-position of the pyridine (meta positions), no stabilization can take place, since delocalization of the radical is only possible within the pyridyl ring.

The reduced form of the pyridinium was thus observed at more negative potentials. Finally, the first porphyrin reductions were measured at -1.57, -1.32, -1.58, and split at -1.26 and -1.55 V *vs.* SCE for **poly-POM-l4,4-ZnOEP**, **poly-POM-l3,3-ZnOEP**, **poly-POM-m3,3-ZnOEP**, and **poly-POM-s4,4-ZnOEP** respectively.

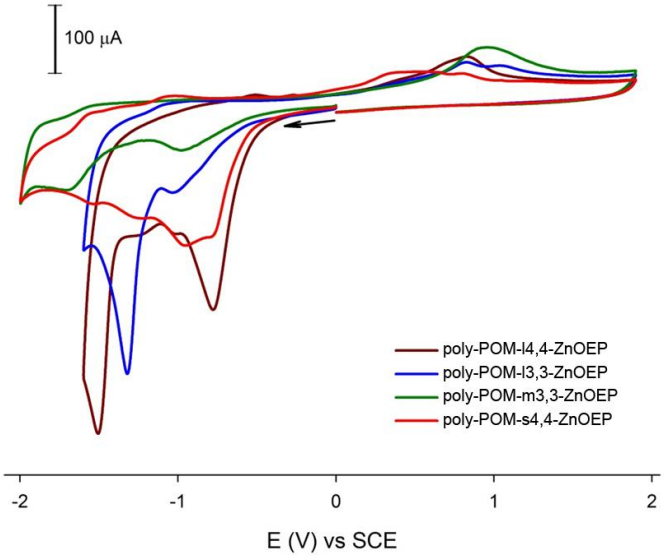

Fig. 4.5 Cyclic voltammograms of **poly-POM-s4,4-ZnOEP**, **poly-POM-m3,3-ZnOEP**, **poly-POM-l3,3-ZnOEP** and **poly-POM-l4,4-ZnOEP** in CH_3CN containing $TBAPF_6$ 0.1mol L^{-1}. Working electrode: ITO, Counter electrode: Pt, Reference: SCE. Scan rate: 0.1 $V.s^{-1}$. (←) Start of the scan.

Table 1 Electrochemical data for **ZnOEP**, fort he organo-POM monomers **POM-l4,4**, **POM-l3,3**, **POM-s4,4**, **POM-m3,3**, and for copolymers **poly-POM-l4,4-ZnOEP**, **poly-POM-l3,3-ZnOEP**, **poly-POM-s4,4-ZnOEP**, **poly-POM-m3,3-ZnOEP**.[a]

	Oxidation			**Reduction**		
	π-ring	V^V/V^{IV}		py^+	π-ring	
POM-l4,4		0.06[b] (113)	-0.31[b] (222)	-0.41[b],*		
POM-l3,3		0.06[b] (87)	-0.26[b] (117)	-0.43[b] (166)		
POM-m3,3		-0.01 (261)	-0.39 (431)	-0.81[b] (583)		
POM-s4,4		-0.04 (83)	-0.39 (264)	-		
ZnOEP	0.94/ 0.68					-1,60[b]
poly-POM-l4,4-ZnOEP	1.15irr,[c]	[e]	[e]	[e]	-0.79irr,[c] (-0.84)[d]	-1.54irr,[c]
poly-POM-l3,3-ZnOEP	1.16irr,[c]	[e]	[e]	[e]	-1.02irr,[c] (-0.95)[d]	-1.32irr,[c]
poly-POM-m3,3-ZnOEP	1.13irr,[c]	[e]	[e]	[e]	-0.98irr,[c] (-0.89)[d]	-1.58[c]
poly-POM-s4,4-ZnOEP	1.24irr,[c]	[e]	[e]	[e]	-0.78irr,[c] -0.95irr,[c] (-0.91)[d]	-1.26irr,[c] -1.55irr,[c]

[a] All potentials in V *vs.* SCE were obtained from cyclic voltammetry in 1,2-$C_2H_4Cl_2$/CH_3CN (7:3) containing 0.1 mol.L^{-1} $TBAPF_6$. Scan rate = 0.1 V s^{-1}. [b] Working electrode: glassy carbon electrode. [c] ITO, S = 1 cm^2 after 25 scans. The given half-wave potentials in the case of the reversible couple are equal to $E_{1/2} = (E_{pa} - E_{pc})/2$. Under bracket for organo-POM monomers: (ΔE_p, peak splitting in mV) ΔE_p is the difference potential between the oxidative and the reductive peak potentials. [d] Under bracket for copolymers: potentials in V *vs.* SCE obtained from cyclic voltammetry in aqueous solution containing 0.1 mol.L^{-1} NaI. [e] not observed. * Measured from DPV.

2.4. UV-vis spectroscopy

All the UV-vis spectra recorded on ITO electrodes coated with the copolymers showed similar characteristics. The absorption intensity of the chromophores increased progressively for each iterative scan during the deposition and eventually reached a plateau (Fig. 4.6A, Fig. 4.7 and Fig. S4.6 in the Appendix). A typical UV-vis spectrum exhibited a large Soret absorption band that was red shifted compared to the **ZnOEP** monomer (Fig. 4.6B). This change can be explained by intra- or intermolecular excitonic interactions between the **ZnOEP** subunits.[6] The shift was less pronounced in DMF, likely due to the reduction of intermolecular interactions between porphyrins in the polar solvent (Fig. 4.6B).

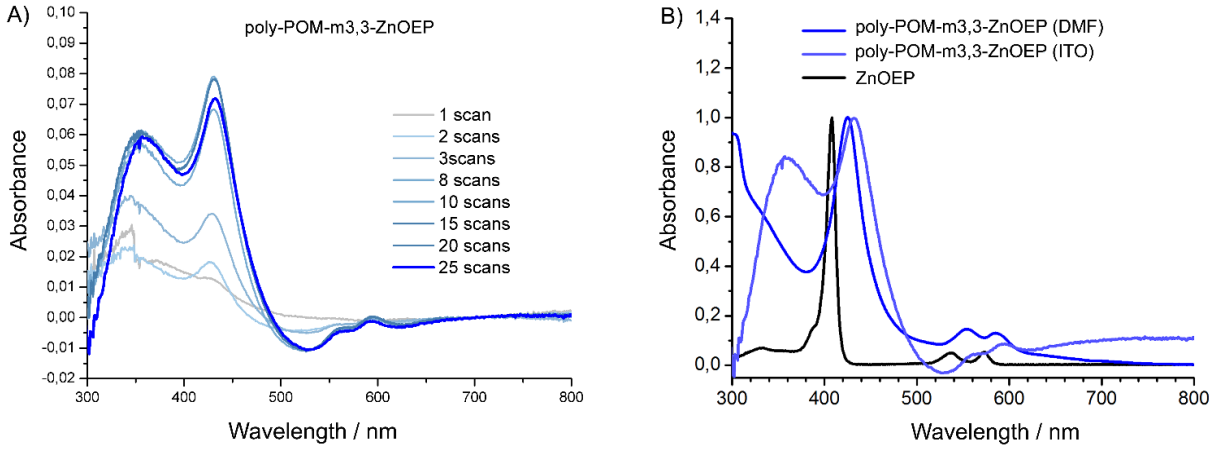

Fig. 4.6 UV-visible absorption spectra of A) **poly-POM-m3,3-ZnOEP** (onto ITO) with different numbers of iterative scans (between -0.05 V and 1.90 V *vs.* SCE). Only one side is recovered by ITO. B) Normalized UV-visible absorption spectra of the ITO electrode modified with **poly-POM-m3,3-ZnOEP**,obtained after 25 iterative scans between -0.05 and +1.90 V *vs.* SCE (light blue), and of **poly-POM-m3,3-ZnOEP** (blue) and **ZnOEP** (black) in DMF solution.

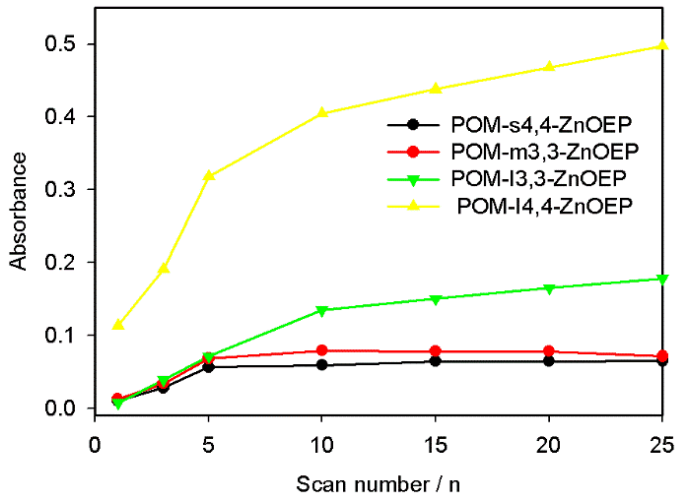

Fig. 4.7 (A) Plots of the absorbance, measured at λ = 427 nm, versus the numbers of iterative scans for **poly-POM-s4,4-ZnOEP**, **poly-POM-m3,3-ZnOEP**, **poly-POM-I3,3-ZnOEP**, and **poly-POM-I4,4-ZnOEP**.

2.5. X-ray photoelectron spectroscopy

This type of characterization has been employed to determine the elemental composition of the films. While XPS is not an accurate quantitative measurement of the individual atoms, it helps to determine the present elements and their oxidation states within the film. For example, the XPS measurement for **poly-POM-I3,3-ZnOEP** (Fig. 4.8) confirms the presence of F, C, N, O, P, V and W for the copolymer onto the ITO electrode.

The film exhibited peaks corresponding to P2p (133.2 eV), O1s (530.6 eV), V2p (V2p1/2 = 522.0 eV and V2p3/2 = 516.2 eV) and W4f levels (W4f5/2 = 37.2 and W4f7/2 = 35.4 eV) coming from the phosphorous, oxygen and tungsten atoms in the POM, while the C1s and N1s signals (at 284.6, and 402.2 eV, respectively) result from the porphyrin ligand and the TBA counter ions. F1s signals (686.6 eV) can also be observed since PF_6^- anions can be trapped in the copolymer structure to balance pyridinium charge. Thus, both POM phosphates and PF_6^- contribute to the P2p peak. The signal of the Zn element is not detectable. The XPS data confirm that we indeed incorporated the Dawson-type phosphovanadotungstate and the zinc metalloporphyrin into the films, which is in agreement with the UV-vis absorption results. Similar XPS spectra (see in Appendix, Fig. S4.7-S4.9) have been obtained for **poly-POM-s4,4-ZnOEP**, **poly-POM-m4,4-ZnOEP** and **poly-POM-I4,4-ZnOEP**.

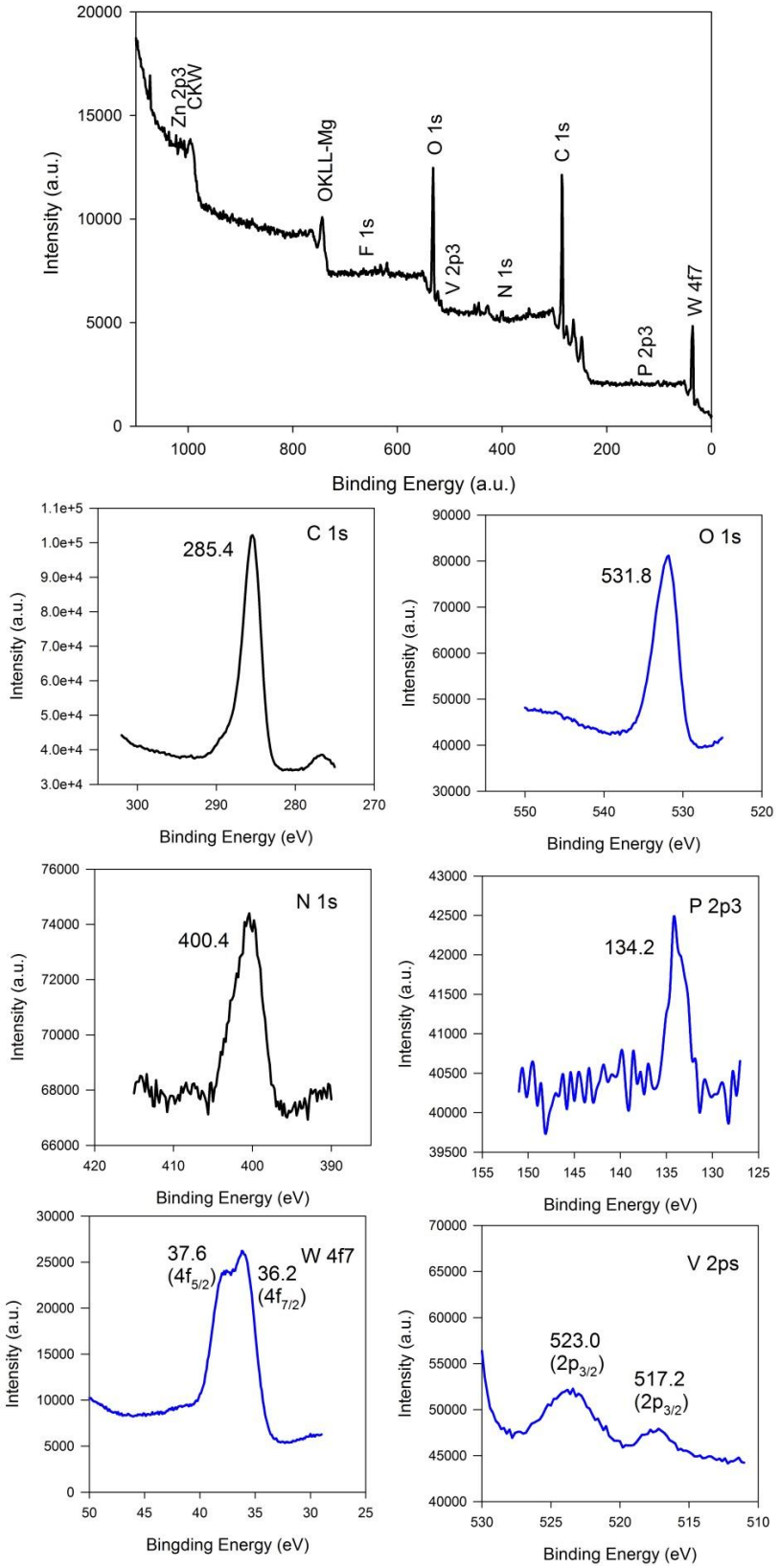

Fig. 4.8 XPS spectra of the modified ITO electrodes with **poly-POM-l4,4-ZnOEP** copolymer obtained after 25 iterative scans between 0 and 1.90 V *vs.* SCE.

2.6. Film morphology (Atomic force microscopy)

The coated electrodes were washed with CH_2Cl_2 to remove any trace of conducting salt present on the film and were examined by scanning AFM. In a typical image, **poly-POM-m3,3-ZnOEP** appeared as tightly packed coils with average diameters of 55–60 nm and a height of 4nm (Fig. 4.9). The root mean square (RMS) surface roughness of the film obtained after 25 iterative scans from -0.05 to +1.90 V versus SCE was 1.9 nm for an area of 1 μm^2. The AFM studies showed an increase in RMS surface roughness with increasing number of iterative scans, and again similar behavior was observed for the e other films (see in the Appendix, Fig. S4.10).

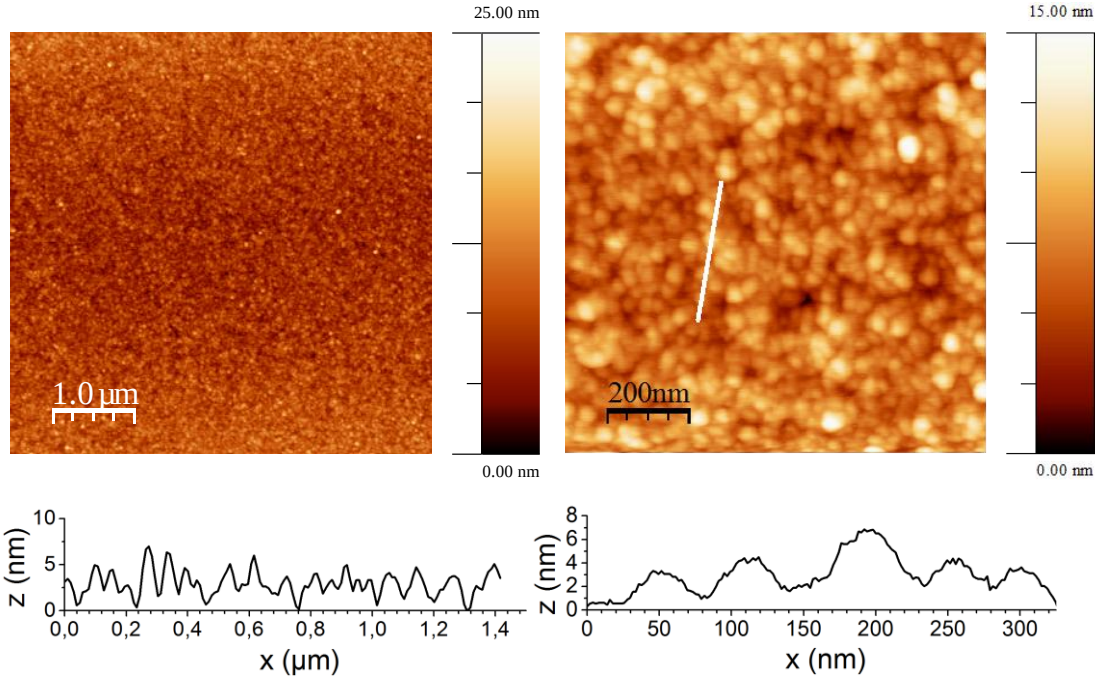

Fig. 4.9 Tapping mode AFM topography of **poly-POM-m3,3-ZnOEP** copolymer films deposited on ITO electrode after 25 iterative scans between -0.05 V and 1.90 V *vs.* SCE. Section analyses of the marked white line on the images are reported under each image.

The starting bare ITO electrode was very smooth and exhibited a lower RMS surface roughness of 0.7 nm (see in the Appendix, Fig. S4.11). To measure the thickness, we removed the polymer by scratching the film with a metallic tip and have used the same method as already described for the other films. Again, as for the other copolymers, the estimated thickness increased with increasing number of scans, following the same trend as the UV-vis absorbance intensity (Fig. 4.7). By using the EQCM and UV-

vis data and the thickness obtained from by AFM after scratching the film, the surface coverage versus the film thickness could be quantified (Table 2).

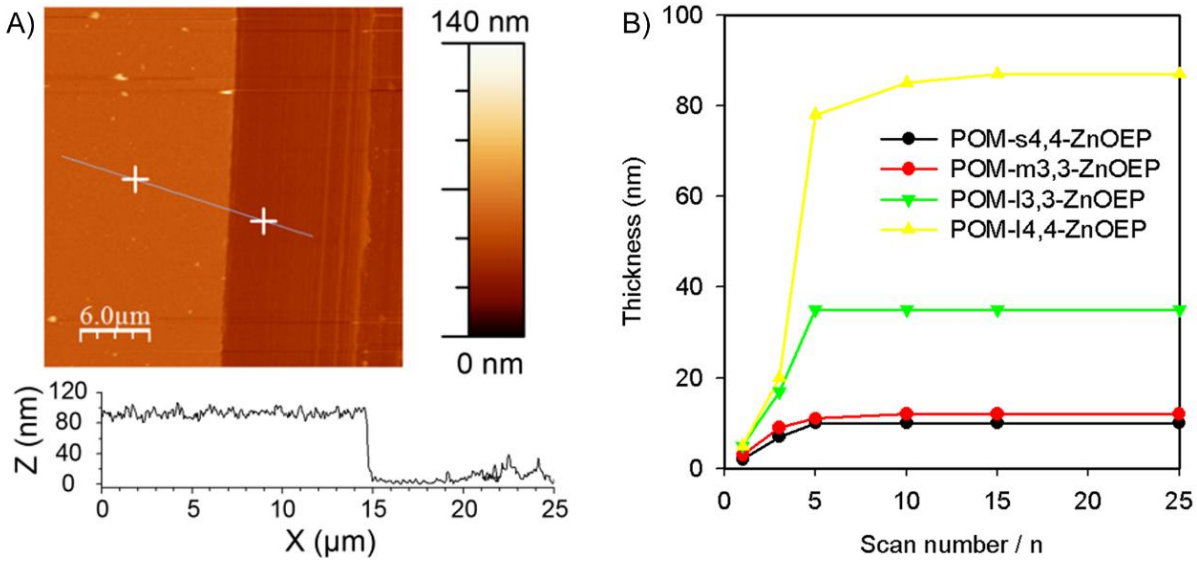

Fig. 4.10 A) AFM image of the ITO electrode modified with **poly-POM-l4,4-ZnOEP** obtained after 25 iterative scans. Bottom: section analysis. B) Thickness measured by AFM versus different numbers of iterative scans.

Table 2 Thickness, Δm (measured from AFM and EQCM respectively) and surface coverage Γ calculated versus the number of iterative scan n.

poly-POM-S4,4-ZnOEP

Number of iterative scan n	Thickness (nm)	Δm ($\mu g/cm^2$)	Γ (10^{-9}mol cm^{-2})
1	2	4.1834	0.81
3	7	8.7421	1.67
5	10	10.0600	1.94
10	10	12.2409	2.36
15	10	12.7736	2.47
20	-	12.9309	2.50
25	10	13.2187	2.55

poly-POM-m3,3-ZnOEP

Number of iterative scan n	Thickness (nm)	Δm ($\mu g/cm^2$)	Γ (10^{-9} mol cm^{-2})
1	3	2.2876	0.44
3	9	6.0133	1.15
5	11	8.5204	1.63
10	12	10.8125	2.07
15	12	11.6704	2.23
20	-	12.2538	2.35
25	12	12.4700	2.39

poly-POM-l4,4-ZnOEP

Number of iterative scan n	Thickness (nm)	Δm ($\mu g/cm^2$)	Γ (10^{-9} mol cm^{-2})
1	5	4.2944	0.82
3	20	11.6582	2.22
5	78	14.9646	2.85
10	85	17.6829	3.37
15	87	18.2634	3.48
20	-	18.4094	3.51
25	87	18.4700	3.52

poly-POM-l3,3-ZnOEP

Number of iterative scan n	Thickness (nm)	Δm ($\mu g/cm^2$)	Γ (10^{-9} mol cm^{-2})
1	5	2.4722	0.47
3	17	7.9118	1.51
5	35	10.0867	1.92
10	35	10.8496	2.07
15	35	10.8954	2.07
20	-	10.9115	2.08
25	35	10.9121	2.08

3. Photocurrent generation

3.1. Effect of the film thickness

Fig. 4.11 shows amperometric J–t curves for the photocurrent response of **poly-POM-l4,4-ZnOEP**

films with various thicknesses (various iterative scans) deposited on ITO electrodes. The films were obtained with increasing scan numbers during the electropolymerization step. The working conditions are all the same like in chapter II and III for the photocurrent generation. As shown in Fig. 4.11, the films showed a photocurrent as the irradiation was switched on, which stopped when it was turned off. The response is not rapid and needs a few seconds to reach the plateau (Fig. 4.11A). This result may be explained by the fact that the electron exchange occurs by hopping. It could be due also to the ion transport associated with movement of charge-compensating ions into and out of the film.

π-conjugated polymers have received much attention because of their high conductivity in the partially oxidized form, and because of their semiconducting properties in the neutral form. Usually, the conductivity is measured by using a four- probe electrode, for which good correlation between the redox currents and in situ conductivity measurements for each potential state are found.[19,20] The effect of light can be also important when an increase of the conductivity of the film in the solid state can be detected on illumination.[21] The presence of molecular oxygen in the solid state can also play some role: indeed, Holderoft et al[22] reported that the conductivity of the poly(3-alkylthiophenes)film increased linearly with the quantity of oxygen present. In the case of this work, we performed some tentative of measurements of the conductivity using the four-probe system. However, because the thickness of the film is not very important and because the films are deposited onto conducting ITO, we were unable to measure the conductivity of the films. The conductivity of the film was illustrated by its permeability toward the uncharged redox mediators ferrocene and 1,1-ferrocenedimethanol (Figs. S4.12–S4.17 in the Appendix).

In all cases the photocurrent response depends on the number of iterative scans n used for preparation of the film. The magnitude of the photocurrent increased appreciably from n=1 to n=3, and then decreased afterwards. This follows the same trend as the peak current corresponding to the oxidation of 1,1-ferrocenedimethanol with the same modified electrode in aqueous solution (Fig. 4.12). It suggests that the photocurrent efficiency is mainly dependent on the conductivity of the film, whereby the best performance for the films is obtained by only three iterative scans between -0.05 and 1.90 V.

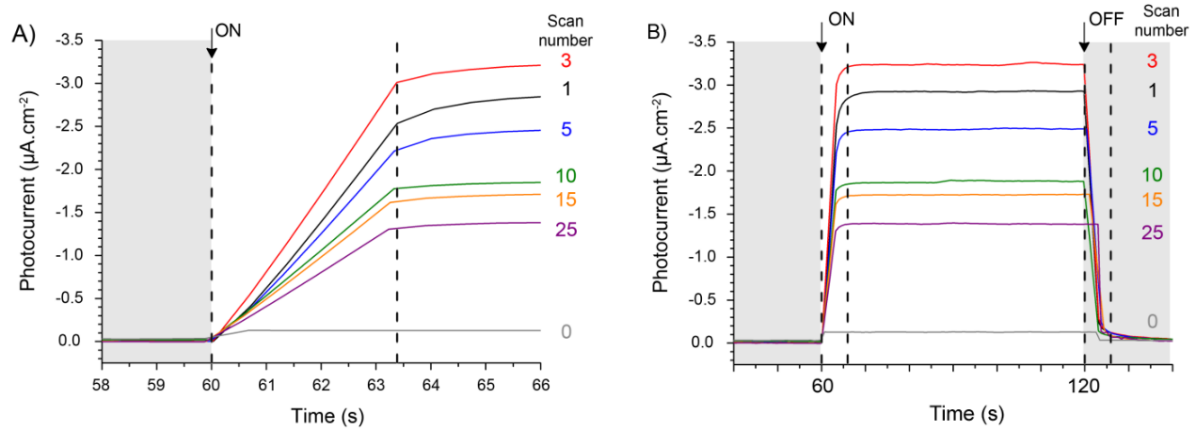

Fig. 4.11 A) and B) photoelectrochemical response of **poly-POM-l4,4-ZnOEP** with different numbers of iterative scans used for the preparation of the film (between –0.05 V and +1.90 V *vs.* SCE). Only one side is covered by ITO with on-off light illumination from 300 W Xe Arc lamp (with $\lambda \geq 385$ nm long pass filter). BIAS potential: -0.1 V. A) plots correspond to the zoom between 58 and 66 s.

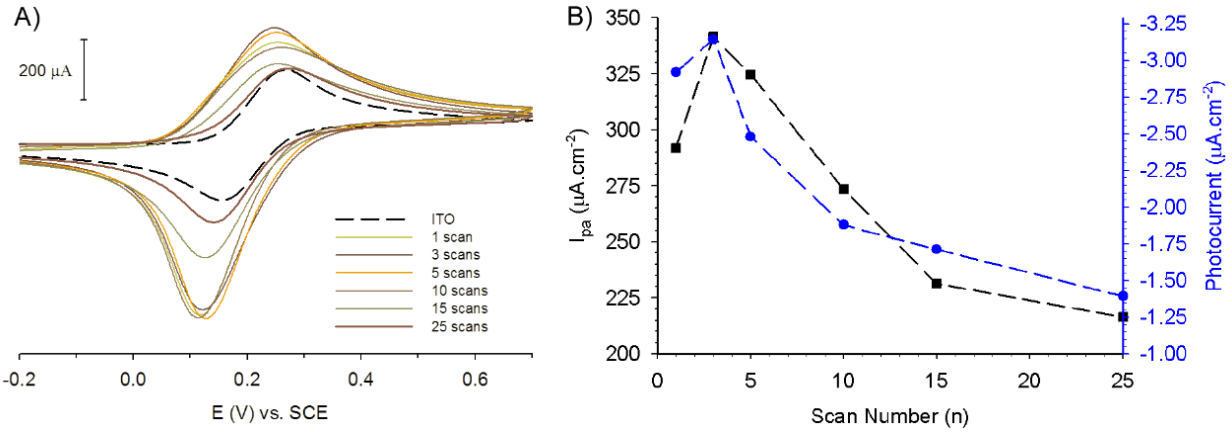

Fig. 4.12 A) CVs of 1 mM 1,1-ferrocenedimethanolin aqueous solution with Na_2SO_4 (0.5 mol.L^{-1}) at modified ITO electrode with **poly-POM-l4,4-ZnOEP** films deposited after 1 to 25 scans between -0.05 and +1.90V *vs.* SCE (full line) and at non-coated ITO electrode (dotted line). v=100 mV s^{-1}. B): (●) plots of the photocurrent measured in aqueous solution containing $Na^+ I_3^-$ 0.1 mol L^{-1} and Na^+I^- 0.5 mol L^{-1} *vs.* the numbers of iterative scans. (▪) plot of the anodic peak current in aqueous solution of 0.5 mol L^{-1} Na_2SO_4 and 1 mmolL^{-1} 1,1-ferrocenedimethanol vs. the numbers of iterative scans.

3.2. Effect of the spacers

The **poly-POM-l4,4-ZnOEP** film generated a higher photocurrent than that of poly-POM-l3,3-ZnOEP (Fig. 4.13), which differs only in the position of the nitrogen atoms. The distance between the chromophore and the porphyrin subunits in the **poly-POM-l3,3-ZnOEP** copolymer is shorter, which could promote charge recombination between the oxidized porphyrin and the reduced POM. This may

also explain the lower photocurrent. A similar explanation could be proposed in the case of the two other copolymers, **poly-POM-s4,4-ZnOEP** and **poly-POM-m3,3-ZnOEP**. The highest oxidation peak current of 1,1-ferrocenedimethanol is also the **poly-POM-l4,4-ZnOEP** modified electrode in aqueous solution (Fig. 4.14) which show **poly-POM-l4,4-ZnOEP** may possess a higher conductivity than others.

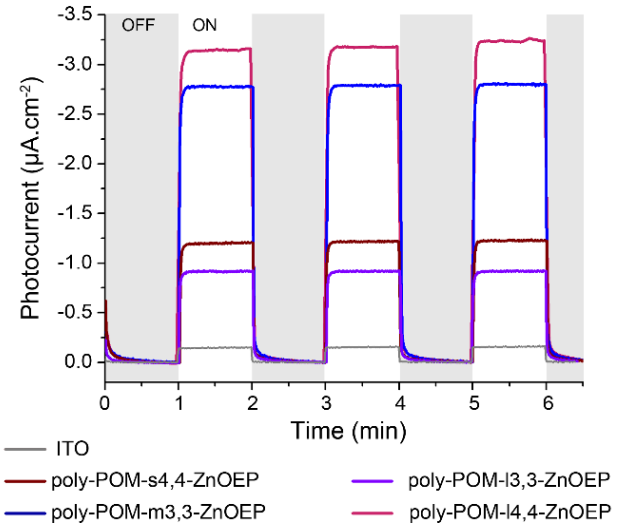

Fig. 4.13 Photoelectrochemical response of **poly-POM-s4,4-ZnOEP, poly-POM-m3,3-ZnOEP, poly-POM-l4,4-ZnOEP** and **poly-POM-l3,3-ZnOEP** (preparation of the film between –0.05 V and +1.90 V *vs.* SCE, 3 iterative scans) in aqueous solution containing $Na^+I_3^-$ 0.1 mol.L^{-1} and Na^+I^- 0.5 mol.L^{-1}. Only one side is covered by ITO with on-off light illumination from 300 W Xe Arc lamp (with $\lambda = 385$ nm long pass filter). BIAS potential: –0.10 V. The grey line corresponds to the photoresponse using bare ITO electrode.

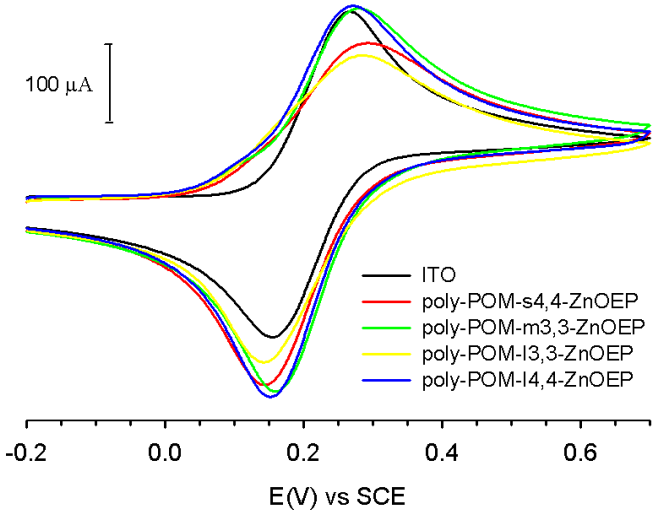

Fig. 4.14 CVs of 1 mmol L^{-1} 1,1-ferrocenedimethanol in aqueous solution with Na_2SO_4 (0.5 mol.L^{-1}) at modified ITO electrode with **poly-POM-s4,4-ZnOEP** (red), **poly-POM-m3,3–ZnOEP** (green), **poly-POM-l3,3-ZnOEP** (yellow), and **poly-POM-l4,4-ZnOEP** (blue) films deposited after 25 scans between -0.05 and +1.90 V *vs.* SCE. v=100 mV s^{-1}.

3.3. Effect of the I_3^- concentration

The photoelectrochemical responses also depend on the concentration of the redox mediator (I_3^-). When no I_3^- was present in the solution, the photocurrent density measured was less than -0.5 µA cm^{-2}. The plot of the photocurrent against time measured in such a case (Fig. 4.15, black curve) showed an exponential decrease under visible-light illumination, due to the diffusion effect. This illustrates a kinetic problem: the film must wait for the arrival of I_3^- formed at the Pt counter electrode to reoxidize the POM subunits. When the concentration of triiodide was increased, the photocurrent was amplified linearly and reached a maximum at [I_3^-] = 0.5 mmol L^{-1}. In these experiments, more and more triiodide ions reach the modified electrode per unit time, where they are able to exchange electrons. At optimized I_3^- concentration, when irradiation was switched on, the photocurrent rapidly increased and reached a plateau. This is consistent with rapid transfer of electrons through the film, and confirms that diffusion is not a problem. At higher triiodide concentration, the decrease in photocurrent could be explained by the absorption of the visible light by the redox mediator itself (Fig. 4.16), which reduces the number of photons reaching the film.

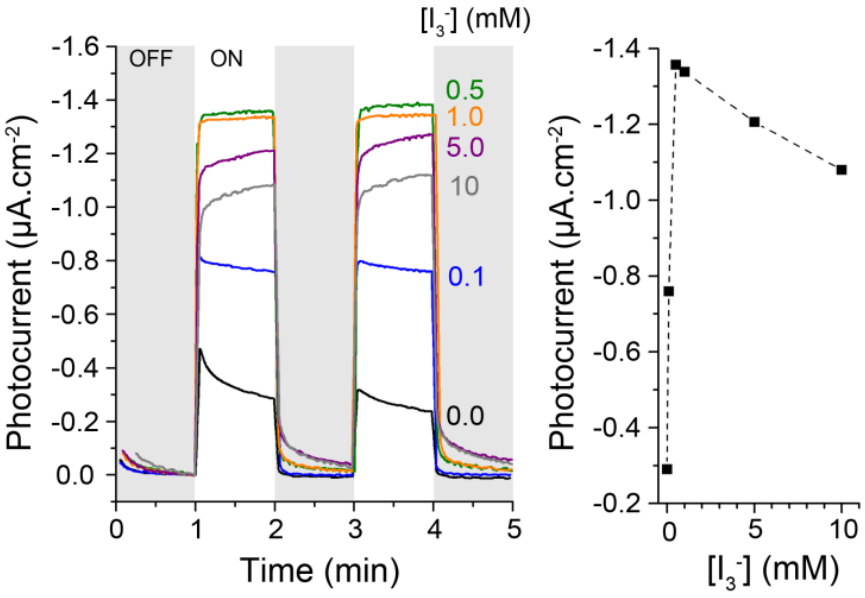

Fig. 4.15 Left: photoelectrochemical response of **poly-POM-l4,4-ZnOEP** with different concentration of $Na^+I_3^-$ used (preparation of the film between –0.05 V and +1.90 V *vs.* SCE, 3 iterative scans). Only one side is covered by ITO with on-off light illumination from 300 W Xe Arc lamp (with λ = 385 nm long pass filter). BIAS potential: –0.1 V. Right: plots of the photocurrent measured in aqueous solution (▪) containing Na^+I^- 0.5 mol L^{-1} and various concentrations of $Na^+I_3^-$ (from 0 to 10.0 mmol L^{-1}).

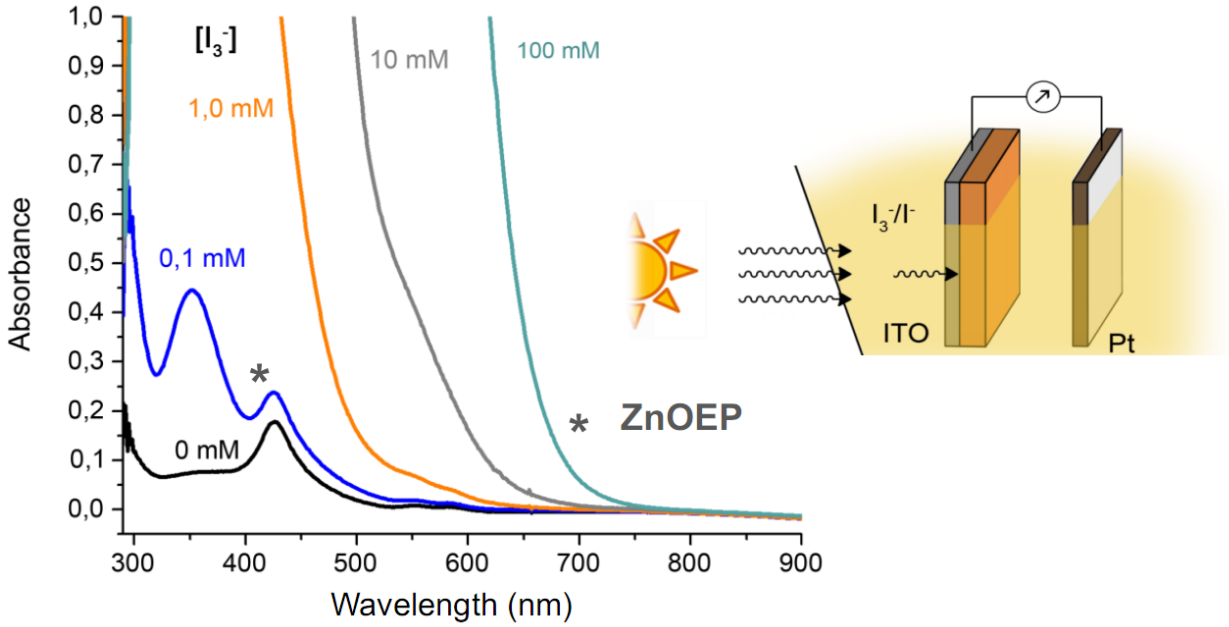

Fig. 4.16 UV-visible absorption spectra of **poly-POM-l4,4-ZnOEP** onto ITO obtained with n = 3 iterative scans (between -0.05 V and 1.90 V *vs.* SCE) in aqueous solution containing I_3^- 0.1 mol L^{-1} and I^- from 0 to 100 mmol L^{-1}. Only one side is covered by ITO.

3.4. Different BIAS potential

The photocurrent response at different BIAS potential in the case of the system **poly-POM-l4,4-ZnOEP** have been exanimate (Fig. 4.17). Two processes are observed both anodic and cathodic process depending to the applied potential: if E < 0 V, a cathodic process is observed, whereas if applied potential is more than 0.0 V anodic process is present.

All the copolymer systems described in this work are very stable. The modified ITO electrodes could be reused many times without changes in their properties. That was not the case in our previous work, in which covalent porphyrin–POM conjugates were transferred by the Langmuir-Schaefer method. These electrodes showed some desorption with time.

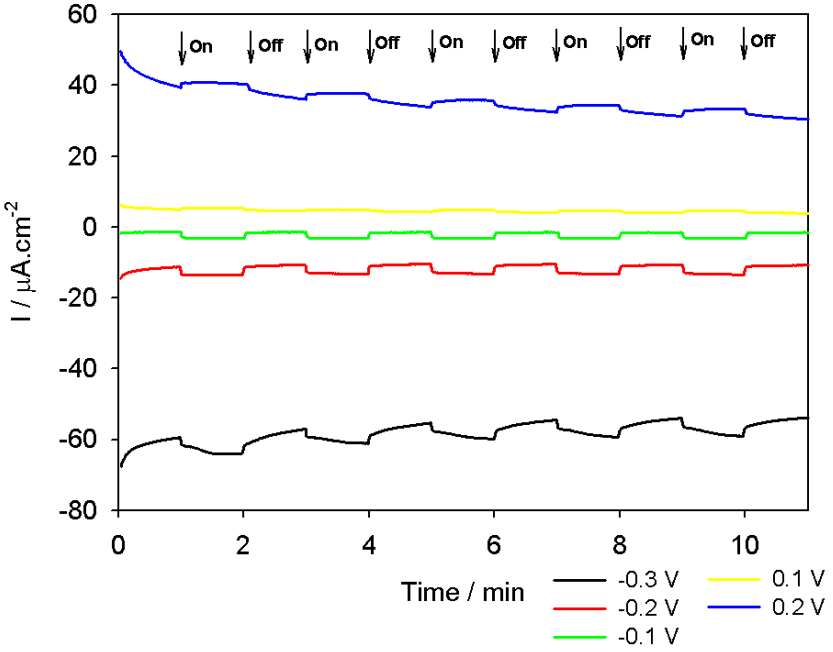

Fig. 4.17 Photoelectrochemical response of **poly-POM-l4,4-ZnOEP** (3 scans) (preparation of the film between -0.05 V and +1.90 V *vs.* SCE) under irradiation from 300 W Xe Arc lamp (with $\lambda \geq 385$ nm long pass filter) in H_2O containing I_3^- 5 mmol L^{-1} and I^- 0.5 mol L^{-1} with different BIAS potential.

3.5. Energy diagram of the electron transfer processes

To study the mechanism of light sensitization of the cathodic photocurrent, the energies of the relevant electronic states must be estimated. In the case of copolymer **poly-POM-l4,4-ZnOEP**, an energy-level diagram can be built by using the oxidation potential measured for **ZnOEP** and the reduction potential measured for the POM and the pyridinium subunits, together with the optical excitation of the porphyrins within the film (Fig. 4.18). It describes the thermodynamics for spectral sensitization of the ITO electrode. The calculated level of the excited state (-3.76 eV for $Porp^{\bullet+}$/Porp*) and the level of the ground state (-5.89 eV for $Porp^{\bullet+}$/Porp) for the film are taken in reference to the oxidation potential of the porphyrin (+1.39 V *vs.* NHE with a band gap of 2.13 eV at λ = 582 nm, measured on the film). The energy level of the couples $V^{V}{}_3POM/V^{IV}$ $V^{V}{}_2POM$, py+/$py^{\bullet}$, and I_3^-/I^- on the absolute scale are -4.80 eV (+0.30 V *vs.* NHE), -3.90 eV (-0.60 V *vs.* NHE), and -5.13 eV (+0.63 V *vs.* NHE) respectively, as shown in Fig. 4.18.

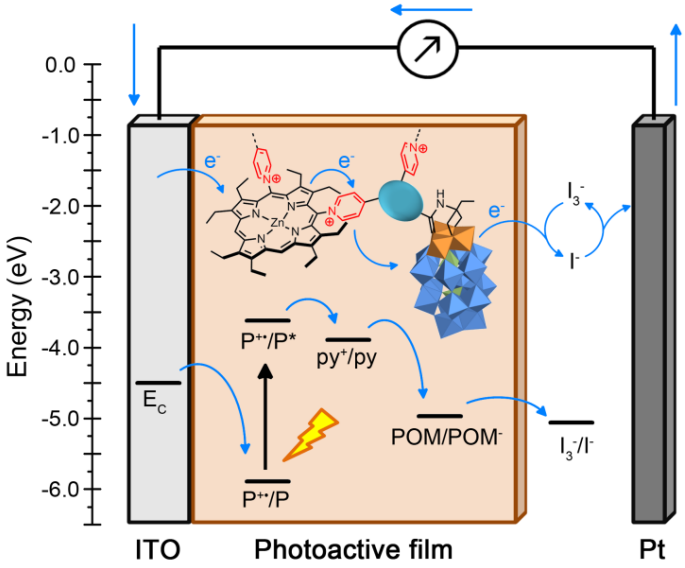

Fig. 4.18 Schematic representation of the internal layer structure of the film and an energy level diagram showing electron transfer processes.

Consequently, the photocurrent enhancement can be explained by the presence of the phosphovanadotungstate $[P_2W_{15}V_3O_{62}]^{9-}$ subunit, which is a strong electron acceptor and can oxidize the pyridyl radical initially formed by electron transfer from the excited porphyrin. The reduced POM can then give one electron to reduced I_3^-, while I^- can be reoxidized at the counter electrode (Fig. 4.18). The phosphovanadotungstate therefore participated in the electron relay via a downhill electrochemical cascade, which stabilized the separated charges (oxidized porphyrin and reduced POM), which are kept apart from each other. This hampers charge recombination and consequently enhances the photocurrent response. However, we must take into account not only the repulsion between I_3^- and the Dawson polyanion ($V^V_3POM^{5-}$), but also the attractive force between I_3^- and the py^+ spacer, which can be in favor of direct electron transfer between I_3^- and py^+.

4. Photocatalytical recovery of metals

4.1. Photocatalytical recovery of silver

Fig. 4.19 shows the evolution of the absorption spectrum during the visible ($\lambda > 385$ nm) irradiation of the sample contained quartz slide covered with **poly-POM-s4,4-ZnOEP** (A), **poly-POM-m3,3–**

ZnOEP (B), **poly-POM-l3,3-ZnOEP** (C), and **poly-POM-l4,4-ZnOEP** (D) films separately, under a deaerated aqueous solution of 8.0 $\times 10^{-5}$ mol L^{-1} Ag_2SO_4 and 0.13 mol L^{-1} propan-2-ol. Moreover, the solution turns pale yellow. After 5 hours of irradiation, all of the spectrum no longer changed, indicating the end of the reaction. Furthermore, no change in the spectrum has also been observed during one week following the experiment, showing that the formed silver nanoparticles are stable over time (at least one week).

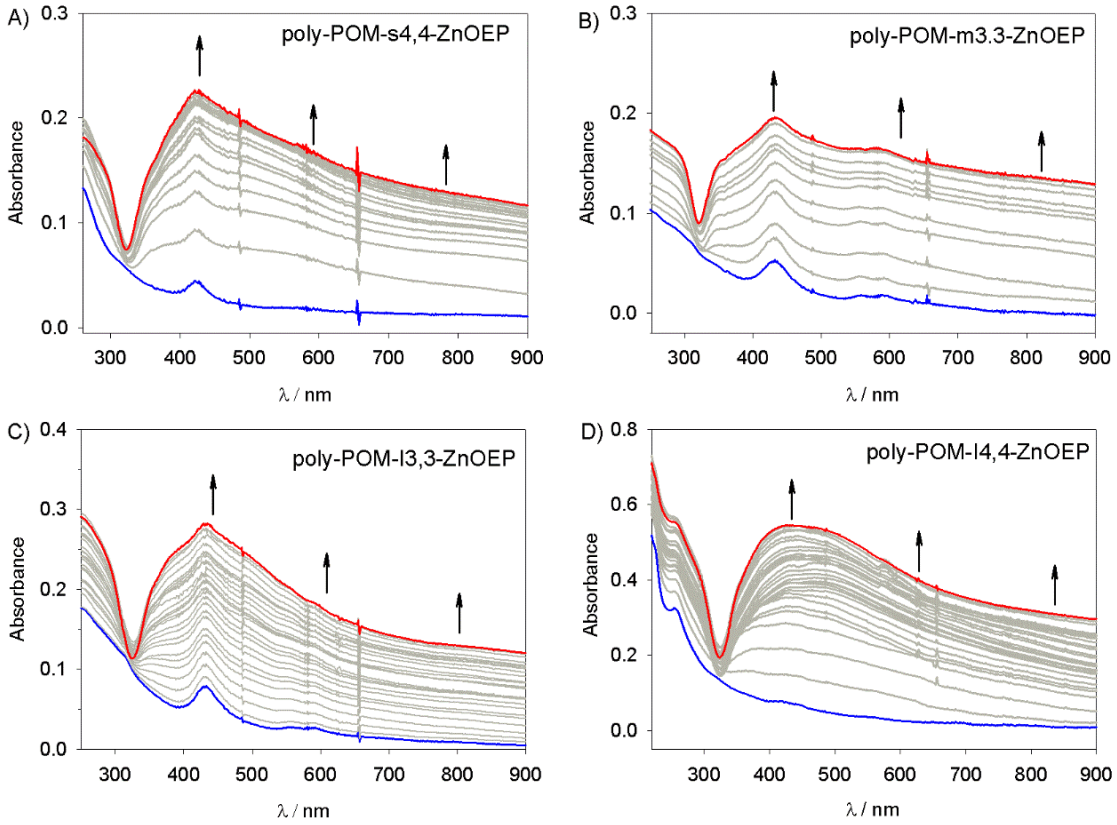

Fig. 4.19 Change in the UV–vis absorption spectrum of a deaerated aqueous solution of 8.0 $\times 10^{-5}$ mol L^{-1} Ag_2SO_4 and 0.13 mol L^{-1} propan-2-ol containing a slide of quartz modified with **poly-POM-s4,4-ZnOEP** (A), **poly-POM-m3,3–ZnOEP** (B), **poly-POM-l3,3-ZnOEP** (C), and **poly-POM-l4,4-ZnOEP** (D) films film under illumination.

During the photocatalysis, the increase in absorbance over the entire spectral range suggests that the Ag^+ cations are reduced to give large nanoparticles with probably inhomogenous shape. Large surface area of plasmon reflects large nano objects. Plot of the intensity of the absorbance (λ = 800 nm) versus the time of visible irradiation in the four systems show that they reach a plateau after nearly 45 minutes of irradiation indicating the end of the photoreduction (Fig. 4.20). The initial rates of Ag^+ reduction based on the four films were almost the same (~ 7.2 $\times 10^{-5}$ mol L^{-1} min^{-1}). UV–visible spectrum of the silver nanoparticle solution without the quartz slide covered with the film shows the presence of the

large plasmon band in the whole visible domain with a maximum around 430 nm (Fig. 4.21), which also suggest that the Ag^+ cations are reduced to give non uniform nanoparticles.[23]

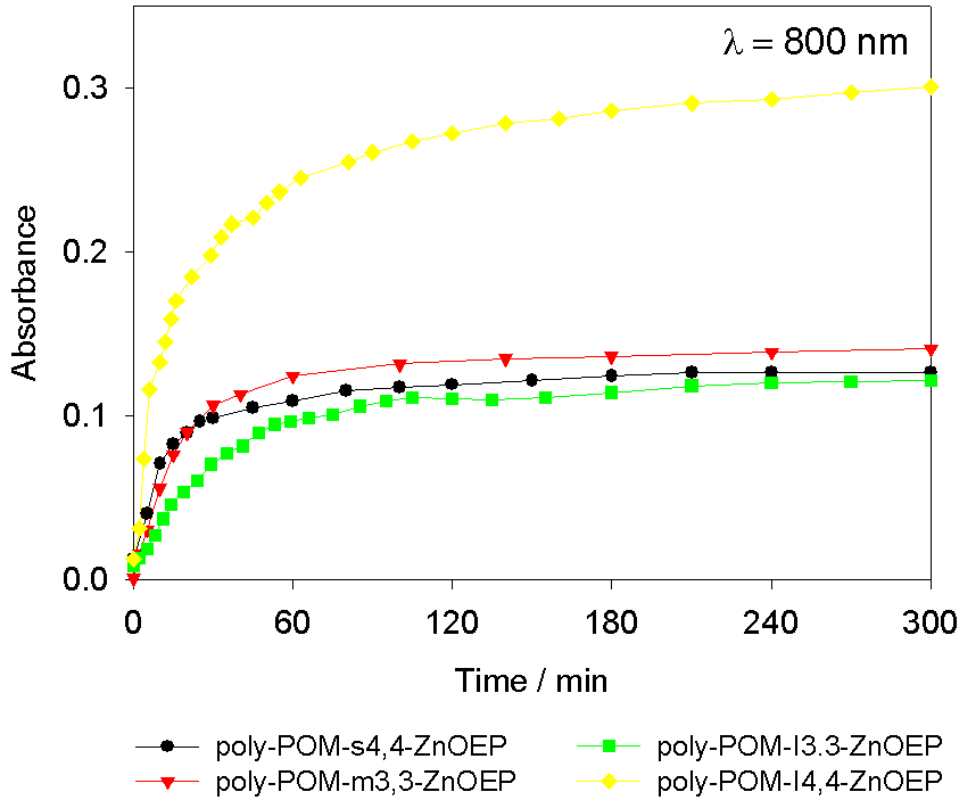

Fig. 4.20 Plots of the intensity of the absorbance at λ = 800 nm versus the time of irradiation.

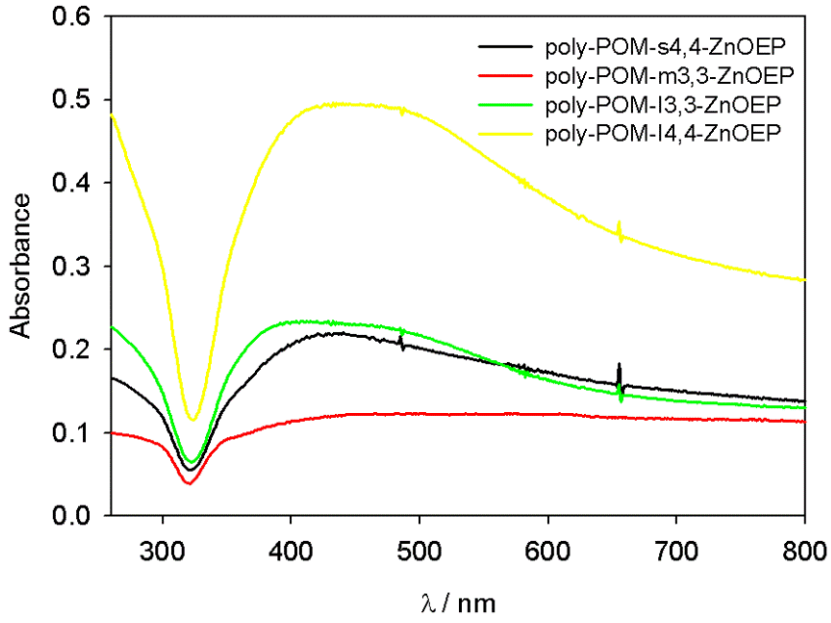

Fig. 4.21 Spectrum of the silver nanoparticles solution after photocatalysis.

All the copolymers gave different size and shape of silver nanoparticles. The transmission electron microscopy (TEM) images of the sample after irradiation confirm the formation of silver nanoparticles (Figs. 4.22-4.25). However, morphology of the obtained Ag nanomaterials by **poly-POM-s4,4-ZnOEP** have a diverse distribution in form and shape. The samples presented not only triangular but also irregular nanosheets (length 100-300 nm), spherical particles (diameter 10-20 nm) and also irregular nanowires (Fig. 4.22). The Ag nanostructures recovered by **poly-POM-m4,4-ZnOEP** showed mainly nanosheets together with nanoparticles. The presence of contrast fringes in TEM images of silver nanosheets could be due to stacking faults during crystallization (Fig. 4.23).

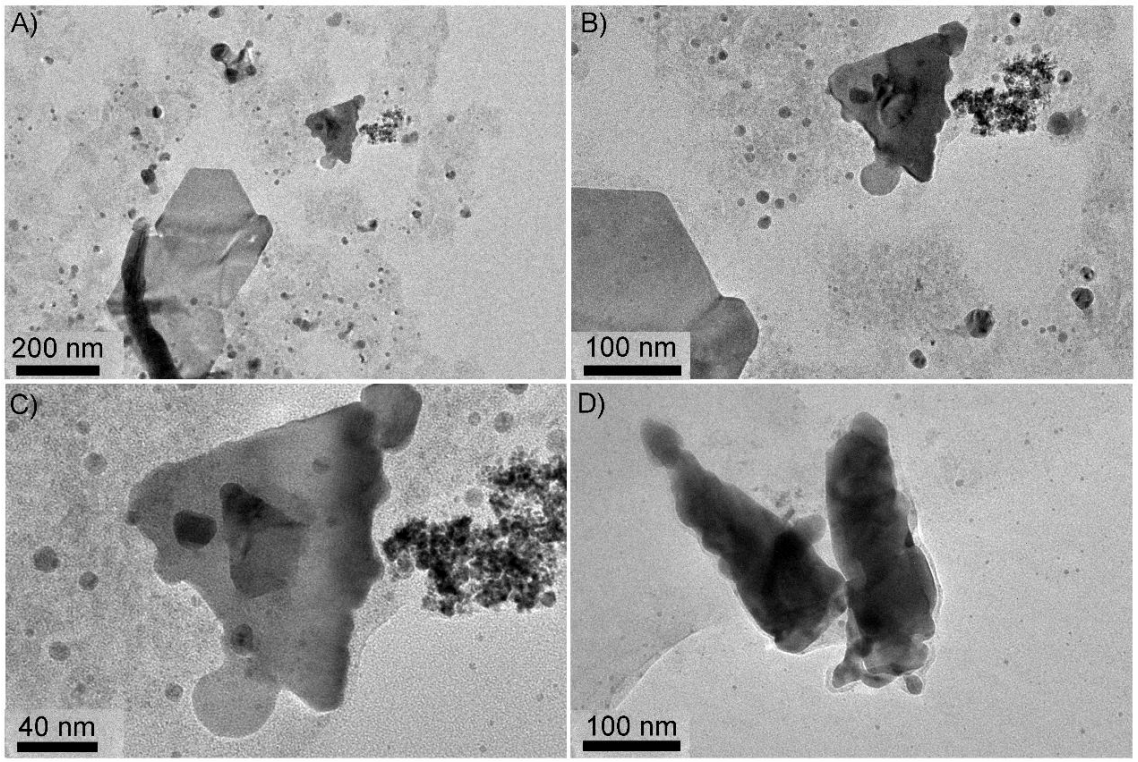

Fig. 4.22 TEM images of the platinum nanomaterials obtained with the **poly-POM-s4,4-ZnOEP** film in deaerated solutions 8×10^{-5} mol L^{-1} Ag_2SO_4.

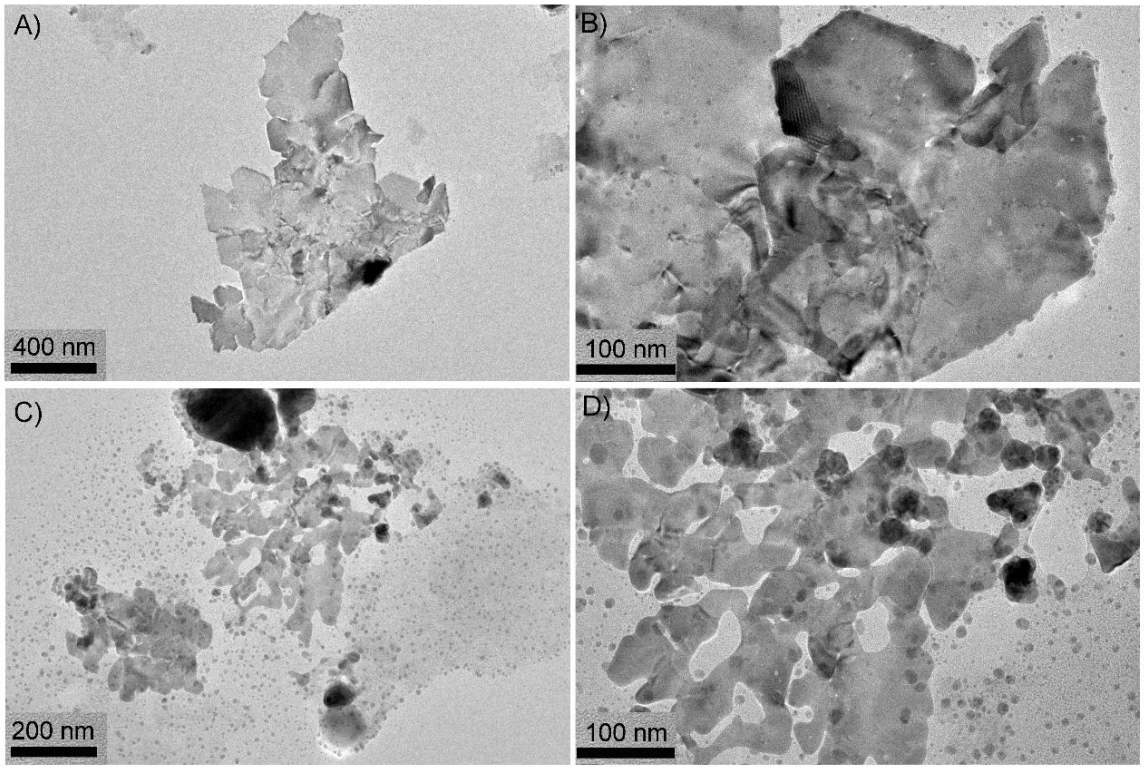

Fig. 4.23 TEM images of the platinum nanomaterials obtained with the **poly-POM-m4,4-ZnOEP** film in deaerated solutions 8×10^{-5} mol L^{-1} Ag_2SO_4.

TEM micrograph represent in Fig. 4.24 silver nanoparticles obtained for **poly-POM-l3,3-ZnOEP** showing mainly the formation of irregular spherical particles with diameters of 5-30 nm. In some part, ten to fifteen nanoparticles come into line like "ellipsis". TEM images of the silver nanostructure obtained for 300 min irradiation by **poly-POM-l4,4-ZnOEP** were in the shape of nanosheet mixed with nanoparticles (Fig. 4.25).

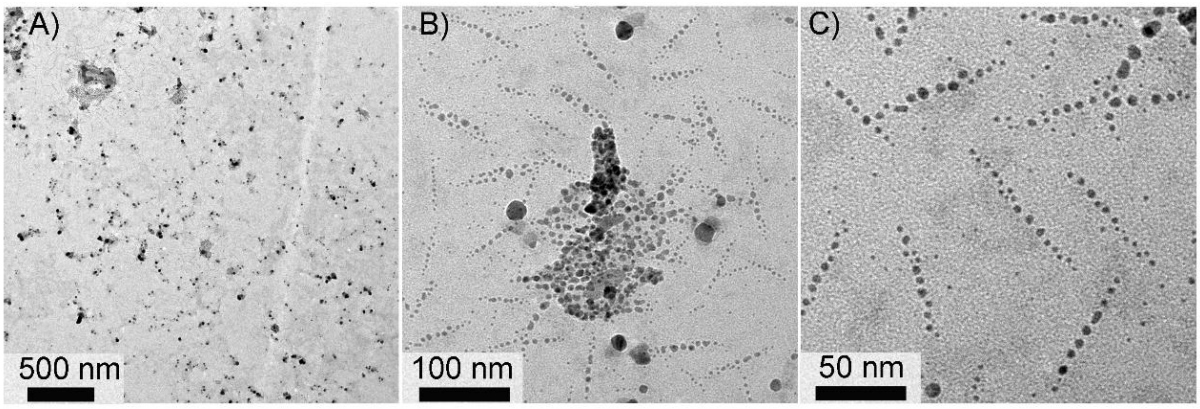

Fig. 4.24 TEM images of the platinum nanomaterials obtained with the **poly-POM-l3,3-ZnOEP** film in deaerated solutions 8×10^{-5} mol L^{-1} Ag_2SO_4.

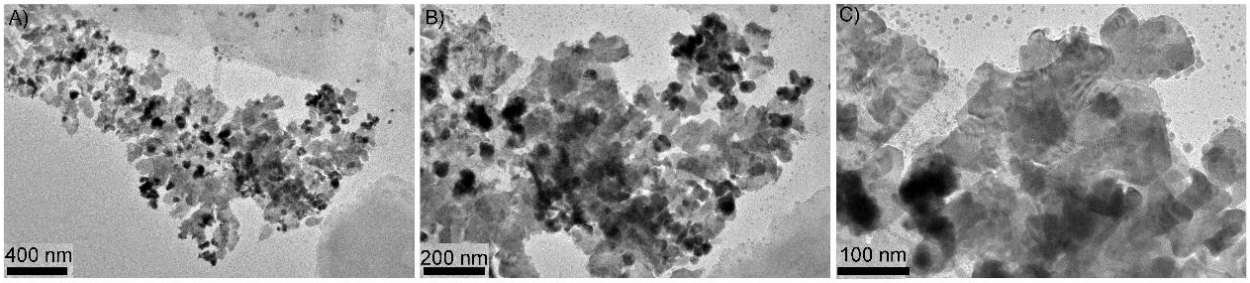

Fig. 4.25 TEM images of the platinum nanomaterials obtained with the **poly-POM-l4,4-ZnOEP** film in deaerated solutions 8×10^{-5} mol L^{-1} Ag_2SO_4.

4.2. Photocatalytical recovery of platinum

Photoreduction tests are also applied for the recovery of platinum ions. Under illumination **poly-POM-l4,4-ZnOEP** is able to rapid reduce Pt^{IV} ions proved by the decrease of characteristic absorption of Pt^{IV} ions, however, it's not accompanied also for this type of copolymers by any increase of the absorbance in the visible range (Fig. 4.26A). After 24 hours irradiation, we got black-brown sediment on the bottom of cuvette (Fig. 4.26A). The TEM pattern of the Pt particles indicated in Fig. 4.27 verify the formation of metal nanoparticles in the process using **poly-POM-l4,4-ZnOEP** as photocatalyst. Fig. 4.28 shows smaller particles of 1.7 ± 0.3 nm diameters were assembled to give larger spheres with an average diameter of 18.0 ± 3.2 nm. The obtained PtNPs using **poly-POM-s4,4-ZnOEP**, **poly-POM-m3,3–ZnOEP** and **poly-POM-l3,3-ZnOEP** as photocatalyst with the similar morphology that obtained from **poly-POM-l4,4-ZnOEP** as photocatalyst. Only that the obtained PtNPs using **poly-POM-m3,3–ZnOEP** as photocatalyst is a little bigger in diameter (average diameter of the assembled larger spheres is 28.0 ± 3.2 nm). The restriction of the size of the assembled spheres is partly depended on the photocatalyst.

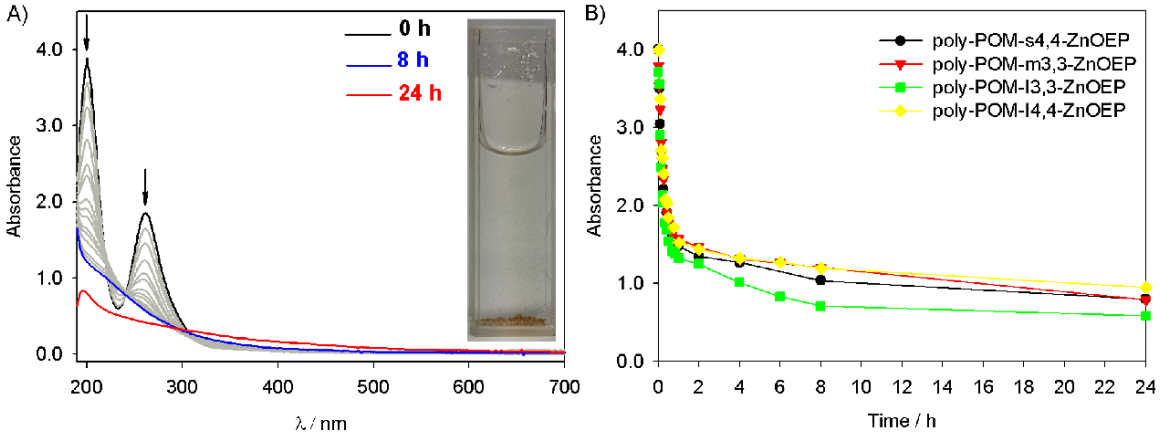

Fig. 4.26 A) Change in the UV–vis absorption spectrum of a deaerated aqueous solution of 1.6×10^{-4} mol L^{-1} H_2PtCl_6 and 0.13 mol L^{-1} propan-2-ol containing a slide of quartz modified with **poly-POM-l4,4-ZnOEP** film under illumination. Inset: photo of the obtained solution in the cuvette after the irradiation. B) Plot of the intensity of the absorbance at λ = 201 nm versus the time of irradiation.

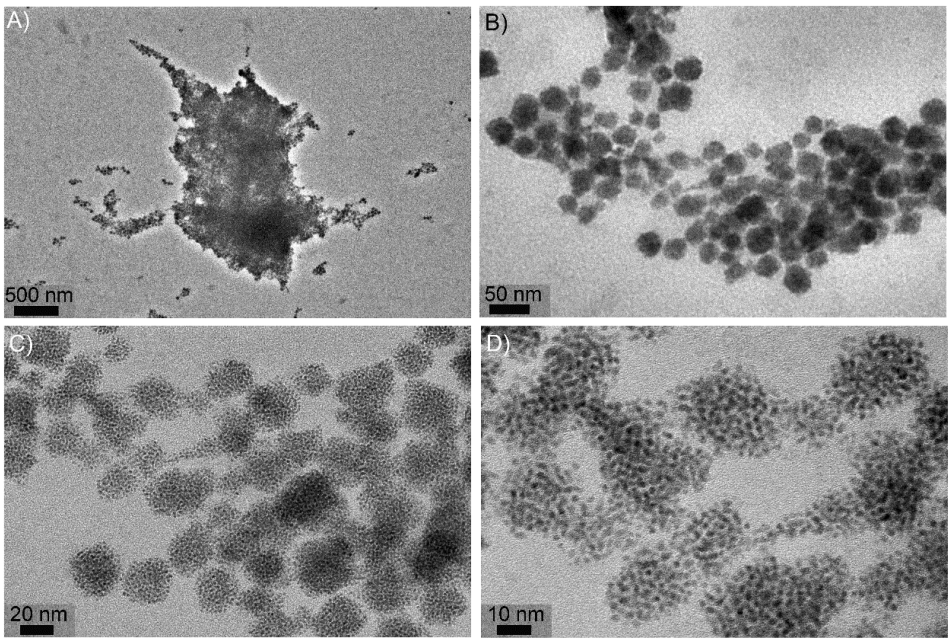

Fig. 4.27 TEM images of the platinum nanomaterials obtained with the **poly-POM-l4,4-ZnOEP** film.

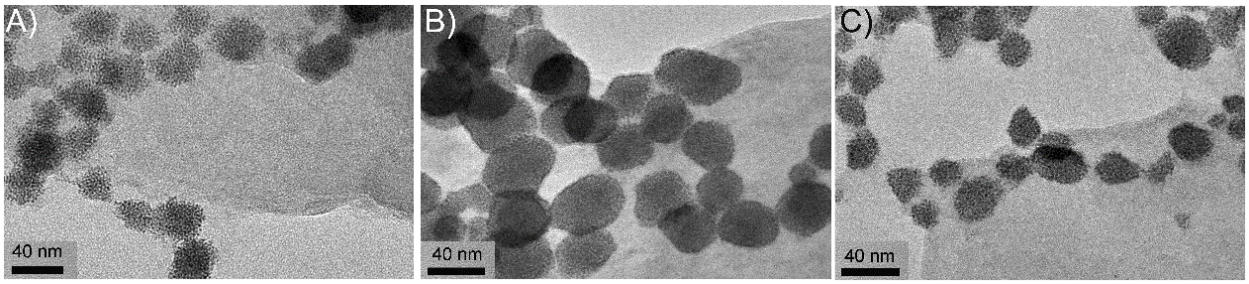

Fig. 4.28 TEM images of the platinum nanomaterials obtained with the **poly-POM-s4,4-ZnOEP** (A), **poly-POM-m3,3–ZnOEP** (B), **poly-POM-l3,3-ZnOEP** (C) film in deaerated solutions 1.6×10^{-4} mol L^{-1} H_2PtCl_6.

5. Conclusion

In this chapter, four conjugated POM-porphyrin electroactive films were obtained on ITO electrode surfaces during repetitive potential cycling. To investigate the effect of spacer between POM and porphyrins, diolamide functionalized Dawson $[P_2W_{15}V_3O_{62}]^{9-}$ framework bearing two pyridyl groups, in which the four POM monomers vary in the relative positions of the nitrogen atoms of the pyridine rings or in the distance from the carbonyl group allows us to form the corresponding copolymer with **ZnOEP**. The **poly-POM-l4,4-ZnOEP** film generated a higher photocurrent than that of **poly-POM-l3,3-ZnOEP**, which differs only in the position of the nitrogen atoms. It may be due to the higher conductivity for **poly-POM-l4,4-ZnOEP**, meantime together with the shorter distance between the chromophore and the porphyrin subunits in the **poly-POM-l3,3-ZnOEP** copolymer, which could promote charge recombination between the oxidized porphyrin and the reduced POM. Controlling the thickness of the film is crucial for the photocurrent-generation efficiency.

We also demonstrated the efficiency of these new copolymers in the photocatalytic reduction of Ag(I) and Pt(IV) using visible light.

Further developments must address the in situ measurement of the conductivity and optimization of the conductivity of the copolymers, as well studying the overall conversion efficiency η of the sealed cell. Improving the conductivity of the films will be also important. One possibility will be to introduce metal nanoparticles onto the surface.

References

(1) Long, D.-L.; Tsunashima, R.; Cronin, L. *Angew. Chem. Int. Ed. Engl.* **2010**, *49* (10), 1736.
(2) Mylonas, a.; Hiskia, a.; Papaconstantinou, E. *J. Mol. Catal. A Chem.* **1996**, *114* (1-3), 191.
(3) Troupis, a.; Hiskia, a.; Papaconstantinou, E. *Appl. Catal. B Environ.* **2003**, *42* (3), 305.
(4) Costa-Coquelard, C.; Schaming, D.; Lampre, I.; Ruhlmann, L. *Appl. Catal. B Environ.* **2008**, *84* (3-4), 835.
(5) Kahef, L. El; Gross, M.; Giraudeau, A. *J. Chem. Soc., Chem. Commun* **1989**, *49*, 1989.
(6) Giraudeau, A.; Ruhlmann, L.; El Kahef, L.; Gross, M. *J. Am. Chem. Soc.* **1996**, *118* (12), 2969.
(7) Ruhlmann, L.; Lobstein, S.; Gross, M.; Giraudeau, A. *J. Org. Chem.* **1999**, *64* (4), 1352.
(8) Giraudeau, A.; Lobstein, S.; Ruhlmann, L.; Melamed, D.; Barkigia, K. M.; Fajer, J. *J. Porphy. Phthalocy.* **2001**, *05* (11), 793.
(9) Ruhlmann, L.; Giraudeau, A. *Chem. Commun.* **1996**, No. 17, 2007.
(10) Ruhlmann, L.; Giraudeau, A. *Eur. J. Inorg. Chem.* **2001**, 659.
(11) Schaming, D.; Allain, C.; Farha, R.; Goldmann, M.; Lobstein, S.; Giraudeau, A.; Hasenknopf, B.; Ruhlmann, L. *Langmuir* **2010**, *26* (7), 5101.
(12) Favette, S.; Hasenknopf, B.; Vaissermann, J.; Gouzerh, P.; Roux, C. *Chem. Commun.* **2003**, No. 21, 2664.
(13) Allain, C.; Favette, S.; Chamoreau, L.; Vaissermann, J.; Ruhlmann, L.; Hasenknopf, B. *Eur. J. Inorg. Chem.* **2008**, *2008* (22), 3433.
(14) Li, J.; Huth, I.; Chamoreau, L. M.; Hasenknopf, B.; Lacôte, E.; Thorimbert, S.; Malacria, M. *Angew. Chemie - Int. Ed.* **2009**, *48* (11), 2035.
(15) Ruhlmann, L.; Schulz, A. *J. Am. Chem. Soc.* **1999**, *121* (8), 6664.
(16) Ruhlmann, L.; Hao, J.; Ping, Z.; Giraudeau, A. *J. Electroanal. Chem.* **2008**, *621* (1), 22.
(17) Azcarate, I.; Ahmed, I.; Farha, R.; Goldmann, M.; Wang, X.; Xu, H.; Hasenknopf, B.; Lacôte, E.; Ruhlmann, L. *Dalton Trans.* **2013**, *42* (35), 12688.
(18) Bruckenstein, S.; Shay, M. *Electrochim. Acta* **1985**, *30* (10), 1295.
(19) Aldebert, P.; Audebert, P.; Armand, M.; Bidan, G.; Pineri, M. *J. Chem. Soc. Chem. Commun.* **1986**, No. 22, 1636.
(20) Audebert, P.; Aldebert, P.; Pineri, M. *Synthetic Metals*, 1989, *32*, 1.
(21) Genies, E. M.; Hany, P.; Lapkowski, M.; Santier, C.; Olmedo, L. *Synth. Met.* **1988**, *25* (1), 29.
(22) Lowe, J.; Holdcroft, S. *Macromolecules* **1995**, *28* (13), 4608.
(23) Keita, B.; Brudna Holzle, L. R.; Ngo Biboum, R.; Nadjo, L.; Mbomekalle, I. M.; Franger, S.; Berthet, P.; Brisset, F.; Miserque, F.; Ekedi, G. a. *Eur. J. Inorg. Chem.* **2011**, *4* (8), 1201.

Chapter V

Poly-ZnOEP / Preyssler type-POM composite films based on electrostatic interaction for photocurrent generation

Chapter V: Poly-ZnOEP / Preyssler type-POM composite films based on electrostatic interaction for photocurrent generation

It is well known that the oxidation of the π-ring of a porphyrin proceeds via two one-electron steps generating respectively the π-radical cation and the dication. The reactivity of porphyrin π-radical cations and dications with nucleophilic compounds has been well studied.[1, 2, 3, 4] In the chapters II, III and IV we have shown that it is possible to form porphyrin-POM copolymers based on the nucleophilic attack of pyridyl groups as Lewis bases onto electrogenerated dications of porphyrins through $E(EC_NEC_B)_nE$ process. In this chapter, similar reaction of electropolymerization has been conducted using only dipyridyl ligands but without polyoxometalate. The polyoxometalates polyanion (POMs) being introduced onto the film by deeping the modified electrode in the aqueous solution of the Preyssler type of polyoxometalate ($[NaP_5W_{30}O_{110}]^{14-}$) giving the electrostatic hybrids film. Thus, in this chapter, two poly-zinc octaethylporphyrin/viologen/POM hybrid films were obtained through incorporating Preyssler type of polyoxometalate ($[NaP_5W_{30}O_{110}]^{14-}$, named **$P_5W_{30}$**) onto the poly-zinc octaethylporphyrin-viologen (poly-ZnOEP-V^{2+}, V = viologen) or onto the poly-zinc octaethylporphyrin-bis-viologen (poly-ZnOEP-V^{2+}-$(CH_2)_3$-V^{2+}) copolymers obtained by electro-oxidation of **ZnOEP** in the presence of 4,4'-bipyridine or 1,1''-(1,3-propanediyl)bis-4,4'-bipyridinium, respectively. Then, by metathesis reaction, the (partial) exchange of the initial counter ion PF_6^- by $[NaP_5W_{30}O_{110}]^{14-}$ gave the target hybrid copolymer (Fig. 5.11).[5] Such copolymers have been characterized by UV-vis spectroscopy, X-ray photoelectron spectroscopy (XPS), atomic force microscopy (AFM), EQCM (electrochemical quartz crystal microbalance) and QCM (quartz crystal microbalance) and electrochemistry. Both poly-ZnOEP-V^{2+}/$[NaP_5W_{30}O_{110}]^{14-}$ (named **poly-ZnOEP1/P_5W_{30}**) and poly-ZnOEP-V^{2+}-$(CH_2)_3$-V^{2+}/$[NaP_5W_{30}O_{110}]^{14-}$ (named **poly-ZnOEP2/P_5W_{30}**) composite film electrodes possessed a 3.4 times and 1.3 times higher photocurrent response than in the absence of polyoxometalate polyanions, respectively (Fig. 5.21). This was due to the appropriate redox potential of $[NaP_5W_{30}O_{110}]^{14-}$ which acted as strong electron acceptor. EQCM and QCM was employed to monitor the mass change during the poly-ZnOEP-V^{2+} (**poly-ZnOEP1**) and poly-ZnOEP-V^{2+}-$(CH_2)_3$-V^{2+} (**poly-ZnOEP2**) copolymers electrodeposition (7.9 and 5.7 $\mu g.cm^{-2}$ respectively, applied potential:

+1.90 V, elapsed time: 180 s) and also for the incorporation process of $[NaP_5W_{30}O_{110}]^{14-}$ (P_5W_{30}) (0.61 and 0.77 $\mu g.cm^{-2}$ respectively, soaking time: 1 hour).

1. Introduction

Solar energy, as the cleanest and least limited energy source, becomes increasingly hot over recent years. Aromatic units with complex structures, such as porphyrins, although have unique photophysical properties, such as strong absorptions, ultrafast photoinduced charge separation, are faced with short-lived charge separation and undesirable backward charge recombination. Polyoxometalates (POMs) are metal-oxygen cluster anions constituted of metal elements in their highest oxidation state.[6] Typically, owing to their robustness and large number of metallic centers, POMs can undergo reversible and multi-electron photoredox processes, like an electron shuttle in the system, without structural alteration. At the same time, it is feasible to modify the structure (Lindqvist, Keggin, Dawson, Sandwich types...) and change the metal (V^V, Nb^V, Mo^{VI}, W^{VI}, Fe^{III},…) of the POMs to adjust the redox potentials, so as to match the thermodynamic energy level of the porphyrin. Preyssler-type POMs $Na_{14}[NaP_5W_{30}O_{110}]$ have been applied to photochromic[7] and thermochromic[8] composite films with good reversibility and stability. Compared with classical POMs, Preyssler-type POMs are less investigated in molecular photovoltaic system.

In the present chapter, we adsorb $[NaP_5W_{30}O_{110}]^{14-}$ (**P_5W_{30}**) onto two kinds of electropolymerized **poly-ZnOEP** films, separately choosing a rigid (viologen) or firstly synthesized and more flexible (bis-viologen, V^{2+}-$(CH_2)_3$-V^{2+}) bridging spacer between the **ZnOEP** macrocycles. XPS analyses and UV-visible absorption spectroscopy have been carried out to determine the elemental composition and spectrum of the films before and after the incorporation of $[NaP_5W_{30}O_{110}]^{14-}$. $[NaP_5W_{30}O_{110}]^{14-}$ was an efficient electron shuttle between the excited **ZnOEP** and viologen (or bis-viologen) which effectively retarded the fast charge pair recombination. We systematically investigated photocurrent generation of **poly-ZnOEP/P_5W_{30}** under visible-light illumination in the presence of I_3^-/I^- as redox mediator.

2. Formation two poly-ZnOEP-Preyssler type-POM composite films

2.1. Electropolymerization of poly-ZnOEP films with viologen or bis-viologen spacer

The general electropolymerization procedure used to deposit the porphyrin-based polymers onto ITO electrode surfaces is relied on the polarization of the working electrode at the second porphyrin-based oxidation potential to produce $ZnOEP^{2+}$, which is readily involved in a series of intermolecular cascade reactions leading to formation of oligomers and polymers (Fig. 5.1).

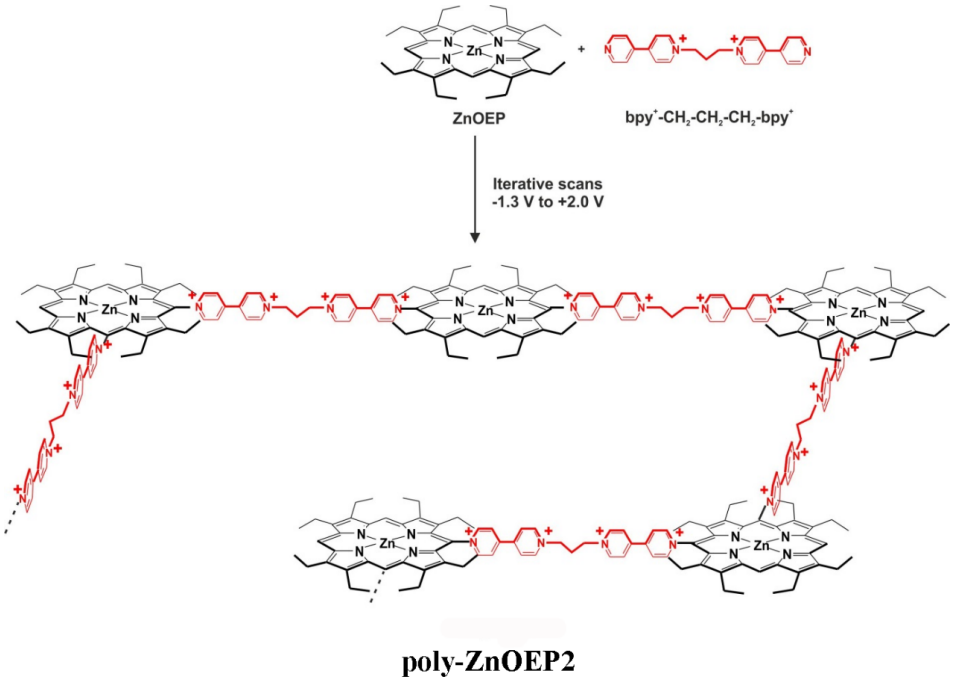

Fig. 5.1 General "zig-zag" polymerization scheme of **ZnOEP** in the presence of $bpy^{+}–CH_2–CH_2–CH_2–{}^{+}bpy\ 2PF_6^{-}$.

In this chapter, we chose a rigid (viologen, named V^{2+}) or a more flexible (bis viologen, named V^{2+}-$(CH_2)_3$-V^{2+})[9] as bridging bis-nucleophile between the **ZnOEP** macrocycles. For convenience, the obtained **ZnOEP** polymers were called **poly-ZnOEP1** and **poly-ZnOEP2**, respectively.

Fig. 5.2 represents the CVs during the iterative scan deposition. During the preparation of **poly-ZnOEP1** (Fig. 5.2A), after the first scan, three reduction peaks appeared. The reduction peaks at ca. 0.00 V and -0.69 V were the reduction of viologens spacers. The small reduction peak in the middle at ca. -0.36 V came from the reduction of the bipyridinium substituents.[3] In the preparation of **poly-ZnOEP2** (Fig. 5.2B), the first scan toward negative potentials reveals one irreversible pyridinium-

centered reduction,[10] whereas several porphyrin-based irreversible oxidation waves are observed on the reverse scan (anodic part), the first ones seen at E_p = +0.68 V and +0.94 V *vs.* SCE being attributed to the first and second porphyrin- based oxidations of the **ZnOEP** monomer. The irreversible waves observed at higher potential values are then attributed to the oxidation of porphyrin or isoporphyrin rings incorporated within the in situ-generated oligomers.[11] As the electrode coating proceeds further with the number of scans, all these oxidation signals are seen to disappear at the expense of one main irreversible oxidation wave observed above +1.5 V. The continuous changes observed on the CV curves depicted in Fig. 5.2A and Fig. 5.2B have unambiguously been attributed to the growth of a copolymeric material adsorbed at the electrode surface. In the cathodic domain of with (bpy^+-CH_2-CH_2-CH_2-$^+$bpy)$2PF_6^-$ as nucleophiles (Fig. 5.2B), the reduction peaks observed at ca. −0.26 V, −0.73 V and −0.93 V *vs.* SCE have been attributed to electron transfers centered on the electrogenerated viologen units introduced between two porphyrins.[11, 4,12] The continuous increase in the peak current values measured on these reduction waves appears therefore as a clear experimental evidence supporting a regular growth of the copolymeric film onto the ITO working electrode.

It should also be mentioned that no polymerization occurred when the initial scan direction was reversed below the second porphyrin-based oxidation potential.[3] The key point in the electropolymerization process is thus clearly the chemical reactivity of the methylylidene carbon atoms linking the pyrrole subunits in the porphyrin dication, a species which is then readily transformed into an isoporphyrin in the presence of nucleophilic species.[13,4,14]

Use of starting materials featuring two accessible nucleophilic sites is thus highly advantageous as such species can be involved in a series of intermolecular cascade reactions leading to polymeric materials. According to statistics, the nucleophilic attack could potentially occur with an equal probability at any of the "free" *meso* positions (5, 10, 15 and 20) of the **ZnOEP** skeleton. Oxidation of the intermediate oligomers might also promote the introduction of up to four pyridine substituents per porphyrin ring and ultimately lead to the formation of a large variety of polymeric materials. Previous works however support the assumption that the electropolymerization procedure in fact mainly leads to "zig-zag" copolymers[15,1] wherein only two viologen units are covalently linked to the 5,10- or 5,20-positions of the porphyrin rings (Fig. 5.1). We also found that the kinetics of the nucleophilic attack on the π-radical cation $ZnOEP^{+\bullet}$ is slow and that the expected substitution reactions does not occur at the electrode

surface but only in the bulk electrolyte. Another consequence of these kinetic issues is that the substitution degree of the porphyrin products evolves quite significantly with the potential value applied during electrolyses.[16,2,1,17] As mentioned above, the electropolymerizations described in this chapter, involving a nucleophilic attack of Lewis bases onto electrogenerated porphyrin-based dications produced in-situ by oxidation at 0.94 V, mainly lead to "zig-zag" copolymers adsorbed at the electrode.[13]

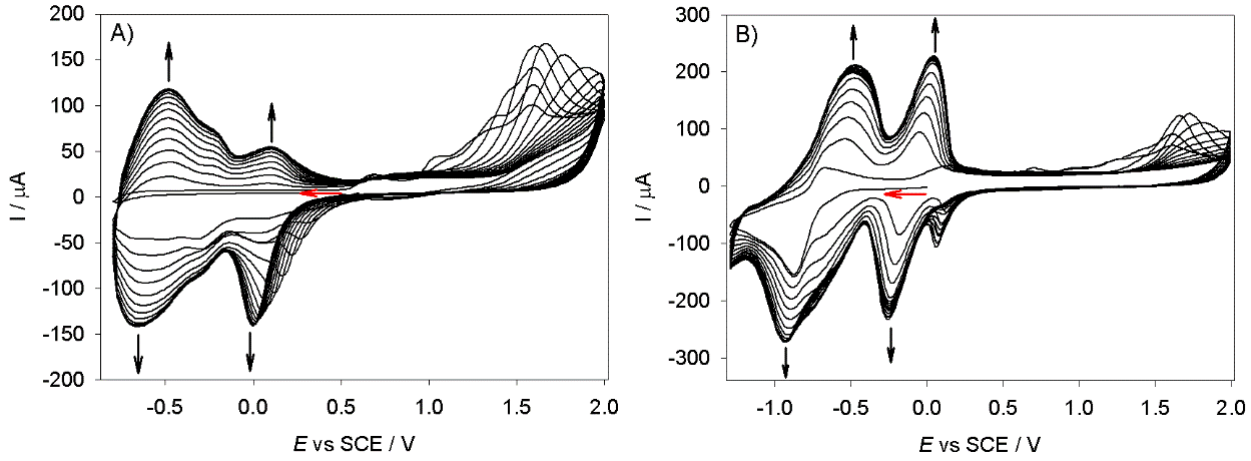

Fig. 5.2 Cyclic voltammograms recorded during 15 iterative scans conducted between −1.30 V and +2.00 V/SCE in a 1,2-$C_2H_4Cl_2$/CH_3CN (4/1) solution of **ZnOEP** (0.25 mmol L^{-1}) in the presence of A) 4,4'-bpy and B) (bpy^+-CH_2-CH_2-CH_2-$^+$bpy)$2PF_6^-$ (0.25 mmol L^{-1}) and $TBAPF_6$ (0.1 mol L^{-1}). WE: ITO. S = 1 cm^2. v = 0.2 V s^{-1}. (*) this wave is attributed to the reduction of an isoporphyrin intermediate.

2.2 Characterization of poly-ZnOEP with viologen or bis-viologen as spacer

2.2.1 EQCM for the copolymer deposition

The electrosynthesis of **poly-ZnOEP1** and **poly-ZnOEP2** by fixed potential (+1.90 V) have been monitored by EQCM. It should be point out that because it is impossible to realize the iterative scan starting on 0.00 V, and for better application, the film synthesis should avoid more electrochemical process such as the redox of pyridiniun to keep the film "purity". Fig. 5.3 illustrates the simultaneously recorded the constant voltage deposition and the mass changes. Indeed, from EQCM, the quartz resonance frequency (Δf) presented a decrease as time go on, which corresponded to the increase of the copolymer mass during the electrosynthesis. Using Sauerbrey's equation,[18] the change in mass of the

working electrode during the electropolymerization was quantified from the changes in the resonance frequency. In the present investigation, coverages after 180s were about 7.9 and 5.7 μg cm^{-2} for **poly-ZnOEP1** and **poly-ZnOEP2**, respectively. And the calculated surface coverage Γ was 7.571×10^{-9} and 4.68×10^{-9} mol cm^{-2} for **poly-ZnOEP1** and **poly-ZnOEP2**, respectively. Moreover, in the case of **poly-ZnOEP2**, the experimental copolymer mass deposited per charge unit gives 0.326 mg/C. The theoretical yield of the copolymer mass deposited per charge unit according to Fig. 5.1 can be calculated and is equal to 3.15 mg/C in the case of **poly-ZnOEP2** (with one V^{2+}-$(CH_2)_3$-V^{2+} spacer per **ZnOEP**). Thus, the calculated current yield is 10.3% for **poly-ZnOEP2**, and 6.6% in the case of **poly-ZnOEP1**.

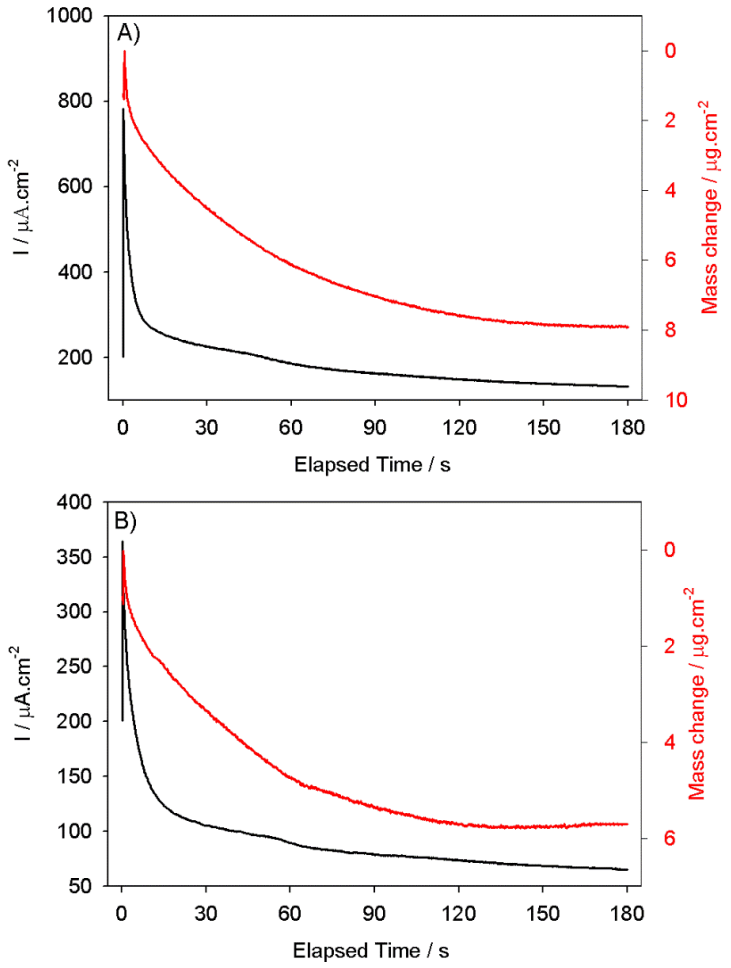

Fig. 5.3 Fixed potential deposition (+1.90 V) and electrochemical quartz crystal microbalance measurements during the electropolymerization of 0.25 mmol L^{-1} 4,4'-bpy A) and bpy^{+}-CH_2-CH_2-CH_2-^{+}bpy $2PF_6^-$ B) with 0.25 mmol L^{-1} **ZnOEP** in CH_3CN/1,2-$C_2H_4Cl_2$ (1/4) in the presence of 0.1 mol L^{-1} $TBAPF_6$. Working electrode: ITO (A = 0.2 cm^2) deposited on a 9.08 MHz AT-cut quartz crystal.

2.2.2 Cyclic voltammetric investigations of the polymeric films

Electroactive polymers deposited by cyclic voltammetry (n iterative scans) on ITO surfaces have been characterized by electrochemical methods. The CV curves shown in Fig. 5.4 have been recorded with a polymer grown on the electrode surface upon repeatedly scanning (25 cycles) its potential between 0.0 V and +2.0 V. The electrode was then removed from the electrochemical cell, washed with CH_3CN and used as working electrode in a clean electrolytic solution containing only the solvent and the supporting electrolyte (Fig. 5.4 and Fig. 5.5). The previous papers have already well discussed the redox process of **poly-ZnOEP1**.[3] The reduction peaks at ca. 0.00 V (peak I) and -0.67 V (peak III) were the reduction of viologens spacers. The small reduction peak in the middle at ca. -0.36 (peak II) came from the reduction of the bipyridinium substituents (Table 1 and Fig. 5.4A). In the case of **poly-ZnOEP2**, five reversible waves are observed in the cathodic domain (Table 1 and Fig. 5.4B). The first well defined, bell-shaped, reduction wave observed at −0.12 V vs. SCE (peak I) is attributed to the formation of viologen radical cations in the polymer ($V^{2+} \rightarrow V^{+\bullet}$). The second viologen-centered electron transfer ($V^{+\bullet} \rightarrow V^{0}$) is then surprisingly observed as two successive waves at −0.52 V and −0.66 V *vs.* SCE (peaks II_a and II_b).

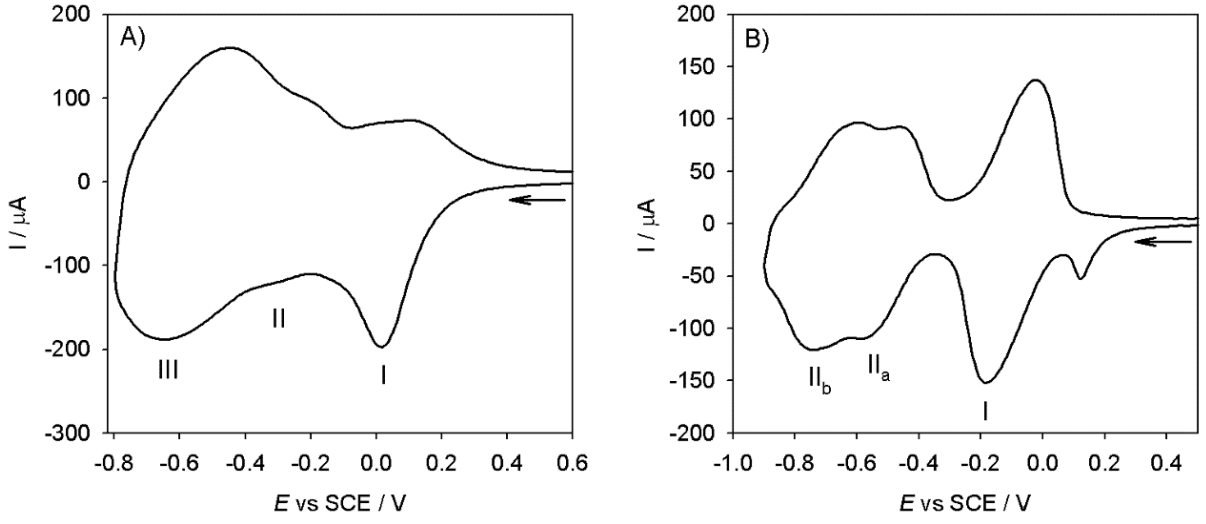

Fig. 5.4 Cyclic voltammograms of A) **poly-ZnOEP1** and B) **poly-ZnOEP2** film obtained after 25 scans in 1,2-$C_2H_4Cl_2$/CH_3CN (4/1) and 0.1 mol L^{-1} $TBAPF_6$. WE: ITO. S = 1 cm^2. *v* = 0.1 V s^{-1}.

A similar splitting appears on the porphyrin-centered reduction observed as two distinct waves at −1.33 V and −1.58 V *vs.* SCE (peaks III_a and III_b, Fig. 5.5). The relative number of electron involved in each

redox process has been estimated by integration of the successive peaks seen on the CV curve. In agreement with the apparent reversibility of the first viologen-centered reduction, a similar charge was obtained by integration of the cathodic (−333 ± 10 μC cm^{-2}) and anodic signals (332 ± 10 μC cm^{-2}) corresponding to the $V/V^{+\bullet}$ redox couple. A similar charge of −351 ± 10 μC cm^{-2} was obtained by simultaneous integration of both following signals, II_a and II_b, and here again the reversibility was checked by integration of the corresponding reoxidation waves yielding a charge of +350 ± 10 μC cm^{-2}. Integration of both porphyrin-based reduction peaks, III_a and III_b, was much more difficult to achieve but to a first approximation, the charge measured for both reduction signals was estimated at 201 ± 10 μC cm^{-2}. Taking as a reference the first viologen-centered reduction wave, attributed to the two-electron reduction of the bis-bipyridinium linker yielding the reduced polymer $–[ZnOEP–V^{+\bullet}–(CH_2)_3–V^{+\bullet}]_n–$, the charges measured on the other signals thus strongly support the assumption that the reduction waves noted II_a and II_b involves 2.1 electrons per repeated subunit while the reduction waves noted III_a and III_b (reduction of the ZnOEP units) involves only 1.1 electron per repeated unit.

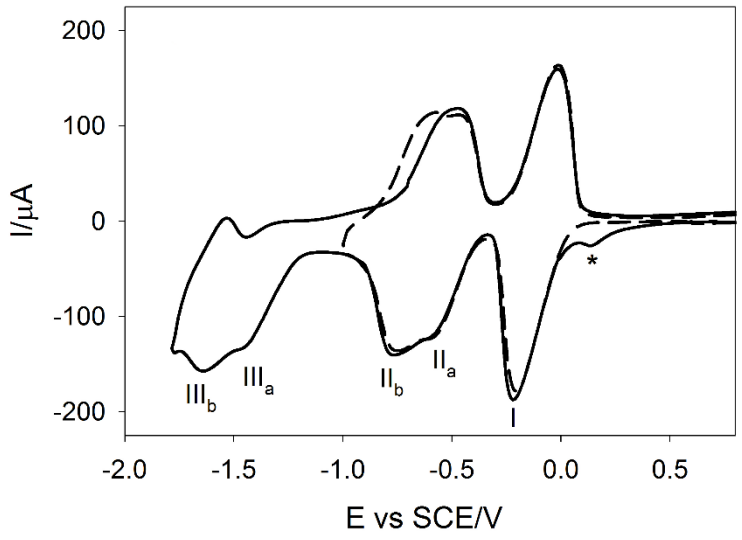

Fig. 5.5 Cyclic voltammograms of poly-ZnOEP2 film obtained after 25 scans in 1,2-$C_2H_4Cl_2$/CH_3CN (4/1) and 0.1 mol L^{-1} $TBAPF_6$. WE: ITO. S = 1 cm^2. v = 0.1 V s^{-1}. Peaks I, II_a and II_b: first and second reduction of the viologen spacers in the polymer, Peaks III_a and III_b are attributed to the first reduction of the ZnOEP porphyrin. (*) this wave is attributed to the reduction of an isoporphyrin intermediate. It is only observed in the first scan.

The surface coverage of the modified ITO electrode was then determined using the equation: $\Gamma = Q/nFA$, where Γ is the surface coverage in mol/cm^2, Q is the charge in coulombs, A is the areas in cm^2, and n is the number of electron transferred during the considered redox transformation. The value of Q was determined by integration of the area under the cathodic peak recorded after 25 iterative scans. Surface coverages, determined using the first or second viologen-based reduction peaks, were found to range from 1.82 to 1.72 $\times 10^{-8}$ mol cm^{-2}.

The most striking feature of the CV curve shown in Fig. 5.5 is that the wave splitting phenomenon is not observed for the first electron transfer leading to the formation of the bis-radical $V^{+\bullet}$-$(CH_2)_3$-$V^{+\bullet}$ but only on the following redox processes leading to the production of $V^{+\bullet}$-$(CH_2)_3$-V^0 and V^0-$(CH_2)_3$-V^0 in the polymer. Assuming that one bis-viologen linker and one **ZnOEP** are involved in the *mer* unit -[ZnOEP-V^{2+}-$(CH_2)_3$-V^{2+}]-, which repeats itself throughout the polymer, it is also quite unexpected to observe two successive reduction centered on the porphyrin ring (III_a et III_b). These successive reductions, observed at -1.33 and -1.58 V, could potentially be attributed either to the first and second porphyrin-centered reductions ($P \rightarrow P^{\bullet -} \rightarrow P^{2-}$) or to the first reduction of two non-equivalent, or interacting, porphyrins in the polymer ($P_a \rightarrow P_a^{\bullet -}$ and $P_b \rightarrow P_b^{\bullet -}$). However, the number of electron exchange measured for the reduction waves noted III_a and III_b (reduction of the **ZnOEP** units) is only 1.1 electron per *mer* unit which is more in favor of the second proposal. Moreover, in the case of copolymer already reported with only one viologen spacer (**poly-ZnOEP1**), the reduction of the **ZnOEP** units were always near -1.3 V *vs.* SCE (without splitting of the wave), close to the first reduction of the porphyrin-ring for the **poly-ZnOEP2** film (peak III_b).[14,17]

These phenomena most probably arise from the specific polymer's structure and from communication/interaction processes occurring between neighboring redox active fragments in the chain or between chains. The exact structure of the polymer is still not well established but the most important result is that such electrochemical signature has never been observed before with other porphyrin/bipyridinium electrode materials build from simple viologens, the resulting electrode material usually showing broad and unresolved bipyridinium and porphyrin-based reduction waves.[1,2,15,19,20]

At first sight, the unusual signature observed when the flexible alkyl-linked bis-viologen is involved,

might be explained by a local desymmetrization occurring in the film after formation of the viologen radical cations. Introduction of a propyl linker in the polymer has actually many electronic and structural effects which might be responsible for the observed experimental data; the resulting materials being for instance much less organized, more flexible and less conjugated than those based on the rigid 4,4'-bis-bipyridinium subunit.

Anion undoping and/or electrostatic attraction/repulsion processes associated to the electrogeneration of the $V^{+\bullet}$-$(CH_2)_3$-$V^{+\bullet}$ units in this "flexible" **poly-ZnOEP2** material might for instance trigger a range of molecular reorganizations within the film leading to symmetry breaking. The relative flexibility of the copolymer could moreover potentially authorize the interchain formation of CT complexes involving the pyridinium acceptors and the porphyrin donors. Depending on the redox state of each subunit in the polymer, such weak associations could be either turned on or of and promote significant structural/electronic changes within the flexible copolymer.

In the absence of further structural data on the copolymer and on the redox properties on the isolated repeating unit, which we have not been able to isolate so far, it is quite difficult to give a definitive explanation for the observed experimental data. As mentioned above, the splitting seen in the viologen and porphyrin-based reduction waves might be due to structural rearrangements occurring within the film after the first viologen-centered reduction yielding the doubly reduced $V^{+\bullet}$-$(CH_2)_3$-$V^{+\bullet}$ unit.

On the cyclic voltammograms depicted in Fig. 5.2B, it is clearly seen that after 12-13 scans, no oxidation signal remains in the investigated positive potential range. This result suggests that the cationic porphyrin rings in the copolymer can only be oxidized at potentials higher than +2.0 V *vs.* SCE.

Another important point to be raised is the absence of a visible signature of the monomer **ZnOEP** from the second iterative scan. It can be explained by the strong electrostatic repulsion during the oxidation between the cationic copolymer and $ZnOEP^{+\bullet}$ or suggesting that the film have a poor conductivity.

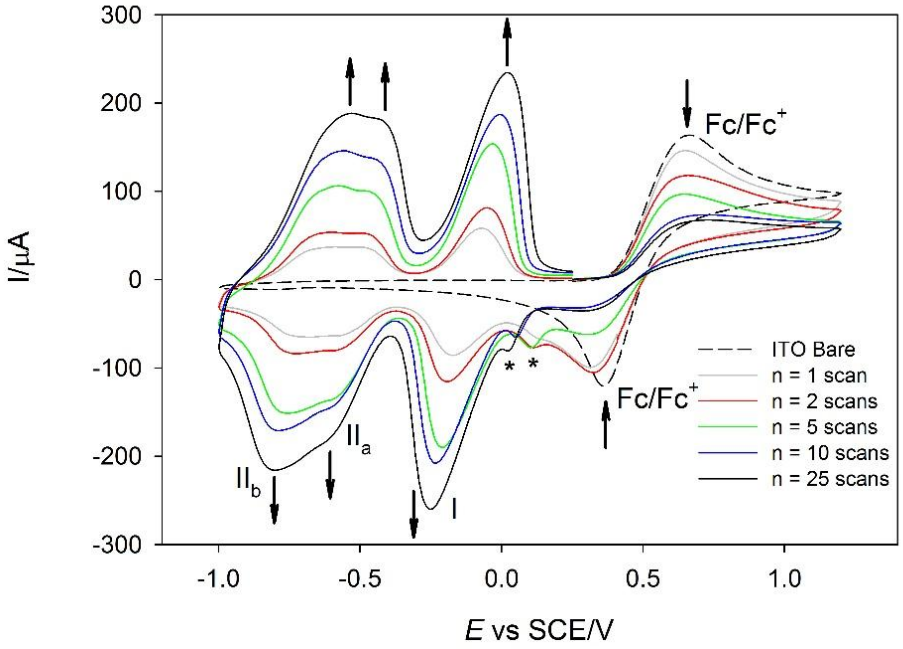

Fig. 5.6 Cyclic voltammograms of poly-ZnOEP2 obtained after n scans (n = 1, 2, 5, 10 and 25) in 1,2-$C_2H_4Cl_2$/CH_3CN (4/1), 0.25 mmol L^{-1} Fc and 0.1 mol L^{-1} $TBAPF_6$. WE: ITO. S = 1 cm^2. v = 0.1 V s^{-1}. Peaks I, II_a and II_b: first and second reduction of the viologen spacers in the polymer. The dotted line corresponds to the cyclic voltammogram of bare ITO in 1,2-$C_2H_4Cl_2$/CH_3CN (4/1), 0.25 mmol L^{-1} Fc and 0.1 mol L^{-1} $TBAPF_6$. (*) This peak is attributed to the reduction of an isoporphyrin intermediate and observed only for the first scan.

The correlation between film thickness and conductivity was appraised upon recording the cyclic voltammogram of ferrocene (Fc), dissolved in the electrolyte, at polymer modified electrodes. The oxidation and reduction of Fc are always observed but the intensity of the signals decreases, while ΔE_p increases, with the thickness of the film. A similar behavior was observed when investigating films generated at constant applied potential (+1.90 V *vs.* SCE, Fig. S5.1 in the Appendix). All these experimental data thus clearly support the fact that the conductivity of the film decreases with increasing film thickness (Fig. 5.6).

Table 1 Electrochemical data for **ZnOEP**, **bpy$^+$-CH$_2$-CH$_2$-CH$_2$-$^+$bpy 2PF$_6^-$**, **TBA$_{14}$[NaP$_5$W$_{30}$O$_{110}$]**, **poly-ZnOEP1**, **poly-ZnOEP2**, **poly-ZnOEP1/P$_5$W$_{30}$** and **poly-ZnOEP2/P$_5$W$_{30}$**.

Compounds	**Ring oxidation[a]**		**Reduction of py$^+$ or viologen (V^{2+})[b]**			**Reduction[b]**		
ZnOEP[c]	0.92	1.18					-1.36	
	(75)	(75)					(65)	
bpy$^+$(CH$_2$)$_3$bpy$^+$ 2PF$_6^-$[c]				-0.57				
				(208)				
TBA$_{14}$[NaP$_5$W$_{30}$O$_{110}$][c]						-0.42	-0.80	-1.01
						(72)	(70)	(110)
poly-ZnOEP1[d]	1.23^{irr}	1.80^{irr}	-0.02	-0.35	-0.62			
			(31)	(105)	(68)			
poly-ZnOEP2[d]	1.25^{irr}	1.82^{irr}	-0.12	-0.47	-0.59			
			(60)	(47)	(57)			
poly-ZnOEP1/P$_5$W$_{30}$[d]	1.18^{irr}	1.82^{irr}	-0.09	-0.36	-0.61			
			(41)	(120)	(60)			
Poly-ZnOEP2/P$_5$W$_{30}$[d]	1.20^{irr}	1.86^{irr}	-0.16	-0.48	-0.60			
			(36)	(59)	(96)			

[a] Potentials in V *vs.* NHE were obtained from cyclic voltammetry in acetonitrile containing 0.1 mol L^{-1} NBu$_4$PF$_6$. Scan rate = 20 mV s^{-1}.
[b] Potentials in V *vs.* NHE were obtained from cyclic voltammetry in acetonitrile containing 0.1 mol L^{-1} NaI. Scan rate = 20 mV s^{-1}.
[c] Working electrode: glass carbon electrode.
[d] Working electrode: ITO, S=1 cm^2. The given half-wave potentials are equal to $E_{1/2} = (E_{pa} + E_{pc})/2$. Under bracket: $\triangle E_p = |E_{pa}-E_{pc}|$.

2.2.3 UV–visible spectroscopy of the polymer

The UV–visible absorption spectra of the monomer in solution and of the polymers deposited on ITO

are shown for comparison in Fig. 5.7. This superimposition reveals that the Soret band, attributed to the main porphyrin-based π-π* electronic transition, is much larger and more red-shifted in **poly-ZnOEP1** and **poly-ZnOEP2** (onto ITO electrode) than in **ZnOEP** (Table 2). Such differences can be interpreted upon considering the existence of intra- and intermolecular exciton-coupling between porphyrin subunits within the polymer. These changes can also be explained by a greater deformation of the macrocycles within the polymer. The red-shift of the Soret band can also be attributed to the electron-withdrawing effects of the viologen substituents on the porphyrin rings.

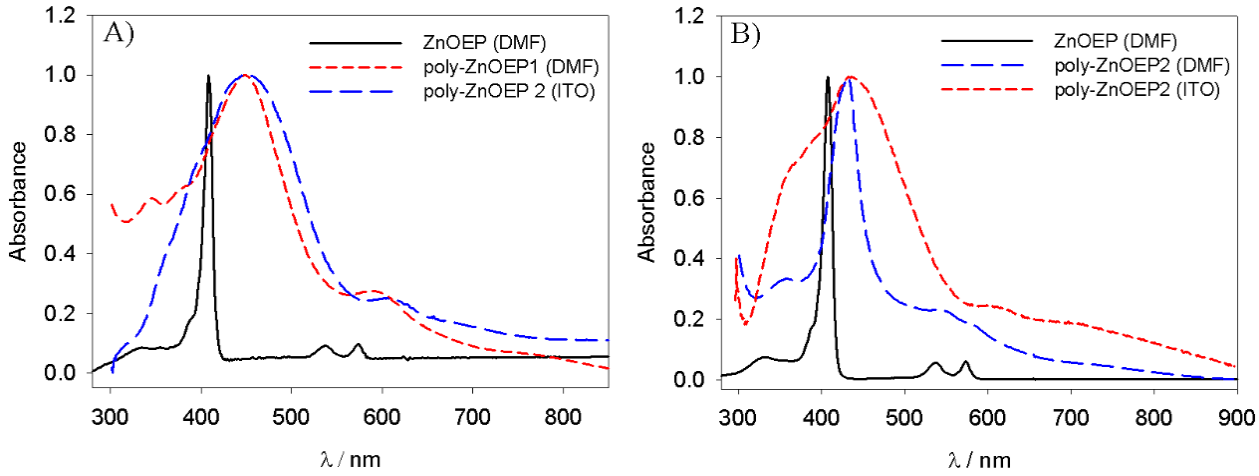

Fig. 5.7 UV–Vis normalized absorption spectrum of A) **poly-ZnOEP1** B) **poly-ZnOEP1** (obtained after 25 iterative scans) onto ITO electrode (red line) or in DMF solution (blue line) compared to **ZnOEP** (black line) in DMF.

After electropolymerization, the films were found to be fully soluble in DMF. Analysis of the resulting solutions by UV-Vis absorption spectroscopy revealed a much sharper Soret band than that recorded on the solid film (Fig. 5.7).

UV-visible absorption spectra of the mother solutions, containing **ZnOEP** and starting spacer, after the deposition of several film clearly shows no demetallation of the starting **ZnOEP** and no demetallation of the **ZnOEP** units of the films.

The spectrum corresponding to the polymer in DMF however still suggests that many interactions between porphyrin chromophores in the copolymer remains in solution.

We have also examined the effects of various experimental parameters used for polymerization on the properties of the ITO coated polymers. In the first experiment, different modified electrodes have been

prepared upon changing the number of iterative scans (Fig. S5.2, see the appendix). Different copolymers have also been grown by constant potential electrolysis (+1.90 V *vs.* SCE) upon varying the deposition time (Fig. 5.8). Plotting the absorbance of the Soret band recorded for **poly-ZnOEP1** and **poly-ZnOEP2** as a function of the number of iterative scans (inset of Fig. S5.2) or deposition time (Fig. 5.8) leads to similar curves featuring an exponential increase reaching a plateau after nearly 25 scans or after a deposition time of 120 seconds.

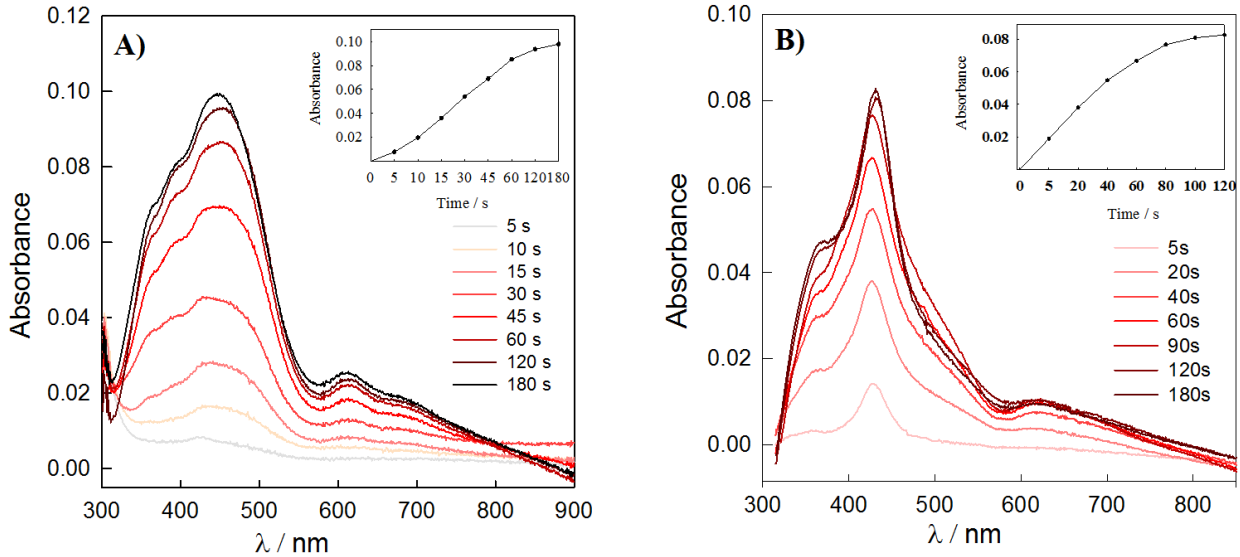

Fig. 5.8 UV–vis absorption spectra of A) **poly-ZnOEP1** and B) **poly-ZnOEP2** obtained after different deposition time under +1.90 V *vs.* SCE.

Table 2 UV–visible spectral data for **ZnOEP**, **4, 4'-bpy** and **bpy^{+}-CH$_2$-CH$_2$-CH$_2$-$^{+}$bpy 2PF$_6^-$** in acetonitrile, **poly-ZnOEP1/P$_5$W$_{30}$** and **poly-ZnOEP2/P$_5$W$_{30}$** on ITO. Under bracket: molar extinction coefficient (ε /10^3 L.M.cm^{-1}).

Compound	**Soret band/nm**	**Q bands/nm**	**π-π^*Band/nm**
ZnOEP	404 (414.2)	533 (187.1),	
		568 (199.8)	
4, 4'-bpy			285 (13.4)
bpy^{+}(CH$_2$)$_3$bpy^{+} 2PF$_6^-$			266 (40.8)
poly-ZnOEP1/P$_5$W$_{30}$	436	602	
poly-ZnOEP2/P$_5$W$_{30}$	434	608	

2.2.4 Thickness measurement of polymeric films

We have also investigated the thickness of the two deposited copolymeric film. Various copolymers coated onto ITO electrodes were prepared just by changing the number of iterative scans n during the electropolymerization. A plot of the absorbance at λ= 433 nm and λ= 426 nm (Soret band of **poly-ZnOEP1** and **poly-ZnOEP2**) as a function of the number of scans n (Fig. 5.8) shows an increase of the thickness during the first 180s fixed potential deposition to reach a plateau corresponding to a thickness of about 31 nm and 25 nm for **poly-ZnOEP1** and **poly-ZnOEP2**, respectively.

These results have been confirmed by AFM experiments (Fig. 5.9). Thickness measurements have been carried out upon scratching the film with a metallic tip. The thickness was then estimated by comparing the height on each side of the scratch. The thickness measured by AFM was found to increase and nearly reach a plateau with the deposition time increase following a similar trend to that obtained by UV-Vis absorption spectroscopy.

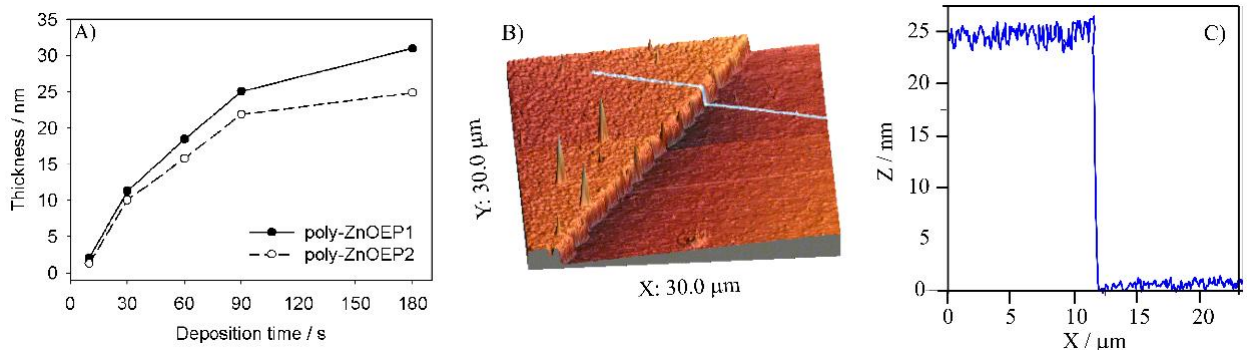

Fig. 5.9 A) Thickness measurement, B) tapping mode AFM topography maps recorded with **poly-ZnOEP2** (deposition on +1.90 V, 180 s) and C) section analysis of the aggregate marked by a blue line.

2.2.5 Spectroelectrochemistry in the solid state

In-situ spectroelectrochemical studies have been carried to gain further insights into the nature of the electrogenerated species (Fig. 5.10 and Fig. S5.3). In-situ spectroelectrochemical analyses have been conducted under an argon atmosphere using **poly-ZnOEP1** (Fig. S5.3, see the appendix) and **poly-ZnOEP2** (Fig. 5.10) modified ITO working electrode placed in a 1,2-$C_2H_4Cl_2$/CH_3CN (4:1) solution containing $TBAPF_6$ as the electrolyte (0.2 mol L^{-1}). Absorption spectra of **poly-ZnOEP2** were recorded

periodically as the viologen centres were submitted to bulk electrochemical reduction at -0.40 V *vs.* SCE. As seen in the array of spectra depicted in Fig. 5.10, the reduction led to a slight increase in intensity of the initial Soret band at 432 nm at the expense of five new absorption bands gradually developing at λ_{max} = 396, 450, 602, 801 and 950 nm (Fig. 5.10A and 3.10B). These changes were furthermore found to be fully reversible under these experimental conditions. The reversibility of the reduction process at the electrolysis time scale was checked by spectroelectrochemistry upon demonstrating that the signature of the starting material [ZnOEP-py^+py^+-$(CH_2)_2$-py^+py^+]$_n$ can be fully recovered after back-electron transfer, by reoxidation at E_{ap} = 0.00 V *vs.* SCE.

Based on literature results, the signals growing at 396 and 602 nm can be safely assigned to the viologen cation radicals whose spectrum, recorded in solution, consists of two intense signals centered at 400 nm and 610 nm with shoulders going from 530 to 800 nm.[5] The porphyrin centered Soret-band is then observed at 450 nm in the reduced polymer.

The origin of the broad absorption band centered at λ_{max} = 950 nm is still not yet fully established but from previous works carried out in solution with a range of bis-bipyridinium derivatives, we believe these transitions to be assigned to the formation of π-dimers. The formation of π-bonded dimers from the spontaneous and reversible association of two organic π-radicals has indeed been observed with a wide range of pyridinium derivatives.[21-23] As a general statement, π-dimer complexes are characterized by cofacial arrangements of two monomeric cation radicals at interplanar distances of around 3.05 ± 0.25 Å, and by diagnostic electronic absorption bands in the near-IR region. Such non covalent complexes are frequently observed at low temperatures or at high concentrations of radicals. The broad absorption in the near infra-red region is moreover a specific diagnostic band whose energy can be directly related to the electronic coupling term between both radicals.[2426]

The broad absorption band seen at λ_{max} = 950 nm in Fig. 5.10A thus most probably arises from the formation of π-dimers formed within the film. Further experiments need however to be carried out in homogeneous phase on well-defined isolated oligomers to accurately determine whether π-dimerization involves two pyridinium or bipyridinum subunits from the same repeated unit [ZnOEP-py^+py^+-$(CH_2)_2$-py^+py^+]$_n$, as seen with previously reported switchable molecular materials,[21,22,23] or from two polymeric chains held at close distances in the polymer.

Similar absorption bands have been observed upon carrying out the bulk reduction in an aqueous

medium containing $TEAPF_6$ (0.2 mol L^{-1}). As seen on the spectra shown in Fig. 5.10C, reduction of **poly-ZnOEP2** at -0.40 V leads to the development of four new signals observed at λ_{max} = 444, 600, 741 and 1013 nm. The first band below 420 nm could not be observed in this case due to the presence of important noise in this region. This spectroscopic signatures recorded for **poly-ZnOEP2** in aqueous and organic media are similar and the slight differences are most probably due to solvation effects. The broad absorption band seen at λ_{max} = 1013 nm in Fig. 5.10C also most probably arises from the formation of π-dimers inside the film.

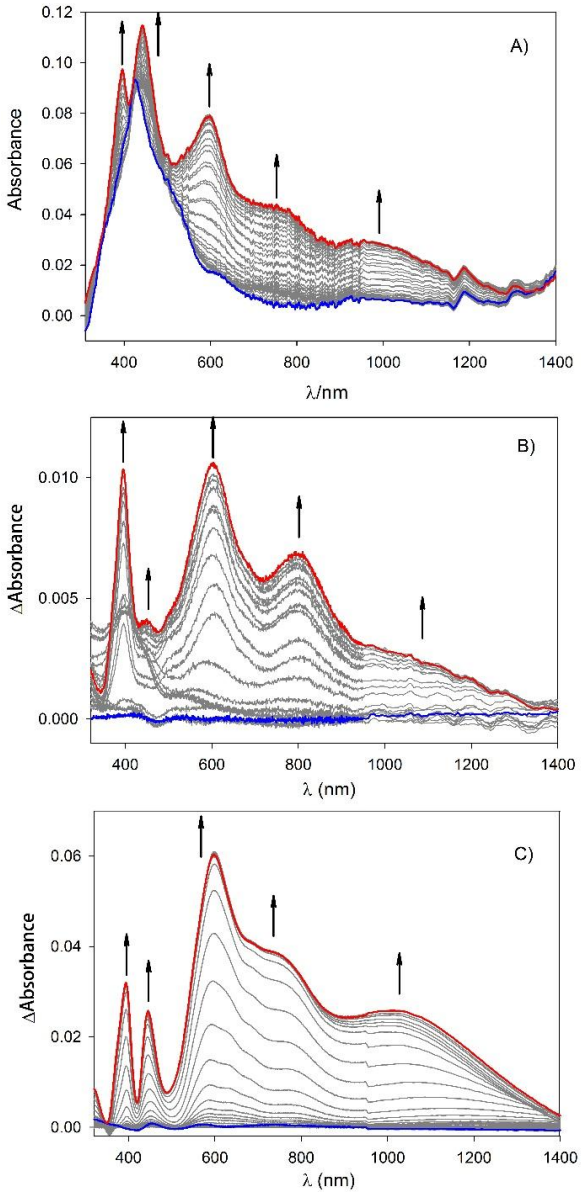

Fig. 5.10 UV-visible-NIR spectra recorded after exhaustive one-electron reduction per viologen in **poly-ZnOEP2** in A) and B) 1,2-$C_2H_4Cl_2$/CH_3CN (4/1) and 0.2 mol L^{-1} $TBAPF_6$ and C) H_2O and 0.2 mol L^{-1} $TEAPF_6$ WE: ITO. S = 1 cm^2. A) Absorbance measurements after (baseline obtained with nude ITO). B) and C) Δ (Absorbance) measured directly (blank obtained from the **poly-ZnOEP2** films on ITO).

Poly-ZnOEP1 copolymers gave similar behaviour with an additional band attributing to the π-dimer (Fig. S5.3). It suggested intermolecular interaction based on its coil structure between the first reduced viologen (or maybe also intramolecular interactions between two close reduced viologen in the same chain).

2.3 Fabrication and characterization of two poly-ZnOEP-Preyssler type-POM composite films

2.3.1 Fabrication the poly-ZnOEP-Preyssler type-POM composite films

Poly-ZnOEP/P_5W_{30} films were prepared following two steps, firstly, the ZnOEP polymers have been electropolymerized using a 0.1 mol L^{-1} solution of $TBAPF_6$ in 1,2-$C_2H_4Cl_2$/CH_3CN (4/1) containing 2.5 × 10^{-4} mol L^{-1} of **ZnOEP** and 2.5×10^{-4} mol L^{-1} of 4, 4'-bpy (**poly-ZnOEP1**) or bpy^+-CH_2-CH_2-CH_2-$^+$bpy $2PF_6^-$ (**poly-ZnOEP2**) under an argon atmosphere.

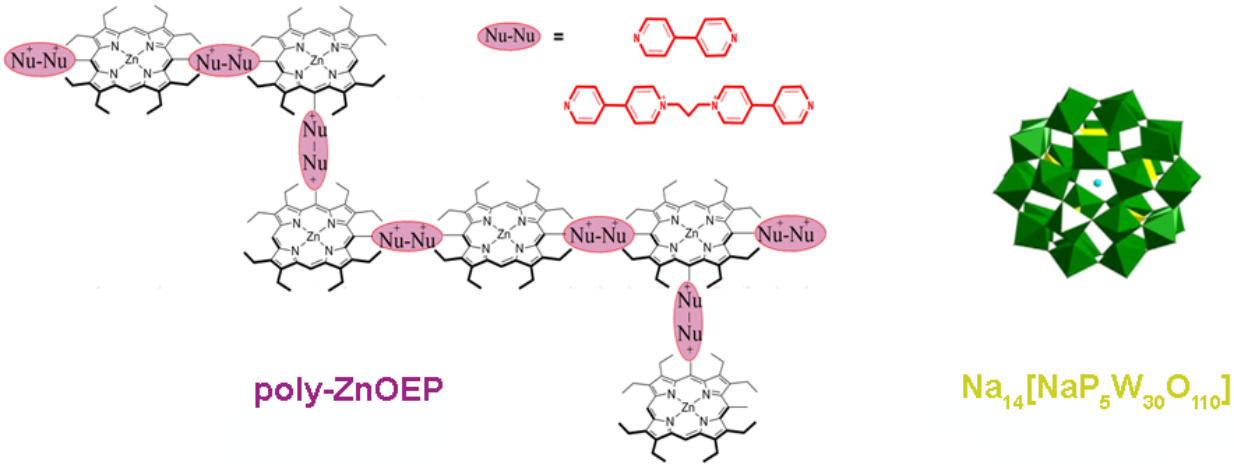

Fig. 5.11 Scheme of the structure of $Na_{14}[NaP_5W_{30}O_{110}]$ (P_5W_{30}) and poly-ZnOEP with 4, 4'-bpy or bpy^+-CH_2-CH_2-CH_2-$^+$bpy $2PF_6^-$ as nucleophiles.

Electropolymerization is carried out at a fixed potential +1.90 V *vs.* SCE for 180 s according to the investigation of section 2.2. After electropolymerization, the ITO electrodes were washed in acetonitrile in order to remove traces of the monomers and the conducting salt present on the deposited films. After drying, P_5W_{30} was equipped by plugging the substrate in 0.1 mmol L^{-1} aqueous $Na_{14}[NaP_5W_{30}O_{110}]$ solution, then, cleaned by dipping into Millipore Q water to obtain poly-ZnOEP/P_5W_{30}.

2.3.2 Characterization of the poly-ZnOEP-Preyssler type-POM composite films

2.3.2.1 X-ray photoelectron spectra

The presence of C, N, O, Zn, Na, P, and F elements enable to confirm the presence of poly-ZnOEP1/P_5W_{30} (red line, Fig. 5.12). In poly-ZnOEP1 film, the Zn 2p3/2 (1022.8 eV) is assigned to the zinc in ZnOEP. Two types of nitrogen with different chemical states are observed, which appear at 402.6 eV due to TBA and 399.7 eV due to the collaboration of N in the porphyrin, pyridium spacers and terminal pyridine (quite small quantity). The P 2p3/2 (136.6, Fig. 5.12E, black curve) and F 1s (686.8 eV, Fig. 5.12I, black curve) is ascribed to counter ion PF_6^-. While O 1s signal (532.9 eV) comes from H_2O on the copolymer surface. Furthermore, plugging the ITO coated with poly-ZnOEP1 film into 0.1 mmol L^{-1} $Na_{14}[NaP_5W_{30}O_{110}]$ aqueous solution, the presence of additional Na 1s (1073.4 eV, Fig. 5.12G, red curve) and W 4f7 (36.4 eV for W4f7/2 and 37.8 eV for W4f5/2, Fig. 5.12H, red curve) peaks, the much lower intensity of F 1s (686.8 eV, Fig. 5.12I, red curve), together with the spectrum signal of O 1s (531.6 eV, Fig. 5.12D, red curve) and P 2p3 (133.3 eV, Fig. 5.12E, red curve) from P−O bond in POM which reflect that we indeed adsorb $[NaP_5W_{30}O_{110}]^{14-}$ on poly-ZnOEP1 film through replacing the PF_6^- counter ions to get poly-ZnOEP1/P_5W_{30}. XPS result of poly-ZnOEP2 *vs*. poly-ZnOEP2/P_5W_{30} is analogous to poly-ZnOEP1 *vs*. poly-ZnOEP1/P_5W_{30}. However, after incorporated P_5W_{30}, the initial N1s peak on 399.7 eV of poly-ZnOEP2 split to two peaks (400.5 eV and 399.1eV). It may be attributed to the interaction between P_5W_{30} and poly-ZnOEP2 (two times more positive charge than for poly-ZnOEP1).

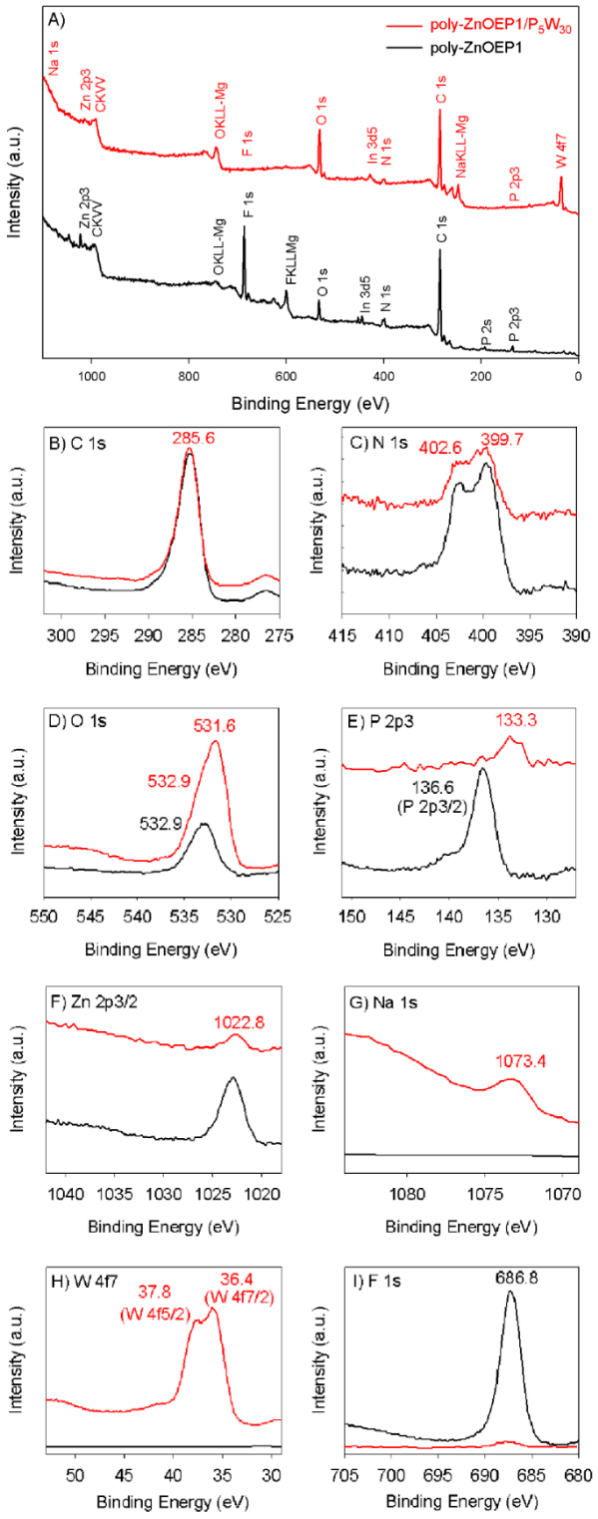

Fig. 5.12 XPS of poly-ZnOEP1 films on ITO with and without P_5W_{30}. Global XPS spectra (A), C 1s (B), N 1s (C), O 1s (D), P 2p3 (E), Zn 2p3 (F), Na 1s (G), W 4f7 (H), F 1s (I).

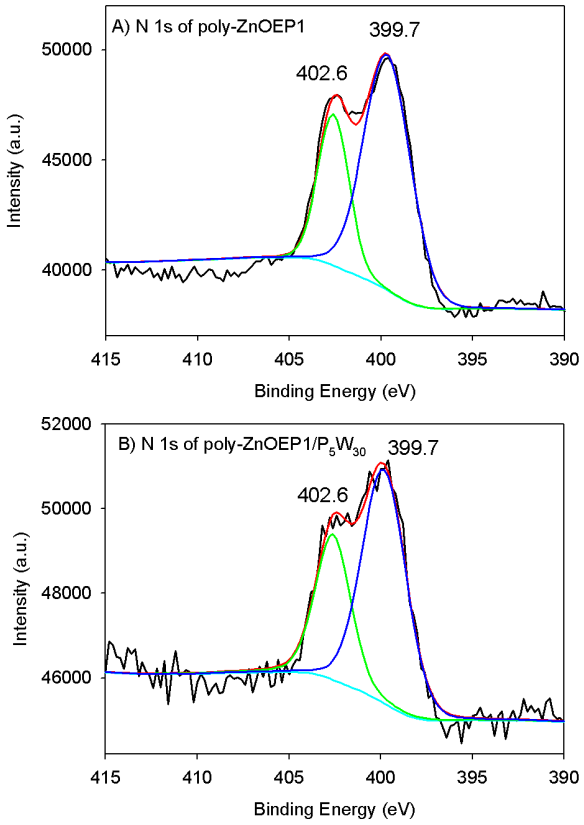

Fig. 5.13 C 1s XPS spectra of poly-ZnOEP1 films on ITO with and without P_5W_{30}.

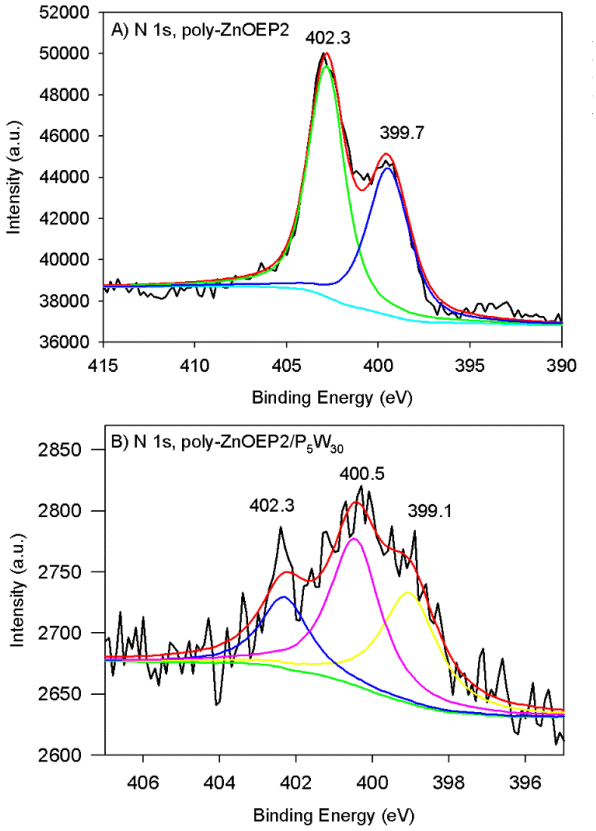

Fig. 5.14 C 1s XPS spectra of poly-ZnOEP2 films on ITO with and without P_5W_{30}.

2.3.2.2 UV–visible spectroscopy of the composite films

After the incorporation of $[NaP_5W_{30}O_{110}]^{14-}$, UV-vis spectra of the two **poly-ZnOEP/P_5W_{30}** films showed a slight red shift (ca. 4 nm) and small decrease of the Soret band accompanied by an increase in the region 600-900 nm (Fig. 5.15) which attested probably the presence of the polyanion and the formation of **P_5W_{30}**-viologen and/or **P_5W_{30}**-bipyridinium ion pairs.

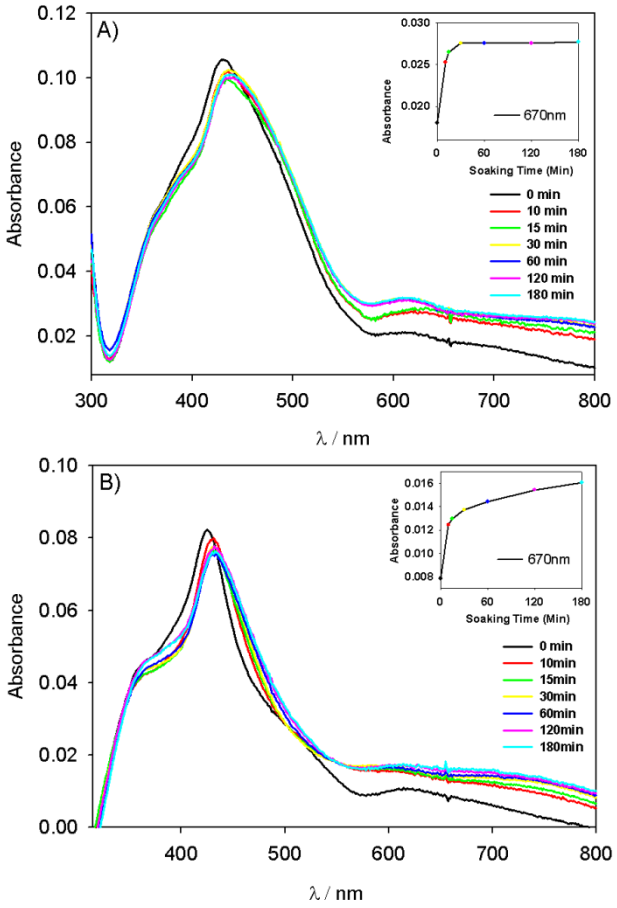

Fig. 5.15 UV-vis spectra of the modified ITO electrode with A) **poly-ZnOEP1** and B) **poly-ZnOEP2** after soaking in 0.1 mmol L^{-1} $Na_{14}[NaP_5W_{30}O_{110}]$ aqueous solution for 10 min, 15 min, 30 min, 60 min, 120 min, and 180min. Inset: absorbance intensity at λ= 670 nm *vs.* time.

2.3.2.3 QCM to monitor $[NaP_5W_{30}O_{110}]^{14-}/PF_6^-$ exchange

To monitor the incorporation kinetics of $[NaP_5W_{30}O_{110}]^{14-}$ onto the **poly-ZnOEP1** and **poly-ZnOEP2** by exchange PF_6^-, *in-situ* QCM measurement in which a QCM electrode covered with a **poly-ZnOEP1** or **poly-ZnOEP2** film was made to contact with the $Na_{14}[NaP_5W_{30}O_{110}]$ aqueous solution. Then, the

frequency change was measured.[28,29] Fig. 5.16 shows the frequency response of QCM sensor to $[NaP_5W_{30}O_{110}]^{14-}$ adsorption onto the **poly-ZnOEP1** film (applied potential: +1.9 V *vs.* SCE, elapsed time: 180 s). From the recorded signal plot, three parameters were evaluated: Δf_1, Δf_2 and Δf_3, which corresponded to the variation of frequency induced by the $[NaP_5W_{30}O_{110}]^{14-}$ adsorption through exchanging PF_6^- during the first hour, the second hour, and the third hour on the surface of the **poly-ZnOEP1** film, respectively.

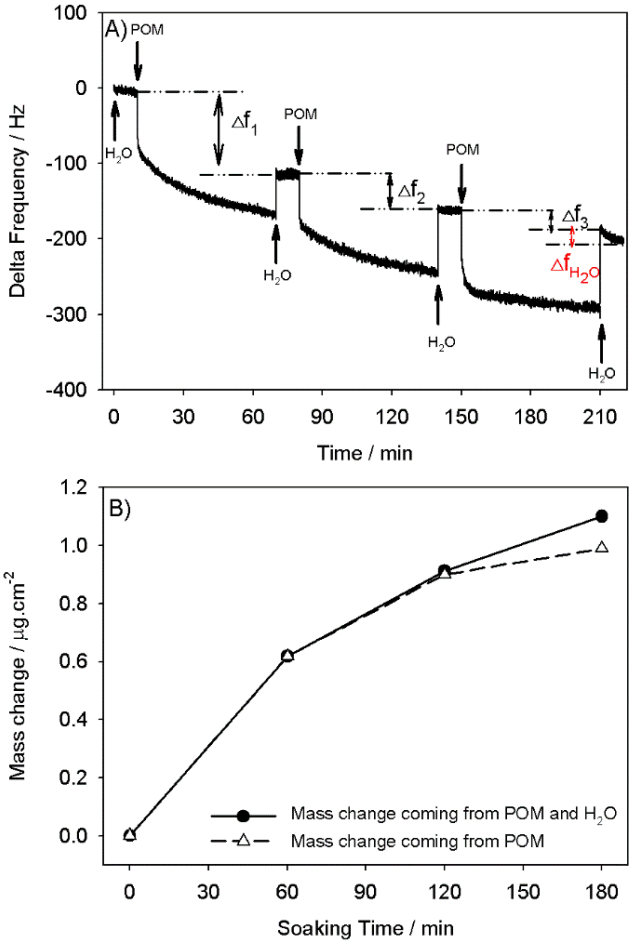

Fig. 5.16 Frequency response of QCM sensor to $Na_{14}[NaP_5W_{30}O_{110}]$ adsorption onto the **poly-ZnOEP1** film **(**deposited onto a 9.08 MHz AT-cut quartz resonator with a thin ITO layer (A = 0.2 cm^2)). The start base line was obtained when the sensor was exposed to H_2O. The arrows ↓ indicated the injection of $Na_{14}[NaP_5W_{30}O_{110}]$ (c = 0.1 mmol L^{-1}). The arrow ↑ indicated the washing using H_2O. B) Mass change (Δm) calculated from Sauerbrey's equation versus the soaking time. Δf_1, Δf_2, and Δf_3 are measured after 60 minutes.

A negative change of frequency corresponds to the mass increase at the sensing area. The mass changes after one hour, two hours, and three hours were 0.618 µg cm^{-2}, 0.912 µg cm^{-2} and 1.101 µg cm^{-2} respectively. However, after two hours, one part of the mass change come from H_2O which adsorbed on

the the surface of **poly-ZnOEP1** film, so the mass of $[NaP_5W_{30}O_{110}]^{14-}$ on the surface of **poly-ZnOEP1** film were 0.618 μg cm^{-2}, 0.900 μg cm^{-2} and 0.990 μg cm^{-2} after the soaking time of one hour, two hours, and three hours, respectively.

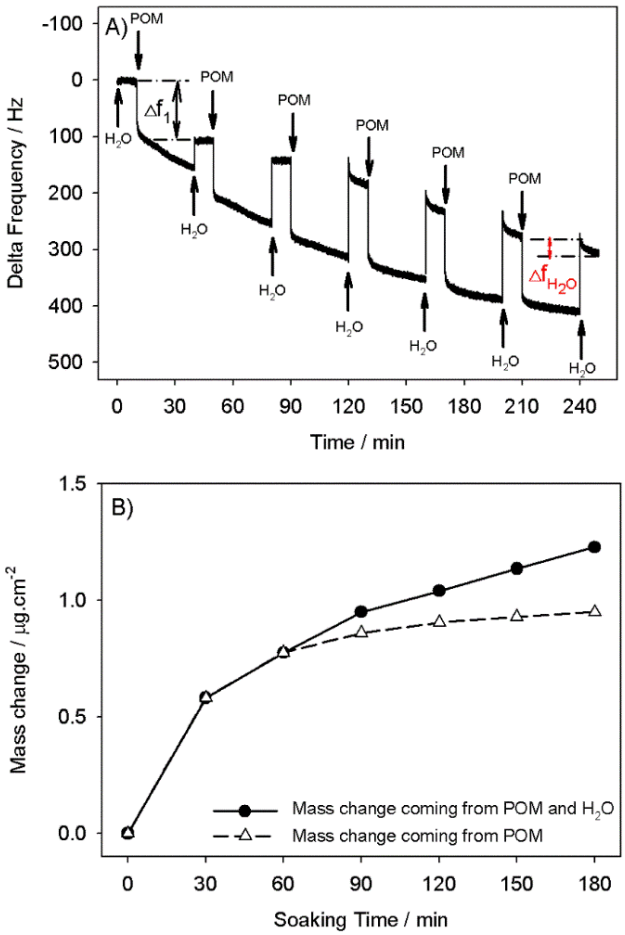

Fig. 5.17 Frequency response of QCM sensor to $Na_{14}[NaP_5W_{30}O_{110}]$ adsorption onto the **poly-ZnOEP2** film **(** deposited onto a 9.08 MHz AT-cut quartz resonator with a thin ITO layer (A = 0.2 cm^2)). The start base line was obtained when the sensor was exposed to H_2O. The arrows ↓ indicated the injection of $Na_{14}[NaP_5W_{30}O_{110}]$ (c = in 0.1 mmol L^{-1}). The arrow ↑ indicated the washing using H_2O. B) Mass change (Δm) calculated from Sauerbrey's equation versus the soaking time. Δf_1 is measured after 30 minutes.

Fig. 5.17 shows the frequency response of QCM sensor to $[NaP_5W_{30}O_{110}]^{14-}$ adsorption onto the **poly-ZnOEP2** film (deposition at applied potential of +1.9 V, elapsed time: 180 s). The incorporation kinetics of $[NaP_5W_{30}O_{110}]^{14-}$ onto **poly-ZnOEP2** was faster than that of **poly-ZnOEP1**, due to the one time higher positive charge of **poly-ZnOEP2**. The H_2O molecular adsorption effect onto the **poly-ZnOEP2** films were more observable than for **poly-ZnOEP1**. It might be tentatively attributed to the stall of the

bilayer of **P_5W_{30}** when the surface was nearly covered by **P_5W_{30}**. At this stage, when we use H_2O to wash the surface of the film, the redundant **P_5W_{30}** will be removed simultaneously taking away the shared H_2O molecules with the "deserved" monolayer of **P_5W_{30}**. As the **P_5W_{30}** is hygroscopic, water from aqueous solution come to complete the solvatation of the polyanion which induce an increase of the mass. This process is not rapid. In the case of **poly-ZnOEP1**, because the copolymer is lower charged, the formation of the monolayer of **P_5W_{30}** need more time. This effect is then becoming observable only after 3 hours.

2.3.2.4 Cyclic voltammetric investigations of the polymeric films

To study the effects of the counter anion on the electrochemistry of the **poly-ZnOEP**, ITO electrodes coated with **poly-ZnOEP1** or **poly-ZnOEP2** were plunged in 0.1 mmol L^{-1} $Na_{14}[NaP_5W_{30}O_{110}]$ aqueous solution for 1 h, in order to replace PF_6^-, and then washed with water (10 mL).

Compared with CVs of the initial **poly-ZnOEP1** and **poly-ZnOEP2** films, CVs of **poly-ZnOEP1/P_5W_{30}** (Fig. S5.5A, red curve in the appendix) and **poly-ZnOEP2/P_5W_{30}** (Fig. S5.5B, red curve in the appendix) revealed similar changes. The first reduction peak of the viologen spacers were shifted cathodically while the other reduction processed remain unchanged.

As a matter of fact, reductive peaks of the **P_5W_{30}** are not perceptible when we measure the cyclic voltammetry of **poly-ZnOEP/P_5W_{30}**. This behavior can be explained to the electron transfer of **P_5W_{30}** subunit might be drastically slowed down. Such behaviour has been already noticed with various POMs–porphyrin systems even in solution.

The first oxidation potential of **ZnOEP** subunit (Porp) of the films provides the measurement of HOMO energy. To the largest extent to close the photocurrent generation conditions, the reduction scan is proceed in acetonitrile with I^- as electrolyte (Fig. 5.18A and Fig. 5.19A). However, the oxidation peak of I^- will cover the oxidation peak of porphyrin. In addition, the oxidation potential of porphyrin remains nearly unchanged in different electrolyte. Thus, measurement of the first oxidation potential of **ZnOEP** subunit of **poly-ZnOEP1/P_5W_{30}** and **poly-ZnOEP2/P_5W_{30}** are carried out in acetonitrile containing 0.1 mol L^{-1} $TBAPF_6$ (Fig. 5.18B and Fig. 5.19B). Moreover, in the present study, $TBA_{14}[NaP_5W_{30}O_{110}]$ shows three successive reduction processes in acetonitrile system. Electrochemical data are gathered in

Table 1 (see page 177).

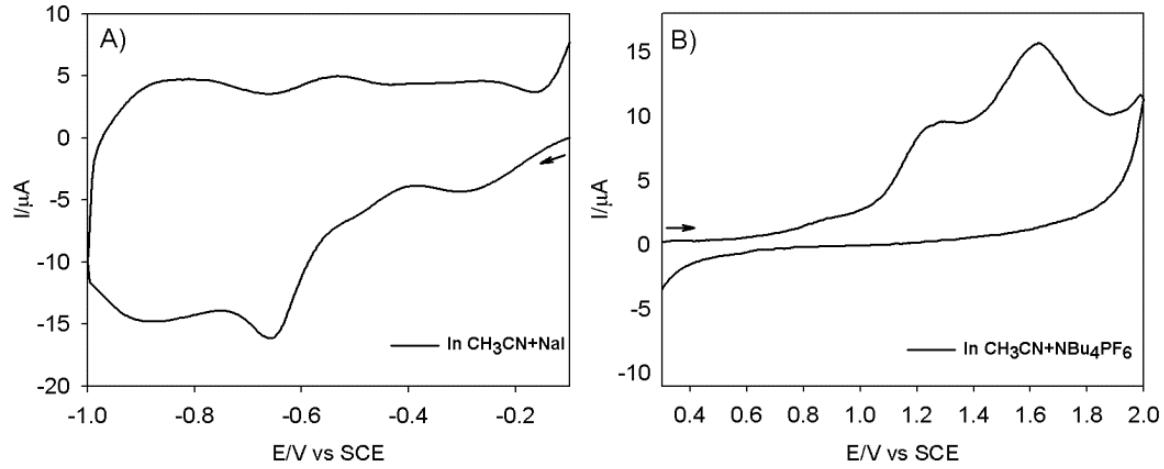

Fig. 5.18 CVs of **poly-ZnOEP1/P_5W_{30}** films in acetonitrile containing (A) 0.5 mol L^{-1} NaI and (B) 0.1 mol L^{-1} $TBAPF_6$. S = 1 cm^2. *v* = 20 mV s^{-1}. (→) shows the scan direction.

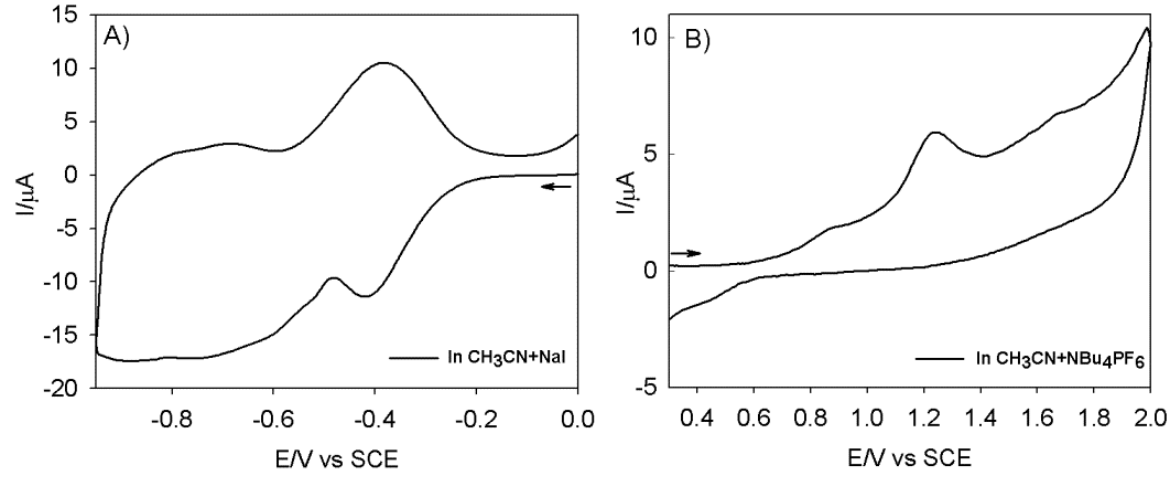

Fig. 5.19 CVs of **poly-ZnOEP2/P_5W_{30}** films in acetonitrile containing 0.5 mol L^{-1} NaI (A) or 0.1 mol L^{-1} $TBAPF_6$ (B). S = 1 cm^2. *v* = 20 mV s^{-1}. (→) shows the scan direction.

2.3.2.5 Electrochemical impedance spectroscopic analysis

Electrochemical impedance spectroscopy (Nyquist plots) was carried out to understand more the change of photocurrent and conversion efficiency of photon. The distance between zero and the start point of the semicircle relates to serials resistant (R_s). Fig. 5.20 shows electrochemical impedance spectra of **poly-ZnOEP1/P_5W_{30}** and of **poly-ZnOEP2/P_5W_{30}** at AC frequency from 0.1 Hz to 10^5 Hz, with DC potential 0.0 V in acetonitrile containing I_3^- 5 mmol L^{-1} and NaI 0.5 mol L^{-1}. Charge transfer resistance (R_{ct}) from the photoelectrodes to redox species in the electrolyte can be calculated by fitting the semi-

arc in the low frequency region.[30] Smaller circular diameter represents lower electron transport resistance and higher separation efficiency of the photogenerated electrons and holes.[31]

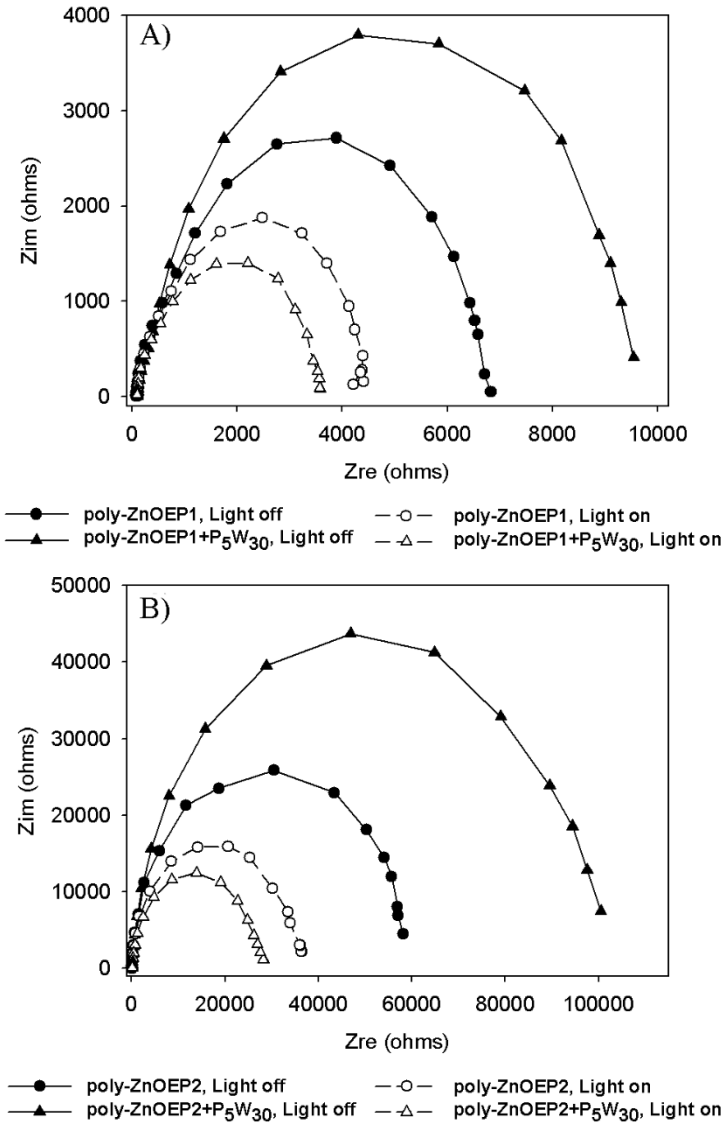

Fig. 5.20 Electrochemical impedance spectroscopy (EIS) for A) **poly-ZnOEP1** and **poly-ZnOEP1/P_5W_{30}** (soaking time 60 min) and B) **poly-ZnOEP2** and **poly-ZnOEP2/P_5W_{30}** (soaking time 30 min) with and without illumination from a 300 W Xe arc lamp (with $\lambda > 385$ nm long pass filter) in acetonitrile containing I_2 5 mmol L^{-1} and NaI 0.5 mol L^{-1} under 0.00 V BIAS potentials. The frequency range explored was 0.1 Hz to 10^5 Hz, with the ac amplitude perturbed at 10 mV. DC potential 0.00 V.

As can be seen from Fig. 5.20A, under visible illumination the R_{ct} of **poly-ZnOEP1/P_5W_{30}** is smaller than that of **poly-ZnOEP1**, demonstrating that **P_5W_{30}** effectively restrain the recombination of photogenerated electrons and holes, thus a larger photocurrents are obtained. The matched potential

positions of **P_5W_{30}** with the oxidation potential of ($Porp^{+\cdot}$/$Porp^{*}$) and reduction potential of viologen promoted the transportation of charge carriers and retards the recombination of electrons and holes under visible irradiation. On the contrary, in the dark, the R_{ct} of **poly-ZnOEP1/P_5W_{30}** is larger than that of **poly-ZnOEP1**. It suggests that **P_5W_{30}** (of the copolymer in the ground state) blocked the charge transfer (by repulsions because of its 14- negative charges) and prevents the migration of I^-. **Poly-ZnOEP2/P_5W_{30}** revealed the same tendency with and without P_5W_{30} (Fig. 5.20B). The higher R_{ct} of **poly-ZnOEP2/P_5W_{30}** than that of **poly-ZnOEP1/P_5W_{30}** was one influence factor resulted in the lower photocurrent respond of **poly-ZnOEP2/P_5W_{30}**.

3. Photocurrent generation

3.1 Optimize the soaking time in $Na_{14}[NaP_5W_{30}O_{110}]$ solution

Fig. 5.21 shows the photocurrent response of poly-ZnOEP1/P_5W_{30} (Fig. 5.21A) and poly-ZnOEP2/P_5W_{30} (Fig. 5.21B) films obtained from soaking in $Na_{14}[NaP_5W_{30}O_{110}]$ solution with different time, under Xe irradiation ($\lambda > 385$ nm) where $Na_{14}[NaP_5W_{30}O_{110}]$ is not expected to be excited. This study is carried out in acetonitrile containing I_3^- 5 mmol L^{-1} and I^- 0.5 mol L^{-1} redox mediators which also act as electrolytes in order to improve the conductivity and thus increase the current magnitude. J-t measurements indicated that the photocurrent response of the poly-ZnOEP1/P_5W_{30} and poly-ZnOEP2/P_5W_{30} film electrodes was dependent on the P_5W_{30} concentration. On 0.00 V BIAS potential, we can see the highest increase of 3.4 times for poly-ZnOEP1/P_5W_{30} (60 min) *vs.* poly-ZnOEP1 and 1.3 times for poly-ZnOEP2/P_5W_{30} (30 min) *vs.* poly-ZnOEP2 respectively. Based on the EQCM measurement of deposition amount of the poly-ZnOEP, and later the adsorption amount of $[NaP_5W_{30}O_{110}]^{14-}$, the molar ratio of unit -ZnOEP-V^{2+}/$[NaP_5W_{30}O_{110}]^{14-}$ (60 min) and poly-ZnOEP-V^{2+}-$(CH_2)_3$-V^{2+}/$[NaP_5W_{30}O_{110}]^{14-}$ (30 min) were 41.71 and 26.89.

The photocurrent transients are prompt, steady and reproducible under continuous 4 hours on–off cycles of the Xe light irradiation. Based on the energy level of components (ZnOEP, P_5W_{30}, viologen (or bis-viologen) and I_3^-/I^-), the P_5W_{30} acted as an efficient electron relay mediator to transport electrons from

the excited ZnOEP to reduce viologen (or bis-viologen) dications into viologen (bis-viologen) cation radicals, so it strengthened the separation of the electron–hole pairs generated in the poly-ZnOEP.

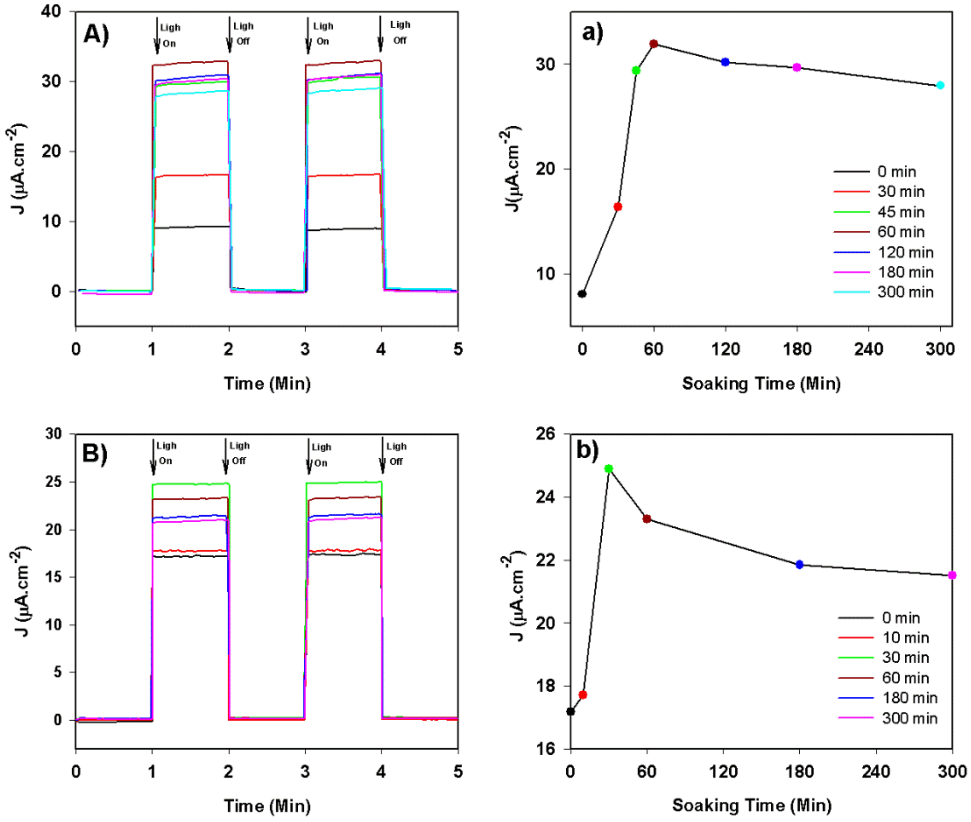

Fig. 5.21 Photoelectrochemical response of **poly-ZnOEP1/P_5W_{30}** (A and a) and **poly-ZnOEP2/P_5W_{30}** (B and b) with different soaking time in $Na_{14}[NaP_5W_{30}O_{110}]$ solution under on–off light illumination from a 300 W Xe arc lamp (with $\lambda > 385$ nm long pass filter) in acetonitrile containing I_3^- 5 mmol L^{-1} and I^- 0.5 mol L^{-1}. BIAS potential: 0.00 V *vs.* OCP.

3.2 Different BIAS potential

To understand the behaviour of electron injection within the two **poly-ZnOEP/P_5W_{30}** film electrodes, the photocurrent response dependence on the BIAS voltage is also investigated. Fig. 5.22 revealed that the rate of heterogeneous electron transfer across the film/electrode interface cannot affect the magnitude of the photocurrent in the present system when we applied 0.0, +0.1 and +0.2 V. However, the BIAS voltage will vary the dark current, because of the redox process of I_3^-/I^-.

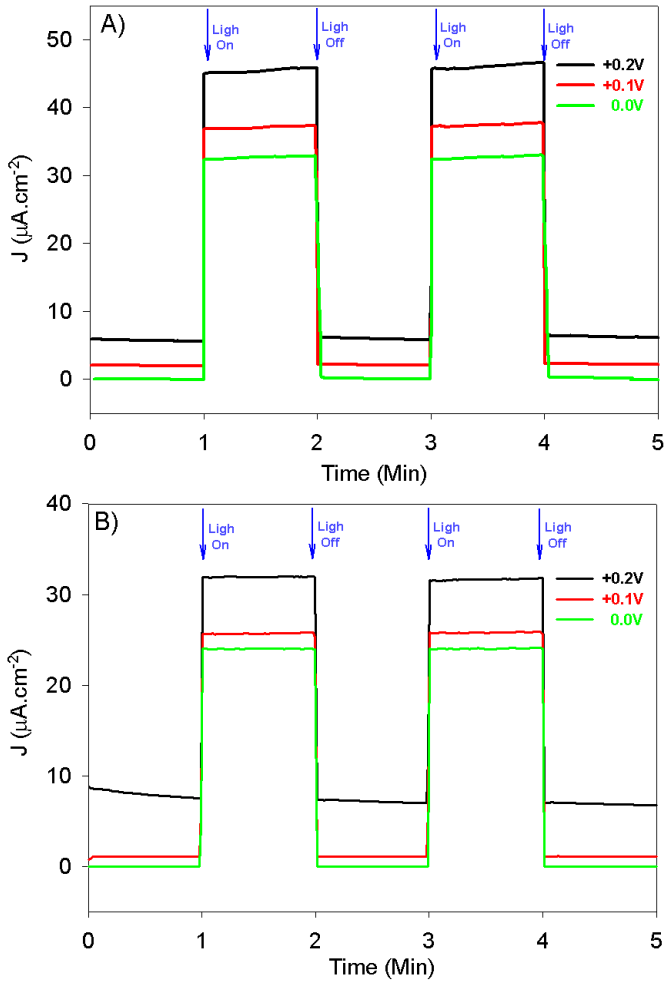

Fig. 5.22 Photocurrent density of **poly-ZnOEP1/P_5W_{30}** (A) and **poly-ZnOEP2/P_5W_{30}** (B) under visible light illumination from a 300 W Xe arc lamp (with $\lambda > 385$ nm long pass filter) in acetonitrile containing I_2 5 mmol L^{-1} and NaI 0.5 mol L^{-1} under different BIAS potentials.

3.3 Energy diagram of the electron transfer processes

The photo-electric conversion mechanism of **poly-ZnOEP1/P_5W_{30}** and **poly-ZnOEP2/P_5W_{30}** film could be explained by the following processes: (1) the band-gap excitation from HOMO to LUMO of the **ZnOEP** macrocycle under illumination, (2) electron transfer from the LUMO of **ZnOEP** to **P_5W_{30}**, circularly, I^- supplement electrons to the HOMO of **ZnOEP**, (3) the reduced **P_5W_{30}** relay electron to the viologen (or the bis-viologen) dications (4) the viologen (or the bis-viologen) cation radicals transmit electrons to the ITO surface.

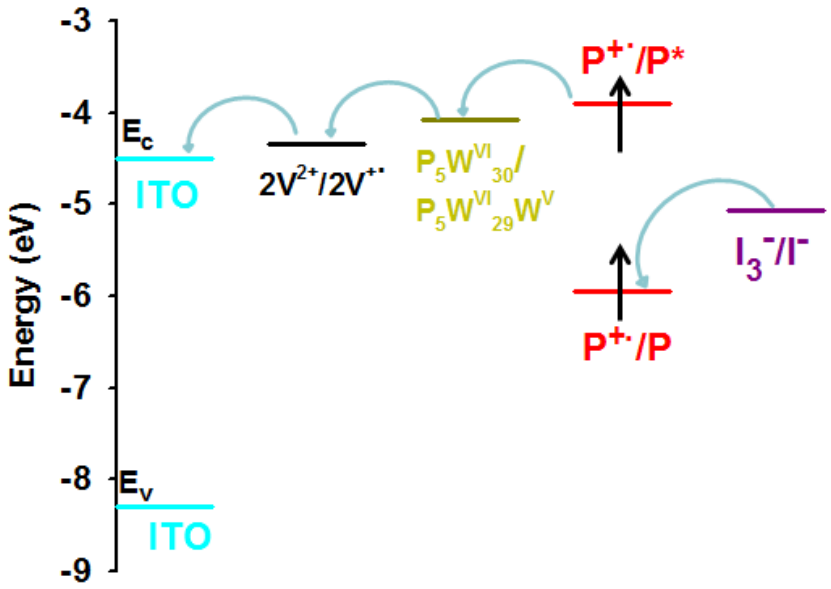

Fig. 5.23 Schematic illustration of the energy level diagram showing electron transfer processes. (V = viologen, P = porphyrin)

The oxidation of ZnOEP (Porp) subunit in the film provides a measurement for the energy of the HOMO level. The potential of porphyrin excited state can be calculated by subtracting the energy for excitation light of the films from oxidation potential value of the ground state, which is correlated with the ability of the excited porphyrin to transfer electrons to P_5W_{30}.

From the electron affinity, the E_c and E_v edges of ITO electrode surface are estimated to be ca. -4.5 and -8.3 eV, respectively. The level of the excited state (couple $Porp^{+\cdot}/Porp^{*}$) and the ground state (couple $Porp^{+\cdot}/Porp$) are -3.92 eV and -5.92 eV for poly-ZnOEP1/P_5W_{30}, and -3.90 eV and -5.94 eV for poly-ZnOEP2/P_5W_{30}, respectively. The energy level of the couples $P_5W^{VI}{}_{30}/P_5W^{V}V^{VI}{}_{29}$, $V^{2+}/V^{+\bullet}$ (or $2V^{2+}/2V^{+\bullet}$) and I_3^-/I^- were -4.08 eV (-0.42 V *vs.* NHE), -4.41 eV (-0.09 V *vs.* NHE) (or -4.34 eV (-0.16 V *vs.* NHE)) and -5.06 eV (+0.56 V *vs.* NHE), respectively, based on the absolute scale. The energy level of P_5W_{30} is lower than the LUMO level of ZnOEP and higher than $V^{2+}/V^{+\bullet}$ (or $2V^{2+}/2V^{+\bullet}$), thus suggesting that the excited ZnOEP to reduce P_5W_{30} is a favorable exothermic process. These results indicate that P_5W_{30} plays the part of an efficient electron shuttle between the excited ZnOEP and the viologen spacers.

4. Conclusion

In summary, firstly, a novel copolymer has been produced by electropolymerization of ZnOEP in the presence of a flexible propyl- linked bispyridinium (1,1''-(1,3-propanediyl)bis-4,4'-bipyridinium). The detailed electrochemical analysis furthermore revealed a splitting of the second viologen-centered reduction wave and of the following porphyrin-based reduction, a phenomenon which has never been observed before with copolymers involving 4,4'-bispyridine as a linker. Spectroelectrochemical studies, carried out on ITO modified electrodes, support the existence of interactions between viologen cation radicals in the film. Observation of a broad absorption band in the near infra-red region of the spectrum recorded for $–[ZnOEP–V^{+\bullet}–(CH_2)_3–V^{+\bullet}]_n–$ suggest the formation of π-dimer complexes in the polymer. Similar behaviour has been obtained for poly-ZnOEP1 suggesting that the formation of π-dimer complexes was mainly intermolecular.

Later, two **poly-ZnOEP/P_5W_{30}** films were obtained through incorporating $[NaP_5W_{30}O_{110}]^{14-}$ onto the two poly-ZnOEP films (one using rigid and short spacer (viologen) and another one using flexible and long spacer (bis viologen) between the **ZnOEP** macrocycles) based on exchanging the initial counter ion (PF_6^-) of the **poly-ZnOEP**. Both **poly-ZnOEP/P_5W_{30}** composite film electrodes possessed a higher photocurrent response than only the poly-ZnOEP electrode. This can be attributed to **P_5W_{30}** as an intermediary between exited **ZnOEP** and spacers.

References

(1) Ruhlmann, L.; Schulz, A. *J. Am. Chem. Soc.* **1999**, *121* (8), 6664.
(2) Ruhlmann, L.; Hao, J.; Ping, Z.; Giraudeau, A. *J. Electroanal. Chem.* **2008**, *621* (1), 22.
(3) Schaming, D.; Ahmed, I.; Hao, J.; Alain-Rizzo, V.; Farha, R.; Goldmann, M.; Xu, H.; Giraudeau, A.; Audebert, P.; Ruhlmann, L. *Electrochim. Acta* **2011**, *56* (28), 10454.
(4) Giraudeau, A.; Ruhlmann, L.; El Kahef, L.; Gross, M. *J. Am. Chem. Soc.* **1996**, *118* (12), 2969.
(5) Hao, J.; Giraudeau, A.; Ping, Z.; Ruhlmann, L. *Langmuir* **2008**, *24* (5), 1600.
(6) Long, D.-L.; Tsunashima, R.; Cronin, L. *Angew. Chem. Int. Ed. Engl.* **2010**, *49* (10), 1736.
(7) Jiang, M.; Wang, E.; Wei, G.; Xu, L.; Kang, Z.; Li, Z. *New J. Chem.* **2003**, *27* (9), 1291.
(8) Jiang, M.; Wang, E.; Xu, L.; Kang, Z.; Lian, S. *J. Solid State Chem.* **2004**, *177* (4-5), 1776.
(9) Huo, Z.; Gisselbrecht, J.-P.; Farha, R.; Goldmann, M.; Saint-Aman, E.; Bucher, C.; Ruhlmann, L. *Electrochim. Acta* **2014**, *122*, 108.
(10) Schaming, D.; Marggi-Poullain, S.; Ahmed, I.; Farha, R.; Goldmann, M.; Gisselbrecht, J.-P.; Ruhlmann, L. *New J. Chem.* **2011**, *35* (11), 2534.
(11) L. El Kahef, M. Gross, and A. G. *ournal Chem. Soc. Commun.* **1989**, 963.
(12) Hünig, S.; Berneth, H. *Org. Chem.* **1980**, *92*, 1.
(13) Kahef, L. El; Gross, M.; Giraudeau, A. *J. Chem. Soc., Chem. Commun* **1989**, *49*, 1989.
(14) Rachlewicz, K.; Latos-Grazynski, L. *Inorg. Chem.* **1995**, *34* (3), 718.
(15) Giraudeau, A.; Schaming, D.; Hao, J.; Farha, R.; Goldmann, M.; Ruhlmann, L. *J. Electroanal. Chem.* **2010**, *638* (1), 70.
(16) Ruhlmann, L.; Giraudeau, A. *Eur. J. Inorg. Chem.* **2001**, 659.
(17) Giraudeau, A.; Lobstein, S.; Ruhlmann, L.; Melamed, D.; Barkigia, K. M.; Fajer, J. *J. Porphyr. Phthalocya.* **2001**, *05* (11), 793.
(18) Bruckenstein, S.; Shay, M. *Electrochim. Acta* **1985**, *30* (10), 1295.
(19) Gervaldo, M.; Liddell, P. A.; Kodis, G.; Brennan, B. J.; Johnson, C. R.; Bridgewater, J. W.; Moore, A. L.; Moore, T. A.; Gust, D. *Photochem. Photobiol. Sci.* **2010**, *9* (7), 890.
(20) Ruhlmann, L.; Gross, M.; Giraudeau, A. *Chem. Eur. J.* **2003**, *9* (20), 5085.
(21) Kannappan, R.; Bucher, C.; Saint-Aman, E.; Moutet, J.-C.; Milet, A.; Oltean, M.; Métay, E.; Pellet-Rostaing, S.; Lemaire, M.; Chaix, C. *New J. Chem.* **2010**, *34* (7), 1373.
(22) Iordache, A.; Kannappan, R.; Métay, E.; Duclos, M.-C.; Pellet-Rostaing, S.; Lemaire, M.; Milet, A.; Saint-Aman, E.; Bucher, C. *Org. Biomol. Chem.* **2013**, *11* (26), 4383.
(23) Iordache, A.; Oltean, M.; Milet, A.; Thomas, F.; Baptiste, B.; Saint-Aman, E.; Bucher, C. *J. Am. Chem. Soc.* **2012**, *134* (5), 2653.
(24) Miyata, Y.; Nishinaga, T.; Komatsu, K. *J. Org. Chem.* **2005**, *70* (4), 1147.
(25) Lü, J.-M.; Rosokha, S. V; Kochi, J. K. *J. Am. Chem. Soc.* **2003**, *125* (40), 12161.
(26) Lee, C.; Lee, Y.; Moon, M.; Park, S. *J. Electroanal. Chem.* **1996**, *416*, 139.
(27) Yokoyama, A.; Kojima, T.; Ohkubo, K.; Fukuzumi, S. *Chem. Commun.* **2007**, *7345* (39), 3997.
(28) Wu, B.-Y.; Hou, S.-H.; Yin, F.; Zhao, Z.-X.; Wang, Y.-Y.; Wang, X.-S.; Chen, Q. *Biosens. Bioelectron.* **2007**, *22*, 2854.
(29) Wu, B. Y.; Hou, S. H.; Yin, F.; Li, J.; Zhao, Z. X.; Huang, J. D.; Chen, Q. *Biosens. Bioelectron.* **2007**, *22*, 838.
(30) Xu, G.; Ji, S.; Miao, C.; Liu, G.; Ye, C. *J. Mater. Chem.* **2012**, *22* (11), 4890.
(31) Liu, Y.; Wang, D.-P.; Yu, Y.-X.; Zhang, W.-D. *Int. J. Hydrogen Energy* **2012**, *37* (12), 9566.

Chapter VI

Poly-*cis*-$H_2Ph_2Py_2P$-ZnOEP / Preyssler POM@MNPs complex based on electrostatic interaction for photocurrent generation

Chapter VI: Poly-*cis*-$H_2Ph_2Py_2P$-ZnOEP / Preyssler POM@MNPs complex based on electrostatic interaction for photocurrent generation

In the last decade, the metal nanoparticles (MNPs) has emerged as a new kind of compound that has attracted intensive attention due to its unique optical, electronic, catalytic, and magnetic properties. Up to now, various methods have been established for the metal nanoparticles synthesis, involving chemical, thermal, radiolytic, electrochemical and photocatalytical processes. The photocatalytic reduction of metallic ions in aqueous solutions is observed in the presence of polyoxometalates as photocatalyst and an organic substrate (propan-2-ol) as sacrificial electron donor. The photochemical excitation of the POM with the UV light in the presence of propan-2-ol leads to its reduction. That photoreduction step induces electron transfer to metallic ions to obtain M^0 metal atoms which form metal nanoparticles stabilized by POM. Using this methods, the direct illumination of the deaerated aqueous solution of the Preyssler type polyoxometalates (P_5W_{30}) leads to its reduction and the formation of P_5W_{30}@MNPs (M = Ag, Au, Pt) (see Fig. 6.4).

Then, we have introduced these nanoparticles P_5W_{30}@MNPs on to the surface of one polycationic bis-porphyrin copolymer (named **poly-*cis*-$H_2Ph_2Py_2P$-ZnOEP**, with pyridiniums as spacers, Fig. 6.1), obtained with the methodology described in chapters II to chapters V via the exchange of the PF_6^- counter anion by the negatively charge P_5W_{30}@MNPs (M = Ag, Au, Pt) nanoparticles. Thus, electrostatic interaction between P_5W_{30}@MNPs and the cationic film lead to the formation of the **poly-*cis*-$H_2Ph_2Py_2P$-ZnOEP/P_5W_{30}@MNPs** composite films. The prepared films were fully characterized by UV-vis spectroscopy, X-ray photoelectron spectroscopy, scan electron microscope, electrochemical quartz crystal microbalance, quartz crystal microbalance, electrochemical impedance spectroscopy, Raman spectroscopy and electrochemistry. Their photovoltaic performance under visible light irradiation was also investigated by photocurrent transient measurements under visible illumination.

1. Introduction

Photoelectric conversion using dye molecules is an important photochemical technique for developing solar cells, in which the conversion of photon energy to electrical energy is achieved.

The metal nanoparticles (MNPs) has emerged as a new kind of compound that has attracted intensive attention due to its unique optical, electronic, catalytic, and magnetic properties.[1,2,3] Significantly, localized surface plasmon resonance (LSPR) that occurs at the surface of silver (or gold) metal has substantially enhanced the electronic excitation of surface-anchored molecules and the charge carrier generation.[4,5] However, pure MNPs are unstable and easily gather together,[1] which restricts their utility in the catalyst industry. In this work, one facile and easier strategy to get stable MNPs (M = Ag, Au, or Pt) with the use of polyoxometalates (POMs) to get various P_5W_{30}@MNPs nanoparticles.[6] Here, the Preyssler's type POMs ($Na_{14}[NaP_5W_{30}O_{110}]$) ($P_5W_{30}$) play a dual role, acting as both reducing agents and stabilizing anions (surfactant).

In the previous chapter, the photoelectrochemical response of poly-porphyrin was enhanced in the presence of POM at the surface of the film. To further increase the conversion efficiency of photon energy to electrical energy, we introduce P_5W_{30}@MNPs (M = Ag, Au, Pt) nanoparticles on to the surface of the bis-porphyrin copolymer (Fig. 6.1) in order to try to promote more the efficiency of the photocurrent generation. It should point out that the bis-porphyrin copolymers (Fig. 6.1) include a free base porphyrin (5,10-dipyridyl-15,20-diphenl-porphyrin named ***cis*-$H_2Ph_2Py_2P$**) and a metalloporphyrin (**ZnOEP**) in order to get broader absorption of the visible light.

In this chapter, we extensively investigated the modification of the optical and the redox properties of the **poly-*cis*-$H_2Ph_2Py_2P$-ZnOEP** film after the incorption of the P_5W_{30}@MNPs nanoparticles (M=Ag, Au and Pt). We checked the change of the properties using the UV-vis spectroscopy, X-ray photoelectron spectroscopy, scan electron microscopy, electrochemical quartz crystal microbalance, quartz crystal microbalance, electrochemical impedance spectroscopy, Raman spectroscopy and electrochemistry. The photovoltaic performances of this composit film were also investigated under visible light irradiation.

2. Formation of poly-cis-$H_2Ph_2Py_2P$-ZnOEP-P_5W_{30}@MNPs

2.1 Electropolymerization of poly-*cis*-$H_2Ph_2Py_2P$-ZnOEP films

2.1.1 Cyclic voltammogram during the film formation

Bis-porphyrin copolymers (Fig. 6.1) have been obtained by an electropolymerization process using **ZnOEP** type macrocycle and one porphyrin functionalized by two pyridyl groups at the *meso* positions 5 and 10 (***cis*-$H_2Ph_2Py_2P$**). This electropolymerization process is again based on a nucleophilic attack of the pyridyl groups onto electrogenerated **ZnOEP** dications.

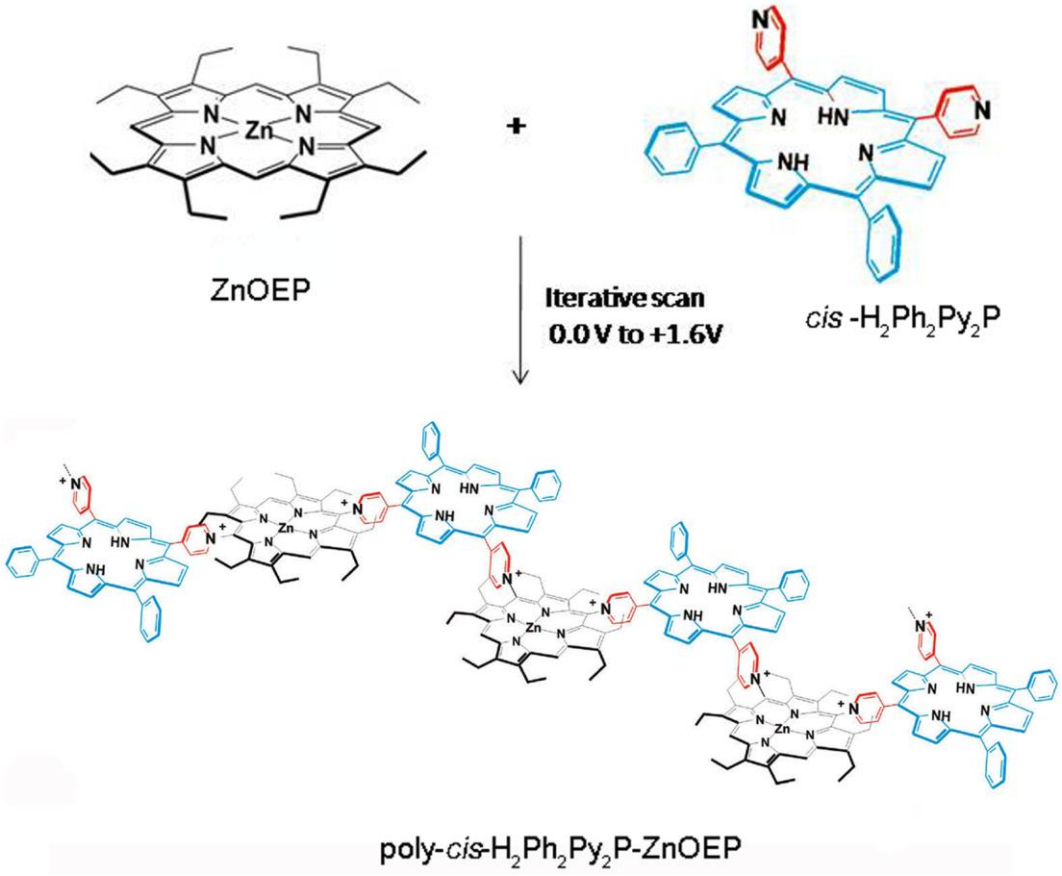

Fig. 6.1 Electropolymerization scheme of **ZnOEP** in the presence of ***cis*-$H_2Py_2Ph_2P$**.

The cyclic voltammograms recorded during electropolymerization of ***cis*-$H_2Ph_2Py_2P$** in the presence of **ZnOEP** shows the growths of three new waves in the cathodic part (Fig. 6.2), at least during the first sweeps (indeed, sometimes, the waves can merge each other when the scan numbers increase). These three waves are always absent during the first scan, i.e. before the oxidation of the **ZnOEP** ring. The

first peak (peak*), around 0.0 and -0.2 V *vs.* SCE, corresponds to the reduction of the isoporphyrin which is formed during the electropolymerization process.[7,8] The two other waves between -0.2 and -0.8 V *vs.* SCE are assigned to the reduction of the pyridinium spacers which are formed between each macrocycle within the polymeric chain.[7,8,9]

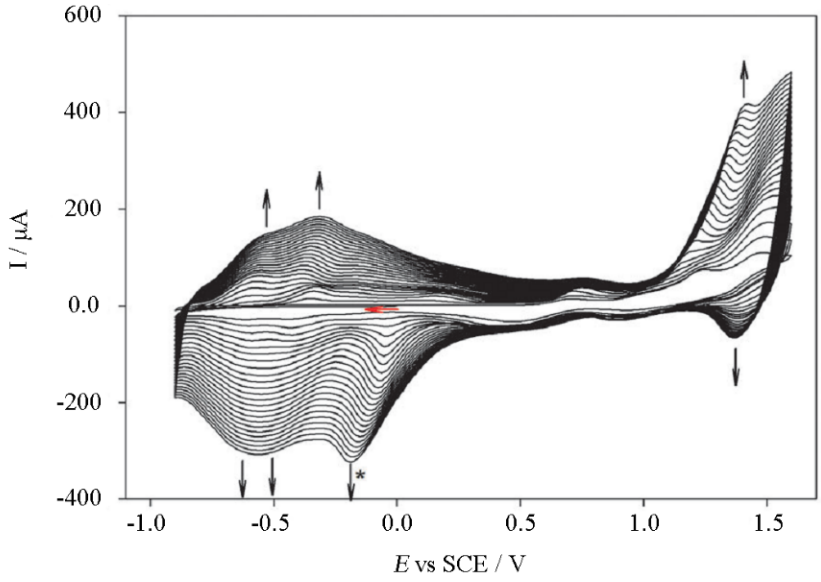

Fig. 6.2 Cyclic voltammograms recorded during 25 iterative scans in a 1,2-$C_2H_4Cl_2$/CH_3CN (7/3) solution of **ZnOEP** (0.25 mmol L^{-1}) in the presence of ***cis*-$H_2Py_2Ph_2P$** (0.25 mmol L^{-1}) and $TBAPF_6$ (0.1 mol L^{-1}). WE: ITO. S = 1 cm^2. v = 0.2 V s^{-1}. (*) This wave is attributed to the reduction of an isoporphyrin intermediate.

2.1.2 EQCM for the copolymer deposition

The electrosynthesis process of **poly-*cis*-$H_2Ph_2Py_2P$-ZnOEP** between 0.00 and +1.60 V has been monitored by EQCM. Fig. 6.3 revealed the simultaneously recorded cyclic voltammograms and mass change.

The quartz resonance frequency (Δf) was decrease at each cycle, which indicated the mass increase of the polymer during the electrosynthesis. Fig. 6.3 shows that a significant decrease of the frequency and consequently the mass increase (calculated from the Sauerbrey's equation[10]) occurred above the second oxidation peak; i.e. electropolymerization happened upon the formation of the dication porphyrin. The steady frequency decrease with time was an indication of the smooth increase of the copolymer mass. The quartz resonance frequency and thus the mass change (Δm) presented a quasi

linear variation in the first ten scans (Fig. 6.3B). In the present investigation, coverage after 25 iterative scans was 9.4 μg cm^{-2}.

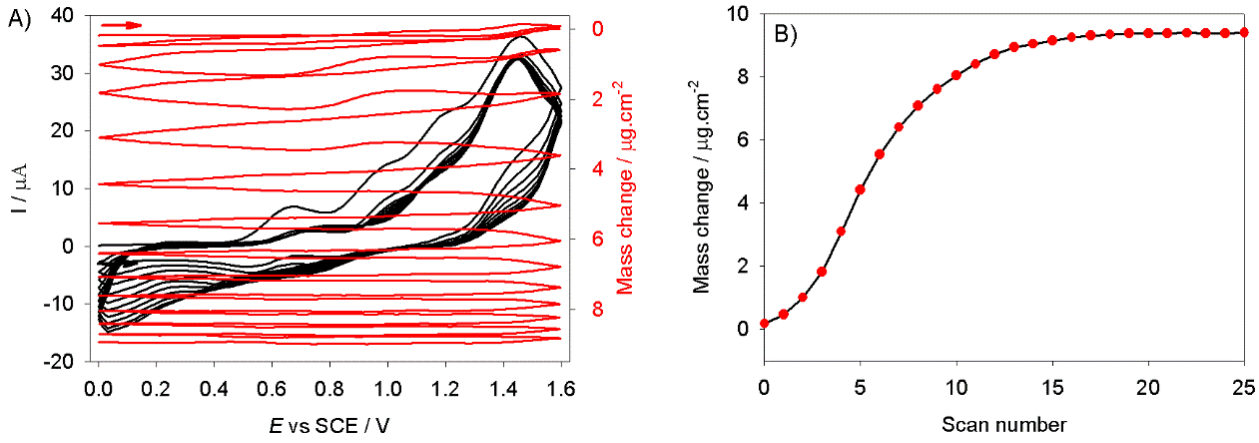

Fig. 6.3 A) Consecutive cyclic voltammograms (first 15 scans) and electrochemical quartz crystal microbalance measurements for the first 15 scans during the electropolymerization of 0.25 mmol L^{-1} **ZnOEP** with 0.25 mmol L^{-1} ***cis*-$H_2Py_2Ph_2P$** in CH_3CN/1,2-$C_2H_4Cl_2$ (3/7) in the presence of 0.1 mol L^{-1} $TBAPF_6$. Working electrode: ITO (A = 0.2 cm^2) deposited on a 9.08 MHz AT-cut quartz crystal. v = 100 mV s^{-1}. B) Mass change (Δm) calculated from Sauerbrey's equation versus the number of scan n.

2.2 Photocatalytic synthesis of metal nanoparticles using Preyssler POM

2.2.1 UV–visible spectrum and TEM study

We present here a low ionic strength photolysis method with near-visible and UV light, which leads to the formation of metal nanoparticles, through a process in which POMs serve both as reducing reagents, and stabilizers. Specifically, three metal ions (Ag^+, $Au^{III}Cl_4^-$, and $Pt^{IV}Cl_6^{2-}$) can form metal nanoparticles in the presence of photochemically reduced POMs in aqueous solutions. This reaction takes place at ambient temperature and without the addition of any stabilizer. A Preyssler-structure polyoxometalate, **$[NaP_5W_{30}O_{110}]^{14-}$** (**$P_5W_{30}$**) was chosen to form the **P_5W_{30}@MNPs**. Reduced **$[NaP_5W_{30}O_{110}]^{15-}$** ion was obtained by photolysis of a deaerated $[NaP_5W_{30}O_{110}]^{14-}$ aqueous solution with λ > 240 nm light, in the presence of propan-2-ol as a sacrificial electron donnor.[11].

Fig. 6.5A-C show the change of the UV-vis spectra during the photocatalysis for the formation of **P_5W_{30}@Ag**, **P_5W_{30}@Au** and **P_5W_{30}@Pt** nanoparticles respectively. The characteristic plasmon bands of the obtained Ag nanostructure (Fig. 6.5A, λ_{max} = 433 nm, yellow color) and Au nanostructure (Fig. 6.5B, λ_{max} = 542 nm, pink color) increased as time go on. On the contrary, no plasmon band was detected

in the case of the photoreduction of the Pt(IV). But, in this case, the increase of the absorbance in the whole visible domain was observed because of the diffusion of the light of the PtNPs. The color of the solution was in this case dark.

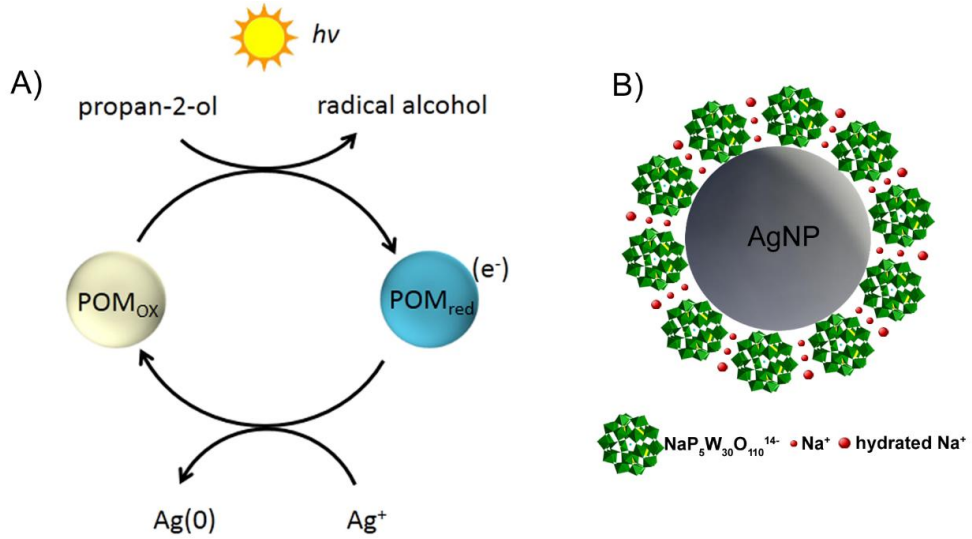

Fig. 6.4 Schematic mechanism of POM-catalyzed photochemical synthesis of Ag^+ to Ag(0) nanoparticles, the model structure of **P_5W_{30}@AgNPs**..

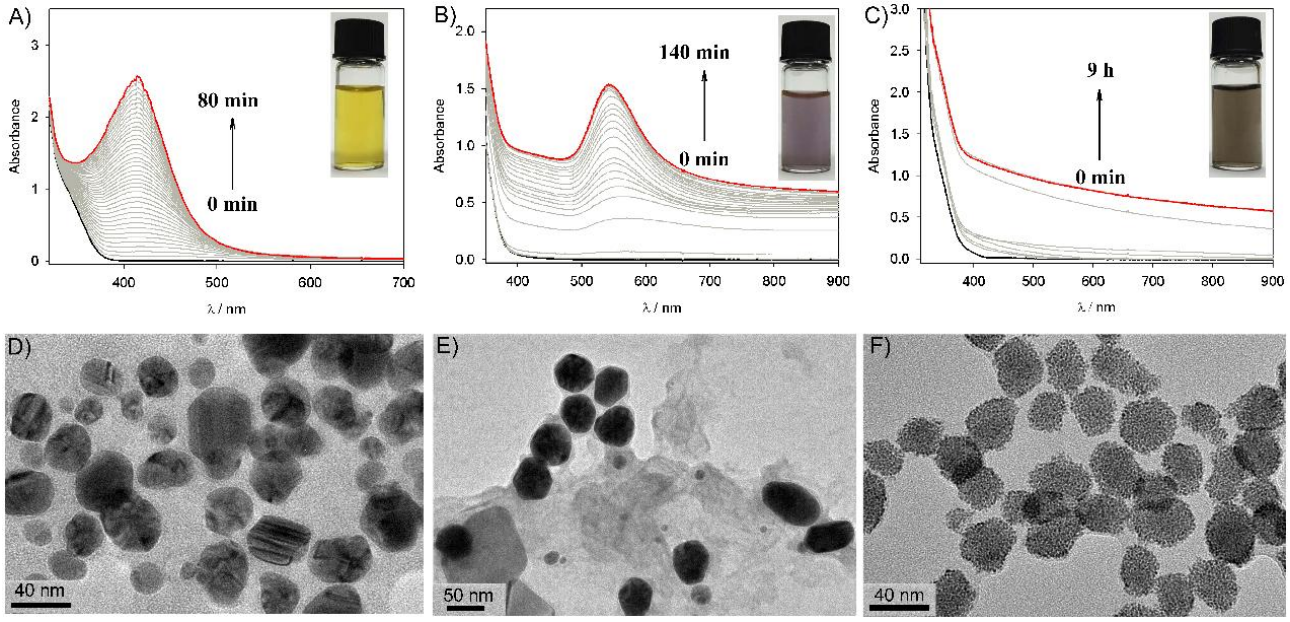

Fig. 6.5 Absorption spectra of metal nanoparticles (Ag, Au, Pt) in aqueous solution, obtained under UV-vis irradiation **$Na_{14}[NaP_5W_{30}O_{110}]$** (**$P_5W_{30}$**) with the corresponding metal ions A) $2Ag^+ SO_4^{2-}$ (0.2 mM), B) $K^+[AuCl_4]^-$ (0.4 mM) or C) $2H^+[PtCl_6]^{2-}$ (0.4 mM)) in the presence of 0.13 M propan-2-ol. Inset: photo of the getting metal nanoparticles in solutions. TEM images of D) **P_5W_{30}@Ag**, E) **P_5W_{30}@Au**, and F) **P_5W_{30}@Pt**.

Transmission electron microscopy (TEM) images of the metal particles indicated in Fig. 6.5D-F verified the formation of metal nanoparticles in the process. The produced Ag nanoparticles were almost spherical with a diameter of 20 − 40 nm. The Au particles obtained were 50 ± 5 nm with the mix morphology of quasi-hexagon and spheroidicity. In the case of platinum, smaller particles of 2.8 ± 0.7 nm diameter were assembled to give larger spheres with an average diameter of 27.0 ± 7.9 nm. The colloids obtained were stable against aggregation for over two months.

2.2.2 Raman spectra

The raman spectrum of **$Na_{14}[NaP_5W_{30}O_{110}]$** exhibits a major band at 968 cm^{-1} and a shoulder at 939 cm^{-1} with both excitation at 457 and 514 nm, which can be attributed to the W=O and W-O-W stretches.[12,13] Interestingly, in the spectra obtained at 514 nm, shoulders at 991 and 1003 cm^{-1} can also be observed. The P-O stretches probably contributes to the signal at 1003 cm^{-1}. Below 300 cm^{-1}, the W-O bending vibrations can be expected. Interaction with Au and Pt NPs does not induce major changes in the spectra. Interaction with AgNPs, however, dramatically enhances the intensity of the bands, and causes a 6 cm^{-1} downshift of the main band. A shoulder at 989 cm^{-1} is visible in both spectra taken at 457 and 514 nm. Silver nanoparticles exhibit several contributions in the 1300-1500 cm^{-1} spectral range.

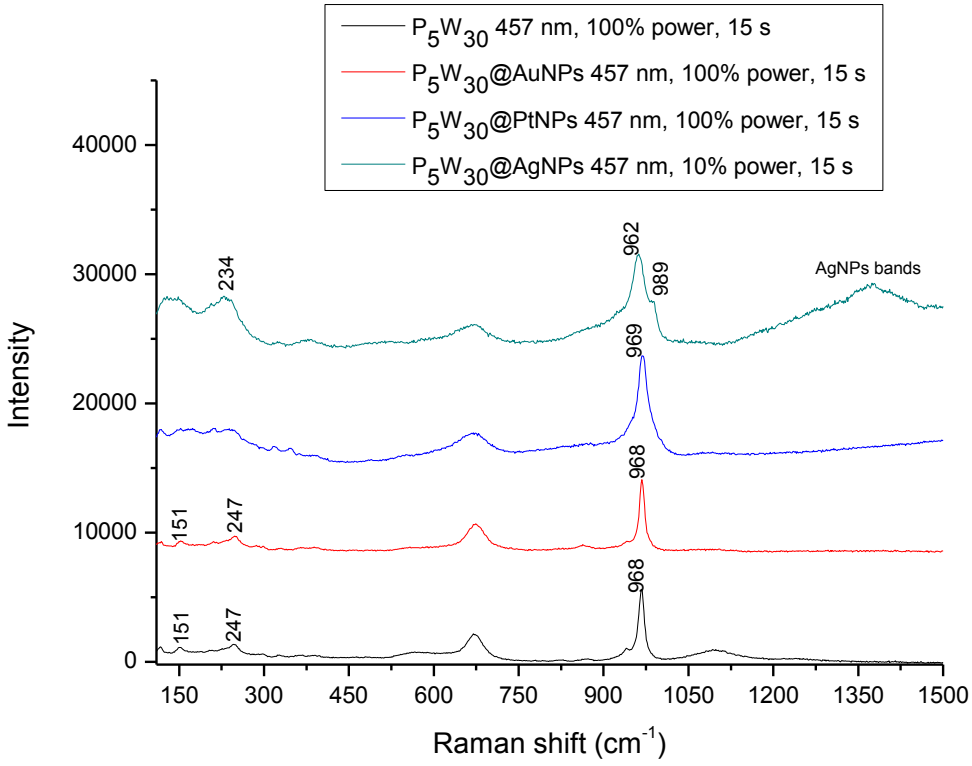

Fig. 6.6 Raman spectra of **P_5W_{30}@MNPs** excited at 457 nm.

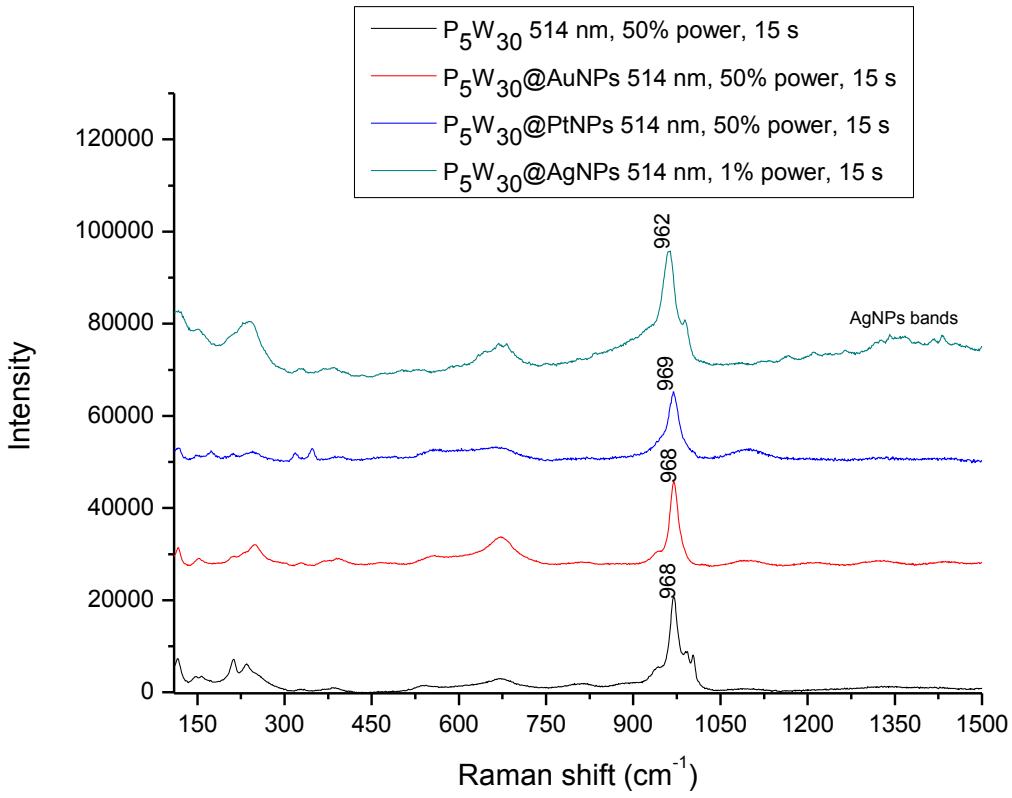

Fig. 6.7 Raman spectra of **P_5W_{30}@MNPs** excited at 514 nm.

2.3 Fabrication poly-*cis*-$H_2Ph_2Py_2P$-ZnOEP/Preyssler POM@MNPs films

2.3.1 Evolution of UV-vis spectra during the POM@MNPs generation

Characterization of **poly-*cis*-$H_2Ph_2Py_2P$-ZnOEP/P_5W_{30}@Ag** was carried out by absorption measurements. Fig. 6.8 shows the evolution of the absorption spectra of the **poly-*cis*-$H_2Ph_2Py_2P$-ZnOEP** film with different soaking time in the **P_5W_{30}@Ag** solution. The slight increase of absorption band around 425 nm can be assigned to the adsorbed isolated AgNPs or the band for the transverse oscillation mode of coupled particles;[14] the small increase of the broadband around 600-900 nm can be allocated to the plasmon band of AgNP aggregates as well as the band for the longitudinal oscillation mode of coupled nanoparticles.[15] In the case of the **poly-*cis*-$H_2Ph_2Py_2P$-ZnOEP/P_5W_{30}@Au** (or Pt) obtained with different soaking time in **P_5W_{30}@Au** (or **P_5W_{30}@Pt**) solution, the UV-visible absorption spectra revealed a much weaker increase of the signals which probably illustrate less electronic interaction between **poly-*cis*-$H_2Ph_2Py_2P$-ZnOEP** and **P_5W_{30}@Au** (or **P_5W_{30}@Pt**), (see appendix,

Fig.S6.1).

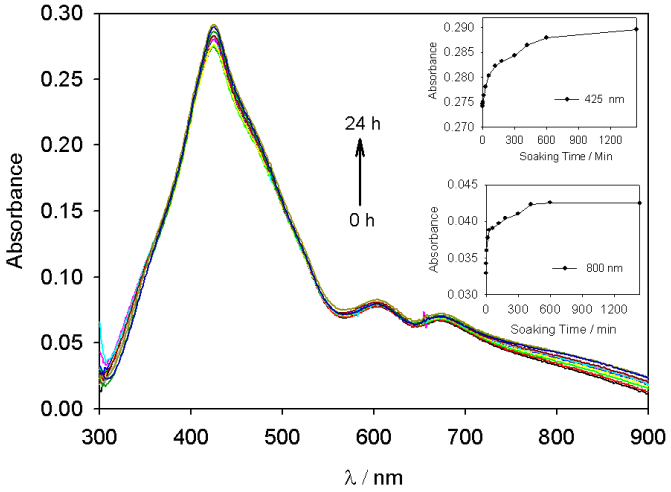

Fig. 6.8 Evolution of UV-vis spectra of the modified ITO electrode with **poly-*cis*-$H_2Ph_2Py_2P$-ZnOEP** after soaking in **P_5W_{30}@Ag** aqueous solution. Inset: absorbance intensity at λ = 425 nm and λ = 800 nm *vs.* time.

2.3.2 X-ray photoelectron spectra

Although the XPS measurement gave only a semi quantitative elemental analysis, the C, N, O, Zn, Na, F, W and Ag elements enable to confirm the presence of poly-*cis*-$H_2Ph_2Py_2P$-ZnOEP/P_5W_{30}@Ag (Fig. 6.9). The Zn 2p3/2 (1021.2 eV) was assigned to the zinc of the ZnOEP porphyrin. Three types of nitrogen with different chemical states were observed and appeared at 402.0 eV for N–C, 400.2 eV for N=C and 398.5 for N–H (free base porphyrin). The F 1s (703.2 eV) was ascribed to counter ion PF_6^-, which indicated that part of PF_6^- also retained in the bis-porphyrin film. The Na 1s (1079.1 eV), W 4f7 (35.8 eV for W4f7/2 and 37.9 eV for W4f5/2) peaks and Ag 3d5/2 (368.0 eV) and Ag 3d3/2 (374.2 eV) in the Ag(0) condition reflected the presence of P_5W_{30}@Ag on to the surface of the film. The XPS of poly-*cis*-$H_2Ph_2Py_2P$-ZnOEP/P_5W_{30}@Au and poly-*cis*-$H_2Ph_2Py_2P$-ZnOEP/P_5W_{30}@Au (see Fig. S6.2 and Fig.S6.3, in the appendix).

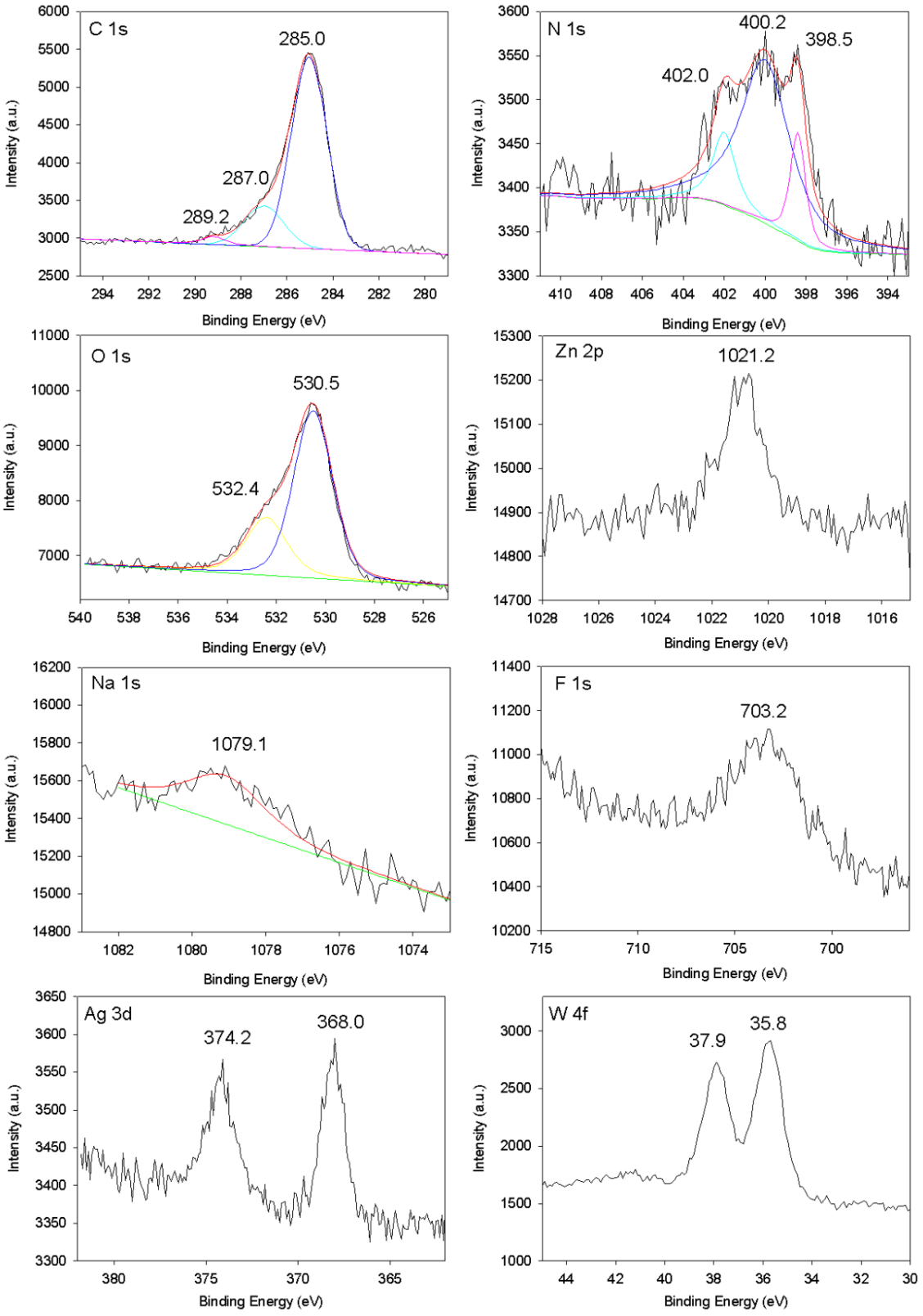

Fig. 6.9 XPS of **poly-*cis*-$H_2Py_2Ph_2P$-ZnOEP-P_5W_{30}@Ag** (0.5 hour) films on ITO.

2.3.3 Electrochemical impedance spectroscopic analysis

Electrochemical impedance spectroscopy (EIS) is a transient technique that measures the current response to the application of a small amplitude AC voltage as a function of the voltage modulation frequency. In the past decade, EIS has been widely used to study the kinetics of electrochemical and photochemical processes in solar cells.[16,17] Usually, the interpretation of EIS spectra is based on electrical equivalent circuits as analogs of the charge transfer processes at the electrified interface.[18]
When the influence of mass transport phenomena on the EIS spectra can be neglected, outer sphere electrochemical reactions at electrified interfaces can be modeled using the equivalent electrical circuit displayed in Fig. 6.10:

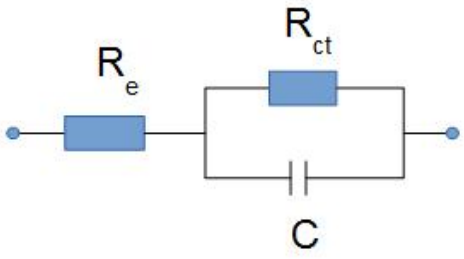

Fig. 6.10 Equivalent circuit n °1 for the electrochemical interface. R_e is the sum of the resistances of the electrolytic solution and of the external circuit, R_{ct} is the charge transfer resistance at the electrode/electrolyte interface and *C* the capacitance at the electrode/electrolyte interface.

The total impedance Z of the equivalent circuit in Fig. 6.10 as a function of the pulsation *w* can be expressed as:

$$Z(w)=R_e+ R_{ct}/[1+R_{ct}C(jw)^n], \qquad \text{equation (1)}$$

where *j* is the imaginary unit and *n* is an empirical constant. For a pure capacitance the value of n is equal to 1. A value of n<1, account for inhomogeneous electrode surfaces and non-ideal capacitor behaviour. The values of the electrolyte and charge transfer resistances (resp. R_e and R_{ct}) can be easily determined from the Nyquist plot, representing *-Z ''(w)* vs. *Z'(w)*. In the case of the equivalent circuit n °1, the corresponding Nyquist diagram is a semicircle and R_e is given by the intercept on the real axis at high frequencies, while R_{ct} is obtained by the intercept on the real axis at low frequencies.

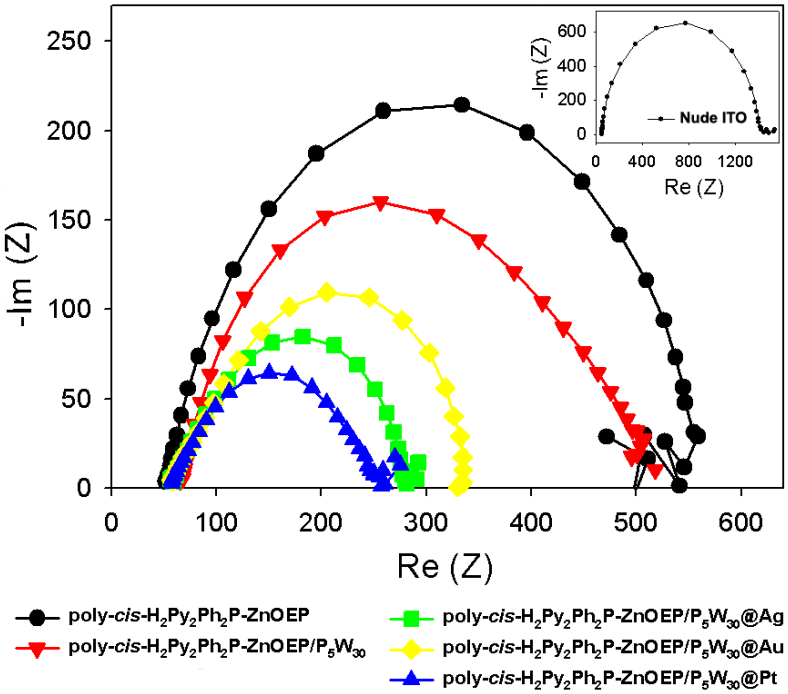

Fig. 6.11 Electrochemical impedance spectroscopy (EIS) under illumination from a 300 W Xe arc lamp (with $\lambda > 385$ nm long pass filter) in H_2O containing I_2 5 mmol L^{-1} and NaI 0.5 mol L^{-1}. The frequency range explored was 0.1 Hz to 10^5 Hz, with the ac amplitude perturbed at 10 mV. DC potential -0.1 V.

Fig. 6.11 shows electrochemical impedance spectra for various electrodes at AC frequency from 0.1 Hz to 10^5 Hz, with DC potential -0.1 V in H_2O containing I_2 5 mmol L^{-1} and NaI 0.5 mol L^{-1} under illumination from a 300 W Xe arc lamp (with $\lambda > 385$ nm long pass filter). The EIS spectrum of the **poly-*cis*-$H_2Py_2Ph_2P$-ZnOEP** and **poly-*cis*-$H_2Py_2Ph_2P$-ZnOEP/P_5W_{30}** electrodes could be satisfactory fitted by using the equation (1), cf. Fig. 6.12a. At variance, when **P_5W_{30}@MNPs** (Ag, Au, Pt) are deposited on the **poly-*cis*-$H_2Py_2Ph_2P$-ZnOEP** electrode, a more sophisticated equivalent circuit (cf. Fig. 6.13) has to be used to reasonnably fit the EIS spectra.

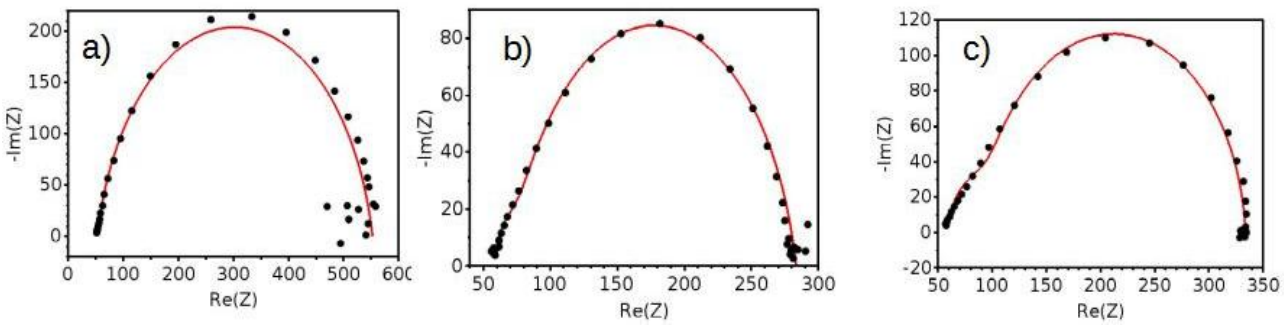

Fig. 6.12 Fits of the **poly-*cis*-$H_2Py_2Ph_2P$-ZnOEP** (a), **poly-*cis*-$H_2Py_2Ph_2P$-ZnOEP/P_5W_{30}@Ag** (b) and **poly-*cis*-$H_2Py_2Ph_2P$-ZnOEP/P_5W_{30}@Au** (c) EIS spectra using equivalent circuits n °1 (a) and n °2 (b) and (c). The parameters used for the fit are given in Table 1.

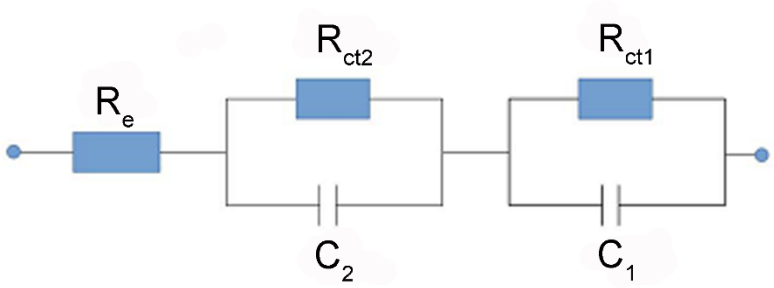

Fig. 6.13 Equivalent circuit n°2 used to model **poly-*cis*-$H_2Py_2Ph_2P$-ZnOEP/P_5W_{30}@MNPs** EIS spectra. R_e is the sum of the resistances of the electrolytic solution and of the external circuit, R_{ct2} and R_{ct1} can be interpretated as the charge transfer resistances from the solution to the MNPs and from the MNPs to the electrode respectively and C_1 and C_2 the corresponding capacitances.

Compared to the equivalent circuit n°1, an additional charge transfer resistance R_{ct2} in parallel with the capacitance C_2 are added in series in the equivalent circuit n°2. R_{ct2} and R_{ct1} can be interpretated as the charge transfer resistances from the solution to the MNPs and from the MNPs to the electrode respectively. The total impedance $Z(w)$ of the circuit n°2 is given by:

$$Z(w)=R_e+ R_{ct1}/(1+R_{ct1}C_1(jw)^n)+R_{ct2}/(1+R_{ct2}C_2jw), \qquad \text{equation(2)}$$

Table 1. The values of the charge transfer resistances and capacitances determined by the fit of the experimental data.

	poly-*cis*-$H_2Py_2PH_2P$-ZnOEP	poly-*cis*-$H_2Py_2Ph_2P$-ZnOEP /P_5W_{30}	poly-*cis*-$H_2Py_2Ph_2P$-ZnOEP/P_5W_{30}/@Ag	poly-*cis*-$H_2Py_2Ph_2P$-ZnOEP/P_5W_{30}/@Pt	poly-*cis*-$H_2Py_2Ph_2P$-ZnOEP/P_5W_{30}/@Au
R_e / Ω	53	61	58	57	59
R_{ct1} / Ω	500	444	210	186	239
R_{ct2} / Ω			15	12	35
C_1 / µF	13	28	24	43	14
C_2 / µF			4.5	4.7	3.4
n	0.87	0.76	0.86	0.78	0.94

As can be seen from Fig. 6.11 and Table 1, under irradiation the *Rct* of **poly-*cis*-$H_2Py_2Ph_2P$-ZnOEP** is about 500 Ω. After incorporating **P_5W_{30}@MNPs** (Ag, Au, Pt), the charge transfer resistances tend to decrease to ca. 200 Ω, revealing the role of the **P_5W_{30}@MNPs** in facilitating the charge transfer and

effectively restraining the recombination of photogenerated electrons and holes. Consequently larger photocurrents are obtained in the presence of nanoparticles in the film. The matched potential positions of P_5W_{30} with the oxidation potential of ($Porp^{+\cdot}$/$Porp^*$) and reduction potential of pyridinium promoted the transportation of charge carriers and retards the recombination of electrons and holes under irradiation, in addition, the catalytic propoerties and the eletronic conductivity of MNPs promoted the electronic transmission. In the three MNPs included films, **poly-*cis*-$H_2Py_2Ph_2P$-ZnOEP/P_5W_{30}@Pt** possessed the lowest Rct (~ 186 Ω).

2.3.4 Raman spectra

Spectra obtained with both excitation at 457 nm (i.e. the porphyrin Soret region) (Fig. 6.14) and 514 nm (i. e. the Q-band region) (Fig. 6.15) of the **poly-*cis*-$H_2Py_2Ph_2P$-ZnOEP** film soaked 0.5 hour in aqueous solution of **P_5W_{30}@MNPs**, yielded several well-resolved bands which can mostly be attributed to the porphyrin. The **P_5W_{30}** polyanions did not exhibit major contributions. Interaction with the **P_5W_{30}** and metallic nanoparticles also did not shift the porphyrin bands. As expected, the silver nanoparticles enhanced significantly the intensity of the bands. The platinium gave also nearly similar behavior. On the contrary, the films containing gold nanoparticles did not show any enhance of the signal probably because the film exhibited a high sensitivity to light, in particular when excited at 514 nm. For a longer soaking time (9 hours) (Fig. 6.16) with again **P_5W_{30}@MNPs** solutions, contribution of the **P_5W_{30}**at 966 cm^{-1} became now clearly visible in the spectra. Interaction with Ag NPs did not shift the porphyrin bands. Interaction with Pt NPs shifted a little bit the porphyrin bands towards lower wavenumbers. Films containing gold nanoparticles still exhibited a high sensitivity to light.

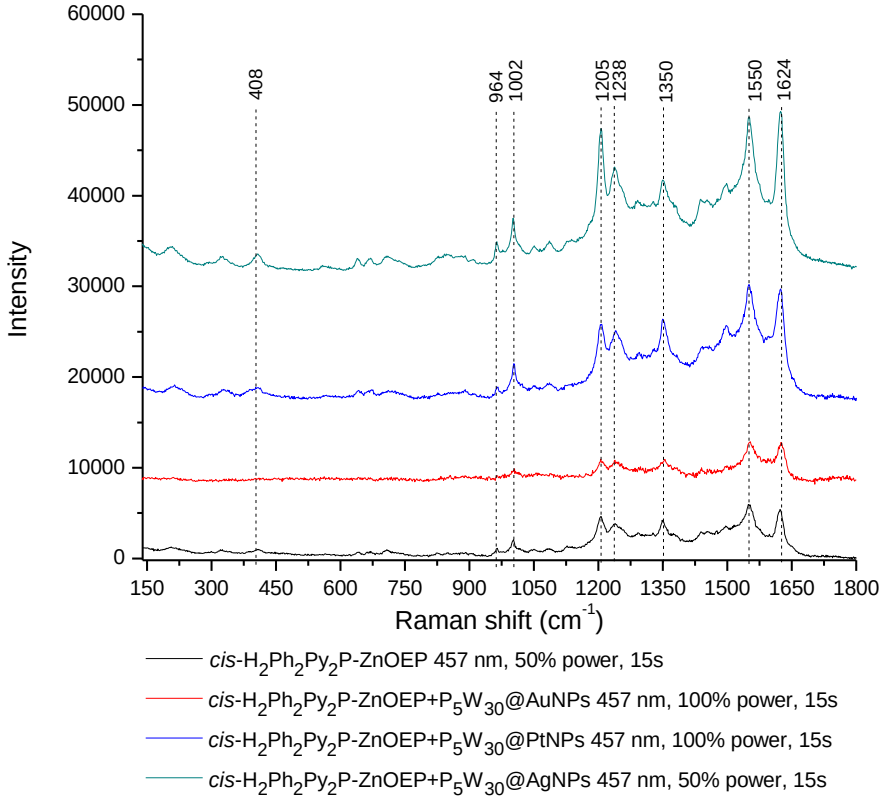

Fig. 6.14 Raman spectra of **poly-*cis*-$H_2Py_2Ph_2P$-ZnOEP/P_5W_{30}@MNPs** (0.5 h) excited at 457 nm.

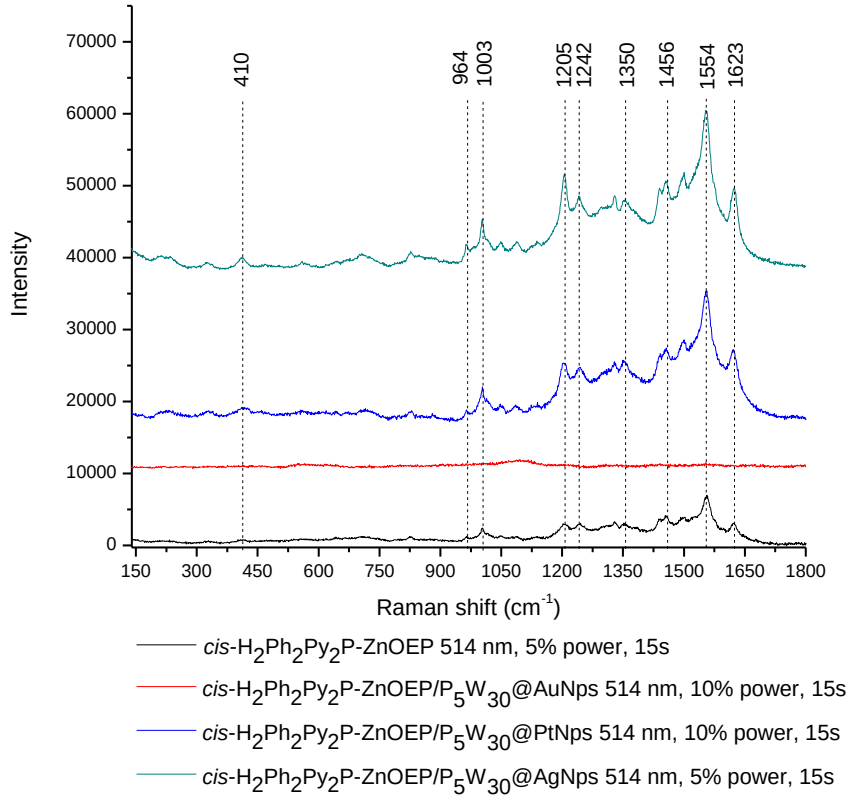

Fig. 6.15 Raman spectra of **poly-*cis*-$H_2Py_2Ph_2P$-ZnOEP/P_5W_{30}@MNPs** (0.5 h) excited at 514 nm.

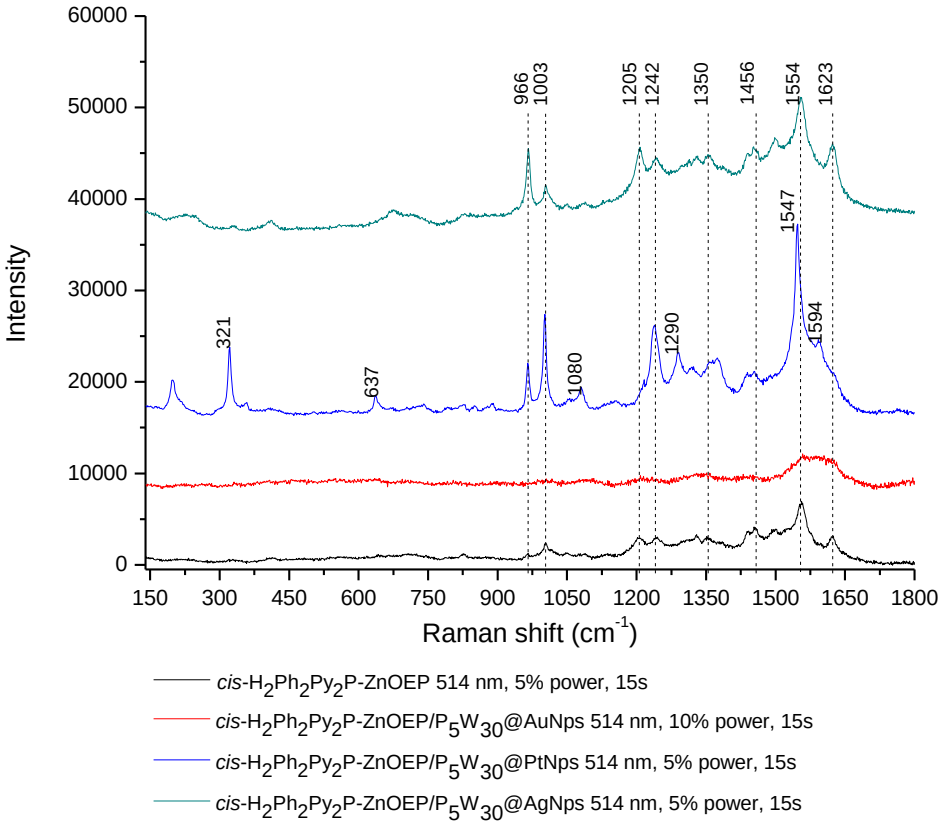

Fig. 6.16 Raman spectra of **poly-*cis*-$H_2Py_2Ph_2P$-ZnOEP/P_5W_{30}@MNPs** (9 h) excited at 514 nm.

2.3.5 SEM graphs of the poly-*cis*-$H_2Ph_2Py_2P$-ZnOEP-P_5W_{30}@MNPs films

Fig. 6.17 shows SEM images of **poly-*cis*-$H_2Py_2Ph_2P$-ZnOEP/P_5W_{30}@Ag**, where AgNPs are indicated as white spots. It is clear that AgNPs incorporated on the bis-porphyrin copolymer films uniformly with diameter of 50 ± 5 nm.

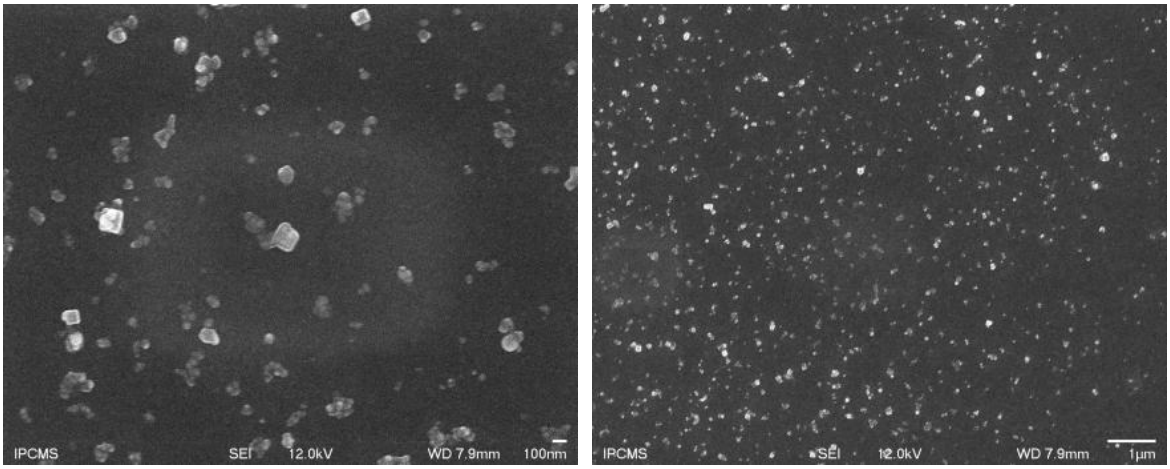

Fig. 6.17 SEM of ***cis*-$H_2Py_2Ph_2P$-ZnOEP-P_5W_{30}@AgNPs** on ITO.

2.3.6 QCM to monitor POM@MNP / PF_6^- exchange on to the poly-cis-$H_2Ph_2Py_2P$-ZnOEP films

QCM was employed to monitor the mass change during **P_5W_{30}@MNPs** (Fig.6.18 −6.20) incorporation process. As we can see, the kinetics of **P_5W_{30}@MNPs** immobilization were quite different: the adsorption amount of **P_5W_{30}@AuNPs** reach the plateau only after 1 hour, while the increase of immobilization amount of **P_5W_{30}@PtNPs** was a linear growth with time (up to 5 hours), whereas the adsorption kinetic of **P_5W_{30}@AgNPs** was in moderation compared the other two. The immobilization of **P_5W_{30}@AgNPs** was 2.82 µg.cm^{-2} after the first 0.5 hour, then the mass increase gently and reached 5.47 µg.cm^{-2} after 5 hours. The different kinetic could be mainly attributed to the difference of the size and morphology of the metal nanoparticles: Au nanoparticles showed a biggest diameter of 50 ± 5 nm (see the TEM, Fig. 6.5E) while the size of Ag nanoparticles were in the range of 20 nm to 40 nm (see the TEM, Fig. 6.5D). In the case of platinum, smaller nanoparticles of 2.8 ± 0.7 nm diameter were assembled to give larger spheres with an average diameter of 27.0 ± 7.9 nm (see the TEM, Fig. 6.5F), **P_5W_{30}@PtNPs** can permeate into the bis-porphyrin film slightly as time go on. However it's hard for the big-sized P_5W_{30}@AuNPs.

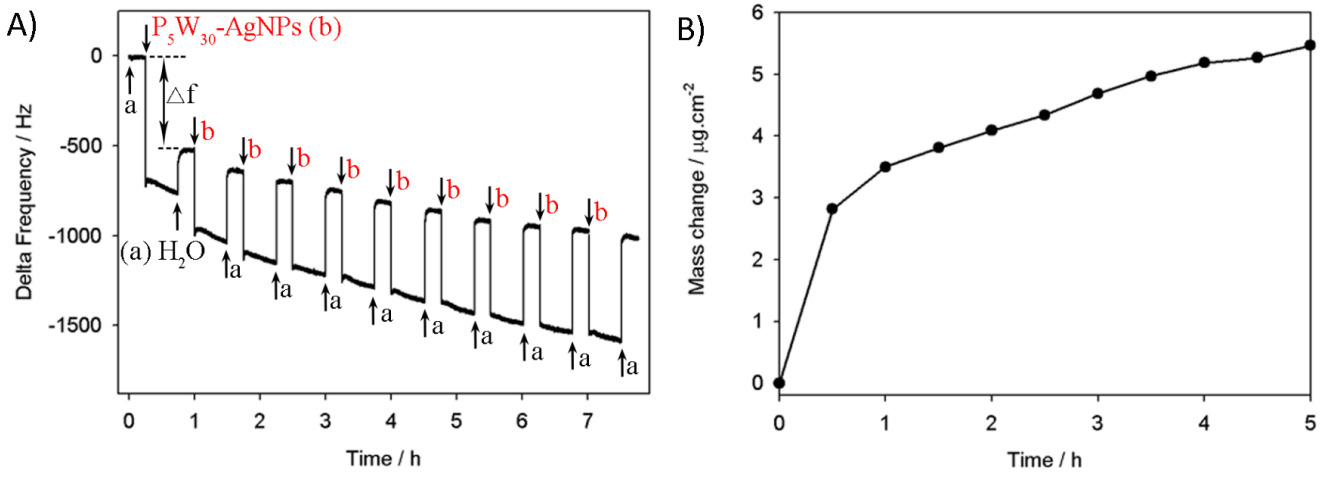

Fig. 6.18 Frequency response of QCM sensor to **$[NaP_5W_{30}O_{110}]^{14-}$@AgNPs** (named b) adsorption onto the **poly-*cis*-$H_2Py_2Ph_2P$-ZnOEP** film **(**pre-electrodeposited onto a 9.08 MHz AT-cut quartz resonator with a thin ITO layer (A = 0.2 cm^2)). The start base line was obtained when the sensor was exposed to H_2O (named a). The arrows ↓ indicated the injection of **P_5W_{30}@Ag**. The arrow ↑ indicated the washing using H_2O. B) Mass change (Δm) calculated from Sauerbrey's equation versus the soaking time.

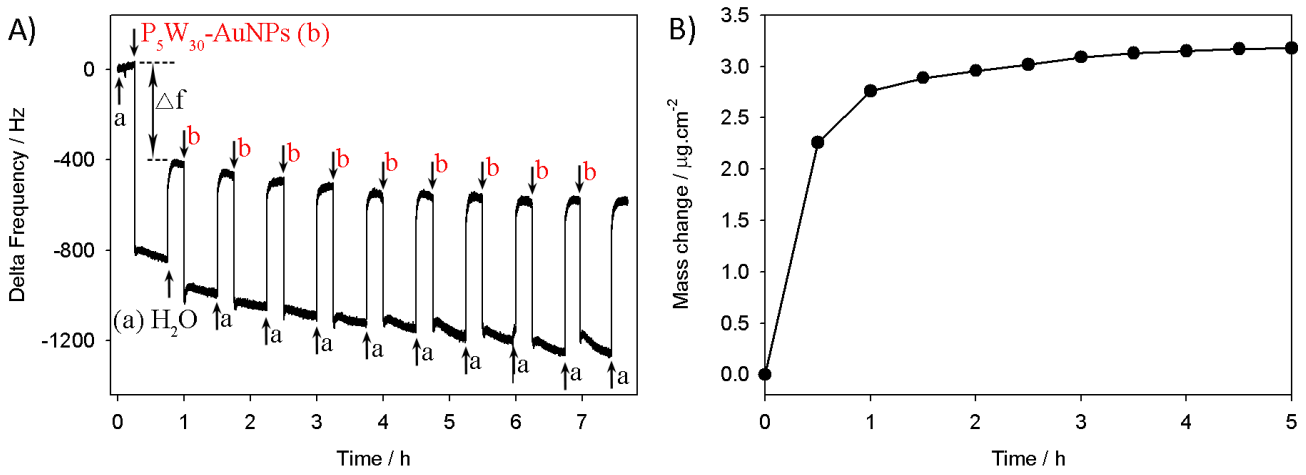

Fig. 6.19 Frequency response of QCM sensor to **$[NaP_5W_{30}O_{110}]^{14-}$@Au** (named b) adsorption onto the **poly-*cis*-$H_2Py_2Ph_2P$-ZnOEP** film **(**pre-electrodeposited onto a 9.08 MHz AT-cut quartz sonator with a thin ITO layer (A = 0.2 cm^2)**).** The start base line was obtained when the sensor was exposed to H_2O (named a). The arrows ↓ indicated the injection of $[NaP_5W_{30}O_{110}]^{14-}$@Pt. The arrow ↑ indicated the washing using H_2O. B) Mass change (Δm) calculated from Sauerbrey's equation versus the soaking time.

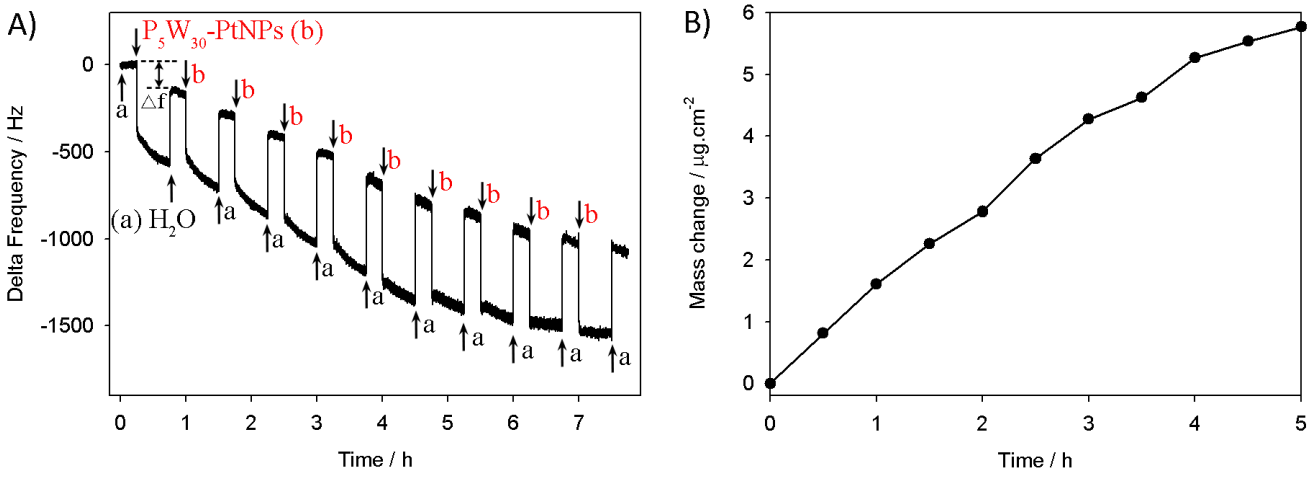

Fig. 6.20 Frequency response of QCM sensor to **$[NaP_5W_{30}O_{110}]^{14-}$@Pt** (named b) adsorption onto the **poly-*cis*-$H_2Py_2Ph_2P$-ZnOEP** film **(**pre-electrodeposited onto a 9.08 MHz AT-cut quartz sonator with a thin ITO layer (A = 0.2 cm^2)**).** The start base line was obtained when the sensor was exposed to H_2O (named a). The arrows ↓ indicated the injection of $[NaP_5W_{30}O_{110}]^{14-}$@Pt. The arrow ↑ indicated the washing using H_2O. B) Mass change (Δm) calculated from Sauerbrey's equation versus the soaking time.

3. Photocurrent generation

3.1 Optimization of the soaking time in P_5W_{30}@MNPs aqueous solution

The immobilization amount of **P_5W_{30}@MNPs** on porphyrin film could be controlled by changing the immersion time into the aqueous colloidal solution of **P_5W_{30}@MNPs**. In order to obtain the maximum enhancement in the photocurrent generation, we have tried to study the photocurrent generation of **poly-*cis*-$H_2Py_2Ph_2P$-ZnOEP/P_5W_{30}@Ag** with different soaking time in **P_5W_{30}@Ag** aqueous ion solution (Fig. 6.21).

In all samples, photocurrents were observed in the cathodic direction. In addition, the maximum enhancements of photocurrents at immersion time of 30 min were observed for **poly-*cis*-$H_2Py_2Ph_2P$-ZnOEP/P_5W_{30}@Ag**. These enhancements of photocurrents due to AgNPs strongly suggest that the local electric fields appearing in the vicinity of AgNPs surface contribute to the enhancement of photocurrent generation based on the porphyrin molecules.[14]

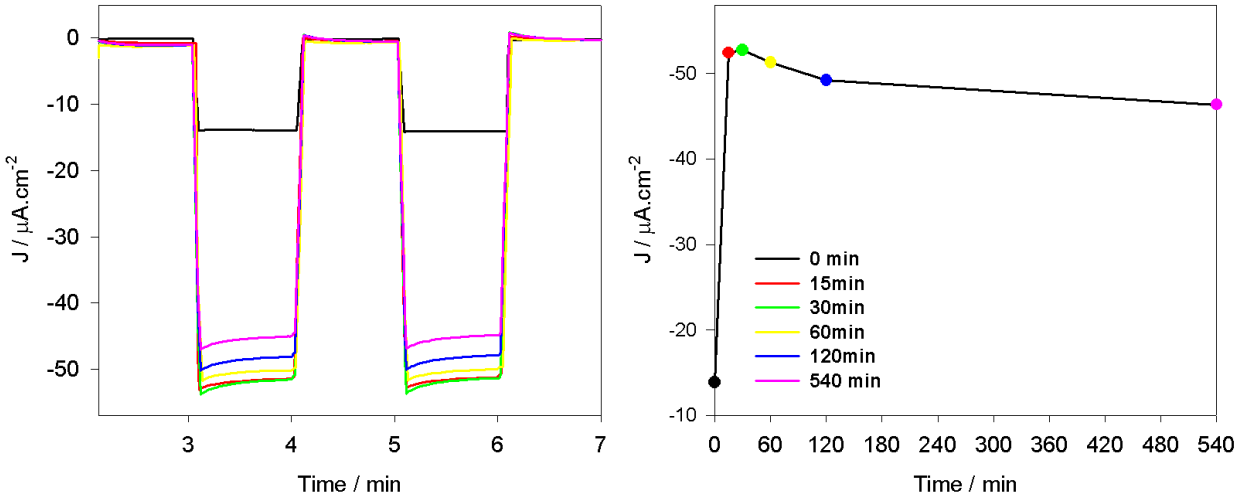

Fig. 6.21 Photoelectrochemical response of **poly-*cis*-$H_2Py_2Ph_2P$-ZnOEP** with different soaking time in **P_5W_{30}@AgNPs** solution under on–off light illumination from a 300 W Xe arc lamp (with $\lambda > 385$ nm long pass filter) in H_2O containing I_3^- 5 mmol L^{-1} and I^- 0.5 mol L^{-1}. BIAS potential: -0.1 V.

Recently, the similar effect of the density of AgNPs on the photocurrents was reported using zinc tetraphenyl porphyrin (ZnTPP)−silver nanoparticle (AgP) composite films on ITO electrodes (ZnTPP/AgP(x h)-OT/PEI/ITO (x h = 1, 2, 4, 6, and 12 h)) by the electrostatic layer-by-layer adsorption technique.[19] In the study, the maximum enhancement (ca. 9 times) of photocurrents in the presence of

AgP (2 h, density: 23%) was observed, while as the density of AgP increase, the relative enhancement of photocurrents decrease. The relative enhancement of photocurrents was ca. 4 times in the presence of AgP (12 h, density: 69%). This difference was ascribed to that the lifetime of ZnTPP* in ZnTPP/AgP(6 h)-OT/PEI/ITO (0.26 ns) was smaller than that in ZnTPP/AgP(2 h)-OT/PEI/ITO (0.97 ns) (see chapter I, section 1.2.2 Porphyrin/metal nanoparticles, Fig. 1.18).

The reduction of photocurrent increase ratio in the **poly-*cis*-$H_2Py_2Ph_2P$-ZnOEP/P_5W_{30}@AgNPs** (540 min) is attributable to the energy transfer from Porp* to surface plasmon on the AgNPs aggregates (nonradiative metallic quenching).[19]

3.2 Effect of noble nanoparticles

The photocurrent comparison of the different films was fully depicted in Fig 6.22 and Table 2. When P_5W_{30} was introduce on to the film, the obtained hybrid film **poly-*cis*-$H_2Py_2Ph_2P$-ZnOEP/P_5W_{30}** possessed a higher photocurrent magnitude (18.1 $\mu A.cm^{-2}$) than for thr initial bis-porphyrin film **poly-*cis*-$H_2Py_2Ph_2P$-ZnOEP** (13.7 $\mu A.cm^{-2}$) in H_2O containing I_3^- 5 mmol L^{-1} and I^- 0.5 mol L^{-1}, under Xe irradiation ($\lambda > 385$ nm) with -0.1 V BIAS potential. The mechanism is similar with that in chapter V. However, the advantage here is the use of aqueous solution, more environmental than the acetonitrile solvent (use in chapter V). The photocurrent enhancement was in a larger extent after adsorption the P_5W_{30}@M nanoparticles (M = Ag, Au or Pt) than for the incorporation of **P_5W_{30}** on the **poly-*cis*-$H_2Py_2Ph_2P$-ZnOEP** film.

The excited state properties of dyes (porphyrin in this work) can be significantly modified by the proximity of a metal nanostructure through the coupling between surface plasmons (AgNPs and AuNPs) and excitons, which may lead to three phenomena: (1) nonradiative metallic quenching, (2) increase in the local excitation field strength, and (3) increase in radiative rate due to plasmon−exciton coupling.[20,21] Metallic quenching of porphyrin molecules is associated with energy and electron-transfer processes. When the excited molecules are close to the metal surface (typically <5 nm), the excited state of porphyrin molecules can be quenched by the metal via nonradiative Förster-like energy transfer or through electron-transfer between porphyrin molecule and the metal. The second phenomenon increases a local excitation field. The third phenomenon results in faster decay rate of fluorescence. In addition,

a scattering of plasmonic nanostructures which increases the optical path of light in chromatic materials enhances the light absorption.[22] Thus, the faster radiative decay rate (third phenomenon: plasmon-exciton coupling), increased local excitation field (second phenomenon: surface plasmon resonance (SPR) - enhanced excitation), and scattering effect which collectively maximize photon competes with the metallic quenching (first phenomenon). The raman spectra study (Fig. 6.14 and Fig. 6.15) revealed that films containing gold nanoparticles exhibit a higher sensitivity to light. Yamada also reported the effect of AuNPs on the photocurrents using the electropolymerized polythiophene−AuNPs composite ITO-electrodes. They revealed that the highest enhancement effect was observed with AuNP density of 14%. In addition, more than 20% of AuNP densities exhibited much smaller enhancement effect of photocurrents. These results indicate that the effects of AuNPs saturate in the fairly low density region, which due to AuNPs perform not only photocurrent enhancement by LSPR (Localized Surface Plasmon Resonance) but also photocurrent decrement by quenching, and that the latter effect should be significantly observed with the dense packing of AuNPs even in the range of submonolayer.[23]

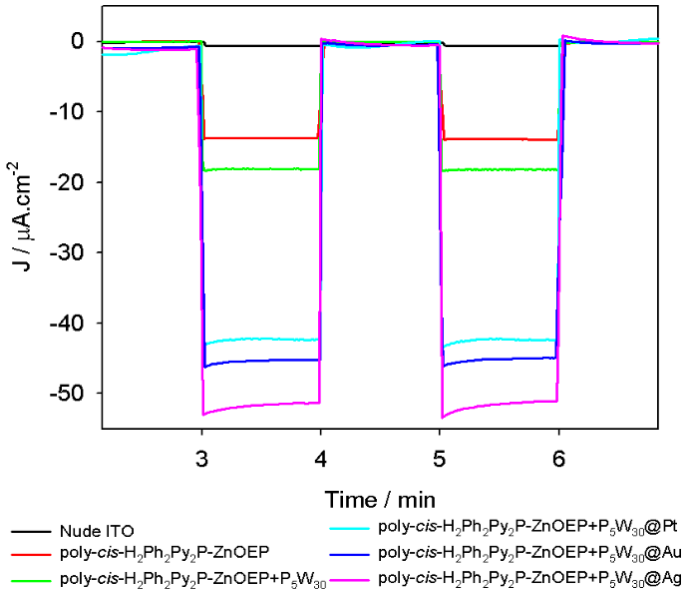

Fig. 6.22 J-t of series copolymers under on–off light illumination in H_2O containing I_3^- 5 mmol L^{-1} and I^- 0.5 mol L^{-1}. BIAS potential: -0.1 V *vs.* OCP. $[NaP_5W_{30}O_{110}]^{14-}$ = P_5W_{30}.

Meantime, the charge transfer resistance of **poly-*cis*-$H_2Py_2Ph_2P$-ZnOEP/P_5W_{30}@Ag** was lower than that **poly-*cis*-$H_2Py_2Ph_2P$-ZnOEP/P_5W_{30}@Au**. Thus, in the two composite films containing plasmonic MNPs (AgNPs and AuNPs), **poly-*cis*-$H_2Py_2Ph_2P$-ZnOEP/P_5W_{30}@Ag** possessed higher photocurrent Table 2). The incorporation of P_5W_{30}@PtNPs could also enhanced the photocurrent, generation mainly due this time to the outstanding conductivity of the PtNPs.

Table 2. The magnitude of the photoelectrical responses.

Systems	J ($\mu A.cm^{-2}$)	BIAS	Conditions
poly-*cis*-$H_2Ph_2Py_2P$-ZnOEP	-13.72	-0.10 V	I_3^-/I^- in H_2O 300 W Xe Arc lamp, λ> 385 nm
poly-*cis*-$H_2Ph_2Py_2P$-ZnOEP /P_5W_{30}	-18.19		
poly-*cis*-$H_2Ph_2Py_2P$-ZnOEP /P_5W_{30}@Ag	-54.21		
poly-*cis*-$H_2Ph_2Py_2P$-ZnOEP /P_5W_{30}@Au	-46.76		
poly-*cis*-$H_2Ph_2Py_2P$-ZnOEP /P_5W_{30}@Pt	-45.58		

3.3 Different BIAS potentials

To reveal the behavior of electron injection within the **poly-*cis*-$H_2Py_2Ph_2P$-ZnOEP/P_5W_{30}@Ag** film electrodes, the photocurrent response dependence on the BIAS voltage is also investigated. Fig. 6.24 depicted that the rate of heterogeneous electron transfer across the film/electrode interface affect the direction and magnitude of the photocurrent in the present system when we applied +0.2 to −0.3 V. Two processes are observed both anodic and cathodic process depending to the applied potential: if E < 0 V, a cathodic process is observed, whereas if applied potential is more than 0.0 V (0.0 V included) anodic process is present. The applied potential can change the rate of heterogeneous electron transfer to the reduced POM. Thus it affected the catalytic activity (regeneration rate) close to electrode surface, which means a larger drift enhance the regeneration rate and it further enhance the catalytic cycles occurring per unit time.[24] When we choosed – 0.1 V BIAS potential, the photocurrent magnitude was the biggest and the respond was prompt, so in this study – 0.1 V BIAS potential was selected.

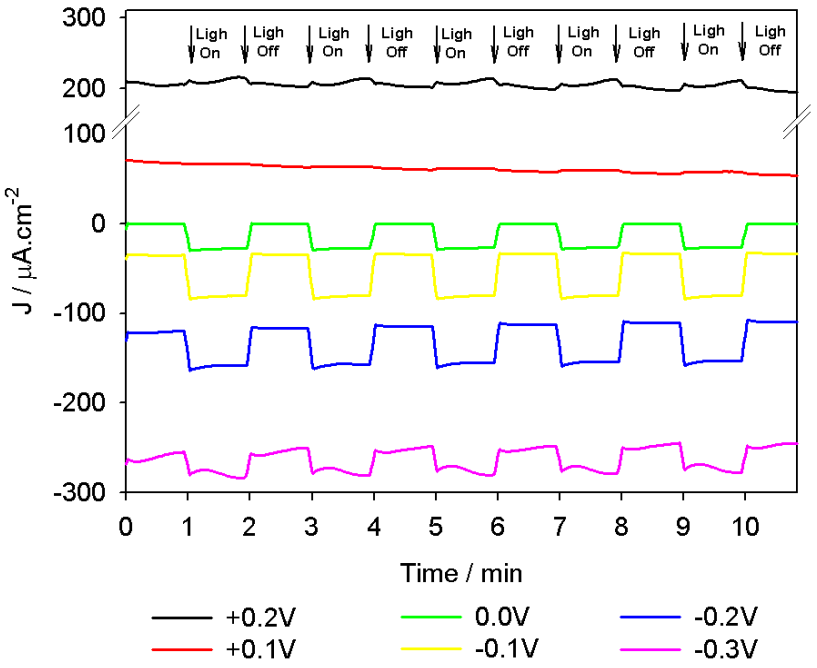

Fig. 6.24 Photocurrent density of **poly-*cis*-$H_2Py_2Ph_2P$-ZnOEP/P_5W_{30}@Ag** (0.5 h) under visible light illumination from a 300 W Xe arc lamp (with $\lambda \geq 385$ nm long pass filter) in H_2O containing I_2 5 mmol L^{-1} and NaI 0.5 mol L^{-1} under different BIAS potentials.

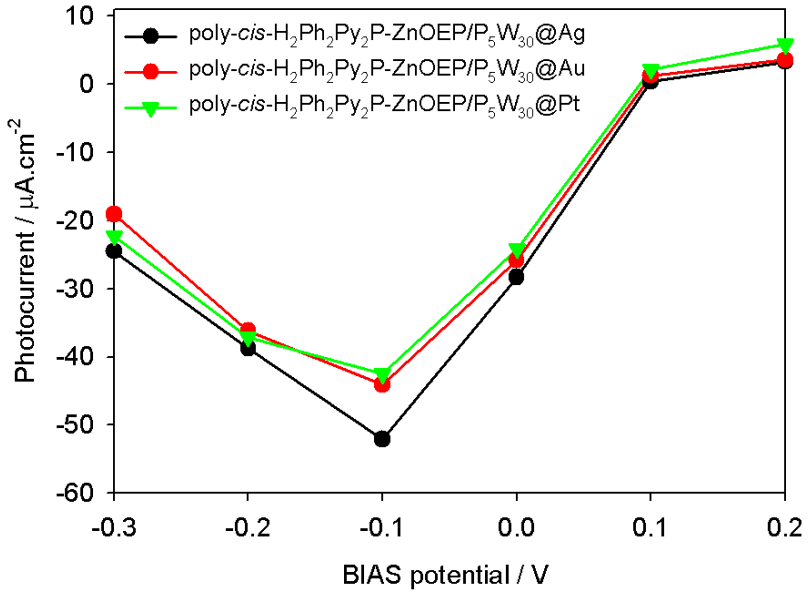

Fig. 6.25 Effects of bias voltage on the photocurrents of **poly-*cis*-$H_2Py_2Ph_2P$-ZnOEP/P_5W_{30}@Ag**, **poly-*cis*-$H_2Py_2Ph_2P$-ZnOEP/P_5W_{30}@Au** and **poly-*cis*-$H_2Py_2Ph_2P$-ZnOEP/P_5W_{30}@Pt** films on to ITO electrode under irradiation from 300 W Xe Arc lamp (with $\lambda \geq 385$ nm long pass filter) in H_2O containing I_3^- 5 mmol L^{-1} and I^- 0.5 mol L^{-1}.

3.4 Energy diagram of the electron transfer processes

The photo-electric conversion mechanism of **poly-*cis*-$H_2Py_2Ph_2P$-ZnOEP/P_5W_{30}@Ag** film could be explained by the following processes: (1) the band-gap excitation from HOMO to LUMO of the

porphyrin macrocycle under illumination and together with the LSPR of AgNPs, (2) electron transfer from the LUMO of porphyrin to the pyridinum spacer, circularly, ITO conduction band supplement electrons to the HOMO of porphyrin (3) reduced pyridine radicals relay electron to W^{VI}POM (4) the reduced W^{V}POM transmit electrons to the redox mediator I_3^- and the generated I^- was reoxidized at the Pt counter electrode which gave the electron to the conduction band of the ITO electrode.

The oxidation of porphyrin subunits (Porp) in the film provides a measurement for the energy of the HOMO level. In the research of the previous chapter (without plasmatic metal nanoparticles), the potential of porphyrin excited state should be calculated as follow:

$$E(\text{Porp}^{+\cdot}/\text{Porp}^{*}) = E(\text{Porp}^{+\cdot}/\text{Porp}) - E_{S0 \rightarrow S1} \qquad (3)$$

The potential of porphyrin in excited state can be calculated by subtracting the energy for excitation light of the films from oxidation potential value of the ground state.

However, LSPR light scattering effection of the AgNPs is able to enhance the interactions between photon and porphyrin. So the level of the excited state (couple $\text{Porp}^{+\cdot}/\text{Porp}^{*}$) should be lower than -4.05 eV calculated from equation 3.[23]

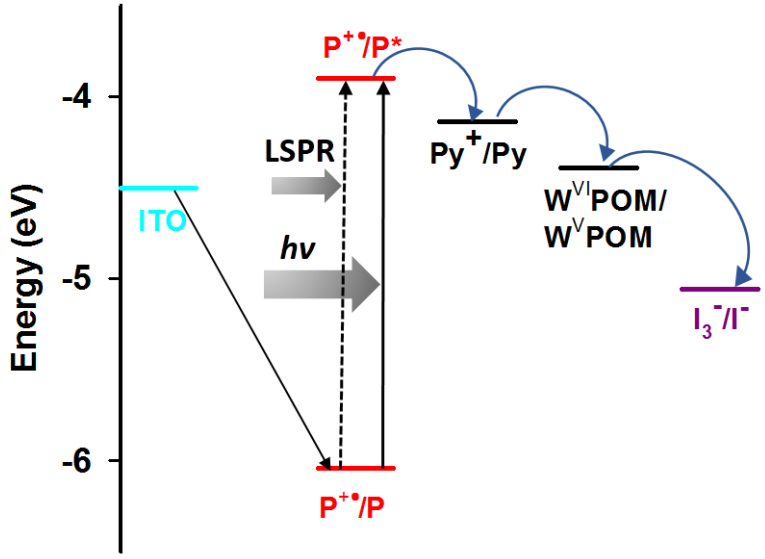

Fig. 6.26 Schematic illustration of the energy level diagram showing electron transfer processes. (Py = pyridine, P = porphyrin).

The energy level of the couples Py^+/Py, $P_5W^{VI}_{30}/P_5W^{V}W^{VI}_{29}$ and I_3^-/I^- were -4.14 eV (-0.36 V *vs.* NHE), -4.39 eV (-0.11 V *vs.* NHE) and -5.06 eV (+0.56 V *vs.* NHE), respectively, on the absolute scale. The

energy level of Py^+/Py is lower than the LUMO level of Porp and higher than $P_5W^{VI}_{30}/P_5W^{V}W^{VI}_{29}$, thus suggesting that the excited **ZnOEP** is able to reduce Py^+ to give $Py^{\bullet}$ and is a favorable exothermic process. Similar to our previous study the photocurrent enhancement can also be explained by the presence of the Preyssler $[Na_{14}P_5W_{30}O_{110}]^{14-}$ subunit, which is a strong electron acceptor and can reoxidize the pyridyl radical ($Py^{\bullet}$) initially formed by electron transfer from the excited porphyrin.

4. Conclusion

In this work, we successfully fabricated the **poly-*cis*-$H_2Py_2Ph_2P$-ZnOEP/P_5W_{30}@M** (M=Ag, Au or Pt) which consisted two steps: firstly, we synthesized bis-porphyrin copolymers covalently linked by pyridinium spacers by electropolymerization from *β*-octaethylporphyrins (**ZnOEP**) and bis-pyridyl substituted free base porphyrins (***cis*-$H_2Py_2Ph_2P$**), secondly, **P_5W_{30}@MNPs** were incorporated onto the prepared **poly-*cis*-$H_2Py_2Ph_2P$-ZnOEP** through electrostatic interaction.

The incorporation of **P_5W_{30}@AgNPs** increases the photocurrent respond of **poly-*cis*-$H_2Py_2Ph_2P$-ZnOEP** (see Table 2) with the greatest extent (about four times). This can be attributed to the occurrence of the photoinduced electron transfer between pyridinium spacers and **P_5W_{30}**, which decrease back electron combination, meantime, the localized surface plasmon resonance that occurs at the surface of silver nanoparticles has substantially enhanced the electronic excitation of the surface-anchored porphyrin, and the excellent eletroconductivity of silver nanoparticles promoted the electronic transmission.

References

(1) Reiss, G.; Hutten, A. *Nat Mater* **2005**, *4* (10), 725.
(2) Singamaneni, S.; Bliznyuk, V. N.; Binek, C.; Tsymbal, E. Y. *J. Mater. Chem.* **2011**, *21* (42), 16819.
(3) Georgakilas, V.; Gournis, D.; Tzitzios, V.; Pasquato, L.; Guldi, D. M.; Prato, M. *J. Mater. Chem.* **2007**, *17* (26), 2679.
(4) Akiyama, T.; Aiba, K.; Hoashi, K.; Wang, M.; Sugawa, K.; Yamada, S. *Chem. Commun. (Camb).* **2010**, *46* (2), 306.
(5) Akiyama, T.; Nakada, M.; Terasaki, N.; Yamada, S. *Chem. Commun.* **2006**, No. 4, 395.
(6) Troupis, A.; Hiskia, A.; Papaconstantinou, E. *Angew. Chem. Int. Ed. Engl.* **2002**, *41* (11), 1911.
(7) Schaming, D.; Ahmed, I.; Hao, J.; Alain-Rizzo, V.; Farha, R.; Goldmann, M.; Xu, H.; Giraudeau, A.; Audebert, P.; Ruhlmann, L. *Electrochim. Acta* **2011**, *56* (28), 10454.
(8) Ruhlmann, L.; Hao, J.; Ping, Z.; Giraudeau, A. *J. Electroanal. Chem.* **2008**, *621* (1), 22.
(9) Giraudeau, A.; Schaming, D.; Hao, J.; Farha, R.; Goldmann, M.; Ruhlmann, L. *J. Electroanal. Chem.* **2010**, *638* (1), 70.
(10) Bruckenstein, S.; Shay, M. *Electrochim. Acta* **1985**, *30* (10), 1295.
(11) Mylonas, A.; Hiskia, A.; Androulaki, E.; Dimotikali, D.; Papaconstantinou, E. *Phys. Chem. Chem. Phys.* **1999**, *1* (3), 437.
(12) Seery, M. K.; Fay, N.; McCormac, T.; Dempsey, E.; Forster, R. J.; Keyes, T. E. *Phys. Chem. Chem. Phys.* **2005**, *7* (19), 3426.
(13) Wang, S.-M.; Liu, L.; Chen, W.-L.; Zhang, Z.-M.; Su, Z.-M.; Wang, E.-B. *J. Mater. Chem. A* **2013**, *1* (2), 216.
(14) Arakawa, T.; Munaoka, T.; Akiyama, T.; Yamada, S. *J. Phys. Chem. C* **2009**, *113* (27), 11830.
(15) Goulet, P. J. G.; Santos, D. S.; Alvarez-puebla, a; Oliveira, O. N.; Aroca, R. F. *Society* **2005**, No. 29, 5576.
(16) Bisquert, J. *J. Phys. Chem. B* **2002**, *106* (2), 325.
(17) Fabregat-Santiago, F.; Garcia-Belmonte, G.; Bisquert, J.; Zaban, A.; Salvador, P. *J. Phys. Chem. B* **2002**, *106* (2), 334.
(18) MacDonald, D. D. *Electrochim. Acta* **2006**, *51* (8-9), 1376.
(19) Matsumoto, R.; Yonemura, H.; Yamada, S. *J. Phys. Chem. C* **2013**, *117* (6), 2486.
(20) Lakowicz, J. R. *Anal. Biochem.* **2001**, *298* (1), 1.
(21) Geddes, C.; Lakowicz, J. *J. Fluoresc.* **2002**, *12* (2).
(22) Atwater, H. a; Polman, A. *Nat. Mater.* **2010**, *9* (3), 205.
(23) Takahashi, Y.; Taura, S.; Akiyama, T.; Yamada, S. *Langmuir* **2012**, *28* (24), 9155.
(24) Zhu, J.; Walsh, J. J.; Bond, A. M.; Keyes, T. E.; Forster, R. J. *Langmuir* **2012**, *28* (37), 13536.

General conclusion

General conclusion

The objective of the present thesis was to investigate new photoactive assemblies based on polyoxometalate – porphyrin hybrids and applied for photocurrent generation and/or photorecovery metal ions (Ag(I) and Pt(IV)). This broad theme can be further subdivided into two main avenues of research according to the linkage of the two subunits (polyoxometalate (POM) moieties and porphyrin moieties). Firstly, covalent POM–porphyrin copolymers were prepared using an electropolymerization method based on the nucleophilic attack of pyridyl groups (bound on the POM framework, Py-POM-Py) onto electrogenerated porphyrin dications. Secondly, electrostatic POM–porphyrin films were constructed by incorporating POM polyanions (or POM@MNPs) onto the surface of the electrogenetated poly-porphyrin film through replacing the initial counter anions (PF_6^-).

In chapter II, Lindqvist – porphyrin copolymers have been prepared. The four times higher coverage of **poly-V_6O_{13}-ZnOEP** (45.8 μg/cm^2) than **poly-V_6O_{13}-H_2T_2P** (8.8 μg/cm^2) films after 20 iterative scans was probably due to the longer chains of the obtained **poly-V_6O_{13}-ZnOEP** and the presence of coordination of one additional **Py-V_6O_{13}-Py** onto the Zn of the **ZnOEP** macrocycle. The properties of the porphyrin (molar extinction coefficient: **ZnOEP** > **H_2T_2P**) dominate the light collection ability of the POM-porphyrin copolymers, and the order of the visible absorbance magnitude is **poly-V_6O_{13}-ZnOEP** > **poly-V_6O_{13}-H_2T_2P**. Thus, based on the higher light collection (higher visible absorbance), together with the lower charge transfer resistance, the **poly-V_6O_{13}-ZnOEP** copolymers with the **ZnOEP** as photosensitizer possessed more efficient photocurrent response and a little higher kinetic performance during photocatalytical process for the reduction of metallic ions than **poly-V_6O_{13}-H_2T_2P**,

In chapter III, covalent Keggin and Dawson silyl polyoxophosphotungstate – porphyrin copolymers have been formed and studied. Their photovoltaic activity and photocatalytic efficiency could be tuned according to structural class of POM (Keggin *vs.* Dawson). The performance of **poly-$P_2W_{17}Si_2$-ZnOEP** in photocurrent generation and photocatalytical kinetic of the reduction of metallic ions were the best during all of the covalent POM-porphyrin copolymers that we have prepared in this thesis (ten covalent copolymers in total). The reasons are following: the organosilyl functionalized Dawson framework offers better compromise between efficient charge separation and long-lived charge-separated state than organosilyl functionalized Keggin framework (Anna Proust et al, Chemical Science, 2013 (4) 1737);

the impedance measurements indicate **poly-$P_2W_{17}Si_2$-ZnOEP** with the lowest charge transfer resistance; and big-size Dawson type POM can provide bigger electron-storage volume.

In chapter IV, we have prepared several conjugated Dawson polyoxophosphovanadotungstate – porphyrin copolymers. We investigated the effect of spacer between bis-alkoxo-amide functionalized Dawson structure $[P_2W_{15}V_3O_{62}]^{9-}$ and **ZnOEP** by varying in the relative positions of the nitrogen atoms of the pyridine rings or in the distance from the carbonyl group. The **poly-POM-l4,4-ZnOEP** film generated higher photocurrent than that of **poly-POM-l3,3-ZnOEP**, which differs only in the position of the nitrogen atoms. This is maybe due to a higher conductivity and longer distance between the POM and the **ZnOEP** subunits (delay charge recombination between the oxidized porphyrin and the reduced POM) for **poly-POM-l4,4-ZnOEP.** A similar explanation can be proposed in the case of the two other copolymers, **poly-POM-s4,4-ZnOEP** and p**oly- POM-m3,3-ZnOEP**.

In chapter V, firstly, one novel porphyrin copolymer (**poly-ZnOEP2**) has been produced by electropolymerization of **ZnOEP** in the presence of a flexible propyl- linked bispyridinium (1,1''-(1,3-propanediyl)bis-4,4'-bipyridinium). Spectroelectrochemical studies in the near infra-red region of the spectrum recorded for $–[ZnOEP–V^{+\bullet}–(CH_2)_3–V^{+\bullet}]_n–$ suggest the formation of π-dimer complexes in the polymer.

We have also prepared one other copolymer with **ZnOEP** and the 4,4'-bipyridine for comparison which leaded to copolymer with single viologen bridges (**poly-ZnOEP1**). Futhermore, due to the appropriate redox potential of $[NaP_5W_{30}O_{110}]^{14-}$ (P_5W_{30}), this POM could acted as strong electron acceptor. Thus, two electrostatic **poly-ZnOEP/P_5W_{30}** (one using rigid and short spacer (viologen) and another one using flexible and long spacer (bis-viologen) between the **ZnOEP** macrocycles) composite film have been prepared. These hybrid systems possessed 3.4 times (**poly-ZnOEP2/P_5W_{30}**) and 1.3 times (**poly-ZnOEP1/P_5W_{30}**) higher photocurrent response than that in the absence of **P_5W_{30}** polyanions, respectively.

In chapter VI, to further improve the efficiency of the photocurrent generation, we have introduced **P_5W_{30}@MNPs** nanoparticles (M=Ag, Au, and Pt) instead of **P_5W_{30}** polyanion to a bis-porphyrin copolymer through metathesis reaction. The incorporation of **P_5W_{30}@AgNPs** increased the photocurrent respond of **poly-*cis*-$H_2Py_2Ph_2P$-ZnOEP** with the greatest extent (about four times). This could be attributed to the occurrence of the photoinduced electron transfer between pyridinium spacers

and **P_5W_{30}**, which retards back electron combination. Meantime, the localized surface plasmon resonance that occurs at the surface in the case of the use of the silver nanoparticles has substantially enhanced the electronic excitation of the surface-anchored porphyrin. Moreover, the excellent eletroconductivity of silver nanoparticles promoted also the electronic transmission. The impedance analysis demonstrated that the charge transfer path was from the solution to the MNPs and from the MNPs to the electrode respectively.

To conclude, for the ten covalent POM-porphyrin films developped in this work (chapters II to IV), the photocurrent is always a cathodic process in aqueous solution using I_3^-/I as redox mediator. The photocurrent intensity is between -0.76 and -7.85 $\mu A.cm^{-2}$ which are comparable to the literatures (see Table 1). **Poly-$P_2W_{17}Si_2$-ZnOEP** possessed the highest photocurrent responds (-7.85 $\mu A.cm^{-2}$). In the case of the electrostatic POM-porphyrin films of which the POMs monolayer was incorporated onto the surface of the poly-porphyrin film (see chapter V), the photocurrent responds were +32.41 $\mu A.cm^{-2}$ for **poly-ZnOEP1/P_5W_{30}** and +24.85 $\mu A.cm^{-2}$ for **poly-ZnOEP2/P_5W_{30}** (anodic process in CH_3CN). The greater performance of the electrostatic POM-porphyrin films than covalent POM-porphyrin films is probably due to the better control of the respective position of the photosensibilisator and the POM in the film which may decrease the kinetic of the back reaction and give also a better control of the direction of the electron transfer. The **poly-*cis*-$H_2Ph_2Py_2P$-ZnOEP/P_5W_{30}@Ag** films obtained a good photocurrent responds (-54.21 $\mu A.cm^{-2}$) where the presence of the nanoparticles onto the surface inscease the photosensibilization of the porphyrin (and also probably the conductivity of the film). Our investigation might initiate new opportunities for the development of a facile synthesis yet highly efficient photoactive system.

To fully reveal the photocurrent responds of all of the systems in this thesis (light green), Table 1 reviews the performance of various type of chromophore / POM assemblies in the literature of other groups (light blue) and also the previous work in our group (light orange).

Further developments will try to address the in situ measurement of the conductivity, investigate monochromatic photocurrent densities to make clear the relationship with the electron excitation of porphyrin and POM@MNPs (or POM) and study the overall conversion efficiency η of the sealed cell.

We will try to controll the size and shape of the obtained POM@MNPs and study the effection of the type of POM used. We also need to investigate the effect of various type of nanoparticles on the photocurrent generation (nanoparticles with citrate as surfactant for instance without POM with various diameters). Finally the photocatalysis application for photodegradation of organic pollutants is also under aerated meadium will be also interesting to be developped.

Table 1. Comparison of the magnitude of the photoelectrical responses. (see Fig. 1 for the representation of the various ruthenium complexes, hemicyanines, phtalocyanines, PVP or porphyrins).

	Systems	J ($\mu A.cm^{-2}$)	BIAS	Conditions
Ru / POM	**$[Ru(bpy)_3]^{2+}$: $[W_{18}O_{54}(SO_4)_2]$** [1]	59.00	1.00 V[a,c]	BnOH in CH_3CN 350 W Oriel Arc lamp, λ>400 nm
	Ru-Co-P :S_2Mo_{18} **Ru-PVP : S_2Mo_{18}** [2]	0.01 0.04	0.40 V[a,c] 0.40 V[a,c]	BnOH in CH_3CN 350 W Oriel Arc lamp,λ>488 nm
	$[Ru(bpy)_2$-$(PVP)_{10}]$: $[S_2Mo_{18}]$ **$[Ru(bpy)_2$-$(PVP)_{10}]$: $[P_2W_{18}]$** [3]	0.04 0.24	0.80 V[a,c] 0.80 V[a,c]	BnOH in CH_3CN 350 W XeArc lamp, λ>480±5 nm
	Polymer / $(W_{72}V_{30}/PPV)_{10}$[d] [4]	1.68	0.00 V[c]	O_2 in H_2O 100 W Xe Arc lamp (UV and visible)
Hemicyanine / POM	**Hemicyanine / SiW_{12}/H^3** [5]	-1.02	-0.20 V	EV^{2+} [e] or O_2 in H_2O 500 W Xe Arc lamp, 325 <λ< 730 nm
	Hemicyanine / $Cd_4(PW_9)_2/N^6$ [6]	-2.40	-0.30 V	MV^{2+} [e] or O_2 in H_2O 500 W Xe Arc lamp, 325 <λ< 730 nm
	Hemicyanine / $Ni_4(PW_9)_2/H^6$ [6]	-3.51		
	Hemicyanine / $Cu_4(PW_9)_2/H^6$ [7]	-3.68		
	Hemicyanine / $Zn_4(PW_9)_2/H^6$ [7]	-2.51		
	Hemicyanine / $Zn_4(PW_9)_2/N^3$ [8]	-13.70		
Phtalocyanine / POM	**Phtalocyanine / P_2Mo_{18}/CoTAPc**[f] [9]	0.03	0.56 V[c]	O_2 in H_2O, 5 W λ = 365 nm
	Phtalocyanine / $SiMo_{12}$/CuPc[f][10]	0.60	0.56 V	O_2 in H_2O, 300 W Xe arc lamp
Porphyrin / POM	**Porphyrin / $P_2V_3W_{15}$-TPP**[g][11]	-1.02	0.10 V[c]	I_3^-/I^- in H_2O 300 W Xe Arc lamp, λ> 385 nm
	Porphyrin / FeP_2W_{17}/ $H_2TPhN(Me)_3P)_{25}$ [12]	-1.78	-0.10 V[c]	I_3^-/I^- in CH_3CN 300 W Xe Arc lamp, λ> 385 nm
Chapter II	**poly-V_6O_{13}-ZnOEP**	-0.83	0.00 V	I_3^-/I^- in H_2O 300 W Xe Arc lamp, λ> 385 nm
	poly-V_6O_{13}-H_2T_2P	-0.76		
Chapter III	**poly-$PW_{11}Si_2$-ZnOEP**	-2.18		
	poly-$PW_{11}Si_2$-H_2T_2P	-1.12		
	poly-$P_2W_{17}Si_2$-ZnOEP	-7.84		
	poly-$P_2W_{17}Si_2$-H_2T_2P	-1.66		
	poly-POM-s4,4-ZnOEP	-1.25		I_3^-/I^- in H_2O

Chapter IV	**poly-POM-m3,3-ZnOEP**	-2.78	-0.10 V	300 W Xe Arc lamp, λ> 385 nm
	poly-POM-l3,3-ZnOEP	-0.92		
	poly-POM-l4,4-ZnOEP	-3.14		
Chapter V	**poly-ZnOEP-V^{2+}**	+9.29	0.00 V	I_3^-/I^- in CH_3CN 300 W Xe Arc lamp, λ> 385 nm
	poly-ZnOEP-V^{2+}/$[NaP_5W_{30}O_{110}]^{14-}$	+32.41		
	poly-ZnOEP-V^{2+}-$(CH_2)_3V^{2+}$	+17.51		
	poly-ZnOEP-V^{2+}-$(CH_2)_3V^{2+}$ /$[NaP_5W_{30}O_{110}]^{14-}$	+24.75		
Chapter VI	**poly-*cis*-$H_2Ph_2Py_2P$-ZnOEP**	-13.72	-0.10 V	I_3^-/I^- in H_2O 300 W Xe Arc lamp, λ> 385 nm
	poly-*cis*-$H_2Ph_2Py_2P$-ZnOEP /P_5W_{30}	-18.19		
	poly-*cis*-$H_2Ph_2Py_2P$-ZnOEP /P_5W_{30}@Ag	-54.21		
	poly-*cis*-$H_2Ph_2Py_2P$-ZnOEP /P_5W_{30}@Au	-46.76		
	poly-*cis*-$H_2Ph_2Py_2P$-ZnOEP /P_5W_{30}@Pt	-45.58		

[a] The [Ru–POM] adduct is excited by incident light to become [Ru–POM]*. This excited [Ru–POM]* species forms is a pre-associated (POM—BnOH) before photo-oxidation of benzylalcohol (BnOH) occurs by hole transfer. Then reoxidation of the reduced [Ru–POM] catalyst occurs at the electrode interface which require high applied potential. [b] Layer-By-Layer (LBL). [c] Three electrodes set up using applied potential versus SCE. [d] Poly(p-phenylenevinylene) derivatives (PPV).[e] Ethylviologen (EV^{2+}), Methylviologen (MV^{2+}). [f] Phtalocyanine (Pc). [g] Tetraphenylporphyrin (TPP). [h] This work.

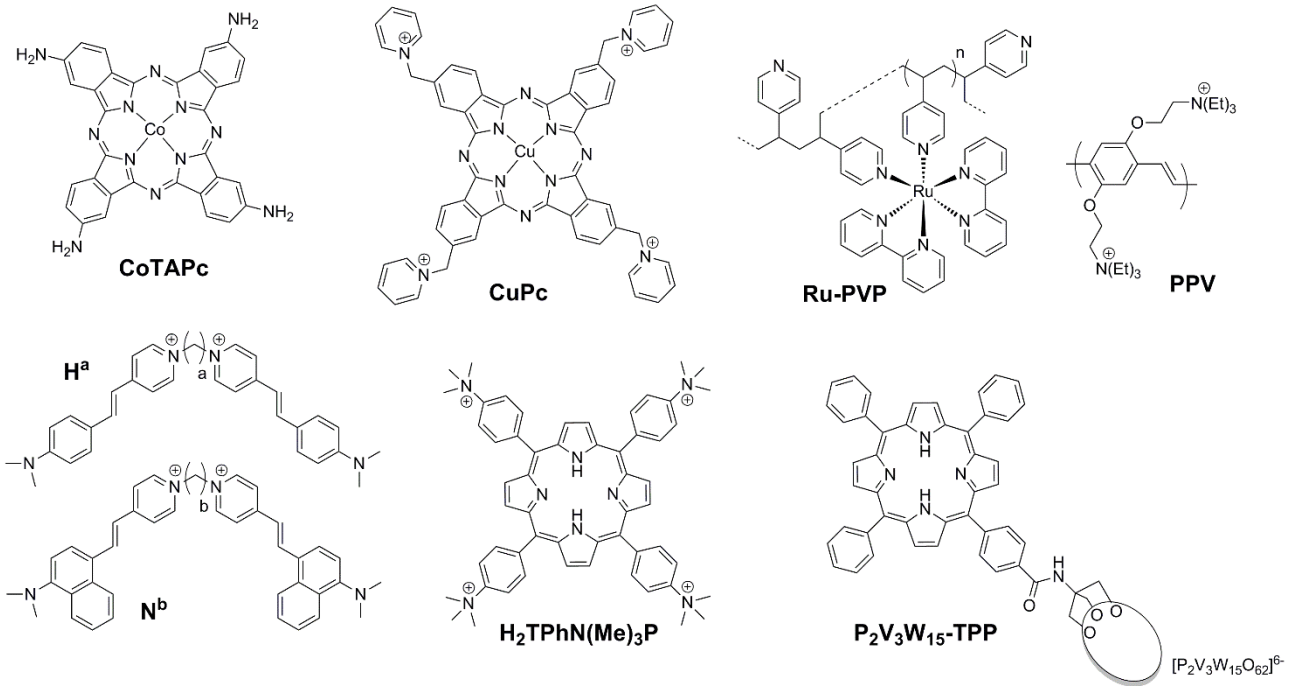

Fig. 1 Representation of some organic part of the systems described in Table 1.

References

(1) Walsh, J. J.; Zhu, J.; Bond, A. M.; Forster, R. J.; Keyes, T. E. *J. Electroanal. Chem.* **2013**, *706*, 93.

(2) Zhu, J.; Zeng, Q.; O'Carroll, S.; Bond, A.; Keyes, T. E.; Forster, R. J. *Electrochem. commun.* **2011**, *13* (9), 899.

(3) Wang, Y.; Hu, C. *Thin Solid Films* **2005**, *476* (1), 84.

(4) Jin, G.; Wang, S.-M.; Chen, W.-L.; Qin, C.; Su, Z.-M.; Wang, E.-B. *J. Mater. Chem. A* **2013**, *1* (23), 6727.

(5) Chen, X.; Gao, L. H.; Zheng, Z. B.; Wang, K. Z. *Mater. Res. Bull.* **2013**, *48* (2), 595.

(6) Gao, L. H.; Sun, Q. L.; Qi, J. M.; Lin, X. Y.; Wang, K. Z. *Electrochim. Acta* **2013**, *92*, 236.

(7) Gao, L.; Sun, Q.; Wang, K. *J. Colloid Interface Sci.* **2013**, *393* (1), 92.

(8) Gao, L.; Sun, Q.; Lin, X.; Qi, J.; Wang, K. *Colloids Surfaces A Physicochem. Eng. Asp.* **2013**, *423*, 162.

(9) Yang, Y.; Xu, L.; Li, F.; Du, X.; Sun, Z. *J. Mater. Chem.* **2010**, *20* (48), 10835.

(10) Sun, Z.; Fang, S.; Li, F.; Xu, L.; Hu, Y.; Ren, J. *J. Photochem. Photobiol. A Chem.* **2013**, *252*, 25.

(11) Ahmed, I.; Farha, R.; Huo, Z.; Allain, C.; Wang, X.; Xu, H.; Goldmann, M.; Hasenknopf, B.; Ruhlmann, L. *Electrochim. Acta* **2013**, *110*, 726.

(12) Ahmed, I.; Farha, R.; Goldmann, M.; Ruhlmann, L. *Chem. Commun. (Camb).* **2013**, *49* (5), 496.

Appendix

Appendix

Reagent and apparatus

Regent

zinc-*β*-octaethylporphyrin	Sigma-Aldrich
5,15-ditolylporphyrin	SAS PorphyChem®
sodium iodide	VWR® Prolabo
iodine	Panreac Quimica Sau
tetrabutylammonium hexaflurophosphate	Fluka
4,4'-dipyridyl	Acros Organics
acetonitrile	Sigma-Aldrich
ferrocene	Fluka
1,1-ferrocenedimethanol	Sigma-Aldrich
dichloroethane	Sigma-Aldrich
dimethylformamide	Sigma-Aldrich
propan-2-ol	Fluka

Electrochemistry and photoelectrochemistry Voltammetric and electrochemical impedance measurements have been performed with a standard three-electrode system using a PARSTAT 2273 potentiate. Glass carbon or single-side coated indium-tin-oxide (ITO, SOLEMS, 25-35 Ω/cm^{-2}) electrodes, with a surface of about 1 cm^2 has been used as working electrode. A platinum wire has been used as an auxiliary electrode. The reference electrode was a saturated calomel electrode. It was electrically connected to the solution by a junction bridge filled with the electrolyte. Photoelectrochemical responses for films were obtained by on-off light illumination of a 300 W Xe arc lamp (with $\lambda > 385$ nm long pass filter).

Photocatalysis The film was prepared on a slide of quartz. Then the slide was plunged in an optical cell of 1 cm path length containing 3 mL of an degassed aqueous solution with 8×10^{-5} mol L^{-1} Ag_2SO_4 or 1.6×10^{-4} mol L^{-1} H_2PtCl_6 and 0.13 mol L^{-1} propan-2-ol. Irradiations were performed using a 300 W Xe lamp equipped with a water cell filter to absorb the near-IR radiations and a 385 nm cut-off filter. According to the sup- plier, the irradiance of the lamp from 320 to 790 nm was around 50 mW $m^{-2}nm^{-1}$.

Electrochemical quartz crystal measurement A QCA-922 (SEIKO EG&G instrument) system combined with Versa STAT 3 was used for simultaneous quartz crystal measurement and cyclic voltammetric measurements. The electrochemical cell was assembled in a glove box using an ITO AT-cut quartz crystal resonator (mirror finished, resonant frequency: 9.08 MHz ± 50 kHz, A = 0.2 cm^2, SEIKO EG&G., LTD) as working electrode, a platinum wire as counter electrode, and a Ag/AgCl wire as a quasi-reference electrode.

UV–visible spectroscopic measurements UV–vis absorption spectra have been recorded on an Agilent 8453 spectrophotometer.

X-ray Photoelectron Spectroscopy (XPS). XPS experiments were carried out on a RBD upgraded PHI-5000C ESCA system (Perkin-Elmer) with MgKR radiation (h =1253.6 eV) or Al KR radiation (h = 1486.6 eV).

Atomic force micrographs (AFM) measurement. AFM have been conducted directly on the ITO surfaces using a Dimension 3100 (Veeco) in the tapping mode under ambient conditions. Silicon cantilevers (Veeco probes) with a spring constant of 300 N/m and a resonance frequency in the range of 120–139 kHz have been used. The scanning rate was 1.0 Hz.

Raman spectroscopy. Raman spectra were recorded on a Renishaw Invia Raman Microscope with the457 or 514-nm emission line of an Ar-laser.

Transmission electronic microscopy (TEM). TEM observations were performed with a JEOL 100 CXII TEM instrument operated at an accelerating voltage of 100 kV.

Scan electronic microscopy (SEM). SEM measurements were performed using Jeol JSM-6700F (Japan) electron microscope with the lattice resolution of 1 nm, at accelerating voltage of 10 kV.

Chapter II: Covalent Lindqvist polyoxovanadate – porphyrin hybrid films for the photocurrent generation and the photocatalytical recovery of metals

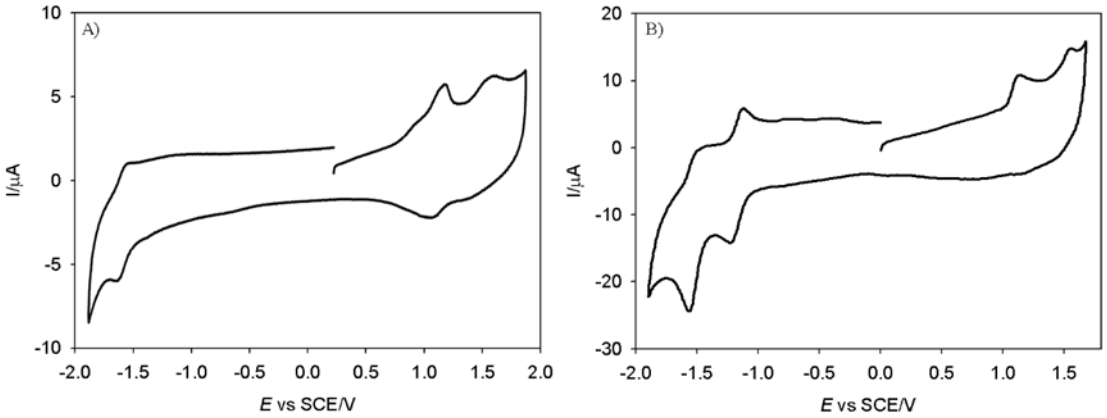

Fig. S2.1 Cyclic voltammograms of 0.25 mmol L^{-1} A) **ZnOEP** and B) **H_2T_2P** in1,2-$C_2H_4Cl_2$ in the presence of 0.1 mol L^{-1} $TBAPF_6$. Working electrode: GC. d =3 mm; scan rate: 0.1 V/s.

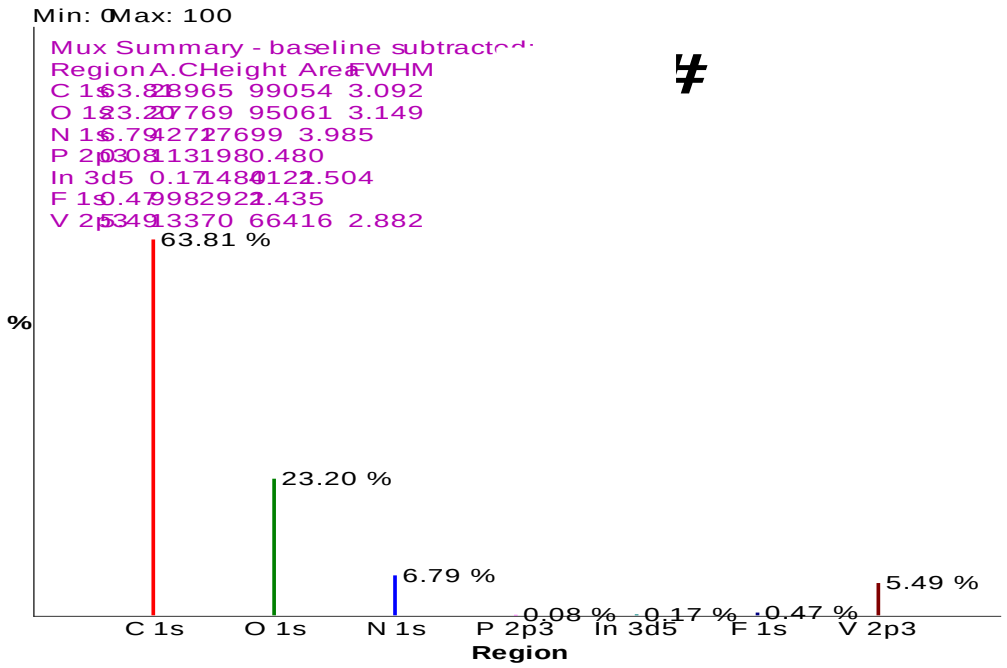

Fig. S2.2 XPS element composition analysis of the modified ITO electrodes with **poly-V_6O_{13}-H_2T_2P** obtained after 20 iterative scans between 0.00 and +1.60 V *vs.* SCE.

From XPS element composition analysis, the experimental atomic ratios are: C:N = 9.4, O:V = 4.2, N:V =1.2

From the proposed formula of the copolymer:

Atomic ratios calculated: C:N = 86:10 = 8.6, O:V = 21:6 = 3.5, N:V = 10:6 = 1.67

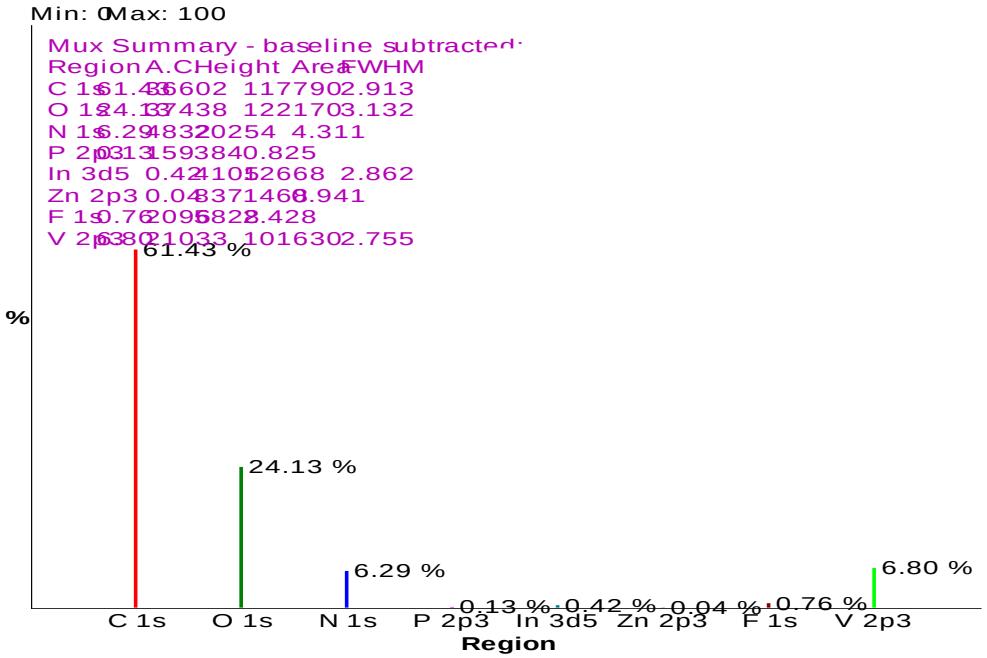

Fig. S2.3 XPS element composition analysis of the modified ITO electrodes with **poly-V_6O_{13}-ZnOEP** obtained after 20 iterative scans between 0.00 and +1.60 V *vs.* SCE.

From XPS, the experimental atomic ratios are: C:N = 9.8, O:V = 3.5, V:Zn = 170*. (* We have observed many times that the detection of the Zn 2p3 signal is very difficult and even something is not detected. Here, because of the ill-defined signals, the ratio calculated is wrong and is very far from the expected value of V:Zn = 12.)

From the proposed formula of the copolymer with one coordination of **Py-V_6O_{13}-Py** between two **ZnOEP** the atomic ratios calculated give: C:N = 140:16 = 8.75, O:V = 42:12 =3.5 (because the O and V atoms come only from Py-POM^{2-}-Py 2TBA), V:Zn = 12:1 =12.

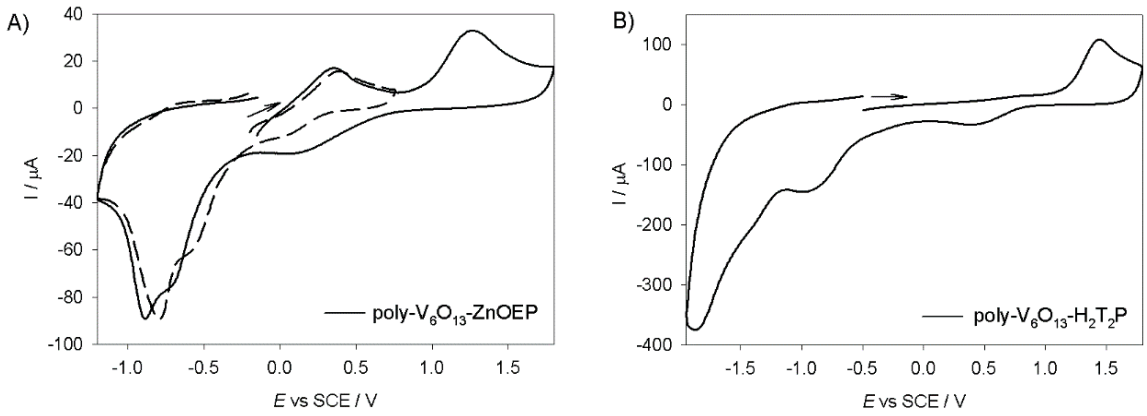

Fig. S2.4 CVs of A) **poly-V_6O_{13}-ZnOEP** and B) **poly-V_6O_{13}-H_2T_2P** (obtained after 25 scans, between 0.00 V and +1.60 V) in CH_3CN/1,2-$C_2H_4Cl_2$ (3/7) with 0.1 mol L^{-1} $TBAPF_6$. (←) Start of the scan. WE=ITO; S =1 cm^2; scan rate: 0.1 V s^{-1}.

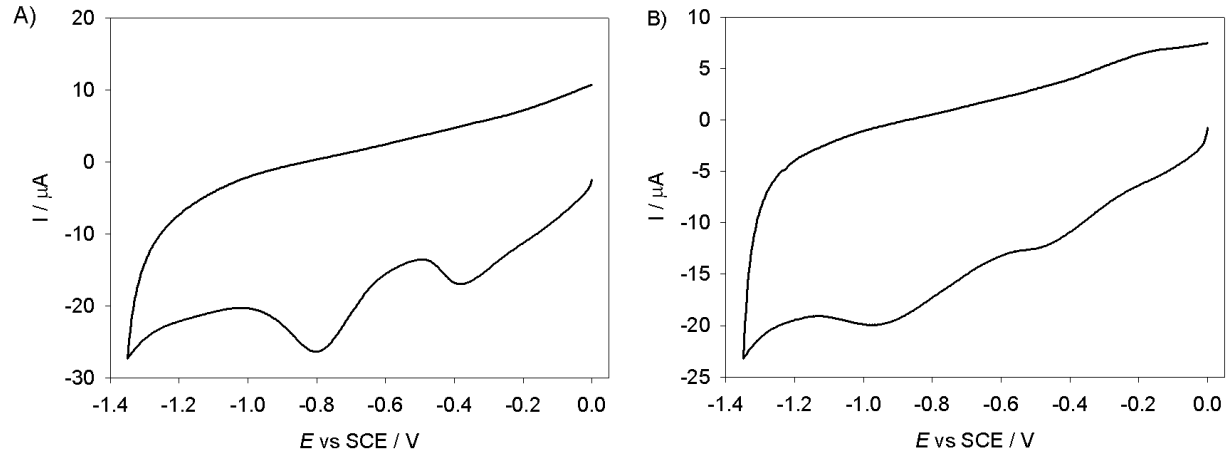

Fig. S2.5 CVs of A) **poly-V_6O_{13}-ZnOEP** and B) **poly-V_6O_{13}-H_2T_2P** (obtained after 25 scans, between 0.00 V and +1.60 V) on GC in H_2O with NaI 0.5 mol L^{-1}. S =1 cm^2; scan rate: 0.1 V s^{-1}.

Chapter III: Covalent Keggin and Dawson silyl polyoxophosphotungstate – porphyrin copolymers for the photocurrent generation and the photocatalytical recovery of metals

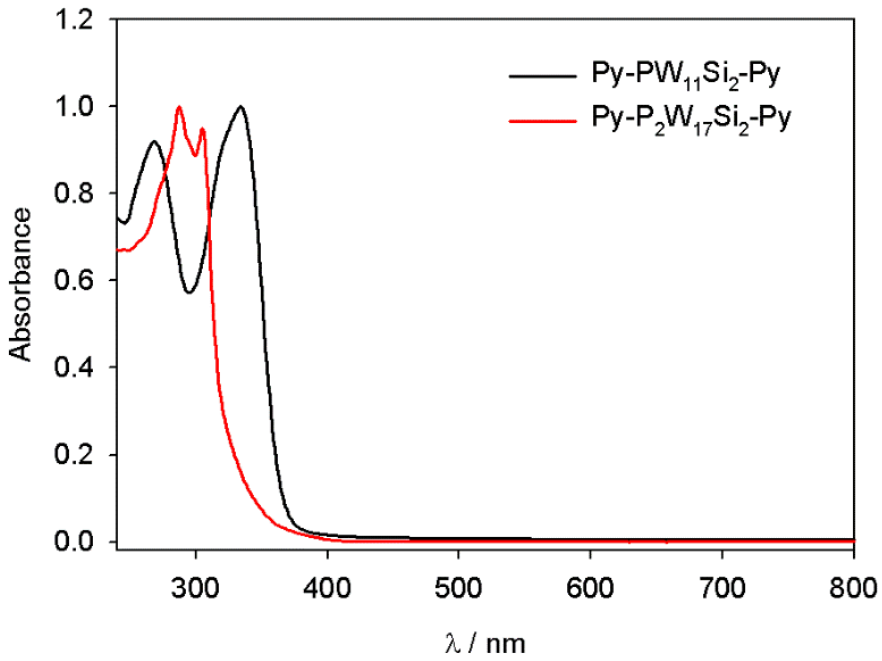

Fig. S3.1 Normalized UV-vis absorption spectra of **Py-$PW_{11}Si_2$-Py** and **Py-$P_2W_{17}Si_2$-Py** in CH_3CN.

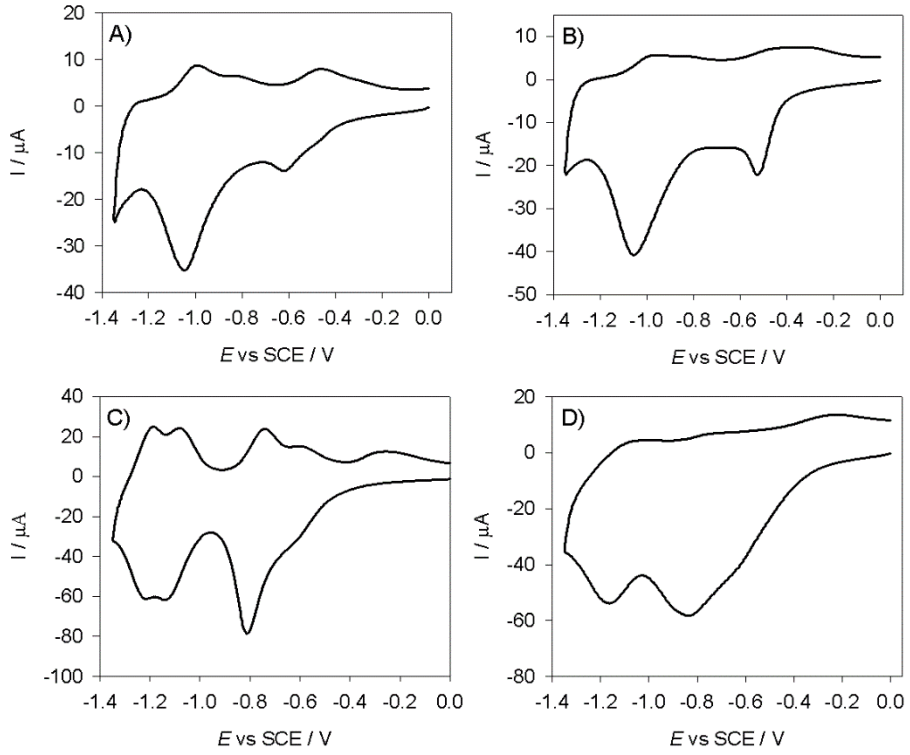

Fig. S3.2 Cyclic voltammograms of A) **poly-$PW_{11}Si_2$-ZnOEP**, B) **poly-$PW_{11}Si_2$-H_2T_2P**, C) **poly-$P_2W_{17}Si_2$-ZnOEP** and D) **poly-$P_2W_{17}Si_2$-H_2T_2P** films (obtained after 25 scans, between 0.00 V and +1.60 V) on GC in H_2O + NaI 0.5 mol L^{-1}. (←) Start of the scan. S =1 cm^2; scan rate: 0.1 V s^{-1}.

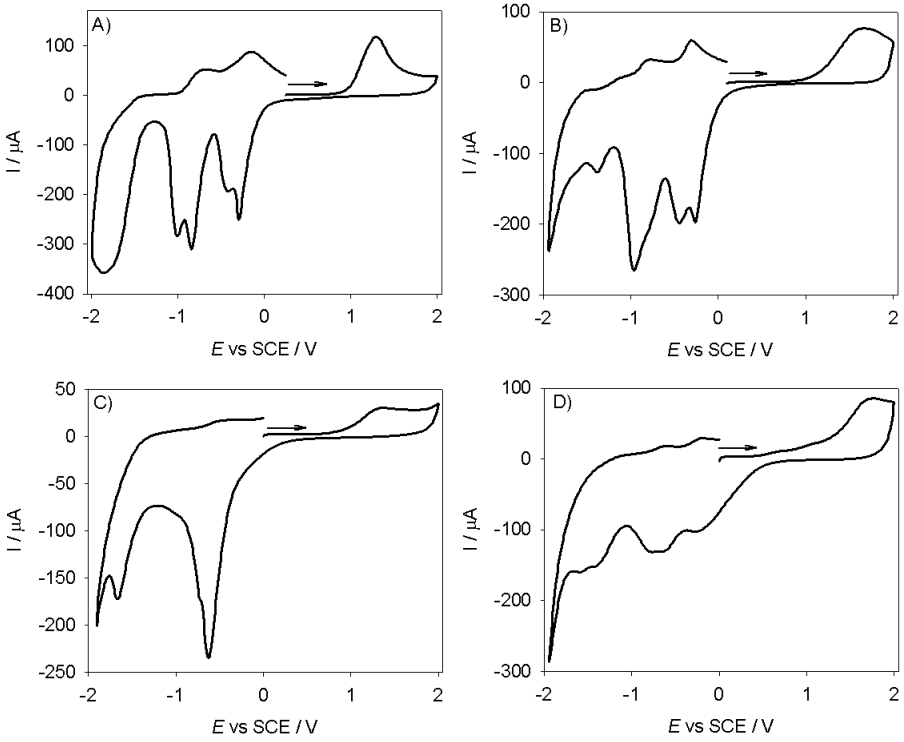

Fig. S3.3 Cyclic voltammograms of A) **poly-$PW_{11}Si_2$-ZnOEP**, B) **poly-$PW_{11}Si_2$-H_2T_2P**, C) **poly-$P_2W_{17}Si_2$-ZnOEP** and D) **poly-$P_2W_{17}Si_2$-H_2T_2P** (obtained after 25 scans, between 0.00 V and +1.60 V) in CH_3CN/1,2-$C_2H_4Cl_2$ (3/7) with 0.1 mol L^{-1} $TBAPF_6$. (←) Start of the scan. S =1 cm^2; scan rate: 0.1 V s^{-1}.

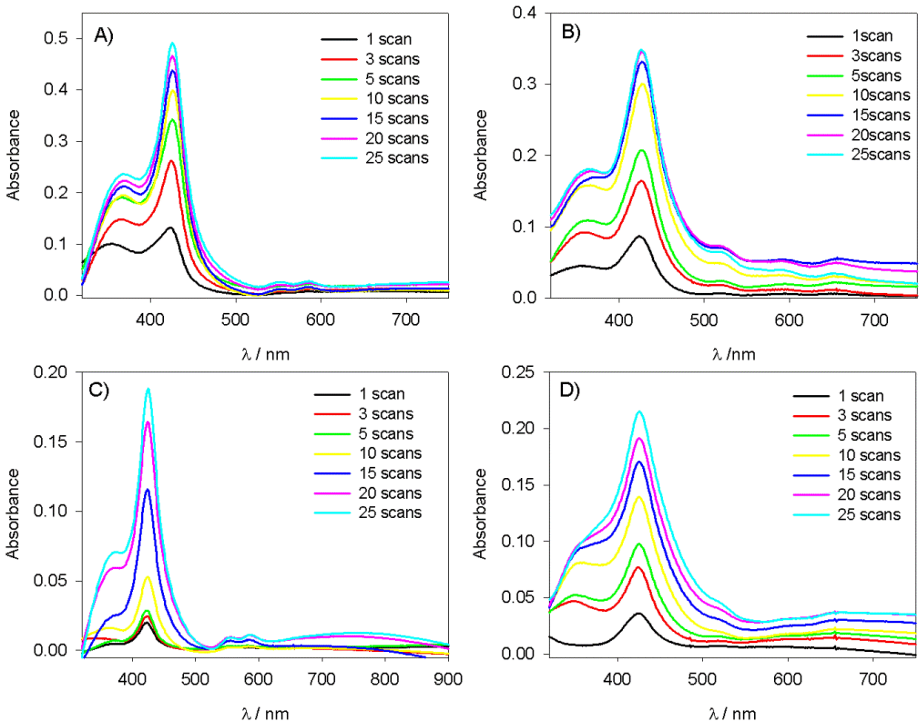

Fig. S3.4 UV–vis spectra of A) **poly-$PW_{11}Si_2$-ZnOEP**, B) **poly-$PW_{11}Si_2$-H_2T_2P**, C) **poly-$P_2W_{17}Si_2$-ZnOEP** and D) **poly-$P_2W_{17}Si_2$-H_2T_2P** obtained after n iterative scans (n = 1, 3, 5, 10, 15, 20 and 25) between 0.00 and +1.60 V *vs.* SCE on ITO.

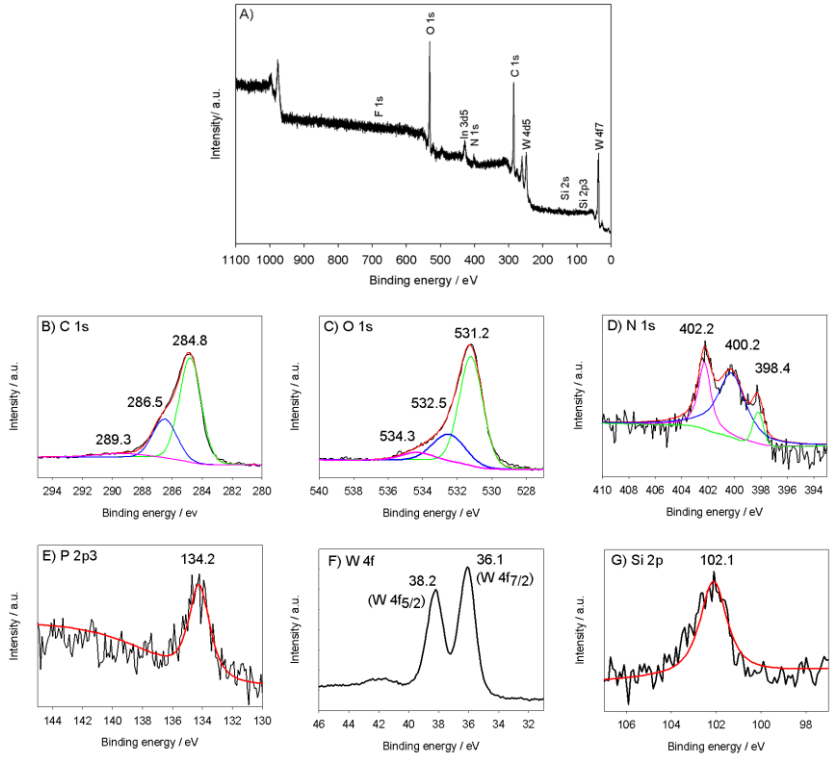

Fig. S3.5 XPS spectra of the modified ITO electrodes with **poly-$PW_{11}Si_2$-H_2T_2P** obtained after 5 iterative scans between 0.00 and +1.60 V *vs.* SCE. (A) Global XPS spectra, (B) C 1s, (C) O 1s, (D) N 1s, (E) P 2p3, (F) W 4f7, (G) Si 2p3.

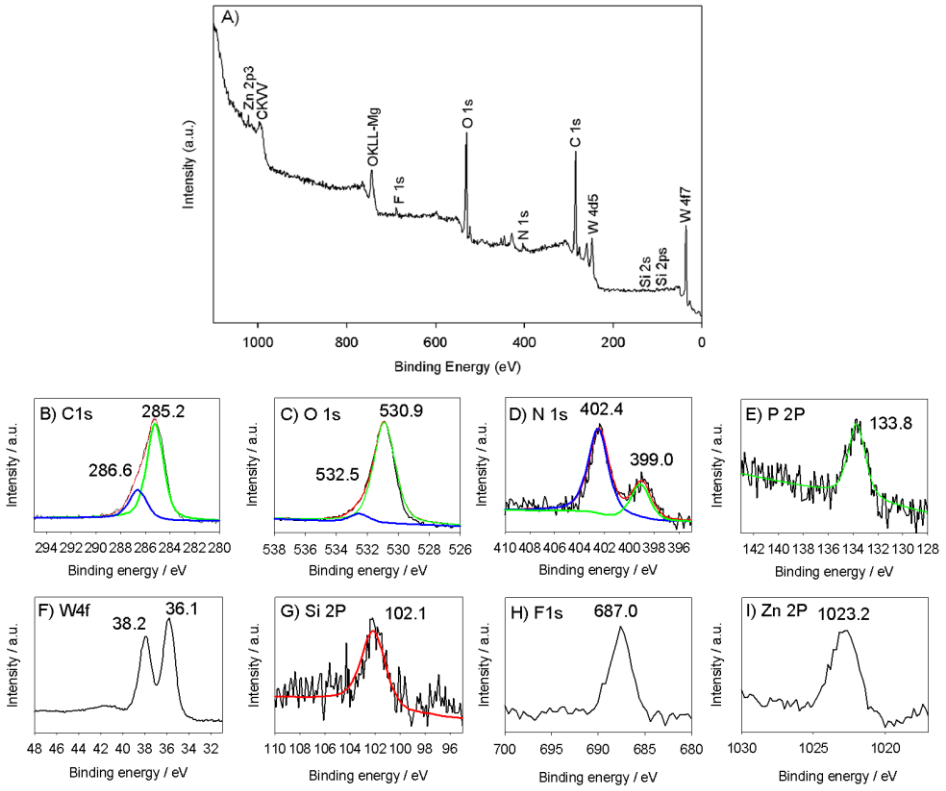

Fig. S3.6 XPS of **poly-$P_2W_{17}Si_2$-ZnOEP** global XPS spectra (A), C 1s (B), O 1s (C), N 1s (D), P 2p3 (E), W 4f7 (H), Si 2p3 (G), F 1s (H), Zn 2p3 (I).

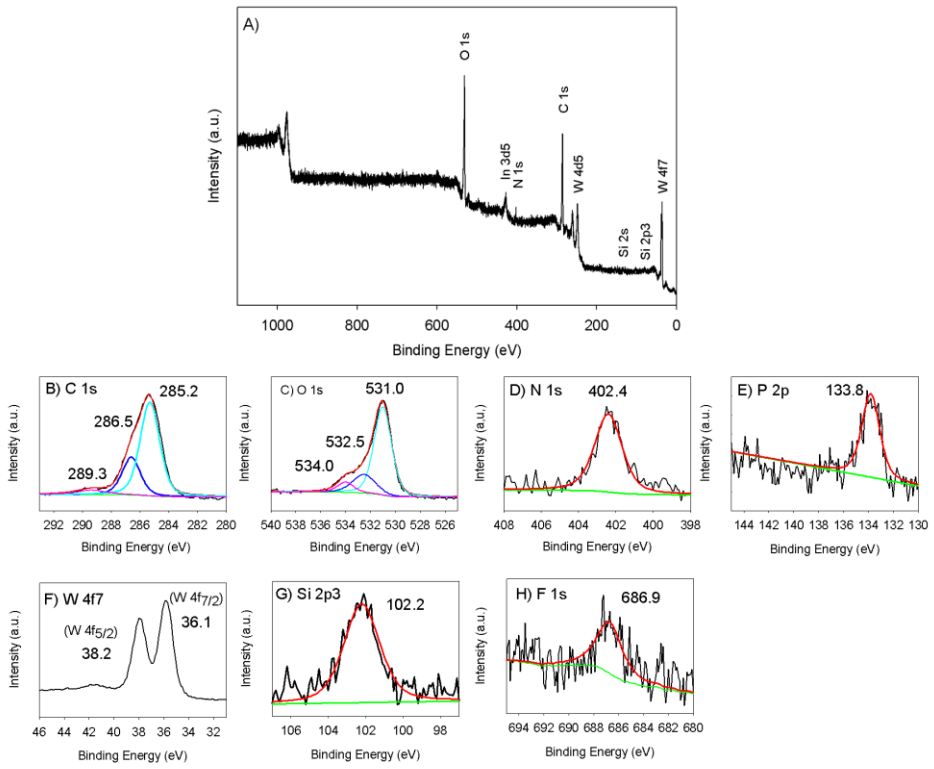

Fig. S3.7 XPS of **poly-$P_2W_{17}Si_2$-H_2T_2P** global XPS spectra (A), C 1s (B), O 1s (C), N 1s (D), P 2p3 (E), W 4f7 (H), Si 2p3 (G), F 1s (H). *Note: the second signals of N 1s near 399 eV is nearly not observed and ill-defined.*

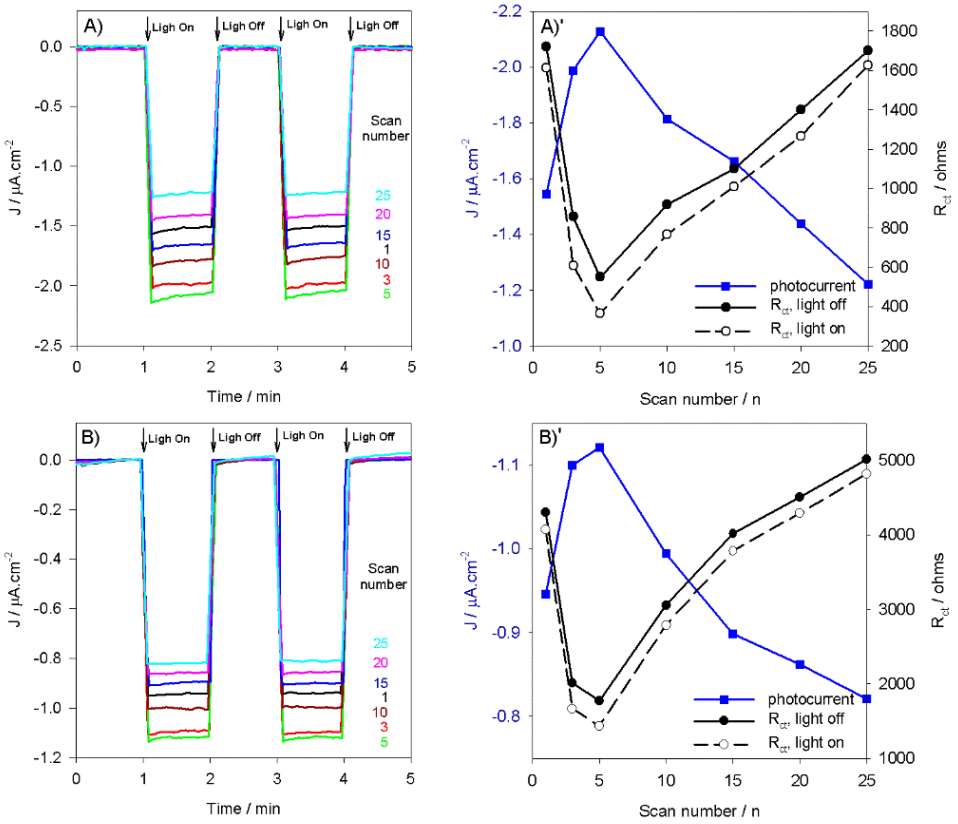

Fig. S3.8 Photoelectrochemical response of A) **poly-$PW_{11}Si_2$-ZnOEP** and B) **poly-$PW_{11}Si_2$-H_2T_2P** with different numbers of iterative scans used for the preparation of the film (between 0.00 V and +1.90 V versus SCE). Only one side is recovered by ITO with on-off light illumination from 300 W Xe Arc lamp (with $\lambda \geq 385$ nm long pass filter). BIAS potential: 0.00 V. A') **poly-$PW_{11}Si_2$-ZnOEP** and B') **poly-$PW_{11}Si_2$-H_2T_2P** (■) plots of the photocurrent, and plots of R_{ct} without illumination (●), and with illumination (○) in aqueous solution containing I_3^- 5 mmol L^{-1} and I^- 0.5 mol L^{-1} versus the numbers of iterative scans.

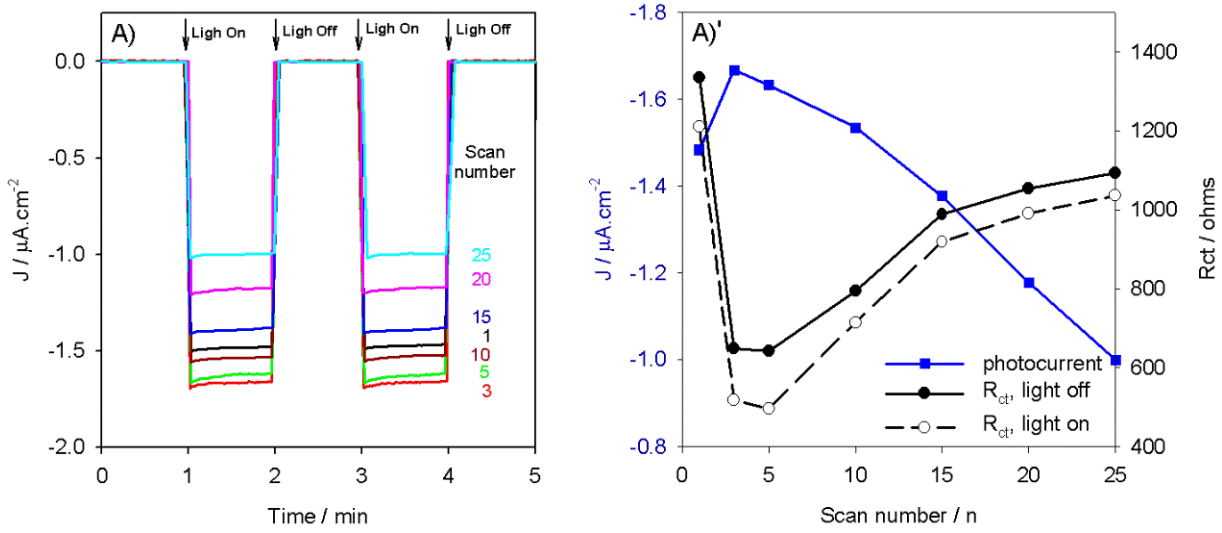

Fig. S3.9 A) Photoelectrochemical response of **poly-$P_2W_{17}Si_2$-H_2T_2P** with different numbers of iterative scans used for the preparation of the film (between 0.00 V and +1.90 V versus SCE). Only one side is recovered by ITO with on-off light illumination from 300 W Xe Arc lamp (with $\lambda \geq 385$ nm long pass filter). BIAS potential: 0.00 V. B) (■) plots of the photocurrent, and plots of R_{ct} without illumination (●), and with illumination (○) in aqueous solution containing I_3^- 5 mmol L^{-1} and I^- 0.5 mol L^{-1} versus the numbers of iterative scans.

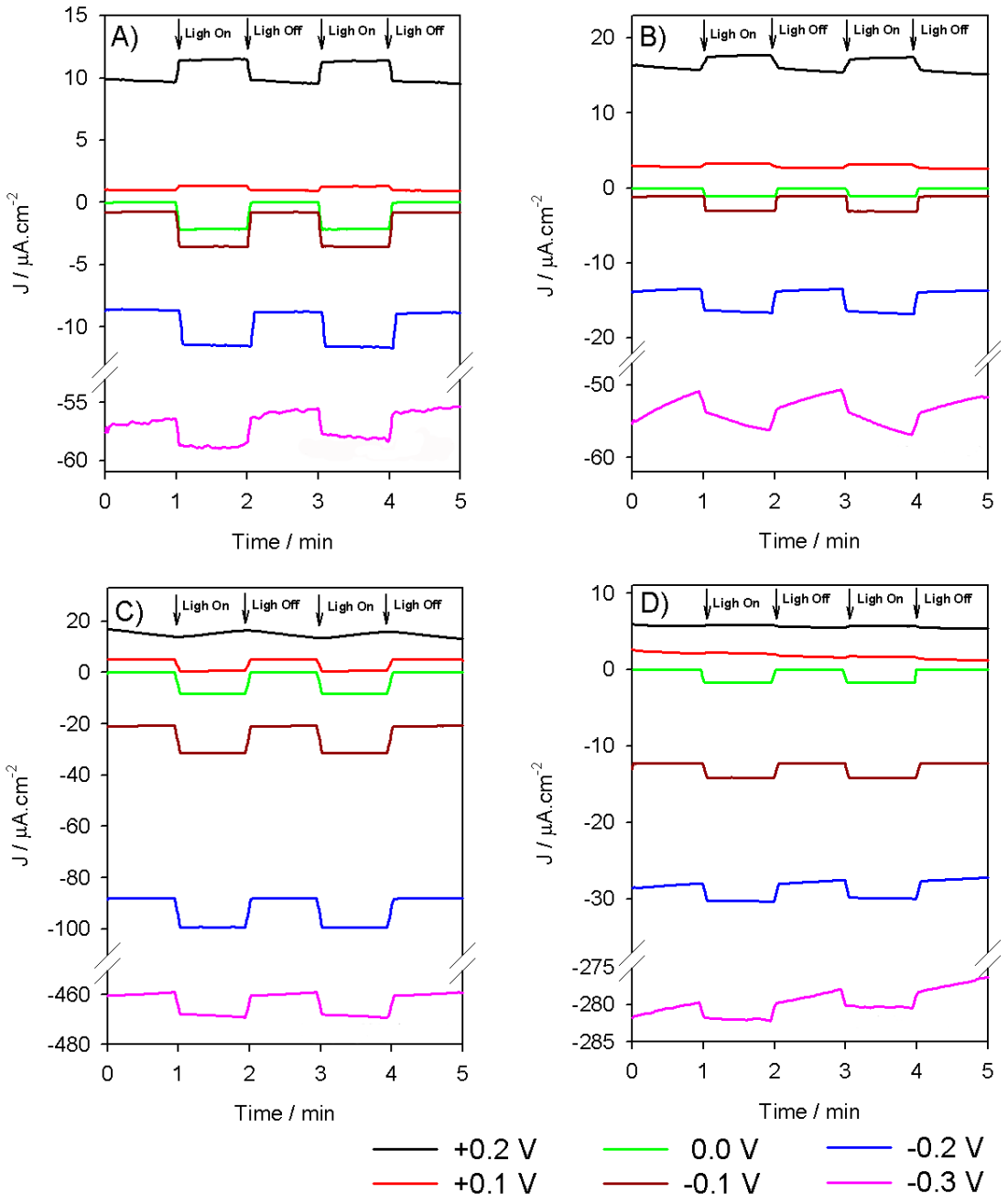

Fig. S3.10 Photoelectrochemical response of **poly-$PW_{11}Si_2$-ZnOEP** (5 scans), **poly-$PW_{11}Si_2$-H_2T_2P** (5 scans), **Poly-$P_2W_{17}Si_2$-ZnOEP** (3 scans) and **poly-$P_2W_{17}Si_2$-H_2T_2P** (3 scans) (preparation of the film between 0.00 V and +1.60 V versus SCE) under irradiation from 300 W Xe Arc lamp (with $\lambda \geq 385$ nm long pass filter) in H_2O containing I_3^- 5 mmol L^{-1} and I^- 0.5 mol L^{-1}, DC (or BIAS) potential 0.00 V.

Chapter IV: Conjugated Dawson polyoxophosphovanadotungstate – porphyrin copolymers for the photocurrent generation and the photocatalytical recovery of metals

UV-vis spectra of POM(py)$_2$ hybrids

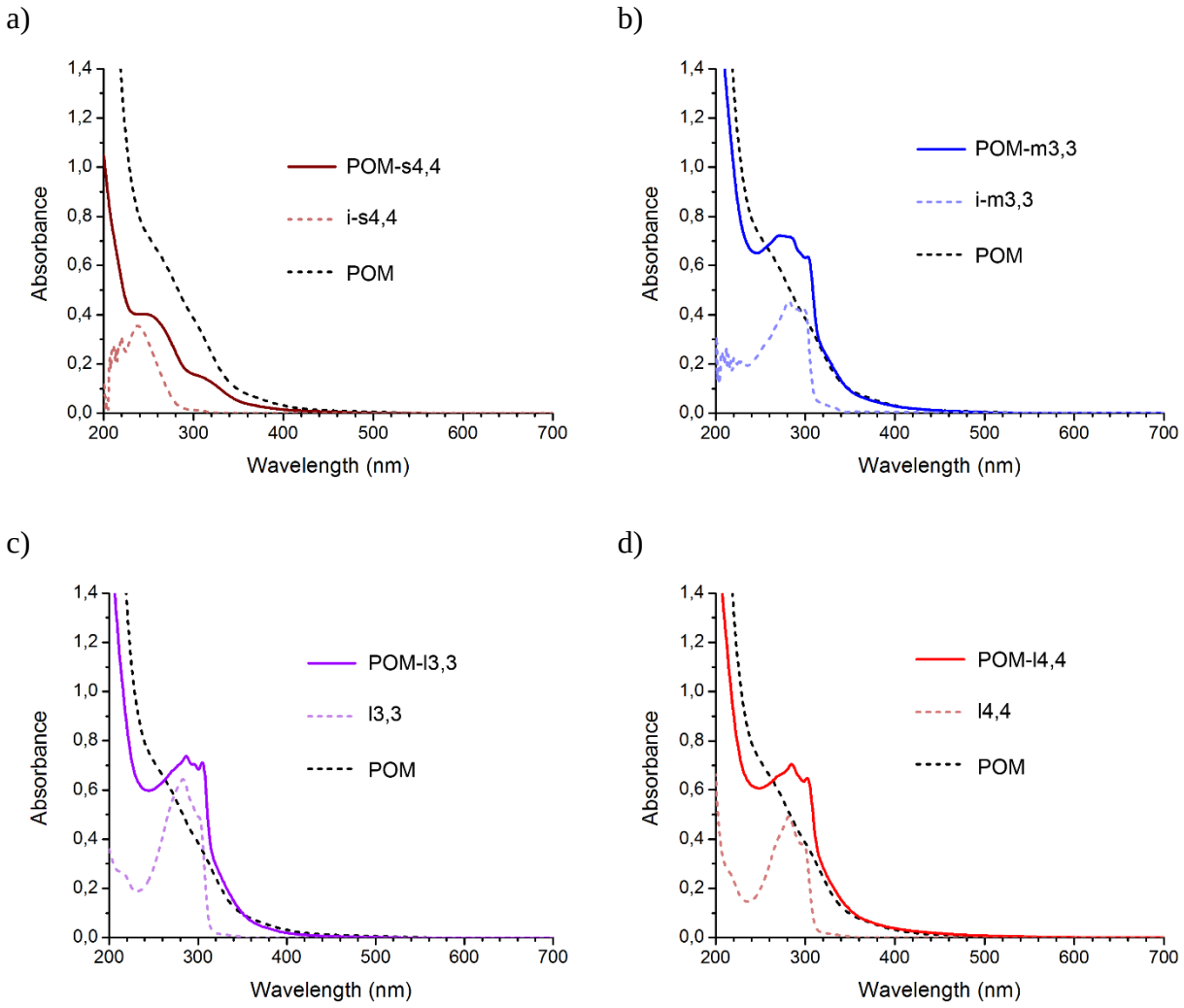

Fig. S4.1 UV-Vis absorption spectra of a) **POM-s4,4**, b) **POM-m3,3**, c) **POM-l3,3**, d) **POM-l4,4** compared to $TBA_5H_4[P_2V_3W_{15}O_{62}]$ and their corresponding non-grafted ligand. Concentration is 6.25 10^{-6} M in CH_3CN.

CV evolution during electropolymerization

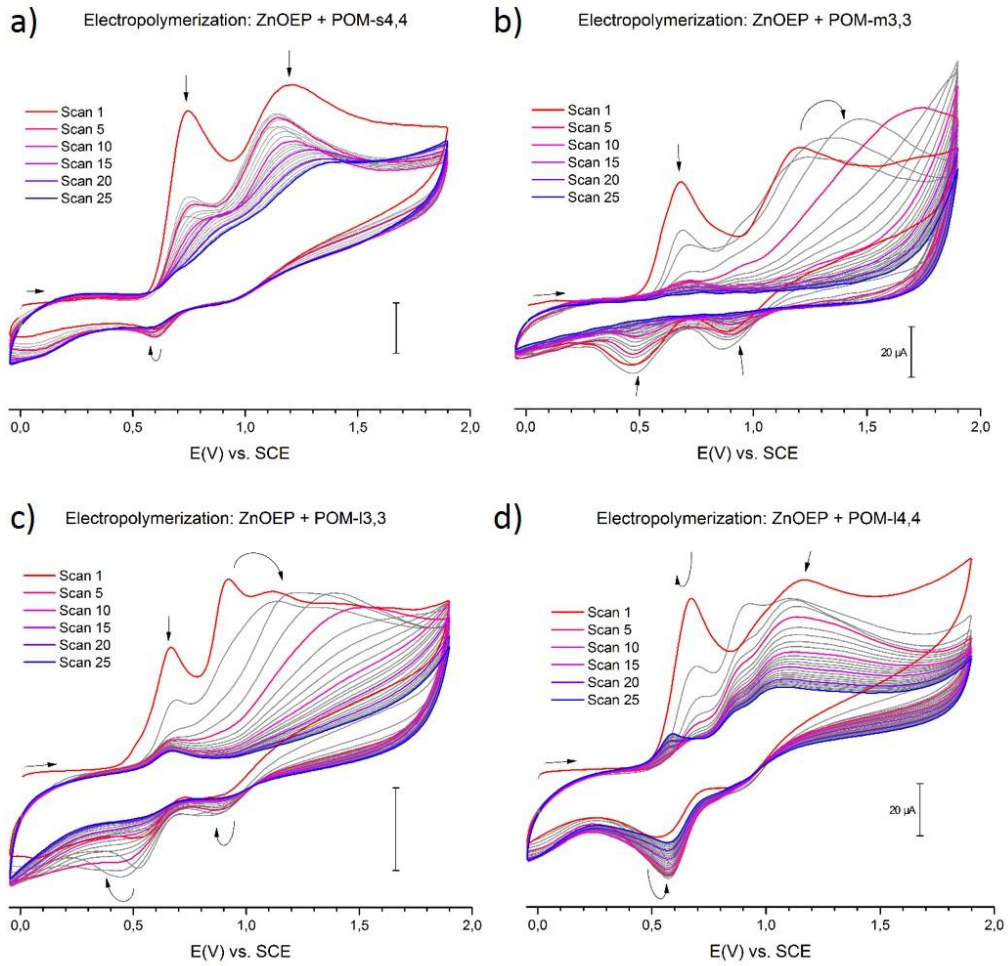

Fig. S4.2 Cyclic voltammograms recorded during the electropolymerization of **ZnOEP** in the presence of a) **POM-s4,4** , b) **POM-m3,3** , c) **POM-l3,3**, d) **POM-l4,4** in 1,2-$C_2H_4Cl_2$/CH_3CN (7:3) (NBu_4)PF6 0.1mol L^{-1}. Working electrode: ITO. S = 1 cm^2. Scan rate: 0.1 $V.s^{-1}$. (←) Start of the scan. Cyclic scanning was applied at potentials -0.05 V and 1.90 V *vs.* SCE.

Redox properties of the films

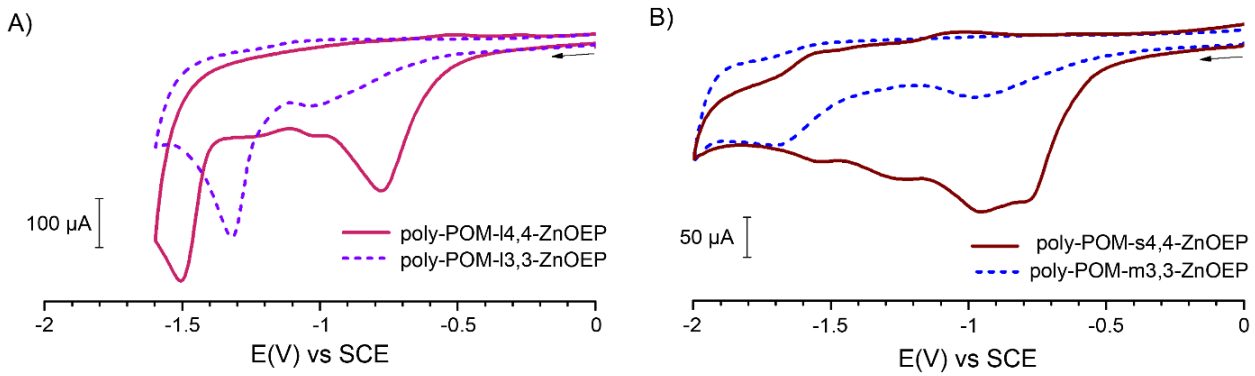

Fig. S4.3 Cyclic voltammograms of A) **poly-POM-l3,3-ZnOEP** (dotted line) and **poly-POM-l4,4-ZnOEP** (full line) and B) **poly-POM-s4,4-ZnOEP** (full line), **poly-POM-m3,3-ZnOEP** (dotted line), in CH_3CN + $TBAPF_6$ 0.1mol L^{-1}. Working electrode: ITO, Counter electrode: Pt, Reference: SCE. Scan rate: 0.1 $V.s^{-1}$. (←) Start of the scan.

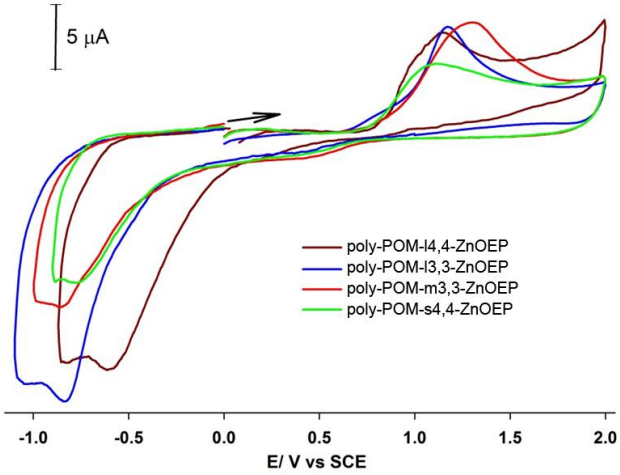

Fig. S4.4 Cyclic voltammograms of **poly-POM-s4,4-ZnOEP, poly-POM-m3,3-ZnOEP**, **poly-POM-l3,3-ZnOEP** and **poly-POM-l4,4-ZnOEP** in CH_3CN + $TBAPF_6$ 0.1mol L^{-1}. Working electrode: ITO, Counter electrode: Pt, Reference: SCE. Scan rate: 0.01 V s^{-1}. (→) Start of the scan.

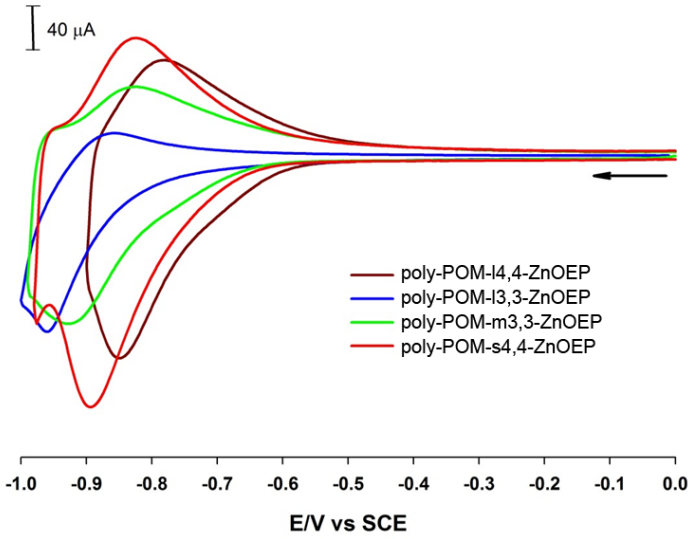

Fig. S4.5 Cyclic voltammograms of **poly-POM-s4,4-ZnOEP**, **poly-POM-m3,3-ZnOEP**, **poly-POM-l3,3-ZnOEP** and **poly-POM-l4,4-ZnOEP** in H_2O + NaI 0.5mol L^{-1}. Working electrode: ITO. Counter electrode: Pt, Reference: SCE. Scan rate 0.1 V.s^{-1}. (←) Start of the scan.

UV-vis evolution

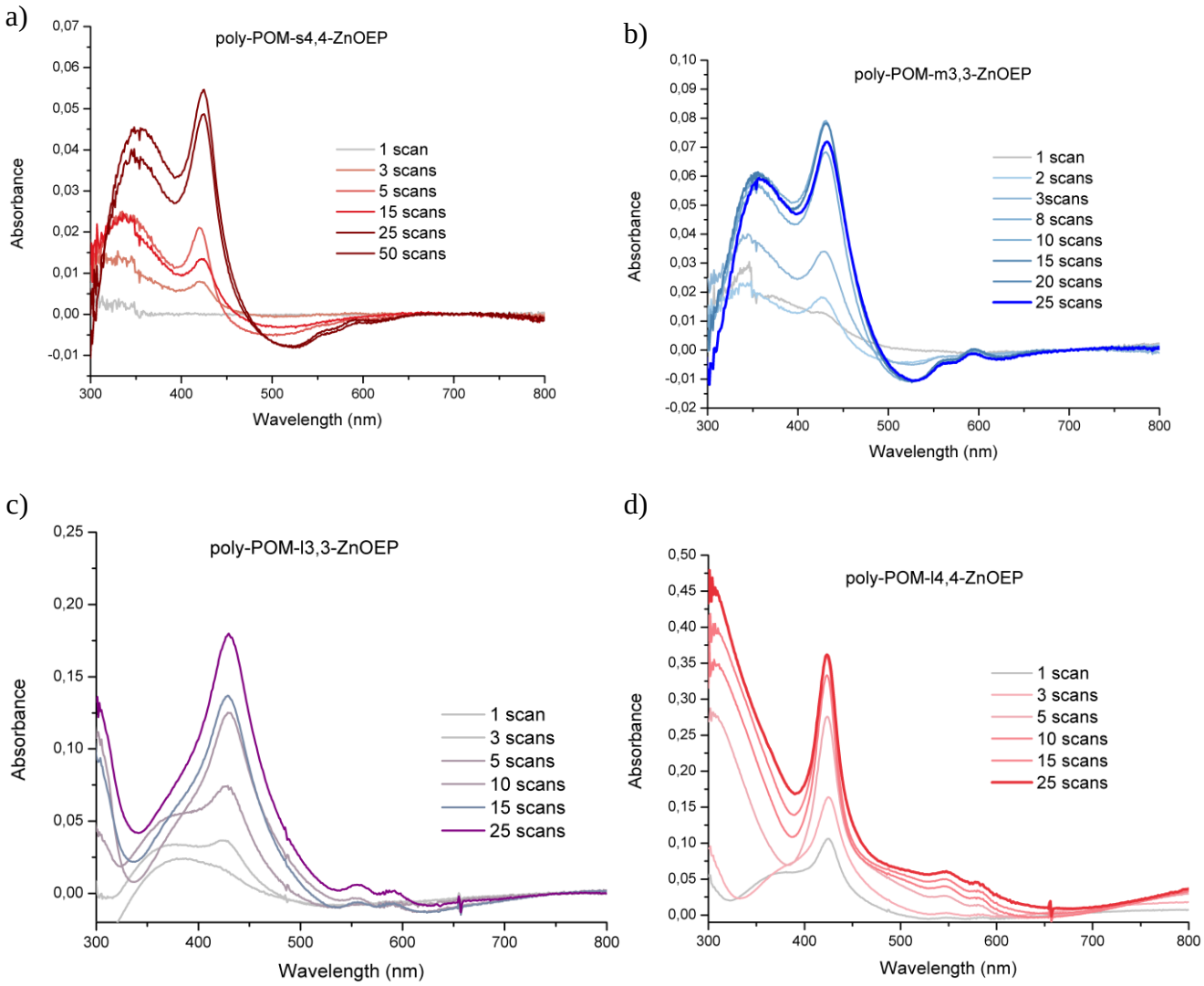

Fig. S4.6 UV-visible absorption spectra of a) **poly-POM-s4,4-ZnOEP**, b) **poly-POM-m3,3-ZnOEP**, c) **poly-POM-l3,3-ZnOEP** and d) **poly-POM-l4,4-ZnOEP** (onto ITO) with different numbers of iterative scans (between -0.05 V and 1.90 V *vs.* SCE). Only one side is recovered by ITO.

X-ray photoelectron spectra (XPS)

poly-POM-s4,4-ZnOEP

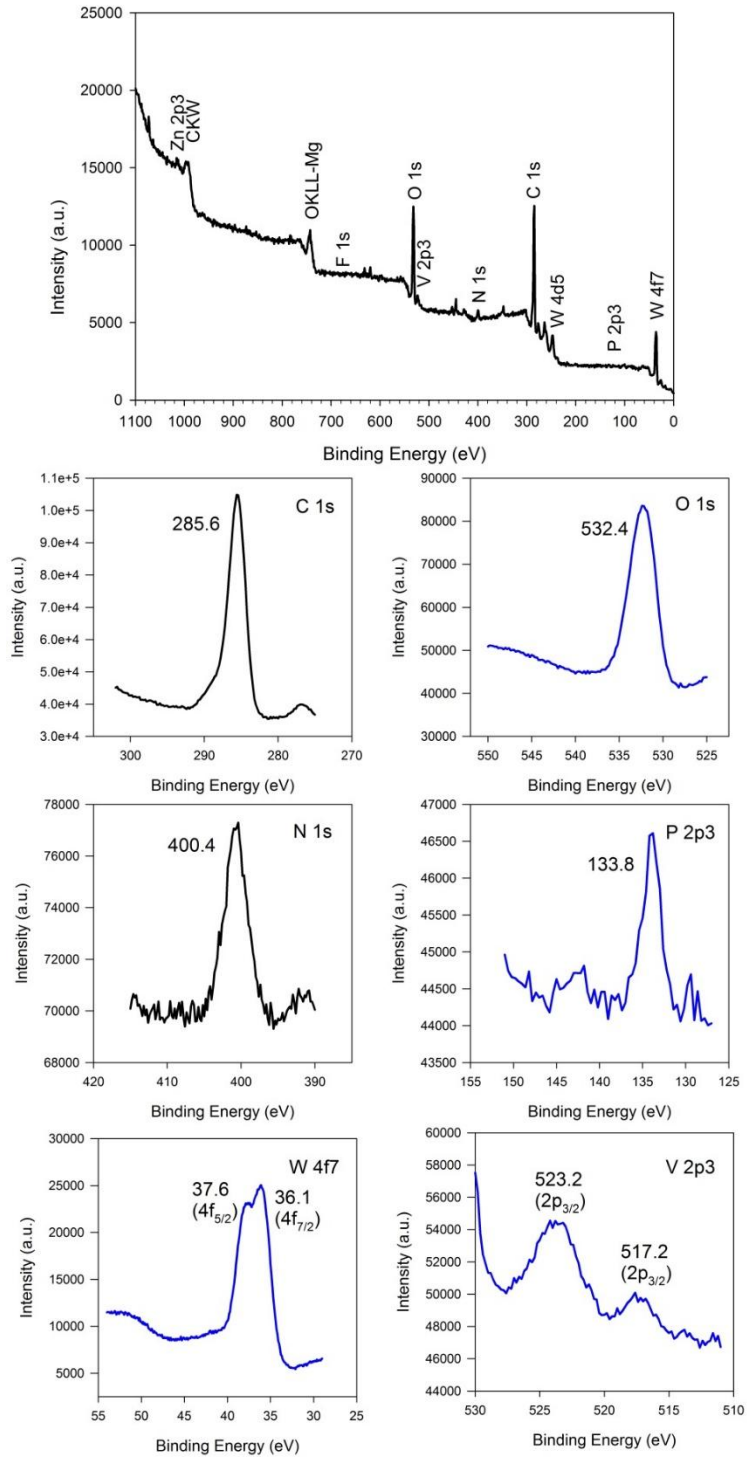

Fig. S4.7 XPS spectra of the modified ITO electrodes with **POM-s4,4-ZnOEP** obtained after 25 iterative scans between 0 and 1.90 V versus SCE.

poly-POM-m3,3-ZnOEP

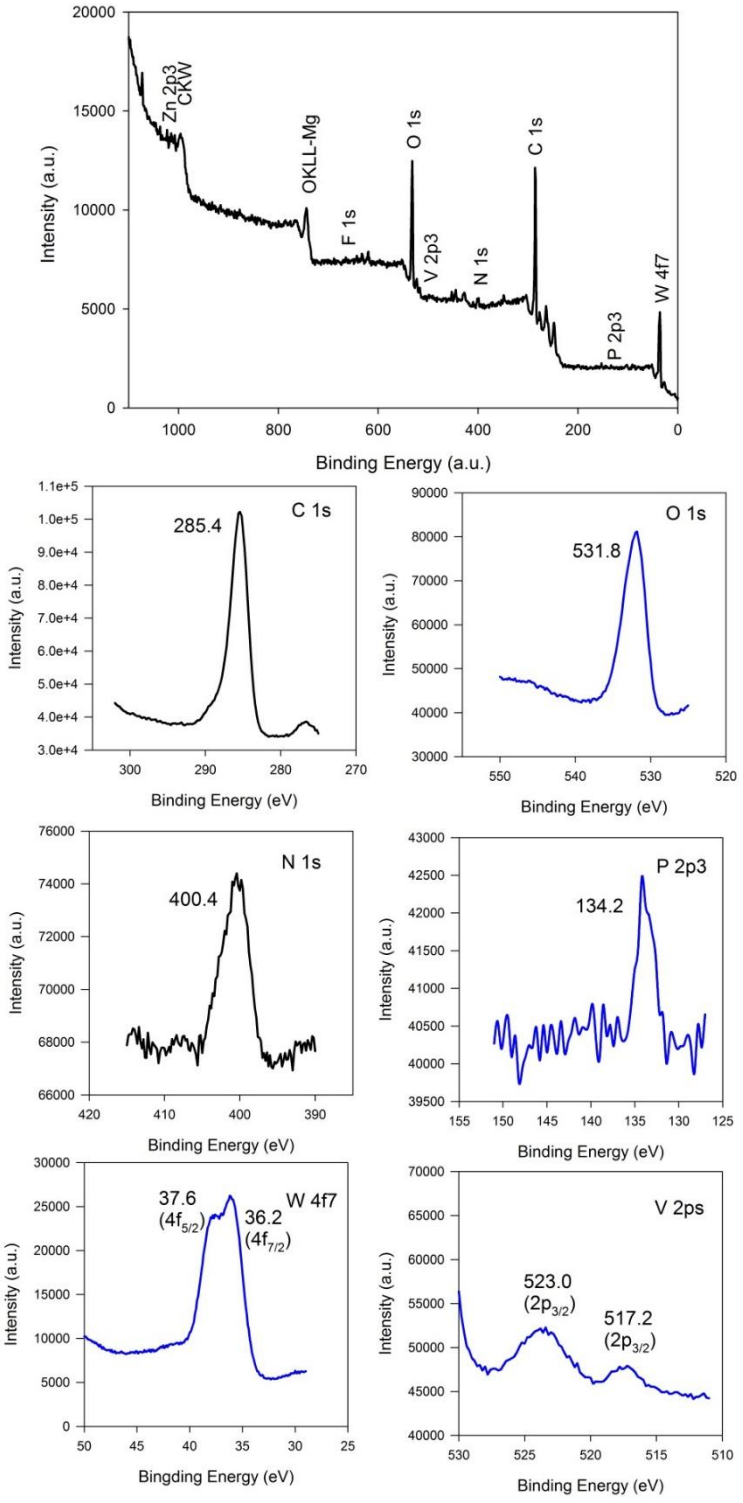

Fig. S4.8 XPS spectra of the modified ITO electrodes with **POM-m3,3-ZnOEP** obtained after 25 iterative scans between 0 and 1.90 V versus SCE.

poly-POM-l4,4-ZnOEP

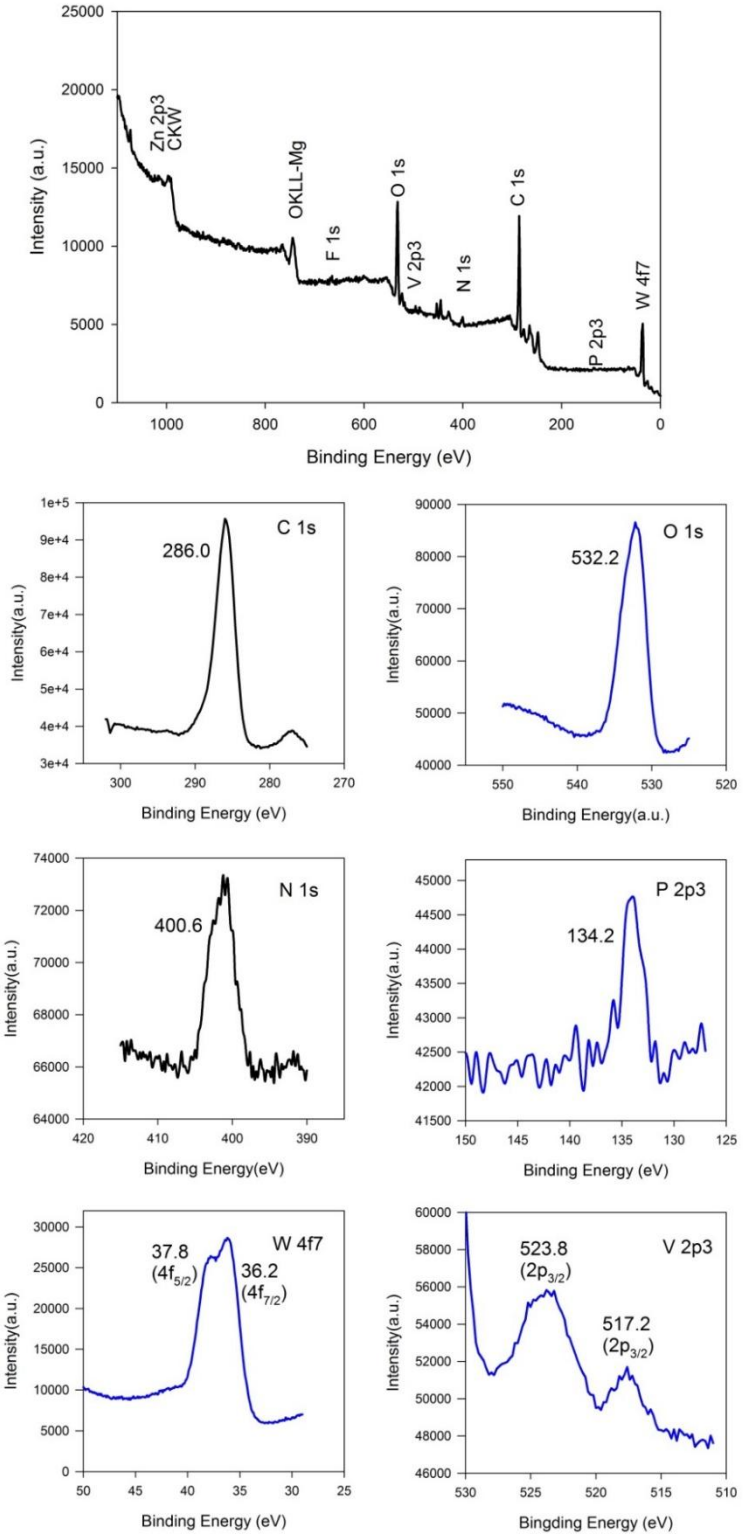

Fig. S4.9 XPS spectra of the modified ITO electrodes with **POM-l4,4-ZnOEP** obtained after 25 iterative scans between 0 and 1.90 V versus SCE.

Copolymer morphology - AFM

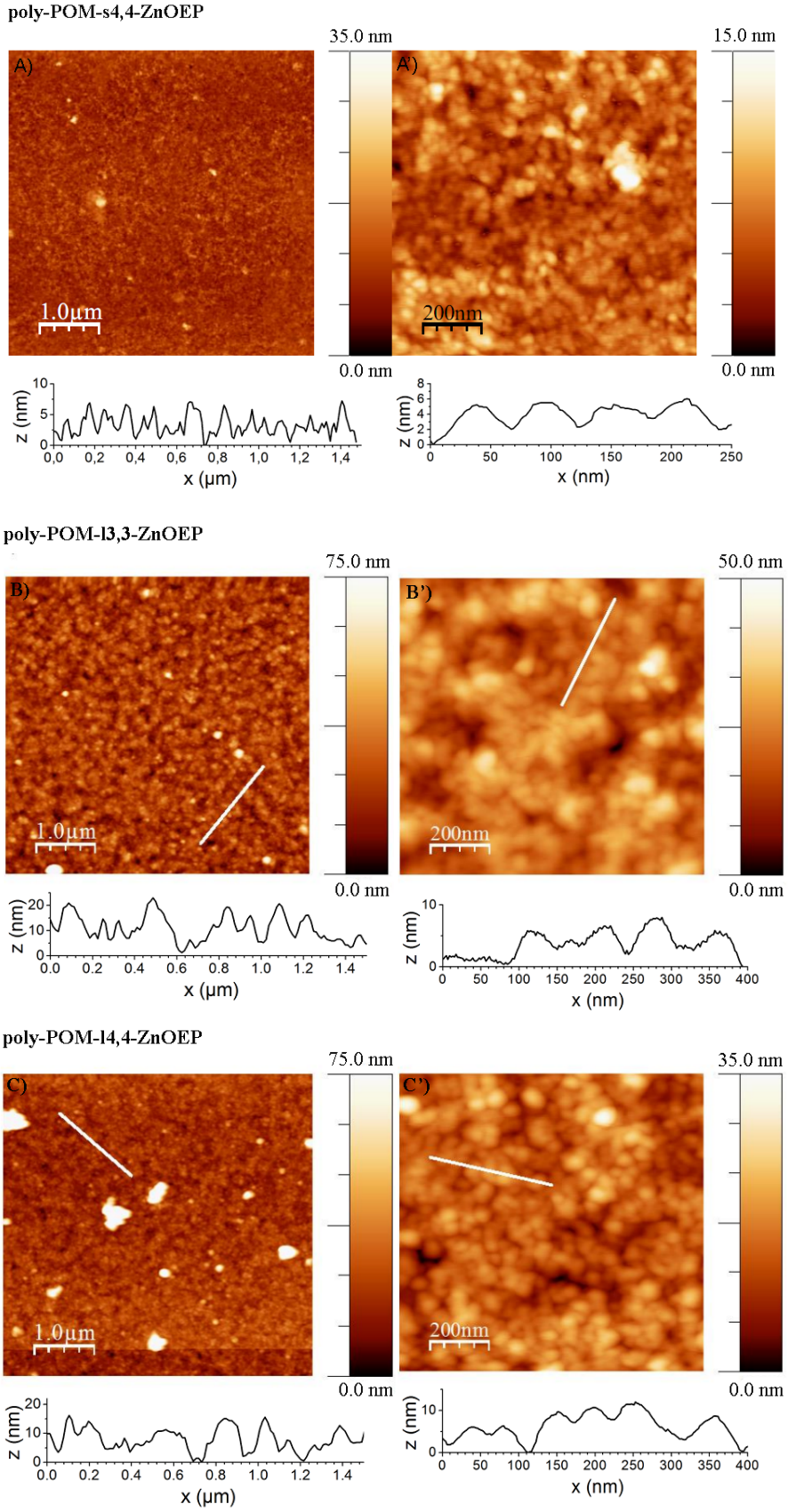

Fig. S4.10 Tapping mode AFM topography of A) **poly-POM-s4,4-ZnOEP**, B) **poly-POM-l3,3-ZnOEP**, C) **poly-POM-l4,4-ZnOEP**.

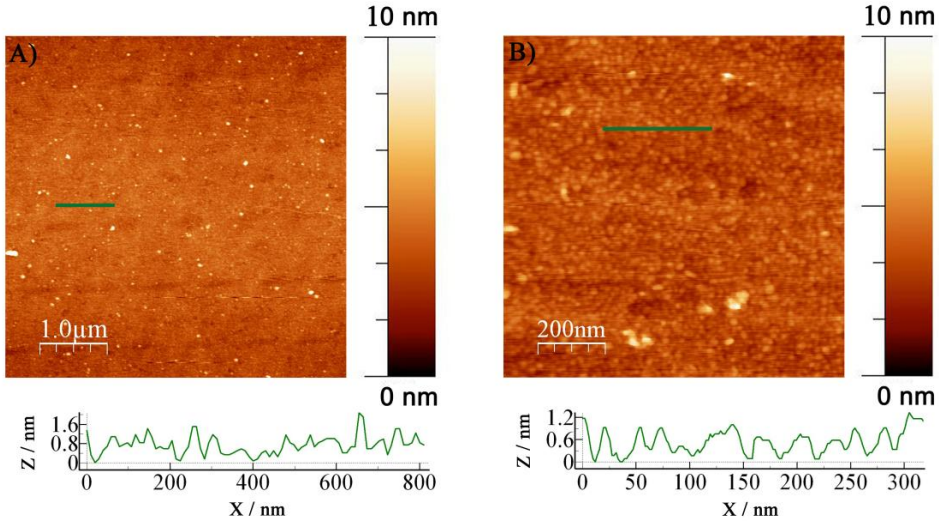

Fig. S4.11 Tapping mode AFM topography of A) and B) **nude ITO** and section analysis of the aggregate marked by blue lines for A) and B).

Permeability

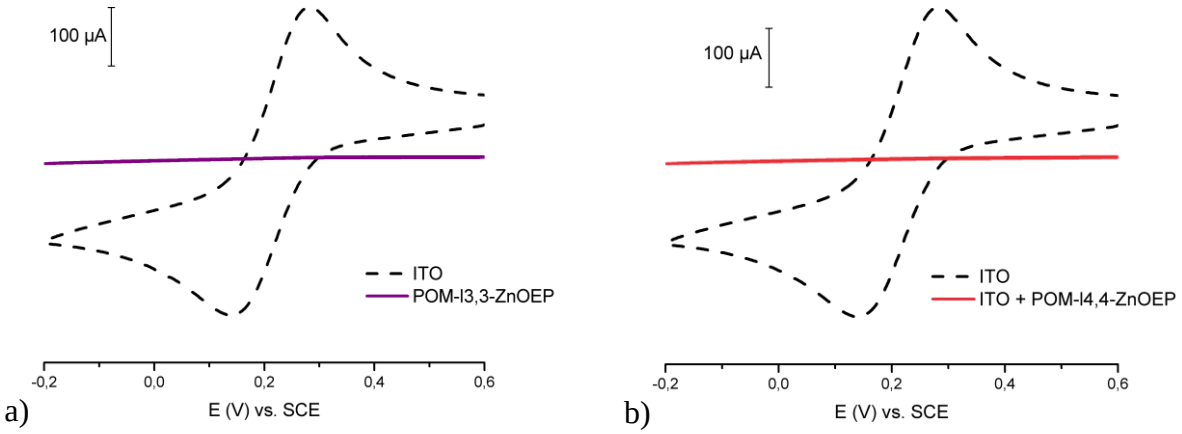

Fig. S4.12 Cyclic voltammogramms of 1 mmol L^{-1} of $K_3Fe(CN)_6$, in 0.5 M Na_2SO_4 at modified ITO electrode with a) **poly-POM-l3,3-ZnOEP**, b) **poly-POM-l4,4-ZnOEP** films (full line) and at noncoated ITO electrode (dotted black line). v =100 mV s^{-1}. Similar behaviours have been obtained for **poly-POM-s4,4-ZnOEP** and **poly-POM-m3,3-ZnOEP** films.

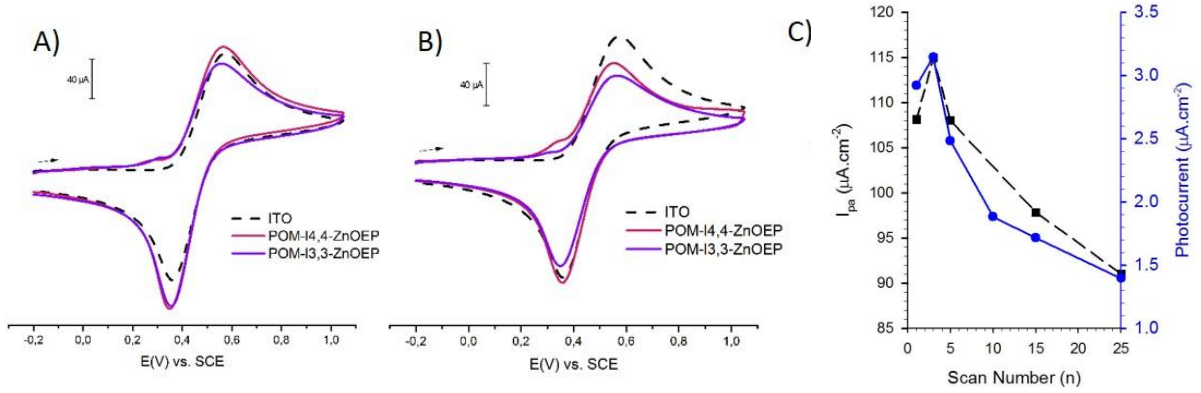

Fig. S4.13 Cyclic voltammogramms of 0.3 mM ferrocene, in $CH_3CN/1,2\text{-}C_2H_4Cl_2$ (3/7) with $TBAPF_6$ (0.1 mol L^{-1}) at modified ITO electrode with **poly-POM-l3,3-ZnOEP**, **poly-POM-l4,4-ZnOEP** films deposited after A) 3 and B) 25 scans between -0.05 and +1.90 V (full line) and at noncoated ITO electrode (dotted black line). v=100 mV s^{-1}. C) (●) plots of the photocurrent measured in aqueous solution containing I_3^- 0.1 mol L^{-1} and I^- 0.5 mol L^{-1} versus the numbers of iterative scans. (▪) plot of the anodic peak current in $CH_3CN/1,2\text{-}C_2H_4Cl_2$ (3/7) with $TBAPF_6$ (0.1 mol L^{-1}) and 0.3 mmol L^{-1} ferrocene *vs*. the numbers of iterative scans.

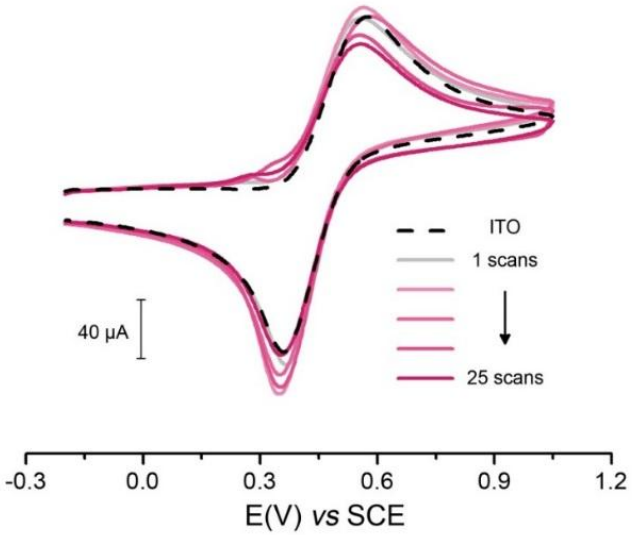

Fig. S4.14 Cyclic voltammogramms of 0.3 mmol L^{-1} ferrocene in $CH_3CN/1,2\text{-}C_2H_4Cl_2$ (3/7) with $TBAPF_6$ (0.1 mol L^{-1}) at modified ITO electrode with **poly-POM-I4,4-ZnOEP** films deposited after 1 to 25 scans between -0.05 and +1.90 V *vs.* SCE (full line) and at noncoated ITO electrode (dotted black line). v=100 mV s^{-1}.

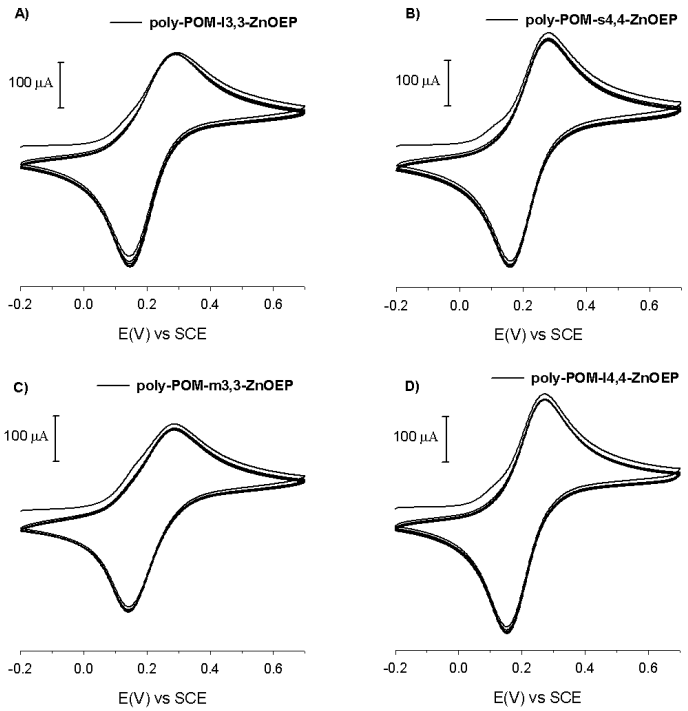

Fig. **S4.15** Cyclic voltammogramms (first 5 scans) of 1 mM 1,1-ferrocenedimethanol in aqueous solution with Na_2SO_4 (0.5 mol L^{-1}) at modified ITO electrode with A) **poly-POM-s4,4-ZnOEP**, B) **poly-POM-m3,3–ZnOEP**, C) **poly-POM-l3,3-ZnOEP** and D) **poly-POM-l4,4-ZnOEP**, D) films deposited after 25 scans between -0.05 and +1.90 V *vs*. SCE. v=100 mV s^{-1}.

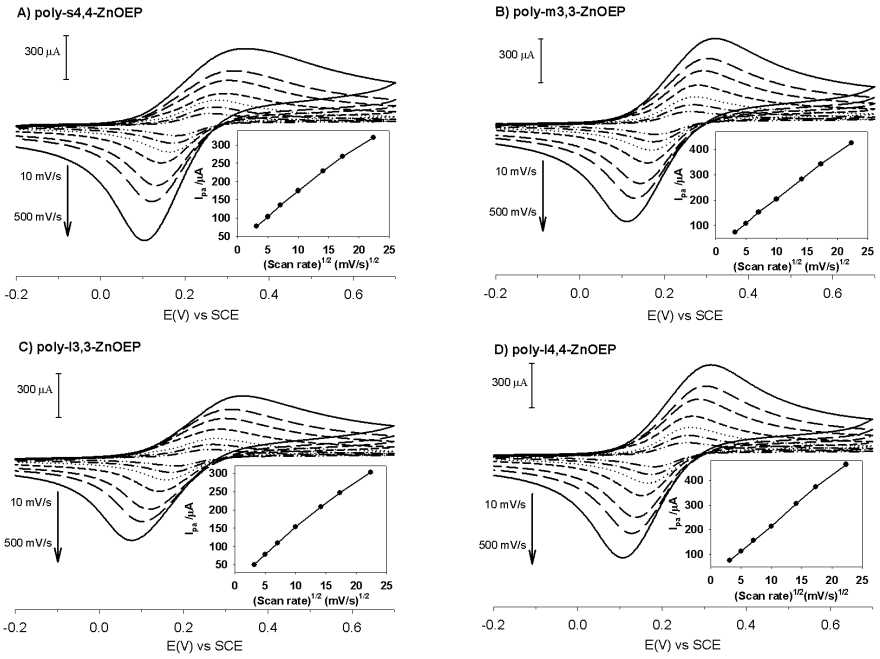

Fig. S4.16 Cyclic voltammogramms of 1 mmol L^{-1} 1,1-ferrocenedimethanol in aqueous solution with Na_2SO_4 (0.5 mol L^{-1}) at modified ITO electrode with A) **poly-POM-s4,4-ZnOEP**, B) **poly-POM-m3,3–ZnOEP**, C) **poly-POM-l3,3-ZnOEP**, and D) **poly-POM-l4,4-ZnOEP** films at various scan rates (10, 25, 50, 100, 200, 300, and 500 mV s^{-1}). Inset: relationship between the anodic peak current and the (scan rate)$^{1/2}$.

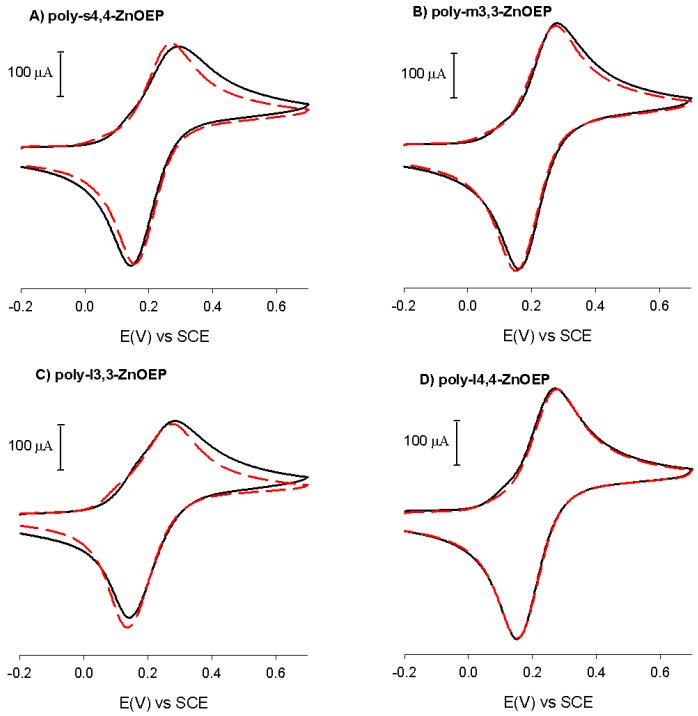

Fig. S4.17 Cyclic voltammogramms of 1 mmol L^{-1} 1,1-ferrocenedimethanol in aqueous solution with 0.5 mol L^{-1} Na_2SO_4 (black full line) and 0.5 mol L^{-1} Li_2SO_4 (red dotted line) at modified ITO electrode with A) **poly-POM-s4,4-ZnOEP**, B) **poly-POM-m3,3–ZnOEP**, C) **poly-POM-l3,3-ZnOEP**, and D) **poly-POM-l4,4-ZnOEP** films deposited after 25 scans between -0.05 and +1.90 V *vs*. SCE. v=100 mV s^{-1}.

Chapter V: Poly-ZnOEP-Preyssler type-POM composite films based on electrostatic interaction for photocurrent generation

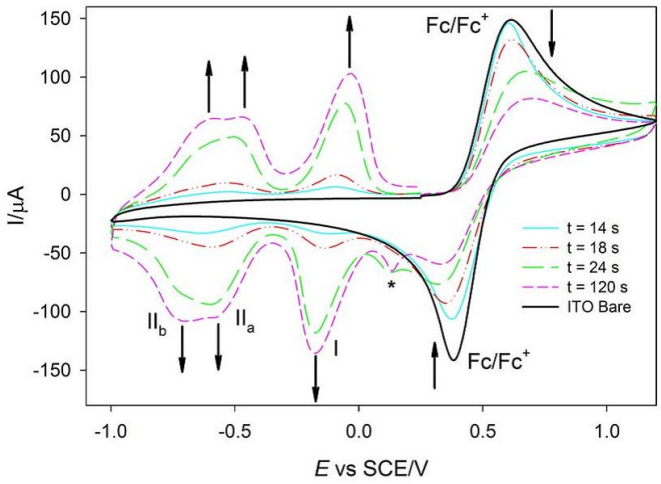

Fig. S5.1 CVs of **poly-ZnOEP2** obtained at +1.9 V *vs.* SCE at different time of deposition (t = 14, 18, 24 and 120 seconds) in 1,2-$C_2H_4Cl_2$/CH_3CN (4/1), 0.25 mmol L^{-1} Fc and 0.1 mol L^{-1} $TBAPF_6$. WE: ITO. S = 1 cm^2. *v* = 0.1 V s^{-1}. Peaks I, II_a and II_b: first and second reduction of the viologen spacers in the polymer. The dotted line corresponds to the cyclic voltammogram of bare ITO in 1,2-$C_2H_4Cl_2$/CH_3CN (4/1), 0.25 mmol L^{-1} Fc and 0.1 mol L^{-1} $TBAPF_6$. (*) This peak is attributed to the reduction of an isoporphyrin intermediate and observed only for the first scan.

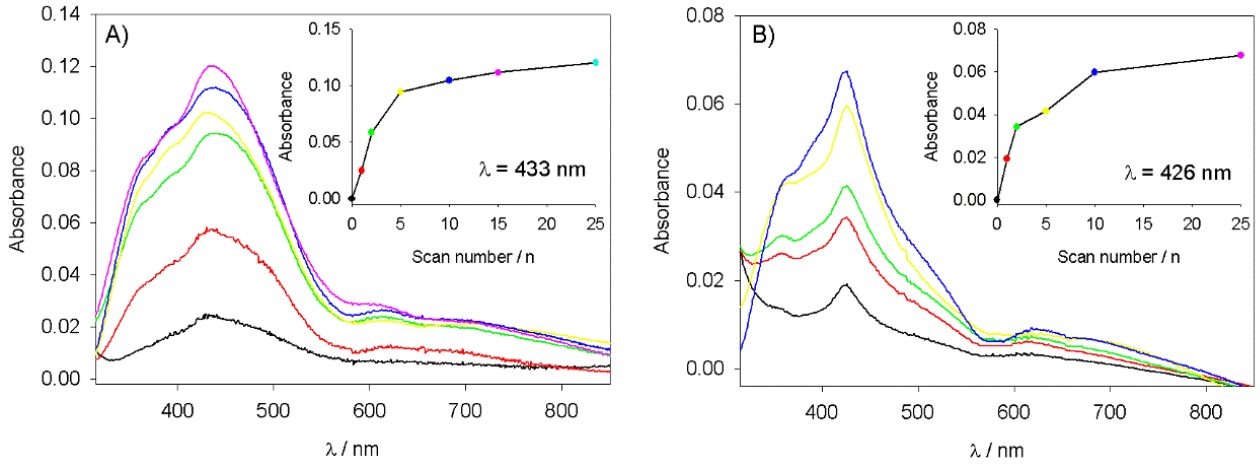

Fig. S5.2 UV–Vis absorption spectra of A) **poly-ZnOEP1** and B) **poly-ZnOEP2** obtained after n iterative scans.

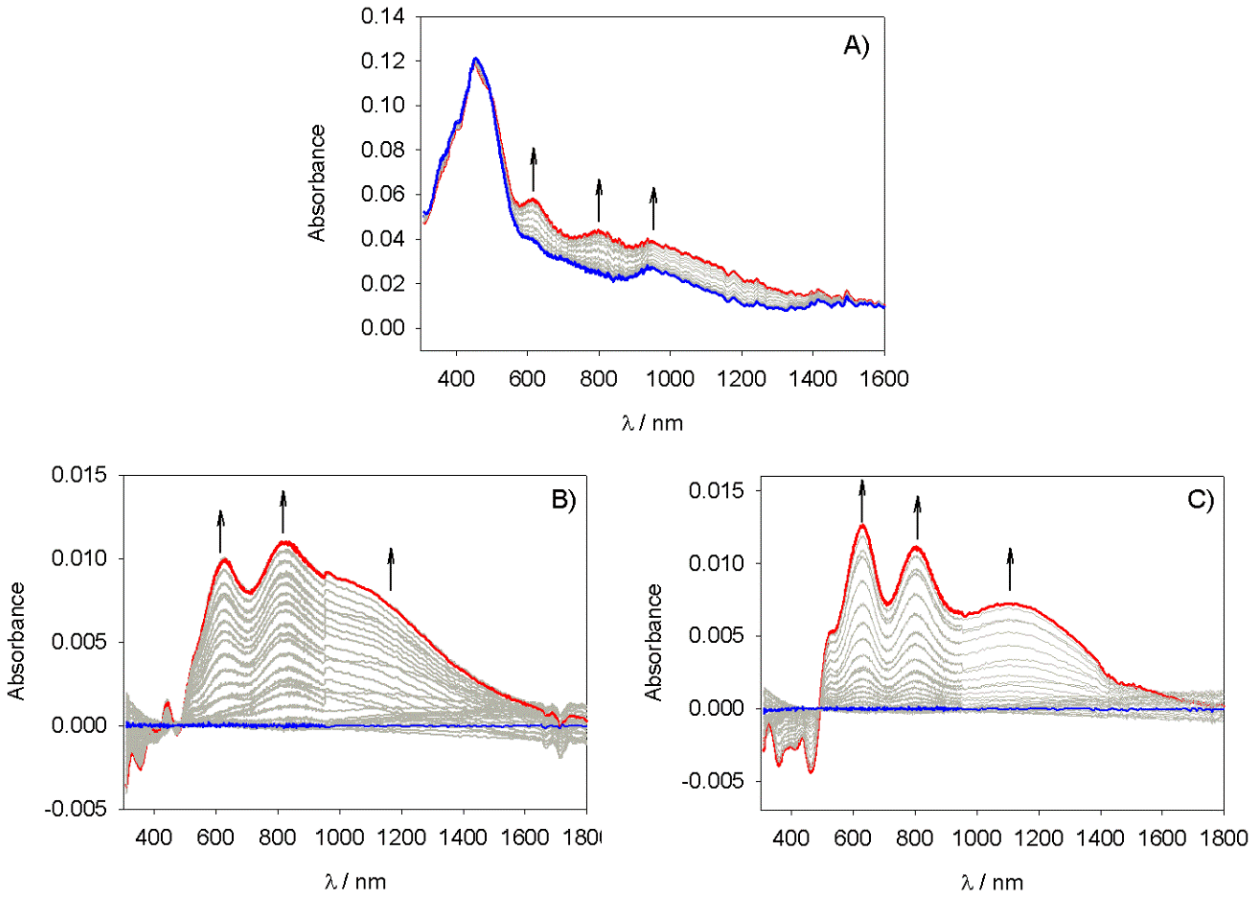

Fig. S5.3 UV-visible-NIR spectra recorded after exhaustive one-electron reduction per viologen in **poly-ZnOEP1** in A) and B) 1,2-$C_2H_4Cl_2$/CH_3CN (4/1) and 0.2 mol L^{-1} $TBAPF_6$ and C) H_2O and 0.2 mol L^{-1} $TEAPF_6$ WE: ITO. S = 1 cm^2. A) Absorbance measurements after (baseline obtained with nude ITO). B) and C) Δ(Absorbance) measured directly (blank obtained from the **poly-ZnOEP1** films on ITO).

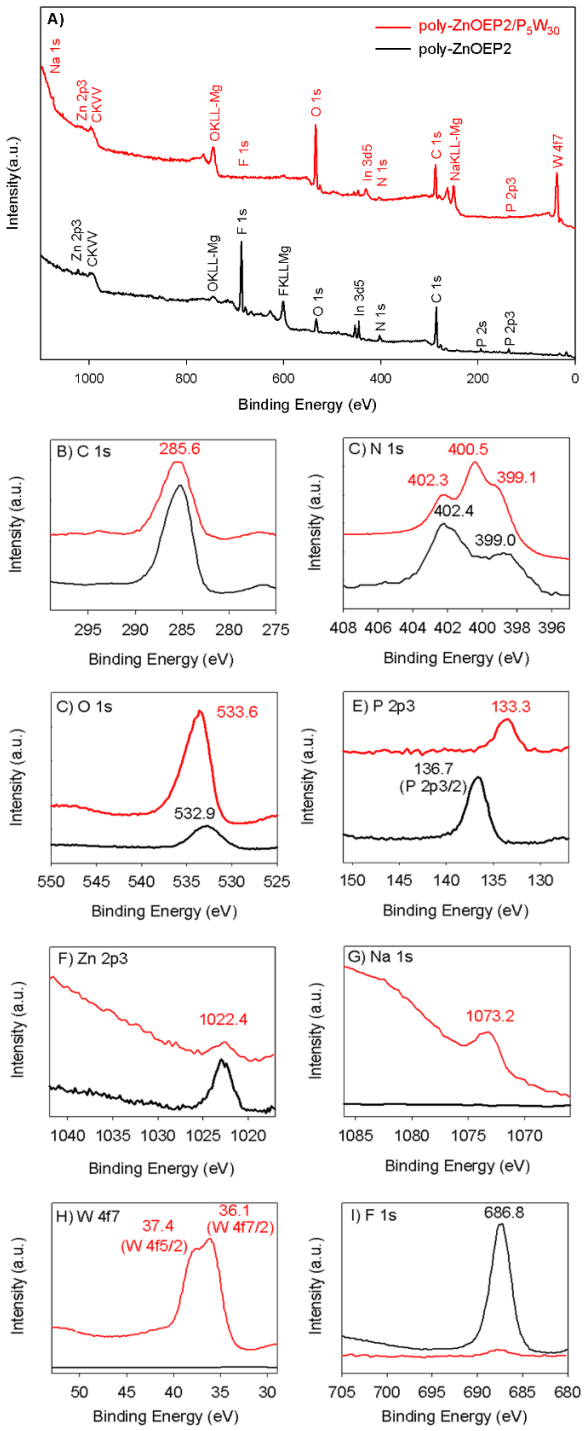

Fig. S5.4 XPS of **poly-ZnOEP2** films on ITO with and without P_5W_{30}. Global XPS spectra (A), C 1s (B), N 1s (C), O 1s (D), P 2p3 (E), Zn 2p3 (F), Na 1s (G), W 4f7 (H), F 1s (I).

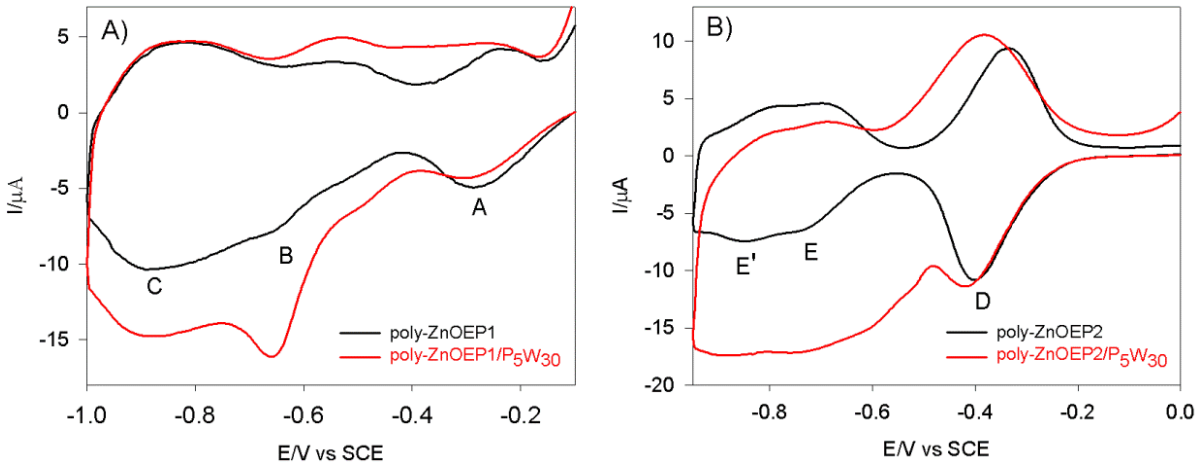

Fig. S5.5 CVs of **poly-ZnOEP1/P_5W_{30}** (A) and **poly-ZnOEP2/P_5W_{30}** (B) (with 60 min soaking time in P_5W_{30} aqueous solution) modified ITO electrodes in acetonitrile containing 0.5 mmol L^{-1} NaI. The dark curves correspond to the **poly-ZnOEP** polymers with PF_6^- as counter anions, the red curves correspond to **poly-ZnOEP/P_5W_{30}**. S = 1 cm^2. ν = 20 mV s^{-1}.

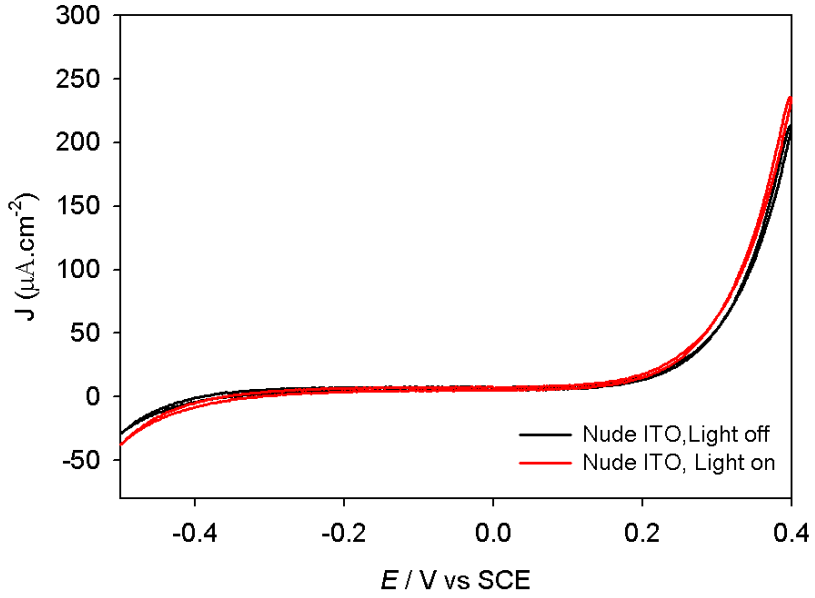

Fig. S5.6 CVs of nude ITO electrode in acetonitrile containing I_2 5 mmol L^{-1} and NaI 0.5 mol L^{-1}.

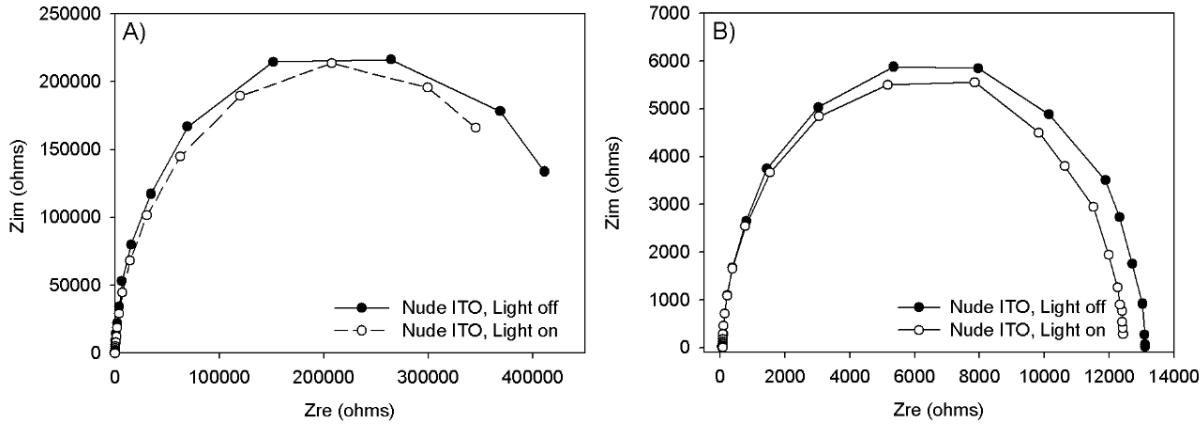

Fig. S5.7 Electrochemical impedance spectroscopy (EIS) for nude ITO electrode in acetonitrile containing I_2 5 mmol L^{-1} and NaI 0.5 mol L^{-1} under A) 0.0 V and B) 0.2 V BIAS potentials. The frequency range explored was 0.01 Hz to 10^5 Hz, with the ac amplitude perturbed at 10 mV. Inset: nude ITO.

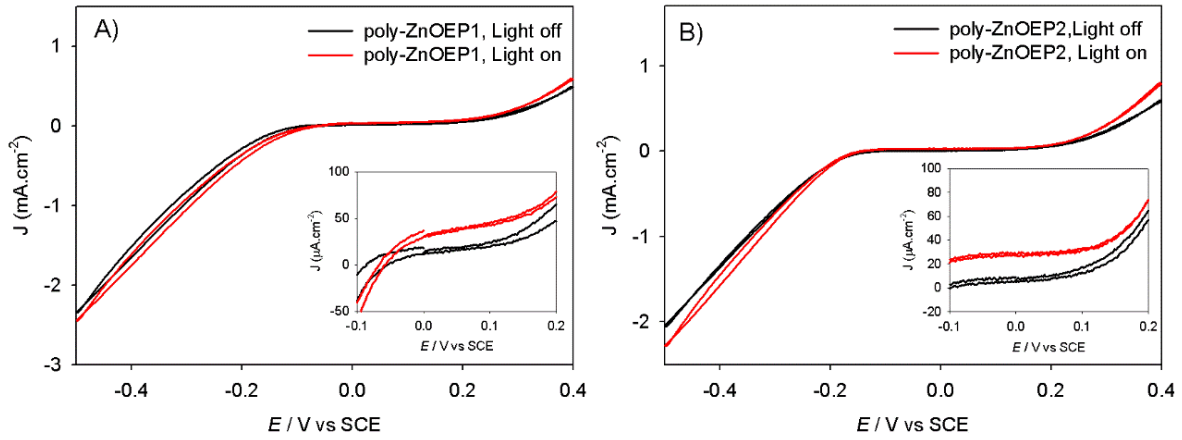

Fig. S5.8 CVs of A) **poly-ZnOEP1**, B) **poly-ZnOEP2** electrodes in acetonitrile containing I_2 5 mmol L^{-1} and NaI 0.5 mol L^{-1}. Inset: zoom of the cyclic voltammograms between -0.1 V and 0.2 V.

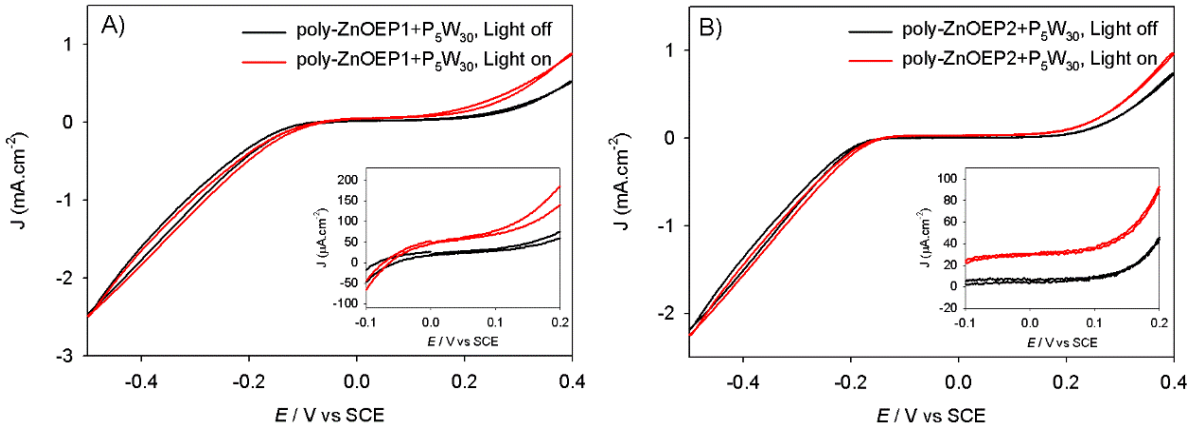

Fig. S5.9 CVs of A) **poly-ZnOEP1/P_5W_{30}**, B) **poly-ZnOEP2/P_5W_{30}** electrodes in acetonitrile containing I_2 5 mmol L^{-1} and NaI 0.5 mol L^{-1}. Inset: zoom of the cyclic voltammograms between -0.1V and 0.2 V.

Chapter VI: Poly-cis-$H_2Ph_2Py_2P$-ZnOEP/Preyssler POM @MNPs complex based on electrostatic interaction for photocurrent generation

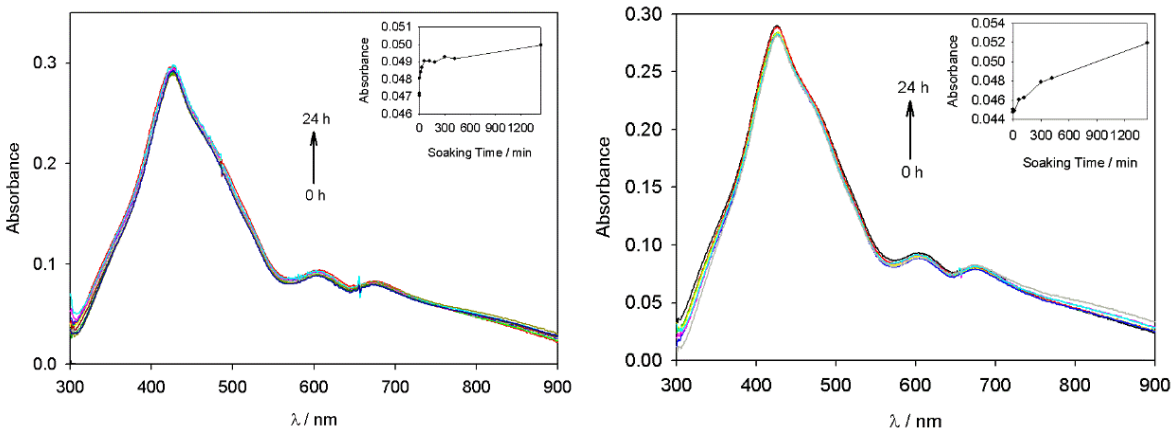

Fig. S6.1 Evolution of UV-vis spectra of the modified ITO electrode with poly-*cis*-$H_2Ph_2Py_2P$-ZnOEP after soaking in $[NaP_5W_{30}O_{110}]^{14-}$@Au (left) or $[NaP_5W_{30}O_{110}]^{14-}$@Pt aqueous solution. Inset: absorbance intensity at λ= 800 nm *vs.* time.

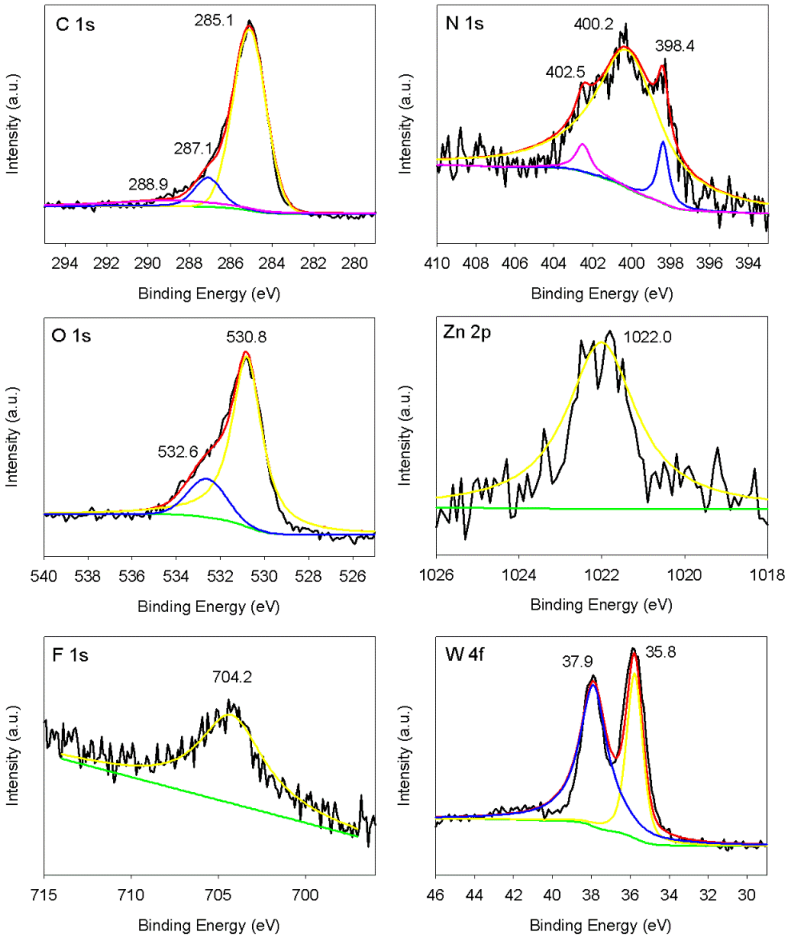

Fig. S6.2 XPS of **poly-*cis*-$H_2Py_2Ph_2P$-ZnOEP-P_5W_{30}@Au** films on ITO.

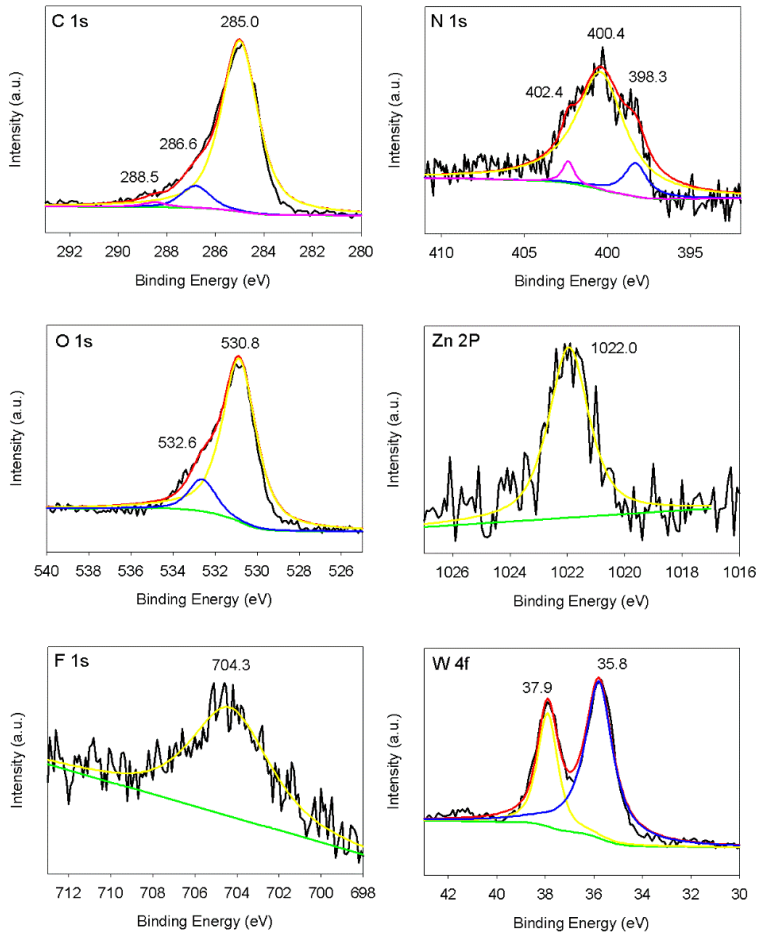

Fig. S6.3 XPS of **poly-*cis*-$H_2Py_2Ph_2P$-ZnOEP-P_5W_{30}@Pt** films on ITO.

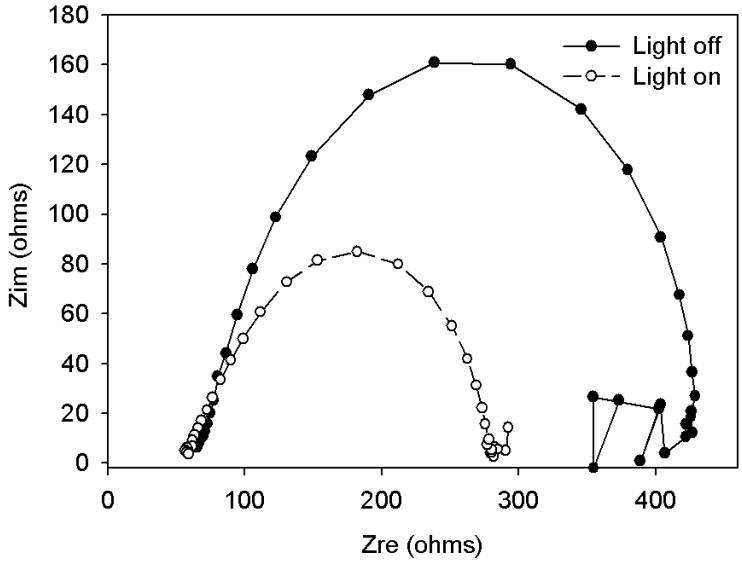

Fig. S6.4 Electrochemical impedance spectroscopy (EIS) for **poly- *cis*-$H_2Py_2Ph_2P$-ZnOEP/P_5W_{30}@Ag** (soaking time 30 min) with and without illumination from a 300 W Xe arc lamp (with $\lambda > 385$ nm long pass filter) in H_2O containing I_2 5 mmol L^{-1} and NaI 0.5 mol L^{-1}. The frequency range explored was 0.1 Hz to 10^5 Hz, with the ac amplitude perturbed at 10 mV. DC potential -0.1 V.

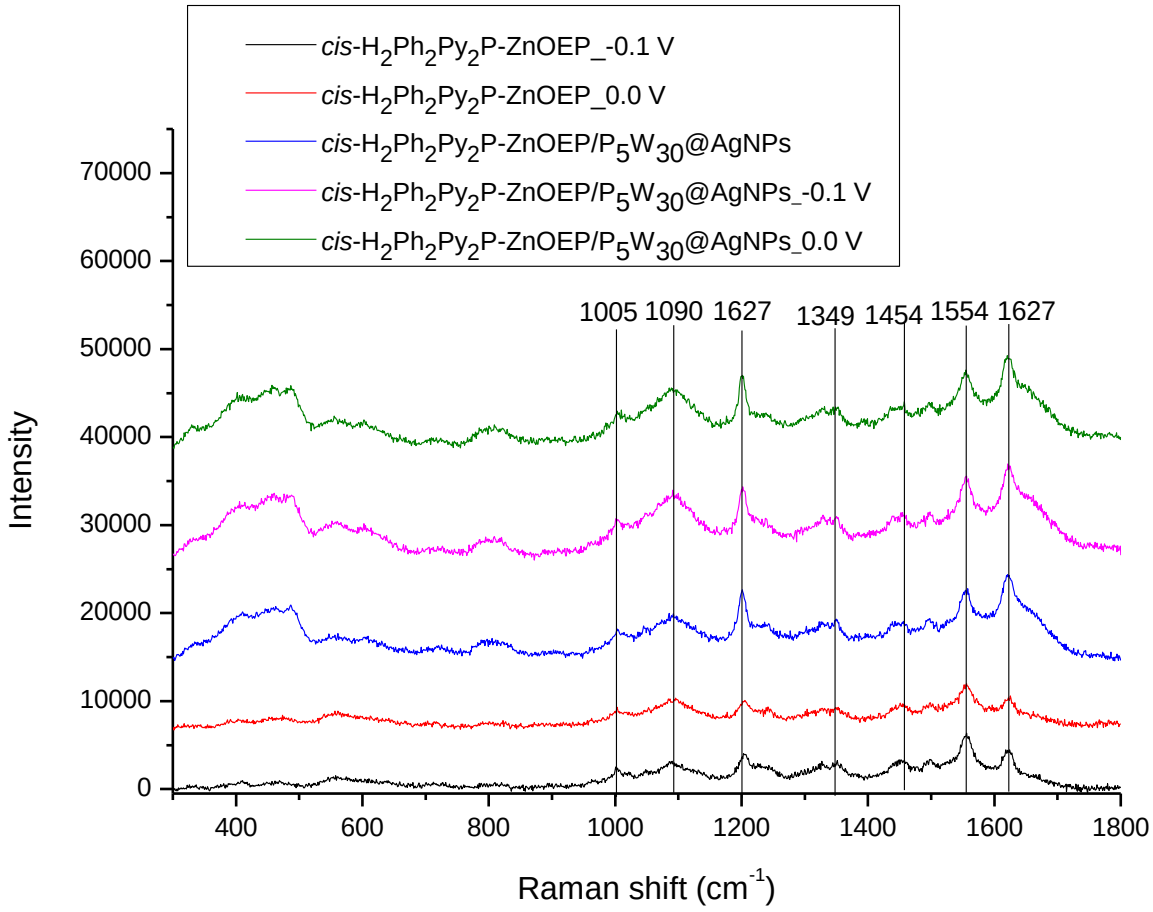

Fig. S6.5 Raman spectra of **poly-*cis*-$H_2Py_2Ph_2P$-ZnOEP/P_5W_{30}@MNPs** (0.5 h) excited at 514nm, in H_2O containing I_3^- 5 mmol L^{-1} and I^- 0.5 mol L^{-1} under polarization.

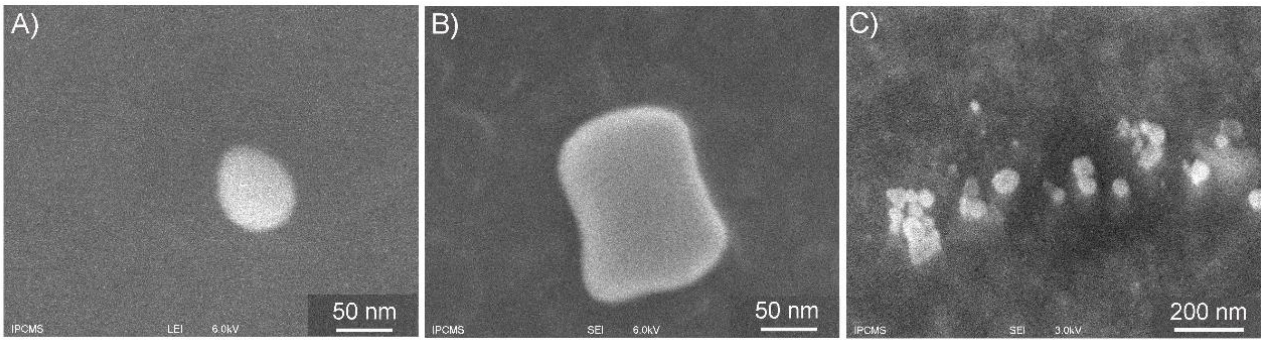

Fig. S6.6 SEM of **poly-*cis*-$H_2Py_2Ph_2P$-ZnOEP-P_5W_{30}@Au** on ITO.

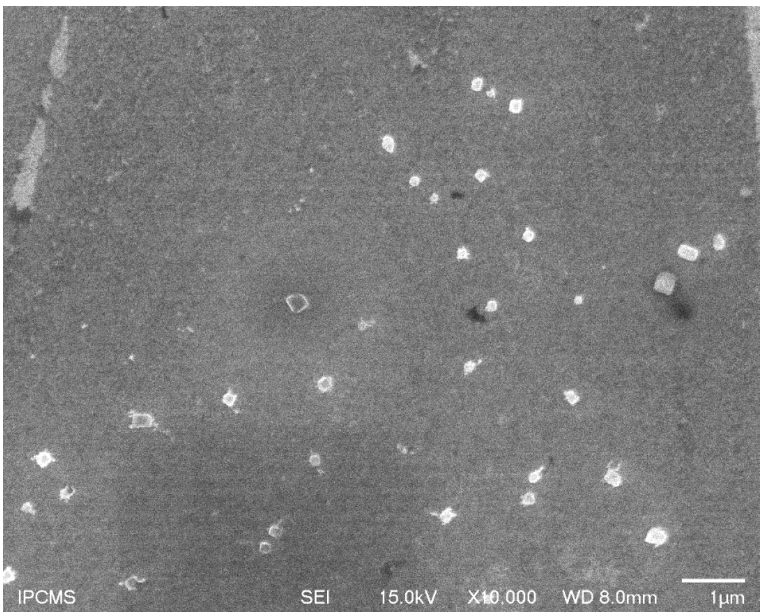

Fig. S6.7 SEM of **poly-*cis*-$H_2Py_2Ph_2P$-ZnOEP-P_5W_{30}@Pt** on ITO.

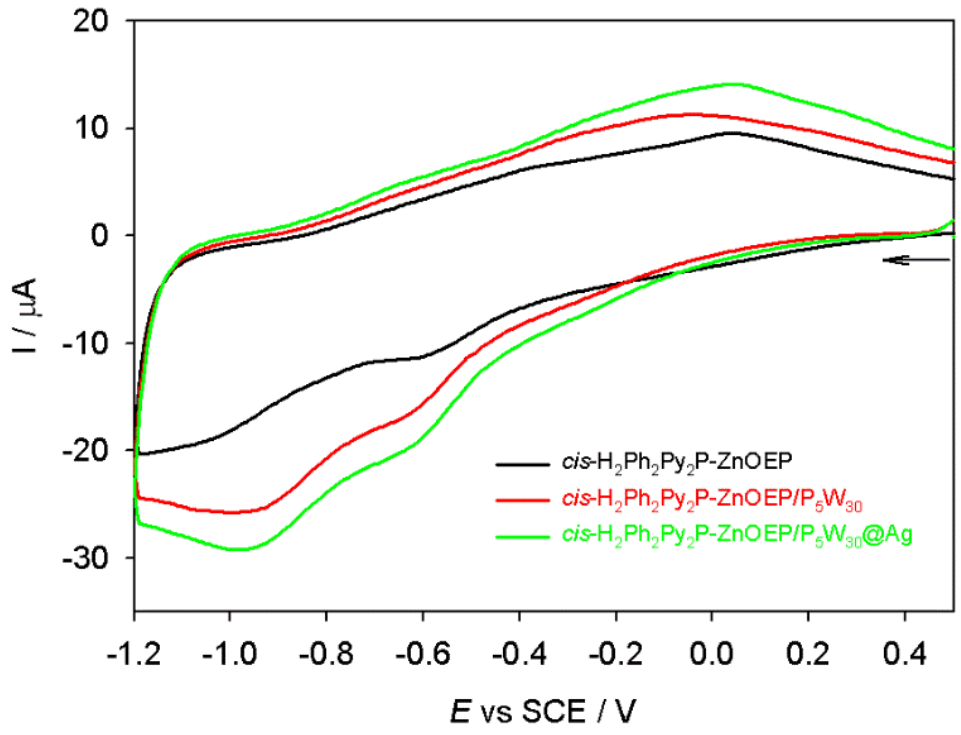

Fig. S6.8 CVs of **poly-*cis*-$H_2Py_2Ph_2P$-ZnOEP** (black curve), **poly-*cis*-$H_2Py_2Ph_2P$-ZnOEP/P_5W_{30}** (red curve), and **poly-*cis*-$H_2Py_2Ph_2P$-ZnOEP/P_5W_{30}@Ag** (green curve) (with 30 min soacking time in P_5W_{30}@AgNPs aquesous solution) modified ITO electrodes in H_2O containing 0.5 mmol L^{-1} NaI. S = 1 cm^2. v = 20 mV s^{-1}.

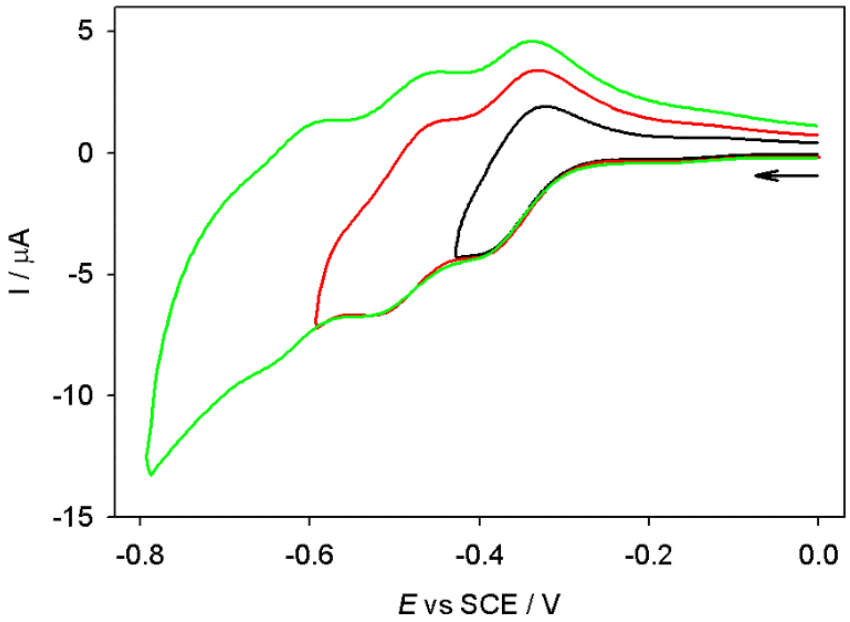

Fig. S6.9 CVs of **$Na_{14}[NaP_5W_{30}O_{110}]$** in H_2O containing 0.5 mmol L^{-1} NaI. Working electrode: GC. d =3 mm; scan rate: 0.02 V s^{-1}.

HUO Zhaohui

Polyoxométallate – porphyrine: application pour la génération de photocourrant et la photocatalyse

Resume

Polyoxometalates-porphyrin hybrid films were synthesized based on covalent or electrostatic interactions. Copolymeric polyoxometalate–porphyrin films were obtained by the electro-oxidation of zinc octaethylporphyrin (ZnOEP) or 5,15-ditolyl porphyrin (H_2T_2P) in the presence of a different type of polyoxometalates (POMs) bearing two pyridyl groups (py-POM-py). Three type of py-POM-py have been used: *i*) a tris-alkoxo functionalized Lindqvist polyoxovanadate, *ii*) an organosilyl functionalized Keggin-type $[PW_{11}Si_2O_{40}C_{26}H_{16}N_2]^{3-}$ and Dawson-type $[P_2W_{17}Si_2O_{62}C_{26}H_{16}N_2]^{6-}$, and *iii*) a bis-pyridine-substituted organo-polyoxometallic bricks using $[P_2W_{15}V_3O_{62}]^{9-}$ diolamide-grafting method with various geometries of the pendant group. All are applied for photocurrent generation and photocatalytical recovery of metals (Ag and Pt). Electrostatic POM-porphyrin films were also prepared by incorporated Preyssler type polyanion $[NaP_5W_{30}O_{110}]^{14-}$ onto the electropolymerized polycationic porphyrin (poly-ZnOEP) with viologen or bis-viologen as spacers. $[NaP_5W_{30}O_{110}]^{14-}$ as an efficient electron shuttle between the excited ZnOEP and viologen (or bis-viologen) which effectively retarded the fast charge pair recombination and enhanced the photocurrent magnitude. Later, we introduced nanoparticles POM@MNPs to a bis-porphyrin copolymer through metathesis reaction to further improve the efficiency of the photocurrent generation in which the localized surface plasmon resonance that occurs at the surface of silver nanoparticles has substantially enhanced the electronic excitation of surface-anchored porphyrin.

Keywords: polyoxometalate, porphyrin, hybrid materials, photocurrent, photocatalysis

Résumé

Des films du type polyoxométallates-porphyrines ont été synthetisés et sont basés sur des interactions du types covalentes ou électrostatiques. Les films polyoxométallates–porphyrines sont obtenus par électro-oxydation de l'octaéthylporphyrine de zinc (ZnOEP) ou la 5,15-ditolylporphyrine (H_2T_2P) en présence de différents types of polyoxométallates (POMs) portant deux groupes pyridyles pendants (py-POM-py) Trois type de systèmes py-POM-py ont été utilises : *i*) un Lindqvist polyoxovanadate fonctionalisé via deux groupes tris-alkoxo , *ii*) un derive organosilyl fonctionalisé du type Keggin ou Dawson ($[PW_{11}Si_2O_{40}C_{26}H_{16}N_2]^{3-}$ et $[P_2W_{17}Si_2O_{62}C_{26}H_{16}N_2]^{6-}$), et iii) des briques du type Dawson $[P_2W_{15}V_3O_{62}]^{9-}$ fonctionalisée avec des groupements organiques bis-pyridine de géométrie variée via un greffage diolamide). Tous ces films ont été testé pour la génération de photocourant et la photocatalyse de la réduction de métaux (Ag et Pt). Des films électrostatiques POM-porphyrin ont été également préparés par incorporation de polyanion du type Preyssler $[NaP_5W_{30}O_{110}]^{14-}$ sur les films de porphyrine polycationic (poly-ZnOEP) électropolymérisés avec des espaceurs viologènes ou bis-viologènes. $[NaP_5W_{30}O_{110}]^{14-}$ agit comme relais d'électron entre une porphyrine excitée ZnOEP* et le viologène (ou le bis-viologène) retardant la recombinaison de charge ce qui permet une augmentation du photocourant. Enfin, des nanoparticules POM@NPs (Pt, Au, Ag) ont été introduitent en surface de copolymère polycationique à base de bis-porphyrine par métathèse afin d'augmenter l'efficacité de la génération de photocourant. La résonance de plasmon de surface localisée qui se produit à la surface des nanoparticules d'argent a sensiblement amélioré l'excitation électronique de porphyrine.

Mots clés : polyoxométallate, porphyrine, matériaux hybrides, photocourrant, photocatalyse